Conditional Moment Closure Methods for Turbulent Combustion Modelling

by

Ahmad El Sayed

A thesis
presented to the University of Waterloo
in fulfillment of the
thesis requirement for the degree of
Doctor of Philosophy
in
Mechanical Engineering

Waterloo, Ontario, Canada, 2013

I hereby declare that I am the sole author of this thesis. This is a true copy of the thesis, including any required final revisions, as accepted by my examiners.

I understand that my thesis may be made electronically available to the public.

Abstract

This thesis describes the application of the first-order Conditional Moment Closure (CMC) to the autoignition of high-pressure fuel jets, and to piloted and lifted turbulent jet flames using classical and advanced CMC submodels. A Doubly-Conditional Moment Closure (DCMC) formulation is further proposed.

In the first study, CMC is applied to investigate the impact of C_2H_6, H_2 and N_2 additives on the autoignition of high-pressure CH_4 jets injected into lower pressure heated air. A wide range of pre-combustion air temperatures is considered and detailed chemical kinetics are employed. It is demonstrated that the addition of C_2H_6 and H_2 does not change the main CH_4 oxidisation pathways. The decomposition of these additives provides additional ignition-promoting radicals, and therefore leads to shorter ignition delays. N_2 additives do not alter the CH_4 oxidisation pathways, however, they reduce the amount of CH_4 available for reaction, causing delayed ignition. It is further shown that ignition always occurs in lean mixtures and at low scalar dissipation rates.

The second study is concerned with the modelling of a piloted CH_4/air turbulent jet flame. A detailed assessment of several Probability Density Function (PDF), Conditional Scalar Dissipation Rate (CSDR) and Conditional Velocity (CV) submodels is first performed. The results of two β-PDF-based implementations are then presented. The two realisations differ by the modelling of the CSDR. Homogeneous (inconsistent) and inhomogeneous (consistent) closures are considered. It is shown that the levels of all reactive scalars, including minor intermediates and radicals, are better predicted when the effects of inhomogeneity are included in the modelling of the CSDR.

The two following studies are focused on the consistent modelling of a lifted H_2/N_2 turbulent jet flame issuing into a vitiated coflow. Two approaches are followed to model the PDF. In the first, a presumed β-distribution is assumed, whereas in the second, the Presumed Mapping Function (PMF) approach is employed. Fully consistent CV and CSDR closures based on the β-PDF and the PMF-PDF are employed. The homogeneous versions of the CSDR closures are also considered in order to assess the effect of the spurious sources which stem from the inconsistent modelling of mixing. The flame response is analysed over a narrow range of coflow temperatures (T_c). The stabilisation mechanism is determined from the analysis of the transport budgets in mixture fraction and physical spaces, and the history of radical build-up ahead of the stabilisation height. The β-PDF realisations indicate that the flame is stabilised by autoignition irrespective of the value of T_c. On the other hand, the PMF realisations reveal that the stabilisation mechanism is susceptible to T_c. Autoignition remains the controlling stabilisation mechanism for sufficiently high

T_c. However, as T_c is decreased, stabilisation is achieved by means of premixed flame propagation. The analysis of the spurious sources reveals that their effect is small but non-negligible, most notably within the flame zone. Further, the assessment of several H_2 oxidation mechanisms show that the flame is very sensitive to chemical kinetics.

In the last study, a DCMC method is proposed for the treatment of fluctuations in non-premixed and partially premixed turbulent combustion. The classical CMC theory is extended by introducing a normalised Progress Variable (PV) as a second conditioning variable beside the mixture fraction. The unburnt and burnt states involved in the normalisation of the PV are specified such that they are mixture fraction-dependent. A transport equation for the normalised PV is first obtained. The doubly-conditional species, enthalpy and temperature transport equations are then derived using the decomposition approach and the primary closure hypothesis is applied. Submodels for the doubly-conditioned unclosed terms which arise from the derivation of DCMC are proposed. As a preliminary analysis, the governing equations are simplified for homogeneous turbulence and a parametric assessment is performed by varying the strain rate levels in mixture fraction and PV spaces.

Acknowledgements

I am indebted to my supervisor, Prof. Roydon Fraser, for his kindness, guidance, and support.

I would like to thank my examining committee members, Profs. Eric Croiset, Kyle Daun, Fue-Sang Lien, and Mikael Mortensen, for reviewing this thesis and for providing valuable comments.

I would also like to extend my thanks to Prof. Andreas Dreizler for providing the velocity measurements of the piloted Sandia flames series and to Profs. Matthew Cleary, Pascale Domingo, Michael Fairweather, and Dr. Amir Baserinia for very useful discussions.

My research was funded by different sources: the University of Waterloo, AUTO21, the Ontario Graduate Scholarship program, and the Natural Sciences and Engineering Research Council of Canada. I am deeply grateful for their financial support.

Many friends made my stay in Waterloo enjoyable. In particular, I would like to thank Nada Zamel, Lori Janbazian, Azad "Palang" Qazi Zade, Sahba Ghiasi, Da Huang and Jean-Claude Cizravi.

Finally, I would like express my profound gratitude to my mother and sisters for their love and support. This thesis is dedicated to them.

Dedication

إلى من أضفت إلى التفاني أوصافاً
إلى أمي

To my mother

Cet extrait du *Petit Prince* vous a toujours fasciné...

"*Ma vie est monotone. Je chasse les poules, les hommes me chassent. Toutes les poules se ressemblent, et tous les hommes se ressemblent. Je m'ennuie donc un peu. Mais, si tu m'apprivoises, ma vie sera comme ensoleillée. Je connaîtrai un bruit de pas qui sera différent de tous les autres. Les autres pas me font rentrer sous terre. Le tien m'appellera hors du terrier, comme une musique. Et puis regarde! Tu vois, là-bas, les champs de blé? Je ne mange pas de pain. Le blé pour moi est inutile. Les champs de blé ne me rappellent rien. Et ça, c'est triste! Mais tu as des cheveux couleur d'or. Alors ce sera merveilleux quand tu m'auras apprivoisé! Le blé, qui est doré, me fera souvenir de toi. Et j'aimerai le bruit du vent dans le blé...*"

Antoine de Saint-Exupéry, *Le Petit Prince*

This excerpt from *The Little Prince* has always fascinated you...

"*My life is monotonous. I hunt chickens, men hunt me. All the chickens are just alike, and all the men are just alike. And, in consequence, I am a little bored. But if you tame me, it will be as if the sun came to shine on my life. I shall know the sound of a step that will be different from all the others. Other steps send me hurrying back underneath the ground. Yours will call me, like music, out of my burrow. And then look! You see the grain-fields down yonder? I do not eat bread. Wheat is of no use to me. The wheat fields have nothing to say to me. And that is sad. But you have hair that is the colour of gold. Think how wonderful that will be when you have tamed me! The grain, which is also golden, will bring me back the thought of you. And I shall love to listen to the wind in the wheat...*"

Antoine de Saint-Exupéry, *The Little Prince*

Table of Contents

List of Tables

List of Figures

Nomenclature

Roman

A_i	Pre-exponential factor in reaction i
$a_{p,\kappa}$	Planck mean absorption coefficient of species κ
B	Beta function
b_i	Temperature exponent in reaction i
c	Progress variable
C_p	Heat capacity at constant pressure
c_p	Specific heat capacity at constant pressure
$c_{p,\kappa}$	Specific heat capacity at constant pressure of species κ
D	Molecular diffusivity, thermal diffusivity, diameter
d	Diameter
D_κ	Molecular diffusivity of species κ
D_t	Turbulent diffusivity
$E_{a,i}$	Activation energy in reaction i
G	Gaussian PDF
$G_{\iota\kappa}$	Conditional covariance of scalars ι and κ
H	Enthalpy, Heaviside step function
h	Specific enthalpy
$h^\circ_{f,\kappa}$	Enthalpy of formation of species κ at standard state
h_κ	Enthalpy of species κ
h_s	Specific sensible enthalpy
J_i^ϕ	Molecular diffusive flux of scalar ϕ in the i^{th} direction
k	Turbulence kinetic energy
k_{bi}	Backward rate constant of reaction i
K_{Ci}	Equilibrium constant of reaction i
k_{fi}	Forward rate constant of reaction i
l	Integral length scale

M_κ	Chemical symbol of species κ
N_r	Number of participating species in the radiative source
N_s	Number of species
N_x	Number of axial grid points
N_y	Number of transverse grid points
N_η	Number of grid points in mixture fraction space
p	Pressure
P,P_ξ	Marginal PDF of the mixture fraction
p_a	Atmospheric pressure
P_c	Marginal PDF of the progress variable
p_κ	Partial pressure of species κ
$P_{\xi,c}$	Joint PDF of the mixture fraction and the progress variable
$P_{c\|\xi}$	Conditional PDF of the progress variable with respect to the mixture fraction
q	Rate of progress of a reaction
Q_κ	Conditional or doubly-conditional mass fraction of species κ
Q_h	Conditional or doubly-conditional enthalpy
q_i	Rate of progress of reaction i
Q_T	Conditional or doubly-conditional temperature
R	Radius
r	Radial coordinate, PDF of the reference field ψ
R_u	Universal gas constant
S	Entropy
S_ϕ	Spurious source of scalar ϕ
T	Temperature
t	Time
T_b	Background temperature
t_d	Ignition delay
$T_{a,i}$	Activation temperature in reaction i
u_i	Velocity component in the i^{th} direction
W_κ	Molecular weight of species κ
X	Mapping function
x_i	Cartesian coordinate in the i^{th} direction
Y_κ	Mass fraction of species κ
Z_k^*	Ignition kernel location

Greek

β	Beta distribution
χ, χ_ξ	Scalar dissipation rate of the mixture fraction

$\chi_\circ$	Peak scalar dissipation rate
χ_c	Scalar dissipation rate of the progress variable
$\chi_{\circ,c}$	Critical value of the peak scalar dissipation rate
$\chi_{\xi,c}$	Mixture fraction-progress variable cross-dissipation
δ	Dirac delta function
δ_{ij}	Kronecker delta
$\dot{\omega}_\kappa$	Chemical source of species κ
$\dot{\omega}_r$	Radiative source
$\dot{\omega}_{h_s}$	Chemical source of the sensible enthalpy
$\dot{\omega}_T$	Chemical source of the temperature
η	Sample space variable of the mixture fraction, Kolmogorov length scale
Γ	Gamma function
γ	Specific heat ratio
λ	Thermal conductivity
μ	Dynamic viscosity, mean of the clipped Gaussian PDF
μ_t	Turbulent viscosity
ν	Kinematic viscosity
$\nu''_{\kappa i}$	Stoichiometric coefficient of product κ in reaction i
$\nu'_{\kappa i}$	Stoichiometric coefficient of reactant κ in reaction i
ν_t	Eddy viscosity
ϕ	Generic scalar, sample space variable of the reference field ψ
Π	Evaporation rate
ψ	Generic scalar, reference field
ρ	Density
σ	Stefan-Boltzmann constant, standard deviation of the clipped Gaussian PDF
τ_η	Kolmogorov time scale
τ_c	Chemical time scale
τ_l	Integral time scale
τ_{ij}	Viscous stress tensor
θ	Sample space variable of the progress variable
ε	Turbulence eddy dissipation
ξ	Mixture fraction

Notation

$\bar{\phi}$	Reynolds average of ϕ
$\Delta\phi$	Change in ϕ
$\langle\phi\rangle$	Expectation of ϕ
$\langle\phi''^2\|\eta\rangle$	Conditional variance of ϕ with respect to η

$\langle\phi\|\eta,\theta\rangle$	Doubly-conditional average of ϕ with respect to η and θ
$\langle\phi\|\eta\rangle$	Conditional average of ϕ with respect to η
$\mathbf{n}_\phi$	Unit vector normal to the ϕ isosurface
ϕ'	Reynolds fluctuation of ϕ
ϕ''	Favre fluctuation of ϕ
$\widetilde{\phi''^2}$	Favre variance of ϕ
$\widetilde{\phi}$	Favre average of ϕ
$\{\phi\}_R$	Area-weighted average of ϕ
$\{\phi\}_{R^+}$	Cross-stream average of ϕ

Dimensionless Numbers

Da	Damköhler number
Le	Lewis Number
Pr	Prandtl Number
Re	Reynolds Number
Sc	Schmidt Number

Acronyms

AMC	Amplitude Mapping Closure
CFD	Computational Fluid Dynamics
CG-PDF	Clipped Gaussian PDF
CMC	Conditional Moment Closure
CSDR	Conditional Scalar Dissipation Rate
CV	Conditional Velocity
DCMC	Doubly-Conditioned Moment Closure
DNS	Direct Numerical Simulation
EDM	Eddy Dissipation Model
LEM	Linear Eddy Model
LES	Large Eddy Simulation
MBPDF	Mortensen's CSDR model based on the β-PDF
MCGPDF	Mortensen's CSDR model based on the CG-PDF
MFM	Multidimensional Flamelet-generated Manifolds
ODE	Ordinary Differential Equation
PDE	Partial Differential Equation
PDF	Probability Density Function
PMF	Presumed Mapping Function
PV	Progress Variable
RSM	Reynolds Stress Model

SLFM	Stationary Laminar Flamelet Model

Additional Subscripts

H	Homogeneous
ign	Ignition
max	Maximum
min	Minimum
mr	Most reactive
st	Stoichiometric
t	Turbulent
1	Value in oxidiser stream
2	Value in fuel stream

Chapter 1

Introduction

1.1 Overview

1.1.1 Turbulent combustion modelling

Turbulent combustion is encountered in many engineering applications, such as engines, gas turbines, burners, furnaces, explosions and fires. The complexity and high cost associated with experimental measurements prompted the need for alternative tools aimed at the understanding of the physics of turbulent combustion phenomena. Turbulent combustion modelling is the branch of Computational Fluid Dynamics (CFD) devoted to the study and analysis of these phenomena.

Turbulence and combustion are strongly coupled in nature. Turbulence promotes the mixing of reactants, and thereby enhances the combustion process. In turn, the heat released by combustion leads to flow instabilities which enhance the transition to turbulence [178]. Turbulent combustion modelling is mainly concerned with the closure of the non-linear chemical reaction rates, which appear in the mean species and energy transport equations. Several models have been devised for the treatment of this quantity based on physical analyses and experimental observations. Some examples are the laminar flamelet model [177], the Probability Density Function (PDF) methods [190], the Eddy Dissipation Concept (EDC) [140], the Linear Eddy Model (LEM) [103, 104] and the Conditional Moment Closure (CMC) [20, 118]. These models have been initially employed in the simulation of the Reynolds-Averaged Navier-Stokes (RANS) equations and later applied in Large Eddy Simulations (LES). When available, experimental measurements are employed

to validate the numerical findings. In recent years, the tremendous increase in computational resources has facilitated the extension of Direct Numerical Simulations (DNS) from non-reacting to reacting flows. Since DNS provides the most accurate numerical solution for a given problem, it is increasingly used as a validation tool for combustion models.

1.1.2 The Conditional Moment Closure

An efficient and versatile turbulent combustion model should meet two criteria. First, it should provide a balance between complexity and computational cost without compromising accuracy. Second, it should be applicable to a wide range of combustion phenomena. Primarily devised for the modelling of non-premixed turbulent combustion, CMC meets these criteria. In CMC, reactive scalars are conditionally averaged with respect to the mixture fraction, a conserved scalar describing the mixedness of reactants and the stoichiometry of the mixture, and their conditional transport equations are solved. The association of reactive scalars with the mixture fraction is motivated by the fact that fluctuations about conditional averages are smaller than their counterparts about unconditional averages. This observation simplifies the modelling of the unclosed chemical reaction rates.

CMC yields a number of unclosed terms that require further modelling. These are the conditional turbulent fluxes, the mixture fraction PDF, the Conditional Velocity (CV), the Conditional Scalar Dissipation Rate (CSDR) and the conditional chemical reaction rates. The conditional turbulent fluxes are typically modelled using the simple gradient diffusion assumption. Several submodels are available in the CMC literature for the closure of the PDF [139, 160, 178], the CSDR [78, 157, 160, 174], and the CV [131, 160, 190]. The conditional mean reaction rates are modelled using a first or second-order closure [120]. In the first-order closure, the conditional fluctuations are neglected and the conditional mean reaction rates are expressed in terms of the conditional density, species mass fractions and temperature. On the other hand, the second-order closure provides an explicit treatment for the conditional fluctuations by incorporating an additional set of variance and covariance equations.

CMC has been successfully applied to variety of non-premixed combustion problems. Some examples are autoignition [50, 59, 116, 143], attached flames [63, 110, 126, 205], piloted flames [61, 62, 65, 65, 66, 113, 170, 198, 199], lifted flames [54, 105, 168, 169, 171, 176, 212], swirl-stabilized flames [64], counterflow flames [106], bluff body flames [111, 112, 167], enclosure fires [43, 44], spray combustion [25, 117, 239], differential diffusion [124], extinction and reignition [115], and engine modelling [51, 238]. A CMC version for premixed combustion wherein reactive scalars are conditioned with respect to a temperature-related Progress

Variable (PV) rather than the mixture fraction is available [18, 218, 219], however, its application thus far has been restricted to a limited number of studies [145, 222].

1.1.3 Some areas of improvements

CMC is a continuously evolving modelling approach. Substantial advances have been accomplished since the inception of the method. In what follows, further improvements related to the consistent implementation of CMC and the treatment of conditional fluctuations are highlighted.

Consistent implementation of CMC

The selected CV and CSDR submodels in CMC should warrant a fully consistent implementation. The CV submodel should be consistent with the modelling of the unconditional fluxes of the first and second moments of the mixture fraction which are used to close the PDF. The CSDR submodel should ensure the full recovery of the unconditional set of equations without any additional spurious source terms upon integrating the PDF-weighted CMC equations over the mixture fraction space. This requirement is met if the CSDR is consistent with the presumed PDF through the PDF transport equation. Recently developed closures based on different PDF modelling approaches [157, 160] satisfy these conditions and hence ensure fully consistent CMC implementations. The application of such advanced closures reinforces the soundness of CMC predictions, and therefore allows for a more accurate computational analysis, ultimately leading to a better understanding of the dynamics of combustion phenomena.

Treatment of conditional fluctuations

It is well established that the second-order closure for the conditional chemical reaction rates outperforms the first-order approximation in situations where the fluctuations about the conditional averages are significant [120, 128]. However, second-order modelling is relatively more expensive due to the necessity of solving an additional, large set of variance and co-variance equations. Despite the remarkable improvement, the anticipated success of this approach was found to be limited. The reasons remain unclear. Possible sources of discrepancy may be related to assumptions specific to the modelling of the unclosed terms in the variance and co-variance equations or to the neglect of the fluctuating terms in the

CMC equations via the primary closure hypothesis [120] (discussed in more detail in Sect. 3.2.1).

A less common, yet attractive approach for the treatment of conditional fluctuations is the introduction of a suitably defined second conditioning variable beside the mixture fraction. This extension is known as the Doubly-Conditional Moment Closure (DCMC) [18,19]. As opposed to the second-order closure, DCMC treats the conditional fluctuations in an implicit fashion. The conditioning of reactive scalars with respect to two variables rather than one is relatively more constrictive. Therefore, doubly-conditional fluctuations are expected to be smaller than their singly-conditional counterparts, and hence may be neglected. As such, the first-order closure for the conditional reaction rates becomes justified in the modelling of highly fluctuating phenomena. Despite this advantage, DCMC yields a number of unclosed terms that require complicated modelling and increases the dimensionality of the governing equations.

The areas of improvement described above are explored in this thesis. The first-order CMC is applied to the modelling of piloted and lifted flames in order to assess the performance of classical (inconsistent) and advanced (consistent) submodels. In addition, a DCMC formulation for the treatment of fluctuations is proposed by introducing a normalised, mixture fraction-dependent PV as a second conditioning variable.

1.2 Objectives

The objectives of this thesis are:

- to analyse the effect of additives on the autoignition of CH_4 using detailed chemical kinetics and classical CMC submodels,
- to assess the performance of classical and advanced CMC submodels in the context of a piloted CH_4/air turbulent jet flame and apply of the first-order closure using consistent submodels,
- to apply the first-order CMC to the modelling of a lifted H_2/N_2 turbulent jet flame using classical and advanced PDF modelling approaches, and
- to propose a new DCMC method for the treatment of fluctuations in non-premixed and partially premixed turbulent combustion.

1.3 Outline

This thesis is structured as follows:

- **Chapter 2**: An overview of turbulent combustion modelling is provided. The conservation equations are presented and turbulence modelling is discussed. Turbulent reacting flows are then described and some of the tools employed in turbulent combustion modelling are presented. This chapter concludes with a brief review of some turbulent combustion models with emphasis on models formulated primarily for the modelling of non-premixed combustion with infinitely fast and finite-rate chemistry.

- **Chapter 3**: The CMC transport equations are derived using the decomposition approach and simplified by invoking the primary closure hypothesis. Submodels for the resulting unclosed terms are discussed. The numerical methods employed in the solution of CMC are highlighted. Recent advances made in CMC are reviewed.

- **Chapter 4**: The first-order cross-stream averaged CMC is employed to investigate the shock tube autoignition of high pressure CH_4, CH_4/C_2H_6, CH_4/H_2, and CH_4/N_2 jets injected into lower pressure heated air over a wide range of pre-combustion air temperatures. The effect of additives on the autoignition of CH_4 is assessed using detailed chemical kinetics. The predictions of ignition delays and ignition kernel locations are compared to experimental measurements.

- **Chapter 5**: A piloted CH_4/air jet flame is investigated using the two-dimensional first-order CMC. Two PDF distributions are employed, the β-PDF and the clipped Gaussian PDF. Several consistent and inconsistent CSDR and CV submodels employing these PDFs are considered. The PDF and CSDR closures are compared to experimental measurements. Consistent and inconsistent combinations of the PDF, CV and CSDR submodels are selected and CMC calculations are performed. The flame response to the inhomogeneous modelling of the CSDR is discussed. The results are compared to available experimental data.

- **Chapter 6**: A lifted H_2/N_2 turbulent jet flame issuing into a vitiated coflow is investigated using the two-dimensional first-order CMC. The PDF is presumed using a β-distribution, and the CV and CSDR submodels are chosen such that they are fully consistent with this choice of PDF. The effect of mixing on liftoff is analysed via the modelling of the CSDR. The response of the flame to small changes in the coflow temperature is investigated. The stabilisation mechanism is determined by analysing the transport budgets in mixture fraction and physical spaces, and the radical history

ahead of the stabilisation height. The influence of the spurious sources is investigated. The role of chemical kinetics is assessed using different kinetic schemes. The results are compared to experimental measurements.

- **Chapter 7**: The lifted jet flame considered in Chapter 6 is revisited to assess the applicability of the PMF approach in the context of the first-order CMC. Rather than presuming the PDF directly, the PMF approach provides a closure for the PDF using a mapping function between the true (unknown) scalar field and a specified (known) reference field. Fully consistent CSDR and CV closures may be derived using the resulting PMF-PDF. These closures are applied in order to investigate the effect of the PMF approach on the stabilisation mechanism over a range of co-flow temperatures. The influence of the spurious sources is reassessed. The results are compared to the β-PDF-based closures of Chapter 6 and to experimental measurements.

- **Chapter 8**: A DCMC method is devised by incorporating a normalised PV beside the mixture fraction. The normalisation of the PV is performed such that the normalisation parameters are mixture fraction-dependent. Simple submodels for the doubly-conditional unclosed arising from the DCMC derivation are proposed and boundary conditions are discussed. The homogeneous version of the method is implemented in order to perform a parametric assessment of the effects of strain in mixture fraction and PV spaces. The conditions of a piloted CH_4/air jet flame are considered.

- **Chapter 9**: A summary of the findings obtained in this thesis is provided and further developments are proposed.

Chapter 2

Turbulent Combustion

An overview of turbulent combustion modelling is provided. The conservation equations are presented and turbulence modelling is discussed with emphasis on the Reynolds-averaged Navier-Stokes equations. The difficulties associated with the averaging of the chemical reaction rate are addressed. The structures and properties of non-premixed, premixed and partially premixed flames are described. The stochastic nature of turbulent reacting flows and the interactions between turbulence and chemistry are discussed. The mixture fraction and progress variables are presented. Finally, some turbulent combustion models from the literature are briefly reviewed. Models for non-premixed combustion with finite-rate and infinitely fast chemistry are emphasised.

2.1 Governing equations

In this section, the conservation equations of mass, momentum, species and energy are presented using Cartesian coordinates and indicial notation. The assumption of unity Lewis numbers is invoked to simplify the species and energy equations.

2.1.1 Conservation of mass

The conservation of mass equation is given by [187]:

$$\underbrace{\frac{\partial \rho}{\partial t}}_{\substack{\text{Local rate} \\ \text{of change}}} + \underbrace{\frac{\partial \left(\rho u_i\right)}{\partial x_i}}_{\text{Convection}} = 0 \tag{2.1}$$

where t denotes time, x_i is the i^{th} Cartesian coordinate, ρ is the density, and u_i is the velocity component in the direction of i^{th} coordinate.

2.1.2 Conservation of momentum

Neglecting body forces, the momentum equation reads [187]:

$$\underbrace{\rho\frac{\partial u_j}{\partial t}}_{\substack{\text{Local rate}\\ \text{of change}}} + \underbrace{\rho u_i\frac{\partial u_j}{\partial x_i}}_{\text{Convection}} = -\underbrace{\frac{\partial p}{\partial x_i}}_{\substack{\text{Pressure}\\ \text{gradient}}} + \underbrace{\frac{\partial \tau_{ij}}{\partial x_i}}_{\substack{\text{Molecular}\\ \text{transport due}\\ \text{to viscosity}}} \tag{2.2}$$

where p is the pressure and τ_{ij} is the viscous stress tensor. This tensor is expressed using the Stokes hypothesis as:

$$\tau_{ij} = -\frac{2}{3}\mu\frac{\partial u_k}{\partial x_k}\delta_{ij} + \mu\left(\frac{\partial u_i}{\partial x_j} + \frac{\partial u_j}{\partial x_i}\right) \tag{2.3}$$

where μ is the dynamic viscosity and δ_{ij} is Kronecker's delta.

2.1.3 Conservation of species

In a mixture of N_s species, the transport equation of a species κ is given by [178]:

$$\underbrace{\rho\frac{\partial Y_\kappa}{\partial t}}_{\substack{\text{Local rate}\\ \text{of change of}}} + \underbrace{\rho u_i\frac{\partial Y_\kappa}{\partial x_i}}_{\text{Convection}} = -\underbrace{\frac{\partial J_i^{Y_\kappa}}{\partial x_i}}_{\text{Diffusion}} + \underbrace{\dot{\omega}_\kappa}_{\substack{\text{Chemical}\\ \text{reaction}\\ \text{rate}}} \qquad \kappa = 1, 2, \ldots, N_s \tag{2.4}$$

where Y_κ, $J_i^{Y_\kappa}$, and $\dot{\omega}_\kappa$ are, respectively, the mass fraction, the i^{th} component of the molecular diffusive flux, and the chemical reaction rate of the species κ. Using Fick's first law of diffusion, $J_i^{Y_\kappa}$ is expressed as:

$$J_i^{Y_\kappa} = -\rho D_\kappa\frac{\partial Y_\kappa}{\partial x_i} \tag{2.5}$$

where D_κ is the binary mass diffusion coefficient of species κ with respect to an abundant species in the mixture [178]. It is often assumed that D_κ is proportional to the thermal diffusivity, $D = \lambda/\rho c_p$, such that the Lewis number of species κ

$$\text{Le}_\kappa = \frac{\lambda}{\rho c_p D_\kappa} = \frac{D}{D_\kappa} \tag{2.6}$$

is constant [178]. Another commonly used simplification is the assumption of unity Lewis numbers for all species, which leads to $D_\kappa = D$. Accordingly, all species diffusivities are equal to the thermal diffusivity. This assumption is adopted here.

The chemical reaction rate, $\dot{\omega}_\kappa$, accounts for the net rate of creation (production) and destruction (consumption) of species κ. A set of I elementary reversible reactions in a mixture consisting of N_s species can be written as [130]:

$$\sum_{\kappa=1}^{N_s} \nu'_{\kappa i} M_\kappa \underset{k_{bi}}{\overset{k_{fi}}{\leftrightarrows}} \sum_{\kappa=1}^{N_s} \nu''_{\kappa i} M_\kappa \qquad i = 1, 2, \ldots, I \tag{2.7}$$

where M_κ is the chemical symbol of species κ and $\nu_{\kappa i}$ denotes the stoichiometric coefficient of the species in reaction i. A single prime superscript is used with $\nu_{\kappa i}$ if M_κ is a reactant, whereas a double prime is used if M_κ is a product. k_{fi} and k_{bi} are the forward and backward rate constants, respectively. The reaction rate of species κ is the sum of the reaction rates corresponding to all the chemical reactions involving this species. Accordingly,

$$\dot{\omega}_\kappa = W_\kappa \sum_{i=1}^{I} \left(\nu''_{\kappa i} - \nu'_{\kappa i}\right) q_i \qquad \kappa = 1, 2, \ldots, N_s \tag{2.8}$$

where W_κ is the molecular weight of species κ and q_i is the rate of progress of the i^{th} reaction. q_i is the difference of the forward and backward reaction rates:

$$q_i = k_{fi} \prod_{\kappa=1}^{N_s} \left(\frac{\rho Y_\kappa}{W_\kappa}\right)^{\nu'_{\kappa i}} - k_{bi} \prod_{\kappa=1}^{N_s} \left(\frac{\rho Y_\kappa}{W_\kappa}\right)^{\nu''_{\kappa i}} \tag{2.9}$$

The forward rate constant, k_{fi}, is expressed using the Arrhenius equation as:

$$k_{fi} = A_i T^{b_i} \exp\left(-\frac{T_{a,i}}{T}\right) = A_i T^{b_i} \exp\left(-\frac{E_{a,i}}{R_u T}\right) \tag{2.10}$$

where A_i is the pre-exponential factor, b_i is the temperature exponent, $T_{a,i}$ and $E_{a,i}$ are, respectively, the activation temperature and energy, R_u is the universal gas constant, and T is the temperature. The backward rate constant, k_{bi}, is related to k_{fi} by:

$$k_{bi} = \frac{k_{fi}}{K_{Ci}} \tag{2.11}$$

where K_{Ci} is the equilibrium constant of reaction i. It is given by [194]:

$$K_{Ci} = \left(\frac{p_a}{R_u T}\right)^{\sum_{\kappa=1}^{N_s} \left(\nu''_{\kappa i} - \nu'_{\kappa i}\right)} \exp\left(\frac{\Delta S_i^\circ}{R_u} - \frac{\Delta H_i^\circ}{R_u T}\right) \tag{2.12}$$

where p_a is the atmospheric pressure (1 bar). The quantities ΔH_i° and ΔS_i° represent the changes in standard state enthalpy and entropy that occur in passing completely from reactants to products in reaction i. They are calculated using:

$$\Delta H_i^\circ = \sum_{\kappa=1}^{N_s} \nu_{\kappa i} H_\kappa^\circ, \quad H_\kappa^\circ = \int_{T_\circ}^{T} C_{p,\kappa}^\circ dT \tag{2.13}$$

and

$$\Delta S_i^\circ = \sum_{\kappa=1}^{N_s} \nu_{\kappa i} S_\kappa^\circ, \quad S_\kappa^\circ = \int_{T_\circ}^{T} \frac{C_{p,\kappa}^\circ}{T} dT \tag{2.14}$$

where H_κ°, S_κ°, and $C_{p,\kappa}^\circ$ are the standard state enthalpy, entropy, and constant-pressure heat capacity of species κ, respectively, and $T_\circ$ is a reference temperature. In practice, $C_{p,\kappa}^\circ$ is evaluated using an N^{th} order polynomial fit of the form [10, 194]:

$$C_{p,\kappa}^\circ = R_u \sum_{n=1}^{N} a_{n,\kappa} T^{n-1} \tag{2.15}$$

where R is the ideal gas constant and $\{a_{n,\kappa} | \kappa = 1, 2, \ldots, N\}$ are the polynomial coefficients. Hence, H_κ° and S_κ° in Eqs. (2.13) and (2.14) are expressed as [194]:

$$H_\kappa^\circ = R_u \left(\sum_{n=1}^{N} \frac{a_{n,\kappa} T^n}{n} + a_{N+1,\kappa} \right) \tag{2.16}$$

and

$$S_\kappa^\circ = R_u \left(a_{1,\kappa} \ln T + \sum_{n=2}^{N} \frac{a_{n,\kappa} T^{n-1}}{n-1} + a_{N+2,\kappa} \right) \tag{2.17}$$

The constants of integration $R_u a_{N+1,\kappa}$ in Eq. (2.16) and $R_u a_{N+2,\kappa}$ in Eq. (2.17) are the standard state entropy and enthalpy at $T_\circ$, respectively. Equations (2.15), (2.16) and (2.17) are expressed for an arbitrary N. The gas-phase chemical kinetics package CHEMKIN-II [194] used throughout this thesis employs the NASA thermodynamic database [10]. In this database, $C_{p,\kappa}^\circ$ is fit to a fourth-order polynomial ($N = 4$ in Eq. (2.15)) and the standard state entropy and enthalpy are provided for $T_\circ = 298.15$ K.

2.1.4 Conservation of energy

The energy equation can be expressed in several forms. The specific enthalpy and temperature transport equations are presented here. The specific enthalpy, h, consists of sensible

and chemical components [187]:

$$\begin{aligned} h = \sum_{\kappa=1}^{N_s} h_\kappa Y_\kappa = \sum_{\kappa=1}^{N_s} \left(\int_{T_\circ}^{T} c_{p,\kappa} dT + \Delta h^\circ_{f,\kappa} \right) Y_\kappa = \int_{T_\circ}^{T} c_p dT + \sum_{\kappa=1}^{N_s} \Delta h^\circ_{f,\kappa} Y_\kappa \\ = \underbrace{h_s}_{\substack{\text{Sensible} \\ \text{component}}} + \underbrace{\sum_{\kappa=1}^{N_s} \Delta h^\circ_{f,\kappa} Y_\kappa}_{\substack{\text{Chemical} \\ \text{component}}} \end{aligned} \tag{2.18}$$

where h_κ, $c_{p,\kappa}$, and $h^\circ_{f,\kappa}$ are, respectively, the specific enthalpy, heat capacity at constant pressure, and enthalpy of formation of species κ, and h_s is the specific sensible enthalpy.

When body forces are neglected, the transport equation of h reads [187]:

$$\underbrace{\rho \frac{\partial h}{\partial t}}_{\substack{\text{Local rate} \\ \text{of change}}} + \underbrace{\rho u_i \frac{\partial h}{\partial x_i}}_{\text{Convection}} = \underbrace{\frac{\partial p}{\partial t} + u_i \frac{\partial p}{\partial x_i}}_{\substack{\text{Total derivative} \\ \text{of pressure}}} - \underbrace{\frac{\partial J_i^h}{\partial x_i}}_{\text{Diffusion}} + \underbrace{\tau_{ij} \frac{\partial u_i}{\partial x_j}}_{\substack{\text{Viscous} \\ \text{heating}}} + \underbrace{\dot{\omega}_r}_{\substack{\text{Radiative} \\ \text{source}}} \tag{2.19}$$

The i^{th} component of the flux of h, J_i^h, is expressed as:

$$J_i^h = -\lambda \frac{\partial T}{\partial x_i} + \sum_{\kappa=1}^{N_s} h_\kappa J_i^{Y_\kappa} = - \underbrace{\frac{\lambda}{c_p}}_{=\rho D \text{Le}} \frac{\partial h}{\partial x_i} - \sum_{\kappa=1}^{N_s} \underbrace{\left(\frac{\lambda}{c_p} - \rho D_\kappa \right)}_{=\rho D_\kappa (\text{Le}_\kappa - 1)} h_\kappa \frac{\partial Y_\kappa}{\partial x_i} \tag{2.20}$$

where λ is the thermal conductivity and c_p is the specific heat at constant pressure. Under the assumption of unity Lewis numbers, the summation in Eq.(2.20) is zero and $\lambda/c_p = \rho D$, leading to $J_i^h = -\rho D \partial h / \partial x_i$.

The sensible enthalpy equation follows from Eqs. (2.18) and (2.19). It has the same form as Eq. (2.19) with h replaced by h_s in addition to the chemical source term $\dot{\omega}_{h_s} = -\sum_{\kappa=1}^{N_s} \Delta h^\circ_{f,\kappa} \dot{\omega}_\kappa$ on the right-hand side (r.h.s.) of the equation.

Alternatively, the energy equation may be expressed in terms of the temperature as [187]:

$$\begin{aligned} \underbrace{\rho c_p \frac{\partial T}{\partial t}}_{\substack{\text{Local rate} \\ \text{of change}}} + \underbrace{\rho c_p u_i \frac{\partial T}{\partial x_i}}_{\text{Convection}} = \underbrace{\frac{\partial p}{\partial t} + u_i \frac{\partial p}{\partial x_i}}_{\substack{\text{Total derivative} \\ \text{of pressure}}} - \underbrace{\frac{\partial}{\partial x_i} \left(\lambda \frac{\partial T}{\partial x_i} \right)}_{\text{Conduction}} + \underbrace{\rho \left(\sum_{\kappa=1}^{N_s} c_{p,\kappa} D_\kappa \frac{\partial Y_\kappa}{\partial x_i} \right) \frac{\partial T}{\partial x_i}}_{\text{Interdiffusion}} \\ + \underbrace{\tau_{ij} \frac{\partial u_i}{\partial x_j}}_{\substack{\text{Viscous} \\ \text{heating}}} + \underbrace{\dot{\omega}_T}_{\substack{\text{Heat release} \\ \text{due to} \\ \text{combustion}}} + \underbrace{\dot{\omega}_r}_{\substack{\text{radiative} \\ \text{source}}} \end{aligned} \tag{2.21}$$

where $\dot{\omega}_T = \sum_{\kappa=1}^{N_s} h_\kappa \dot{\omega}_\kappa$. If unity Lewis numbers are assumed, $\lambda = \rho c_p D$ in the diffusion term and $D_\kappa = D$ in the interdiffusion term.

2.2 Turbulence modeling

Reacting and non-reacting fluid flows are classified as either laminar or turbulent. The majority of flows encountered in engineering applications belong to the latter category because fluids are transported and mixed more efficiently in the presence of turbulence [192]. The design and optimisation of a given application require a detailed understanding of turbulence. This field of study is complicated in nature. Turbulent flows comprise eddies of different sizes. Large eddies transfer their energy and break up into smaller eddies. This energy transfer, referred to as the energy cascade, continues until the smallest eddies disappear due to viscous forces [178]. As such, turbulent motions take place over a wide range of length and time scales, and local properties undergo significant fluctuations. Simplified experiments provide a deep insight into the nature of turbulence, however, detailed measurements can be difficult, expensive, and time-consuming. To overcome these limitations, several computational approaches have been developed. These approaches enable the anticipation and prediction of the behaviour of fluid flows with lesser dependence on experimental measurements. This section provides a brief overview of Reynolds-Averaged Navier-Stokes (RANS) models, Large Eddy Simulation (LES), and Direct Numerical Simulation (DNS).

2.2.1 Overview of computational approaches in fluid dynamics

The RANS, LES, and DNS approaches may be best described by referring to the turbulence kinetic energy spectrum. Some basic definitions of the relevant length and time scales are first provided.

Length and time scales of turbulence

The integral length scale, l, is associated with the size of the largest eddies. Using dimensional analysis, it can be shown that [134, 178]:

$$l = \frac{k^{3/2}}{\varepsilon} \tag{2.22}$$

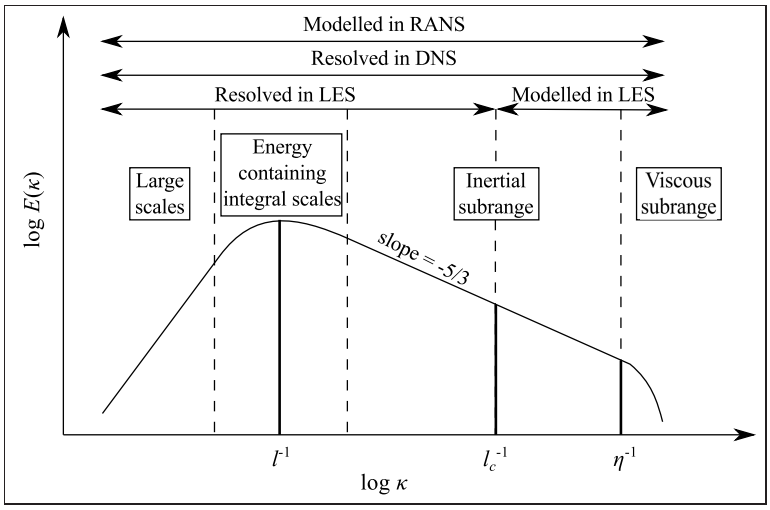

Figure 2.1: Turbulence kinetic energy spectrum of a large Reynolds number flow as a function of the wavenumber [178, 187].

where k is the turbulence kinetic energy and ϵ is its dissipation. The associated time scale, also referred to as the turnover time, is proportional to l and is given by [134, 178]:

$$\tau_l = \frac{k}{\varepsilon} \tag{2.23}$$

The transfer of turbulence kinetic energy from integral scale to smaller size eddies occurs at a rate ε up to the point where the size of the eddies is smallest [134]. The length scale associated with the smallest eddies is the Kolmogorov length scale, η, which is related to ν and ε by [134, 178]:

$$\eta = \left(\frac{\nu^3}{\varepsilon}\right)^{1/4} \tag{2.24}$$

where ν is the kinematic viscosity ($\nu = \mu/\rho$). The corresponding time scale is given by [134, 178]:

$$\tau_\eta = \left(\frac{\nu}{\varepsilon}\right)^{1/2} \tag{2.25}$$

The turbulent kinetic energy spectrum

Figure 2.1 depicts the kinetic energy spectrum, $E(\kappa)$, of a large Reynolds number (Re) flow as a function of the wavenumber, κ. $E(\kappa)$ represents the density of kinetic energy per

unit wavenumber [178]. Four regions can be distinguished. The first corresponds to large scale eddies. In this region, $E(\kappa)$ increases with a power law between κ^2 and κ^4 [178]. The second region corresponds to the energy-containing eddies. The peak of $E(\kappa)$ is reached at the wavenumber corresponding to the integral length scale, l. The third region represents the inertial subrange where $E(\kappa)$ decays following the $\kappa^{-5/3}$ law [178]. The fourth region extending beyond the wavenumber corresponding to the Kolmogorov length scale, η, is referred to as the viscous subrange. In this region, $E(\kappa)$ decreases exponentially as the kinetic energy is dissipated by means of viscosity effects [178].

Computational approaches

Three computational approaches are described in reference to Fig. 2.1. In RANS simulation, all the scales of turbulence are modelled. RANS models supply submodels for the unclosed terms arising from the averaging of the different conservation equations. Therefore, these models yield the mean values of the flow variables. Conversely, all the scales of turbulence are determined explicitly or resolved in DNS [187]. The instantaneous conservation equations in DNS are solved directly without the need for averaging or modelling. The level of modelling in LES is intermediate between RANS and DNS: large scales are resolved, whereas smaller scales are modelled using subgrid closures [187].

The next three sections describe these computational approaches in more detail with emphasis on RANS modelling, which is the approach of choice in this work.

2.2.2 Simulation of the Reynolds-averaged Navier-Stokes equations

In this section, the mean conservation equations are presented and the closures required for the modelling of the unclosed terms that arise from averaging are discussed.

Reynolds and Favre averaging

An instantaneous random variable $\psi(\mathbf{x}, t)$ in a non-reacting turbulent flow is decomposed into a Reynolds average, $\bar{\psi}(\mathbf{x}, t)$, and a fluctuation about $\bar{\psi}(\mathbf{x}, t)$, $\psi'(\mathbf{x}, t)$:

$$\psi(\mathbf{x}, t) = \bar{\psi}(\mathbf{x}, t) + \psi'(\mathbf{x}, t) \tag{2.26}$$

such that

$$\bar{\psi}'(\mathbf{x}, t) = 0 \tag{2.27}$$

This is referred to as Reynolds decomposition. Since turbulent reacting flows involve substantial density variations, it is more convenient to use a density-weighted average, $\tilde{\psi}(\mathbf{x},t)$, referred to as the Favre average [67]. Similar to Reynolds decomposition, the Favre decomposition of $\psi(\mathbf{x},t)$ performed as:

$$\psi(\mathbf{x},t) = \tilde{\psi}(\mathbf{x},t) + \psi''(\mathbf{x},t) \tag{2.28}$$

where $\psi''(\mathbf{x},t)$ is a fluctuation about $\tilde{\psi}(\mathbf{x},t)$. A double prime superscript is used to distinguish Favre fluctuations from Reynolds fluctuations. The difference between the two decomposition methods lies in treatment of the mean of the fluctuation. In Reynolds decomposition, Eq. (2.27) follows from the averaging of Eq. (2.26), whereas in Favre decomposition, the mean of the density-fluctuation product is required to be zero, i.e.:

$$\overline{\rho\psi''(\mathbf{x},t)} = 0 \tag{2.29}$$

Accordingly, when Eq. (2.28) is multiplied by ρ and averaged,

$$\overline{\rho\psi(\mathbf{x},t)} = \overline{\rho\big[\tilde{\psi}(\mathbf{x},t) + \psi''(\mathbf{x},t)\big]} = \overline{\rho\tilde{\psi}(\mathbf{x},t)} + \overline{\rho\psi''(\mathbf{x},t)} = \bar{\rho}\tilde{\psi}(\mathbf{x},t) \tag{2.30}$$

and therefore,

$$\tilde{\psi}(\mathbf{x},t) = \frac{\overline{\rho\psi(\mathbf{x},t)}}{\bar{\rho}} \tag{2.31}$$

The averaging of the transport equation of ψ is performed in two steps. First, ψ is decomposed following Eq. (2.28) and inserted into its governing transport equation. The resulting expression is then averaged and simplified using Eqs. (2.29) and (2.31). This procedure leads to several unclosed terms that require further modelling.

The Favre-averaged conservation equations

The averaging of Eqs. (2.1), (2.2), (2.4) and (2.19) results in:

$$\frac{\partial\bar{\rho}}{\partial t} + \frac{\partial(\bar{\rho}\tilde{u}_i)}{\partial x_i} = 0 \tag{2.32}$$

$$\bar{\rho}\frac{\partial\tilde{u}_i}{\partial t} + \bar{\rho}\tilde{u}_i\frac{\partial\tilde{u}_j}{\partial x_i} = -\frac{\partial\bar{p}}{\partial x_i} + \frac{\partial\bar{\tau}_{ij}}{\partial x_i} - \frac{\partial(\bar{\rho}\widetilde{u_i''u_j''})}{\partial x_i} \tag{2.33}$$

$$\bar{\rho}\frac{\partial\tilde{Y}_\kappa}{\partial t} + \bar{\rho}\tilde{u}_i\frac{\partial\tilde{Y}_\kappa}{\partial x_i} = -\frac{\partial\overline{J_i^{Y_\kappa}}}{\partial x_i} - \frac{\partial(\bar{\rho}\widetilde{u_i''Y_\kappa''})}{\partial x_i} + \overline{\dot{\omega}}_\kappa \qquad \kappa = 1,2,\ldots,N_s \tag{2.34}$$

$$\bar{\rho}\frac{\partial \tilde{h}}{\partial t} + \bar{\rho}\tilde{u}_i\frac{\partial \tilde{h}}{\partial x_i} = \frac{\partial \bar{p}}{\partial t} + \tilde{u}_i\frac{\partial \bar{p}}{\partial x_i} + \overline{u_i''\frac{\partial p}{\partial x_i}} - \frac{\partial \overline{J_i^h}}{\partial x_i} - \frac{\partial(\bar{\rho}\widetilde{u_i''h''})}{\partial x_i} + \overline{\tau_{ij}\frac{\partial u_i}{\partial x_j}} + \overline{\dot{\omega}}_r \tag{2.35}$$

The mean viscous stress tensor, $\bar{\tau}_{ij}$, the mean viscous dissipation, $\overline{\tau_{ij}\partial u_i/\partial x_j}$, the Reynolds stresses, $\widetilde{u_i''u_j''}$, the mean molecular diffusive fluxes, $\overline{J_i^{Y_\kappa}}$ and $\overline{J_i^h}$, the turbulent fluxes, $\widetilde{u_i''Y_\kappa''}$ and $\widetilde{u_i''h''}$, the pressure-velocity correlation, $\overline{u_i''\partial p/\partial x_i}$, the mean chemical reaction rate, $\overline{\dot{\omega}}_\kappa$, and the mean radiative source, $\overline{\dot{\omega}}_r$, are all unclosed and require additional modelling.

The Reynolds stresses

A model is required for the closure of the Reynolds stresses $\widetilde{u_i''u_j''}$ which appear on the r.h.s. of Eq. (2.33). This quantity is closed using either a turbulent viscosity model or the Reynolds Stress Model (RSM).

Turbulent viscosity models In the framework of this class of models, the Reynolds stresses are expressed using the Boussinesq hypothesis [98, 134, 187]:

$$\widetilde{u_i''u_j''} = \frac{2}{3}\left(\tilde{k} + \nu_t\frac{\partial \tilde{u}_k}{\partial x_k}\right)\delta_{ij} - \nu_t\left(\frac{\partial \tilde{u}_i}{\partial x_j} + \frac{\partial \tilde{u}_j}{\partial x_i}\right) \tag{2.36}$$

where

$$\tilde{k} = \frac{1}{2}\widetilde{u_i''u_i''} \tag{2.37}$$

is the turbulence kinetic energy and ν_t is the eddy viscosity, which is equal to the ratio of the turbulent viscosity to the mean density ($\nu_t = \mu_t/\bar{\rho}$). The turbulent flux of a scalar ϕ, $\widetilde{u_i''\phi''}$, is modelled using the gradient diffusion assumption by analogy to Fick's law. The closure of the turbulent flux is achieved by assuming that $\widetilde{u_i''\phi''}$ is be proportional to the negative of the gradient of $\tilde{\phi}$ with the proportionality constant being a turbulent transport coefficient [134]:

$$\widetilde{u_i''\phi''} = -\frac{\nu_t}{\sigma_\phi}\frac{\partial \tilde{\phi}}{\partial x_i} \tag{2.38}$$

where σ_ϕ is a turbulent Schmidt or Prandtl number.

In order to close Eqs. (2.36) and (2.38), ν_t needs to be determined. For this purpose, several modelling approaches have been proposed. Zero-equation models are the simplest among the turbulent viscosity models since the closure of ν_t is algebraic and therefore, does not introduce any additional transport equations. On the other hand, one-equation models

require the solution of an additional equation for $\tilde{k}$. The major drawback of these two models is necessity to specify a turbulence length scale. Two-equation models overcome this difficulty by introducing beside the $\tilde{k}$-equation, an additional equation describing a variable related to the turbulence length scale. Several variables have been proposed in the literature. Two examples are the dissipation of turbulence kinetic energy ε [94, 98] and the specific dissipation rate ω (the ratio of ε to k) [237]. The resulting models are known as the k-ε and k-ω models, respectively. The former is presented here.

In the k-ε model, ν_t is modelled as [98, 134, 187]:

$$\nu_t = C_\mu \frac{\tilde{k}^2}{\tilde{\varepsilon}} \tag{2.39}$$

where $C_\mu = 0.09$. Thus, the evaluation of ν_t requires the knowledge of $\tilde{k}$ and $\tilde{\varepsilon}$. Neglecting transport by molecular diffusion, buoyancy effects, and body forces, the modelled $\tilde{k}$ and $\tilde{\varepsilon}$ equations[1] are given by [98]:

$$\underbrace{\bar{\rho}\frac{\partial \tilde{k}}{\partial t}}_{\substack{\text{Local rate}\\ \text{of change}}} + \underbrace{\bar{\rho}\tilde{u}_i\frac{\partial \tilde{k}}{\partial x_i}}_{\text{Convection}} = \underbrace{\frac{\partial}{\partial x_i}\left(\frac{\bar{\rho}\nu_t}{\sigma_k}\frac{\partial \tilde{k}}{\partial x_i}\right)}_{\text{Turbulent diffusion}} \underbrace{-\frac{\nu_t}{\bar{\rho}\mathrm{Sc}_t}\frac{\partial \bar{\rho}}{\partial x_i}\frac{\partial \bar{p}}{\partial x_i}}_{\substack{\text{Transport by the mean}\\ \text{pressure gradient}}} \underbrace{-\bar{\rho}\widetilde{u_i'' u_j''}\frac{\partial \tilde{u}_j}{\partial x_i}}_{\text{Production}} \underbrace{-\bar{\rho}\tilde{\varepsilon}}_{\text{Dissipation}} \tag{2.40}$$

and

$$\underbrace{\bar{\rho}\frac{\partial \tilde{\varepsilon}}{\partial t}}_{\substack{\text{Local rate}\\ \text{of change}}} + \underbrace{\bar{\rho}\tilde{u}_i\frac{\partial \tilde{\varepsilon}}{\partial x_i}}_{\text{Convection}} = \underbrace{\frac{\partial}{\partial x_i}\left(\frac{\bar{\rho}\nu_t}{\sigma_\varepsilon}\frac{\partial \tilde{\varepsilon}}{\partial x_i}\right)}_{\text{Turbulent diffusion}} \underbrace{-\frac{\tilde{\varepsilon}}{\tilde{k}}\frac{\nu_t}{\bar{\rho}\mathrm{Sc}_t}\frac{\partial \bar{\rho}}{\partial x_i}\frac{\partial \bar{p}}{\partial x_i}}_{\substack{\text{Transport by the mean}\\ \text{pressure gradient}}} \underbrace{-C_{\varepsilon 1}\frac{\tilde{\varepsilon}}{\tilde{k}}\bar{\rho}\widetilde{u_i'' u_j''}\frac{\partial \tilde{u}_j}{\partial x_i}}_{\text{Production}} \underbrace{-C_{\varepsilon 2}\bar{\rho}\frac{\tilde{\varepsilon}^2}{\tilde{k}}}_{\text{Dissipation}} \tag{2.41}$$

The Reynolds stresses in the production terms of Eqs. (2.40) and (2.41) are expressed using Eq. (2.36). The standard model constants are $C_{\varepsilon 1} = 1.44$, $C_{\varepsilon 2} = 1.92$, $\sigma_k = 1.0$, $\sigma_\varepsilon = 1.3$ and $\mathrm{Sc}_t = 0.7$ [98, 134, 187]. The turbulence length and time scales are determined from $\tilde{k}$ and $\tilde{\varepsilon}$ as $l = \tilde{k}^{3/2}/\tilde{\varepsilon}$ and $\tau = \tilde{k}/\tilde{\varepsilon}$, respectively.

The k-ε model is one of the most widely used two-equation models due to its simplicity, completeness, and wide range of applicability. It is the model of choice for most of the calculations performed in this thesis. When applied to a round jet, it is known to overpredict the spreading rate. One way to resolve this issue is to adjust the values of $C_{\varepsilon 1}$ and $C_{\varepsilon 2}$ [155, 189]. This approach is followed in this work.

[1] Equation (2.38) is employed in the modelling of the transport by turbulent diffusion (turbulent fluxes and pressure work) and by the mean pressure gradient.

The Reynolds Stress Model In RSM, the Boussinesq hypothesis is not invoked to model the Reynolds stresses. Instead, transport equations derived directly from the momentum equations are solved for the individual stresses. Neglecting transport by molecular diffusion, buoyancy effects, and body forces, the Reynolds stress transport equation reads [202]:

$$\underbrace{\bar{\rho}\frac{\partial\widetilde{u_i''u_j''}}{\partial t}}_{\substack{\text{Local rate}\\ \text{of change}}}+\underbrace{\tilde{\rho}\tilde{u}_k\frac{\partial\widetilde{u_i''u_j''}}{\partial x_k}}_{\text{Convection}}=\underbrace{P_{ij}}_{\substack{\text{Stress}\\ \text{production}}}+\underbrace{\Pi_{ij}}_{\substack{\text{Deviatoric part}\\ \text{of the pressure-}\\ \text{strain correlation}}}+\underbrace{T_{ij}}_{\substack{\text{Turbulent}\\ \text{diffusion}}}-\underbrace{\varepsilon_{ij}}_{\text{Dissipation}}+\frac{2}{3}\overline{p'\frac{\partial u_k'}{\partial x_k}}\delta_{ij}$$
$$-\left(\overline{u''}_i\frac{\partial\bar{p}}{\partial x_j}+\overline{u_j''}\frac{\partial\bar{p}}{\partial x_i}\right)+\left(\overline{u_i''}\frac{\partial\bar{\tau}_{jk}}{\partial x_k}+\overline{u''}_j\frac{\partial\bar{\tau}_{ik}}{\partial x_i}\right) \tag{2.42}$$

where

$$\begin{aligned}
P_{ij}&=-\bar{\rho}\left(\widetilde{u_i''u_k''}\frac{\partial\tilde{u}_j}{\partial x_k}+\widetilde{u_j''u_k''}\frac{\partial\tilde{u}_i}{\partial x_k}\right)\\
\Pi_{ij}&=\overline{p'\frac{\partial u_i'}{\partial x_j}}+\overline{p'\frac{\partial u_j'}{\partial x_i}}-\frac{2}{3}\overline{p'\frac{\partial u_k'}{\partial x_k}}\delta_{ij}\\
T_{ij}&=-\frac{\partial}{\partial x_k}\left[\bar{\rho}\widetilde{u_i''u_j''u_k''}+(\overline{p'u_i'}\delta_{jk}+\overline{p'u_j'}\delta_{ik})-(\overline{\tau_{ik}'u_j'}+\overline{\tau_{jk}'u_i'})\right]\\
\varepsilon_{ij}&=\overline{\tau_{ik}'\frac{\partial u_j'}{\partial x_k}}+\overline{\tau_{jk}'\frac{\partial u_i'}{\partial x_k}}
\end{aligned} \tag{2.43}$$

The term P_{ij} is in closed form. On the other hand, the terms Π_{ij}, T_{ij} and ε_{ij} require further modelling. Several closures are available for Π_{ij}, e.g. the models of Launder et al. [133] (LRR), Fu et al. [74] (FLT) and Speziale et al. [208] (SSG). The details of these closures are conveniently summarised in [207] and omitted here for brevity. The diffusion term may be modelled using the generalised gradient-diffusion hypothesis of Daly and Harlow [47]:

$$T_{ij}=-C_s\frac{\partial}{\partial x_k}\left(\rho\frac{\tilde{k}}{\tilde{\varepsilon}}\widetilde{u_k''u_l''}\frac{\partial\widetilde{u_i''u_j''}}{\partial x_l}\right) \tag{2.44}$$

where $C_s=0.22$. Lien and Leschziner [137] note that the expansion of Eq. (2.44) results in a number of cross-diffusion terms, which may lead to numerical instabilities. Alternatively, they suggest the simpler isotropic model

$$T_{ij}=-\frac{\partial}{\partial x_k}\left(\frac{\bar{\rho}\nu_t}{\sigma_k}\frac{\partial\widetilde{u_i''u_j''}}{\partial x_k}\right) \tag{2.45}$$

where $\sigma_k = 0.82$ when $C_s = 0.22$ [137]. The dissipation term is modelled as [202]:

$$\varepsilon_{ij} = \frac{2}{3}\bar{\rho}\tilde{\varepsilon}_s(1 + \alpha \mathrm{Ma}_t^2)\delta_{ij} \tag{2.46}$$

where ε_s is the solenoidal dissipation, $\alpha = 1$ is a model constant, $\mathrm{Ma}_t = (2\tilde{k}/a^2)^{1/2}$ is the turbulent Mach number, $a = (\gamma R\tilde{T})^{1/2}$ is the speed of sound, and γ is the specific heat ratio. The transport equation of ε_s is given by [202]:

$$\underbrace{\bar{\rho}\frac{\partial \tilde{\varepsilon}_s}{\partial t}}_{\substack{\text{Local rate}\\ \text{of change}}} + \underbrace{\bar{\rho}\tilde{u}_i\frac{\partial \tilde{\varepsilon}_s}{\partial x_i}}_{\text{Convection}} = \underbrace{C_\varepsilon \frac{\partial}{\partial x_k}\left(\bar{\rho}\frac{\tilde{k}}{\tilde{\varepsilon}_s}\widetilde{u_k'' u_j''}\frac{\partial \tilde{\varepsilon}_s}{\partial x_j}\right)}_{\text{Turbulent diffusion}} + \underbrace{C_{\varepsilon 1}\frac{\tilde{\varepsilon}_s}{\tilde{k}}\frac{P_{ii}}{2}}_{\text{Production}} \underbrace{-C_{\varepsilon 2}\bar{\rho}\frac{\tilde{\varepsilon}_s^2}{\tilde{k}}}_{\text{Dissipation}} \tag{2.47}$$

where $C_{\varepsilon 1} = 1.44$ and $C_{\varepsilon 1} = 1.92$ and $C_\varepsilon = 1.8$. If diffusion is assumed to be isotropic, Eq. (2.47) becomes very similar to the $\tilde{\varepsilon}$ equation of the $k - \varepsilon$ model, except that the model constant σ_ε needs to be modified to 1.0 [137]. The means of the Favre velocity fluctuations in Eq. (2.43) are modelled as [202]:

$$\overline{u_i''} = \frac{\nu_t}{\bar{\rho}\mathrm{Sc}_t}\frac{\partial \bar{\rho}}{\partial x_i} \tag{2.48}$$

Obviously, the r.h.s. of Eq. (2.48) is zero in constant-density flows. In such flows, the last two terms on the r.h.s. of Eq. (2.42) vanish. The turbulence kinetic energy is computed from the trace of the Reynolds stress tensor following Eq. (2.37). As in the $k - \varepsilon$ model, the eddy viscosity is computed using Eq. (2.39).

The Reynolds stress model is applicable to any turbulent flow [192]. In general, it is more accurate than two-equation models. However, it is relatively more complicated and computationally expensive. Seven additional equations need to be solved (six for $\widetilde{u_i'' u_j''}$ and one for $\tilde{\varepsilon}_s$) compared to two in the case of two-equation models.

The mean viscous stress tensor

If the turbulent fluctuations of μ are assumed to be negligible, the mean viscous stress tensor in Eq. (2.33) may be written as [207]:

$$\bar{\tau}_{ij} = \overline{\mu\left(\frac{\partial u_i}{\partial x_j} + \frac{\partial u_j}{\partial x_i} - \frac{2}{3}\frac{\partial u_k}{\partial x_k}\delta_{ij}\right)} \approx \bar{\mu}\left(\frac{\partial \tilde{u}_i}{\partial x_j} + \frac{\partial \tilde{u}_j}{\partial x_i} - \frac{2}{3}\frac{\partial \tilde{u}_k}{\partial x_k}\delta_{ij}\right) \tag{2.49}$$

The mean viscous dissipation

The mean viscous dissipation is approximated as [207]:

$$\overline{\tau_{ij}\frac{\partial u_i}{\partial x_j}} = \bar{\tau}_{ij}\frac{\partial \tilde{u}_i}{\partial x_j} + \bar{\tau}_{ij}\frac{\partial \overline{u_i''}}{\partial x_j} + \bar{\rho}\tilde{\varepsilon}_s(1+\alpha \mathrm{Ma}_t^2) \tag{2.50}$$

where $\overline{u_i''}$ is closed using Eq. (2.48).

The pressure-velocity correlation

This term appears on the r.h.s. of Eq. (2.35). It is usually neglected in RANS [187]. Using the decomposition $p = \bar{p} + p'$, it may be expanded as [134]:

$$\overline{u_i''\frac{\partial p}{\partial x_i}} = \overline{u_i''}\frac{\partial \bar{p}}{\partial x_i} + \overline{u_i''\frac{\partial p'}{\partial x_i}} \tag{2.51}$$

The first term on the r.h.s. of Eq. (2.51) is modelled using Eq. (2.48). It vanishes in constant-density flows.

The mean molecular diffusive fluxes

Neglecting the turbulent fluctuations of the density and diffusivity, the mean molecular diffusive flux of species κ in Eq. (2.34) is approximated as [187]:

$$\overline{J_i^{Y_\kappa}} = -\overline{\rho D\frac{\partial Y_\kappa}{\partial x_i}} \approx -\bar{\rho}\bar{D}\frac{\partial \tilde{Y}_\kappa}{\partial x_i} \tag{2.52}$$

where $\bar{D}$ is the mean molecular diffusivity. Similarly, under the assumption of unity Lewis number, the mean molecular diffusive flux of h in Eq. (2.35) is expressed as:

$$\overline{J_i^h} = -\overline{\rho D\frac{\partial h}{\partial x_i}} \approx -\bar{\rho}\bar{D}\frac{\partial \tilde{h}}{\partial x_i} \tag{2.53}$$

The species and enthalpy turbulent fluxes

In the framework of eddy viscosity models, the species and enthalpy turbulent fluxes are modelled using the gradient diffusion assumption:

$$\widetilde{u_i''Y_\kappa''} = -\frac{\nu_t}{\mathrm{Sc}_t}\frac{\partial \tilde{Y}_\kappa}{\partial x_i} \tag{2.54}$$

$$\widetilde{u_i''h''} = -\frac{\nu_t}{\mathrm{Pr}_t}\frac{\partial \tilde{h}}{\partial x_i} \tag{2.55}$$

where Sc_t and Pr_t are, respectively, the turbulent Schmidt and Prandtl numbers, and ν_t is computed from Eq. (2.39). Under the assumption of unity Lewis number, Sc_t and Pr_t are equal. Unless indicated, Sc_t is set to 0.7 following Jones and Whitelaw [98]. For simplicity of notation, the turbulent diffusivity

$$D_t = \frac{\nu_t}{\mathrm{Sc}_t} \tag{2.56}$$

is employed hereafter in the representation of turbulent fluxes. In high Reynolds number flows, the magnitude of D_t is much larger than that of $\bar{D}$. Therefore, transport by turbulent fluxes dominates and transport by molecular diffusion may be neglected for simplicity.

On the other hand, in RSM, transport equations for the turbulent fluxes of passive or reactive scalars can be derived and solved. These equations can be found in [95, 134]. Alternatively, the generalised gradient-diffusion hypothesis [47] may be employed. When the latter approach is adopted and diffusion is further assumed to be isotropic, Eqs. (2.54) and (2.55) may be used [137].

The mean chemical reaction rate

As described in Sect. 2.1.3, $\dot{\omega}_\kappa$ ($\kappa = 1, 2, \ldots, N_s$) is a non-linear function of the density, temperature and species mass fractions. Therefore, its mean, $\overline{\dot{\omega}}_\kappa$, cannot be simply expressed in terms of the means of these quantities, i.e. $\overline{\dot{\omega}}_\kappa(\rho, T, Y_\kappa) \neq \dot{\omega}_\kappa(\bar{\rho}, \widetilde{T}, \widetilde{Y}_\kappa)$. This can be demonstrated by considering the irreversible one-step reaction between fuel F and oxidiser O with products P:

$$\mathrm{F} + \mathrm{O} \rightarrow \mathrm{P} \tag{2.57}$$

Following Eqs. (2.8)-(2.10), the fuel burning rate is

$$\dot{\omega}_F(\rho, T, Y_\mathrm{F}, Y_\mathrm{O}) = -A\rho^2 T^b \frac{Y_\mathrm{F}}{W_\mathrm{F}}\frac{Y_\mathrm{O}}{W_\mathrm{O}}\exp\left(-\frac{T_a}{T}\right) \tag{2.58}$$

It is obvious from Eq.(2.58) that $\dot{\omega}_\mathrm{F}$ is non-linear. It can be shown using a Taylor series expansion that the mean reaction rate has the form [26, 187, 230]:

$$\begin{aligned}\overline{\dot{\omega}}_\mathrm{F} = \dot{\omega}_F(\bar{\rho}, \widetilde{T}, \widetilde{Y}_\mathrm{F}, \widetilde{Y}_\mathrm{O})\Bigg[1 + \frac{\widetilde{Y_\mathrm{F}''Y_\mathrm{O}''}}{\widetilde{Y}_\mathrm{F}\widetilde{Y}_\mathrm{O}} + (P_1 + Q_1)\left(\frac{\widetilde{Y_\mathrm{F}''T''}}{\widetilde{Y}_\mathrm{F}\widetilde{T}} + \frac{\widetilde{Y_\mathrm{O}''T''}}{\widetilde{Y}_\mathrm{O}\widetilde{T}}\right) \\ + (P_2 + Q_2 + P_1Q_1)\left(\frac{\widetilde{T''^2}}{\widetilde{T}^2} + \frac{\widetilde{Y_\mathrm{F}''T''^2}}{\widetilde{Y}_\mathrm{F}\widetilde{T}^2} + \frac{\widetilde{Y_\mathrm{O}''T''^2}}{\widetilde{Y}_\mathrm{O}\widetilde{T}^2}\right) + \cdots\Bigg]\end{aligned} \tag{2.59}$$

where

$$P_n = \sum_{k=1}^{n} (-1)^{n-k} \frac{(n-1)!}{(n-k)![(k-1)!]^2 k} \left(\frac{T_a}{\widetilde{T}}\right)^k; \quad Q_n = \frac{1}{n!} \prod_{k=1}^{n} (b-k) \tag{2.60}$$

To a first-order approximation, Eq. (2.59) reduces to $\overline{\dot{\omega}}_{\mathrm{F}} = \dot{\omega}_F(\bar{\rho}, \widetilde{T}, \widetilde{Y}_{\mathrm{F}}, \widetilde{Y}_{\mathrm{O}})$. Three difficulties are associated with Eq. (2.59) when the higher-order terms are retained [26, 187, 230]:

1. The correlations $\widetilde{Y''_{\mathrm{F}} Y''_{\mathrm{O}}}$, $\widetilde{T''^n}$ and $\widetilde{Y_\kappa T''^n}$ ($\kappa = \mathrm{O}, \mathrm{F}$) are unclosed. Their closure requires either using algebraic models or solving their respective transport equations.

2. The chemical reaction rate may be poorly estimated if only few terms of the expansion are retained in Eq. (2.59) due to large truncation errors. Such errors become substantial when the magnitudes of the correlations are significant.

3. Equation (2.59) is only applicable to an irreversible one-step chemical reaction. Extension to realistic multi-step chemical kinetics is complicated and impractical due to the emergence of a large number of unclosed correlations.

Based on the above, the mean reaction rate is not closed using Eq. (2.59). Alternatively, a combustion model is employed in order to fulfil this requirement. Some modelling strategies will be reviewed in Sect. 2.3.6.

The mean radiative source

The mean radiative source $\overline{\dot{\omega}}_r$ in the enthalpy equation, Eq. (2.35), should be retained in situations where radiative heat transfer influences the local enthalpy balance [178]. Temperature variations due to radiation can affect the local flame structure and have significant influence on flammability, ignition, extinction, flame propagation, and pollutant formation.

The modelling of the turbulence-combustion-radiation interactions is complicated in nature. Beside the necessity for a detailed description of the spectral characteristics of the main chemical species, the accurate modelling of radiation requires the solution of the radiative transfer equations [187]. Therefore, accounting for radiative effects entails additional computational costs. A number of statistical, zonal and flux methods commonly employed for the modelling of radiative heat transfer are reviewed in [38, 232].

Since detailed radiation modelling is beyond the scope of this work, a simplified and inexpensive approach is adopted. The radiative source is modelled by assuming that the

medium is optically thin with cold non-reflecting boundaries. This assumption is suitable for open non-sooting flames that are distant from their surrounding boundaries. According to this assumption, there is no incident energy from the boundaries of the system and the emitted energy passes within the system without attenuation by absorption or scattering [204]. Since absorption and scattering are neglected in the optically thin limit, radiative heat losses due solely to emission may be overestimated. This observation is confirmed in the numerical findings of Barlow et al. [15], who note, however, that such treatment can yield superior results compared to adiabatic calculations. The rate of radiative heat loss per unit volume is calculated as [14]:

$$\dot{\omega}_r = 4\sigma \sum_{\kappa=1}^{N_r} p_\kappa a_{p,\kappa} (T^4 - T_b^4) \tag{2.61}$$

where $\sigma = 5.669 \times 10^8$ W/m^{2}K^4 is the Stefan-Boltzmann constant, N_r is the number of the participating species included in the radiation calculations, p_κ and $a_{p,\kappa}$ are the partial pressure and the Planck mean absorption coefficient of participating species κ, respectively, and T_b is the background temperature. T_b is included in Eq. (2.61) in order to avoid the unphysical scenario where the mixture cools below the temperature of the surroundings [14]. The set of participating species depends on the nature of the fuel. Two fuels are mainly considered in this work, CH_4 and H_2. In CH_4 combustion, the predominantly participating species are H_2O, CH_4, CO_2, and CO, whereas in H_2 combustion, only H_2O is considered. Curve fits for the Planck mean absorption coefficients are available in [14,144]. In this work, the fits and their corresponding coefficients are obtained from [14]. These fits are constructed using the RADCAL program [81] and are valid for temperatures ranging between 300 K and 2500 K. They are given by [14]:

$$\begin{aligned}
a_{p,\mathrm{H_2O}} &= C_{0,\mathrm{H_2O}} + C_{1,\mathrm{H_2O}} \frac{10^3}{T} + C_{2,\mathrm{H_2O}} \left(\frac{10^3}{T}\right)^2 + C_{3,\mathrm{H_2O}} \left(\frac{10^3}{T}\right)^3 + C_{4,\mathrm{H_2O}} \left(\frac{10^3}{T}\right)^4 \\
&\quad + C_{5,\mathrm{H_2O}} \left(\frac{10^3}{T}\right)^5 \\
a_{p,\mathrm{CH_4}} &= C_{0,\mathrm{CH_4}} + C_{1,\mathrm{CH_4}} T + C_{2,\mathrm{CH_4}} T^2 + C_{3,\mathrm{CH_4}} T^3 + C_{4,\mathrm{CH_4}} T^4 \\
a_{p,\mathrm{CO_2}} &= C_{0,\mathrm{CO}} + C_{1,\mathrm{CO_2}} \frac{10^3}{T} + C_{2,\mathrm{CO_2}} \left(\frac{10^3}{T}\right)^2 + C_{3,\mathrm{CO_2}} \left(\frac{10^3}{T}\right)^3 + C_{4,\mathrm{CO_2}} \left(\frac{10^3}{T}\right)^4 \\
&\quad + C_{5,\mathrm{CO_2}} \left(\frac{10^3}{T}\right)^5 \\
a_{p,\mathrm{CO}} &= C_{0,\mathrm{CO}} + T\{C_{1,\mathrm{CO}} + T[C_{2,\mathrm{CO}} + T(C_{3,\mathrm{CO}} + TC_{4,\mathrm{CO}})]\}
\end{aligned} \tag{2.62}$$

The coefficients $C_{0-5,\kappa}$ employed in Eq. (2.62) are provided in Table 2.1.

Table 2.1: Coefficients employed in the curve fits of the Planck mean absorption coefficients given in Eq. (2.62) [14].

Species (κ)	H_2O	CH_4	CO_2	CO	
				$300 \leq T\,[\mathrm{K}] \leq 750$	$750 < T\,[\mathrm{K}] \leq 2500$
$C_{0,\kappa}$	-0.23093	6.6334	18.741	4.7869	10.09
$C_{1,\kappa}$	-1.1239	-0.0035686	-121.31	-0.06953	-0.01183
$C_{2,\kappa}$	9.4153	1.6682×10^{8}	273.5	2.95775×10^{4}	4.7753×10^{6}
$C_{3,\kappa}$	-2.9988	2.5611×10^{10}	-194.05	-4.25732×10^{7}	5.87209×10^{10}
$C_{4,\kappa}$	0.51382	-2.6558×10^{14}	56.31	2.02894×10^{10}	-2.5334×10^{14}
$C_{5,\kappa}$	1.8684×10^{5}	–	-5.8169	–	–

2.2.3 Direct Numerical Simulation

In DNS, all the scales of motion are resolved by directly solving the instantaneous three-dimensional (3D) Navier-Stokes equations for a given set of initial and boundary conditions, without performing any averaging or applying any modelling. Each DNS computation yields a single realisation of the flow. Therefore, DNS is considered to be the simplest yet the most accurate approach in CFD [68]. However, the computational cost associated with DNS is extremely high due to the necessity of resolving all the scales of motion. The computational domain is usually chosen to be a box of side L, such that L is large enough to represent the energy-containing integral scales. Therefore, L must be a few times the integral scale, l. The grid spacing in 1D, Δx, needs to be at least as small as the Kolmogorov scale, η, in order to resolve the small dissipative scales of the energy spectrum (see Fig. 2.1). To satisfy this requirement, the number of grid points in each dimension, N, must be at least L/η (for a uniform grid distribution), which is proportional to $\mathrm{Re}_l^{3/4}$ where Re_l is the Reynolds number based on the magnitude of the velocity fluctuations and l [68]. Thus, the overall resolution in 3D is at least of the order of $\mathrm{Re}_l^{9/4}$. For this reason, DNS is restricted to small Re_l flows. Another important consideration in DNS is the time step employed to advanced the solution in time. The choice of this quantity is limited by the desired level of numerical accuracy. The Navier-Stokes equations are typically solved using pseudo-spectral methods, which introduce aliasing errors [192]. Time-stepping strategies, error control, implementation and other aspects of DNS are discussed in more detail in [68, 192].

The DNS of turbulent reacting flows imposes further computational challenges. First, an additional set of transport equations needs to be solved for the species mass fractions and temperature (or enthalpy). This requirement increases the computational cost tremen-

dously. In practice, global or reduced chemical kinetics consisting of a small number of species and limited number of steps are employed in order to decrease the number of the governing equations.

Due to the limitations highlighted above, DNS is restricted to low Re_l reacting flows with simplified chemistry. It is, however, a valuable validation tool for turbulence modellers as it provides the most accurate solution for a given problem.

2.2.4 Large Eddy Simulation

LES is a three-dimensional time-dependent computational approach wherein large scale eddies are resolved and small scale eddies are modelled. Therefore, LES is more accurate than RANS, but less accurate than DNS. The idea behind LES originates from the fact that the transport of conserved properties is primarily achieved by the large energetic eddies, whereas transport by the smaller eddies is weaker [68].

In LES, a flow variable f is decomposed into resolved (grid) and subgrid scale components. The LES equation of f is obtained by applying a spatial filter to its transport equation. The Favre filtering of f is performed using $\bar{\rho}\tilde{f}(x_i) = \int_{\mathcal{D}} \rho F(x_i', \Delta) f(x_i - x_i') dx_i'$ where $\mathcal{D}$ denotes the integration domain, F is a filter function, Δ is the filter width, and $\bar{\rho}$ is the filtered density. Some examples of filters are the Gaussian, box and cutoff filters. A comprehensive overview of these functions is available in [187, 192]. The filter width Δ is a length scale associated with every filter function such that eddies larger than Δ are considered to be large eddies, whereas smaller ones are considered to be small eddies [68]. There are two differences between Favre filtering and Favre averaging [187]: (1) the filtered and double filtered values of f are not equal in general and (2) the filtered fluctuation of f is not zero. The filtered conservation equations can be found in [187]. The Favre-filtered conservation equations are similar in form to the Favre-averaged equations. Filtering yields several unclosed terms such as the unresolved Reynolds stresses and turbulent fluxes and the filtered molecular diffusion fluxes and chemical reaction rate. The modelling of these quantities and the integration of turbulent combustion models in the framework of LES are discussed in [187].

The computational cost of LES is high due to the necessity of resolving the large scales of motions. However, the length scale requirements are less restrictive compared to DNS [187]. Evidently, the integral length scale must be contained in the computational domain. Therefore, $l < N\Delta x$. The cutoff scale between the resolved and unresolved eddies, l_c, must lie in the inertial subrange of the turbulence kinetic energy spectrum (see Fig. 2.1). Hence, $\eta < l_c < l$. Assuming $l_c = q\eta$ with $1 < q < \mathrm{Re}_l^{3/4}$, the resolution of l_c requires

$l_c > \Delta x$, which leads to $N > \mathrm{Re}_l^{3/4}/q$ with $q > 1$. This requirement is less stringent than the $N > \mathrm{Re}_l^{3/4}$ requirement necessary in DNS. Therefore, the cost of LES is lower. Further details on LES can be found in [68, 187, 192].

2.3 Turbulent combustion modelling

2.3.1 Modes of combustion

This section provides a brief overview of non-premixed, premixed, and partially premixed combustion. The distinction between the three combustion modes is based on the nature of the initial mixing between the fuel and oxidiser.

Non-premixed combustion

Non-premixed combustion is encountered in gas turbines, jet and diesel engines, furnaces, burners and fires. Most non-premixed problems are concerned with the mixing and reaction of two streams, one supplying a fuel and the other providing an oxidiser [21]. The two streams are initially unmixed. They enter separately into the combustion domain where they mix and burn. The resulting flame is referred to as a diffusion flame because the rate of molecular diffusion is slower than that of chemical reaction. As shown in Fig. 2.2(a), the fuel and oxidiser are located on both sides of the reaction zone, which is wide due to the continuous interdiffusion of reactants and products. In this zone, reactants are consumed and the temperature increases, leading to heat release. The flame is incapable of propagating towards the fuel due to the lack of oxidiser, and likewise, it is incapable of propagating towards the oxidiser due to the lack of fuel [187].

When the diffusion time scale is much larger than the chemical time scale, diffusion is the rate-controlling process and the chemistry is considered to be infinitely fast. In this situation, the assumption of chemical equilibrium becomes suitable [178]. When the orders of two scales are comparable, the assumption of chemical equilibrium does not hold and non-equilibrium effects due to finite-rate chemistry have to be taken into account [178]. The discussion of the relative magnitude of these scales is deferred to Sect. 2.3.3.

Premixed combustion

Premixed combustion is encountered in gas turbines, jet and spark-ignition engines, afterburners and explosions [21]. In premixed problems the fuel and oxidiser are initially

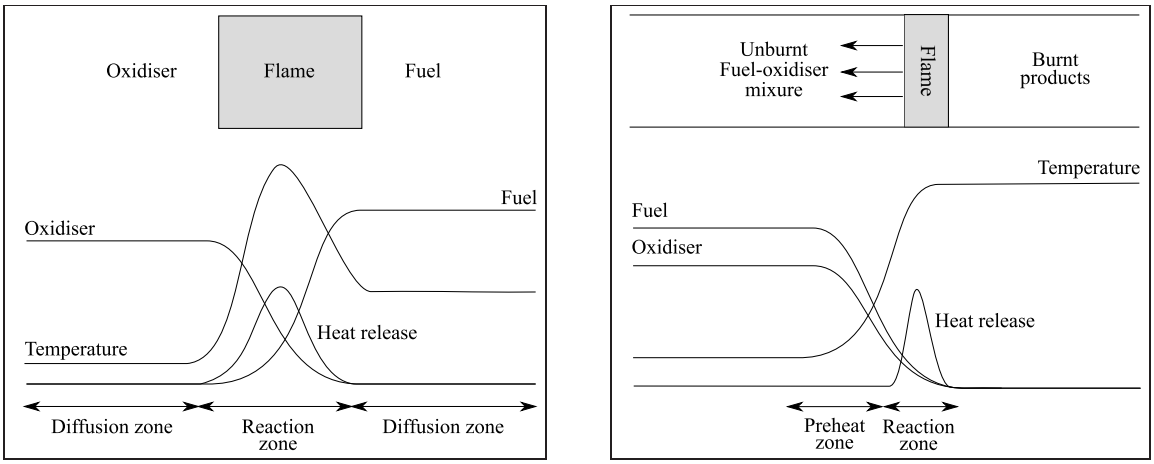

(a) Non-premixed flame

(b) Premixed flame

Figure 2.2: Structures of non-premixed and premixed flames (reproduced from [230]).

mixed. The pre-mixing process should take place at sufficiently low temperatures in order to prevent fuel oxidation [178]. As depicted in Fig. 2.2(b), the unburnt fuel-oxidiser mixture and burnt products are separated by a thin reaction zone where a sharp temperature gradient develops. In contrast to non-premixed flames, premixed flames are capable of propagating towards the unburnt fuel-oxidiser mixture. The sharp temperature gradient leads to thermal fluxes out of reaction zone. These fluxes pre-heat the unburnt mixtures causing them to burn. The propagation mechanism is due to the local imbalance between heat diffusion and chemical consumption [230].

Partially premixed combustion

When the fuel and oxidiser enter the combustion domain separately and undergo some partial mixing before burning, combustion occurs in a stratified medium where the partially premixed parcels are ignited by an adjacent flame zone. This mode of combustion is referred to as partially premixed [178]. It is encountered in aircraft gas turbines, direct-injection gasoline engines, and diesel engines [178].

2.3.2 Stochastic description of turbulent reacting flows

Turbulent combustion is a stochastic process in which the velocity components and scalar quantities such as the temperature, pressure and species mass fractions are fluctuating

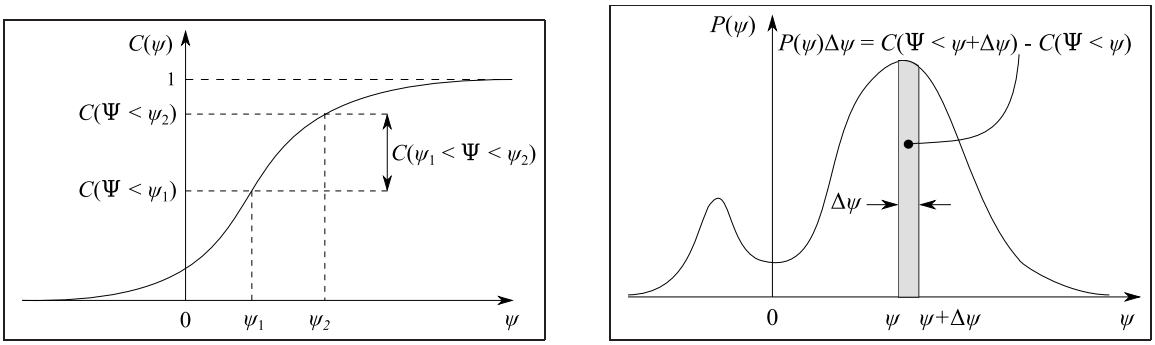

(a) (b)

Figure 2.3: (a) cumulative distribution function and (b) probability of the event $\psi < \Psi < \psi + \Delta\psi$ (reproduced from [120]).

variables. One way to quantify these variables is to characterize them by their Probability Density Functions (PDF) [120]. Given a stochastic variable Ψ with a sample space variable, ψ, the cumulative probability $C(\Psi < \psi)$ is defined as the probability of occurrence of Ψ such that $\Psi < \psi$. With this definition in mind, C is an increasing function bounded by 0 and 1 since $\lim_{\psi \to -\infty} C(\Psi < \psi) = 0$ and $\lim_{\psi \to +\infty} C(\Psi < \psi) = 1$. This is illustrated in Fig. 2.3(a). Given two values of ψ, ψ_1 and ψ_2, $C(\psi_1 < \Psi < \psi_2) = C(\Psi < \psi_2) - C(\Psi < \psi_1)$. Referring to Fig. 2.3(b), the PDF of ψ, $P(\psi)$, is related to C by:

$$P(\psi) = \lim_{\Delta\psi \to 0} \frac{C(\Psi < \psi + \Delta\psi) - C(\Psi < \psi)}{\Delta\psi} = \frac{dC(\Psi < \psi)}{d\psi} \tag{2.63}$$

such that

$$\int_{-\infty}^{+\infty} P(\psi) d\psi = 1 \tag{2.64}$$

The expectation of Ψ is given by:

$$\langle \Psi \rangle = \int_{-\infty}^{+\infty} \psi P(\psi) d\psi \tag{2.65}$$

and the expectation of a given deterministic function definition $F(\Psi)$ is given by:

$$\langle F(\Psi) \rangle = \int_{-\infty}^{+\infty} F(\psi) P(\psi) d\psi \tag{2.66}$$

Given two stochastic variables Ψ_1 and Ψ_2 with sample space variables ψ_1 and ψ_1, the joint PDF of ψ_1 and ψ_2, $P(\psi_1, \psi_2)$, is expressed using Bayes' theorem as:

$$P(\psi_1, \psi_2) = P(\psi_1 | \Psi_2 = \psi_2) P(\psi_2) \tag{2.67}$$

where $P(\psi_1|\Psi_2 = \psi_2)$ is the conditional PDF of ψ_1 with respect to ψ_2 and $P(\psi_2)$ is the marginal PDF of ψ_2. If ψ_1 and ψ_2 are statistically independent, $P(\psi_1|\Psi_2 = \psi_2) = P(\psi_1)$ and Eq. (2.67) becomes:

$$P(\psi_1, \psi_2) = P(\psi_1)P(\psi_2) \tag{2.68}$$

The conditional expectation of Ψ_1 such that $\Psi_2 = \psi_2$ is given by:

$$\langle \Psi_1|\Psi_2 = \psi_2\rangle = \int_{-\infty}^{+\infty} \psi_1 P(\psi_1|\Psi_2 = \psi_2)d\psi_1 = \frac{\int_{-\infty}^{+\infty} \psi_1 P(\psi_1, \psi_2)d\psi_1}{P(\psi_2)} \tag{2.69}$$

and the conditional expectation of any deterministic function $F(\Psi_1)$ conditioned at $\Psi_2 = \psi_2$ is given by:

$$\langle F(\Psi_1)|\Psi_2 = \psi_2\rangle = \int_{-\infty}^{+\infty} F(\psi_1)P(\psi_1|\Psi_2 = \psi_2)d\psi_1 = \frac{\int_{-\infty}^{+\infty} F(\psi_1)P(\psi_1, \psi_2)d\psi_1}{P(\psi_2)} \tag{2.70}$$

The unconditional expectation of $F(\Psi_1)$ is retrieved from $\langle F(\Psi_1)|\Psi_2 = \psi_2\rangle$ as:

$$\langle F(\Psi_1)\rangle = \int_{-\infty}^{+\infty} \langle F(\Psi_1)|\Psi_2 = \psi_2\rangle P(\psi_2)d\psi_2 \tag{2.71}$$

The relations above are extensively used in the modelling of turbulent combustion (Sect. 2.3.6 and Chaps. 3 and 8) and may be extended to an arbitrary number of stochastic variables.

2.3.3 Turbulence-chemistry interactions

The interactions between turbulence and chemistry can be described in terms of the Damköhler number, Da, which is defined as the ratio of a characteristic residence time scale, τ_r, to the chemical time scale, τ_c. A possible definition for τ_r in non-premixed flames is the diffusion (or mixing) time scale, τ_d, which is inversely proportional to the stoichiometric scalar dissipation rate, χ_{st}. The scalar dissipation rate measures the local rate of mixing (discussed in more detail in Sect. 2.3.4). τ_c corresponds to the time scale of the rate-determining chemical reaction. Thus, Da is written as:

$$D_a = \frac{\tau_d}{\tau_c} \tag{2.72}$$

Three chemical regimes may be distinguished based on the relative magnitudes of τ_d and τ_c, which enables their classification in terms of Da:

1. **Fast chemistry:** if Da $>$ 1 ($\tau_c < \tau_d$), the reaction time is shorter than the mixing time and chemical reactions take place at a faster rate than diffusion. In the case where $\mathrm{D_a} \gg 1$ (in the limit Da $\to \infty$), chemical reactions are considered to be infinitely fast. This leads to the local chemical equilibrium assumption wherein chemical reactions proceed locally in a fast manner such that equilibrium is reached instantaneously [187]. In this situations, the reactive scalars tend to their equilibrium values.

2. **Slow chemistry:** if Da $<$ 1 ($\tau_c > \tau_d$), the reaction time is longer than the mixing time and the chemistry is considered to be slow. In this case, the species are mixed by the flow before chemical reactions start to take place. When Da $\ll$ 1 (in the limit Da $\to$ 0) the chemical time scale becomes very small and pure (frozen or inert) mixing occurs without any reaction [230].

3. **Finite-rate chemistry:** this regime is intermediate between the slow and fast chemistry regimes. It manifests when the chemical and turbulent time scales are of comparable orders, i.e. when Da $\sim$ 1. In this situation, chemistry and mixing are both influential. The assumption of local chemical equilibrium is invalid and non-equilibrium effects must be accounted for [178, 187].

2.3.4 The mixture fraction variable

The mixture fraction, ξ, plays a key role in the modelling of non-premixed and partially-premixed combustion. It is a conserved (passive) scalar that describes the mixedness of reactants. In order to define ξ, the single-step reversible reaction between a fuel F and an oxidiser O with products P is considered:

$$\nu'_{\mathrm{F}}\,\mathrm{F} + \nu'_{\mathrm{O}}\,\mathrm{O} \leftrightarrows \nu''_{\mathrm{P}}\,\mathrm{P} \tag{2.73}$$

Assuming unity Lewis numbers, the mass fractions of the reacting species are governed by:

$$\rho\frac{\partial Y_\kappa}{\partial t} + \rho u_i\frac{\partial Y_\kappa}{\partial x_i} = \frac{\partial}{\partial x_i}\left(\rho D\frac{\partial Y_\kappa}{\partial x_i}\right) + \dot{\omega}_\kappa, \quad \kappa = \mathrm{F,\ O\ and\ P} \tag{2.74}$$

where the diffusivities of all species are assumed to be constant and equal to D. Using Eq. (2.8), $\dot{\omega}_{\mathrm{F}} = W_{\mathrm{F}}\nu'_{\mathrm{F}}q$ and $\dot{\omega}_{\mathrm{O}} = W_{\mathrm{O}}\nu'_{\mathrm{O}}q$. Introducing the stoichiometric oxidiser-to-fuel mass ratio, $r = \nu'_{\mathrm{O}}W_{\mathrm{O}}/\nu'_{\mathrm{F}}W_{\mathrm{F}}$, $\dot{\omega}_{\mathrm{O}} = r\dot{\omega}_{\mathrm{F}}$. Setting $\kappa = \mathrm{F}$ in Eq.(2.74) and multiplying the resulting equation by r, then subtracting Eq.(2.74) with $\kappa = \mathrm{O}$, yield:

$$\rho\frac{\partial \hat{\xi}}{\partial t} + \rho u_i\frac{\partial \hat{\xi}}{\partial x_i} = \frac{\partial}{\partial x_i}\left(\rho D\frac{\partial \hat{\xi}}{\partial x_i}\right) \tag{2.75}$$

where $\hat{\xi} = rY_F - Y_O$. In two-feed systems, $\hat{\xi}$ may be normalized as:

$$\xi = \frac{\hat{\xi} - \hat{\xi}_2}{\hat{\xi}_1 - \hat{\xi}_2} = \frac{rY_F - Y_O + Y_{O,2}}{rY_{F,1} + Y_{O,2}} \tag{2.76}$$

where $\hat{\xi}_1 = rY_{F,1}$ and $\hat{\xi}_2 = -Y_{O,2}$ denote $\hat{\xi}$ in the fuel and oxidiser streams, respectively. ξ in Eq.(2.76) is the mixture fraction. It varies between 0 (pure oxidiser) and 1 (pure fuel), and it is governed by the transport equation:

$$\rho\frac{\partial \xi}{\partial t} + \rho u_i \frac{\partial \xi}{\partial x_i} = \frac{\partial}{\partial x_i}\left(\rho D \frac{\partial \xi}{\partial x_i}\right) \tag{2.77}$$

Mixture fraction-based combustion models such as the flamelet models [177, 178] (Sect. 2.3.6) and CMC [120] (Chap. 3) require the knowledge of the Favre mean, variance and dissipation of the mixture fraction, $\tilde{\xi}$, $\widetilde{\xi''^2}$ and $\tilde{\chi}$, respectively. The variables are required for the construction of the two-parameter presumed PDF of ξ and for the quantification of mixing.

The mixture fraction mean

Using the decomposition $\xi = \tilde{\xi} + \xi''$ in Eq. (2.77) and averaging results in the Favre-averaged transport equation of ξ:

$$\bar{\rho}\frac{\partial \tilde{\xi}}{\partial t} + \bar{\rho}\tilde{u}_i \frac{\partial \tilde{\xi}}{\partial x_i} = \underbrace{\frac{\partial}{\partial x_i}\left(\overline{\rho D \frac{\partial \xi}{\partial x_i}}\right)}_{\substack{\text{Transport by} \\ \text{molecular diffusion}}} - \underbrace{\frac{\partial(\bar{\rho}\widetilde{u_i'' \xi''})}{\partial x_i}}_{\substack{\text{Turbulent} \\ \text{transport}}} \tag{2.78}$$

Transport by molecular diffusion is often neglected in high Re flows. The turbulent flux $\widetilde{u_i'' \xi''}$ appearing in the turbulent transport term is usually closed using the gradient diffusion assumption:

$$\widetilde{u_i'' \xi''} = -D_t \frac{\partial \tilde{\xi}}{\partial x_i} \tag{2.79}$$

With these assumptions, Eq. (2.78) simplifies to:

$$\bar{\rho}\frac{\partial \tilde{\xi}}{\partial t} + \bar{\rho}\tilde{u}_i \frac{\partial \tilde{\xi}}{\partial x_i} = \frac{\partial}{\partial x_i}\left(\bar{\rho} D_t \frac{\partial \tilde{\xi}}{\partial x_i}\right) \tag{2.80}$$

The mixture fraction variance

The transport equation of the Favre-averaged mixture fraction variance, $\widetilde{\xi''^2}$, is obtained using Eqs. (2.77) and (2.78). The derivation is outlined in [187]. The resulting expression is given by:

$$\bar{\rho}\frac{\partial\widetilde{\xi''^2}}{\partial t}+\bar{\rho}\tilde{u}_i\frac{\partial\widetilde{\xi''^2}}{\partial x_i}=\underbrace{\frac{\partial}{\partial x_i}\left(\overline{\rho D\frac{\partial\xi''^2}{\partial x_i}}\right)+2\overline{\xi''\frac{\partial}{\partial x_i}\left(\rho D\frac{\partial\tilde{\xi}}{\partial x_i}\right)}}_{\text{Transport by molecular diffusion}}\\ \underbrace{-\frac{\partial(\bar{\rho}\widetilde{u_i''\xi''^2})}{\partial x_i}}_{\substack{\text{Turbulent}\\ \text{transport}}}\underbrace{-2\bar{\rho}\widetilde{u_i''\xi''}\frac{\partial\tilde{\xi}}{\partial x_i}}_{\text{Production}}\underbrace{-2\overline{\rho D\frac{\partial\xi''}{\partial x_i}\frac{\partial\xi''}{\partial x_i}}}_{\text{Dissipation}} \tag{2.81}$$

As in Eq. (2.78), transport by molecular diffusion is neglected in high Re flows and the turbulent flux $\widetilde{u_i''\xi''}$ in the production term is modelled using Eq. (2.79). The gradient diffusion assumption is reinvoked to close $\widetilde{u_i''\xi''^2}$ in the turbulent transport term:

$$\widetilde{u_i''\xi''^2}=-D_t\frac{\partial\widetilde{\xi''^2}}{\partial x_i} \tag{2.82}$$

By definition, the scalar dissipation is expressed as:

$$\chi=2D\frac{\partial\xi}{\partial x_i}\frac{\partial\xi}{\partial x_i} \tag{2.83}$$

Multiplying Eq. (2.83) by ρ and taking the mean results in:

$$\bar{\rho}\tilde{\chi}=\underbrace{2\overline{\rho D}\frac{\partial\tilde{\xi}}{\partial x_i}\frac{\partial\tilde{\xi}}{\partial x_i}}_{\bar{\rho}\tilde{\chi}_m}+4\overline{\rho D\frac{\partial\xi''}{\partial x_i}\frac{\partial\tilde{\xi}}{\partial x_i}}+\underbrace{2\overline{\rho D\frac{\partial\xi''}{\partial x_i}\frac{\partial\xi''}{\partial x_i}}}_{\bar{\rho}\tilde{\chi}_p} \tag{2.84}$$

where $\tilde{\chi}_m$ and $\tilde{\chi}_p$ are the scalar dissipation rates due to $\tilde{\xi}$ and ξ'', respectively. In constant-density flows, the second term on the r.h.s. is zero. In RANS, mean gradients (first term on the r.h.s.) are usually neglected against fluctuation gradients (third term on the r.h.s.). Accordingly, Eq. (2.84) reduces to:

$$\bar{\rho}\tilde{\chi}\approx\bar{\rho}\tilde{\chi}_p=2\overline{\rho D\frac{\partial\xi''}{\partial x_i}\frac{\partial\xi''}{\partial x_i}} \tag{2.85}$$

As such, Eq. (2.81) may be written as:

$$\bar{\rho}\frac{\partial\widetilde{\xi''^2}}{\partial t}+\bar{\rho}\tilde{u}_i\frac{\partial\widetilde{\xi''^2}}{\partial x_i}=\frac{\partial}{\partial x_i}\left(\bar{\rho}D_\mathrm{t}\frac{\partial\widetilde{\xi''^2}}{\partial x_i}\right)+\underbrace{2\bar{\rho}D_\mathrm{t}\frac{\partial\tilde{\xi}}{\partial x_i}\frac{\partial\tilde{\xi}}{\partial x_i}-\bar{\rho}\tilde{\chi}}_{\substack{\text{Source term of the } \widetilde{\xi''^2} \\ \text{transport equation, } \tilde{S}_{\widetilde{\xi''^2}}}} \tag{2.86}$$

The scalar dissipation rate

The scalar dissipation rate, which appears as a source term in Eq. (2.86), measures the local rate of mixing. Its inverse provides a characteristic mixing (or diffusion) time scale. It is standard practice to model this quantity algebraically as [177, 178, 187, 201]:

$$\tilde{\chi}=C_\chi\frac{\tilde{\varepsilon}}{\tilde{k}}\widetilde{\xi''^2} \tag{2.87}$$

where C_χ is a model constant usually set to 2. In this model, it is assumed that the flow time ($\tilde{k}/\tilde{\varepsilon}$) is proportional to the time scale of scalar turbulence ($\widetilde{\xi''^2}/\tilde{\chi}$), with C_χ being the proportionality constant (the time scale ratio). In situations where C_χ is not constant, Eq. (2.87) becomes incapable of capturing all the characteristics of scalar dissipation. To resolve this issue, a transport equation for $\tilde{\chi}$ must be solved. This equation reads [95]:

$$\begin{aligned}\bar{\rho}\frac{\partial\tilde{\chi}}{\partial t}+\bar{\rho}\tilde{u}_i\frac{\partial\tilde{\chi}}{\partial x_i}=&\underbrace{\frac{\partial}{\partial x_i}\left(C_s\bar{\rho}\widetilde{u_i''u_j''}\frac{\tilde{k}}{\tilde{\varepsilon}}\frac{\partial\tilde{\chi}}{\partial x_j}\right)}_{\text{Turbulent transport}}-\underbrace{C_1\bar{\rho}\frac{\tilde{\chi}^2}{\widetilde{\xi''^2}}}_{\substack{\text{Dissipation due to} \\ \text{scalar destruction} \\ \text{of fluctuations}}}-\underbrace{C_2\bar{\rho}\frac{\tilde{\varepsilon}}{\tilde{k}}\tilde{\chi}}_{\substack{\text{Dissipation due to} \\ \text{mechanical destruc-} \\ \text{tion of fluctuations}}}\\&-\underbrace{2C_3\bar{\rho}\frac{\tilde{\varepsilon}}{\tilde{k}}\widetilde{u_i''\xi''}\frac{\partial\tilde{\xi}}{\partial x_i}}_{\substack{\text{Production due to} \\ \text{mean scalar gradients}}}-\underbrace{C_4\bar{\rho}\frac{\tilde{\chi}}{\tilde{k}}\widetilde{u_i''u_j''}\frac{\partial\tilde{u}_i}{\partial x_j}}_{\substack{\text{Production due to} \\ \text{mean velocity gradients}}}\end{aligned} \tag{2.88}$$

where C_s and C_{1-4} are model constants. Sanders and Gökalp [201] provide a comprehensive review of the constants available in the literature. Here, the constants proposed by Jones and Musonge [95] are adopted when Eq. (2.88) is solved: $C_s=0.22$, $C_1=1$, $C_2=C_{\varepsilon 2}-1$, $C_3=1.70$ and $C_4=C_{\varepsilon 1}$. The turbulent flux $\widetilde{u_i''\xi''}$ is modelled using the gradient diffusion assumption, Eq. (2.79). When the Reynolds stress model is employed, the Reynolds stresses $\widetilde{u_i''u_j''}$ appearing in the fifth term on the r.h.s. of Eq. (2.88) are readily available

from the solution of their transport equations. When the $k-\varepsilon$ model is employed, $\widetilde{u_i'' u_j''}$ is modelled using the Boussinesq hypothesis provided in Eq. (2.36). The tensor $C_s \bar{\rho} \widetilde{u_i'' u_j''} \tilde{k}/\tilde{\varepsilon}$ appearing in the first term on the r.h.s. of Eq. (2.88) represents the anisotropic diffusivity. When expanded, this term may lead to numerical instabilities and convergence issues [137]. Therefore, for simplicity, the diffusivity is assumed to be isotropic and the simplifying approach of Lien and Leschziner [137] is adopted:

$$\frac{\partial}{\partial x_i}\left(C_s \bar{\rho} \widetilde{u_i'' u_j''} \frac{\tilde{k}}{\tilde{\varepsilon}} \frac{\partial \tilde{\chi}}{\partial x_j}\right) \approx \frac{\partial}{\partial x_i}\left(\frac{\bar{\rho}\nu_t}{\sigma_\chi} \frac{\partial \tilde{\chi}}{\partial x_i}\right) \tag{2.89}$$

where $\sigma_\chi = 0.82$ when $C_s = 0.22$. With the modelling assumptions outlined above, Eq. (2.88) simplifies to:

$$\begin{aligned} \bar{\rho}\frac{\partial \tilde{\chi}}{\partial t} + \bar{\rho}\tilde{u}_i \frac{\partial \tilde{\chi}}{\partial x_i} =& \frac{\partial}{\partial x_i}\left(\frac{\bar{\rho}\nu_t}{\sigma_\chi}\frac{\partial \tilde{\chi}}{\partial x_i}\right) - C_1 \bar{\rho}\frac{\tilde{\chi}^2}{\widetilde{\xi''^2}} - C_2 \bar{\rho}\frac{\tilde{\varepsilon}}{\tilde{k}}\tilde{\chi} + 2C_3 \bar{\rho} D_t \frac{\tilde{\varepsilon}}{\tilde{k}} \frac{\partial \tilde{\xi}}{\partial x_i}\frac{\partial \tilde{\xi}}{\partial x_i} \\ & - C_4 \bar{\rho}\frac{\tilde{\chi}}{\tilde{k}} \widetilde{u_i'' u_j''} \frac{\partial \tilde{u}_i}{\partial x_j} \end{aligned} \tag{2.90}$$

2.3.5 Progress variables

A PV is a tool employed in the modelling of premixed and partially premixed turbulent combustion. A PV serves as marker for the distinction between burnt and unburnt mixtures. It allows the determination of the flame position by tracking the evolution of reaction. A PV may be defined as the mass fraction of a species (or a combination of species) or the temperature (or a temperature-related quantity such as the sensible enthalpy) [36, 230]. The selected PV is usually normalised such that it varies between zero and one. A normalised PV is written as:

$$c = \frac{\phi - \phi_{min}}{\phi_{max} - \phi_{min}} \tag{2.91}$$

where ϕ is a generic PV governed by the transport equation:

$$\underbrace{\rho\frac{\partial \phi}{\partial t}}_{\substack{\text{Local rate} \\ \text{of change}}} + \underbrace{\rho u_i \frac{\partial \phi}{\partial x_i}}_{\text{Convection}} = \underbrace{\frac{\partial}{\partial x_i}\left(\rho D_\phi \frac{\partial \phi}{\partial x_i}\right)}_{\text{Diffusion}} + \underbrace{\dot{\omega}_\phi}_{\substack{\text{Chemical} \\ \text{source}}} \tag{2.92}$$

The normalisation parameters ϕ_{min} and ϕ_{max} are the minimum and maximum values of ϕ. For a given equivalence ratio, ϕ_{min} and ϕ_{max} in premixed flames are set to the inert

(unburnt) and equilibrium (fully burnt) values of ϕ, respectively. As such, the position of the flame corresponds to values of c lying between zero and one [230]. The transport equation of c is obtained by introducing $\phi = c(\phi_{max} - \phi_{min}) + \phi_{min}$ in Eq. (2.92). The final result is given by [187, 230]:

$$\underbrace{\rho\frac{\partial c}{\partial t}}_{\substack{\text{Local rate}\\ \text{of change}}} + \underbrace{\rho u_i \frac{\partial c}{\partial x_i}}_{\text{Convection}} = \underbrace{\frac{\partial}{\partial x_i}\left(\rho D_\phi \frac{\partial c}{\partial x_i}\right)}_{\text{Diffusion}} + \underbrace{\dot{\omega}_c}_{\substack{\text{Chemical}\\ \text{source}}} \quad ; \qquad \dot{\omega}_c = \frac{\dot{\omega}_\phi}{\phi_{max} - \phi_{min}} \tag{2.93}$$

The transport equations of the Favre mean and variance of c can be found in [187].

In the modelling of partially premixed combustion, ϕ_{min} and ϕ_{max} are defined as functions of ξ in order to account for the presence of non-premixed parcels in the mixture [28, 55, 56, 138]. When this is the case, additional terms involving the dissipation of ξ and the cross-dissipation of ξ and c arise on the r.h.s. of Eq. (2.93). The derivation of this equation is deferred to Sect. 8.2.

2.3.6 Turbulent combustion models

The difficulties associated with the direct averaging of the chemical reaction rate, which were discussed in Sect. 2.2, prompted the need for alternative closures. Such closures are formulated from physical analysis [187].

Before proceeding to the description of CMC (Chap. 3), some of the turbulent combustion models available in the literature are reviewed in this section. Models devised primarily for non-premixed (and in some cases applicable to premixed and/or partially premixed) combustion with infinitely fast and finite-rate chemistry are emphasised.

Eddy dissipation model

The Eddy Dissipation Model (EDM) of Magnussen and Hjertager [141] is applicable to flames exhibiting infinitely fast chemistry (Da $\gg 1$). In such flames, since the chemical time scale is much smaller than the mixing time scale, the latter is viewed as the rate-determining scale. Accordingly, EDM assumes that the rate of burning is controlled by turbulent mixing, and therefore eliminates the effect of chemical kinetics. Considering the one-step irreversible reaction between a fuel F and oxidiser O with products P and stoichiometric oxidiser-to-fuel mass ratio r

$$\mathrm{F} + r\mathrm{O} \rightarrow (1 + r)\mathrm{P} \tag{2.94}$$

the mean burning rate rate is taken as the lowest of three reaction rates [141, 178, 187]:

$$\overline{\dot{\omega}} = A\frac{\bar{\rho}}{\tau_t}\min\left(\widetilde{Y}_{\mathrm{F}}, \frac{1}{r}\widetilde{Y}_{\mathrm{O}}, \frac{B}{1+r}\widetilde{Y}_{\mathrm{P}}\right), \tag{2.95}$$

where $\widetilde{Y}_{\mathrm{F}}$, $\widetilde{Y}_{\mathrm{O}}$ and $\widetilde{Y}_{\mathrm{P}}$ are, respectively, the mean mass fractions of F, O and P, and τ_t is the turbulent mixing time scale. τ_t is set equal to the integral time scale ($\tau_t = \tau_l = \tilde{k}/\tilde{\varepsilon}$). A and B are model constants assigned the values 4 and 0.5, respectively [141].

EDM is attractive due to its simplicity and ease of implementation, however, it presents several limitations. The model is only applicable in the fast chemistry limit to kinetics described by Eq. (2.94) and two-step kinetics with intermediate species. Further, the constants A and B are not universal and need to be adjusted for a particular application [178, 187].

Eddy dissipation concept

To overcome the restrictions of EDM , Magnusen [140] extends the EDM in order to allow the inclusion of multi-step and finite-rate chemical kinetics. The extension is known as the Eddy Dissipation Concept (EDC). In this model, chemical reactions are assumed to take place in small turbulent structures referred to as "fine structures". The fraction of the flow occupied by these regions, or the length fraction, is obtained from [80]:

$$\gamma = \left(\frac{3C_{D2}}{4C_{D1}^2}\right)^{1/4}\left(\frac{\nu\tilde{\varepsilon}}{\tilde{k}^2}\right)^{1/4} \tag{2.96}$$

The time scale for mass transfer between the fine structures and their surroundings (the characteristic time scale of the fine structures) is expressed in terms of the Kolmogorov time scale as:

$$\tau^* = \left(\frac{C_{D2}}{3}\right)^{1/2}\underbrace{\left(\frac{\nu}{\tilde{\varepsilon}}\right)^{1/2}}_{\substack{\text{Kolmogorov}\\ \text{time scale}}} \tag{2.97}$$

where $C_{D1} = 0.134$ and $C_{D2} = 0.5$ are model constants. The mean chemical reaction rate of species κ is obtained from:

$$\overline{\dot{\omega}}_\kappa = \bar{\rho}\frac{\gamma^2}{\tau^*(1-\gamma^3)}(Y_\kappa^* - \widetilde{Y}_\kappa) \tag{2.98}$$

Where Y_κ^* is the mass fractions of species κ in the fine structure. The effect of chemical kinetics, which is absent in EDM, is accounted for in EDC through this quantity. Y_κ^* is calculated by assuming that reaction in the fine structure occurs at constant pressure. As such, the fine structures are viewed as constant-pressure homogeneous reactors. The details of this approach are provided in [80]. Essentially, reactions proceed over the time scale τ^* via Eq. (2.8) and the governing equations of the reactor are solved numerically for a given chemical kinetics mechanism. Since τ^* is a fraction of the Kolmogorov scale, the system of equations, which is highly non-linear in nature due to reaction, is very stiff. For this reason, the computational cost of EDM is high.

Linear eddy model

The Linear Eddy Model (LEM) was initially developed by Kerstein [101, 102] for non-reacting flows, and later extended by the author to reacting flows [103, 104]. The idea behind LEM is to treat molecular diffusion and chemical reaction separately from convective stirring. The distinction among these processes is achieved by means of a reduced one-dimensional (1D) description of the scalar field [150]. The physical interpretation of the 1D domain depends on the configuration of the application. For instance, in turbulent round jets, reactive scalars $\phi_\alpha(x_i, t)$ are computed along transverse lines that move with the mean fluid velocity. Two simultaneous steps are required to determine $\phi_\alpha(x_i, t)$. In the first, the 1D time evolution of $\phi_\alpha(x_i, t)$ by means of diffusion and reaction is treated explicitly [150]. This requires the numerical solution of the 1D parabolic diffusion-reaction equations:

$$\frac{\partial(\rho\phi_\alpha)}{\partial t} = \frac{\partial}{\partial x}\left(\rho D_\alpha \frac{\partial \phi_\alpha}{\partial x}\right) + \dot{\omega}_\alpha \tag{2.99}$$

In the second step, convective stirring is accounted for stochastically by means of randomly occurring rearrangement events of the scalar field along the domain [150]. Each event involves a permutation of the cells of the spatially-discretized concentration field. Each permutation is confined to a finite segment of the computational domain, and may be viewed as a local representation of the effect of an individual eddy on the concentration field [103]. Permutation rules such as "block inversion" and the "triplet map" are discussed in [103]. In order to represent all the eddies, the size of the permutation events ranges between the Kolmogorov and integral length scales. Therefore, the computational cost of LEM is high.

Laminar flamelet model

Peters [178] defines flamelets as "thin reactive-diffusive layers embedded within an otherwise nonreacting turbulent flow field". As such, a turbulent diffusion flame is viewed as an ensemble of laminar diffusion flamelets [177]. This approach is valid when chemistry is fast compared to mixing (Da > 1), such that chemical activity is highest within a very thin layer. If the thickness of this layer is smaller than the size of a Kolmogorov eddy, turbulence does not affect the local structure of the flame and the flame is therefore considered to be locally laminar [178].

The idea behind this modelling approach is to separate the solution of the turbulent flow and mixing mixture fields from chemistry. The latter is precomputed and tabulated prior to performing the turbulence calculations, which leads to substantial reductions in computational cost. Coupling between turbulence and chemistry is achieved through ξ and χ. To accomplish this, a coordinate system attached to the surface of stoichiometric mixture is first introduced such that the first coordinate x_1, which is by definition locally normal to the surface, is replaced by ξ, whereas the tangential coordinates x_2 and x_3 lie within the surface. The flamelet equations are then derived by applying the coordinate transformation described in [177, 178]. In the process, asymptotic arguments are invoked in order to show that the derivatives of reactive scalars in the tangential directions are negligible in comparison to those in the normal direction [177, 178]. Neglecting pressure and radiation effects while assuming unity mixture fraction Lewis number and constant (but unequal) species Lewis numbers, the species and temperature equations are given by [184]:

$$\rho\frac{\partial Y_\kappa}{\partial t} = \underbrace{\frac{\rho}{\mathrm{Le}_\kappa}\frac{\chi}{2}\frac{\partial^2 Y_\kappa}{\partial \xi^2}}_{\text{Diffusion}} \underbrace{-\frac{1}{4}\left(1-\frac{1}{\mathrm{Le}_\kappa}\right)\frac{\partial(\rho\chi)}{\partial\xi}\frac{\partial Y_\kappa}{\partial\xi}}_{\text{Differential diffusion}} + \underbrace{\dot{\omega}_\kappa}_{\substack{\text{Chemical}\\ \text{reaction}\\ \text{rate}}} \qquad \kappa = 1, 2, \cdots, N_s \tag{2.100}$$

and

$$\rho\frac{\partial T}{\partial t} = \underbrace{\rho\frac{\chi}{2}\left[\frac{1}{c_p}\left(\frac{\partial c_p}{\partial\xi} + \sum_{\kappa=1}^{N_s}\frac{c_{p,\kappa}}{\mathrm{Le}_\kappa}\frac{\partial Y_\kappa}{\partial\xi}\right)\frac{\partial T}{\partial\xi} + \frac{\partial^2 T}{\partial\xi^2}\right]}_{\text{Conduction and diffusion}} \underbrace{-\frac{1}{c_p}\sum_{\kappa=1}^{N_s} h_\kappa\dot{\omega}_\kappa}_{\text{Heat release}} \tag{2.101}$$

These equations may be simplified further if Le_κ is assumed to be equal to unity. The scalar dissipation rate is related to the mixture fraction by [107]:

$$\chi = \frac{a}{\pi}Cf(\xi); \quad C = \frac{3}{8}\frac{[(\rho_O/\rho)^{1/2}+1]^2}{(\rho_O/\rho)^{1/2}+1}; \quad f(\xi) = \exp -2[\mathrm{erf}^{-1}(2\xi-1)]^2 \tag{2.102}$$

where a is the strain rate, ρ_O is the density of the oxidiser stream, and erf^{-1} is the inverse error function. The factor C accounts for density variations and reduces to unity in constant-density flows. Equivalently, the above relation can be expressed in terms of the stoichiometric scalar dissipation rate, χ_{st}, by evaluating Eq. (2.103) at $\xi = \xi_{st}$:

$$\chi = \chi_{st} \frac{C f(\xi)}{C_{st} f(\xi_{st})} \tag{2.103}$$

where C_{st} is the value of C at stoichiometry. The Favre averages of the species mass fractions and the temperature are obtained from [187]:

$$\tilde{Y}_\kappa = \frac{1}{\bar{\rho}} \int_0^{+\infty} \int_0^1 \rho Y_\kappa(\xi, \chi_{st}) \tilde{P}(\xi, \chi_{st}) d\xi d\chi_{st} \tag{2.104}$$

and

$$\tilde{T} = \frac{1}{\bar{\rho}} \int_0^{+\infty} \int_0^1 \rho T(\xi, \chi_{st}) \tilde{P}(\xi, \chi_{st}) d\xi d\chi_{st} \tag{2.105}$$

where the mean density is computed from [178]:

$$\bar{\rho} = \left(\int_0^1 \rho^{-1}(\xi) \tilde{P}(\xi) d\xi \right)^{-1} \tag{2.106}$$

In Eqs. (2.104) and (2.105), $\tilde{P}(\xi, \chi_{st})$ is the Favre joint PDF of ξ and χ_{st}. These two variables are often assumed to be statistically independent leading to [187]:

$$\tilde{P}(\xi, \chi_{st}) = \tilde{P}(\xi) \tilde{P}(\chi_{st}) \tag{2.107}$$

where $\tilde{P}(\xi)$ and $\tilde{P}(\chi_{st})$ are the marginal PDFs of ξ and χ_{st}. $\tilde{P}(\xi)$ is usually presumed using the β-PDF [178] which requires the solution of the $\tilde{\xi}$ and $\widetilde{\xi''^2}$ transport equations (Eqs. (2.80) and (2.86)). This probability distribution is discussed in more detail in Sect. 3.3.1. If the fluctuations of χ_{st} are neglected, $\tilde{P}(\chi_{st})$ is represented using a Dirac-delta function:

$$\tilde{P}(\chi_{st}) = \delta(\chi_{st} - \widetilde{\chi}_{st}) \tag{2.108}$$

Otherwise, it is commonly presumed to follow the log-normal distribution given by [58]:

$$\tilde{P}(\chi_{st}) = \frac{1}{\chi_{st} \sigma (2\pi)^{1/2}} \exp\left[-\frac{(\ln \chi_{st} - \mu)^2}{2\sigma^2} \right] \tag{2.109}$$

where the parameters μ and σ are related to the first and second moments χ_{st} by:

$$\widetilde{\chi}_{st} = \exp\left(\mu + \frac{\sigma^2}{2} \right) \tag{2.110}$$

and

$$\widetilde{\chi_{st}''^2} = \tilde{\chi}_{st}^2[\exp(\sigma^2) - 1] \tag{2.111}$$

To determine $\widetilde{\chi}_{st}$, Eq. (2.103) is weighted by $\tilde{P}(\xi)$ and integrated over the mixture fraction space. This leads to:

$$\widetilde{\chi}_{st} = \tilde{\chi}\frac{C_{st}f(\xi_{st})}{\int_0^1 Cf(\xi)\tilde{P}(\xi)d\xi} \tag{2.112}$$

$\tilde{\chi}$ can be obtained either from the algebraic model given by Eq. (2.87) or from the solution of its transport equation, Eq. (2.90). The parameter σ is assumed to be constant. Effelsberg and Peters [58] suggest setting it to unity, which leads to $\widetilde{\chi_{st}''^2} \approx 1.7183\tilde{\chi}_{st}^2$ via Eq. (2.111). Using this value of σ in Eq. (2.110) along with $\widetilde{\chi}_{st}$ from Eq. (2.112) provides the parameter μ.

The assumption of negligible transient effects in Eqs. (2.100) and (2.101) leads to the so-called Stationary (or Steady) Laminar Flamelet Model (SLFM). The underlying assumption in SLFM is that the scalar dissipation rate varies slowly [178], which is the case when Da > 1. To generate the SLFM library, discrete values of χ_{st} are first inserted in Eq. (2.103). Equations (2.100) and (2.101) are then solved subject to the mass fractions and temperature boundary conditions at $\xi = 0$ and $\xi = 1$, which are obtained from the conditions of the oxidiser and fuel streams, respectively. The steady-state solutions of $Y_\kappa(\xi, \chi_{st})$ and $T(\xi, \chi_{st})$ are finally stored in the library. This procedure is performed for several χ_{st} values ranging between the chemical equilibrium value ($\chi_{st} = 0$) to a quenching value χ_q. When Da ~ 1 (finite rate chemistry) or Da < 1 (slow chemistry), the scalar dissipation rate varies rapidly. Therefore, transient effects are retained, leading to the so-called unsteady laminar flamelet model. Two modelling approaches are briefly described here: the Lagrangian flamelet model [183] and the Eulerian particle flamelet model [17]. In the first, the scalar dissipation rate is a function of time, space and mixture fraction, and the unsteady flamelet equations are solved interactively with the turbulent flow and mixing solver. In the second, numerical tracer particles are introduced into the turbulent flow field, with each particle representing a flamelet. The tracking of the particles is accomplished by solving a marker equation for each particle.

Various extensions to the classical laminar flamelet theory are available in the literature. For instance, the two-mixture fraction flamelet model of Hasse et al. [83] which allows the modelling of three-feed combustion systems (two fuel and one oxidiser streams). Another example is the flamelet/progress variable approach of Pierce and Moin [180] where reactive scalars are tabulated in terms of ξ and a reaction progress variable. The incorporation of the latter makes the modelling of local extinction, re-ignition and lift-off possible. Another extension is the Multidimensional Flamelet-generated Manifolds (MFM) of Nguyen et al.

[172] wherein the full set of species conservation equations is projected into a restricted subset of the composition space, thus allowing the modelling of flames where the premixed, partially premixed, and non-premixed regimes coexist. As will be shown in Chap. 8, MFM is closely related to the homogeneous version of the proposed DCMC method.

PDF methods

PDF methods [190, 191] are very versatile as they are valid for both premixed and non-premixed turbulent combustion modes and applicable to infinitely fast and finite-rate chemistry. The major advantage of PDF methods over combustion models that seek closure for the chemical reaction rate is that this quantity appears in closed form, and therefore does not require any modelling. Two methods are briefly described here: the composition and the velocity-composition joint PDF methods.

Composition joint PDF method Considering a set of $\sigma \geq 1$ composition variables $\boldsymbol{\phi} = \{\phi_1, \phi_2, \cdots, \phi_\sigma\}$, and introducing σ sample space variables $\boldsymbol{\psi} = \{\psi_1, \psi_2, \cdots, \psi_\sigma\}$, the joint PDF of $\boldsymbol{\phi}$, $P_{\boldsymbol{\phi}}(\boldsymbol{\psi})$, is defined as the probability density of the compound event $\boldsymbol{\phi} = \boldsymbol{\psi}$, or in other words, the probability density of the events $\phi_1 = \psi_1$, $\phi_2 = \psi_2$, ..., $\phi_\sigma = \psi_\sigma$ [191]. The composition joint PDF transport equation is derived starting from the general transport equation:

$$\rho \frac{\partial \phi_\alpha}{\partial t} + \rho u_i \frac{\partial \phi_\alpha}{\partial x_i} = -\frac{\partial J_i^\alpha}{\partial x_i} + \dot{\omega}_\phi \tag{2.113}$$

where J_i^α and $\dot{\omega}_\phi$ are, respectively, the i^{th} component of the molecular diffusive flux and the chemical reaction rate of ϕ_α. The Favre-averaged equation is given by [190, 191]:

$$\underbrace{\frac{\partial \tilde{P}_{\boldsymbol{\phi}}}{\partial t}}_{\substack{\text{local rate} \\ \text{of change}}} + \underbrace{\tilde{u}_i \frac{\partial \tilde{P}_{\boldsymbol{\phi}}}{\partial x_i}}_{\text{Convection}} = \underbrace{-\frac{\partial}{\partial \psi_\alpha}\left(\frac{1}{\rho}\dot{\omega}_\alpha(\boldsymbol{\psi})\tilde{P}_{\boldsymbol{\phi}}\right)}_{\substack{\text{Divergence of the flux} \\ \text{of probability due} \\ \text{to chemical reaction}}} \underbrace{-\frac{1}{\bar{\rho}}\frac{\partial(\bar{\rho}\langle u_i''|\boldsymbol{\psi}\rangle \tilde{P}_{\boldsymbol{\phi}})}{\partial x_i}}_{\text{Turbulent transport}} + \underbrace{\frac{\partial}{\partial \psi_\alpha}\left(\left\langle \frac{1}{\rho}\frac{\partial J_i^\alpha}{\partial x_i}\middle|\boldsymbol{\psi}\right\rangle \tilde{P}_{\boldsymbol{\phi}}\right)}_{\text{Molecular mixing}} \tag{2.114}$$

where $\tilde{P}_{\boldsymbol{\phi}} = \tilde{P}_{\boldsymbol{\phi}}(\boldsymbol{\psi}; x_i, t)$ is the Favre-joint PDF of $\boldsymbol{\phi}(x_i, t)$. It is related to the PDF $P_{\boldsymbol{\phi}}(\boldsymbol{\psi}; x_i, t)$ and the mass density function $\mathcal{P}_{\boldsymbol{\phi}}(\boldsymbol{\psi}; x_i, t)$ by [190, 191]:

$$\bar{\rho}\tilde{P}_{\boldsymbol{\phi}}(\boldsymbol{\psi}; x_i, t) = \rho(\boldsymbol{\psi}) P_{\boldsymbol{\phi}}(\boldsymbol{\psi}; x_i, t) = \mathcal{P}_{\boldsymbol{\phi}}(\boldsymbol{\psi}; x_i, t) \tag{2.115}$$

The first term on the r.h.s. of Eq. (2.114) is in closed form because $\dot{\omega}_\alpha(\boldsymbol{\psi})$ depends directly on the local variables of the composition field $\boldsymbol{\psi}$ [190]. In contrast, the second and third

terms on the r.h.s. are unclosed and require further modelling. The quantity $\bar{\rho}\langle u_i''|\boldsymbol{\psi}\rangle\tilde{P}_{\boldsymbol{\phi}}$ in the second term, which involves the conditional mean of the Favre velocity fluctuations, is modelled using the gradient diffusion assumption [190, 191]:

$$\bar{\rho}\langle u_i''|\boldsymbol{\psi}\rangle\tilde{P}_{\boldsymbol{\phi}} = -\bar{\rho}D_t\frac{\partial\tilde{P}_{\boldsymbol{\phi}}}{\partial x_i} \tag{2.116}$$

The closure of the third term is achieved using a stochastic model that simulates the process of scalar dissipation [190, 191]. Three mixing models are the Interaction by Exchange with the Mean (IEM) [231], the Modified Curl (MC) [93], and the Euclidean Minimum Spanning Tree (EMST) [214] models.

Pope [190, 191] identifies two shortcomings in the composition PDF model. First, although common, the usage of the gradient diffusion assumption described by Eq. (2.116) is questionable in the context of variable-density reactive flows [190, 191]. Second, the model is not self-contained because the velocity and turbulence fields must be treated separately. The solution of Eq. (2.114) must be complemented with the mean momentum equation (to determine $\tilde{u}_i$) and a turbulence model (to determine D_t) [190, 191]. The velocity-composition PDF method described next overcomes these shortcomings.

Velocity-composition joint PDF method The velocity-composition joint PDF transport equation is derived using the equation of ϕ_α, Eq. (2.113), and the momentum equation, Eq. (2.2) [190, 191]. Neglecting gravitational effects, the equation of the mass density function $\mathcal{P}(\mathbf{V},\boldsymbol{\psi};x_i,t) = \rho(\boldsymbol{\psi})P(\mathbf{V},\boldsymbol{\psi};x_i,t)$ is given by:

$$\underbrace{\frac{\partial\mathcal{P}}{\partial t}}_{\substack{\text{local rate}\\ \text{of change}}} + \underbrace{V_j\frac{\partial\mathcal{P}}{\partial x_j}}_{\text{Convection}} = \underbrace{-\frac{\partial}{\partial\psi_\alpha}\left(\frac{1}{\rho(\boldsymbol{\psi})}\dot{\omega}_\alpha(\boldsymbol{\psi})\mathcal{P}\right)}_{\substack{\text{Divergence of the flux}\\ \text{of probability due}\\ \text{to chemical reaction}}} + \underbrace{\frac{1}{\rho(\boldsymbol{\psi})}\frac{\partial\bar{p}}{\partial x_j}\frac{\partial\mathcal{P}}{\partial V_j}}_{\substack{\text{Transport in velocity}\\ \text{space by the mean}\\ \text{pressure gradient}}}$$
$$+ \underbrace{\frac{\partial}{\partial V_j}\left(\frac{1}{\rho(\boldsymbol{\psi})}\left\langle -\frac{\partial\tau_{ij}}{\partial x_i} + \frac{\partial p'}{\partial x_j}\middle|\mathbf{V},\boldsymbol{\psi}\right\rangle\mathcal{P}\right)}_{\substack{\text{Transport in velocity space by viscous stresses}\\ \text{and the fluctuating pressure gradient}}} + \underbrace{\frac{\partial}{\partial\psi_\alpha}\left(\frac{1}{\rho(\boldsymbol{\psi})}\left\langle\frac{\partial J_j^\alpha}{\partial x_j}\middle|\mathbf{V},\boldsymbol{\psi}\right\rangle\mathcal{P}\right)}_{\substack{\text{Transport in composition space}\\ \text{by molecular mixing}}} \tag{2.117}$$

where $\mathbf{V} = \{V_1, V_2, V_3\}$ are three independent velocity variables. The first two terms on the r.h.s. of Eq. (2.117) are in closed form, whereas the last two require additional modelling. Stochastic approaches are employed to model these terms. Further details can be found in [190, 191].

Solution method Due to the high dimensionality of Eq. (2.117) and the associated large memory requirements, finite difference and finite volume discretisation methods are impractical [178]. Alternatively, the Lagrangian Monte Carlo method devised by Pope [190, 191] is employed. In this grid-free method, the mass of the fluid is discretised into a large number of N_p stochastic particles. From a Lagrangian point of view, each particle is described by its own position, velocity and composition. The details on this approach and its solution algorithm are available in [190, 191]. The main drawback of this technique is that statistical errors decrease slowly with increasing N_p [190]. Therefore, a large number of particles must be used, leading to increased computational requirements.

2.4 Summary

This chapter presented the conservation equations employed in the computations of reacting flows. Different computational approaches for the modelling of turbulence were presented, with emphasis on the eddy viscosity and Reynolds stress models. The modes of combustion, the stochastic nature of turbulent reacting flows, and the interactions between turbulence and chemistry were described. The mixture fraction and reaction progress variables were presented. Several models for non-premixed turbulent combustion with infinitely fast and finite-rate chemistry were reviewed.

The next chapter provides a detailed description of CMC and its numerical implementation, and a brief review of the advances made in the field.

Chapter 3

The Conditional Moment Closure

The CMC method employed in the four subsequent chapters is presented. The conditional transport equations are derived using the decomposition approach and the primary closure hypothesis is applied. Submodels for the resulting unclosed terms such as the PDF, the conditional turbulent fluxes, velocity, scalar dissipation rate, reaction rate, and radiative source are discussed. The numerical methods employed to solve the CMC equations are highlighted. A brief review of the advances made in CMC is provided. The topic discussed are the second-order closure for the conditional reaction rate, spray (two-phase) combustion, differential diffusion, premixed combustion, LES, and double-conditioning.

3.1 Background

Independently devised by Klimenko [118] and Bilger [18, 20], CMC is a mixture fraction-based turbulent combustion model primarily formulated for the description of turbulence-chemistry interactions in non-premixed combustion. In CMC, fluctuations of reactive scalars, such as the species mass fractions and temperature, are associated with those of the mixture fraction, ξ. This association is motivated by some exclusive features of ξ:

1. The magnitude of fluctuations about the averages of the reactive scalars conditioned on ξ are smaller than their counterparts about the unconditional averages.

2. ξ describes the mixedness of reactants and the stoichiometry of the reacting mixture.

3. ξ is a conserved scalar which is a desirable feature for modelling. Its transport equation does not involve any source terms, and hence no modelling assumptions are required.

4. The PDF of ξ can be accurately described by means of simple distributions requiring its mean and variance.

Therefore, reactive scalars in CMC are conditionally averaged on ξ, and their conditional transport equations are solved. Although the model equations attained by Klimenko [118] and Bilger [18, 20] are mathematically identical, different methodologies and assumptions are employed in the two derivations. In Klimenko's approach, the conditional transport equation of a given reactive scalar is obtained by first manipulating and combining the transport equations of the reactive scalar and the fine-grained PDF, then taking the expectation of the result (averaging). Bilger's derivation relies on the decomposition of the reactive scalar into a conditional mean and a fluctuation about this mean. The sum is introduced in the scalar's transport equation, and then the conditional average of the resulting expression is taken, ultimately leading to the same conditional transport equation obtained in the Klimenko's approach.

The next two sections present the governing CMC equations and the submodels necessary for the closure of the system of equations.

3.2 Conditional transport equations

3.2.1 Conditional species equation

Assuming unity Lewis numbers and equal mass diffusivities, the transport equation of a species κ (Eq. (2.4)) simplifies to:

$$\rho\frac{\partial Y_\kappa}{\partial t} + \rho u_i\frac{\partial Y_\kappa}{\partial x_i} = \frac{\partial}{\partial x_i}\left(\rho D\frac{\partial Y_\kappa}{\partial x_i}\right) + \dot{\omega}_\kappa \tag{3.1}$$

The conditional average of Y_κ is defined as:

$$Q_\kappa(\eta, \mathbf{x}, t) = \langle Y_\kappa(\mathbf{x}, t)|\xi(\mathbf{x}, t) = \eta\rangle \tag{3.2}$$

where $\langle\cdot|\cdot\rangle$ denotes the conditional average of the quantity to the left of the vertical bar subject to the quantity to its right, and η is a sample variable of ξ, such that $0 \leq \eta \leq 1$.

Following the decomposition approach proposed by Bilger [18,20], Y_κ is written as the sum of its conditional average Q_κ and a fluctuation y''_κ:

$$Y_\kappa(\mathbf{x},t) = Q_\kappa(\xi(\mathbf{x},t), x_i, t) + y''_\kappa(\mathbf{x},t) \tag{3.3}$$

such that $\langle y''_\kappa | \xi(\mathbf{x},t) = \eta \rangle = 0$. Substituting the transformations

$$\frac{\partial Y_\kappa}{\partial t} = \frac{\partial Q_\kappa}{\partial \eta}\frac{\partial \xi}{\partial t} + \frac{\partial Q_\kappa}{\partial t} + \frac{\partial y''_\kappa}{\partial t} \tag{3.4}$$

$$\frac{\partial Y_\kappa}{\partial x_i} = \frac{\partial Q_\kappa}{\partial \eta}\frac{\partial \xi}{\partial x_i} + \frac{\partial Q_\kappa}{\partial x_i} + \frac{\partial y''_\kappa}{\partial x_i} \tag{3.5}$$

$$\begin{aligned}\frac{\partial}{\partial x_i}\left(\rho D \frac{\partial Y_\kappa}{\partial x_i}\right) =& \frac{\partial Q_\kappa}{\partial \eta}\frac{\partial}{\partial x_i}\left(\rho D \frac{\partial \xi}{\partial x_i}\right) + \rho D \left(\frac{\partial \xi}{\partial x_i}\frac{\partial \xi}{\partial x_i}\right)\frac{\partial^2 Q_\kappa}{\partial \eta^2} \\ &+ \rho D \frac{\partial \xi}{\partial x_i}\frac{\partial}{\partial x_i}\left(\frac{\partial Q_\kappa}{\partial \eta}\right) + \frac{\partial}{\partial x_i}\left(\rho D \frac{\partial Q_\kappa}{\partial x_i}\right) + \frac{\partial}{\partial x_i}\left(\rho D \frac{\partial y''_\kappa}{\partial x_i}\right)\end{aligned} \tag{3.6}$$

into Eq. (3.1) and rearranging yield:

$$\begin{aligned}\rho\frac{\partial Q_\kappa}{\partial t} =& -\rho u_i \frac{\partial Q_\kappa}{\partial x_i} + \rho D\left(\frac{\partial \xi}{\partial x_i}\frac{\partial \xi}{\partial x_i}\right)\frac{\partial^2 Q_\kappa}{\partial \eta^2} + \dot{\omega}_\kappa \\ &+ \left[\frac{\partial}{\partial x_i}\left(\rho D \frac{\partial Q_\kappa}{\partial x_i}\right) + \rho D \frac{\partial \xi}{\partial x_i}\frac{\partial}{\partial x_i}\left(\frac{\partial Q_\kappa}{\partial \eta}\right)\right] \\ &- \left[\rho\frac{\partial y''_\kappa}{\partial t} + \rho u_i \frac{\partial y''_\kappa}{\partial x_i} - \frac{\partial}{\partial x_i}\left(\rho D \frac{\partial y''_\kappa}{\partial x_i}\right)\right] \\ &- \frac{\partial Q_\kappa}{\partial \eta}\left[\rho\frac{\partial \xi}{\partial t} + \rho u_i \frac{\partial \xi}{\partial x_i} - \frac{\partial}{\partial x_i}\left(\rho D \frac{\partial \xi}{\partial x_i}\right)\right]\end{aligned} \tag{3.7}$$

The bracketed quantity in the last term on the r.h.s. of Eq. (3.7) is zero via the mixture fraction transport equation (Eq. (2.77)). Taking the conditional average of Eq. (3.7) with respect to $\xi(x_i,t) = \eta$ while neglecting the density fluctuations results in[1]:

$$\frac{\partial Q_\kappa}{\partial t} = -\langle u_i|\eta\rangle \frac{\partial Q_\kappa}{\partial x_i} + \frac{\langle \chi|\eta\rangle}{2}\frac{\partial^2 Q_\kappa}{\partial \eta^2} + \frac{\langle \dot{\omega}_\kappa|\eta\rangle}{\langle \rho|\eta\rangle} + \frac{e_{Q_\kappa} + e_{y''_\kappa}}{\langle \rho|\eta\rangle} \tag{3.8}$$

where

$$e_{Q_\kappa} = \frac{\partial}{\partial x_i}\left(\rho D \frac{\partial Q_\kappa}{\partial x_i}\right) + \left\langle \rho D \frac{\partial \xi}{\partial x_i}\frac{\partial}{\partial x_i}\left(\frac{\partial Q_\kappa}{\partial \eta}\right)\middle|\eta\right\rangle, \tag{3.9}$$

[1]The notation $\langle\cdot|\eta\rangle$ is used in Eqs. (3.8)-(3.10) instead of $\langle\cdot|\xi(\mathbf{x},t)=\eta\rangle$ for simplicity.

$$e_{y''_\kappa} = -\left\langle \rho\frac{\partial y''_\kappa}{\partial t} + \rho u''_i\frac{\partial y''_\kappa}{\partial x_i} - \frac{\partial}{\partial x_i}\left(\rho D\frac{\partial y''_\kappa}{\partial x_i}\right)\middle|\eta\right\rangle, \tag{3.10}$$

and

$$\chi = 2D\frac{\partial\xi}{\partial x_i}\frac{\partial\xi}{\partial x_i} \tag{3.11}$$

is the scalar dissipation rate. The quantities $\langle u_i|\eta\rangle$, $\langle\chi|\eta\rangle$, and $\langle\dot{\omega}_\kappa|\eta\rangle$ are the conditional velocity, the conditional scalar dissipation rate, and the conditional chemical source, respectively. These terms are unclosed and require further modelling. The submodels employed in the implementation of CMC are discussed in Sect. 3.3. The primary closure hypothesis [18, 20, 120] is first invoked to model e_{Q_κ} (Eq. (3.9)) and $e_{y''_\kappa}$ (Eq. (3.10)).

By definition, the Schmidt number is given by:

$$\mathrm{Sc} = \frac{\mu}{\rho D} \tag{3.12}$$

Therefore, when Sc is finite, ρD scales as μ, which in turn scales as the inverse of the Reynolds number, Re^{-1}. As such, given finite Sc and high Re, all the terms in Eq. (3.9) can be neglected, leading to:

$$e_{Q_\kappa} \approx 0 \tag{3.13}$$

The unconditional mean of $e_{y''_\kappa}$ is expanded as [120]:

$$\begin{aligned}
\int_0^1 e_{y''_\kappa}P(\eta)d\eta &= -\int_0^1\left\langle\left[\rho\frac{\partial y''_\kappa}{\partial t} + \rho u_i\frac{\partial y''_\kappa}{\partial x_i} - \frac{\partial}{\partial x_i}\left(\rho D\frac{\partial y''_\kappa}{\partial x_i}\right)\right]\middle|\eta\right\rangle P(\eta)d\eta \\
&= -\left\langle\rho\frac{\partial y''_\kappa}{\partial t} + \rho u_i\frac{\partial y''_\kappa}{\partial x_i} - \frac{\partial}{\partial x_i}\left(\rho D\frac{\partial y''_\kappa}{\partial x_i}\right)\right\rangle \\
&= -\left\langle\frac{\partial\left(\rho y''_\kappa\right)}{\partial t}\right\rangle - \left\langle\frac{\partial\left(\rho u_i y''_\kappa\right)}{\partial x_i}\right\rangle + \left\langle\frac{\partial}{\partial x_i}\left(\rho D\frac{\partial y''_\kappa}{\partial x_i}\right)\right\rangle \\
&= -\frac{\partial\left\langle\rho y''_\kappa\right\rangle}{\partial t} - \frac{\partial\left\langle\rho u_i y''_\kappa\right\rangle}{\partial x_i} + \frac{\partial}{\partial x_i}\left\langle\rho D\frac{\partial y''_\kappa}{\partial x_i}\right\rangle
\end{aligned} \tag{3.14}$$

where the continuity equation was used in the transition from the second step to the third. If the conditional fluctuation of ρ are neglected,

$$\left\langle\rho y''_\kappa\right\rangle = \left\langle\left(\langle\rho|\eta\rangle + \rho''\right)y''_\kappa\right\rangle \approx \langle\rho|\eta\rangle\left\langle y''_\kappa\right\rangle \tag{3.15}$$

If the conditional fluctuations of D are also neglected,

$$\left\langle\rho D\frac{\partial y''_\kappa}{\partial x_i}\right\rangle = \left\langle\left(\langle\rho|\eta\rangle + \rho''\right)\left(\langle D|\eta\rangle + D''\right)\frac{\partial y''_\kappa}{\partial x_i}\right\rangle \approx \langle\rho|\eta\rangle\langle D|\eta\rangle\frac{\partial\left\langle y''_\kappa\right\rangle}{\partial x_i} \tag{3.16}$$

The fact that $\langle y''_\kappa|\eta\rangle = 0$ implies:

$$\langle y''_\kappa\rangle = \int_0^1 \langle y''_\kappa|\eta\rangle\, P(\eta)d\eta = 0 \tag{3.17}$$

Using Eq. (3.17) in Eqs. (3.15) and (3.16) leads to:

$$\langle \rho y''_\kappa\rangle \approx 0 \quad \text{and} \quad \left\langle \rho D \frac{\partial y''_\kappa}{\partial x_i} \right\rangle \approx 0 \tag{3.18}$$

Accordingly, the first and third terms on the r.h.s. of Eq. (3.14) are neglected, which results in:

$$\int_0^1 e_{y''_\kappa} P(\eta)d\eta \approx -\frac{\partial}{\partial x_i}\langle \rho u_i y''_\kappa\rangle \tag{3.19}$$

Equation (3.19) may be simplified further by decomposing the velocity and the density as follows:

$$\begin{aligned}
\frac{\partial}{\partial x_i}\langle \rho u_i y''_\kappa\rangle &= \frac{\partial}{\partial x_i}\langle \rho\left(\langle u_i|\eta\rangle + u''_i\right) y''_\kappa\rangle \\
&= \langle u_i|\eta\rangle \frac{\partial \overbrace{\langle \rho y''_\kappa\rangle}^{\approx 0}}{\partial x_i} + \underbrace{\langle \rho y''_\kappa\rangle}_{\approx 0}\frac{\partial \langle u_i|\eta\rangle}{\partial x_i} + \frac{\partial}{\partial x_i}\langle \rho u''_i y''_\kappa\rangle \\
&= \frac{\partial}{\partial x_i}\int_0^1 \langle\rho|\eta\rangle\,\langle u''_i y''_\kappa|\eta\rangle\, P(\eta)d\eta \\
&= \int_0^1 \frac{\partial}{\partial x_i}\left(\langle\rho|\eta\rangle\,\langle u''_i y''_\kappa|\eta\rangle\, P(\eta)\right)d\eta
\end{aligned} \tag{3.20}$$

where $\langle u''_i y''_\kappa|\eta\rangle$ is the conditional turbulent flux of species κ. Substituting Eq. (3.20) in Eq. (3.19) and using $\langle\rho|\eta\rangle P(\eta) = \langle\rho\rangle\tilde{P}(\eta)$ finally result in:

$$e_{y''_\kappa} \approx -\frac{\langle\rho|\eta\rangle}{\langle\rho\rangle\tilde{P}(\eta)}\frac{\partial}{\partial x_i}\left(\langle\rho\rangle\,\langle u''_i y''_\kappa|\eta\rangle\,\tilde{P}(\eta)\right) \tag{3.21}$$

where the mean density is obtained from [120]:

$$\langle\rho\rangle = \left(\int_0^1 \langle\rho|\eta\rangle^{-1}\tilde{P}(\eta)d\eta\right)^{-1} \tag{3.22}$$

The substitution of Eqs. (3.13) and (3.21) in Eq (3.8) finally leads to:

$$\underbrace{\frac{\partial Q_\kappa}{\partial t}}_{\substack{\text{Local rate}\\ \text{of change}}} = \underbrace{-\langle u_i|\eta\rangle \frac{\partial Q_\kappa}{\partial x_i}}_{\text{Convection}} \underbrace{-\frac{1}{\langle\rho\rangle \tilde{P}(\eta)} \frac{\partial}{\partial x_i}\left[\langle\rho\rangle \langle u_i'' y_\kappa''|\eta\rangle \tilde{P}(\eta)\right]}_{\text{Diffusion in physical space}} + \underbrace{\frac{\langle\chi|\eta\rangle}{2}\frac{\partial^2 Q_\kappa}{\partial\eta^2}}_{\substack{\text{diffusion in } \eta\text{-space}\\ \text{(micro-mixing)}}} + \underbrace{\frac{\langle\dot{\omega}_\kappa|\eta\rangle}{\langle\rho|\eta\rangle}}_{\substack{\text{Chemical}\\ \text{source}}} \tag{3.23}$$

Upon solving Eq. (3.23), the Favre-averaged mass fraction of species κ is obtained using:

$$\tilde{Y}_\kappa = \int_0^1 \langle Y_\kappa|\eta\rangle \tilde{P}(\eta) d\eta = \int_0^1 Q_\kappa \tilde{P}(\eta) d\eta \tag{3.24}$$

3.2.2 Conditional temperature equation

The conditional temperature equation is derived using the same procedure outlined in the previous section. Assuming unity Lewis number and equal species diffusivities, and neglecting the pressure convection and viscous heating terms, the temperature transport equation (Eq. (2.21)) simplifies to:

$$\rho c_p \frac{\partial T}{\partial t} + \rho c_p u_i \frac{\partial T}{\partial x_i} = \frac{\partial}{\partial x_i}\left(\rho c_p D \frac{\partial T}{\partial x_i}\right) + \sum_{\kappa=1}^{N_s} \rho c_{p,\kappa} D \frac{\partial Y_\kappa}{\partial x_i}\frac{\partial T}{\partial x_i} + \frac{\partial p}{\partial t} - \sum_{\kappa=1}^{N_s} h_\kappa \dot{\omega}_\kappa - \dot{\omega}_r \tag{3.25}$$

The temperature is first decomposed into a conditional mean and a fluctuation:

$$T(\mathbf{x},t) = Q_T(\xi(\mathbf{x},t) = \eta, \mathbf{x}, t) + T''(\mathbf{x},t) \tag{3.26}$$

Similar transformations to the ones described in Eqs. (3.4)-(3.6) are then applied and substituted in Eq. (3.25). Neglecting the fluctuations of the density and those of the specific heats, and assuming that the specific heat of the mixture is independent of $\mathbf{x}$, the

conditional averaging of the resulting expression yields[2]:

$$\begin{aligned}\frac{\partial Q_T}{\partial t} =& -\langle u_i|\eta\rangle\frac{\partial Q_T}{\partial x_i} + \frac{\langle\chi|\eta\rangle}{2}\left\{\frac{\partial^2 Q_T}{\partial\eta^2} + \frac{1}{\langle c_p|\eta\rangle}\left[\frac{\partial\langle c_p|\eta\rangle}{\partial\eta}\right.\right.\\ &\left.\left.+\sum_{\kappa=1}^{N_s}\left(\langle c_{p,\kappa}|\eta\rangle\frac{\partial Q_\kappa}{\partial\eta}\right)\right]\frac{\partial Q_T}{\partial\eta}\right\} + \frac{1}{\langle\rho|\eta\rangle\langle c_p|\eta\rangle}\left\langle\frac{\partial p}{\partial t}\middle|\eta\right\rangle\\ &-\frac{\sum_{\kappa=1}^{N_s}\langle h_\kappa|\eta\rangle\langle\dot\omega_\kappa|\eta\rangle}{\langle\rho|\eta\rangle\langle c_p|\eta\rangle} - \frac{\langle\dot\omega_r|\eta\rangle}{\langle\rho|\eta\rangle\langle c_p|\eta\rangle} + \frac{e_{Q_T}+e_{T''}+e_{c_p}}{\langle\rho|\eta\rangle\langle c_p|\eta\rangle}\end{aligned} \tag{3.27}$$

where

$$e_{Q_T} = \frac{\partial}{\partial x_i}\left(\rho c_p D\frac{\partial Q_T}{\partial x_i}\right) + \left\langle\rho c_p D\frac{\partial\xi}{\partial x_i}\frac{\partial}{\partial x_i}\left(\frac{\partial Q_T}{\partial\eta}\right)\middle|\eta\right\rangle \tag{3.28}$$

$$e_{T''} = -\left\langle\rho c_p\frac{\partial T''}{\partial t} + \rho c_p u_i''\frac{\partial T''}{\partial x_i} - \frac{\partial}{\partial x_i}\left(\rho D c_p\frac{\partial T''}{\partial x_i}\right)\middle|\eta\right\rangle \tag{3.29}$$

$$\begin{aligned}e_{c_p} =& \left\langle\rho D\left\{\sum_{\kappa=1}^{N_s}\left[c_{p,\kappa}\frac{\partial Q_\kappa}{\partial\eta}\frac{\partial\xi}{\partial x_i}\left(\frac{\partial Q_T}{\partial x_i}+\frac{\partial T''}{\partial x_i}\right) + \left(\frac{\partial Q_\kappa}{\partial x_i}+\frac{\partial y_\kappa''}{\partial x_i}\right)\times\right.\right.\right.\\ &\left.\left.\left.\left(\frac{\partial Q_T}{\partial\eta}\frac{\partial\xi}{\partial x_i}+\frac{\partial Q_T}{\partial x_i}+\frac{\partial T''}{\partial x_i}\right)\right] + \frac{\partial\xi}{\partial x_i}\left(\frac{\partial Q_T}{\partial x_i}+\frac{\partial T''}{\partial x_i}\right)\frac{\partial\langle c_p|\eta\rangle}{\partial\eta}\right\}\middle|\eta\right\rangle\end{aligned} \tag{3.30}$$

The quantities $\langle h_\kappa|\eta\rangle$ and $\langle\dot\omega_r|\eta\rangle$ are the conditional enthalpy of species κ and the conditional radiative source term, respectively. As in the conditional species equation, the terms e_{Q_T} and $e_{T''}$ are simplified by means of the primary closure hypothesis:

$$e_{Q_T} \approx 0 \tag{3.31}$$

and

$$e_{T''} - \frac{\langle\rho|\eta\rangle\langle c_p|\eta\rangle}{\langle\rho\rangle\tilde P(\eta)}\frac{\partial}{\partial x_i}\left(\langle\rho\rangle\,\langle u_i''T''|\eta\rangle\,\tilde P(\eta)\right) \tag{3.32}$$

De Paola [49] obtains a similar expression for e_{c_p}. He suggests neglecting this term in high Re flows since $\rho D \sim \mathrm{Re}^{-1}$. However, he notes that the scalar product of the gradients of two fluctuating quantities multiplied by the diffusivity is finite. Such terms are neglected here, leading to:

$$e_{c_p} \approx 0 \tag{3.33}$$

[2]A detailed derivation with double-conditioning is provided in Appendix B. The resulting doubly-conditional temperature equation degenerates to Eq. (3.27) when the second conditioning variable is omitted.

The substitution of Eqs. (3.31), (3.32) and (3.33) in Eq (3.27) results in:

$$\underbrace{\frac{\partial Q_T}{\partial t}}_{\substack{\text{Local rate}\\ \text{of change}}} = \underbrace{-\langle u_i|\eta\rangle\frac{\partial Q_T}{\partial x_i}}_{\substack{\text{Convection,}\\ T_{C,x}\text{ and }T_{C,y}}} \underbrace{-\frac{1}{\langle\rho\rangle\tilde{P}(\eta)}\frac{\partial}{\partial x_i}\left[\langle\rho\rangle\langle u_i''T''|\eta\rangle\tilde{P}(\eta)\right]}_{\substack{\text{Diffusion in physical space,}\\ T_{D,x}\text{ and }T_{D,y}}}$$
$$\underbrace{+\frac{\langle\chi|\eta\rangle}{2}\left\{\frac{\partial^2 Q_T}{\partial\eta^2}+\frac{1}{\langle c_p|\eta\rangle}\left[\frac{\partial\langle c_p|\eta\rangle}{\partial\eta}+\sum_{\kappa=1}^{N_s}\left(\langle c_{p,\kappa}|\eta\rangle\frac{\partial Q_\kappa}{\partial\eta}\right)\right]\frac{\partial Q_T}{\partial\eta}\right\}}_{\text{Diffusion in }\eta\text{-space (micro-mixing), }T_{MM}} \tag{3.34}$$
$$\underbrace{+\frac{1}{\langle\rho|\eta\rangle\langle c_p|\eta\rangle}\left\langle\frac{\partial p}{\partial t}\middle|\eta\right\rangle}_{\substack{\text{Local rate of}\\ \text{change of pressure}}} \underbrace{-\frac{\sum_{\kappa=1}^{N_s}\langle h_\kappa|\eta\rangle\langle\dot{\omega}_\kappa|\eta\rangle}{\langle\rho|\eta\rangle\langle c_p|\eta\rangle}}_{\text{Chemical source, }T_{CS}} \underbrace{-\frac{\langle\dot{\omega}_r|\eta\rangle}{\langle\rho|\eta\rangle\langle c_p|\eta\rangle}}_{\text{Radiative source, }T_{RS}}$$

Once Eq. (3.34) is solved, the Favre-averaged temperature is obtained using:

$$\tilde{T}=\int_0^1\langle T|\eta\rangle\tilde{P}(\eta)d\eta=\int_0^1 Q_T\tilde{P}(\eta)d\eta \tag{3.35}$$

3.3 CMC submodels

The quantities $\tilde{P}(\eta)$, $\langle u_i''y_\kappa''|\eta\rangle$, $\langle u_i''T''|\eta\rangle$, $\langle u_i|\eta\rangle$, $\langle\chi|\eta\rangle$, $\langle\dot{\omega}_\kappa|\eta\rangle$, and $\langle\dot{\omega}_r|\eta\rangle$ are unclosed and need to be modelled in order to fully close the CMC equations. The following sections provide a description of the closures employed throughout this work.

3.3.1 Presumed probability density function

When Eq. (2.114) is rewritten with the mixture fraction being the only sample space variable, the end result provides the mixture fraction PDF transport equation:

$$\bar{\rho}\frac{\partial\tilde{P}}{\partial t}+\bar{\rho}\tilde{u}_i\frac{\partial\tilde{P}}{\partial x_i}=-\frac{\partial(\bar{\rho}\langle u_i''|\eta\rangle\tilde{P})}{\partial x_i}+\frac{\partial}{\partial x_i}\left(\bar{\rho}D\frac{\partial\tilde{P}}{\partial x_i}\right)-\frac{1}{2}\frac{\partial^2(\bar{\rho}\langle\chi|\eta\rangle\tilde{P})}{\partial\eta^2} \tag{3.36}$$

No chemical source appears on the r.h.s. of Eq. (3.36) since the mixture fraction is a conserved scalar. Two modelling approaches are possible thorough this equation [160]:

1. The transported PDF approach: a model for $\langle\chi|\eta\rangle$ implies $\tilde{P}(\eta)$.
2. The presumed PDF approach: a model for $\tilde{P}(\eta)$ implies $\langle\chi|\eta\rangle$.

The latter approach is adopted in CMC. The PDF is presumed using smooth or intermittent distributions that rely on the moments of the mixture fraction and $\langle\chi|\eta\rangle$ is deduced from the double-integration of Eq. (3.36) (discussed in more detail in Sect. 3.3.4).

Klimenko and Bilger [120] provide a comprehensive overview on smooth and intermittent PDFs. Essentially, the classification of these distributions in two-stream systems depends on the behaviour of the PDF at the unmixed fluid states, i.e. $\eta = 0$ (pure oxidiser) and 1 (pure fuel). It is common in two-stream mixing problems to encounter patches of unmixed fuel and/or oxidiser that are intermittently present near the outer edges of turbulent flows. Two points of view may be argued to be valid:

1. When the unmixed fuel and/or oxidiser patches are viewed as being uncontaminated by the other stream, the PDF must be represented by Dirac delta functions at $\eta = 0$ and 1. PDFs providing such description are referred to as "intermittent".
2. Based on the convection-diffusion equation, unmixed patches must be always contaminated by the other stream, even if the contamination levels are very small. Therefore, the PDF must be continuous near $\eta = 0$ and 1. Such PDFs are referred to as "smooth".

In this work, both smooth and intermittent PDFs are considered.

The β-PDF

The β-distribution is a smooth PDF that is widely used in the modelling two-feed combustion systems (binary mixing) due to the fact the mixture fraction varies between zero and one [178]. The Favre β-PDF is given by:

$$\tilde{P}(\eta; v, w) = \frac{\eta^{v-1}(1-\eta)^{w-1}}{B(v,w)} \tag{3.37}$$

where the parameters v and w are related to the mean and variance of the mixture fraction (first and second moments) by:

$$v = \gamma\tilde{\xi} \tag{3.38}$$

and

$$w = \gamma(1 - \tilde{\xi}) \tag{3.39}$$

where

$$\gamma = \frac{\tilde{\xi}(1 - \tilde{\xi})}{\widetilde{\xi''^2}} - 1 \geq 0 \tag{3.40}$$

$B(v, w)$ in the denominator of Eq. (3.37) is the beta function defined by:

$$B(v, w) = \int_0^1 \eta^{v-1}(1 - \eta)^{w-1} d\eta = \frac{\Gamma(v)\Gamma(w)}{\Gamma(v + w)} \tag{3.41}$$

where Γ is the gamma function. The β-PDF develops singularities at $\eta = 0$ and $\eta = 1$ if $v < 1$ and $w < 1$, respectively. Girimaji [77] shows that this PDF reduces to a Gaussian PDF in the limit of very small $\widetilde{\xi''^2}$. This behavior is usually observed in well-mixed regions characterized by a low scalar dissipation rate. Using the DNS of Eswaran and Pope [60], Girimaji [77] and Swaminathan and Mahalingam [221] show that this distribution characterizes the evolution of the scalar PDF accurately at all stages of mixing in statistically-stationary, homogeneous, isotropic turbulence.

One weakness of the β-PDF is its inability to describe the intermittency of unmixed patches that manifest near the outer edges of shear flows. In such regions, the β-PDF tends asymptotically to infinity at the corresponding bound [120]. To remedy this behavior, Effelsberg and Peters [57] propose a composite PDF consisting of the sum of three parts: a fully turbulent part represented by the β-distribution, a superlayer part, and a outer flow part. The resulting PDF has four parameters and an intermittency factor. Algebraic relations between these parameters and the first four moments of the mixture fraction are obtained by integrating the PDF. These relations are solved iteratively as outlined in [57]. The composite PDF is not implemented here. Alternatively, the simpler clipped Gaussian PDF, which will be discussed shortly, is considered.

Beside lacking a mechanism for the description intermittency, the β-PDF cannot describe the turbulent mixing of multiple injections, i.e. the mixing of multiple streams. Nevertheless, some attempts have been made in order to extend its applicability to the mixing of three streams (trinary mixing). For instance, Kim et al. [114] propose a trimodal β-PDF for the trinary mixing that takes place in double scalar mixing layers.

The clipped Gaussian PDF

By definition, the Gaussian PDF of a random variable describes the probability distribution of this variable as it varies from $-\infty$ to $+\infty$. Since the mixture fraction varies between 0

and 1, Lockwood and Naguib [139] suggest "reconstructing" the Gaussian PDF by clipping the "unwanted tails" present at $\eta < 0$ and $\eta > 1$ and lumping them into Dirac delta functions at $\eta = 0$ and $\eta = 1$, leading to the so-called Clipped Gaussian PDF (CG-PDF). The CG-PDF is intermittent in nature as it accounts for the presence of unmixed fuel and/or oxidiser patches that might be present in certain flows. Klimenko and Bilger [120] show that the CMC equations preserve the conservation integrals for the intermittent PDFs. The CG-PDF is given by:

$$\tilde{P}(\eta) = \gamma_1 \delta(\eta) + \tilde{G}(\eta)\left[H(\eta) - H(\eta - 1)\right] + \gamma_2 \delta(\eta - 1) \tag{3.42}$$

where

$$G(\eta) = \frac{1}{\sigma\sqrt{2\pi}} \exp\left[-\frac{1}{2}\left(\frac{\eta - \mu}{\sigma}\right)^2\right] \tag{3.43}$$

μ and σ are the mean and the standard deviation of the CG-PDF, δ is the Dirac delta function, and H is the Heaviside step function. The first and last terms on the right hand side of Eq. (3.42), $\gamma_1\delta(\eta)$ and $\gamma_2\delta(1-\eta)$, account for the clipped tails of the Gaussian distribution for $\eta < 0$ and $\eta > 1$, respectively. The parameters γ_1 and γ_2 represent the strengths of the delta functions. They are given by:

$$\gamma_1 = \int_{-\infty}^{0} G(\eta) d\eta = \frac{1}{2}\left[1 + \mathrm{erf}\left(\frac{-\mu}{\sqrt{2}\sigma}\right)\right] \tag{3.44}$$

and

$$\gamma_2 = \int_{1}^{\infty} G(\eta) d\eta = \frac{1}{2}\left[1 - \mathrm{erf}\left(\frac{1 - \mu}{\sqrt{2}\sigma}\right)\right] \tag{3.45}$$

The quantities μ and σ in Eq. (3.43) are not simple moments of $G(\eta)$. However, they are related to the mean and variance of the mixture fraction by taking the first and second moments about $\eta = 0$ and $\eta = \tilde{\xi}$:

$$\tilde{\xi} = \int_{-\infty}^{\infty} \eta \tilde{P}(\eta) d\eta \tag{3.46}$$

and

$$\widetilde{\xi''^2} = \int_{-\infty}^{\infty} \eta^2 \tilde{P}(\eta) d\eta - \tilde{\xi}^2 \tag{3.47}$$

Inserting Eq. (3.42) in Eqs. (3.46) and (3.47) and integrating yields:

$$\tilde{\xi} = 1 - \mu K(x_1) + (1 - \mu) K(x_2) + \frac{\sigma}{\sqrt{(2\pi)}}\left[\exp\left(-\frac{x_1^2}{2}\right) - \exp\left(-\frac{x_2^2}{2}\right)\right] \tag{3.48}$$

and

$$\begin{aligned}\widetilde{\xi''^2} =& 1 - (\sigma^2 + \mu^2)K(x_1) + (1 + \sigma^2\mu^2)K(x_2) \\ &+ \frac{\sigma^2}{\sqrt{(2\pi)}}\left[x_1 \exp\left(-\frac{x_1^2}{2}\right) - x_2 \exp\left(-\frac{x_2^2}{2}\right)\right] \\ &+ \frac{2\sigma\mu}{\sqrt{(2\pi)}}\left[\exp\left(-\frac{x_1^2}{2}\right) - \exp\left(-\frac{x_2^2}{2}\right)\right] - \tilde{\xi}^2\end{aligned} \tag{3.49}$$

where

$$x_1 = -\frac{\mu}{\sigma}, \tag{3.50}$$

$$x_2 = \frac{(1-\mu)}{\sigma}, \tag{3.51}$$

and

$$K(x) = \frac{1}{\sqrt{2\pi}}\int_{-\infty}^{x} \exp\left(-\frac{x^2}{2}\right) dx = \frac{1}{2}\left[1 + \text{erf}\left(\frac{x}{\sqrt{2}}\right)\right] \tag{3.52}$$

The mean and the standard deviation of the CG-PDF are finally obtained by solving the non-linear expressions given by Eqs. (3.48) and (3.49).

The Presumed Mapping Function PDF

In most presumed PDF models an assumed form is chosen directly for the PDF, such as the β-PDF and the CG-PDF presented earlier. In the Presumed Mapping Function (PMF) approach, on the other hand, a known reference field is chosen and a mapping function between the true, unknown, scalar field and this reference field is computed. Following the notation employed in [160], the reference field is denoted by ψ with a sample space variable ϕ, and as defined in Sect. 3.2, the true (unknown) scalar field is denoted by ξ with a sample space variable η. The reference fields is mapped to the scalar field via:

$$X(\psi) = \xi \quad \text{and} \quad X(\phi) = \eta \tag{3.53}$$

where X is a unique mapping function. The PDF of ξ, $\tilde{P}$, and that of ψ, r, are related by:

$$\tilde{P}(X(\phi)) = \tilde{P}(\eta) = r(\phi)\left(\frac{\partial X}{\partial \phi}\right)^{-1} \tag{3.54}$$

Mortensen and Andersson [160] employ a Gaussian distribution with a zero mean to represent $r(\phi)$. This choice of PDF is motivated by the fact that only a Gaussian distribution yields an analytical solution for the mapping closure. As such,

$$r(\phi) = \frac{1}{\sqrt{2\pi}\sigma_r}\exp\left(-\frac{\phi^2}{2\sigma_r^2}\right) \tag{3.55}$$

where

$$\sigma_r^2 = 1 - 2\tau \tag{3.56}$$

is the variance and τ is a scaled time parameter bounded by 0 (no mixing) and 0.5 (complete mixing). Using the cumulative distribution functions of $\tilde{P}$ and r, it can be shown that [160]:

$$X(\phi) = \frac{1}{2\sqrt{\pi\tau}} \int_{-\infty}^{+\infty} X(s, \tau = 0) \exp\left[-\frac{(s-\phi)^2}{4\tau}\right] ds \tag{3.57}$$

where $X(s, \tau = 0)$ is the initial mapping between ξ and ψ. The initial binary mixing PDF reads:

$$\tilde{P}(\eta, \tau = 0) = (1 - \tilde{\xi})\delta(\eta) + \tilde{\xi}\delta(\eta - 1) \tag{3.58}$$

where δ is the Dirac delta function. Accordingly, the initial mapping is:

$$X(\phi, \tau = 0) = H(\phi - \alpha) \tag{3.59}$$

where H is the Heaviside step function and the parameter α is determined from:

$$1 - \tilde{\xi} = \int_{-\infty}^{\alpha} r(\phi, \tau = 0) d\phi \tag{3.60}$$

Equation 3.60 has the analytical solution:

$$\alpha = \sqrt{2}\mathrm{erf}^{-1}(1 - 2\tilde{\xi}) \tag{3.61}$$

where erf^{-1} is the inverse error function. The substitution of Eq. (3.59) in Eq. (3.57) yields:

$$X(\phi) = \frac{1}{2}\left[1 + \mathrm{erf}\left(\frac{\phi - \alpha}{2\sqrt{\tau}}\right)\right] \tag{3.62}$$

Finally, inserting Eq. (3.62) in Eq. (3.54) results in:

$$\tilde{P}(X(\phi)) = \tilde{P}(\eta) = \sqrt{\frac{2\tau}{\sigma_r^2}} \exp\left[E^2(\eta) - \frac{\phi^2}{2\sigma_r^2}\right] \tag{3.63}$$

where

$$\phi = \alpha + 2\sqrt{\tau}E(\eta) \tag{3.64}$$

and

$$E(\eta) = \mathrm{erf}^{-1}(2\eta - 1) \tag{3.65}$$

The parameter τ is obtained from the solution of the integral:

$$\tilde{\xi}^2 + \widetilde{\xi''^2} = \int_{-\infty}^{+\infty} X^2(\phi) r(\phi) d\phi \tag{3.66}$$

The PMF-PDF given by Eq. (3.63) is valid for binary mixing. A distinctive feature of the PMF approach is the ability to construct presumed PDFs for multiple injections scenarios starting from an initial combination of delta functions. As such, the PMF approach is in general applicable to flows consisting of any number of streams. Further details can be found in [160].

3.3.2 Conditional turbulent fluxes

The conditional turbulent fluxes $\langle u_i'' y_\kappa'' | \eta \rangle$ and $\langle u_i'' T'' | \eta \rangle$ are modelled using the gradient diffusion assumption. This assumption states that transport by the conditional flux of a given scalar is down the gradient of the conditional mean of the scalar. Accordingly, there exists a positive scalar, D_t, the turbulent diffusivity, such that

$$\langle u_i'' y_\kappa'' | \eta \rangle = -D_t \frac{\partial \langle Y_\kappa | \eta \rangle}{\partial x_i} = -D_t \frac{\partial Q_\kappa}{\partial x_i} \tag{3.67}$$

and

$$\langle u_i'' T'' | \eta \rangle = -D_t \frac{\partial \langle T | \eta \rangle}{\partial x_i} = -D_t \frac{\partial Q_T}{\partial x_i} \tag{3.68}$$

where D_t is given by Eq. (2.56). The gradient diffusion assumption does not account for counter-gradient effects, which are mostly encountered in premixed flames. Richardson and Mastorakos [196] suggest adding a correction to Eqs. (3.67) and (3.68) in order to account for these effects. When applied to a lifted flame, they conclude that the inclusion of counter-gradient effects leads to a slight increase in liftoff height and to a decrease in flame thickness. This extension is not employed in the current work. However, it is worth investigating in future studies.

3.3.3 Conditional velocity

The linear velocity model

The linear velocity model of Kuznetsov and Sabel'nikov [131] assumes that joint PDF of the velocity and the mixture fraction is Gaussian. Based on this assumption, the conditional

velocity fluctuations are linearly related to η. This model reads:

$$\langle \tilde{u}_i|\eta\rangle = \tilde{u}_i + \frac{\widetilde{u_i''\xi''}}{\widetilde{\xi''^2}}(\eta - \tilde{\xi}) \tag{3.69}$$

The gradient diffusion assumption is usually employed to model the turbulent flux as $\widetilde{u_i''\xi''} = -D_t \partial\tilde{\xi}/\partial x_i$. Equation (3.69) is exact only if the joint PDF of the velocity and the mixture fraction is Gaussian, which is not in general the case for inhomogeneous flows [23]. However, this condition is not necessary for Eq. (3.69) to be an appropriate approximation [120]. By comparing Eq. (3.69) to experimental measurements, Kuznetsov and Sabel'nikov [131] show that performance of this model is satisfactory when η is within two standard deviations from the mixture fraction mean, i.e. when $|\eta - \tilde{\xi}| \lesssim 2(\widetilde{\xi''^2})^{1/2}$, and report deviations from the linear relationship between the velocity fluctuations and η outside this range. Similar observations are reported in the measurements of Li and Bilger [131]. Another anomaly of this model is that it is only consistent with the first moment of the mixture fraction [43]. Hence, inconsistencies arise when this model is used with presumed PDFs that depend on the second moment of mixture fraction, such as the β-PDF, the CG-PDF and the PMF-PDF. Despite the shortcomings discussed above, Eq. (3.69) is widely used due to its simplicity and ease of implementation.

The PDF gradient diffusion model

In the PDF-gradient model of Pope [188,190], the gradient diffusion assumption is invoked to close the conditional velocity fluctuations. This closure can be obtained by taking the first moment of the mixture fraction PDF transport equation and using the mixture fraction mean equation (see [43]). The resulting expression for the conditional velocity takes the form:

$$\begin{aligned}
\langle u_i|\eta\rangle &= \tilde{u} - \frac{D_t}{\tilde{P}(\eta)}\frac{\partial \tilde{P}(\eta)}{\partial x_i} \\
&= \tilde{u} - D_t \frac{\partial \ln[\tilde{P}(\eta)]}{\partial x_i} \\
&= \tilde{u}_i - D_t \left\{ \frac{\partial \ln[\tilde{P}(\eta)]}{\partial \tilde{\xi}}\frac{\partial \tilde{\xi}}{\partial x_i} + \frac{\partial \ln[\tilde{P}(\eta)]}{\partial \widetilde{\xi''^2}}\frac{\partial \widetilde{\xi''^2}}{\partial x_i} \right\}
\end{aligned} \tag{3.70}$$

One important feature of this model is its consistency with the first and second moments of the PDF [43] and with the modelling of the unconditional passive and reactive scalar

fluxes [160,162]. As such, the closure provided by the PDF-gradient guarantees a consistent CMC implementation. It is evident from Eq. (3.70) that $\langle u_i|\eta\rangle$ depends on the form of the presumed PDF.

β-PDF closure

When the PDF in Eq. (3.70) is presumed using the β distribution, $\langle u_i|\eta\rangle$ diverges to $\pm\infty$ if $\tilde{P}(\eta)$ tends to zero and the magnitude of $\partial\tilde{P}(\eta)/\partial x_i$ is large compared to $\tilde{P}(\eta)$. This behavior is of minor importance because low-probability events have a negligible effect on mixing [48]. However, this may lead to numerical instabilities and convergence issues. The partial derivatives of $\tilde{P}(\eta)$ with respect to $\tilde{\xi}$ and $\widetilde{\xi''^2}$ are computed numerically.

CG-PDF closure

When $\tilde{P}(\eta)$ is presumed using the CG-PDF, $\langle u_i|\eta\rangle$ does not overshoot significantly at low probabilities. Therefore, in comparison to the β-PDF closure, the CG-PDF formulation is better-behaved over the whole mixture fraction space. As in the β-PDF closure, the partial derivatives of $\tilde{P}(\eta)$ with respect to $\tilde{\xi}$ and $\widetilde{\xi''^2}$ are obtained numerically.

PMF-PDF closure

By inserting Eq. (3.63) in Eq. (3.70), Mortensen and Andersson [160] show that:

$$\langle u_i|\eta\rangle = \tilde{u}_i + \frac{D_\mathrm{t}}{\sigma_r^2}\left\{\frac{\partial\tilde{\xi}}{\partial x_i}\frac{d\alpha}{d\tilde{\xi}}\phi(\eta) - \frac{1}{2\tau}\left[\frac{\partial\tau}{\partial\tilde{\xi}}\frac{\partial\tilde{\xi}}{\partial x_i} + \frac{\partial\tau}{\partial\widetilde{\xi''^2}}\frac{\partial\widetilde{\xi''^2}}{\partial x_i}\right]\left[1+\alpha\phi(\eta) - \frac{\phi^2(\eta)}{\sigma_r^2}\right]\right\} \quad (3.71)$$

where $d\alpha/d\tilde{\xi} = -\sqrt{2\pi}\exp(\alpha^2/2)$. Similar to the CG-PDF closure, the PMF-PDF closure does not overshoot significantly at low probabilities.

3.3.4 Conditional scalar dissipation rate

The conditional scalar dissipation rate, $\langle\chi|\eta\rangle$, is a measure of the intensity of micro-mixing or diffusion in mixture fraction space. It is proportional to the inverse of the diffusion time scale. Accurate modelling of this quantity is critical. Several homogeneous and inhomogeneous closures are available in the literature.

The Amplitude Mapping Closure

The Amplitude Mapping Closure (AMC) was introduced by O'Brien and Jiang [174]. This closure is a particular solution of the homogeneous PDF transport equation. It employs

the mapping closure solution of Gao [76] with a Gaussian reference field. The AMC is given by:

$$\langle \chi|\eta \rangle = \chi_{\circ} G(\eta) \tag{3.72}$$

where $G(\eta)$ is a function independent of $\tilde{\xi}$ and $\widetilde{\xi''^2}$. It is given by:

$$G(\eta) = \exp\left\{-2\left[\mathrm{erf}^{-1}(2\eta - 1)\right]^2\right\} \tag{3.73}$$

$\chi_{\circ}$ is obtained by integrating Eq. (3.72) weighted by $\tilde{P}(\eta)$ over the mixture fraction space:

$$\chi_{\circ} = \frac{\int_0^1 \langle \chi|\eta \rangle \tilde{P}(\eta) d\eta}{\int_0^1 G(\eta)\tilde{P}(\eta) d\eta} = \frac{\tilde{\chi}}{\int_0^1 G(\eta)\tilde{P}(\eta) d\eta} \tag{3.74}$$

The CG-PDF is employed instead of the Gaussian distribution to presume $\tilde{P}(\eta)$ in Eq. (3.74). This adjustment introduces some mathematical inconsistencies with the standard AMC formulation, however, it confines the mixture fraction range to $[0, 1]$ rather than $]-\infty, +\infty[$, as discussed in Section 3.3.1. One limitation of the AMC is that it requires the presence of some unmixed fluid in the mixture. This restriction does not apply to the models discussed next.

Girimaji's model

Girimaji [78] derives a model for $\langle \chi|\eta \rangle$ by doubly integrating the homogeneous PDF transport equation. This formulation is based on the observation that a presumed β-PDF is capable of accurately characterizing the evolution of the scalar PDF over all stages of two-scalar, constant-density mixing in statistically stationary, isotropic turbulence. The model is given by:

$$\langle \chi|\eta \rangle = -2\tilde{\chi}\frac{\tilde{\xi}(1-\tilde{\xi})}{(\widetilde{\xi''^2})^2}\frac{I(\eta)}{\tilde{P}(\eta)} \tag{3.75}$$

where $\tilde{\chi}$ is the Favre-averaged scalar dissipation rate and $I(\eta)$ is given by the integral:

$$I(\eta) = \int_0^{\eta} \left\{\tilde{\xi}(\ln\eta' - I_1) + (1-\tilde{\xi})[\ln(1-\eta') - I_2]\right\}\tilde{P}(\eta')(\eta - \eta')d\eta' \tag{3.76}$$

where

$$I_1 = \int_0^1 \ln\eta \tilde{P}(\eta) d\eta \tag{3.77}$$

and

$$I_2 = \int_0^1 \ln(1-\eta)\tilde{P}(\eta) d\eta \tag{3.78}$$

Mortensen's model

In a similar fashion, Mortensen [157] derives an expression for $\langle\chi|\eta\rangle$ by doubly integrating the mixture fraction PDF transport equation. However, in this derivation, the inhomogeneous terms are retained. The conditional velocity fluctuations appearing in the transport equation are modelled using the PDF gradient model of Pope [188] and the PDF is presumed using a functional form described by the vector of mixture fraction moments, μ. This model is given by:

$$\langle\chi|\eta\rangle = \frac{2}{\tilde{P}(\eta;\mu)}\left(-\frac{\partial II(\eta;\mu)}{\partial\mu_j}S_j + D_{\text{eff}}\frac{\partial^2 II(\eta;\mu)}{\partial\mu_j\partial\mu_k}\frac{\partial\mu_j}{\partial x_i}\frac{\partial\mu_k}{\partial x_i}\right) \tag{3.79}$$

where

$$II(\eta,\mu) = \int_0^\eta\int_0^{\eta'}\tilde{P}(\eta'';\mu)d\eta''d\eta' = \int_0^\eta I(\eta';\mu)d\eta' \tag{3.80}$$

$I(\eta';\mu)$ in Eq. (3.80) is the cumulative distribution function of $\tilde{P}(\eta;\mu)$. The quantity S_j represents the sum of the source terms in the transport equation of the moment μ_j, and D_{eff} is the effective diffusivity which is equal to the sum of the turbulent and molecular diffusivities ($D_{\text{eff}} = D_{\text{t}} + D$). The boundary conditions $\langle\chi|\eta = 0\rangle = 0$ and $\langle\chi|\eta = 1\rangle = 0$ are used in the process of obtaining Eq. (3.79). These boundary conditions are valid for both smooth and intermittent PDFs [120]. It is obvious from Eq. (3.79) that the final expression of the conditional scalar dissipation depends on the choice of the presumed PDF. When the PDF is described by the first two moments of the mixture fraction, $\tilde{\xi}$ and $\widetilde{\xi''^2}$, Eq. (3.79) takes the form [156]:

$$\begin{aligned}\langle\chi|\eta\rangle = \frac{2}{\tilde{P}(\eta)}\Bigg\{ &-\frac{\partial II(\eta)}{\partial\widetilde{\xi''^2}}S_{\widetilde{\xi''^2}} + D_{\text{t}}\Bigg[\frac{\partial^2 II(\eta)}{\partial\widetilde{\xi''^2}\partial\widetilde{\xi''^2}}\frac{\partial\widetilde{\xi''^2}}{\partial x_i}\frac{\partial\widetilde{\xi''^2}}{\partial x_i} \\ &+ \frac{\partial^2 II(\eta)}{\partial\tilde{\xi}\partial\tilde{\xi}}\frac{\partial\tilde{\xi}}{\partial x_i}\frac{\partial\tilde{\xi}}{\partial x_i} + 2\frac{\partial^2 II(\eta)}{\partial\tilde{\xi}\partial\widetilde{\xi''^2}}\frac{\partial\tilde{\xi}}{\partial x_i}\frac{\partial\widetilde{\xi''^2}}{\partial x_i}\Bigg]\Bigg\}\end{aligned} \tag{3.81}$$

It is assumed in Eq. (3.81) that $D_{\text{eff}} \approx D_{\text{t}}$ since $D_{\text{t}} \gg D$. The first moment of the mixture fraction, $\tilde{\xi}$, does not contribute a source term. Thus, $S_{\tilde{\xi}} = 0$. However, the second moment, $\widetilde{\xi''^2}$, incorporates the source term:

$$S_{\widetilde{\xi''^2}} = -\tilde{\chi} + 2D_{\text{t}}\frac{\partial\tilde{\xi}}{\partial x_i}\frac{\partial\tilde{\xi}}{\partial x_i} \tag{3.82}$$

The homogeneous version of Mortensen's model, $\langle\chi|\eta\rangle_H$, is obtained by discarding the inhomogeneous terms from Eqs. (3.81) and (3.82), which leads to:

$$\langle\chi|\eta\rangle_H = 2\frac{\tilde{\chi}}{\tilde{P}(\eta)}\frac{\partial II(\eta)}{\partial\widetilde{\xi''^2}} \tag{3.83}$$

The two-parameter presumed PDF distributions discussed in Sect. 3.3.1 are now applied to Eqs. (3.80) and (3.81):

β-PDF closure

When the β-PDF is employed, $I(\eta; v, w)$ in Eq. (3.80) becomes the cumulative distribution of the β-PDF, i.e. the incomplete β-function, which is given by:

$$I(\eta; v, w) = \int_0^\eta \tilde{P}(\eta; v, w)d\eta = \frac{1}{B(v, w)}\int_0^\eta \eta^{v-1}(1-\eta)^{w-1}d\eta \tag{3.84}$$

where v and w are given by Eqs. (3.38) and (3.39), respectively. By applying some identities and integral properties of the incomplete β-function, Mortensen [156] shows that $II(\eta; v, w)$ simplifies to:

$$II(\eta; v, w) = (\eta - \tilde{\xi})I(\eta; v, w) + \widetilde{\xi''^2}\tilde{P}(\eta; v+1, w+1) \tag{3.85}$$

The partial derivatives of II appearing in Eq. (3.81) are calculated numerically. Mortensen's model based on the β-PDF, referred to hereafter as the MBPDF model, reduces exactly to Girimaji's when the inhomogeneous terms are discarded. Hence, Eq. (3.75), is the equivalent of Eq. (3.83).

CG-PDF closure

When the CG-PDF is used, II assumes a different functional form. Substituting Eq. (3.42) in Eq. (3.80), and using some integral properties of the Dirac delta function and the Heaviside function, it can be shown that:

$$\begin{aligned} II(\eta; \mu, \sigma) =& \frac{\eta-\mu}{2}\left[\operatorname{erf}\left(\frac{\eta-\mu}{\sigma\sqrt{2}}\right) + \operatorname{erf}\left(\frac{\mu}{\sigma\sqrt{2}}\right)\right] \\ &+ \frac{\sigma}{\sqrt{2\pi}}\left\{\exp\left[-\left(\frac{\eta-\mu}{\sigma\sqrt{2}}\right)^2\right] - \exp\left[-\left(\frac{\mu}{\sigma\sqrt{2}}\right)^2\right]\right\} \end{aligned} \tag{3.86}$$

where μ and σ are obtained from $\tilde{\xi}$ and $\widetilde{\xi''^2}$ by solving the non-linear system of equations given by Eqs. (3.48) and (3.49). As in the β-PDF closure, the partial derivatives of II

involved in Eq. (3.81) are calculated numerically. Hereafter, Mortensen's model based on the CG-PDF will be referred to as the MCGPDF model.

PMF-PDF closure

Using Eqs. (3.63) and (3.80) in Eq. (3.81), Mortensen and Andersson [160] show that CSDR can be expressed analytically as [3]:

$$\begin{aligned}\langle\chi|\eta\rangle =& \left\{\tilde{\chi} - 2D_\mathrm{t}\left[\left(\frac{\partial\tilde{\xi}}{\partial x_i}\right)^2\left(2+\frac{\tau_m^2\tau_{vv}}{\tau_{vv}^3}-\frac{\tau_{mm}}{\tau_v}\right) - 2\frac{d\alpha}{d\tilde{\xi}}\frac{\partial\tilde{\xi}}{\partial x_i}\frac{\partial\widetilde{\xi''^2}}{\partial x_i}A(\eta)\right.\right.\\ &\left.\left. - \left(\left(\frac{\partial\widetilde{\xi''^2}}{\partial x_i}\right)^2\tau_v + 2\frac{\partial\tilde{\xi}}{\partial x_i}\frac{\partial\widetilde{\xi''^2}}{\partial x_i}\tau_m + \left(\frac{\partial\tilde{\xi}}{\partial x_i}\right)^2\frac{\tau_m^2}{\tau_v}\right)B(\eta)\right]\right\}\frac{\langle\chi|\eta\rangle_H}{\tilde{\chi}}\\ &- 2D_\mathrm{t}\left(\frac{\partial\tilde{\xi}}{\partial x_i}\right)^2 C(\eta)\end{aligned} \tag{3.87}$$

where

$$\begin{aligned}A(\eta) &= \frac{\alpha}{1-\tau} - \frac{\phi(\eta)}{\sigma_r^2},\\ B(\eta) &= \frac{\alpha^2}{2(1-\tau)^2} - \frac{1}{\sigma_r^2}\left(\frac{\phi(\eta)E(\eta)}{\sqrt{\tau}} + \frac{\phi^2(\eta)}{\sigma_r^2} - \frac{1}{1+\sigma_r^2}\right),\\ C(\eta) &= \sqrt{\frac{2}{\pi}}\left(\alpha_1 + \frac{1}{\tau}\frac{\partial\tau}{\partial\tilde{\xi}}\frac{\phi(\eta)}{\sigma_r^2}\right)\exp\left[-2E^2(\eta)+\frac{\alpha^2}{2}\right],\\ \tau_m &= \frac{\partial\tau}{\partial\tilde{\xi}},\ \tau_v = \frac{\partial\tau}{\partial\widetilde{\xi''^2}},\ \tau_{mm} = \frac{\partial^2\tau}{\partial\tilde{\xi}^2},\ \tau_{vv} = \frac{\partial^2\tau}{\partial\widetilde{\xi''^2}^2}\end{aligned} \tag{3.88}$$

and $\langle\chi|\eta\rangle_H$ is given by Eq. (3.83). Using Eqs. (3.63) and (3.80), it can be shown that [160]:

$$\langle\chi|\eta\rangle_H = \tilde{\chi}\sqrt{\frac{1-\tau}{\tau}}\exp\left(-2E^2(\eta)+\frac{\alpha^2}{\sigma_r^2+1}\right) \tag{3.89}$$

This closure is the exact equivalent of the AMC (Eq. (3.72)) and the counterflow model of Peters [177] as implied by the PMF approach.

[3] Mortensen [158] reports a typographical error in the first term of the second line of Eq. (38) in [160]: τ_2 (the equivalent of τ_v) should not be raised to the power two. This error is rectified in Eq. (3.87).

3.3.5 Conditional chemical source

As demonstrated in Sect. 2.2.2, the chemical source of species κ, $\dot{\omega}_\kappa$, is a non-linear function of ρ, T and $\mathbf{Y} = \{Y_\kappa | \kappa = 1, 2, \ldots, N_s\}$. Thus $\widetilde{\dot{\omega}}_\kappa$ cannot be expressed as a linear function of $\bar{\rho}$, $\tilde{T}$, and $\mathbf{Y}$, i.e. $\widetilde{\dot{\omega}}_\kappa(\rho, T, \mathbf{Y}) \neq \dot{\omega}_\kappa(\bar{\rho}, \tilde{T}, \tilde{\mathbf{Y}})$. In CMC, the quantity of interest is the conditional average of the chemical source term, $\langle \dot{\omega}_\kappa(\rho, T, \mathbf{Y}) | \eta \rangle$. In situations where conditional fluctuations are negligible, it is possible to model $\langle \dot{\omega}_\kappa(\rho, T, \mathbf{Y}) | \eta \rangle$ to a first-order approximation as a function of $\langle \rho | \eta \rangle$, $\langle T | \eta \rangle$ and $\langle \mathbf{Y} | \eta \rangle$ [120]:

$$\langle \dot{\omega}_\kappa (\rho, T, \mathbf{Y}) | \eta \rangle \approx \langle \dot{\omega}_\kappa (\langle \rho | \eta \rangle, \langle T | \eta \rangle, \langle \mathbf{Y} | \eta \rangle) | \eta \rangle = \dot{\omega}_\kappa (\langle \rho | \eta \rangle, Q_T, \mathbf{Q}) \tag{3.90}$$

where $\mathbf{Q} = \{Q_\kappa | \kappa = 1, 2, \ldots, N_s\}$. To investigate the validity of this closure, Klimenko and Bilger [120] analyse the conditional chemical source of a simple one-step irreversible chemical reaction $\mathrm{R} + \mathrm{S} \rightarrow \mathrm{P}$. The corresponding reaction rates are:

$$\dot{\omega}(\rho, T, \mathbf{Y}) = \rho^2 A T^b \frac{Y_R}{W_R} \frac{Y_S}{W_S} \exp\left(-\frac{T_a}{T}\right). \tag{3.91}$$

By taking the Taylor series expansion for the reaction rate around the conditional means of the reactive scalars and then conditionally averaging the resulting expression, they show that to a second-order accuracy:

$$\begin{aligned} \langle \dot{\omega} | \eta \rangle = \dot{\omega} (\langle \rho | \eta \rangle, Q_T, \mathbf{Q}) \Bigg\{ 1 + \Bigg[\frac{\langle y_R'' y_S'' | \eta \rangle}{Q_R Q_S} + \left(b + \frac{T_a}{Q_T} \right) \left(\frac{\langle y_R'' T'' | \eta \rangle}{Q_R Q_T} + \frac{\langle y_S'' T'' | \eta \rangle}{Q_S Q_T} \right) \\ + \frac{1}{2} \left(b(b-1) + \frac{2(b-1)T_a}{Q_T} + \frac{T_a^2}{Q_T^2} \right) \frac{\langle T''^2 | \eta \rangle}{Q_T^2} \Bigg] \Bigg\} \end{aligned} \tag{3.92}$$

To a first-order approximation, this expression reduces to the first-order closure given by Eq. (3.90). In order for the error in this closure to be small, the conditional covariances in Eq. (3.92) need to be small compared to the product of the conditional means. Thus, Eq. (3.90) is valid only when the magnitudes of the conditional fluctuations are sufficiently small. A more detailed description of the second-order closure is provided in Sect. 3.6.2.

3.3.6 Conditional radiative source

For simplicity, the conditional radiative source, $\langle \dot{\omega}_r | \eta \rangle$, is modelled using the optically thin assumption. To a first-order approximation, the conditional averaging of Eq. (2.61) yields:

$$\langle \dot{\omega}_r | \eta \rangle = 4\sigma \sum_{\kappa=1}^{N_r} p_\kappa a_{p,\kappa} (\langle T | \eta \rangle^4 - T_b^4) = 4\sigma \sum_{\kappa=1}^{N_r} p_\kappa a_{p,\kappa} (Q_T^4 - T_b^4) \tag{3.93}$$

where σ, N_r p_κ, $a_{p,\kappa}$ and T_b are defined as in Eq. (2.61). Here, T_b set to 300 K. The coefficients $a_{p,\kappa}$ are obtained from the curve fits provided in Sect. 2.2.2.

3.4 Spurious sources in CMC

The integration of the PDF-weighted CMC equations over η-space should ideally yield the unconditional set of equations without any additional source terms [120, 226]. This outcome is guaranteed when fully consistent CSDR models (e.g. the inhomogeneous models of Mortensen) are employed [4]. On the other hand, when inconsistent CSDR models (e.g. Girimaji's model, the homogeneous versions of Mortensen's models, and the AMC) are used, the integration of the CMC equations results in spurious (or false) source terms. The analysis of these sources is a valuable tool that enables the identification of the flaws of inconsistent CMC implementations. The spurious source associated with species κ is calculated through [120, 226]:

$$\tilde{S}\kappa = \frac{1}{2}\int_0^1 \left[\langle\chi|\eta\rangle_i - \langle\chi|\eta\rangle_c\right]\frac{\partial^2 Q_{\kappa,i}}{\partial\eta^2}\tilde{P}(\eta)d\eta \tag{3.94}$$

where $\langle\chi|\eta\rangle_i$ and $\langle\chi|\eta\rangle_c$ are the inconsistent and consistent CSDR models, respectively (the same presumed PDF is used in both), and $Q_{\kappa,i}$ is the conditional mass fraction of the species κ obtained in the inconsistent CMC realisation. Similarly, the spurious source associated with the temperature is calculated as:

$$\begin{aligned}\tilde{S}_T = \frac{1}{2}\int_0^1 \left[\langle\chi|\eta\rangle_i - \langle\chi|\eta\rangle_c\right]\Bigg\{\frac{\partial^2 Q_{T.i}}{\partial\eta^2} + \frac{1}{\langle c_p|\eta\rangle_i}\Bigg[\frac{\partial\langle c_p|\eta\rangle_i}{\partial\eta} \\ + \sum_{\kappa=1}^{N_s}\left(\langle c_{p,\kappa}|\eta\rangle_i\frac{\partial Q_{\kappa,i}}{\partial\eta}\right)\Bigg]\frac{\partial Q_{T,i}}{\partial\eta}\Bigg\}\tilde{P}(\eta)d\eta\end{aligned} \tag{3.95}$$

where $Q_{T,i}$ is the conditional temperature, and $\langle c_p|\eta\rangle_i$ and $\langle c_{p,\kappa}|\eta\rangle_i$ are the specific heats obtained in the inconsistent CMC realisation. When a consistent inhomogeneous CSDR

[4] In order for an inhomogeneous CSDR model to be fully consistent, the CV model employed in the derivation should be consistent with the moments of the mixture fraction PDF. This condition is satisfied in Moretnsen's model due to the usage of the PDF-gradient model, which is consistent with both the first and second moments. An example of an inhomogeneous yet inconsistent CSDR model is the closure proposed in [53] wherein the CV fluctuations are closed by means of the linear velocity model (Eq (3.69)). The inconsistency arises from the fact that the employed CV model is not consistent with the second moment of the mixture fraction PDF [43].

model is benchmarked against its inconsistent homogeneous version, the difference $\left[\langle\chi|\eta\rangle_i - \langle\chi|\eta\rangle_c\right]$ in Eqs. (3.94) and (3.95) represents the negative of the inhomogeneous portion of the model.

3.5 Numerical solution

This section provides an overview of the numerical aspects CMC. The topics discussed are: grid resolution in physical and mixture fraction spaces, discretisation schemes, time-stepping, boundary conditions, and the implementation of the submodels and thermochemistry.

3.5.1 Grid resolution

All the problems considered in this work are axisymmetric. Therefore, the CMC equation are solved solved in 2D physical and mixture fraction spaces. The configurations considered in Chaps. 5–7 are treated in this fashion. In turbulent shear flows, the dimensionality of CMC in physical space can be further reduced to 1D by invoking the shear flow approximation [119, 120]. This technique is discussed and applied in Chap. 4.

In what follows, some aspects of grid generation are briefly highlighted in the contexts of autoignition problems and attached and lifted flames.

Resolution in physical space

Grid resolution in physical space depends on the nature of the problem. In problems involving attached jet flames, a coarse grid may be adequate because gradients in physical space are in general small [128]. On the other hand, a relatively higher resolution is required in the calculations of lifted jet flames, particularly around the stabilisation height. This treatment is necessary due to the presence of sharp gradients at the base of the flame. In all cases, a sufficiently high resolution is necessary in reaction zones and in regions with sharp gradients.

Resolution in η-space

As in physical space, grid resolution in η space depends on the nature of the problem. In the simulation of attached jet flames, the η-grid must be clustered about the stoichiometric

mixture fraction value [128]. Such resolution is employed in the piloted flame calculations of Chap 5. In autoignition calculations where flame propagation in the post-ignition phase is not considered, the grid density must be highest in lean mixtures, specifically around the most reactive mixture fraction value. Such resolution is used in the autoignition calculations of Chap. 4. On the other hand, when flame propagation is taken into consideration, the grid must be sufficiently fine across the whole range of η in order to resolve the propagation of reaction fronts across η-space [128]. This treatment is applied in the simulation of lifted jet flames in Chaps. 6 and 7.

The accurate computation of the Favre averages from the conditional means via Eqs. (3.24) and (3.35) requires the adaptation of the η-grid such that the resolution is highest around $\eta = \tilde{\xi}$. This procedure is necessary because the presumed PDF peaks in the neighbourhood of $\tilde{\xi}$ and varies sharply in this region. Throughout this work, the PDF is recomputed and a third-order piecewise polynomial interpolation is applied to evaluate the conditional means on the adapted grid prior to the usage of Eqs. (3.24) and (3.35).

3.5.2 Discretisation

The CMC equations are discretised using the finite difference method. The first-order derivatives of the convective terms are discretised using the Upwind Difference Scheme (UDS). Backward differencing is employed when the velocity is in the direction of the flow, otherwise forward differencing is used. The simplest UDS discretisation is the first-order accurate scheme. However, this scheme is known for causing numerical diffusion in the presence of sharp gradients on coarse grids. Issues pertaining to numerical diffusion can be controlled by strategically refining the grid in regions where gradients vary substantially. This approach was found to be successful in many CMC studies [51, 59, 105, 106, 116, 117]. It is adopted Chaps. 4 and 5. In situations where grid refinement is computationally expensive, a higher-order scheme, such as the second-order UDS, becomes necessary. However, this scheme suffers from oscillatory behaviour (overshooting and undershooting). To overcome this shortcoming, a second-order UDS with high resolution (total variation diminishing) may be employed. In this approach, oscillation are treated with a flux limiter. This scheme and the most common flux limiters are thoroughly discussed in [42, 86]. In this work, the limiter proposed by Koren [121] is employed. This approach has been successfully applied in [176]. It is employed in the calculations of Chaps. 6 and 7. As for the second-order derivatives of the diffusive terms (in physical and mixture fraction spaces), discretisation is performed using the second-order Central Difference Scheme (CDS) [42,86]. This usage of this scheme is common in most CMC studies [128].

3.5.3 Fractional time-stepping

Given the resolutions $N_x \times N_y = 60 \times 30$ in 2D physical space and $N_\eta = 50$ in η-space, and a chemical kinetics mechanism including $N_s = 30$ species[5], a total of $N_x \times N_y \times N_\eta \times N_s = 2.7 \times 10^6$ equations need to be solved at every time step in order to advance the solution from t to $t + \Delta t$. In addition to this expensive requirement, the stiffness arising from the varying time scales of chemical kinetics adds further complications to the solution of the system of equations. Therefore, an efficient and robust solution strategy is essential.

The fractional step method, also known as operator splitting, is a coupling approach in which a complicated Partial Differential Equation (PDE) is split into a set of simpler and segregated PDEs [175]. These split PDEs are solved sequentially over consecutive fractions of the time step and each PDE provides the subsequent one with the necessary initial conditions. The main advantage of this method is that the different parts of the PDE are treated separately, which allows the usage of the most robust numerical method for each [175]. Splitting errors arise if the variable solved for varies quickly in any of the split PDEs. The usage of a sufficiently small time step guarantees a slow change, and therefore prevents the occurrence of large splitting errors.

A three-step fractional method (Strang operator splitting [213]) is employed throughout this work. The current implementation allows the reduction of the size of the system of equations in each fractional step and permits the separate treatment of the stiff chemical sources. The details of the implementation are provided here for the conditional species equation. The temperature equation is treated exactly the same way. To advance the solution from time $t = t_\circ$ to $t = t_\circ + \Delta t$, the PDEs are split as follows:

- **Step 1** Convection and diffusion in physical space are solved over the first half of the time step:

$$\frac{\partial Q_\kappa}{\partial t} = \underbrace{-\langle u_i|\eta\rangle \frac{\partial Q_\kappa}{\partial x_i}}_{\text{Convection}} \underbrace{-\frac{1}{\langle\rho\rangle \tilde{P}(\eta)} \frac{\partial}{\partial x_i}\left[\langle\rho\rangle \langle u_i'' y_\kappa''|\eta\rangle \tilde{P}(\eta)\right]}_{\text{Diffusion in physical space}}; \quad t_\circ \le t \le t_\circ + \frac{\Delta t}{2} \tag{3.96}$$

  The size of the system of equations at every grid point in η space is $N_x \times N_y \times N_s$.

- **Step 2** Diffusion in mixture fraction space and chemistry are solved over the whole

[5] $N_s - 1$ species are accounted for with species N_s obtained from conservation of mass. Therefore, in addition to the temperature (or enthalpy), the total number of variables in N_s.

time step:

$$\frac{\partial Q_\kappa}{\partial t} = \underbrace{\frac{\langle\chi|\eta\rangle}{2}\frac{\partial^2 Q_\kappa}{\partial \eta^2}}_{\substack{\text{diffusion in } \eta\text{-space} \\ \text{(micro-mixing)}}} + \underbrace{\frac{\langle\dot{\omega}_\kappa|\eta\rangle}{\langle\rho|\eta\rangle}}_{\substack{\text{Chemical} \\ \text{source}}}; \quad t_\circ \leq t \leq t_\circ + \Delta t \tag{3.97}$$

The size of the system of equations at every grid point in physical space is $N_\eta \times N_s$.

- **Step 3** Convection and diffusion in physical space are solved over the second half of the time step:

$$\frac{\partial Q_\kappa}{\partial t} = \underbrace{-\langle u_i|\eta\rangle\frac{\partial Q_\kappa}{\partial x_i}}_{\text{Convection}} \underbrace{-\frac{1}{\langle\rho\rangle\tilde{P}(\eta)}\frac{\partial}{\partial x_i}\left[\langle\rho\rangle\,\langle u_i'' y_\kappa''|\eta\rangle\,\tilde{P}(\eta)\right]}_{\text{Diffusion in physical space}}; \quad t_\circ + \frac{\Delta t}{2} \leq t \leq t_\circ + \Delta t \tag{3.98}$$

As in step 1, the size of the system of equations at every grid point in η space is $N_x \times N_y \times N_s$.

Each step is initialised using the solution of the previous one. The non-stiff/stiff solvers VODE [31] (Chap. 4) and VODPK [30, 31, 33] (Chaps. 5–7) are employed in this work to solve each of the steps. The non-stiff steps 1 and 3 are treated using Adam's method. On the other hand, step 2 is stiff and therefore solved using the Backward Differentiation Formula (BDF). A time-step of 10^{-5} is employed. The absolute tolerances for the major and minor species are set to 10^{-7} and 10^{-10}, respectively, and the absolute tolerance for the temperature is set to 10^{-5}. A relative tolerance of 10^{-5} is employed. When a steady-state solution is desired, the transient CMC transport equations are solved by relaxation of the time step. Convergence is considered to be reached when the following criterion is met:

$$\max\left(\frac{|Q_T^{t+\Delta t} - Q_T^t|}{Q_T^t}\right) < 10^{-10} \tag{3.99}$$

3.5.4 Boundary conditions in mixture fraction space

The species and temperature Boundary Conditions (BCs) at $\eta = 0$ and $\eta = 1$ are obtained from the conditions of the oxidiser and fuel streams, respectively. Since these streams are non-reacting, the BCs at fuel and oxidiser inlets correspond to the adiabatic inert mixing between fuel and oxidiser over the range $0 \leq \eta \leq 1$. If a pilot is present between the fuel and oxidiser inlets (Chap. 5), the BCs are set by assuming adiabatic inert mixing between the oxidiser and the pilot streams for $0 \leq \eta \leq \tilde{\xi}_p$ and between the fuel and the pilot streams

for $\tilde{\xi}_p < \eta \leq 1$, where $\tilde{\xi}_p$ is the mean mixture fraction at the pilot [205]. Zero-gradient BCs are employed at entrainment boundaries and outlets if these are sufficiently far from the reaction zone.

3.5.5 Implementation of submodels and thermochemistry

CMC submodels

The integrals appearing in Girimaji's model (Eq. (3.75)) and the AMC (Eq. (3.72)) are computed using the quadrature integration package QUADPACK [181]. In Mortensen's β-PDF-based CSDR model, the incomplete beta-function $I(\eta; v, w)$ (Eq. (3.84)) is calculated using the method of continued fractions [193] and the partial derivatives of $II(\eta; v, w)$ (Eq. (3.85)) with respect to the $\tilde{\xi}$ and $\widetilde{\xi''^2}$ are computed using Ridders' method of polynomial extrapolations [193, 197]. Due to division by the PDF in the PDF-gradient model and Mortensen's β-PDF-based CSDR model, numerical instabilities may arise at low probabilities. To resolve this issue, $\langle u_i|\eta\rangle$ is set equal to its unconditional value, $\tilde{u}_i$, and $\langle\chi|\eta\rangle$ is set to zero when η falls outside $\tilde{\xi} \pm 7(\widetilde{\xi''^2})^{1/2}$. Additionally, in the event where Moretnsen's model yields unphysical negative values, $\langle\chi|\eta\rangle$ is set to zero.

Thermochemistry

The chemical kinetics package CHEMKIN II [194] is employed to compute all of the necessary thermochemical quantities appearing in the CMC equations for a given chemical kinetics mechanism.

3.6 Advances in CMC

This section reviews the applications of CMC and the advances made in the field since the introduction of the model.

3.6.1 Applications of the first-order closure and assessment of CMC submodels

The first-order closure for the conditional reaction rate, which is employed throughout this work, has been successfully applied to a variety of combustion problems. Some examples are

autoignition [59,116,143], attached flames [205], piloted flames [61,62,65,66,170,198,199], lifted flames [54,105,168,169,171,176,212], swirl-stabilized flames [64], counterflow flames [106], bluff body flames [111,112,167], enclosure fires [43,44], spray combustion [25,117,239] (Sect. 3.6.3), differential diffusion [124] (Sect. 3.6.4), and engine modelling [51,238].

Several assessment studies have been conducted with the aid of DNS and experimental measurements to validate the applicability of the different CMC submodels: the reaction rate closure [148,216,221], the scalar dissipation rate submodels [39,157,160,163,210,221], the velocity submodels [162, 210], the radiation submodels [15, 199], and the presumed PDF [39,160,163].

3.6.2 The second-order closure

As demonstrated in Eq. (3.92), the second order closure requires the knowledge of the conditional variances and covariances of the reactive scalars. The species covariance equations is presented here. For simplicity of notation, the conditional covariance of species ι and κ is denoted by $G_{\iota\kappa} = \langle y''_\iota y''_\kappa|\eta\rangle$. Assuming unity Lewis numbers and invoking the primary closure hypothesis, the transport equation of $G_{\iota\kappa}$ reads [128]:

$$\begin{aligned}\frac{\partial G_{\iota\kappa}}{\partial t} =& -\langle u_i|\eta\rangle\frac{\partial G_{\iota\kappa}}{\partial x_i} + \frac{\langle\chi|\eta\rangle}{2}\frac{\partial^2 G_{\iota\kappa}}{\partial\eta^2} - \frac{1}{\langle\rho|\eta\rangle P(\eta)}\frac{\partial}{\partial x_i}\left[\langle\rho|\eta\rangle\langle u''_i y''_\iota y''_\kappa|\eta\rangle P(\eta)\right] \\ &- \langle u''_i y''_\kappa|\eta\rangle\frac{\partial Q_\iota}{\partial x_i} - \langle u''_i y''_\iota|\eta\rangle\frac{\partial Q_\kappa}{\partial x_i} + \frac{1}{\langle\rho|\eta\rangle P(\eta)}\frac{\partial J_{g,\iota\kappa}}{\partial x_i} - 2\left\langle D\frac{\partial y''_\iota}{\partial x_i}\frac{\partial y''_\kappa}{\partial x_i}\middle|\eta\right\rangle \\ &+ \langle\dot\omega''_\kappa y''_\iota|\eta\rangle + \langle\dot\omega''_\iota y''_\kappa|\eta\rangle + \frac{\langle\chi'' y''_\kappa|\eta\rangle}{2}\frac{\partial^2 Q_\iota}{\partial\eta^2} + \frac{\langle\chi'' y''_\iota|\eta\rangle}{2}\frac{\partial^2 Q_\kappa}{\partial\eta^2}\end{aligned} \tag{3.100}$$

The equation of the conditional variance of species ι, $G_{\iota\iota} = \langle y''_\iota y''_\iota|\eta\rangle$, is obtained by setting $\kappa = \iota$ in Eq. (3.100). The governing equation of the conditional covariance of a species ι and the temperature, $G_{\iota T} = \langle y''_\iota T''|\eta\rangle$, is identical in form to Eq. (3.100) [128]. All the terms on the r.h.s are unclosed and require further modelling. Several closures are available in the literature for $\langle u_i|\eta\rangle$ (Sect. 3.3.3) and $\langle\chi_\xi|\eta\rangle$ (Sect. 3.3.4). The conditional turbulent fluxes in the third, fourth and fifth r.h.s. terms ($\langle u''_i y''_\iota y''_\kappa|\eta\rangle$, $\langle u''_i y''_\kappa|\eta\rangle$ and $\langle u''_i y''_\iota|\eta\rangle$) may be modelled using the gradient diffusion assumption. The turbulent flux in η-space appearing in the sixth term, J_g, is modelled following the closure proposed by Kim [109]:

$$J_{g,\iota\kappa} = C_g\langle\rho|\eta\rangle P(\eta)\frac{\langle\chi|\eta\rangle}{2}\frac{\partial G_{\iota\kappa}}{\partial\eta} \tag{3.101}$$

where C_g is a model constant set to 1. Different closures have been suggested for the remaining terms. Li and Bilger [136] model the seventh term as:

$$2\left\langle D\frac{\partial y_\iota''}{\partial x_i}\frac{\partial y_\kappa''}{\partial x_i}\middle|\eta\right\rangle = 2a_T\frac{\tilde{\varepsilon}}{\tilde{k}}G_{\iota\kappa} \tag{3.102}$$

where a_T is a model constant of the order of unity. Kim and Huh [113] replace a_T by $\sqrt{C_\iota C_\kappa}$ and set $C_\iota = 1$ for major species and temperature and $C_\iota = 2$ for radicals. Kim et al. [110] later suggest setting $C_\iota = 1/\sqrt{\xi_{st}(1-\xi_{st})}$ for major species and temperature and $C_\iota = 1/\xi_{st}$ for radicals. Based on the SLFM theory, Swaminathan and Bilger [217] propose the model:

$$2\left\langle D\frac{\partial y_\iota''}{\partial x_i}\frac{\partial y_\kappa''}{\partial x_i}\middle|\eta\right\rangle = \left\{\int \frac{\partial}{\partial\eta}\ln[y_\iota''^S(\eta,\chi_{st})]\frac{\partial}{\partial\eta}\ln[y_\kappa''^S(\eta,\chi_{st})]P_\chi(\chi_{st})d\chi_{st}\right\}\langle\chi|\eta\rangle G_{\iota\kappa} \tag{3.103}$$

where $y_\iota''^S(\eta,\chi_{st})$ is the conditional fluctuation approximated by the SLFM (see [217] for details) and χ_{st} is the stoichiometric scalar dissipation rate. Kim et al. [115] provide the first-order approximation for the reaction rate-species correlation (eighth and ninth terms):

$$\langle\dot{\omega}_\kappa'' y_\iota''|\eta\rangle = \left.\frac{\partial\dot{\omega}_\kappa}{\partial Y_l}\right|_{\mathbf{Y}=\mathbf{Q}} G_{\iota l} \tag{3.104}$$

Li and Bilger [136] model the scalar dissipation-species correlation (tenth and eleventh terms) as:

$$\langle\chi'' y_\iota''|\eta\rangle = R\langle\chi|\eta\rangle G_{\iota\iota}^{1/2} \tag{3.105}$$

where the correlation coefficient R depends on the Reynolds number. It is often assumed to be constant and set to unity. Using the SLFM theory, Kim et al. [110] propose an alternative approach for the modelling of $\langle\dot{\omega}_\kappa'' y_\iota''|\eta\rangle$ and $\langle\chi'' y_\iota''|\eta\rangle$. Their closures are given by:

$$\begin{aligned}\langle\dot{\omega}_\kappa'' y_\iota''|\eta\rangle =& \frac{G_{\iota\iota}^{1/2}}{\sigma_\iota}\left[\int \dot{\omega}_\kappa^S(\eta,\chi_{st})Y_\iota^S(\eta,\chi_{st})P_\chi(\chi_{st})d\chi_{st}\right.\\ &\left.-\left(\int\dot{\omega}_\kappa^S(\eta,\chi_{st})P_\chi(\chi_{st})d\chi_{st}\right)\left(\int Y_\iota^S(\eta,\chi_{st})P_\chi(\chi_{st})d\chi_{st}\right)\right]\end{aligned} \tag{3.106}$$

and

$$\begin{aligned}\langle\chi'' y_\iota''|\eta\rangle =& \frac{\langle\chi_\xi|\eta\rangle}{\langle\chi_\xi|\eta_{st}\rangle}\frac{G_{\iota\iota}^{1/2}}{\sigma_\iota}\left[\int \chi_{st}Y_\iota^S(\eta,\chi_{st})P_\chi(\chi_{st})d\chi_{st}\right.\\ &\left.-\left(\int\chi_{st}P_\chi(\chi_{st})d\chi_{st}\right)\left(\int Y_\iota^S(\eta,\chi_{st})P_\chi(\chi_{st})d\chi_{st}\right)\right]\end{aligned} \tag{3.107}$$

where $\dot{\omega}_\kappa^S(\eta, \chi_{\xi,st})$ and $Y_\iota^S(\eta, \chi_{\xi,st})$ are the SLFM solutions and σ_ι is the root mean square fluctuation of Y_ι^S.

It is evident from the above that the level of modelling is much higher compared to the first-order closure. The main issue with this approach is the requirement to solve a large number of conditional variance and co-variance equations. This requirement increases as the detail of chemical kinetics (the number of species) increases, making the computations extremely expensive. Techniques have been developed in order to make these computations tractable [115, 126]. Successful applications of the second-order closure span a number of combustion problems such as autoignition [50], piloted flames [65, 113], attached flames [63, 110, 126], and flames exhibiting extinction and reignition [115].

3.6.3 Spray combustion

The description of interactions between liquid fuel droplets and the surrounding gas in spray (two-phase) combustion requires more elaborate modelling compared to the case of single-phase gaseous flows. Smith et al. [206] derive the CMC equations for spray combustion. Essentially, the conditional species and temperature equations have the same form as Eqs. (3.23) and (3.34) with an additional source term accounting for the influence of the liquid phase on the gaseous phase on the r.h.s. of each. For convenience, the species and temperature sources are denoted by S_κ and S_T, respectively. They are given by [117, 206]:

$$S_\kappa = -\langle \Pi | \eta \rangle \frac{\partial Q_\kappa}{\partial \eta} \quad \text{and} \quad S_T = -\langle \Pi | \eta \rangle \frac{\partial Q_T}{\partial \eta} \tag{3.108}$$

where $\langle \Pi | \eta \rangle$ is the conditional evaporation rate[6]. Kim and Huh [117] investigate three methodologies for the treatment of droplet evaporation: (1) the no source method: the evaporation sources are neglected, (2) the boundary flux method: evaporation is assumed to occur at $\eta = 1$ with an external flux imposed at the boundary, and (3) the one-droplet model [195]: the droplets are arranged in clouds which are embedded homogeneously in freely decaying turbulence and the evaporation sources are treated as a monotonic function η. Kim and Huh [117] apply these modelling approaches to investigate autoignition in an n-heptane spray. Their results indicate that the conditional profiles do not vary noticeably near the stoichiometric mixture fraction where most reactions occur (after ignition takes place at the most reactive mixture fraction). Based on these findings, Wright et al. [239] adopt the no source approach to model autoignition and flame establishment in the same n-heptane spray.

[6] The notation $\langle \dot{s}_\xi | \eta \rangle$ is employed in [117, 206] instead of $\langle \Pi | \eta \rangle$.

In a recent theoretical study, Mortensen and Bilger [161] use the joint PDF approach [118,120] to derive the CMC equations in two-phase flow. Borghesi et al. [25] consider the case of dilute sprays with pure liquid fuel droplets. The conditional species equation is given by Eq. (3.23) in addition to the term

$$S_\kappa = \left[\delta_{\kappa f} - Q_\kappa - (1-\eta)\frac{\partial Q_\kappa}{\partial \eta}\right]\langle \Pi|\eta\rangle - \frac{1}{\bar{\rho}\tilde{P}(\eta)}\frac{\partial}{\partial \eta}\left[(1-\eta)\bar{\rho}\tilde{P}(\eta)\langle y_\kappa'' \Pi''|\eta\rangle\right] \tag{3.109}$$

on its r.h.s. and the conditional temperature equation is given by Eq. (3.34) supplemented by the term

$$S_T = -\left[\frac{h_{fg}}{\langle c_p|\eta\rangle} + Q_T - (1-\eta)\frac{\partial Q_T}{\partial \eta}\right]\langle \Pi|\eta\rangle - \frac{1}{\bar{\rho}\tilde{P}(\eta)}\frac{\partial}{\partial \eta}\left[(1-\eta)\bar{\rho}\tilde{P}(\eta)\langle T'' \Pi''|\eta\rangle\right] \tag{3.110}$$

on its r.h.s. $\delta_{\kappa f}$ is equal to 1 for the fuel species and 0 otherwise, $\langle \Pi|\eta\rangle$ is the conditional evaporation rate and h_{fg} is the enthalpy of vaporization. Borghesi et al. [25] assume that the joint fluctuations of Π and the reactive scalars to be negligible ($\langle y_\kappa'' \Pi''|\eta\rangle \approx 0$ and $\langle T'' \Pi''|\eta\rangle \approx 0$), and thereby neglect the second terms on the r.h.s. of Eqs. (3.109) and (3.110). To model the conditional evaporation rate, they assume that the mixture fraction at saturation, ξ_s, is equal to the fuel mass fraction at the droplet surface, $Y_{f,s}$, for which an estimate is provided in terms of the saturation pressure, p_s. They obtain p_s by integrating the Clausius-Clapeyron equation between a reference state and the saturation state. The closure conditional evaporation rate takes the form:

$$\langle \Pi|\eta\rangle = \sum_{d=1}^{N_d} \frac{\tilde{\Pi}\delta(\eta - \xi_{s,d})}{\tilde{P}(\eta)} \tag{3.111}$$

where N_d is the number of droplets within a given computational cell. The Favre-averaged evaporation rate, $\tilde{\Pi}$, is closed using the PSI-cell model wherein droplets are treated as sources of mass to the gaseous phase. The remaining unclosed terms $\langle \dot{\omega}_\kappa|\eta\rangle$, $\langle u_i|\eta\rangle$, $\langle \chi|\eta\rangle$ and $\tilde{P}(\eta)$ are modelled using the first-order closure, the linear velocity model, the AMC and the β-PDF, respectively. In order to account for the presence of fuel vapour, corrections are applied to $\langle \chi|\eta\rangle$ and $\tilde{P}(\eta)$ and additional source terms are included in the $\tilde{\xi}$ and $\widetilde{\xi''^2}$ transport equations (see [25] for further details). The model is applied in [25] to an n-heptane spray burning under conditions relevant to a diesel engine. The results show that the inclusion of droplet evaporation affects the predictions of the mixing field, but has a small effect on ignition delay, and almost no impact on the flame propagation and anchoring mechanisms.

3.6.4 Differential diffusion

The effects of differential diffusion can be included in the CMC equations by employing non-unity Lewis numbers. Kronenburg and Bilger investigate these effects in non-reacting [123,125] and reacting [124] flows. By setting the diffusivity of species κ to D_κ and that of ξ to D_ξ, and following the same procedure outlined in Sect. 3.2.1, it can be easily shown that the conditional species transport equation in the reacting case takes the form [124]:

$$\frac{\partial Q_\kappa}{\partial t} = -\langle u_i|\eta\rangle\frac{\partial Q_\kappa}{\partial x_i} + \frac{\mathrm{Le}_\xi}{\mathrm{Le}_\kappa}\frac{\langle\chi|\eta\rangle}{2}\frac{\partial^2 Q_\kappa}{\partial\eta^2} + \frac{\langle\dot{\omega}_\kappa|\eta\rangle}{\langle\rho|\eta\rangle} + \frac{e_{Q_\kappa}+e_{y''_\kappa}}{\langle\rho|\eta\rangle} \tag{3.112}$$

where

$$e_{Q_\kappa} = \frac{\partial}{\partial x_i}\left(\rho D_\kappa\frac{\partial Q_\kappa}{\partial x_i}\right) + \left\langle\frac{\partial Q_\kappa}{\partial\eta}\frac{\partial}{\partial x_i}\left[\rho D_\xi\left(\frac{\mathrm{Le}_\xi}{\mathrm{Le}_\kappa}-1\right)\frac{\partial\xi}{\partial x_i}\right] + \rho D_\kappa\frac{\partial\xi}{\partial x_i}\frac{\partial}{\partial x_i}\left(\frac{\partial Q_\kappa}{\partial\eta}\right)\middle|\eta\right\rangle, \tag{3.113}$$

$$e_{y''_\kappa} = -\left\langle\rho\frac{\partial y''_\kappa}{\partial t} + \rho u''_i\frac{\partial y''_\kappa}{\partial x_i} - \frac{\partial}{\partial x_i}\left(\rho D_\kappa\frac{\partial y''_\kappa}{\partial x_i}\right)\middle|\eta\right\rangle, \tag{3.114}$$

and

$$\chi = 2D_\xi\frac{\partial\xi}{\partial x_i}\frac{\partial\xi}{\partial x_i} \tag{3.115}$$

is the dissipation rate of ξ. It is obvious that by setting $D_\kappa = D_\xi = D$, the ratio $\mathrm{Le}_\xi/\mathrm{Le}_\kappa$ becomes equal to unity, and Eqs. (3.8), (3.9) and (3.11) are recovered. According to the primary closure hypothesis, the contribution of e_{Q_κ} is small and hence neglected. However, the new term in Eq. (3.113) (the second on the r.h.s.) needs to be retained if differential diffusion is to be considered. Assuming constant but non-unity Le, it may be written as:

$$\left\langle\frac{\partial Q_\kappa}{\partial\eta}\frac{\partial}{\partial x_i}\left[\rho D_\xi\left(\frac{\mathrm{Le}_\xi}{\mathrm{Le}_\kappa}-1\right)\frac{\partial\xi}{\partial x_i}\right]\middle|\eta\right\rangle = \left(\frac{\mathrm{Le}_\xi}{\mathrm{Le}_\kappa}-1\right)\langle M|\eta\rangle\frac{\partial Q_\kappa}{\partial\eta} \tag{3.116}$$

where

$$\langle M|\eta\rangle = \left\langle\frac{\partial}{\partial x_i}\left(\rho D_\xi\frac{\partial\xi}{\partial x_i}\right)\middle|\eta\right\rangle \tag{3.117}$$

is the conditional diffusion. This quantity is related to $\langle\chi|\eta\rangle$ by [120]:

$$\langle M|\eta\rangle = \frac{1}{P(\eta)\langle\rho|\eta\rangle}\frac{\partial}{\partial\eta}\left[\frac{\langle\chi|\eta\rangle}{2}P(\eta)\langle\rho|\eta\rangle\right] \tag{3.118}$$

the inclusion of the first term on the r.h.s. of Eq. (3.113) is straightforward and poses no modelling issues. To model $e_{y''_\kappa}$, Kronenburg and Bilger [124, 125] propose the DNS-based closure:

$$e_{y''_\kappa} = -C\left|\frac{\mathrm{Sc}_\kappa - \mathrm{Sc}_\xi}{\mathrm{Sc}_\kappa}\right|^{1/8}\frac{Q_{z,\kappa}}{\eta} \tag{3.119}$$

where C is a model constant set to 0.4, η is the Kolmogorov time scale (not to be confused with the sample space variable of ξ) and $Q_{z,\kappa}$ is the conditional average of the differential diffusion variable z_κ. This variable is defined as $z_\kappa = Y_\kappa - Y_\kappa^+$ where Y_κ^+ is governed by the same transport equation as Y_κ except that diffusion coefficient D_κ is set to D_ξ (the chemical sources in both equations are identical). Kronenburg and Bilger [124, 125] also derive an equation for the conditional enthalpy and suggest a similar treatment for the term involving conditional fluctuations. The authors apply the proposed formulation to a turbulent hydrogen/air jet flame in [124] and conclude that the inclusion of differential diffusion effects improves the predictions of radicals and capture super-equilibrium effects.

3.6.5 Premixed combustion

CMC for premixed combustion was first proposed by Bilger [18]. The idea behind this method is very similar to the non-premixed CMC. The difference lies in the nature of the conditioning variable. In the premixed CMC, scalars are conditioned on a normalised PV instead of ξ. This choice of conditioning variable is motivated by the fact that a PV is capable of distinguishing between unburnt and burnt mixtures, and allows the determination of the flame position. Following the procedure outlined in Sect. 3.2.1, the conditional average of Y_κ is defined as $Q_\kappa(\theta, \mathbf{x}, t) = \langle Y_\kappa(\mathbf{x}, t)|c(\mathbf{x}, t) = \theta\rangle$. Here c is a normalised PV defined as in Eq. (2.91) and governed by the transport equation given by Eq. (2.93), and θ is a sample space variable of c, such that $0 \leq \theta \leq 1$. Y_κ is decomposed as $Y_\kappa(\mathbf{x}, t) = Q_\kappa(c(\mathbf{x}, t), \mathbf{x}, t) + y''_\kappa(\mathbf{x}, t)$ such that $\langle y''_\kappa|c(\mathbf{x}, t) = \theta\rangle = 0$. The conditional transport equation of Y_κ is derived by substituting this decomposition into the transport equation of Y_κ (Eq. (2.4) with $\mathrm{Le}_\kappa \neq 1$), and subsequently applying the transformations given by Eqs. (3.4)–(3.6) with ξ and η replaced by c and θ, respectively. Further assuming negligible density fluctuations, the equation of Q_κ becomes [218][7]:

$$\frac{\partial Q_\kappa}{\partial t} = -\langle u_i|\theta\rangle\frac{\partial Q_\kappa}{\partial x_i} + \frac{\langle\chi_{c,\kappa}|\theta\rangle}{2}\frac{\partial^2 Q_\kappa}{\partial\theta^2} + \frac{\langle\dot{\omega}_\kappa|\theta\rangle}{\langle\rho|\theta\rangle} - \frac{\langle\dot{\omega}_c|\theta\rangle}{\langle\rho|\theta\rangle}\frac{\partial Q_\kappa}{\partial\theta} + \frac{e_{Q_\kappa} + e_{y''_\kappa}}{\langle\rho|\theta\rangle} \tag{3.120}$$

[7] In [218], the thermal diffusivity (α) is employed instead of a diffusion coefficient (D_c) in the equation of c, which allows the incorporation of the Lewis number ($\mathrm{Le}_\kappa = \alpha/D_\kappa$) in the governing equations.

where

$$e_{Q_\kappa} = \frac{\partial}{\partial x_i}\left(\rho D_\kappa \frac{\partial Q_\kappa}{\partial x_i}\right) + \left\langle \frac{\partial Q_\kappa}{\partial \theta}\frac{\partial}{\partial x_i}\left[\rho(D_\kappa - D_c)\frac{\partial c}{\partial x_i}\right] + \rho D_\kappa \frac{\partial c}{\partial x_i}\frac{\partial}{\partial x_i}\left(\frac{\partial Q_\kappa}{\partial \theta}\right)\middle|\theta\right\rangle, \quad (3.121)$$

$$e_{y''_\kappa} = -\left\langle \rho\frac{\partial y''_\kappa}{\partial t} + \rho u''_i \frac{\partial y''_\kappa}{\partial x_i} - \frac{\partial}{\partial x_i}\left(\rho D_\kappa \frac{\partial y''_\kappa}{\partial x_i}\right)\middle|\theta\right\rangle, \quad (3.122)$$

and

$$\chi_{c,\kappa} = 2D_\kappa \frac{\partial c}{\partial x_i}\frac{\partial c}{\partial x_i} \quad (3.123)$$

is the scalar dissipation rate of c. The conditional enthalpy and temperature equations can be obtained in a similar fashion. Apart from the fourth term on the r.h.s. of Eq. (3.120), Eqs. (3.120)-(3.123) are essentially identical in form to Eqs. (3.112)-(3.115). Although chemical in nature, this term may be interpreted as convective in θ-space when $\langle \dot{\omega}_c|\eta,\theta\rangle$ is viewed as "reaction progress velocity" [3]. The quantities $\langle u_i|\theta\rangle$, $\langle \chi_{c,\kappa}|\theta\rangle$, $\langle \dot{\omega}_\kappa|\theta\rangle$, e_{Q_κ} and $e_{y''_\kappa}$ are all unclosed and require further modelling. As in non-premixed CMC, Swaminathan and Bilger [218] invoke the primary closure hypothesis to model e_{Q_κ} and $e_{y''_\kappa}$. It can be shown that the first and third terms of e_{Q_κ} are negligible for finite Sc and high Re, whereas the second term is important and should not be neglected. For $\partial Q_\kappa/\partial\theta > 0$, this term is responsible for heat diffusion away from a point in θ-space if $D_c < D_\kappa$ and towards it if $D_c > D_\kappa$ [218]. Neglecting density and diffusivity fluctuations, it can be shown that $e_{y''_\kappa}$ reduces to [218]:

$$e_{y''_\kappa} \approx -\frac{\langle\rho|\theta\rangle}{\langle\rho\rangle\tilde{P}(\theta)}\frac{\partial}{\partial x_i}\left(\langle\rho\rangle\,\langle u''_i y''_\kappa|\theta\rangle\,\tilde{P}(\theta)\right) \quad (3.124)$$

where $\langle u''_i y''_\kappa|\theta\rangle$ is the conditional turbulent flux of species κ and $\tilde{P}(\theta)$ is the marginal PDF of c. Swaminathan and Bilger [218,219] propose closures for all of the unclosed terms and validate them against DNS. The reader is referred to refs. [218,219] for further details. The assessment of the performance of the first-order closure for $\langle \dot{\omega}_\kappa|\theta\rangle$ is highlighted here. This closure is found to be satisfactory in general with some discrepancies in the predictions of the reaction rates of minor species. The authors attribute these discrepancies to the neglect of the conditional fluctuations.

The application of the premixed CMC is limited to a small number of studies. Examples are the calculations of Martin et al. [145] who apply the method to a lean premixed gas turbine combustor and the more recent study of Thornber et al. [222] who employ the premixed CMC-LES approach to investigate a lean premixed slot Bunsen burner.

3.6.6 LES-CMC

All of the CMC methods discussed thus far are applicable in the context of RANS. Navarro-Martinez et al. [170] derive the CMC equations for LES. The density-weighted conditionally filtered average of a scalar Φ is defined as:

$$\widetilde{\Phi|\eta}(\eta;\mathbf{x},t) = \frac{\int_V \rho(\mathbf{x}',t)\Phi(\mathbf{x}',t)\psi_\eta[\xi(\mathbf{x},t)-\eta]G(\mathbf{x}-\mathbf{x}',\Delta)dV'}{\bar{\rho}(\mathbf{x},t)\tilde{P}(\eta;\mathbf{x},t)} \tag{3.125}$$

where V is the volume of the computational domain, $\psi_\eta[\xi(\mathbf{x},t)-\eta] = \delta[\xi(\mathbf{x},t)-\eta]$ is the fine-grained PDF, $G(\mathbf{x}-\mathbf{x}',\Delta)$ is a positive filter function of specified filter width Δ, $\bar{\rho}(\mathbf{x},t)$ is the filtered density, and $\tilde{P}(\eta;\mathbf{x},t)$ is the density-weighted Filtered probability Density Function (FDF). The FDF is defined as:

$$\tilde{P}(\eta;\mathbf{x},t) = \frac{1}{\bar{\rho}(\mathbf{x},t)}\int_V \rho(\mathbf{x}',t)\psi_\eta[\xi(\mathbf{x},t)-\eta]G(\mathbf{x}-\mathbf{x}',\Delta)dV' \tag{3.126}$$

The filtered density and the filtered value of Φ are obtained from:

$$\bar{\rho}(\mathbf{x},t) = \left\{\int_0^1 \left[\widetilde{\rho|\eta}(\eta;\mathbf{x},t)\right]^{-1}\tilde{P}(\eta;\mathbf{x},t)d\eta\right\}^{-1} \tag{3.127}$$

and

$$\tilde{\Phi}(\mathbf{x},t) = \int_0^1 \widetilde{\Phi|\eta}(\eta;\mathbf{x},t)\tilde{P}(\eta;\mathbf{x},t)d\eta \tag{3.128}$$

A detailed derivation of the conditionally filtered transport equation of Φ is available in [170]. Its outline is provided here. The equation of $\widetilde{\Phi|\eta}$ is derived starting from the transport equations of ψ_η and $\Phi\psi_\eta$. These two equations are first multiplied by $G(\mathbf{x}-\mathbf{x}',\Delta)$ and then integrated over the physical domain, ultimately leading to the transport equations of $\tilde{P}$ and $\widetilde{\Phi|\eta}\tilde{P}$. The latter equation involves the conditionally filtered flux of Φ, $\widetilde{J_\Phi|\eta}$. This quantity is linearised using the diffusion approximation described in [120]. The equation of $\widetilde{\Phi|\eta}$ is finally obtained by multiplying the transport equation of $\tilde{P}$ by $\widetilde{\Phi|\eta}$ and subtracting the resulting expression from the transport equation of $\widetilde{\Phi|\eta}\tilde{P}$. The conditionally filtered transport equation of species κ is obtained by setting $\Phi = Y_\kappa$, leading to [170]:

$$\frac{\partial Q_\kappa}{\partial t} = -\widetilde{u_i|\eta}\frac{\partial Q_\kappa}{\partial x_i} + \frac{\widetilde{\chi|\eta}}{2}\frac{\partial^2 Q_\kappa}{\partial \eta^2} + \frac{\widetilde{\dot{\omega}_\kappa|\eta}}{\widetilde{\rho|\eta}} + e_{y''_\kappa} \tag{3.129}$$

where $Q_\kappa = \widetilde{Y_\kappa|\eta}$ is the conditionally filtered species mass fraction, and $\widetilde{u_i|\eta}$, $\widetilde{\chi|\eta}$ and $\widetilde{\dot{\omega}_\kappa|\eta}$ are the conditionally filtered velocity, scalar dissipation rate, and chemical reaction rate,

respectively. Unity Lewis numbers are assumed and simplifications valid for high Re are applied in the process of obtaining Eq. (3.129) (see [170]). The term $e_{y''_\kappa}$ is given by:

$$e_{y''_\kappa} = -\frac{1}{\bar{\rho}\tilde{P}(\eta)}\frac{\partial}{\partial x_i}\left[\bar{\rho}\Big(\underbrace{\widetilde{u_i Y_\kappa|\eta} - \widetilde{u_i|\eta} Q_\kappa}_{\widetilde{u''_i y''_\kappa|\eta}}\Big)\tilde{P}(\eta)\right] \tag{3.130}$$

The conditionally filtered enthalpy equation is obtained by setting $\Phi = h$. It has the same form as Eq. (3.129) in addition to a conditionally filtered radiative source on the r.h.s.

In most CMC-LES studies, the FDF is presumed using the two-parameter β distribution, which requires the knowledge of the resolved mixture fraction and the sub-grid scale variance. The modelled equation for the resolved mixture fraction is given by [170]:

$$\bar{\rho}\frac{\partial\tilde{\xi}}{\partial t} + \bar{\rho}\tilde{u}_i\frac{\partial\tilde{\xi}}{\partial x_i} = \frac{\partial}{\partial x_i}\left[\bar{\rho}(D + D_\mathrm{t})\frac{\partial\tilde{\xi}}{\partial x_i}\right] \tag{3.131}$$

where D_t is the sub-grid scale turbulent diffusivity. This quantity is modelled as [170]:

$$D_t = (C_D\Delta)^2(2\tilde{S}_{ij}\tilde{S}_{ij})^{1/2} \tag{3.132}$$

where C_D is a model constant and $\tilde{S}_{ij}$ is the filtered strain rate tensor. The sub-grid scale variance may be modelled using [170]:

$$\widetilde{\xi''^2_\mathrm{sgs}} = C_\xi\Delta^2\frac{\partial\tilde{\xi}}{\partial x_i}\frac{\partial\tilde{\xi}}{\partial x_i} \tag{3.133}$$

where C_ξ is a constant assigned the value 0.1. The conditionally filtered turbulent flux $\widetilde{u''_i y''_\kappa|\eta}$ appearing in Eq. (3.135) is usually modelled using the gradient diffusion assumption:

$$\widetilde{u''_i y''_\kappa|\eta} = -D_t\frac{\partial Q_\kappa}{\partial x_i} \tag{3.134}$$

The conditionally filtered velocity is often assumed to be equal to its unconditional counterpart:

$$\widetilde{u_i|\eta} = \tilde{u}_i \tag{3.135}$$

Two approaches are common for the modelling of the conditionally filtered scalar dissipation rate: the inversion method employed in [170] and the AMC. Both approaches require the knowledge of the filtered scalar dissipation, which is given by:

$$\tilde{\chi} = 2D\widetilde{\frac{\partial\xi}{\partial x_i}\frac{\partial\xi}{\partial x_i}} \tag{3.136}$$

$\tilde{\chi}$ is split into resolved and sub-grid scale parts:

$$\tilde{\chi} = \tilde{\chi}_{\text{res}} + \tilde{\chi}_{\text{sgs}} \tag{3.137}$$

The resolved part is computed from:

$$\tilde{\chi}_{\text{res}} = 2D \frac{\partial \tilde{\xi}}{\partial x_i} \frac{\partial \tilde{\xi}}{\partial x_i} \tag{3.138}$$

and the sub-grid scale part is obtained using [170]:

$$\tilde{\chi}_{\text{sgs}} = C_\chi (2\tilde{S}_{ij}\tilde{S}_{ij})^{1/2} \widetilde{\xi''^2}_{\text{sgs}} \tag{3.139}$$

where C_χ is a constant of the order of unity.

LES-CMC implementations employing the first-order closure for the modelling of $\widetilde{\dot{\omega}_\kappa|\eta}$ have been successfully applied to attached flames [9, 170, 243], lifted flames [168, 169, 171, 212], bluff-body flames [167, 223, 224], and spray combustion [227].

3.6.7 Double-conditioning

As discussed in Sect. 3.6.2, the second-order modelling of the conditional chemical reaction rates overcomes the shortcomings of the first-order closure in the presence of substantial conditional fluctuations. Another approach for the treatment of these fluctuations is to introduce a second conditioning variable beside ξ. First suggested by Bilger [18,19], this extension is referred to as DCMC. The first-order closure in DCMC is justified on the grounds that doubly-conditional fluctuations are of smaller order than their singly-conditional counterparts, and hence may be safely neglected. However, DCMC yields a number of unclosed term that require complicated modelling. DCMC modelling will be addressed in depth in Chapter 8.

3.7 Summary

The first-order CMC was presented in this chapter. The decomposition approach and the primary closure hypothesis were used to demonstrate the derivation of the conditional species and temperature transport equations. Several submodels for the unclosed conditional terms resulting from the CMC derivation were presented. The numerical methods

employed throughout this work were highlighted. A brief review of advances in CMC was provided.

In the next four chapters, the first-order CMC is applied to simulate the autoignition of methane-based fuel blends in a shock-tube (Chap. 4), a piloted methane/air turbulent jet flame (Chap. 5) and a lifted hydrogen/nitrogen turbulent jet flame (Chaps. 6 and 7). In Chap. 8, the first-order CMC is extended to include a normalised temperature-related second conditioning variable beside the mixture fraction.

Chapter 4

Modelling of Shock Tube Autoignition of Methane-Based Fuel Blends

The first-order CMC is applied to investigate the shock tube autoignition of several high-pressure CH_4-based fuel blends injected into lower pressure heated air over a wide range of pre-combustion air temperatures. Mixture consisting of 100% CH_4, 90% CH_4/10% C_2H_6, 80% CH_4/20% H_2, and 80% CH_4/20% N_2 are considered. The turbulent flow field and CMC calculations are decoupled based on the frozen mixing assumption. The standard k-ε turbulence model is used to perform the flow and mixing fields calculations. The CMC equations are cross-stream averaged due to the weak radial dependence of the conditional scalars in shear flows. Two formulations are implemented to model the CSDR. Detailed and optimized chemical kinetics mechanisms are used for each fuel blend. The predicted ignition delays and kernel locations are compared to experimental measurements. It is found that C_2H_6 and H_2 additives do not change the main CH_4 oxidisation pathways but provide additional ignition-promoting reactions. The decomposition of these two additives supplies active radicals, which in turn promote the decomposition of CH_4 via different chain-branching reactions, leading to shorter ignition delays. On the other hand, N_2 additives reduce the amount of CH_4 available for reaction, causing delayed ignition. It is further shown that ignition in all mixtures always occurs in lean mixtures and at low scalar dissipation rates.

4.1 Introduction

Autoignition can be defined as the process in which a fuel-oxidiser mixture reacts in a self-heating fashion, leading to the ignition of the mixture. The autoignition mechanism involves a series of chain reactions and a large number of species that emerge during the oxidisation of the fuel. This results in complex and strongly coupled interactions between chemistry and turbulent mixing. Two key quantities of interest for engine designers are the location of the ignition kernel and ignition delay. Due to the difficulties and high costs associated with the experimental measurements of a reacting mixture inside an running engine, it is crucial to develop reliable chemical kinetics and turbulent combustion models that are able to accurately predict autoignition in conditions relevant to engine operation.

In the past few years, several experimental studies were conducted in order to improve the understanding of the ignition chemistry of methane and to investigate the effect of additives on the ignition process [52, 72, 166, 215, 240]. Research on methane combustion is motivated by some exclusive features of natural gas such as its low cost, abundance, and low emissions. Natural gas consists of different hydrocarbons of varying concentrations, primarily methane. The strategy of using additives such as hydrogen, is increasingly utilised in order to reduce emissions. The combustion of natural gas is encountered in many engineering applications such as direct-injection compression-ignition engines, industrial burners, and gas turbines. The requirement for versatile, high-efficiency, and low-emission engines has prompted the need for reliable turbulent combustion models and detailed chemical kinetics that can accurately predict autoignition and subsequent flame propagation. The modelling of autoignition of non-premixed transient fuel jets in direct-injection systems is a challenging task due to the unsteady and turbulent nature of the ignition phenomenon, and due to the stiff and non-linear chemical kinetics involved in the oxidisation of the fuel.

Different approaches have been applied to model the turbulence-chemistry interactions, such as the flamelet models [24, 108, 234] and PDF methods [96, 97, 132]. First-order CMC has been successfully applied to several autoignition problems [59, 116, 117, 143, 239]. Further developments related to the effect of conditional fluctuations were investigated using a second-order closure for the conditional chemical source [148]. However, reasonable agreement has been achieved in previous studies using the simpler first-order closure [59, 116, 117, 143, 239]. This approach is further supported by the DNS results of Sreedhara and Lakshmisha [209]. Also using DNS, it is shown that ignition always occurs at a specific value of mixture fraction, referred to as "the most reactive mixture fraction", and at low scalar dissipation rates [147, 149].

The objective of this study is to apply the first-order CMC to predict the ignition delay and the ignition kernel location of methane (CH_4), methane-ethane (CH_4/C_2H_6), methane-

Table 4.1: Composition of the fuel blends (in volume).

Mixture	Fuel blend
A	100% CH_4
B	90% CH_4 + 10% C_2H_6
C	80% CH_4 + 20% H_2
D	80% CH_4 + 20% N_2

hydrogen (CH_4/H_2), and methane-nitrogen (CH_4/N_2) jets under engine relevant conditions over a wide range of pre-combustion air temperatures. Each fuel blend is treated separately with suitable detailed chemical kinetics, and the results are compared to the experimental measurements of Wu [240]. To the author's best knowledge, CMC was never previously applied to these recent sets of experimental data and conditions. Although conditional fluctuations may be large in autoignition scenarios [148], it is useful first to evaluate the performance of first-order CMC placed in the perspective of the level of accuracy required for practical engine calculations.

4.2 Shock tube experiments

The current numerical study focuses on the experimental measurements conducted by Wu [240]. In these experiments, a shock tube facility is used to investigate the autoignition of non-premixed CH_4, CH_4/C_2H_6, CH_4/H_2, and CH_4/N_2 air mixtures. The compositions of the four fuel blends are shown in Table 4.1. A schematic of the experimental apparatus is shown in Fig. 4.1. The shock tube has a circular cross-section with an inner diameter of 5.9 cm and a total length of 7.90 m, the driver and driven sections being 3.11 m and 4.79 m long, respectively. An electronically controlled injector is used to inject the gaseous fuel into the preheated and compressed air. The injector has a central hole of 0.275 mm in diameter (d) and is mounted at the centre of the endplate of the shock tube in order to inject the fuel along the centreline. To provide optical access to the experimental area, a stainless steel section equipped with a quartz windows is attached to the end of the driven section. A high-speed digital camera (31000 frames per second) is used to capture the location of the initial ignition kernel. The location of this kernel is identified by the appearance of a non-contiguous flame region that is able to develop into a fully fledged jet flame. Accordingly, ignition delay, t_d, is defined as the time from the start of the injection of the fuel to the appearance of the ignition kernel. The experimental conditions are summarised in Table 4.2.

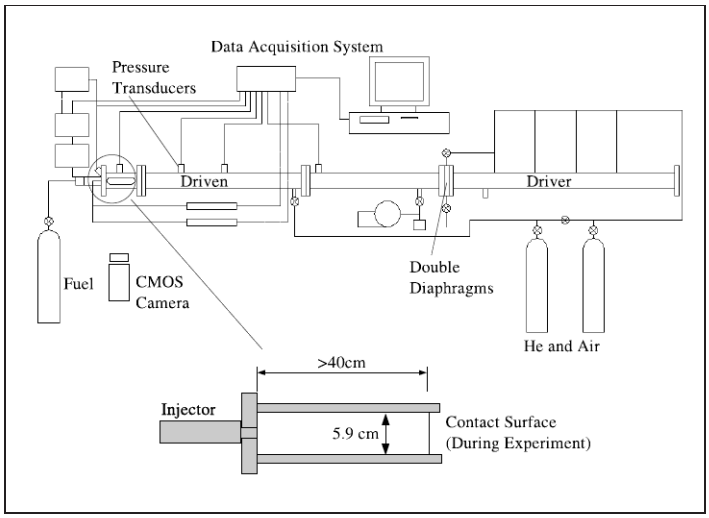

Figure 4.1: Schematic of the shock tube facility [240].

Table 4.2: Experimental conditions [240].

t_i [ms]	P_i [bar]	P_o [bar]	T_i [K]	T_o [K]
1.5	120	∼30	294	1200–1400

Nomenclature: t_i, injection duration; P_i, injection pressure; P_o, initial air pressure; T_i, fuel temperature; T_o, air temperature.

Wu [240] gives an estimate in the change of the average ignition delay ($\bar{t}_d$) and average normalised ignition kernel location ($\bar{Z}_k^*$). The latter is defined as the average of $Z_k^* = Z_k/d^*$, where $d^* = d(P_i/P_o)^{1/2}$, P_i is the fuel injection pressure, P_o initial air pressure and d the injector hole diameter. A 7% decrease is reported in $\bar{t}_d$ when H_2 is added to CH_4, while $\bar{Z}_k^*$ remains almost unaffected. On the other hand, the addition of N_2 increases $\bar{t}_d$ and $\bar{Z}_k^*$ by 13% and 28%, respectively. As for the case where C_2H_6 is added, Wu [240] finds the quantification of the change in $\bar{t}_d$ through the experimental data difficult due to large scatter. However, exponential curve fitting suggests an overall 14% decrease for $\bar{t}_d$ and 28% increase for $\bar{Z}_k^*$. Experimental uncertainties are estimated to be (+0.106 ms, -0.073 ms) for t_d and ±2% for Z_k^* [240]. No differential diffusion for CH_4/H_2 is reported in the experiments.

4.3 Mathematical model

4.3.1 Conditional Moment Closure

In the current CMC implementation, radiative heat transfer and pressure work are neglected. Therefore, the conditional enthalpy, Q_h, is conserved. As such, only the conditional species transport equation, Eq. (3.23), is solved and the conditional temperature, Q_T, is obtained from the knowledge of the calculated $\{Q_\kappa|\kappa = 1, 2, \cdots, N_s\}$ and the conserved Q_h. The PDF is presumed using the β-distribution given by Eq. (3.37). Two expressions are separately implemented to model the conditional scalar dissipation rate: Girimaji's model, Eq. (3.75), and the AMC, Eq. (3.72). The conditional velocity is approximated following the linear model, Eq. (3.69). The conditional turbulent fluxes of the species are modelled using the gradient diffusion assumption, Eq. (3.67). A turbulent Schmidt number of 0.9 is employed in Eq. (2.56) to compute the turbulent diffusivity following [89, 239]. The first-order closure given by Eq. (3.90) is implemented to model the conditional chemical source term.

4.3.2 Turbulent flow field calculations

The turbulent flow field and the CMC calculations are decoupled. The turbulent flow field calculations are first performed, and then used as input to the CMC calculations. This strategy is valid in the current autoignition problem since the reaction rates are slow before ignition takes place, which results in small density variations. By neglecting these changes, it is possible to perform the flow field and the CMC calculations separately. This technique was successfully implemented by Devaud and Bray [54], Markides et al. [143], and El Sayed and Devaud [59].

The axisymmetric computational domain has dimensions of 0.1 m (length) $\times$ 0.0295 m (radius). ANSYS CFX [4] is used to perform the turbulent velocity and mixing field calculations based on an unstructured computational mesh consisting of 259 $\times$ 72 unevenly-spaced nodes in the axial and radial directions, respectively. The computational domain is initialized with pure air at a given average temperature and pressure calculated from the experimental data. The walls of the shock tube are assumed to be smooth and adiabatic, and no slip conditions apply. The inlet boundary conditions are defined by assuming an isentropic expansion of the fuel jet at the tip of the injector with the upstream pressure and temperature equal to 120 bar and 295 K, respectively, and the downstream pressure and temperature equal to the initial experimental conditions ($\simeq$ 30 bar and air temperature, T_o,

between 1200 K and 1400 K). The resulting injection velocity depends on the composition of the fuel mixture, and was found to be around 600 m/s. In the simulations the pressure variations are found to be less than 10% of the initial pressure in the shock tube and are confined in a small region close to the nozzle exit far from potential ignition regions. Thus, pressure work is assumed negligible. The standard k-ε turbulence model is employed in the calculations. The second-order high resolution scheme [16] is used for the discretization of the advection terms. The transient terms are discretized using the second-order backward Euler scheme. An adaptive time step is utilized and convergence is achieved based on a maximum residual target of 10^{-3}.

4.3.3 The CMC implementation

When CMC is applied to turbulent shear flows, the dependence of conditional averages on the cross-flow (radial) coordinate is weak, and hence may be neglected. This is known as the shear flow approximation. This assumption is supported by the asymptotic analysis of Klimenko [119] and validated by experimental measurements [20, 220]. Klimenko [119] notes that the PDF is a stronger function of the cross-stream coordinate compared to conditional averages. Therefore, the cross-stream variation of the PDF needs to be taken into account.

In cylindrical coordinates, the area-weighted average of a scalar $\phi(t, x, r, \eta)$ is defined as:

$$\{\phi\}_R (t, x, \eta) = \frac{2}{R^2} \int_0^R \phi(t, x, r, \eta) r dr \tag{4.1}$$

The cross-stream average of $\phi(t, x, r, \eta)$ is defined as ratio of the area-weighted average of the product $\phi(t, x, r, \eta)\tilde{P}(t, x, r, \eta)$, to the area-weighted average of $\tilde{P}(t, x, r, \eta)$:

$$\{\phi\}_{R^+} (t, x, \eta) = \frac{\{\phi\tilde{P}\}_R(t, x, \eta)}{\{\tilde{P}\}_R(t, x, \eta)} = \frac{\int_0^R \phi(t, x, r, \eta)\tilde{P}(t, x, r, \eta) r dr}{\int_0^R \tilde{P}(t, x, r, \eta) r dr} \tag{4.2}$$

where R is a large radius determined according to a cutoff imposed on the Favre-averaged mixture fraction in the flow field calculations. A cutoff value of 10^{-4} is used throughout the calculations. Smaller cutoff values were tested and the differences in the cross-stream averages were found to be negligible. Expanding the physical space diffusion term in the axial component of Eq. (3.23), then applying Eq. (4.2) to the resulting expression, the cross-stream averaged conditional transport equation of species κ takes the form:

$$\frac{\partial Q_\kappa}{\partial t} = \underbrace{-\left[\{\langle u_x|\eta\rangle\}_{R^+} - \left\{\frac{D_t}{\tilde{P}(\eta)}\frac{\partial \tilde{P}(\eta)}{\partial x}\right\}_{R+} - \left\{\frac{\partial D_t}{\partial x}\right\}_{R^+}\right]\frac{\partial Q_\kappa}{\partial x} + \{D_t\}_{R^+}\frac{\partial^2 Q_\kappa}{\partial x^2}}_{\text{Spatial transport}} + \underbrace{\frac{1}{2}\{\langle\chi|\eta\rangle\}_{R^+}\frac{\partial^2 Q_\kappa}{\partial \eta^2}}_{\text{Micro-mixing}} + \underbrace{\frac{\langle\dot{\omega}_\kappa|\eta\rangle}{\langle\rho|\eta\rangle}}_{\text{Chemicalsource}} \tag{4.3}$$

where x is the axial coordinate. As such the spatially two-dimensional (axisymmetric) configuration in hand reduces to a one-dimensional problem. The conditional temperature is computed iteratively from Q_κ and Q_h. The mesh consists of 63 nodes in mixture fraction space refined in lean mixtures and around stoichiometry, and 29 unevenly spaced grid points in the axial direction. Finite differences are used to discretise the transport equations. The three-step fractional method described in Sect. 3.5.3 is implemented to advance the solution in time. The first step accounts for spatial transport over the time interval $[t, t + \Delta t/2]$, the second step treats the micro-mixing term and the chemical source over $[t, t + \Delta t]$, and the third step involves spatial transport over $[t + \Delta t/2, t + \Delta t]$. The first and third steps are non-stiff and solved using LU-decomposition. On the other hand, the second step is stiff and requires a stiff ODE solver. The solver VODE [31] is employed here. Trapezoidal integration is employed to compute the cross-stream averages appearing in Eq. (4.3). The turbulent mixing field parameters are updated every 50 μs in the CMC calculations from pre-computed transient libraries, and 10 intermediate steps in each CMC time step are used in order to facilitate convergence. The ignition criterion is based on a 75 K increase in the conditional temperature at any point in the domain [59, 82]. Negligible differences were obtained between the ignition delay based on conditional temperatures and that using Favre-averaged temperatures. The results presented in the next section are grid independent.

4.4 Results

CMC simulations are performed for four fuel blends and the chemical kinetics used, along with the number of species and chemical reactions, are shown in Table 4.3. UBC Mech 1.0 [90] is based on GRI-Mech 1.2 [73]. This mechanism is optimized for the combustion of pure CH_4 under high pressures and engine-relevant temperatures. UBC Mech 2.0 [88] and UBC Mech 2.1 [91] are extensions of UBC Mech 1.0 [90] suitable for the combustion of CH_4 with small additions of C_2H_6 and H_2, respectively.

Table 4.3: Chemical kinetic mechanisms used with the different mixtures.

Mixture	Mechanism	Number of species	Number of reactions
A	UBC Mech 1.0 [90]	38	192
B	UBC Mech 2.0 [88]	54	277
C	UBC Mech 2.1 [91]	40	194
D	UBC Mech 1.0 [90]	38	192

4.4.1 Ignition delay

Figure 4.2 shows the predicted ignition delays of Mixture A compared with the experimental data of Wu [240]. Two sets of simulations were run with each scalar dissipation model (AMC and Girimaji's). Good agreement with the experimental data is achieved over the range of air temperatures as the predictions fall within the experimental scatter. The trend of increasing ignition delay with decreasing air temperature is well reproduced. Both scalar dissipation models yield comparable ignition delays, with the AMC model predicting ignition slightly earlier. This can be explained by the fact that $\{\langle\chi|\eta\rangle\}_{R^+,ign}$ determined from Girimaji's model is slightly higher than that obtained using the AMC model. Consequently, ignition occurs slightly earlier with the AMC model. Swaminathan and Mahalingham [221] also noted that the AMC model could capture well the inhomogeneity of the flow at the early stage of mixing, even though the model is based on local homogeneity. Thus, the AMC mode may provide more accurate values for the present case of autoignition.

Figures 4.3, 4.4 and 4.5 present the effect of additives on the ignition delay compared with the experimental data for mixture B, C and D, respectively. For comparison, the results obtained for pure methane (A) are also included. Good agreement with the experimental data is found again for the different blends. The ignition delay seems to be underpredicted for $T_{air} \simeq 1400$ K whereas it is overpredicted at $T_{air} \simeq 1200$ K. However, these observations should be balanced with the fact that a large scatter in the measured ignition delays exists, in particular for low temperatures. As shown in Fig.4.3, C_2H_6 has the largest impact on ignition delay compared to the results obtained for H_2 and N_2. The addition of 10% of C_2H_6 decreases t_d by 24 % on average. The effect of the other additives is more modest. Hydrogen decreases the ignition delay by 13 % and nitrogen increases t_d by 7 %. Comparable trends were found in the experiments [240].

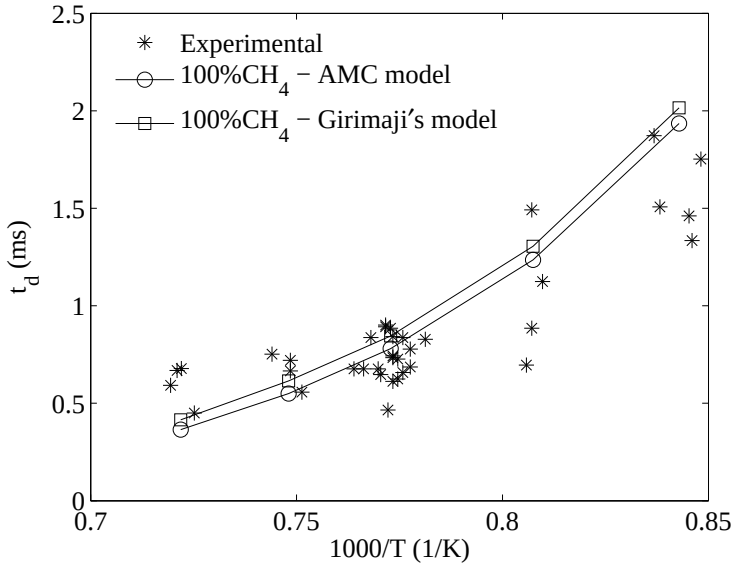

Figure 4.2: Ignition delay of mixture A ($100\%CH_4$).

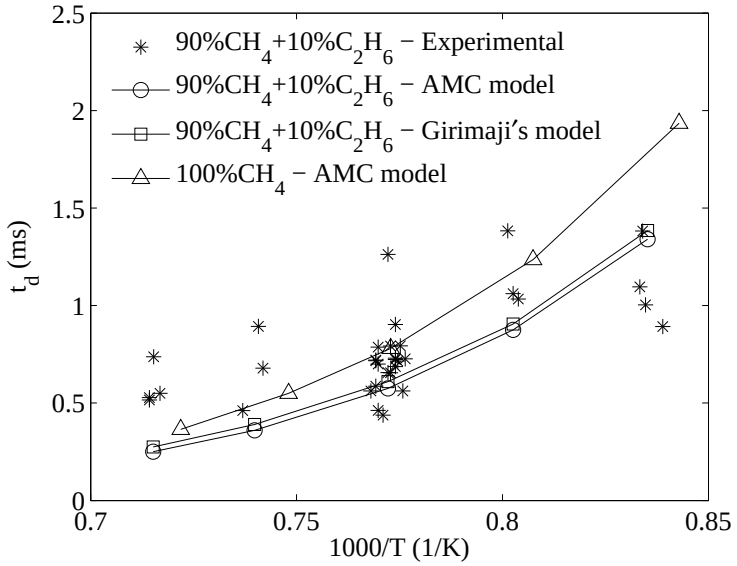

Figure 4.3: Ignition delay of mixture B (90% CH_4+10 % C_2H_6).

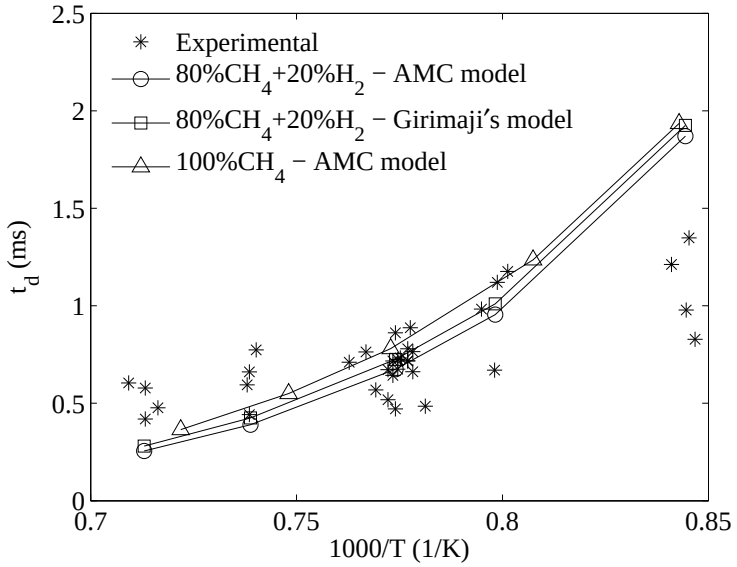

Figure 4.4: Ignition delay of mixture C (80% CH_4+20% H_2).

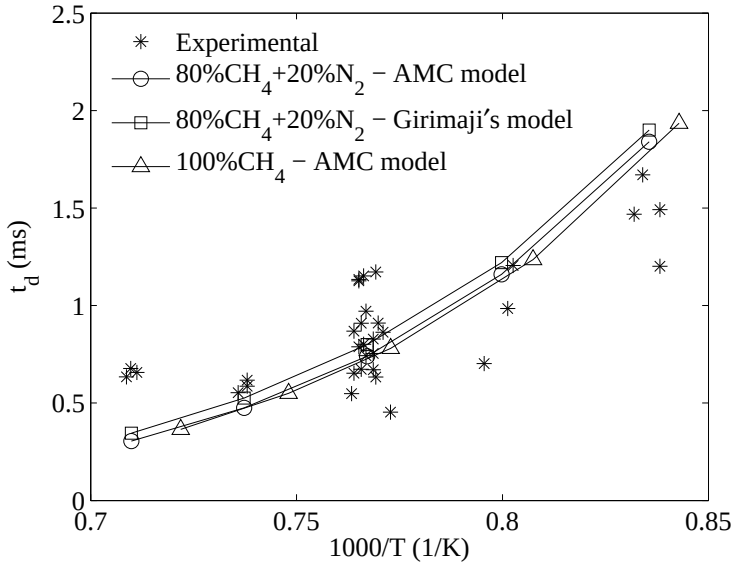

Figure 4.5: Ignition delay of mixture D (80% CH_4+20% N_2).

4.4.2 Ignition location

Ignition location in physical space

For comparison with the experimental data the normalised ignition kernel location Z_k^* is used. Figure 4.6 shows the variation of Z_k^* with the pre-combustion air temperature for mixtures A and B. For clarity, only the AMC model is included but similar observations are obtained with Girimaji's model. The results are in good agreement with the experimental data for most temperatures. Similar to what was observed for the ignition delay, the ignition location is underpredicted for the highest temperature (T $\simeq$ 1400 K) and overpredicted for the lowest temperature (T $\simeq$ 1200 K). The trend of decreasing Z_k^* with decreasing air temperature is well captured. In comparison with the results obtained for pure methane, the addition of C_2H_6 decreases $\bar{Z}_k^*$ by 15%. Wu [240] reported a 28% increase in the experiments whereas Sullivan et al. [215] observed an opposite trend in their data using the same experimental setup. Figures 4.7 and 4.8 present the predicted ignition locations for the two remaining mixtures C and D, respectively. The effect of adding H_2 is negligible and the change due to N_2 is also very small, 8% at most. The largest impact can be seen in Fig.4.8 at low temperatures (between 1200 and 1250 K). These results are consistent with the experimental observations. Wu [240] noted a more significant impact (around 28% increase) based on his curve fitting when N_2 was added to methane. However, these values need to be considered with caution due to the limited number of experimental points and large scatter.

Ignition location in mixture fraction space

As shown in Table 4.4, ignition always occurs on the lean side of stoichiometry. The smallest value of η_{ign} corresponds to the highest air temperature ($\simeq$ 1400 K) and η_{ign} increases with decreasing air temperature. After ignition, the temperature peak moves to richer mixtures close to stoichiometry. This is due to initial radical build-up taking place on the oxidiser side and as time increases, radicals diffuse away towards richer mixtures. The temperature profiles also become wider in mixture fraction space. Hot combustion products are moved away from the reaction zone through molecular diffusion and chemical reaction rates further increase with time for a larger range of mixture fraction values.

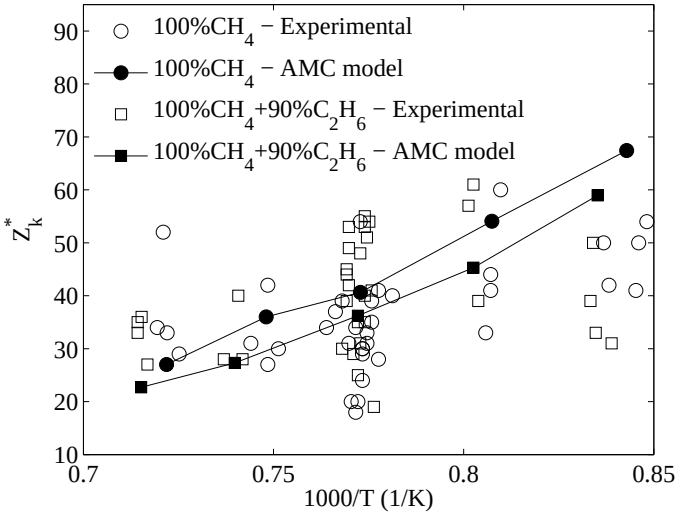

Figure 4.6: Ignition kernel locations of mixtures A (100% CH_4) and B (90% CH_4+10% C_2H_6).

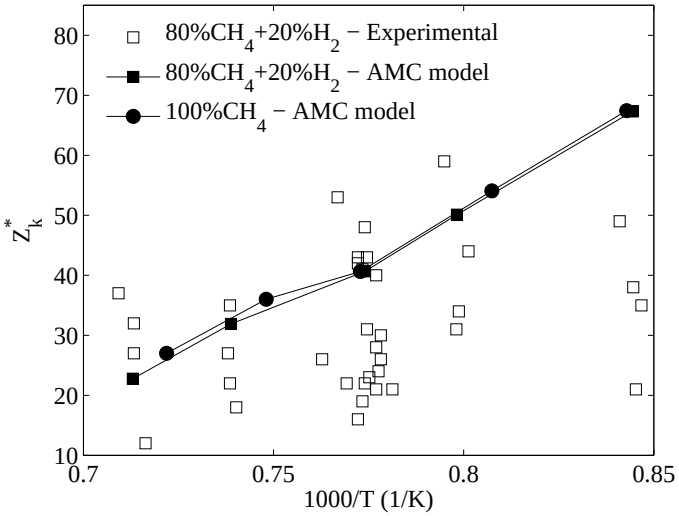

Figure 4.7: Ignition kernel locations of mixtures A (100% CH_4) and C (80% CH_4+20% H_2).

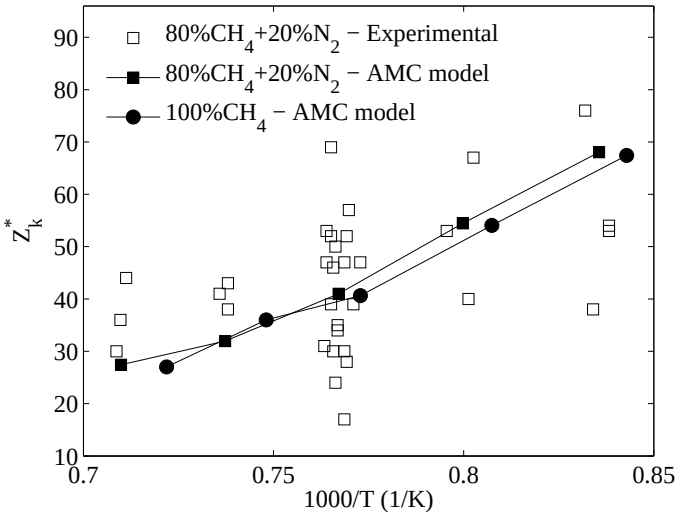

Figure 4.8: Ignition kernel locations of mixtures A (100% CH_4) and D (80% CH_4+20% N_2).

Table 4.4: Range of ignition mixture fraction values, $\eta_{ign} \times 10^2$ for the different mixtures and the stoichiometric value ($\eta_{st} \times 10^2$) for each blend.

Mixture	AMC	Girimaji's	Z_{st}
A	1.34 – 2.20	1.65 – 2.20	5.55
B	1.65 – 2.75	1.93 – 2.75	5.58
C	2.20 – 2.48	1.93 – 2.48	5.35
D	1.65 – 2.75	1.93 – 3.02	7.70

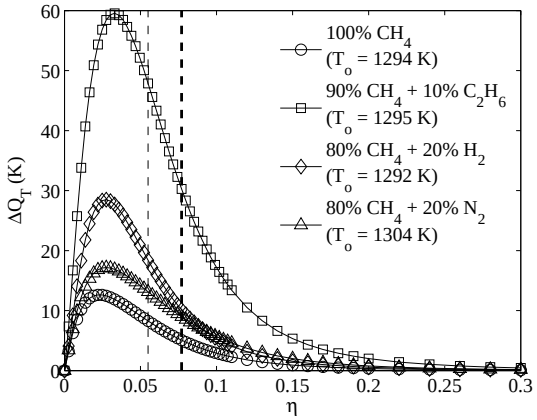

Figure 4.9: Change in conditional temperature profiles for each fuel blend at $x = 2.25$ cm and $t = 0.55$ ms.

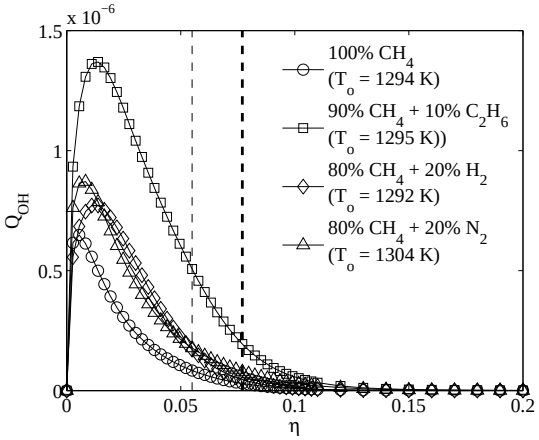

Figure 4.10: Conditional mass fraction of OH for each fuel blend at $x = 2.25$ cm and $t = 0.55$ ms.

4.4.3 Discussion

The effect of additives on the reaction pathways of CH_4 oxidation

In the present study the turbulent flow and mixing fields are very similar for the four blends considered due to small fuel density changes. The jet penetration length was compared for each mixture (not shown here) and the differences were negligible. Thus, the differences in the predicted ignition delay stem from the chemistry. Figure 4.9 presents the conditional temperature profiles just before the ignition of mixture B. As expected, the highest temperature occurs for mixture B. The lowest temperature is for pure methane. However, addition of N_2 has the effect of retarding ignition. This small discrepancy is explained by the slightly higher air temperature used in mixture D compared to A. The addition of C_2H_6 promotes the formation of H radicals as well as of OH and HO_2 and contributes to accelerate the methane oxidation (see Fig.4.10). Addition of N_2 is not expected to change the chemical kinetics but reduces the amount of CH_4 available for reaction, leading to delayed ignition. In order to investigate further the effect of additives on ignition, the main reaction pathways are examined at ignition time and mixture fraction for $T \simeq 1300$ K in Figs. 4.11 and 4.12. For clarity, the reaction numbers are specified following the order in UBC-Mech 1.0 [90], UBC-Mech 2.0 [88] and UBC-Mech 2.1 [91]. As shown in Fig. 4.11, C_2H_6 and H_2 do not change the main CH_4 oxidisation pathways but provide additional ignition-promoting reactions. CH_4 dissociation mainly occurs through hydrogen abstrac-

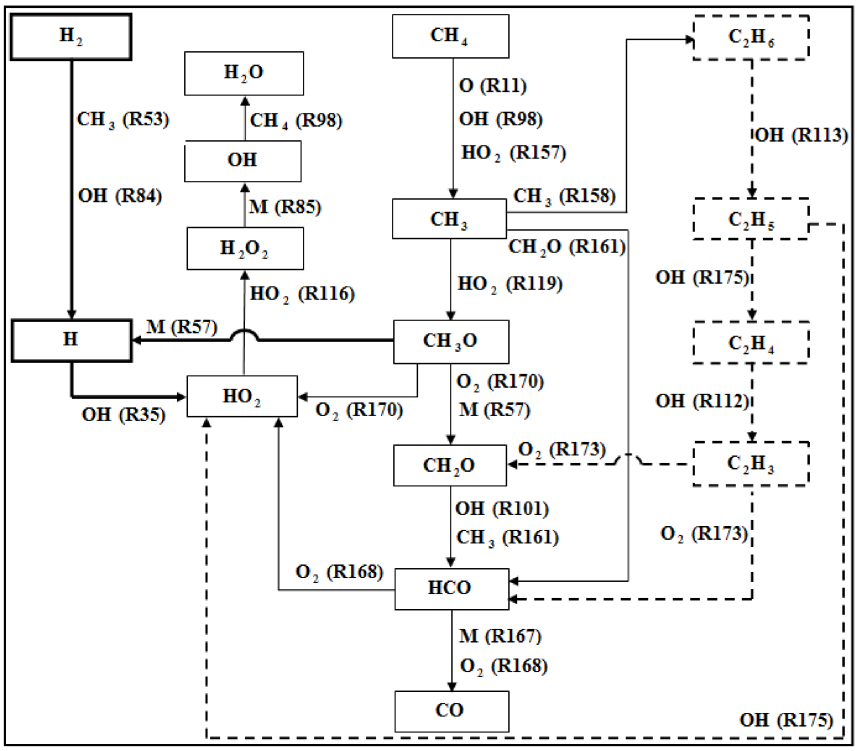

Figure 4.11: Main reaction pathways of pure CH_4 (thin solid lines), and CH_4/C_2H_6 (thin solid and dashed lines) and CH_4/H_2 (thin and thick solid lines) mixtures.

tion via the ignition-promoting reactions R11, 98 and 157, yielding methyl (CH_3) radicals. The chain reaction R98, in which CH_4 reacts with hydroxyl (OH) radicals, contributes the most to the formation of CH_3. Here, the dominant role of CH_3 is to promote the formation of hydroperoxy (HO_2) radicals to form methoxy (CH_3O) radicals, followed by oxidisation into formaldehyde (CH_2O) via R57 and R170. The production of the active HO_2 radicals also occurs through R170. Further oxidisation takes place to produce carbon monoxide (CO) and hydrogen peroxide (H_2O_2). When C_2H_6 is added (mixture B), the equilibrium of R158 is shifted resulting in reduced CH_3 consumption compared to pure CH_4. Further, C_2H_6 undergoes a series of hydrogen abstraction reactions to form ethyl (C_2H_5), ethene (C_2H_4) and vinyl (C_2H_3) radicals (R113, 175 and 112, respectively). Another product of R175 is the highly active HO_2 radicals. In addition, C_2H_3 decomposes into CH_2O and HCO via R173, favouring the formation of HO_2 (R168). For mixture C the addition of H_2 produces H radicals via R53, R57 and R84 that react with OH to form HO_2 (R35), as shown in Fig.4.12. Thus, C_2H_6 and H_2 additives promote the formation of HO_2 leading to

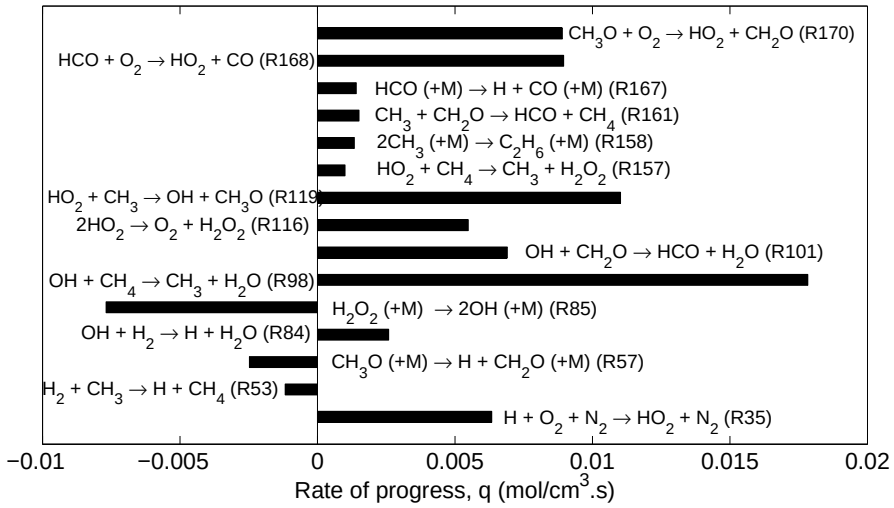

Figure 4.12: Net rate of progress of the main steps during the oxidisation of CH_4/H_2 (mixture C).

OH (R85), the major CH_4 dissociation agent (R98). Shorter ignition delays for mixture B can be explained by the additional CH_2O and HCO contribution.

The scalar dissipation rate at ignition

The conditional scalar dissipation rate measures the intensity of micro-mixing in mixture fraction space and characterizes the diffusive losses of heat and radicals. Previous work on autoignition of high-pressure methane jets in a shock tube showed that spatial transport of conditional species was small at ignition [59]. This implies that the scalar dissipation rate and the chemical source are the dominant terms in the present CMC formulation. Figure 4.13 displays the values of $\{\langle\chi|\eta\rangle_{\rm ign}\}_{R+}$ determined from the AMC model at ignition for the four fuel blends over a range of air temperatures. Ignition always occurs at low scalar dissipation rates, consistent with previous studies [116, 143]. Further, $\{\langle\chi|\eta\rangle_{\rm ign}\}_{R+}$ at ignition decreases with decreasing air temperature. This is explained by the fact that chemical activity is larger at higher temperatures and can compete with more intense turbulent mixing, hence ignition occurs earlier. Thus, the mixing model plays a crucial role in controlling the ignition process. Both mixing models used in the present study are based on homogeneous turbulence. A formulation including the effect of non-homogeneous turbulence may improve the ignition delay predictions.

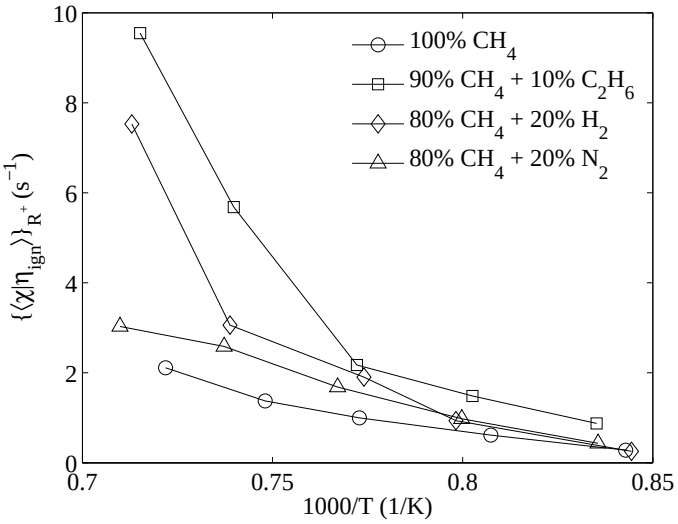

Figure 4.13: Comparison of the ignition conditional scalar dissipation rate of the different mixtures using the AMC model.

Sources of discrepancy

One source of discrepancy may be the $k-\varepsilon$ model. No experimental data is available for the flow and mixing fields. Good agreement between the predicted jet penetration length and the correlation derived by Hill and Ouellette [85] was found. Jet spreading corrected k-ε, as well as different eddy viscosity models (RNG k-ε and k-ω), were tested and negligible differences were found for the ignition delays and locations in CMC. However, a better description of turbulence may bring further improvement.

The effect of conditional fluctuations is not accounted for in the first-order closure. De Paola et al. [50] show that this closure is sufficient to model autoignition if the conditional scalar dissipation rate decays rapidly below its critical value downstream of the injector. This corresponds to what is observed in the present calculations and would explain the good agreement with the experimental data.

4.5 Conclusions

The first-order CMC was applied to the autoignition of different CH_4-based fuel blends in a shock tube over a range of pre-combustion air temperatures. The predicted ignition

delays and ignition locations are in reasonable agreement with the experimental data. Most numerical results fall within the experimental scatter. Around 1400 K, ignition is slightly underpredicted, while a larger overprediction is noticed at 1200 K. The effect of fuel additives is well reproduced. The addition of C_2H_6 and H_2 leads to shorter ignition delay, whereas N_2 additives result in longer delays. Ignition in all blends always occurs in lean mixtures and at low scalar dissipation rates.

For the present conditions, the first-order CMC appears to be suitable for the modelling autoignition. The effect of conditional fluctuations needs to be investigated further.

Chapter 5

Modelling of a Piloted Methane/Air Turbulent Jet Flame

The piloted CH_4/air turbulent jet flame Sandia D is investigated using the two-dimensional first-order CMC. This study is focused on the assessment of the PDF, CSDR and CV submodels and on the implementation of CMC in a fully consistent fashion. Two presumed PDF distributions are examined, the β-PDF and the CG-PDF. These PDFs and several CSDR and CV submodels relying on them are assessed and compared to available experimental measurements. The results of two CMC realisations employing the presumed β-PDF are presented. These realisations differ by the modelling of the CSDR. Homogeneous (inconsistent) and inhomogeneous (consistent) closures for the CSDR are considered in order to investigate the effect of the spurious sources on the CMC predictions. The comparison of the results with experimental measurements reveals that the levels of all reactive scalars, including minor intermediates and radicals, are in general better predicted when the effects of inhomogeneity are accounted for consistently in the modelling of the CSDR. It is concluded that the spurious sources have a non-negligible effect on the modelling of the flame under investigation, most notably in the inlets region.

5.1 Introduction

Since the release of their experimental data, the piloted Sandia flame series [12] have been employed as a benchmark for the validation of non-premixed turbulent combustion models. These flames are operated at different jet and pilot velocities. Flame A ($\mathrm{Re}_{jet} =$

$1,100$) is laminar, whereas flames B–F ($\mathrm{Re}_{jet} = 8,200 - 44,800$) are turbulent. Flame B ($\mathrm{Re}_{jet} = 8,200$) does not display any signs of local extinction. On the other hand, flames C ($\mathrm{Re}_{jet} = 13,400$) and D ($\mathrm{Re}_{jet} = 22,400$) show a small degree of local extinction. Flames E ($\mathrm{Re}_{jet} = 33,600$) and F ($\mathrm{Re}_{jet} = 44,800$) exhibit, respectively, moderate and significant levels of extinction, with the latter being close to global extinction. These flames are the subject of a large number of numerical studies. Some examples include the joint velocity-composition-turbulence frequency PDF approach [241], the steady flamelet model [235], the unsteady Lagrangian flamelet model [185], the unsteady Eulerian particle flamelet model [46], the flamelet/progress variable approach [92], the conditional source estimation model [236], and the multiple mapping conditioning model [233].

The Sandia flames are also investigated extensively using CMC. The order of the closure of the conditional chemical reaction rate is investigated by several authors. Roomina and Bilger [199] apply the first-order closure to flame D and assess a number of chemical kinetic mechanisms. They obtain a good agreement between the experimental measurements and the predicted conditional temperature and major species in lean mixtures, and report varying levels of discrepancy in rich mixtures, depending on the employed chemical kinetics mechanism. They identify the tested chemical kinetics and the first-order closure as possible sources of discrepancy. Among other flames, Fairweather and Woolley [62] apply the first-order closure to flames D and E. The latter exhibits a moderate level of local extinction. Their predictions of flame D are in line with those of Roomina and Bilger [199]. As for flame E, they report substantial overpredictions in stoichiometric and rich mixtures. They attribute the discrepancies to the inadequacy of the first-order closure. Kim and Huh [114] and Fairweather and Woolley [65] obtain improved predictions by applying the second-order closure to flames D, E, and F. The conditional profiles of the temperature and major species are better predicted in stoichiometric and rich mixtures. Moreover, substantial improvements are obtained for minor species. Fairweather et al. [66] explore the role of chemical kinetic mechanisms using the first-order closure. They show that simple reduced mechanisms derived from detailed mechanisms are capable of reproducing the numerical predictions of the parent mechanisms to a high degree of accuracy.

Sreedhara et al. [210] assess the applicability of several CV and CSDR submodels to flame D. However, they do not examine the influence of these submodels on the CMC predictions. They consider three CV submodels, namely, the uniform (Favre-average) approximation, the linear model [131], and the PDF-gradient model [190]. Three CSDR submodels are also investigated. The first two, Girimaji's model [78] and the AMC [174], are valid for homogeneous turbulence, whereas the third is based on the numerical double integration of the inhomogeneous mixture fraction PDF transport equation. The PDF required for construction of the CV and CSDR submodels is presumed to follow a β distri-

bution. Their results show minor differences between the CV submodels. As for the CSDR, the AMC and Girimajis model show qualitatively similar symmetric profiles, whereas the third yields asymmetric profiles. In a more recent study, Brizuela and Roudsari [29] apply the first-order CMC and the PMF approach to the modelling of Sandia flame D. The trinary PMF-PDF is employed in the pilot region and the binary PMF-PDF is used elsewhere. PDF gradient modelling is applied to the CV. The CSDR is closed using the homogeneous versions of the binary and trinary PMF closures proposed in [160]. The binary CSDR, which is given by Eq. (3.89), is the exact equivalent of the AMC when the PDF in Eq. (3.74) is modelled using the PMF approach. In another realisation, the PDF is presumed using the β-distribution, and the CV and the CSDR are closed using the PDF gradient model and the AMC, respectively. Their results show that the PMF approach yields more accurate predictions in the near field, as it is capable of capturing the features of mixing near the fuel, pilot and oxidiser streams.

This chapter complements the works of Sreedhara et al. [210] and Brizuela and Roudsari [29]. A more comprehensive assessment of CMC submodels is performed in the context of Sandia flame D. This flame is further simulated using fully consistent β-PDF-based submodels in order to quantify the impact of the spurious sources. This chapter is structured as follows. The experimental configuration of the considered flame is first summarized, then the mathematical and numerical details of CMC and the flow field calculations are described, and finally, the results are presented and analysed.

5.2 Experimental Configuration

The flame under investigation is shown in Fig. 5.1. The burner consists of a fuel nozzle surrounded by a coaxial pilot. The diameter of the nozzle, d, is 7.2 mm and the inner and outer diameters of the pilot are 7.7 and 18.2 mm, respectively. The nozzle issues a mixture of 25% CH_4 and 75% air (in volume), and the pilot burns a lean mixture of C_2H_2, H_2, air, CO_2 and N_2 with the same nominal enthalpy and equilibrium composition as CH_4/air at an equivalence of 0.77. The experimental conditions of the fuel, pilot and air streams are provided in Table 5.1. Compared to pure CH_4 and N_2-diluted CH_4 fuels, the partial premixing of CH_4 with air results in a relatively smaller flame length and yields a more robust flame. As such, it is possible to operate the flame at a relatively higher Reynolds number with little or no local extinction [11]. The Reynolds number of the fuel jet in flame D is 22,400 and the probability of local extinction is reported to be small [12]. Although CH_4 in the fuel stream is premixed with air, the mixing rates are sufficiently high so that the flame burns as diffusion flame with a single reaction zone near the stoichiometric mix-

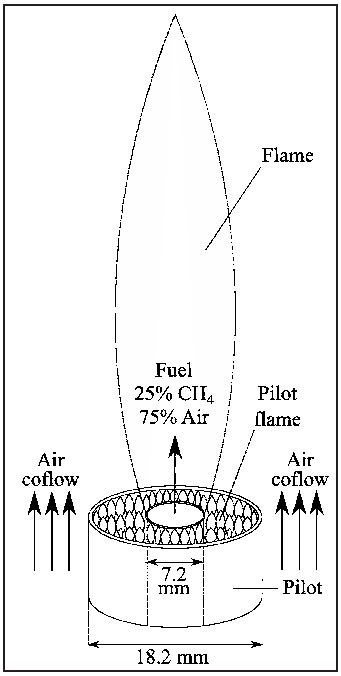

Figure 5.1: The piloted CH_4/air flame of Barlow et al. [12]

Table 5.1: Conditions of the fuel, pilot and oxidiser streams in Sandia flame D [11].

	Fuel	Pilot	Air
U [m/s]†,‡	49.6 ($\pm$2)	11.4 ($\pm$0.5)	0.9 ($\pm$0.05)
T [K]‡	294	1880 ($\pm$50)	291
ξ	1	0.27	0
Y_{N_2}	0.6471	0.7342	0.7671
Y_{O_2}	0.1965	5.4×10^{-2}	0.2329
Y_{CH_4}	0.1564	–	–
Y_{O}	–	7.47×10^{-4}	–
Y_{H_2}	–	1.29×10^{-4}	–
Y_{H}	–	2.48×10^{-5}	–
Y_{H_2O}	–	9.42×10^{-2}	–
Y_{CO}	–	4.07×10^{-3}	–
Y_{CO_2}	–	0.1098	–
Y_{OH}	–	2.8×10^{-3}	–
Y_{NO}	–	4.8×10^{-6}	–

† Bulk velocities.
‡ Values between parentheses correspond to the experimental uncertainties.

ture fraction (0.351). Moreover, there is no sign of substantial premixed reaction in the fuel-rich CH_4/air mixtures [11]. The multiscalar measurements are available from [2, 11] and the velocity measurements can be obtained from [203].

5.3 The Mathematical model

5.3.1 Turbulent flow and mixing fields

The CMC submodels require the knowledge of $\tilde{u}_i$, $\tilde{k}$, $\tilde{\varepsilon}$, $\tilde{\xi}$, and $\widetilde{\xi''^2}$. Ideally, the CMC combustion solver should be fully coupled with a flow and mixing CFD solver. For simplicity, the two solvers are decoupled here. However, the CFD calculations include a relatively less expensive combustion model in order to account for density variations in the flow and mixing fields. Upon obtaining a converged CFD solution, $\tilde{u}_i$, $\tilde{k}$, $\tilde{\varepsilon}$, $\tilde{\xi}$, and $\widetilde{\xi''^2}$ are fed as input to the CMC solver which in turn solves the conditional species and temperature equations

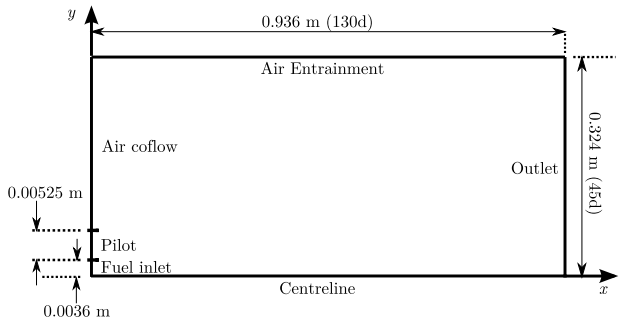

Figure 5.2: Computational domain.

independently, without any feedback to the CFD solver. Fairweather and Woolley [61–65], Fairweather et al. [66], Kim and Mastorakos [106], and Sreedhara et al. [210] employ the same simplifying approach.

The CFD calculations are performed using the commercial software FLUENT [5]. The Reynolds stress model is employed in conjunction with the partially premixed combustion model in FLUENT. The latter is a combination of the laminar flamelet model [177] (non-premixed combustion) and the Zimont Turbulent Flame Closure [244] (premixed combustion). Further information on these models and their implementation can be found in [6]. A two-dimensional axisymmetric computational domain is employed in the current calculations. A schematic is shown in Figure 5.2. The domain is $130\,d$ long in and $45\,d$ wide, with the centre of the fuel nozzle placed at the origin. The thickness of the nozzle and pilot walls are neglected. A quadratic unstructured mesh is generated using ANSYS ICEM CFD [8]. It consists of $2,500 \times 279$ nodes (axial $\times$ radial), resulting in a total of 694,722 control volumes. The Semi-Implicit Method for Pressure-Linked Equations (SIMPLE) algorithm is used for pressure-velocity coupling. The PREssure Staggering Option (PRESTO) pressure interpolation scheme is employed to compute the pressure at cell faces. Spatial discretization is performed using the second-order upwind scheme. Default model constants are employed, except for $C_{\varepsilon 1}$ in the Reynolds stress model which is modified from the standard value of 1.44 to 1.52 in order to improve the spreading rate predictions. The detailed chemical kinetics mechanism GRI-MECH 2.11 [27] is used in the combustion calculations. This mechanism includes 49 species and 279 chemical reactions. The flamelet library is generated using 75 points for both the mixture fraction and mixture fraction variance. The boundary conditions for the species mass fractions are specified as prescribed in the experiments [11] (see Table 5.1). The fuel and oxidiser temperatures are set to 300 K, which is slightly higher than the experimentally reported values. The inlet velocity boundary condition is specified using the 1/7 power law with the centreline velocity set

to 62.95 m/s, as reported by Schneider et al. [203]. The profile of the turbulence kinetic energy, $\tilde{k}$, is calculated from the experimentally measured shear stresses by assuming axial symmetry. The turbulence eddy dissipation, $\tilde{\varepsilon}$, is computed according to:

$$\tilde{\varepsilon} = \frac{C_{\mu}^{3/4}\tilde{k}^{3/2}}{l_m} \tag{5.1}$$

where l_m is the Prandtl mixing length. For fully developed pipe flow, l_m is usually set to 7% of the diameter, i.e. $l_m = 0.07d$. The factor 0.07 is based on the maximum value of the mixing length in fully developed turbulent pipe flow [7]. Here, l_m is calculated using the expression proposed by Merci et al. [151]:

$$l_m = D\left\{1 - \exp\left[-2\times 10^{-6}\left(\frac{y^*}{D_h}\right)^3\right]\right\}\left[\frac{1}{15} - \left(\frac{1}{2} - \frac{y^*}{D_h}\right)^4\right] \tag{5.2}$$

where D_h is the hydraulic diameter and y^* is the distance from the nearest solid boundary to the location of interest. In the flame under investigation, D_h is equal to the diameter of the inlet, d, and y^* is the distance from the wall of the inlet to y, i.e. $y^* = d/2 - y$ where $0 \leq y < d/2$. The profiles of the inlet Reynolds stresses are set by curve-fitting the experimental data of Schneider et al. [203]. The pilot and coflow boundary conditions are set using the bulk experimental values (see Table 5.1). The turbulence eddy dissipation at the pilot is specified according to Eq.(5.1) and (5.2) with $D_h = d_p - d$ and $y^* = \min(y - d/2, d_p/2 - y)$, d_p being the pilot diameter. Pressure boundary conditions are set at the entrainment and outlet boundaries.

5.3.2 The CMC implementation

The physical CMC domain has the same dimensions as the CFD domain (130 d in length and 45 d in width). The grid resolution is 120×40 (axial $\times$ radial), with the mesh density being highest near the inlet and pilot areas and within the reaction zone. The mixture fraction grid consists of 50 unevenly-spaced points, refined around the stoichiometric mixture fraction ($\eta_{st} = 0.351$). Steady laminar flamelet calculations performed with higher resolution grids yield negligible differences in the conditional scalars (not shown here). Therefore, the 50-point resolution ensures grid independence. The required variables $\tilde{u}_i$, $\tilde{k}$, $\tilde{\varepsilon}$, $\tilde{\xi}$, and $\widetilde{\xi''^2}$ are transferred from FLUENT to the CMC solver by applying bilinear interpolation. This interpolation scheme was found to be accurate due to the high resolution of CFD grid. The Favre scalar dissipation rate is calculated using the algebraic model given by Eq. (2.87). The steady-state solution is obtained from the transient CMC transport

Table 5.2: ARM2 chemical kinetics mechanism [1].

Step	Reaction
1	$2H + O_2 \rightleftharpoons 2OH$
2	$2H_2 + O_2 \rightleftharpoons 2H + 2OH$
3	$2HO_2 \rightleftharpoons O_2 + 2OH$
4	$O2 + 2H_2O_2 \rightleftharpoons 2OH + 2HO_2$
5	$O_2 + C_2H_2 \rightleftharpoons 2H + 2CO$
6	$2CH_3 + 2CO + 2C_2H_4 \rightleftharpoons O_2 + 2CH_4 + 3C_2H_2$
7	$O_2 + 4CH_3 \rightleftharpoons 2H_2 + 2CH_4 + 2CO$
8	$O_2 + 2CH_3 \rightleftharpoons 2H + 2CH_2O$
9	$O_2 + 2CH_4 \rightleftharpoons 2OH + 2CH_3$
10	$O_2 + 2CO \rightleftharpoons 2CO_2$
11	$O_2 + 2C_2H_6 \rightleftharpoons 2CH_4 + 2CH_2O$
12	$H + OH \rightleftharpoons H_2O$
13	$2H + 2CH_4 + 2NO + 2HCN \rightleftharpoons O_2 + 4CH_3 + 2N_2$
14	$2H + O2 + 2CH_4 + 2HCN \rightleftharpoons 4CH_3 + 2NO$
15	$O_2 + 2CH_4 + 2NH_3 + 2HCN \rightleftharpoons 2H_2O + 4CH_3 + 2N_2$

equations, Eqs.(3.23) and (3.34), by relaxation of the time step for which a value of 10^{-5} s is used. The three-step fractional method described in Sect. 3.5.3 is implemented in order to treat the stiff chemical source term separately. The equations are discretized using the finite difference method. The first and second-order derivatives are discretized using the first-order upwind and the second-order central difference schemes, respectively. The non-stiff/stiff solver VODPK [30, 31, 33] is employed to solve the system of equations. The boundary conditions for Q_κ and Q_T are specified following Smith et al. [205] by assuming non-reacting adiabatic mixing between the oxidiser and the pilot streams for $0 \leq \eta \leq \tilde{\xi}_p$ and between the fuel and the pilot streams for $\tilde{\xi}_p < \eta \leq 1$ where $\tilde{\xi}_p = 0.27$ is the mean mixture fraction at the pilot. The composition of the fuel, oxidiser and pilot streams are set following Table 5.1. To speed up the calculations, a steady laminar flamelet computed with a stoichiometric scalar dissipation rate of 100 s^{-1} is employed to initialise the flame in the reaction zone. The details of the submodels employed in the different CMC realisations will be described in Sect. 5.4.3. For computational efficiency, the augmented reduced chemical kinetics mechanism ARM2 [1] is used in the present calculations. This mechanism is based on the GRI-MECH 2.11 mechanism employed in the FLUENT calculations. It consists of 19 species and 15 steps including NO chemistry. The reactions are provided in Table 5.2. This mechanism is one of several reduced chemical kinetic schemes assessed by Barlow et al. [14] and Fairweather et al. [66]. Their calculations show that ARM2 is capable of reproducing the trends of its parent mechanism GRI-MECH 2.11 accurately.

5.4 Results and Discussion

5.4.1 Flow field results

Figure 5.3(a) shows a comparison of the predicted Favre-averaged axial velocity, $\tilde{u}$, with the centreline measurements of Schneider et al. [203]. The experimental data is overpredicted between $x/d = 20$ and 60 and slightly underpredicted elsewhere. The centreline profiles of $\tilde{\xi}$ and $\widetilde{\xi''^2}$ are shown in Figs. 5.3(b) and (c), respectively, along with the experimental measurements of Barlow and Frank [12]. As displayed in Fig. 5.3(b), the predicted profile of $\tilde{\xi}$ is in excellent agreement with the measurements. As for $\widetilde{\xi''^2}$, Fig. 5.3(c) shows that the experimental data is highly underpredicted between $x/d = 30$ and 45 with a reasonable agreement elsewhere. This behaviour is most likely attributed to the inaccuracy of the algebraic modelling of $\tilde{\chi}$.

The radial profiles of $\tilde{u}$ are shown in Fig. 5.4(a). The experimental measurements are very well reproduced at $x/d = 1$, 7.5, 15, 30 and 45 except near the centreline. Better predictions are obtained close the centreline at $x/d = 60$, however, the agreement with the experiments deteriorates for large radii. No measurements are available at $x/d = 75$. Fig. 5.4(b) displays the radial predictions of $\tilde{\xi}$. At $x/d = 1$ and 7.5, the measurements are accurately predicted at all radial locations. At $x/d = 15$, 30 and 45, a very good agreement is achieved near the centreline with slight overpredictions at larger radii. An opposite trend is obtained at $x/d = 60$. Further downstream at $x/d = 75$, the measurements are predicted to a very good degree of accuracy. The radial profiles of $\widetilde{\xi''^2}$ are displayed in Fig. 5.4(c). The measurements at $x/d = 1$, 7.5 and 15 are fairly well predicted except near the peaks. A lower degree of agreement is achieved at $x/d = 30$, most notably between $y/d = 0.5$ and 2. At $x/d = 45$, the measurements are underpredicted between $y/d = 0$ and ~ 2.8, and accurately reproduced elsewhere. A similar trend is obtained at $x/d = 60$. Downstream at $x/d = 75$, the experimental data is overall underpredicted.

Barlow and Frank [11, 12] report a stoichiometric flame length of $47d$. This quantity is calculated as the distance on the centreline of the flame where the mixture fraction is equal to the stoichiometric value 0.351. The contour of the stoichiometric mixture fraction ($\tilde{\xi}_{\text{st}} = 0.351$) is plotted in Fig. 5.5 along with the locations of the measured and predicted stoichiometric flame lengths. As shown, the calculated value is approximately equal to $48.8d$, which is 3.83% in excess of the measured value. This result proves further the reliability of the mean mixture fraction field.

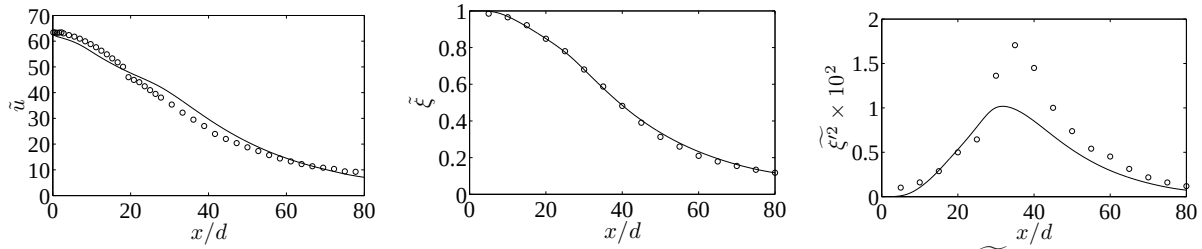

(a) $\tilde{u}$ (b) $\tilde{\xi}$ (c) $\widetilde{\xi''^2} \times 10^2$

Figure 5.3: Centreline profiles of (a) $\tilde{u}$, (b) $\tilde{\xi}$ and (a) $\widetilde{\xi''^2} \times 10^2$. Symbols, experimental data ($\tilde{u}$, [203]); $\tilde{\xi}$ and $\widetilde{\xi''^2}$ [12]); lines, predictions.

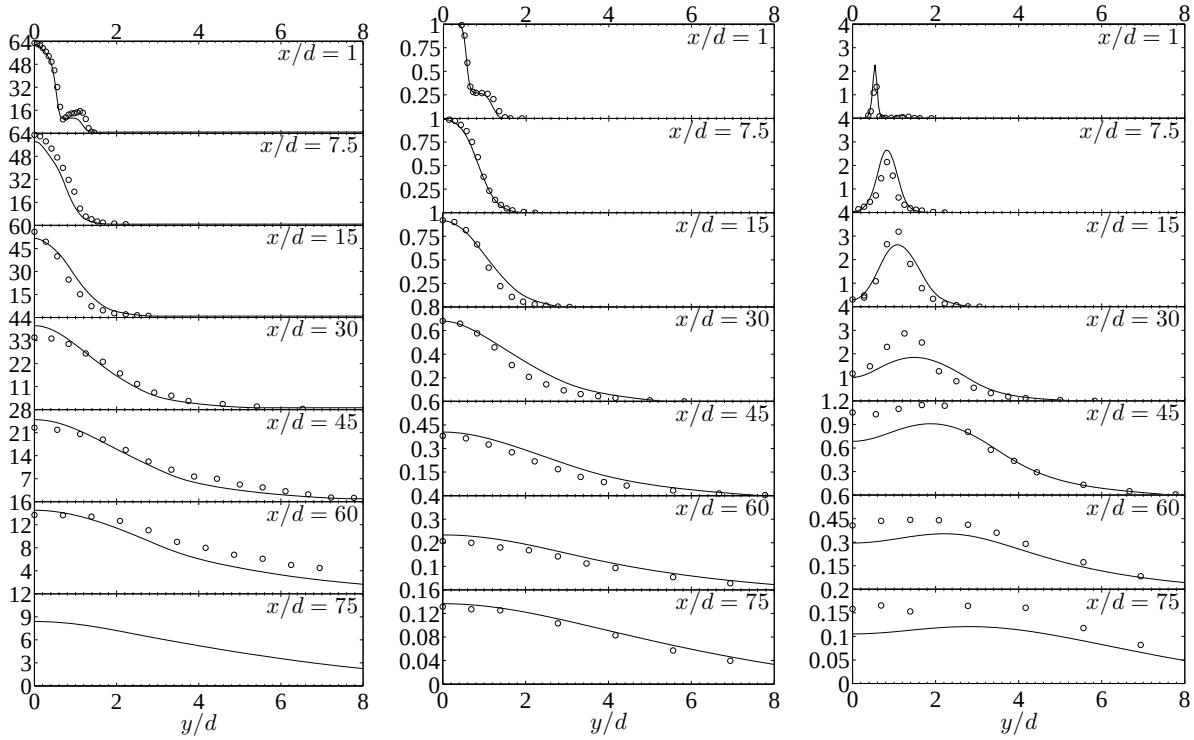

(a) $\tilde{u}$ (b) $\tilde{\xi}$ (c) $\widetilde{\xi''^2} \times 10^2$

Figure 5.4: Radial profiles of (a) $\tilde{u}$, (b) $\tilde{\xi}$ and (a) $\widetilde{\xi''^2} \times 10^2$. Symbols, experimental data ($\tilde{u}$, [203]; $\tilde{\xi}$ and $\widetilde{\xi''^2}$ [12]); lines, predictions.

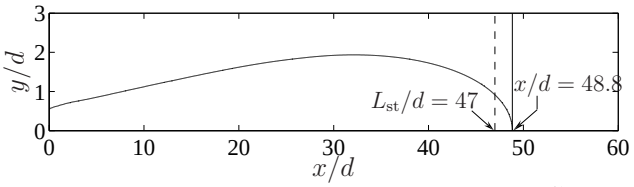

Figure 5.5: Contour of the stoichiometric mixture fraction ($\tilde{\xi}_{\rm st} = 0.351$) showing the experimentally measured (- - -) and predicted (——) stoichiometric flame lengths.

5.4.2 Assessment of the CMC Submodels

In this section, the submodels of $\tilde{P}(\eta)$, $\langle\chi|\eta\rangle$ and $\langle u_i|\eta\rangle$ are assessed. Comparison to available experimental measurements is performed.

The probability density function

Figure 5.6 shows a comparison of the β-PDF and the CG-PDF with the measurements of Barlow et al. [13]. The two distribution are compared to the experimental data at the axial locations $x/d = 15$, 30 and 45 for several radial locations. The numerical results are reported at the grid points that are closest to the locations where the measurements are taken. Both distributions capture the trends of the experimental data. However, the locations and magnitudes of the peaks are not in general well predicted. This is most likely attributed to the discrepancies in the predictions of the moments $\tilde{\xi}$ and $\widetilde{\xi''^2}$. In Fig. 5.6(a), both presumed PDFs show good agreement with the experiments at small radii, e.g. $y = 0$ and 3 mm. At larger radii, e.g. $y = 9$ and 12 mm, substantial discrepancies are obtained and the misprediction of the locations of the peaks becomes more pronounced. Moving downstream to $x/d = 30$ and 45, the presumed PDFs show better agreement with the experiments and the locations the peaks are better predicted, as displayed in 5.6(b) and 5.6(c). Overall, the β-PDF outperforms the CG-PDF. Nevertheless, unlike the latter, it is incapable of capturing the intermittency of the unmixed fuel and/or oxidiser close to the outer edge of the fuel jet. This is demonstrated at $x/d = 15$ for $y = 0$ mm and for large radii at all of the considered axial locations. It is important to note that some of the measured PDF profiles display more than one local maximum, e.g. at $y = 9$ and 12 mm at $x/d = 15$, $y = 6$ and 12 mm at $x/d = 30$, and $y = 9$ and 18 mm at $x/d = 45$. The β-PDF and the CG-PDF are incapable of predicting such structure due to the fact that distributions do not allow for more than one local maximum in the range $0 < \eta < 1$.

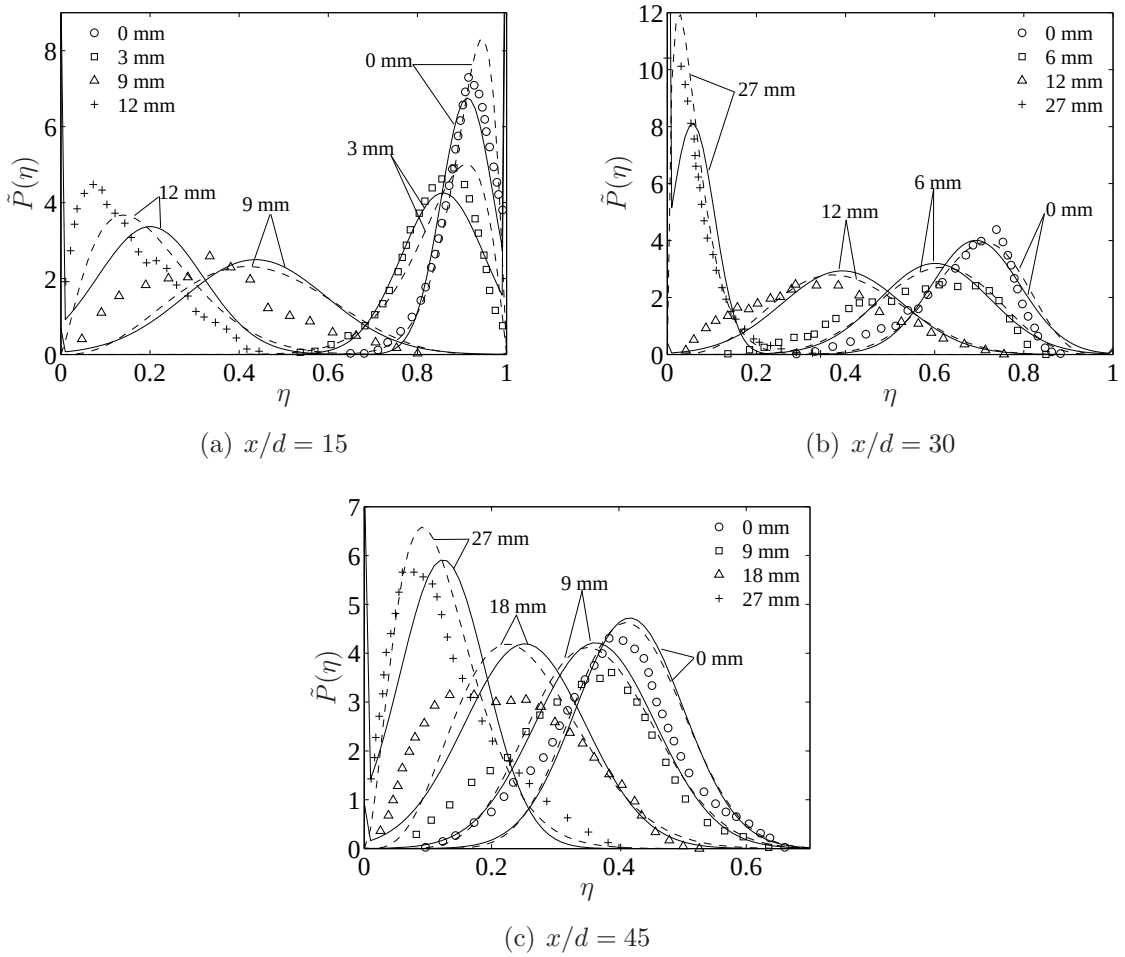

(a) $x/d = 15$

(b) $x/d = 30$

(c) $x/d = 45$

Figure 5.6: Comparison of the radial variation of the presumed probability density functions with the experimental measurements of Barlow et al [13] at different axial locations. Solid lines, CG-PDF; dashed lines β-PDF; symbols, experimental data.

The conditional scalar dissipation rate

Karpetis and Barlow [99] provide measurements for the one-dimensional (1D) and three-dimensional (3D) CSDR, $\langle \chi_r | \eta \rangle$ and $\langle \chi | \eta \rangle$, respectively. χ_r represents the radial component of the scalar dissipation rate ($\chi_r = 2D_\xi(\partial\xi/\partial r)^2$). The data presented in [99] reveals that the 3D measurements are larger in magnitude than their 1D counterparts, but very similar in shape. Further, the differences between the 1D and 3D measurements become more substantial with increasing axial location. Figure 5.7 compares the different CSDR models with the 3D data reported by Karpetis and Barlow [99] at the grid points nearest to the stoichiometric isocontour at $x/d = 7.5$, 15, 30 and 45 (no experimental measurements are available at $x/d = 45$). At $x/d = 7.5$ (Fig. 5.7(a)), the MBPDF model yields a narrower profile compared to the AMC and Girimaji's models, and $\langle \chi | \eta \rangle$ decays faster to zero near the boundaries of the mixture fraction space, successfully mimicking the trend observed in the experiments. Nevertheless, this model overpredicts the measurements over most of the range of mixture fraction. The AMC and Girimaji's model result in a better agreement around the stoichiometric mixture fraction, but tend to be more overpredictive than the MBPDF model as η approaches 0 and 1. As for the MCGPDF model, it yields best agreement amongst all models in the range $0 \lesssim \eta \lesssim 0.5$, however, decays abruptly to zero at $\eta \approx 0.55$. Moving downstream to $x/d = 15$ (Fig. 5.7(b)), the AMC, Girimaji's model and the MBPDF model result in a very good agreement with the experimental data over $0 \leq \eta \lesssim 0.25$, but tend to be overpredictive in rich mixtures. The MCGPDF model shows best agreement with the measurements up to $\eta \approx 0.45$, however, performs poorly thereafter. Further downstream at $x/d = 30$ (Fig. 5.7(c)), the profiles of the AMC, Girimaji's model and the MBPDF model are very similar. The measurements are underpredicted by all three models over $0.2 \lesssim \eta \lesssim 0.7$ and overpredicted elsewhere. On the other hand, the MCGPDF model underpredicts the experimental data over most of the mixture fraction space. None of the CSDR models in Figs. 5.7(a)-(c) is capable of reproducing the double-peak structures observed in the experiments. The inability of the current models to do so is due to the nature of the presumed PDFs which do not allow for two local maxima in the range $0 < \eta < 1$. This discrepancy can be remedied using the PMF approach [160]. Taking into consideration the experimental limitations and uncertainties, all models apart from the MCGPDF model result in reasonable agreement with the experiments. The CSDR at $x/d = 45$ is displayed in Fig. 5.7(d). The profiles obtained using the AMC and Girimaji's model are similar as in the upstream axial locations. The MBPDF model yields a substantially different, positively skewed distribution. The MCGPDF model results in a relatively narrower yet flatter profile.

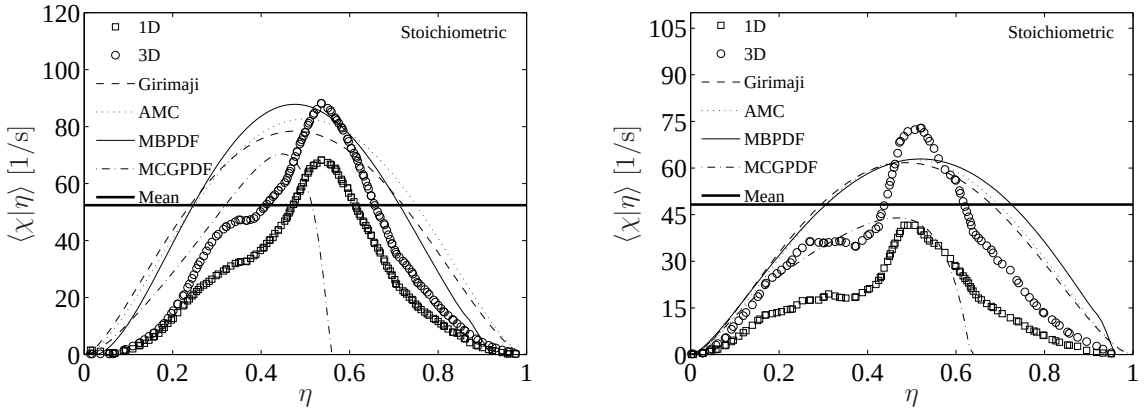

(a) $x/d = 7.5$ (b) $x/d = 15$

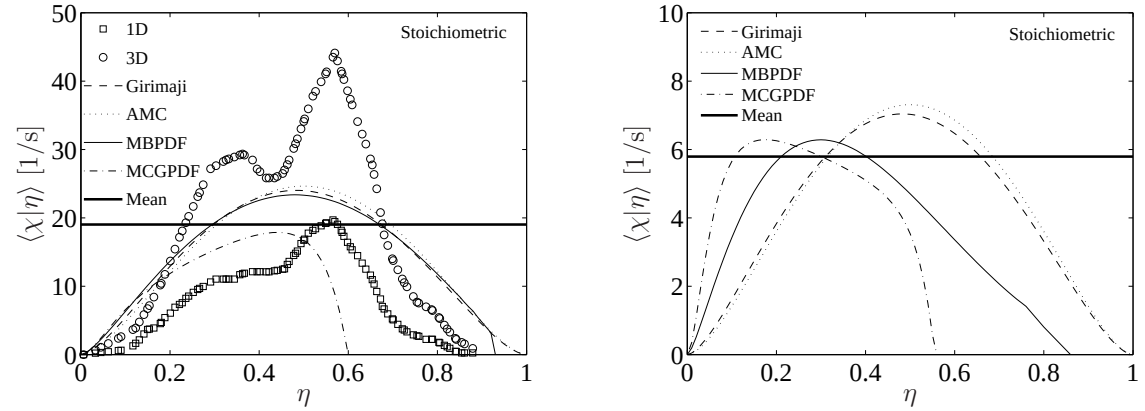

(c) $x/d = 30$ (d) $x/d = 45$

Figure 5.7: Comparison of the CSDR models with the one-dimensional ($\langle\chi_r|\eta\rangle$) and three-dimensional ($\langle\chi|\eta\rangle$) measurements of Karpetis and Barlow [99] taken near the stoichiometric isocontour: (a) $x/d = 7.5$, (b) $x/d = 15$, (c) $x/d = 30$ and (d) $x/d = 45$.

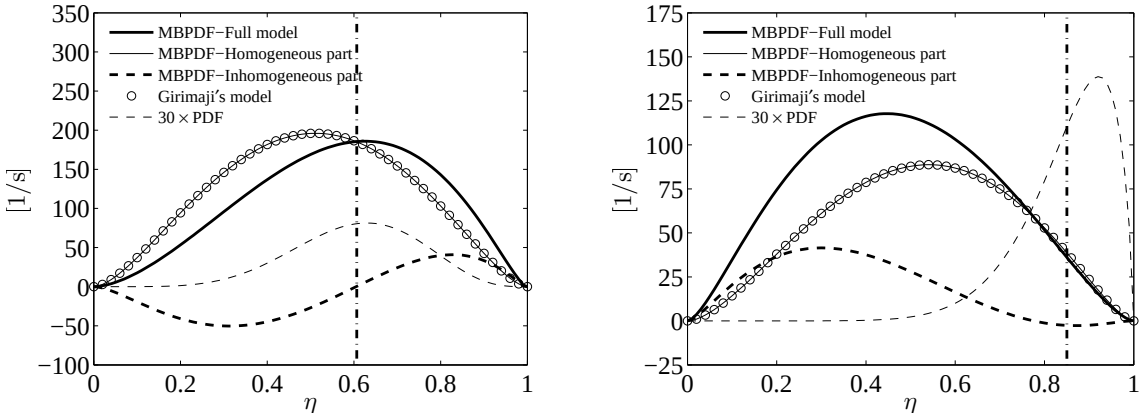

(a) $x/d = 3$, $y/d = 0.646$ (b) $x/d = 7.5$, $y/d = 0.5$

Figure 5.8: Recovery of Girimaji's model from the MBPDF model at (a) $x/d = 3$ and $y/d = 0.646$ and (b) $x/d = 7.5$ and $y/d = 0.5$. The vertical line corresponds to $\eta = \tilde{\xi}$.

Relation between Girimaji's model and the MBPDF model The MBPDF model reduces exactly to Girimaji's when the inhomogeneous terms are discarded from it. In other words, the homogeneous part of the MBPDF model given by Eq. (3.83) (with $II(\eta)$ obtained from Eq. (3.85)) is equivalent to Eq. (3.75). A graphical demonstration is provided in Fig. 5.8. Figures 5.8(a) and (b) display the MBPDF model and its homogeneous and inhomogeneous parts, along with Girimaji's model and the β-PDF at $(x/d = 3, y/d = 0.646)$ and $(x/d = 7.5, y/d = 0.5)$, respectively. The recovery of Girimaji's model is obvious at both locations. The homogeneous part of the MBPDF model overlaps with the CSDR profile computed using Girimaji's. This figure reflects the effect of the inhomogeneity of the flow on the CSDR. Consistent with the observation of Mortensen [157], the major differences between the inhomogeneous and homogeneous versions of the MBPDF model manifest far from the mean of the mixture fraction where the PDF becomes small. Close to the mean, the sum of the inhomogeneous terms in Eq. (3.81) presents zero-ordinate inflection points as in Fig. 5.8(a) or local minima as in Fig. 5.8(b). Therefore, the profiles of the homogeneous and full models cross-one another near the mean and yield the same CSDR value.

Analysis of the MBPDF model This section examines the MBPDF model at the locations considered in Fig. 5.8. The right hand side terms of Eq. (3.81) are isolated as

follows:

$$
\begin{aligned}
T_1 &= 2\frac{\tilde{\chi}}{\tilde{P}(\eta)}\frac{\partial II(\eta)}{\partial\widetilde{\xi''^2}} \quad \text{(homogeneous portion)} \\
T_2 &= -4\frac{D_\mathrm{t}}{\tilde{P}(\eta)}\frac{\partial II(\eta)}{\partial\widetilde{\xi''^2}}\frac{\partial\tilde{\xi}}{\partial x_i}\frac{\partial\tilde{\xi}}{\partial x_i} = -4\frac{D_\mathrm{t}}{\tilde{P}(\eta)}\frac{\partial II(\eta)}{\partial\widetilde{\xi''^2}}\left[\left(\frac{\partial\tilde{\xi}}{\partial x}\right)^2+\left(\frac{\partial\tilde{\xi}}{\partial y}\right)^2\right] \\
T_3 &= 2\frac{D_\mathrm{t}}{\tilde{P}(\eta)}\frac{\partial^2 II(\eta)}{\partial\tilde{\xi}\partial\tilde{\xi}}\frac{\partial\tilde{\xi}}{\partial x_i}\frac{\partial\tilde{\xi}}{\partial x_i} = 2\frac{D_\mathrm{t}}{\tilde{P}(\eta)}\frac{\partial^2 II(\eta)}{\partial\tilde{\xi}\partial\tilde{\xi}}\left[\left(\frac{\partial\tilde{\xi}}{\partial x}\right)^2+\left(\frac{\partial\tilde{\xi}}{\partial y}\right)^2\right] \\
T_4 &= 2\frac{D_\mathrm{t}}{\tilde{P}(\eta)}\frac{\partial^2 II(\eta)}{\partial\widetilde{\xi''^2}\partial\widetilde{\xi''^2}}\frac{\partial\widetilde{\xi''^2}}{\partial x_i}\frac{\partial\widetilde{\xi''^2}}{\partial x_i} = 2\frac{D_\mathrm{t}}{\tilde{P}(\eta)}\frac{\partial^2 II(\eta)}{\partial\widetilde{\xi''^2}\partial\widetilde{\xi''^2}}\left[\left(\frac{\partial\widetilde{\xi''^2}}{\partial x}\right)^2+\left(\frac{\partial\widetilde{\xi''^2}}{\partial y}\right)^2\right] \\
T_5 &= 4\frac{D_\mathrm{t}}{\tilde{P}(\eta)}\frac{\partial^2 II(\eta)}{\partial\tilde{\xi}\partial\widetilde{\xi''^2}}\frac{\partial\tilde{\xi}}{\partial x_i}\frac{\partial\widetilde{\xi''^2}}{\partial x_i} = 4\frac{D_\mathrm{t}}{\tilde{P}(\eta)}\frac{\partial^2 II(\eta)}{\partial\tilde{\xi}\partial\widetilde{\xi''^2}}\left(\frac{\partial\tilde{\xi}}{\partial x}\frac{\partial\widetilde{\xi''^2}}{\partial x}+\frac{\partial\tilde{\xi}}{\partial y}\frac{\partial\widetilde{\xi''^2}}{\partial y}\right)
\end{aligned}
\tag{5.3}
$$

such that $\langle\chi|\eta\rangle = T_1+T_2+T_3+T_4+T_5$. Before analysing the relative importance of the terms T_1–T_5, it is important to note that T_1 scales as $-T_2$ when certain assumptions are invoked. To demonstrate this, T_2 is first rewritten as:

$$
T_2 = \frac{2}{\tilde{P}(\eta)}\frac{\partial II(\eta)}{\partial\widetilde{\xi''^2}}\left[2\left(-D_\mathrm{t}\frac{\partial\tilde{\xi}}{\partial x_i}\right)\frac{\partial\tilde{\xi}}{\partial x_i}\right] \tag{5.4}
$$

Using the gradient diffusion assumption, $-D_t\partial\tilde{\xi}/\partial x_i \approx \widetilde{u_i''\xi''}$ and Eq. (5.4) becomes:

$$
T_2 \approx -\frac{2}{\tilde{P}(\eta)}\frac{\partial II(\eta)}{\partial\widetilde{\xi''^2}}\left(-2\widetilde{u_i''\xi''}\frac{\partial\tilde{\xi}}{\partial x_i}\right) \tag{5.5}
$$

The term $-2\widetilde{u_i''\xi''}\partial\tilde{\xi}/\partial x_i$ on the right hand side of Eq.(5.5) represents the production of scalar fluctuations in the mixture fraction variance transport equation, Eq. (2.81). If the production and dissipation of scalar fluctuations in this equation are of the same order (for instance when convective transport and transport by turbulent fluxes are weak or of the same order under steady-state conditions), $-2\widetilde{u_i''\xi''}\partial\tilde{\xi}/\partial x_i \sim \tilde{\chi}$ and Eq. (5.5) yields:

$$
T_2 \sim 2\frac{\tilde{\chi}}{\tilde{P}(\eta)}\frac{\partial II(\eta)}{\partial\widetilde{\xi''^2}} = -T_1 \tag{5.6}
$$

Table 5.3: Partial derivatives of $\tilde{\xi}$ and $\widetilde{\xi''^2}$.

Location	$x/d = 3$ $y/d = 0.646$	$x/d = 7.5$ $y/d = 0.5$
$\partial\tilde{\xi}/\partial x$	10.149	-0.597
$\partial\tilde{\xi}/\partial y$	-302.901	-82.236
$\partial\widetilde{\xi''^2}/\partial x$	0.331	0.049
$\partial\widetilde{\xi''^2}/\partial y$	-0.430	6.799

Hence, under such circumstances, T_1 should be essentially counterbalanced by T_2 and the contribution of their sum to $\langle\chi|\eta\rangle$ is expected to be small relative to the individual contributions of T_3, T_4 and T_5.

Figures 5.9(a) and (b) show the contributions of the terms T_1–T_5 and the partial derivatives of $II(\eta)$ at $x/d = 3$ and $y/d = 0.646$ (same location as in Fig. 5.8(a)). The terms T_1–T_3 are dominant in Fig. 5.9(a) and the balance between T_1 and T_2 is obvious. Although $\partial^2 II(\eta)/\partial\widetilde{\xi''^2}\partial\widetilde{\xi''^2}$ and $\partial^2 II(\eta)/\partial\tilde{\xi}\partial\widetilde{\xi''^2}$ in Fig. 5.9(b) are relatively more important than the remaining partial derivatives of $II(\eta)$, the contributions of T_4 and T_5 are not significant because $\partial\widetilde{\xi''^2}/\partial x$ and $\partial\widetilde{\xi''^2}/\partial y$ are small at the present location (see Table 5.3). Therefore, $\langle\chi|\eta\rangle$ is largely determined by T_3. To verify these observations, $\langle\chi|\eta\rangle$, $T_1 + T_2$, and $T_3 + T_4 + T_5$ are plotted in Fig. 5.9(c). It is evident that $T_1 + T_2$ is small compared to $T_3 + T_4 + T_5$ ($\approx T_3$). However, $T_1 + T_2$ is non-negligible, as $\max(|T_1 + T_2|)$ is equal to 24.5% of $\max(\langle\chi|\eta\rangle)$. Hence, T_1 is primarily counterbalanced T_2 and $\langle\chi|\eta\rangle$ is predominantly composed of the contribution of T_3. The negative and non-negligible contribution of $T_1 + T_2$ indicates that the magnitude of production of scalar fluctuations is larger than that dissipation. The imbalance between production and dissipation reveals that convective transport and transport by turbulent fluxes in Eq. (2.81) are important. This behavior is expected since the present location is situated near the fuel-pilot shear layer where the velocity is high and the mean scalar fluxes and gradients are large.

Figure 5.10(a) displays the terms T_1–T_5 at $x/d = 7.5$ and $y/d = 0.5$ (same location as in Fig. 5.8(b)). Similar to Fig. 5.9(a), there is a clear a balance between T_1 and T_2. The contribution of T_3 is important but less prevalent due to the smaller magnitudes of $\partial\tilde{\xi}/\partial x$ and $\partial\tilde{\xi}/\partial y$ (see Table 5.3). Conversely, T_4 and T_5 are relatively more important because $\partial^2 II(\eta)/\partial\widetilde{\xi''^2}\partial\widetilde{\xi''^2}$ and $\partial^2 II(\eta)/\partial\tilde{\xi}\partial\widetilde{\xi''^2}$ are dominant in comparison to the remaining partial derivatives of $II(\eta)$, as shown in Fig. 5.10(b), and due to the large magnitude of $\partial\widetilde{\xi''^2}/\partial y$ (see Table 5.3). Therefore, $\langle\chi|\eta\rangle$ is mostly determined from T_3, T_4 and T_5. This can be

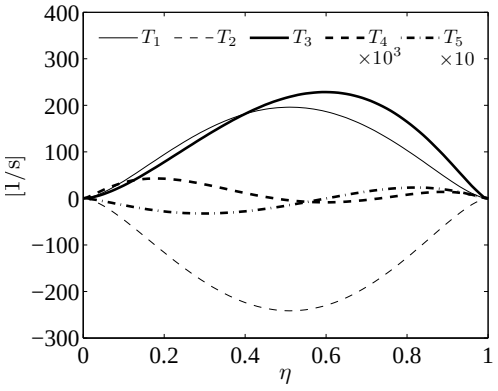

(a) T_1–T_5

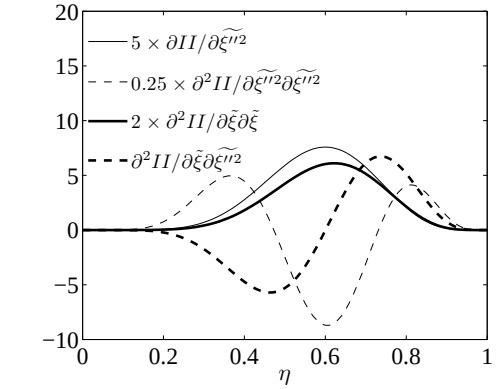

(b) Partial derivatives of $II(\eta)$

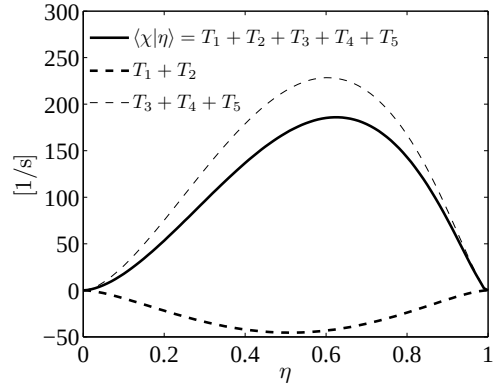

(c) CSDR

Figure 5.9: The CSDR computed using the MBPDF model at $x/d = 3$ and $y/d = 0.646$.

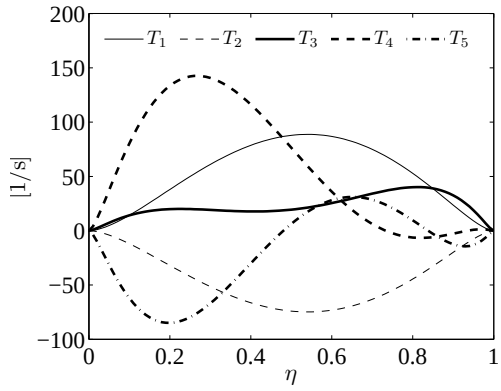

(a) T_1–T_5

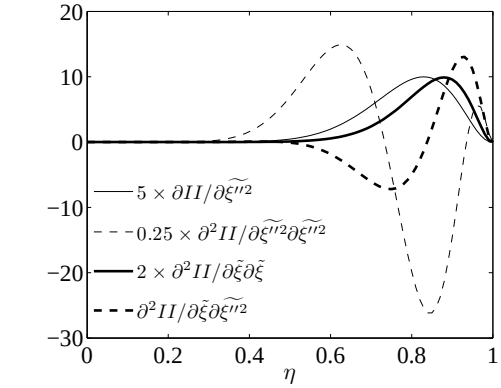

(b) Partial derivatives of $II(\eta)$

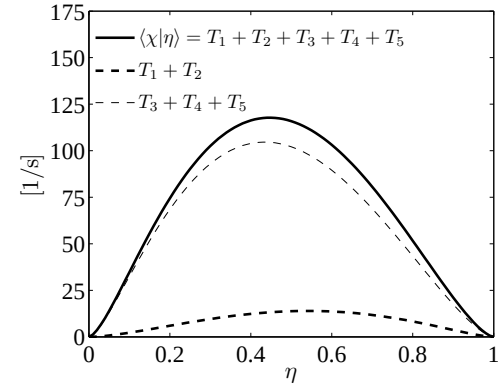

(c) CSDR

Figure 5.10: The CSDR computed using the MBPDF model at $x/d = 7.5$ and $y/d = 0.5$.

confirmed from Fig. 5.10(c) where the contribution of T_1+T_2 to the overall budget of $\langle\chi|\eta\rangle$ is smaller than that of $T_3+T_4+T_5$. Here, $\max(T_1+T_2)$ is equal to 11.8% of $\max(\langle\chi|\eta\rangle)$, which is substantially lower than what is observed in Fig. 5.9(c). This behaviour is due to the lower level of production and dissipation of scalar fluctuations, which are in turn caused by the lower local velocity and the weaker mean scalar fluxes and gradients. The overall positive contribution of T_1+T_2 indicates that dissipation is larger than production.

Recovery of the Favre-averaged scalar dissipation rate from the CSDR In order to examine the validity of the considered CSDR models, one would expect to recover the Favre-averaged scalar dissipation, $\tilde{\chi}$, upon integrating a given CSDR model weighted by its corresponding presumed PDF over the mixture fraction space, hence satisfying:

$$\tilde{\chi} = \int_0^1 \langle\chi|\eta\rangle \tilde{P}(\eta) d\eta \tag{5.7}$$

Figure 5.11 shows axial profiles of $\tilde{\chi}$ computed from Eq.(2.87) and from Eq.(5.7) at several radial locations. The MBPDF and Girimaji's models are weighted by the β-PDF, whereas the MCGPDF and AMC models are weighted by the CG-PDF. In Figure 5.11(a) ($y/d=0$) and (b) ($y/d=0.5$), $\tilde{\chi}$ is fully recovered using all CSDR models. Moving radially outward, recovery is achieved by all models except MCGPDF, as shown in Figure 5.11(c) ($y/d=1$) and (d) ($y/d=2$). The discrepancies at $y/d=1$ are only observed over a narrow range of x centred about the peak of $\tilde{\chi}$. The recovery of $\tilde{\chi}$ at $y/d=2$ is not achieved over a much wider range. The failure to recover $\tilde{\chi}$ at these two radial locations is most likely attributed to the numerical errors involved in the calculation of the partial derivatives of $II(\eta)$ with respect to $\tilde{\xi}$ and $\widetilde{\xi''^2}$. When the MCGPDF model is employed, the computation of these spatial derivatives using Ridders' method is not straightforward as it requires the calculation of the mean and the variance of the CG-PDF from $\tilde{\xi}$ and $\widetilde{\xi''^2}$ in an iterative fashion at every polynomial extrapolation. Therefore, the accuracy of these derivatives is debatable at some locations in the flow field, and the resulting CSDR may involve some errors. Another possible source of error is the presence of discontinuities in the integrand of Eq. (5.7) due to the clipping of the PDF.

In a recent autoignition study focusing on mixture A in Table 4.1, Milford and Devaud [154] show very large departures from Eq. (2.87) upon applying Eq. (5.7) to a CSDR model that is similar in derivation to the MBPDF model (see Eq. (11) in [154]). They attribute this anomaly to the behavior of the PDF gradient CV model at low probabilities (with $\tilde{P}(\eta)$ presumed using the β-PDF), and resort to scaling $\langle\chi|\eta\rangle$ by $\tilde{\chi}$ in order to match Eq.(5.7). As shown in Fig. 5.11, such departures do not occur when the MBPDF model

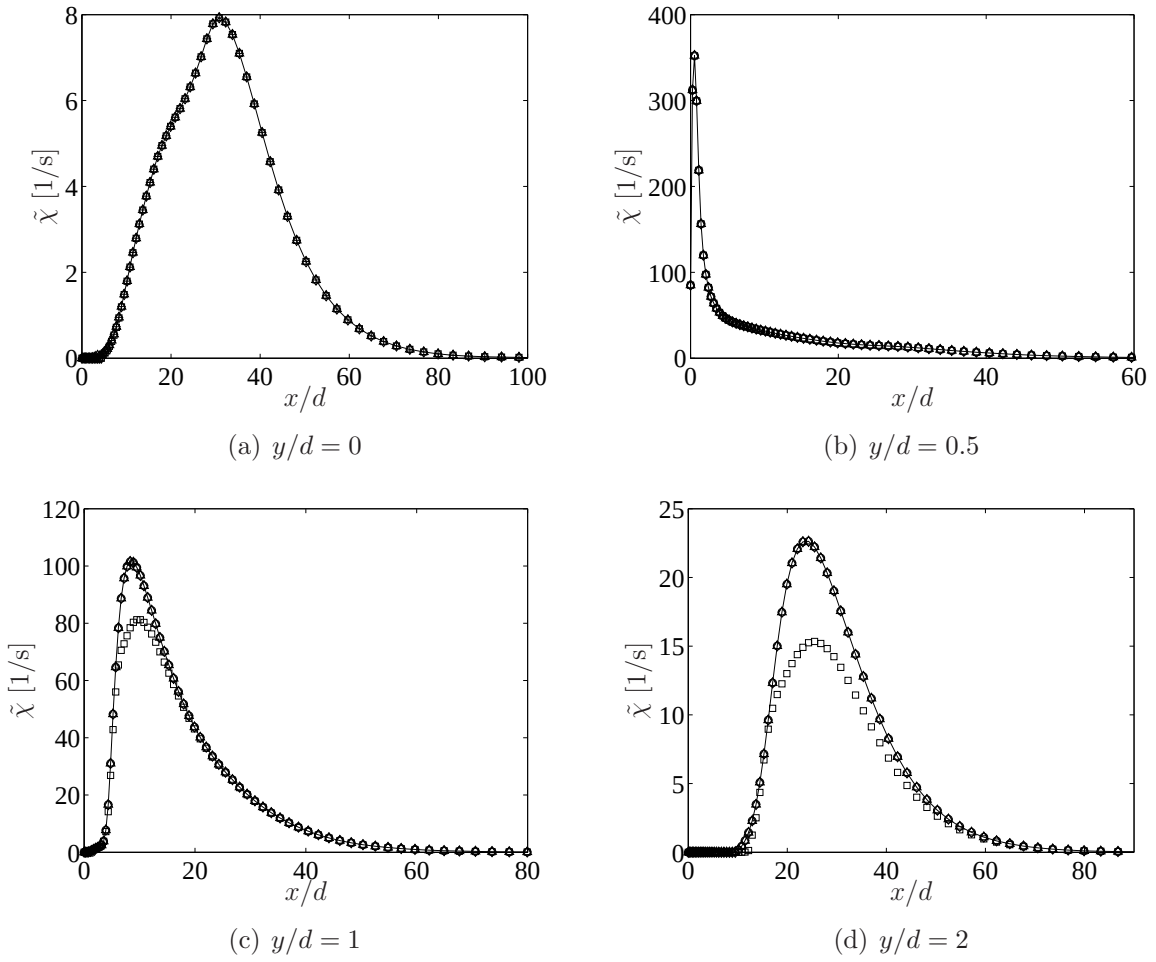

Figure 5.11: Axial profiles of the Favre-averaged scalar dissipation rate (solid line) and the integrated CSDR (symbols) at different radial locations. Symbols: △, Girimaji's model; ◇, AMC; ∘, MBPDF; □, MCGPDF.

is employed. It is well known that the PDF gradient model is not well-behaved in regions where the probabilities are low, as demonstrated in [48]. However, when applying Eq. (5.7), these regions should have a negligible effect on the integration due to the small magnitude of $\tilde{P}(\eta)$. If the product $\langle\chi|\eta\rangle\tilde{P}(\eta)$ is substantial at low $\tilde{P}(\eta)$, then $\langle\chi|\eta\rangle$ has to be several orders of magnitude larger than $\tilde{P}(\eta)$ in order for the r.h.s. Eq. (5.7) to deviate from Eq.(2.87). For example, if $\tilde{P}(\eta)$ is $O(10^{-6})$, then $\langle\chi|\eta\rangle$ has to be much higher than $O(10^{6})$, which may be unphysical. Therefore, this anomaly may be due to some different aspect in the implementation of Eq. (11) in [154]. The major challenge in this equation corresponds to the computation of the gradient and the time derivative of a definite integral (See Eq. (6) in [154]). Beside being a function of time and space, the integrand also depends on the first and second moments of the mixture fraction (via the PDF), which are in turn functions of time and space. The direct computation of the gradient and the time derivative of this integral without accounting for the fact that the integrand is a composite function may lead to numerical errors, especially if coarse grids and large time steps are employed. In the current study, the direct implementation of Eq. (9) in [157] wherein the derivatives of $II(\eta)$ with respect to x_i are not expanded leads to large errors (not shown here). On the other hand, the final form of Mortensen's model, Eq. (3.79) (Eq.(13) in [157]), does not yield such errors due to the expansion of the spatial derivatives.

The conditional velocity

Figures 5.12 and 5.13 compare the axial and radial components of the linear and PDF gradient CV models at the same locations considered in Fig. 5.7, that is at $x/d = 7.5$, 15, 30 and 45 near the stoichiometric mixture fraction isocontour. Five common observations can be made:

1. The trends of the profiles obtained using the β- and CG-PDF gradient models are similar. The differences between the two models manifest away from $\eta = \tilde{\xi}$.

2. The β-PDF gradient model tends to infinity at the boundaries of η-space as the PDF decays to zero $\eta = 0$ and 1.

3. The CG-PDF gradient model is finite at the boundaries of η-space since the PDF is clipped ($\neq 0$) at $\eta = 0$ and 1.

4. The fluctuations of the linear CV model are in general smaller in magnitude than those of the β- and CG-PDF models.

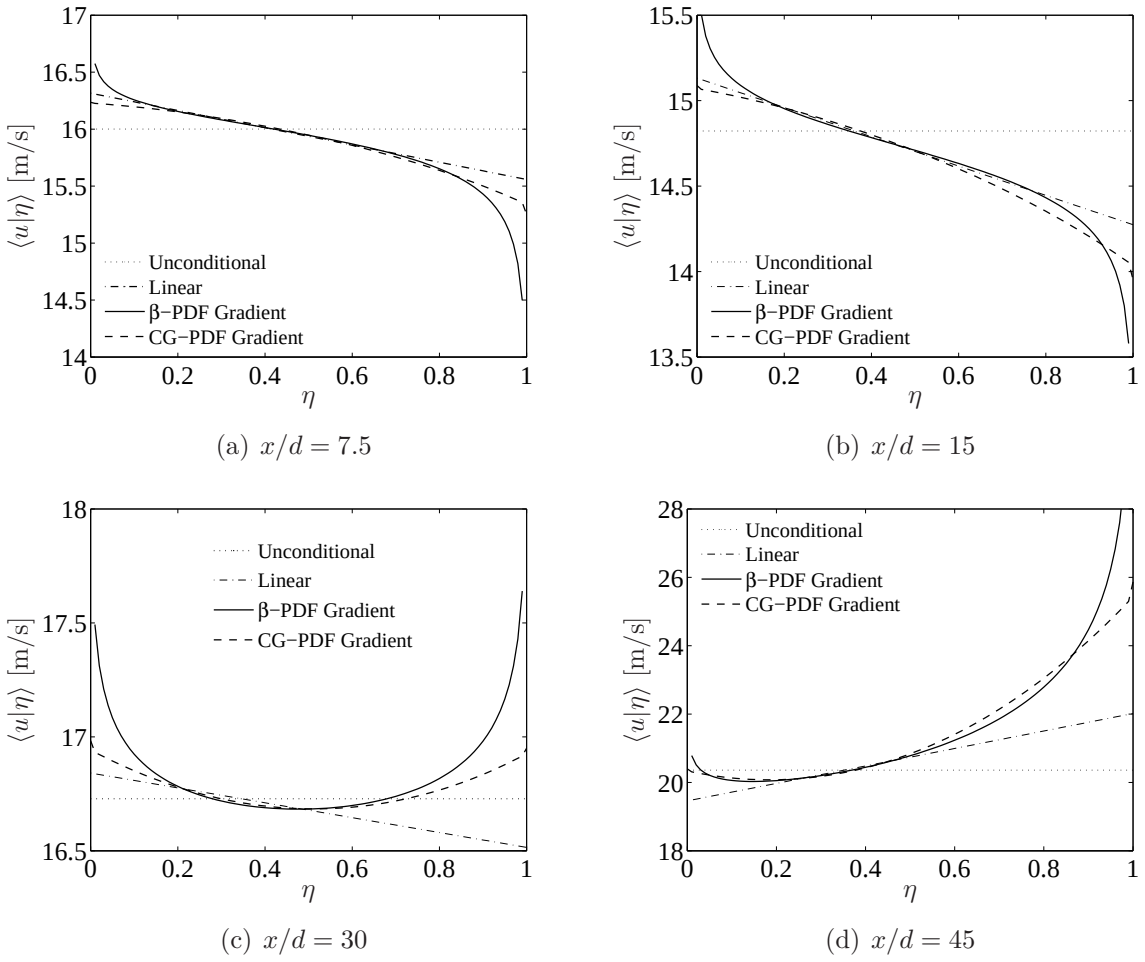

(a) $x/d = 7.5$ (b) $x/d = 15$

(c) $x/d = 30$ (d) $x/d = 45$

Figure 5.12: Comparison of the axial components of the conditional velocity models near the stoichiometric isocontour: (a) $x/d = 7.5$, (b) $x/d = 15$, (c) $x/d = 30$, and (d) $x/d = 45$.

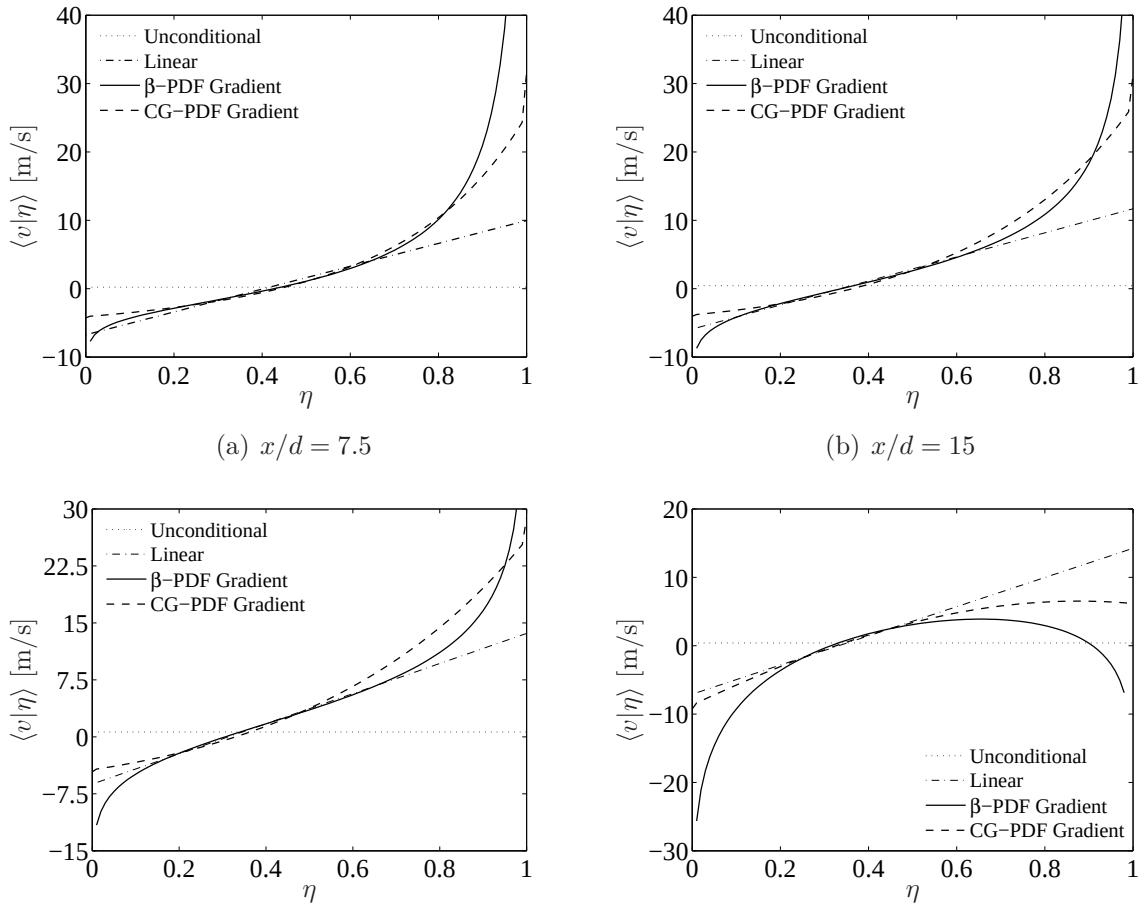

(a) $x/d = 7.5$ (b) $x/d = 15$

(c) $x/d = 30$ (d) $x/d = 45$

Figure 5.13: Comparison of the radial components of the conditional velocity models near the stoichiometric isocontour: (a) $x/d = 7.5$, (b) $x/d = 15$, (c) $x/d = 30$ and (d) $x/d = 45$.

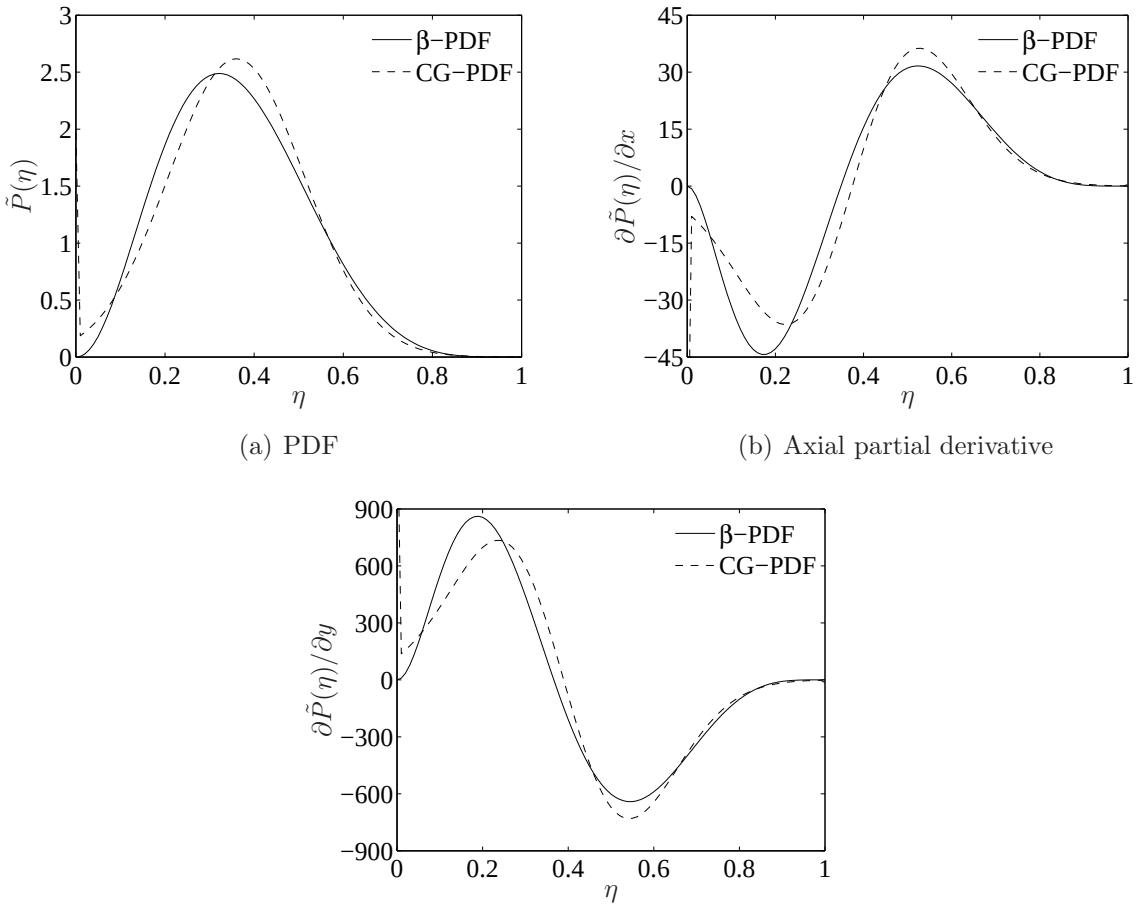

(a) PDF

(b) Axial partial derivative

(c) Radial partial derivative

Figure 5.14: The β-PDF and CG-PDF and their gradients at $x/d = 15$ near the stoichiometric isocontour: (a) $\tilde{P}(\eta)$, (b) $\partial\tilde{P}(\eta)/\partial x$, and (c) $\partial\tilde{P}(\eta)/\partial y$.

5. The linear and PDF gradient models yield very similar results within approximately two standard deviations of the mean mixture fraction (between $\eta \approx 0.2$ and 0.5 at all locations).

The β-PDF and CG-PDF along with their axial and radial partial derivatives at $x/d = 15$ are plotted in Fig. 5.14. As shown in Fig. 5.14(a), the two PDFs differ in shape over $0 < \eta < 1$ and behave differently at $\eta = 0$ and 1. The β-PDF decays to zero at the boundaries of η-space, whereas the CG-PDF is non-zero by virtue of clipping ($\tilde{P}(\eta = 1) \neq 0$, however it is very small). As a result, the spatial derivatives of $\tilde{P}(\eta)$ are substantially different, as shown in Figs. 5.14(b) and (c). By investigating these two figures, it is apparent that the radial derivatives of both PDFs, $\partial\tilde{P}(\eta)/\partial y$, are approximately one order of magnitude higher than their axial counterparts, $\partial\tilde{P}(\eta)/\partial x$. This is due to the sharper variation of $\tilde{P}(\eta)$ across the flame. Therefore, the radial CV fluctuations are larger than the axial ones. This is evident in Figs. 5.12(b) where $-1/\tilde{P}(\eta)\partial P(\eta)/\partial x$ is small compared to $\tilde{u}$ and 5.13(b) where $-1/\tilde{P}(\eta)\partial P(\eta)/\partial y$ is very large compared to $\tilde{v}$. As such, $\langle v|\eta\rangle$ is mainly dominated by radial conditional fluctuations.

In the absence of experimental measurements, it is difficult to judge the performance of the considered models. Despite its divergent behaviour at low probabilities, the PDF gradient model is better suited than the linear approximation for a consistent CMC implementation.

5.4.3 CMC calculations using β-PDF-based closures

Calculations for two CMC realisations employing the presumed β-PDF are performed. In the first, CMC-G, Girimaji's homogeneous model (Eq. (3.75)) is employed to close the CSDR, whereas in the second, CMC-M, the inhomogeneous and fully consistent MBPDF model is used (Eq. (3.81) with $II(\eta)$ computed from Eq. (3.85)). In both realisations, the CV is closed using the β-PDF gradient model (Eq. (3.70)), the conditional reaction rates are modelled using the first-order closure (Eq. (3.90)), and the conditional radiative source is computed using the optically thin assumption (Eq. (3.93)). The subset of participating species comprises H_2O, CH_4, CO_2, and CO. Transport in physical space by conditional turbulent fluxes is neglected following previous studies investigating the same flame [62, 199]. The pressure term in Eq. (3.34)) is neglected because the flame is open to the atmosphere (pressure changes are small). As such, the two realisations only differ in the modelling of the CSDR. Since the inhomogeneous MBPDF model reduces exactly to Girimaji's homogeneous model when the inhomogeneous terms are omitted from Eq. (3.81) (Eq. (3.75) becomes the exact equivalent of Eq. (3.83)), the CMC-M realisation

complements CMC-G by accounting for the inhomogeneity of the CSDR. Therefore, the comparison of the results of the two realisations enables the quantification of the effect of the spurious sources.

The profiles of the CSDR, the PDF, and the conditional temperature and species mass fractions are shown at two locations in the near field: $x/d = 2$ (Fig. 5.15) and $x/d = 3$ (Fig. 5.16) near the fuel-pilot shear layer ($y/d = 0.646$), and at three locations in the far field: $x/d = 15$ (Fig. 5.17), $x/d = 30$ (Fig. 5.18) and $x/d = 45$ (Fig. 5.19) near the stoichiometric isocontour (at the radial grid point closest to $\tilde{\xi}(x_i) = \xi_{st}$). In all figures, the lines correspond to CMC-G (dashed) and CMC-M (solid), and the symbols correspond to the experimental measurements of the temperature ($\circ$) and the mass fractions of O_2 ($\triangle$), CH_4 ($\square$), H_2O ($\diamond$), CO_2 ($\times$), CO ($*$), OH ($+$), H_2 ($\triangledown$) and NO ($\triangleright$). For clarity, OH and H_2 are scaled by factors of 10 and 5, respectively The vertical lines indicate the location of the stoichiometric mixture fraction, $\eta = \xi_{st} = 0.351$.

The trends in the predicted conditional profiles are discussed elsewhere [62, 199] and will not be repeated here for brevity. In summary, a very good agreement with the experimental data is achieved in lean mixtures, while discrepancies are obtained around $\eta = \xi_{st}$ and in rich mixtures. These discrepancies are mainly attributed to the modelling of the conditional chemical sources using the first-order closure. The deviation from experimental measurements could be also due to the neglect of differential diffusion or to the employed chemical kinetics mechanism [62, 66, 199]. In what follows, the discussion of the results is focused on the impact of the modeling of the CSDR on the conditional predictions.

Two common observations can be made at all locations concerning the distributions of the CSDR (Figs. 5.15(a), 5.16(a), 5.17(a) and 5.19(a)): Girimaji's model yields nearly symmetric profiles, whereas the MBPDF model results in asymmetric profiles. The two CSDR distributions intersect at $\eta = \tilde{\xi}$ (located near the peak of $\tilde{P}(\eta)$), and therefore yield the same CSDR value at this location in η-space. The differences between the profiles manifest far from $\eta = \tilde{\xi}$ where the PDF is small.

At $x/d = 2$ (Fig. 5.15(a)), substantial differences between the two CSDR models are obtained over the whole range of η-space. Girimaji's model produces high dissipation levels in stoichiometric mixtures, while the MBPDF model tends to be less dissipative there due to the sharp negative skewness of the CSDR. Pitsch and Steiner [186] note that the scalar dissipation rate within the pilot stream is zero because the scalar gradient is zero at $x/d = 0$. Hence, the CSDR at $\eta = \tilde{\xi}_p = 0.27$, $\langle \chi | \eta = \tilde{\xi}_p \rangle$, is zero. This causes the CSDR to be small at the stoichiometric mixture fraction. They also note that this effect propagates to downstream locations and the shape of the CSDR remains influenced by the pilot. This behavior is well predicted by the MBPDF model at $x/d = 2$, as shown in Fig.

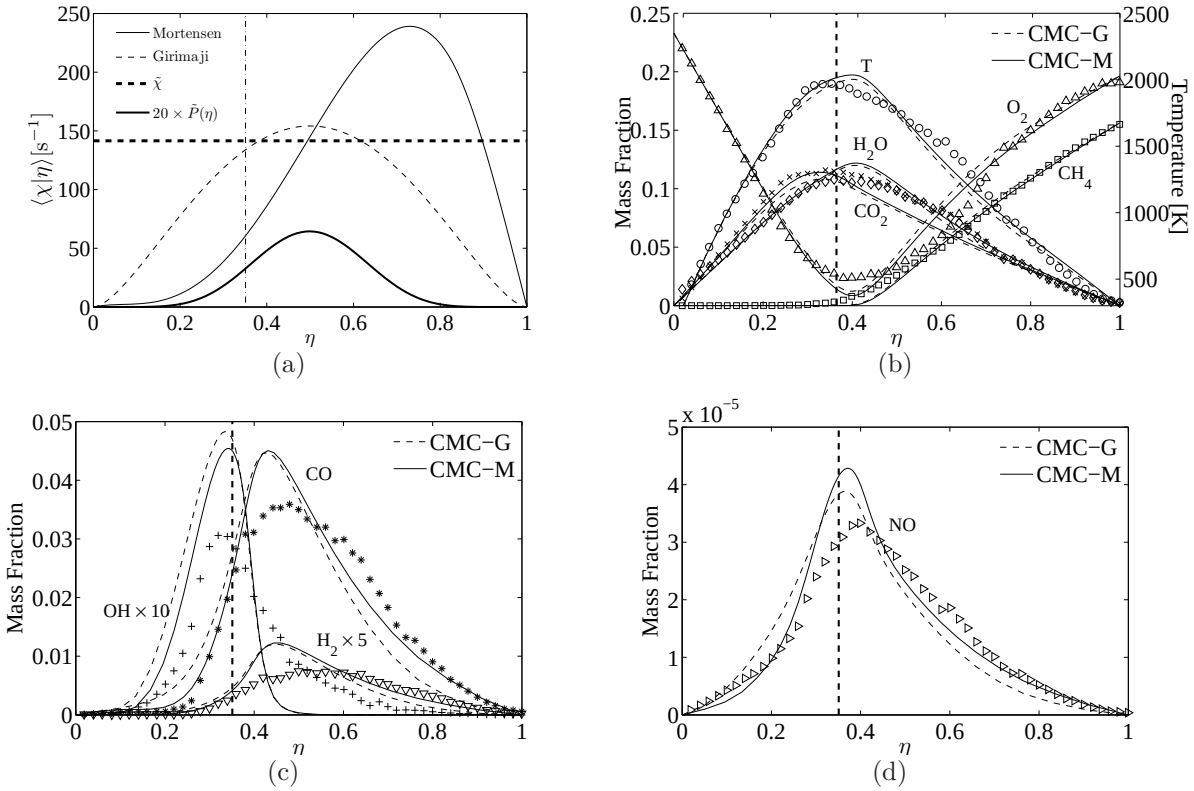

Figure 5.15: Predicted (lines) and measured (symbols) profiles of the conditional temperature and species mass fractions at $x/d = 2$ near the inflow-pilot shear layer ($y/d = 0.646$).

5.15(a). The lower CSDR levels lead to a decrease in the leakage of O_2 from stoichiometric towards lean and rich mixtures. Therefore, the oxidation of fuel becomes more intense in the vicinity of the stoichiometric mixture fraction. As a direct consequence, higher temperature and product mass fractions and lower reactant mass fractions are obtained there. This is evident in Figs. 5.15(b)-(d). The higher CSDR levels on the rich side ($\eta \gtrsim 0.5$) enhance the diffusion of O_2 from the (O_2-containing) fuel stream towards less rich mixtures, thus promoting oxidation there. Therefore, the temperature and product mass fractions increase and the reactant mass fractions decrease as a larger fraction of fuel is consumed by the incoming O_2. On the lean side of stoichiometry, the low CSDR levels result in slower diffusion of O_2 from the oxidiser stream. This results in lower intermediate species and radical mass fractions, as displayed in Figs. (c) and (d). In comparison with the experimental measurements, the results of CMC-M are in general superior to those of CMC-G. All reactive scalars show some improvement over the whole range of mixture

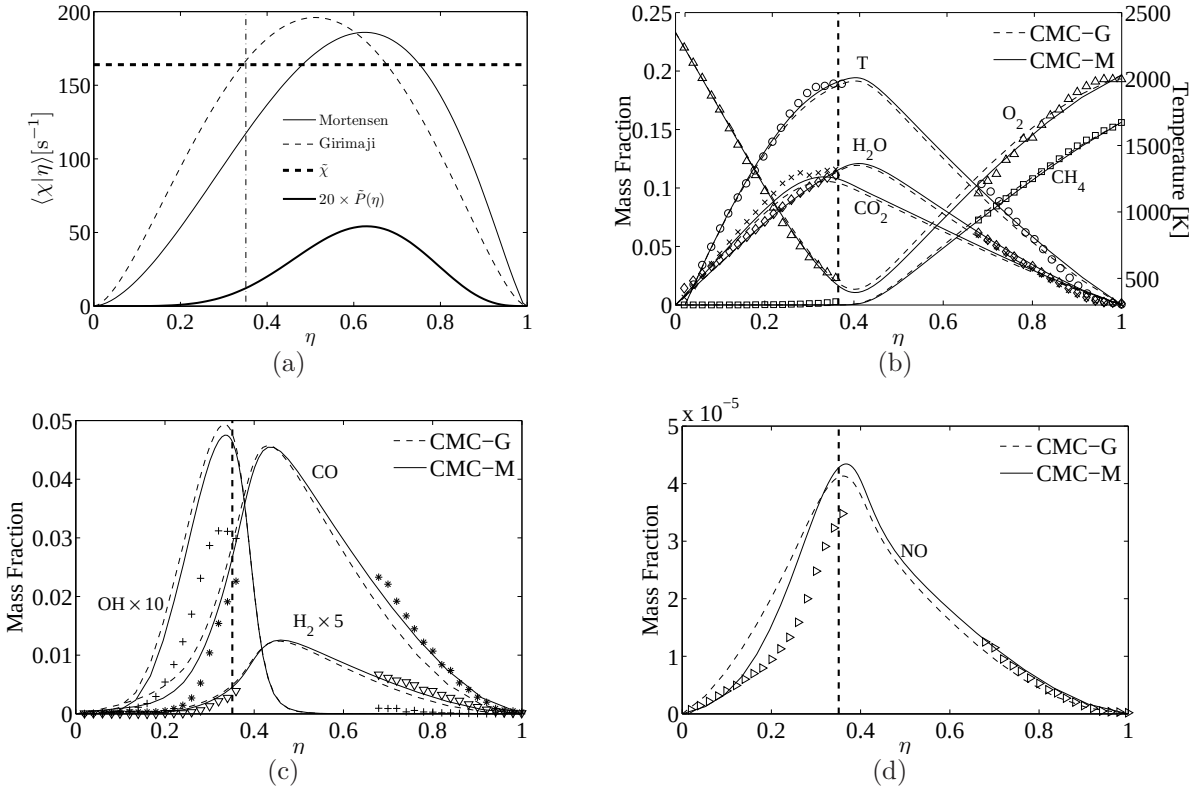

Figure 5.16: Predicted (lines) and measured (symbols) profiles of the conditional temperature and species mass fractions at $x/d = 3$ near the inflow-pilot shear layer ($y/d = 0.646$).

fraction space except in the region between $\eta \approx 0.35$ and $\eta \approx 0.45$. This discrepancy is most likely attributed to the excessive underestimation of the CSDR by the MBPDF model in this range of η.

The trends of the CSDR distributions at $x/d = 3$ (Fig. 5.16(a)) are similar to those observed at $x/d = 2$ (Fig. 5.15(a)). The MBPDF and Girimaji's models yields negatively-skewed and symmetric profiles, respectively. The skewness is due to the influence of the pilot stream. However, in comparison to $x/d = 2$, the CSDR is not as skewed at the current location. This behaviour is expected since the effect of the pilot diminishes gradually in the streamwise direction. The CSDR computed from the MBPDF model remains relatively lower in lean mixtures and around η_{st} and higher in rich mixtures in comparison to the nearly symmetric CSDR obtained using Girimaji's model. Hence, similar trends in the conditional profiles of the reactive scalars are obtained, as shown in Figs. 5.16(b)-(d). The profiles of temperature and major species show a slightly better agreement with the

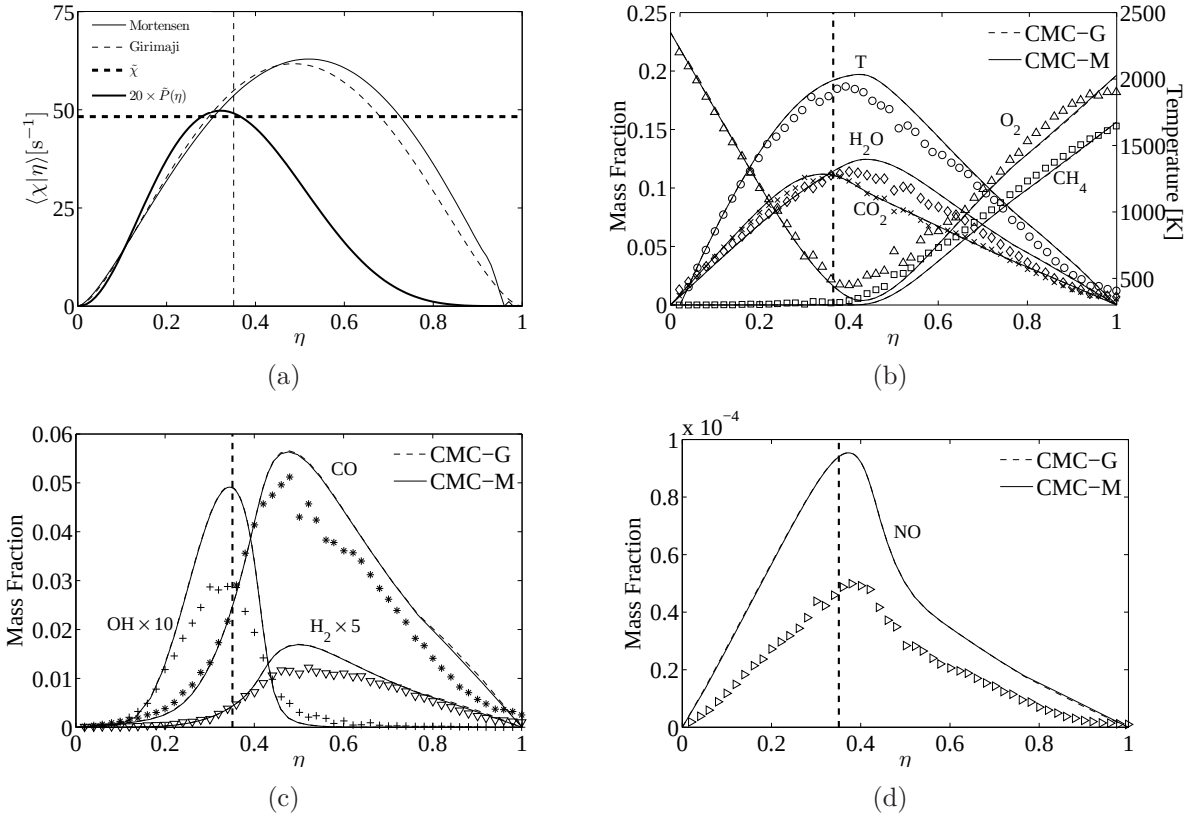

Figure 5.17: Predicted (lines) and measured (symbols) profiles of the conditional temperature and species mass fractions at $x/d = 15$ near the stoichiometric isocontour.

experimental measurements in rich mixtures (Fig. 5.16(b)), whereas those of intermediates and radicals display a more noticeable improvement in both lean and rich mixtures (Figs. 5.16(c) and (d)).

Further downstream at $x/d = 15$ (Fig. 5.17(a)) and 30 (Fig. 5.18(a)), the two CSDR models yield very similar profiles, with the MBPDF model showing a slight skewness. Therefore, the usage of either model is expected to yield very similar results. This is confirmed in Figs. 5.17(b)-(d) and 5.18(b)-(d) where the conditional temperature and species mass fraction in CMC-G and CMC-M are virtually identical.

At $x/d = 45$, the MBPDF model yields a positively-skewed CSDR distribution. Compared to the profile obtained using Girimaji's model, the CSDR is higher in lean mixtures and lower in rich ones. Therefore, trends opposite to those observed at $x/d = 2$ and 3

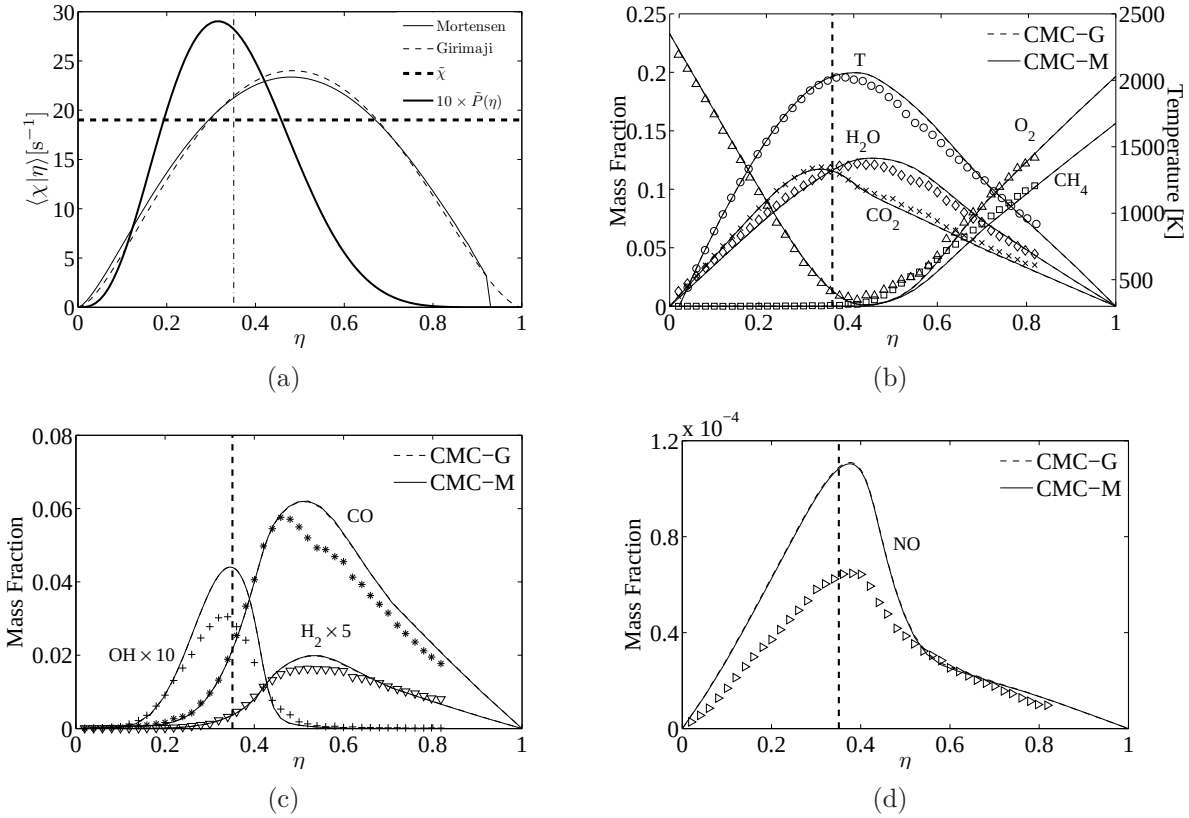

Figure 5.18: Predicted (lines) and measured (symbols) profiles of the conditional temperature and species mass fractions at $x/d = 30$ near the stoichiometric isocontour.

are expected. This is demonstrated in Figs. 5.19(b)-(d). The lower CSDR levels in rich mixtures hinder the diffusion of O_2 from the fuel stream towards less rich mixtures, and therefore suppress oxidation on the rich side. Consequently, the temperature and product mass fractions decrease and the reactant mass fractions increase as a smaller fraction of fuel is oxidised. Conversely, the higher CSDR levels in lean mixtures enhance the diffusion of O_2 from the oxidiser stream. As a result, the mass fraction of intermediates and radicals are slightly higher on the lean side, as displayed in Figs. (c) and (d).

To summarise, the presented results reveal that the levels of all reactive scalars, most notably minor intermediates and radicals, are better predicted when the effects of inhomogeneity are included in the modelling of the CSDR (the MBPDF model). This suggests that the spurious sources, which arise from the homogeneous modelling of the CSDR (Gir-

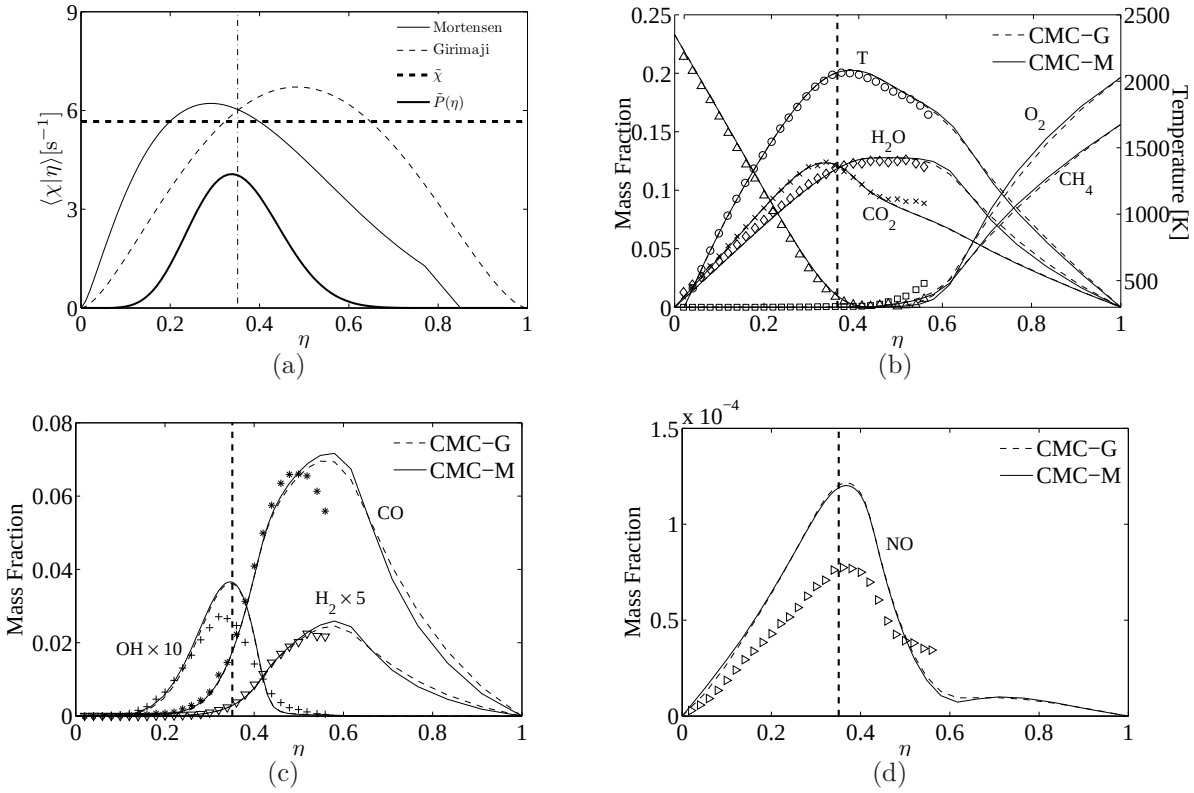

Figure 5.19: Predicted (lines) and measured (symbols) profiles of the conditional temperature and species mass fractions at $x/d = 45$ near the stoichiometric isocontour.

imaji's model), have a non-negligible effect on the modelling of the piloted jet flame under investigation.

5.5 Conclusions

The piloted CH_4/air jet flame Sandia D was investigated using the first-order CMC. Several CMC submodels were assessed and consistent combinations were employed to simulate the flame. In light of the results, the following conclusions are drawn:

1. The β-PDF is more suited for the modelling of the flame under investigation, although the CG-PDF is capable of detecting the presence of intermittency at the outer edge

of the jet. Better results can be obtained by using a trinary PDF in the nozzle-pilot-coflow region and a binary PDF elsewhere because the fuel and air streams do not mix directly due to the presence of the pilot. This can be be achieved using the PMF approach.

2. The AMC and Girimaji's model yield very similar symmetric profiles. On the other had, Mortensen's model based on the β-PDF leads to asymmetric profiles. When the CG-PDF is used in Mortensen's model, the CSDR profiles are sharply skewed. This version of the model shows strong deviation from measurements in rich mixtures. All other models are in fair agreement with the experimental data.

3. It is demonstrated that Girimaji's model can be fully recovered from Mortensen's model based on the β-PDF when the inhomogeneous terms are eliminated from the later. The CSDR profiles resulting from the two models intersect at the value of η located near the local mixture fraction mean. Differences in the CSDR distributions manifest far from the mean where the PDF is small.

4. The analysis of Mortensen's model reveals that the homogeneous portion of the model represented by term T_1 in Eq. (5.3) is essentially counterbalanced by term T_2 when the production and dissipation of scalar fluctuations are of the same order. When this situation arises, the contribution of the sum of these two terms to the overall budget of the model is relatively smaller than the sum remaining terms.

5. It is shown that $\tilde{\chi}$ is fully recovered when the considered CSDR models are weighted by their respective PDFs and integrated over η-space. Mortensen's model based on the CG-PDF does not achieve full recovery in some regions of the flow field. The discrepancies are possibly due to the numerical errors associated with the computation of the mean and variance of the CG-PDF from $\tilde{\xi}$ and $\widetilde{\xi''^2}$ or to the discontinuities introduced by the CG-PDF.

6. The linear and PDF gradient CV models yield very similar distributions within two standard deviations of $\eta = \tilde{\xi}$ and deviate from one another elsewhere. As opposed to the β-PDF gradient model, the CG-PDF gradient model is well-behaved (finite) at the boundaries of the η-space due to clipping. It is further shown that the radial CV fluctuations in the PDF gradient model are substantially larger than the axial ones due to the sharper variations of the PDF across the flow.

7. CMC realisations using consistent and inconsistent CSDR models (the homogeneous model of Girimaji and the inhomogeneous model of Mortensen, respectively) show that the inclusion of the effects of inhomogeneity yields better predictions for all

reactive scalars in lean and rich mixtures, most notably in the near field. Therefore, it is concluded that the spurious sources resulting from the homogeneous modelling of the CSDR have a non-negligible effect on the predictions of the considered flame.

Chapter 6

Modelling of a Lifted Hydrogen/Nitrogen Turbulent Jet Flame using Consistent β-PDF-based Submodels

A lifted H_2/N_2 turbulent jet flame issuing into a vitiated coflow is investigated using the two-dimensional first-order CMC and a modified version of the $k-\varepsilon$ model. The CV and the CSDR submodels are chosen such that they are fully consistent with the mixture fraction PDF transport equation. The conditional fluctuations of the velocity are modelled in terms of the gradient of the PDF. Two CSDR submodels based on the double integration of the homogeneous and inhomogeneous PDF transport equations are implemented. An additional transport equation for the Favre-averaged scalar dissipation rate is solved rather employing the traditional algebraic approach wherein the flow and scalar turbulence time scales are assumed to be proportional. The effect of the modelling of the CSDR over a range of coflow temperatures is investigated and the stabilisation mechanism is determined from the analysis of transport budgets in mixture fraction and physical spaces, and from the history of radical build-up ahead of the stabilisation height. Using both CSDR submodels and for all coflow temperatures, the balance between chemistry, axial convection and micro-mixing, and the absence of axial diffusion upstream of the stabilisation height indicate that the flame is stabilised by autoignition rather than premixed flame propagation. This conclusion is further confirmed from the early and rapid build-up of the intermediate HO_2 ahead of the radicals H, O and OH. It is also found that the inclusion of the effects of inhomogeneity in the modelling of the CSDR yields higher dissipation level at the "most

reactive" mixture fraction, which results in delayed ignition and larger liftoff heights. The effect of the spurious sources which arise from inconsistent CSDR modelling is found to be small but non-negligible, mostly notably within the flame zone. The role of chemical kinetics is additionally investigated. The results show that the flame is very sensitive to chemistry.

6.1 Introduction

A non-premixed jet flame remains attached to the fuel nozzle provided that the velocity of the fuel jet, U_j, is sufficiently low [178]. As U_j is increased, there exists a critical velocity at which the flame lifts off and stabilises at a certain distance H from the nozzle, as shown in Fig. 6.1. This critical velocity is defined as the liftoff velocity and the distance H is referred to as the liftoff height. As U_j is increased beyond the liftoff velocity, H keeps increasing

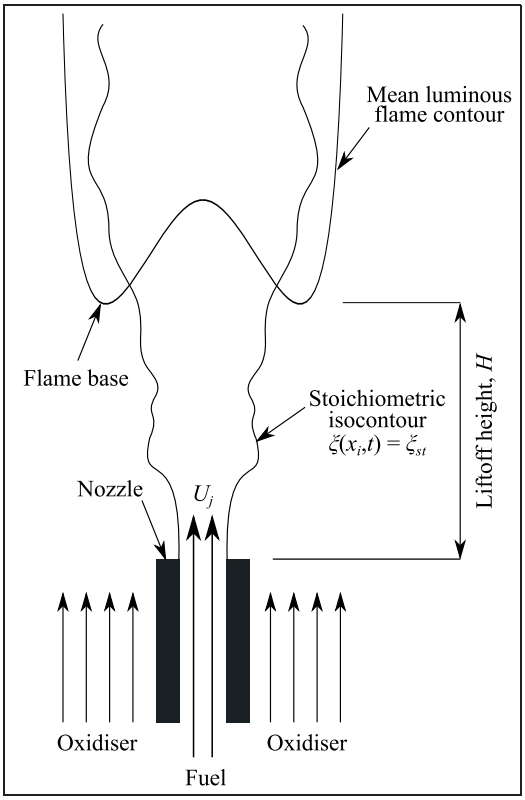

Figure 6.1: Schematic of a lifted flame (reproduced from [178]).

up to a critical height at which the flame blows out. When U_j is decreased, there exists a critical velocity (different from the liftoff velocity) at which the flame reattaches to the nozzle. Therefore, there is hysteresis phenomenon between flame liftoff and reattachment [178].

The investigation of stabilisation mechanisms of lifted flames is an active area in combustion research. A substantial number of experimental and numerical studies have been dedicated to the understanding and analysis of the process by which lifted flames are stabilised. Several theories have been proposed in the literature. Vanquickenborne and van Tiggelen [228] suggest the premixed flame propagation stabilisation theory. Their experimental findings indicate that the fuel and the oxidiser are premixed ahead of the base of lifted diffusion flames and that stabilisation takes place at stoichiometric locations where the local mean velocity and the turbulent burning velocity of a stoichiometric premixed flame are equal. Peters and Williams [179] suggest that stabilisation is achieved by the local quenching of diffusion flamelets due to excessive straining. Cabra et al. [35] conduct experimental measurements for a lifted turbulent H_2/N_2 jet flame issuing into a coaxial vitiated coflow consisting of the hot combustion products of a lean premixed H_2/Air flame. The coflow conditions allow for the possibility of stabilisation by means of autoignition. It is postulated that autoignition takes place as inert fuel parcels are convected downstream and become well mixed with the hot coflow. However, premixed flame propagation remains another possible stabilisation mechanism.

The Cabra flame is attractive for the validation of combustion models due to its simple configuration and well-defined boundary conditions. It is extensively investigated using PDF methods [35,37,79,146]. Masri et al. [146] use the composition PDF approach coupled with the $k-\varepsilon$ turbulence model and conclude that flame is largely controlled by chemical kinetics. They identify key reactions and show that the predicted liftoff height and the composition at the base of the flame are highly sensitive to the rate parameters of these reactions. Gordon et al. [79] use the same computational methodology in order to determine the underlying stabilisation mechanism. They develop two numerical indicators for the distinction between stabilisation via autoignition and premixed flame propagation. These indicators are based on the analysis of the transport budgets of convection, diffusion and reaction and the history of radical build-up ahead of the reaction zone. A convection-reaction balance without significant contribution from axial diffusion, along with an early and rapid build-up of HO_2 ahead of the remaining radicals indicate that stabilisation occurs via autoignition. Whereas an axial diffusion-convection balance with negligible reaction accompanied by a simultaneous build-up of all radicals point to stabilisation by means of premixed flame propagation. With the aid of these indicators, Gordon et al. [79] conclude that autoignition is the controlling mechanism for a wide range of coflow temperatures.

Cao et al. [37] employ the joint velocity-turbulence frequency-composition PDF method and perform a detailed parametric study using several mixing models and chemical kinetics mechanisms, over a wide range of jet and coflow conditions. They show that although the modelling of mixing affects the prediction of liftoff height, the flame is mainly controlled by chemical kinetics. They also demonstrate that the liftoff height increases with increasing jet and coflow velocities and decreases with increasing jet and coflow temperatures. In all of the PDF studies described above, autoignition was found to be the controlling stabilisation mechanism. In the context of CMC, Stanković and Merci [212] and Navarro-Martinez and Kronenburg [169] investigate this flame using LES with a first-order closure for the conditional chemical source. The main difference between the two LES-CMC studies lies in the treatment of the CSDR. The first employs the AMC [174], which produces symmetric profiles in mixture fraction space. The second employs a different conditioning technique described in [170], which allows for skewed profiles with the possibility of local minima and maxima in mixture fraction space. In both sets of calculations the coflow temperature ranges between 1020 and 1080 K. The first authors conclude that stabilisation is controlled by autoignition for all coflow temperature. The second authors draw the same conclusions for high coflow temperatures, however, they report a transition to flame stabilization by premixed flame propagation as the coflow temperature is reduced. The different conclusions are most likely attributed to the treatment of the CSDR, and to a lesser extent, to the employed numerical methods, discretization schemes and grid resolutions in physical and mixture fraction spaces. Patwardhan et al. [176] also use the first-order CMC to study this flame. They employ the standard $k-\varepsilon$ model for the computation of the turbulence and mixing fields. To a certain degree, their conclusions in regards to the controlling stabilisation mechanism are in line with those of Navarro-Martinez and Kronenburg [169]. Premixed flame propagations is found to be the controlling stabilisation mechanism of the lifted flame for low and intermediate coflow temperatures (1025 and 1045 K), whereas the flame stabilised by autoignition for high coflow temperatures (1080 K). To close the CMC equations, they employ the β-distribution for the PDF, the linear velocity model [131] for the CV, and the AMC for the CSDR. The assumption of homogeneous Gaussian turbulence is inherent to the adopted CV and CSDR closures. The linear velocity model is exact only if the velocity and the mixture fraction are jointly Gaussian [22, 120], which is in general not the case for inhomogeneous flows. Although consistent with the first moment of the PDF, this CV model is inconsistent with the second moment [43]. As for the AMC, this closure is a particular solution of the homogeneous PDF transport equation, wherein the employed mapping function is Gaussian. Patwardhan et al. [176] use a β-distribution instead. Further, the fact that the AMC does not account for inhomogeneous effects leads to an inconsistent CMC implementation. When such closure is employed, the integration of the PDF-weighted CMC equations over the mixture fractions space yields

the unconditional equations in addition to extra spurious sources [120, 226]. These sources may lead to inaccurate results and misleading conclusions, depending on their magnitudes. As such, the CV and CSDR closures employed in [176] do not provide a fully consistent CMC implementation.

In this chapter, the lifted hydrogen jet flame of Cabra et al. [35] is revisited and investigated using the two-dimensional first-order CMC and a modified version of the $k-\varepsilon$ model. The conditional submodels required for the closure of the CMC equations are selected such that they are fully consistent with the mixture fraction PDF transport equation. Additionally, a transport equation is solved for the Favre-averaged scalar dissipation rate rather employing the traditional "equal time scales" algebraic approach. The simulations are set-up such that the settings of Patwardhan et al. [176] are reproduced as closely as possible. This study is aimed at determining (1) the effect of micro-mixing on liftoff via the modelling of the CSDR, (2) the response of the flame to changes in the coflow temperature, (3) the controlling stabilisation mechanism, (4) the influence of the spurious sources, and (5) the impact of chemical kinetics.

6.2 Experimental configuration

The flame under investigation is the lifted turbulent jet flame of Cabra et al. [35]. The burner consists of a central H_2/N_2 jet surrounded with a coaxial flow composed of the hot combustion products of a lean premixed H_2/Air flame stabilized on a perforated disk. The perforated disk is surrounded by an exit collar for the purpose of delaying the entrainment of ambient air into the coflow. The nozzle exit is placed above the surface of the disk in order to allow the fuel to exit into the coflow with a uniform composition. A schematic of the experimental setup is shown in Fig. 6.2 and the flow conditions are summarized in Table 6.1. The experimental criterion for the determination of the liftoff height (H_{exp}) is taken as the first location where the mass fraction of OH reaches 600 ppm. The normalised measured height is $H_{\text{exp}}/d = 10$.

6.3 Mathematical model

6.3.1 Conditional Moment Closure

The modelling of the turbulence-chemistry interactions is carried out using CMC. The conditional species and temperature equations are given by Eqs. (3.23) and (3.34), respec-

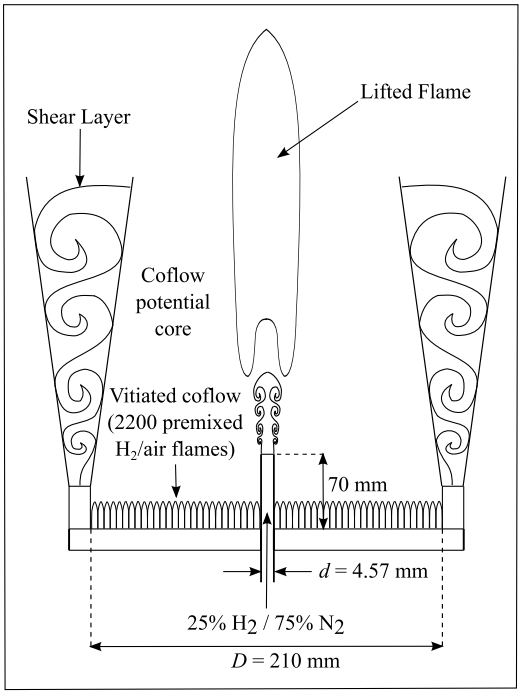

Figure 6.2: The lifted H_2/N_2 flame of Cabra et al. [35]

Table 6.1: Conditions of the lifted flame of Cabra et al. [35].

	Jet		Coflow
d [mm]	4.57	D [mm]	210
T_j [K]	305	T_c [K]	1045
U_j [m/s]	107	U_c [m/s]	3.5
X_{H_2}	0.2537	X_{H_2}	0.0005
X_{O_2}	0.0021	X_{O_2}	0.1474
X_{N_2}	0.7427	X_{N_2}	0.7534
X_{H_2O}	0.0015	X_{H_2O}	0.0989
ξ_{st}	0.474	ϕ	0.25

Nomenclature: d = jet diameter; D = coflow diameter; T = temperature; U = velocity; X = mole fraction; ξ = mixture fraction; ϕ = equivalence ratio. Subscripts: j = jet; c = coflow; st = stoichiometric.

tively. The unsteady pressure term in Eq. (3.34) is neglected due to the fact that the investigated flame is open to the atmosphere, and hence pressure changes are expected very small. In order to fully close the system of equations, submodels for $\tilde{P}(\eta)$, $\langle u_i|\eta\rangle$, $\langle\chi|\eta\rangle$, $\langle u_i'' y_\kappa''|\eta\rangle$, $\langle u_i'' T''|\eta\rangle$, $\langle\dot{\omega}_\kappa|\eta\rangle$, and $\langle\dot{\omega}_r|\eta\rangle$ are required. Throughout this study, $\tilde{P}(\eta)$ is presumed to follow a β-distribution (Eq. (3.37)). For consistency with this choice, the submodels employed to close $\langle u_i|\eta\rangle$ and $\langle\chi|\eta\rangle$ are based on this distribution. The PDF gradient diffusion model of Pope [188,190], Eq. (3.70), is used to model $\langle u_i|\eta\rangle$. The partial derivatives of $\tilde{P}(\eta)$ with respect to $\tilde{\xi}$ and $\widetilde{\xi''^2}$ are computed numerically. As stressed in Sect. 3.3.3, this model is consistent with the first and second moments of the PDF and with the modelling of the unconditional passive and reactive scalar fluxes. As for $\langle\chi|\eta\rangle$, two β-PDF based closures are investigated: the model of Girimaji [78], Eq. (3.75), and the model of Mortensen [157], Eq. (3.81). In the latter, $II(\eta)$ is given by Eq. (3.85). Girimaji's model is valid for homogeneous turbulence. Therefore, its usage in the CMC of inhomogeneous flows is inconsistent and results in spurious sources. On the other hand, Mortensen's model ensures a fully consistent CMC implementation as it accounts for the inhomogeneous terms of the PDF transport equation and employs a consistent closure for the CV fluctuations. As such, this model does not yield any spurious sources. It is important to note that Girimaji's model is the equivalent of the homogeneous portion of Mortensen's, $2\tilde{\chi}/\tilde{P}(\eta)\partial II(\eta)/\partial\widetilde{\xi''^2}$. The gradient diffusion assumption is used to model the conditional turbulent fluxes. The closures for $\langle u_i'' y_\kappa''|\eta\rangle$ and $\langle u_i'' T''|\eta\rangle$ are given by Eqs. (3.67) and (3.68), respectively. The gradient diffusion assumption does not account for counter-gradient effects, which are mostly encountered in premixed flames. Therefore, this approximation may not be suitable when lifted flames are stabilised by premixed flame propagation. In this situation, a correction such as the one proposed by Richardson and Mastorakos [196] may be necessary. When applied to a lifted flame, they conclude that the inclusion of counter-gradient effects leads to a slight increase in liftoff height and to a decrease in flame thickness. This correction is not applied in the current study, following previous CMC investigations of the same flame considered here [169, 176, 212]. The conditional chemical source, $\langle\dot{\omega}_\kappa|\eta\rangle$, is modelled using the first-order closure given by Eq. (3.90). In this closure, the conditional fluctuations about the conditional averages of the reactive scalars are assumed to be small. Accordingly, $\langle\dot{\omega}_\kappa|\eta\rangle$ is modelled as a function of the conditional species mass fractions, temperature and density. This closure has been successfully applied in the CMC of lifted flames [105,169,176,212]. The conditional radiative source, $\langle\dot{\omega}_r|\eta\rangle$, is closed using the optically thin assumption via Eq. (3.93), with H_2O being the predominantly participating species.

6.3.2 Turbulent flow field calculations

The Favre averages of the velocity, mixture fraction mean and variance, turbulence kinetic energy, and turbulence eddy dissipation are obtained from an inert flow calculation using the commercial CFD software FLUENT [5]. This approach was successfully applied in the CMC calculations of lifted flames performed by Kim and Mastorakos [105]. They justify the validity of this simplification by the fact that the flow remains frozen until the stabilisation height. Nevertheless, they note that density changes caused by the flame are non-negligible and may affect the flow field.

A two-dimensional axisymmetric computational domain is employed to perform the inert flow calculations. The domain extends 55 nozzle diameters above the nozzle exit in the axial direction and 15 diameters in the radial direction with the origin of the domain placed at the centre of the nozzle. The thickness of the wall of the nozzle is neglected [34, 35]. A quadratic unstructured mesh is generated using ANSYS ICEM CFD [8]. It consists of $1,000 \times 265$ nodes (axial $\times$ radial). The $k-\varepsilon$ model is employed to perform the calculations. Default model constants are employed, except for $C_{\varepsilon 1}$ which is modified from the standard value of 1.44 to 1.6 in order to improve the prediction of the spreading rate of the jet [189]. The SIMPLE algorithm is used for pressure-velocity coupling. The PRESTO pressure interpolation scheme is employed to compute the pressure at cell faces. Spatial discretization is performed using the second-order upwind scheme. The inlet velocity boundary condition is specified using the 1/7 power law with the centreline velocity set to 5/4 times the experimentally estimated mean value of 107 m/s as in [34]. The coflow velocity is assumed to be uniform and is set to 3.5 m/s. The turbulence intensity is taken to be 5% at both the inlet and the coflow. The boundary conditions of the temperature and species mass fractions are specified following Table 6.1. Transport equations for the mean and variance of the mixture fraction, Eqs. (2.80) and (2.86), are added to the solver. The algebraic model given in Eq. (2.87) was adopted in the early stages of this study in order to model the Favre-averaged scalar dissipation rate $\tilde{\chi}$ which appears as a source term in Eq. (2.86). However, this approach was abandoned later because the calculation yielded very short liftoff heights for moderate and low T_c and nearly attached flames for sufficiently high T_c. This behavior was not observed in the lifted flames simulations of Patwardhan et al. [176] and Kim and Mastorakos [105]. Alternatively, the transport equation of $\tilde{\chi}$, Eq. (2.90), is solved. The inclusion of this equation in the context of CMC was first employed in the counterflow flames calculations of Kim and Mastorakos [106]. The authors solve an additional transport equation for $\widetilde{u_i'' \xi''}$ rather than resorting to gradient diffusion modelling.

6.3.3 The CMC implementation

Numerical details

A smaller physical domain is employed in the CMC calculations for computational efficiency. The chosen domain is 30 nozzle diameters in length and 5 diameters in width. The mesh consists of 70×40 (axial $\times$ radial) non-uniformly distributed nodes, with the mesh density being highest near the experimentally measured stabilization height ($10d$) [35]. The mixture fraction grid consists of 80 points. These resolutions ensure grid independence. The CMC equations are discretized using the finite difference method. The first-order derivative appearing in the convective term is discretized using the second-order upwind difference scheme with the kappa flux limiter of Koren [121], following Patwardhan et al. [176]. The second-order derivatives in physical and mixture fraction spaces are discretized using the second-order central difference scheme. The steady-state solution is obtained from the transient CMC transport equations, Eqs. (3.23) and (3.34), by relaxation of the time step, for which a value of 10^{-5} s is used. The three-step fractional method described in Sect. 3.5.3 is implemented in order to treat the stiff chemical source term separately. The boundary conditions for Q_κ and Q_T at the inlet and the coflow are specified using the inert mixing solution. The composition of the fuel and coflow streams are obtained from the experiments [35]. Zero-gradient boundary conditions are specified at the remaining boundaries. The solution is initialized by igniting some nodes above the experimentally measured stabilization height with a steady laminar flamelet computed with a strain rate of 1000 s^{-1}. The Inert mixing solution is set elsewhere. The Favre-averaged velocity, mixture fraction mean and variance, turbulence kinetic energy, and turbulence eddy dissipation are transferred from FLUENT to the CMC solver by applying bilinear interpolation. This interpolation scheme is accurate enough given the high resolution of the CFD grid. The numerical implementation of the different CMC submodels is described in Sect. 3.5.5.

Chemical kinetic mechanisms

The chemical kinetics mechanisms developed by Mueller et al. [164], Li et al. [135], Burke et al. [32] and Ó Conaire et al. [173] are considered in this study. The corresponding number of species and reactions are summarised in Table 6.2. All four mechanisms have a comparable level of detail, with the Mueller and Burke mechanisms being the least and most detailed, respectively. The former is used in most of the calculations. The corresponding reactions are provided in Table 6.3.

Table 6.2: Number of species and reactions in the considered chemical kinetics mechanisms.

Mechanism	Species	Reactions	Ref.
Mueller	9	21	[164]
Li	13	25	[135]
Burke	13	27	[32]
Ó Conaire	10	21	[173]

Table 6.3: Chemical kinetics mechanism of Mueller et al. [164].

Step	Reaction	Step	Reaction
R1	$H + O_2 \rightleftharpoons O + OH$	R11	$HO_2 + H \rightleftharpoons OH + OH$
R2	$O + H_2 \rightleftharpoons H + OH$	R12	$HO_2 + O \rightleftharpoons O2 + OH$
R3	$H_2 + OH \rightleftharpoons H_2O + H$	R13	$HO_2 + OH \rightleftharpoons H_2O + O_2$
R4	$O + H_2O \rightleftharpoons OH + OH$	R14	$HO_2 + HO_2 \rightleftharpoons H_2O_2 + O_2$[†]
R5	$H_2 + M \rightleftharpoons H + H + M$	R15	$H_2O_2(+M) \rightleftharpoons OH + OH(+M)$
R6	$O + O + M \rightleftharpoons O_2 + M$	R16	$H_2O_2 + H \rightleftharpoons H_2O + OH$
R7	$O + H + M \rightleftharpoons OH + M$	R17	$H_2O_2 + H \rightleftharpoons HO_2 + H_2$
R8	$H + OH + M \rightleftharpoons H_2O + M$	R18	$H_2O_2 + O \rightleftharpoons OH + HO_2$
R9	$H + O_2(+M) \rightleftharpoons HO_2(+M)$	R19	$H_2O_2 + OH \rightleftharpoons HO_2 + H_2O$[†]
R10	$HO_2 + H \rightleftharpoons H_2 + O_2$		

[†] R14 and R19 are expressed as the sum of two rate expressions. Hence, the mechanism has a total of 21 reactions.

6.4 Results and discussion

6.4.1 Flow field results

The radial profiles of the Favre-averaged axial velocity are compared to the experimental measurements of Kent [100] in Fig. 6.3(a). The predictions are in very good agreement with the experimental data up to $x/d = 11$. The measurements are slightly underpredicted at $x/d = 14$ for $y/d > 0.5$. No velocity measurements are available at $x/d = 26$. The profile at this location is provided for completeness. The radial profiles of the Favre-averaged mixture fraction mean are displayed in Fig. 6.3(b) along with the experimental data of Cabra et al. [35]. The predictions are in very good agreement with the experiments at $x/d = 1$, 8, 9, 10 and 11. Slight underpredicitions are obtained at $x/d = 14$ and 26 for $0 \leq y/d \leq 1$. Figure 6.3(c) shows a comparison of the radial Favre-averaged mixture fraction variance profiles with the experimental measurements. A very good agreement is obtained at all axial locations except at $x/d = 26$. The discrepancies at this locations are attributed to the underprediction of the mixture fraction mean (bottom pane in Fig. 6.3(b)). The results obtained with the algebraic modelling of $\tilde{\chi}$ (Eq. (2.87)) tend to be undepredictive near the centreline and overpredictive around the peaks of the experimental data (not shown here). Therefore, it is concluded that the alternative approach of incorporating an additional transport equation for $\tilde{\chi}$ (Eq. (2.90)) provides more accurate mixture fraction variance predictions. Overall, the results presented in Fig. 6.3 show that the inert flow calculations employed in this study provide reliable flow and mixing fields for the CMC calculations.

The centreline evolution of the time scale ratio, C_χ, is shown in Fig. 6.4. Here, C_χ is computed using Eq. (2.87) with $\tilde{\chi}$ obtained from the solution of Eq. (2.90). In the vicinity of the nozzle, C_χ is well above the commonly used constant value of 2. Away from the nozzle, C_χ decays gradually and tends asymptotically to 2.76. This suggests that the usage of Eq. (2.87) with $C_\chi = 2$ would generally underpredict the centreline scalar dissipation levels, especially near the nozzle area. The trend obtained in Fig. 6.4 is in line with the experimental observations of Markides [142] who perform scalar dissipation measurements in autoignitive nitrogen-diluted fuel jets injected into coflowing heated air, a configuration similar to the one under investigation. His results show that the centreline values of C_χ decay from high levels near the injector to a constant value around 2 at downstream locations . Accordingly, in a subsequent CMC study in the same context, Markides et al. [143] tune C_χ in Eq. (2.87) in the vicinity of the injector in order to emulate the decay of the time scale ratio and set it to 2 downstream. In the absence of scalar dissipation measurements, as in the present case, such treatment is *ad hoc* and tedious: C_χ must be tuned by trial and error until a reasonable agreement between the predicted and measured

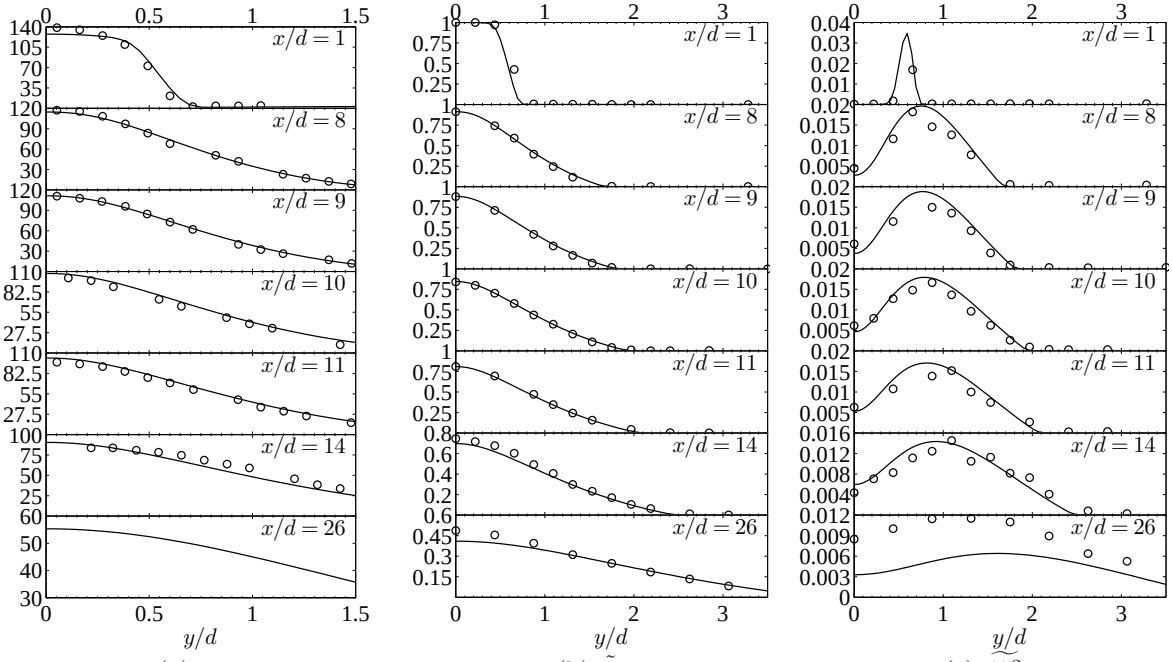

(a) $\tilde{u}$ (b) $\tilde{\xi}$ (c) $\widetilde{\xi''^2}$

Figure 6.3: Radial profiles of (a) $\tilde{u}$, (b) $\tilde{\xi}$ and (c) $\widetilde{\xi''^2}$. Lines, numerical results; Symbols, experimental data ($\tilde{u}$ obtained from [100]; $\tilde{\xi}$ and $\widetilde{\xi''^2}$ obtained from [35]). No velocity measurements are available at $x/d = 26$.

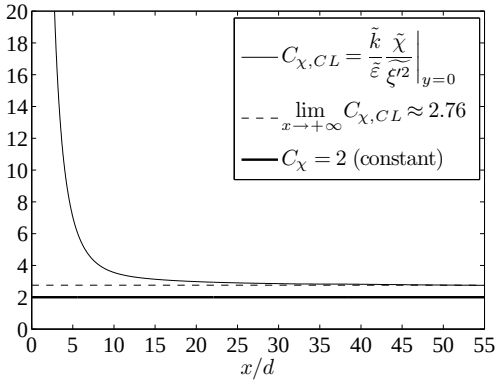

Figure 6.4: Evolution of the time scale ratio along the centreline.

$\widetilde{\xi''^2}$ profiles is achieved, and most likely, a non-constant functional form for C_χ may be necessary. This process is easily avoided by means of solving Eq. (2.90).

6.4.2 Effect of the CSDR modelling for various coflow temperatures

The effect of the modelling of the CSDR is investigated using the homogeneous model of Girimaji [78] and the inhomogeneous model of Mortensen [157]. The reader is reminded that the latter model degenerates to the former when the inhomogeneous terms in Eq. (3.81) are discarded. Calculations are performed for three coflow temperatures. In addition to the experimentally reported value $T_c = 1045$ K [35], two other temperatures are investigated: $T_c = 1030$ and 1060 K. Given the experimental uncertainty of 3% in the temperature measurements [35], these two values lie within the experimental error. The chemical kinetics mechanism of Mueller et al. [164] is employed throughout this section.

Results in physical space

The radial profiles of the Favre-averaged reactive scalars are shown in Fig. 6.5(a)–(e) at the axial locations $x/d = 8$, 9, 10, 11, 14 and 26. For $T_c = 1045$ K (thick black lines), the results obtained using the two CSDR models are almost identical, except for some minor differences at $x/d = 10$ and 11. When T_c is decreased to 1030 K (thin black lines), the predictions remain in good agreement with the experiments up to $x/d = 10$ and the two CSDR models yield very similar results. Farther downstream, the temperature and products mass fractions are underpredicted and the reactants mass fractions are overpredicted, most notably at $x/d = 11$ and 14. The influence of the CSDR modelling becomes more apparent at these axial locations. Overall, the results remain in reasonable agreement with the experiments. When T_c is increased to 1060 K (grey lines), the CSDR models yield distinct results for $x/d \leq 14$. Using both models, the temperature and products mass fractions are grossly overpredicted and the reactants mass fractions are underpredicted. All three coflow temperatures result in very similar profiles at $x/d = 26$, irrespective of the CSDR model. As a general observation in Fig. 6.5, the usage of Girimaji's model always yields lower temperatures and product mass fractions and higher reactant mass fractions when compared to Mortensen's, which leads to a shorter liftoff height. This is attributed to the fact that Girimaji's model results in earlier ignition delays and hence shorter ignition kernels for all coflow temperatures. This phenomenon will be discussed shortly in more detail. Before doing so, the liftoff heights obtained from the cases considered in Fig. 6.5 are first presented.

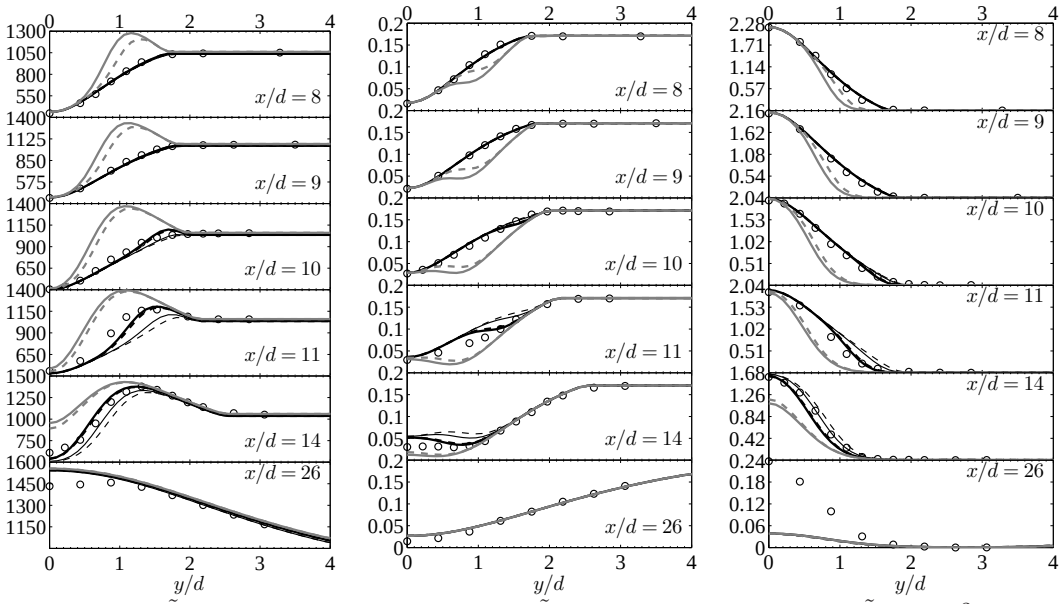

(a) $\tilde{T}$ [K] (b) $\tilde{Y}_{O_2}$ (c) $\tilde{Y}_{H_2} \times 10^2$

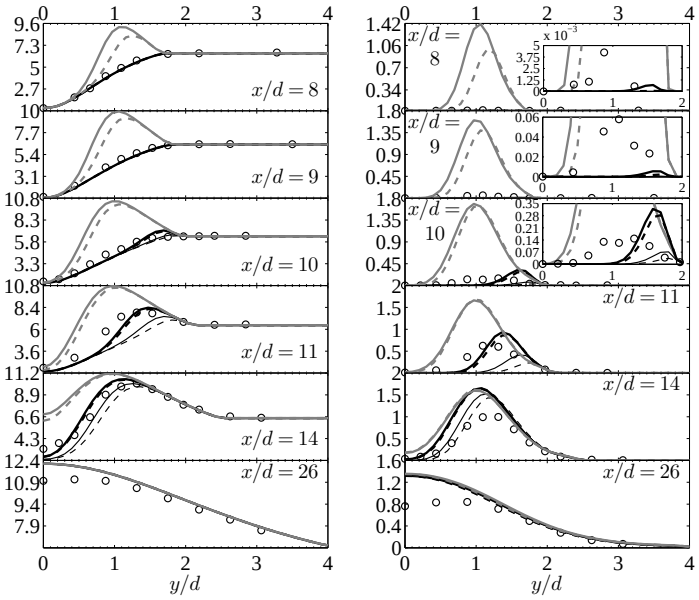

(d) $\tilde{Y}_{H_2O} \times 10^2$ (e) $\tilde{Y}_{OH} \times 10^3$

Figure 6.5: Radial profiles of (a) $\tilde{T}$, (b) $\tilde{Y}_{O_2}$, (c) $\tilde{Y}_{H_2}$ ($\times 10^2$), (d) $\tilde{Y}_{H_2O}$ ($\times 10^2$), and (e) $\tilde{Y}_{OH}$ ($\times 10^3$) using Girimaji's and Mortensen's CSDR models. In (a)–(e): solid lines, Girimaji's model; dashed lines, Mortensen's model; symbols, experimental data [35]. Colours: black (thin), $T_c = 1030$ K; black (thick), $T_c = 1045$ K; grey, $T_c = 1060$ K.

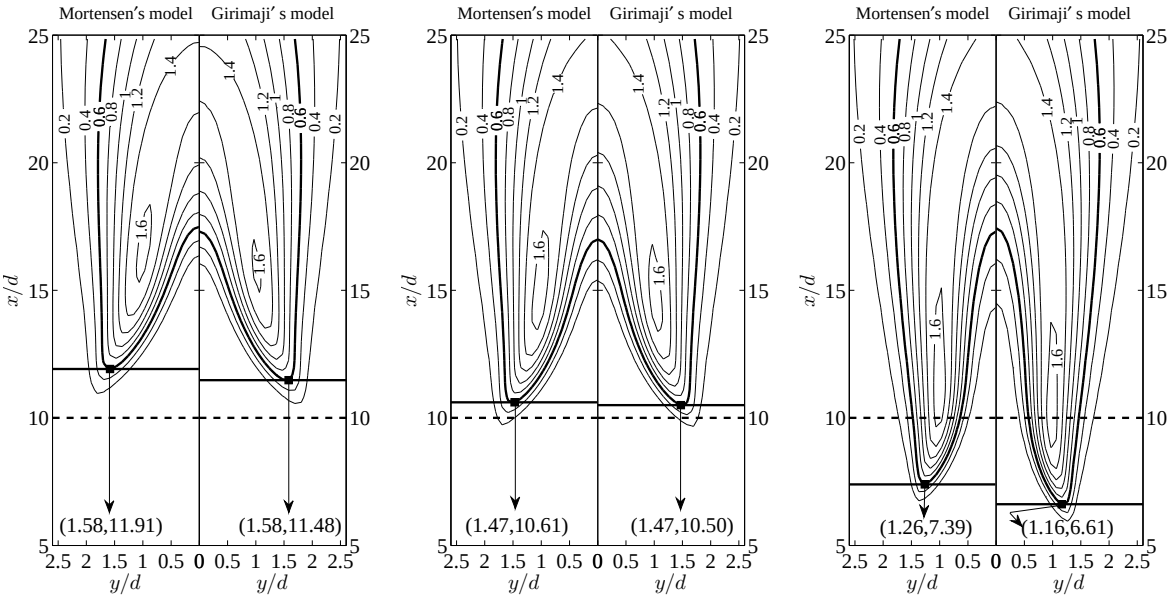

(a) $T_c = 1030$ K (b) $T_c = 1045$ K (c) $T_c = 1060$ K

Figure 6.6: Contours of $\tilde{Y}_{\mathrm{OH}}$ ($\times 10^3$): (a) $T_c = 1030$ K, (b) $T_c = 1045$ K and (c) $T_c = 1060$ K obtained using Mortensen's model (left panes) and Girimaji's model (right panes). The thick contour corresponds to 600 ppm. The solid and dashed horizontal lines correspond to the numerical and experimental liftoff heights, respectively.

The contours of $\tilde{Y}_{\mathrm{OH}}$ ($\times 10^{-3}$) are shown in Figs. 6.6(a) for $T_c = 1030$ K, (b) for $T_c = 1045$ K and (c) for $T_c = 1060$ K. In each sub-figure, the left and right panes correspond to the results obtained with Mortensen's and Girimaji's models, respectively. As shown in Fig. 6.6(a), stabilization takes place at slightly distinct locations due to the very small $\tilde{Y}_{\mathrm{OH}}$ differentials (see the radial profiles in Fig. 6.5(e) for $T_c = 1030$ K). Mortensen's model (left) results in $H/d = 11.91$ (19.1% in excess of H_{exp}/d) while Girimaji's model (right) gives $H/d = 11.48$ (14.8% in excess of H_{exp}/d). The same scenario is observed in Fig. 6.6(b) where $T_c = 1045$ K. However, in this case, the location of stabilisation is better predicted. Mortensen's model (left) yields $H/d = 10.61$ (6.1% in excess of H_{exp}/d) while Girimaji's model (right) results in $H/d = 10.50$ (5% in excess of H_{exp}/d). The advantage of the inclusion of the effects of inhomogeneity Mortensen's model is judged to be insignificant for these two coflow temperatures. Conversely, the differences in the stabilisation locations are more substantial for $T_c = 1060$ K, as displayed in Fig. 6.6(c). This is due to the much larger $\tilde{Y}_{\mathrm{OH}}$ differentials (see the radial profiles in Fig. 6.5(e) for $T_c = 1060$ K). Mortensen's model (left) yields $H/d = 7.39$ (26.1% below H_{exp}/d) while Girimaji's model (right) gives

$H/d = 6.61$ (33.9% below H_{exp}/d). As for the radial location of stabilisation (the radial distance from the stabilisation point to the centreline normalised d, denoted here by W/d), the values obtained using the two CSDR models for $T_c = 1030$ K and 1045 K are the same (1.58 and 1.47, respectively). As for $T_c = 1060$ K, the two models yield slightly different values (Mortensen's, 1.26; Girimaji's, 1.16). It is obvious from the above results that the liftoff height becomes smaller and that flame base becomes narrower as T_c is decreased. This is due to the fact that at lower T_c, the mixture can autoignite in areas closer to the nozzle which are characterised by high scalar dissipation rate levels. This behaviour will be addressed in more detail in Sect. 6.4.2.

The stabilisation mechanism

The numerical indicators developed by Gordon et al. [79] for the distinction between stabilisation by autoignition and premixed flame propagation are employed here to determine the underlying controlling mechanism. For this purpose, the transport budget of the temperature and the history of radical build-up ahead of the stabilisation height are analysed.

Budgets in mixture fraction space Figure 6.7 shows the transport budget of the steady-state conditional temperature equation, that is the individual contributions of the r.h.s. terms of Eq. (3.34). Only the results obtained using Girimaji's model are presented here. Mortensen's model produces similar trends. For each T_c, the budgets are displayed at several axial locations around the corresponding liftoff height. The radial locations are held fixed and set to the W/d value obtained with each T_c. As such, the chosen coordinates cover the pre-flame, liftoff and post-flame regions. Before analysing the balance in these budgets, the axial evolution of the chemical source term, T_{CS}, is first examined. As shown in Fig. 6.7(a), (b) and (c), common trends are observed in the evolution of this term for all three coflow temperatures. Below the stabilisation height (first two locations in the pre-flame regions, Pre-F1 and Pre-F2), as x/d increases, T_{CS} shifts from very lean to less lean mixtures and its amplitude increases dramatically. At liftoff (middle panes), T_{CS} peaks at $\eta \approx 0.24$ with a significantly higher amplitude. Within approximately two to three nozzle diameters downstream the stabilisation height (first locations in the post-flame regions, Post-F1) the peak of T_{CS} increases further and occurs around the stoichiometric mixture fraction. Further downstream (second locations in the post-flame regions, Post-F2), the magnitude of T_c decreases substantially from the Post-F1 locations. The reaction zone becomes wider and presents two peaks. The first occurs around the stoichiometric mixture fraction and the second in rich mixtures. The second peak is most likely attributed to the propagation of a rich reaction zone towards stoichiometric mixtures [105]. All of the

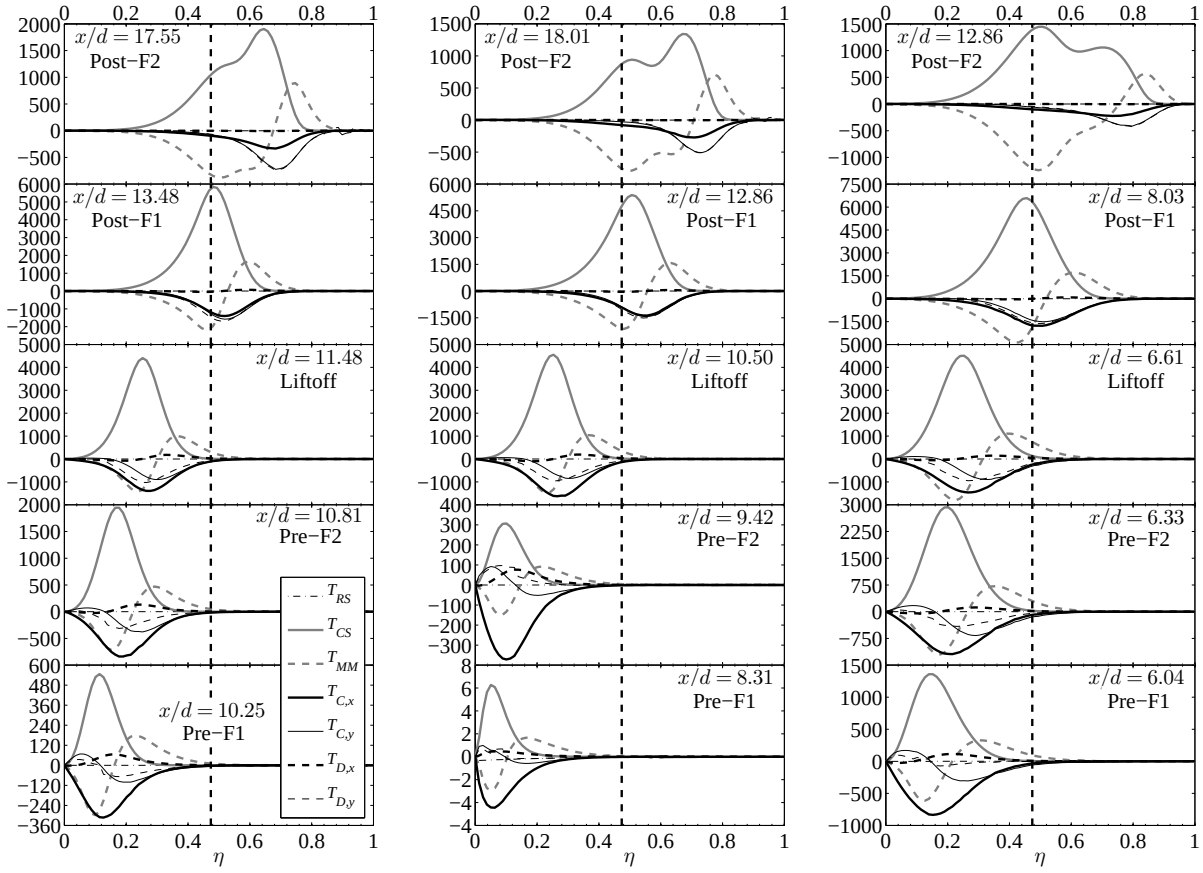

(a) $T_c = 1030$ K, $y/d = 1.58$ (b) $T_c = 1045$ K, $y/d = 1.47$ (c) $T_c = 1060$ K, $y/d = 1.16$

Figure 6.7: Transport budget of the steady-state Q_T equation (r.h.s. terms of Eq.(3.34)): (a) $T_c = 1030$ K ($y/d = 1.58$), (b) $T_c = 1045$ K ($y/d = 1.47$) and (c) $T_c = 1060$ K ($y/d = 1.16$). T_{RS}, radiative source; T_{CS}, chemical source; T_{MM}, micro-mixing; $T_{C,x}$, axial convection; $T_{C,y}$ radial convection; $T_{D,x}$, axial diffusion; $T_{D,y}$, radial diffusion. The vertical dashed line corresponds to the location of η_{st}. All terms are scaled down by a factor of 10^3 and the units are K/s. The CSDR is modelled using Girimaji's model.

above trends are consistent with the direct numerical simulation Yoo et al. [242]. As in the evolution of T_{CS}, common trends are observed in the axial variation of the remaining terms contributing to the r.h.s. of Eq. (3.34). In the pre-flame region (locations Pre-F1 and Pre-F2), there is a clear balance in lean mixtures between T_{CS}, the axial convection term, $T_{C,x}$, and micro-mixing, T_{MM}. The axial and radial diffusion terms, $T_{D,x}$ and $T_{D,y}$, and the radial convection term, $T_{C,y}$ are non-negligible but have little contribution to the overall budget. This balance suggests that stabilisation by premixed flame propagation wherein $T_{D,x}$ balances $T_{C,x}$ in the pre-heat zone with negligible T_{CS} is not the case. Instead, stabilisation occurs via autoignition as can be seen from the T_{CS}-$T_{C,x}$-T_{MM} balance. At liftoff, the balance shifts to $\eta \approx 0.24$. The role of $T_{C,x}$ in balancing T_{CS} diminishes but this term remains a major contributor to the overall balance, and T_{MM} prevails. As for the remaining terms, $T_{D,x}$ becomes much weaker while $T_{D,y}$ and $T_{C,y}$ remain important. In the post flame regions (locations Post-F1 and Post-F2), the role of $T_{c,x}$ diminishes further, T_{MM} becomes more dominant, and $T_{D,x}$ is virtually null. The contributions of $T_{D,y}$ and $T_{C,y}$ are as significant as that of $T_{C,x}$ at Post-F1 and supersede it at Post-F2. As T_{CS} increases in mixture fraction space, the contributions of $T_{D,y}$, $T_{C,y}$ and $T_{C,x}$ remain smaller than that of T_{MM}, which acts as the major heat sink. In contrast, as T_{CS} decays, T_{MM} increases and acts as a source (notice its positive contribution), and both of these terms are counterbalanced by $T_{D,y}$, $T_{C,y}$ and $T_{C,x}$. Thus, beyond the stabilisation height, the flame budgets indicate the structure of a non-premixed flame, which is largely characterised by a T_{CS}-T_{MM} balance. To be noted that the radiative source, T_{RS}, is negligible at all locations for all coflow temperatures due to the fact that hydrogen in the fuel stream is highly diluted with nitrogen. Therefore, this term can be safely neglected without loss of accuracy.

Budgets in physical space The fact that autoignition is the controlling stabilisation mechanism can be further confirmed by analysing the transport budget of Q_T in physical space. To do so, the PDF-weighted integration of the r.h.s. terms of Eq. (3.34) is performed over the mixture fractions space. This yields IT_{RS}, IT_{CS}, IT_{MM}, $IT_{C,x}$, $IT_{C,y}$, $IT_{D,x}$ and $IT_{D,y}$ ("IT" stands for "Integrated Transport"). The axial profiles of these terms are plotted in Fig. 6.8(a) for Girimaji's model and in (b) for Mortensen's model at the respective W/d locations obtained with each T_c. The parallels between the observation made in Fig. 6.7 and this figure are evident. IT_{CS} is mostly balanced by $IT_{C,x}$ and IT_{MM} in the pre-flame regions, with the former being more dominant. The remaining terms are small but non-negligible. The absence of $IT_{D,x}$ eliminates the possibility of stabilisation by premixed flame propagation and the current balance indicates that autoignition is the controlling mechanism. Right ahead of liftoff, $IT_{C,y}$ and $IT_{D,y}$ emerge and IT_{MM} becomes more important. These three terms start to dominate at the expense of $IT_{C,x}$, which

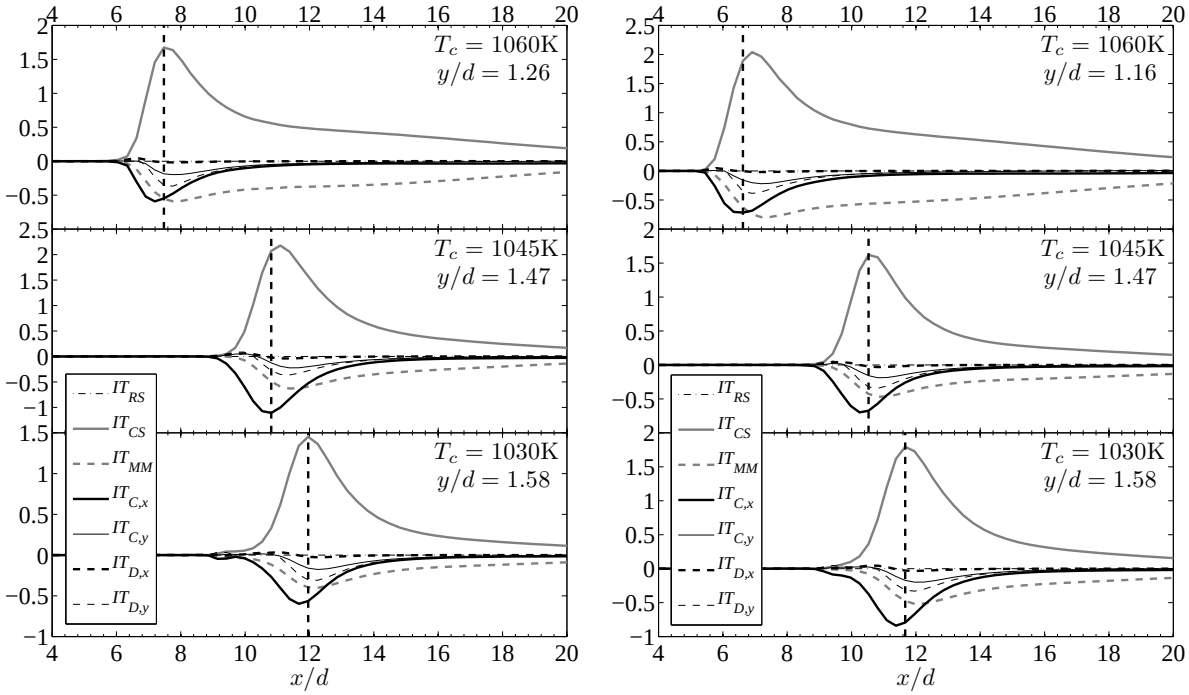

(a) Girimaji's model

(b) Mortensen's model

Figure 6.8: Axial profiles of the Integrated Transport (IT) budget of the steady-state Q_T equation (integrated r.h.s. terms of Eq.(3.34)): (a) Girimaji's model and (b) Mortensen's model. The bottom, middle and top panes correspond to $T_c = 1030$ K, $T_c = 1045$ K and $T_c = 1060$ K, respectively. IT_{RS}, radiative source; IT_{CS}, chemical source; IT_{MM}, micro-mixing; $IT_{C,x}$, axial convection; $IT_{C,y}$ radial convection; $IT_{D,x}$, axial diffusion; $IT_{D,y}$, radial diffusion. All terms are scaled down by a factor of 10^6 and the units are K/s.

remains the main heat sink. Downstream of the stabilisation height, $IT_{C,x}$, $IT_{C,y}$ and $IT_{D,y}$ diminish gradually and IT_{MM} becomes more important. Further downstream IT_{CS} is mostly counterbalanced by IT_{MM}, with smaller contributions $IT_{C,x}$, $IT_{C,y}$ and $IT_{D,y}$, which indicates the structure of a non-premixed flame.

Radical history ahead of the stabilisation height The transport budgets of the temperature in mixture fraction and physical spaces are both indicative of stabilisation via autoignition. In order ascertain this conclusion, the history of radical build-up ahead of the reaction zone is now investigated. Figure 6.9 displays the axial profiles of the normalised

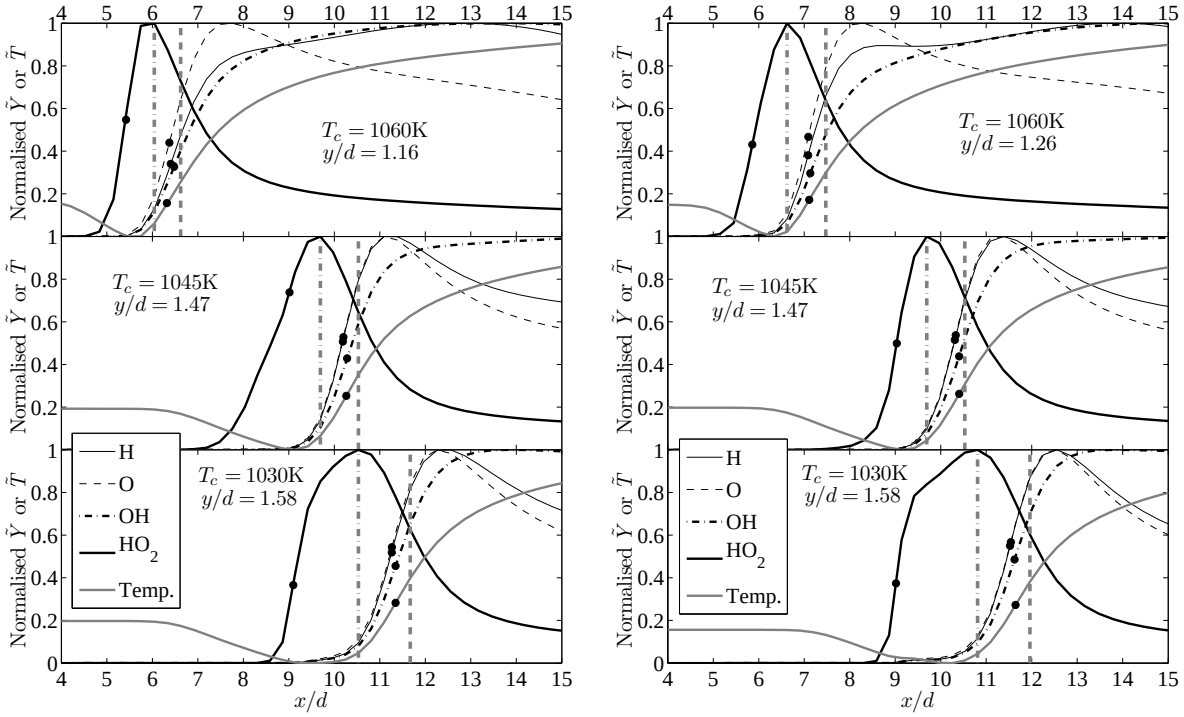

(a) Girimaji's model

(b) Mortensen's model

Figure 6.9: Axial profiles of the normalised Favre-averaged temperature and mass fractions of H, O, OH, and HO_2 obtained at the radial locations of stabilisation corresponding to each T_c: (a) Girimaji's model and (b) Mortensen's model. The vertical dash-dotted and dashed lines correspond the axial locations of maximum HO_2 and liftoff height, respectively. The circles indicate the locations of the maximum slopes.

Favre-averaged temperature $((\tilde{T} - \tilde{T}_{\min})/(\tilde{T}_{\max} - \tilde{T}_{\min}))$ and mass fractions $(\tilde{Y}/\tilde{Y}_{\max})$ of H, O, OH, and HO_2. The subscripts "min" and "max" denote the minimum and maximum values of the reactive scalars at $y/d = W/d$. The results are reported for Girimaji's and Mortensen's models in Figs. 6.9(a) and (b), respectively. Common trends are observed ahead of the stabilisation height for the different combinations of T_c values and CSDR models:

1. The production of the intermediate HO_2 initiates upstream of the axial locations where the radicals H, O and OH emerge.

2. H, O and OH start building up before the consumption of HO_2 begins. As shown, the

mass fractions of these three species start to increase before HO_2 reaches its peak.

3. HO_2 builds-up rapidly prior to the runaway of H, O and OH, as can be seen from the axial locations of the maximum slopes.

Therefore, radicals do not build-up simultaneously as in premixed flame propagation, but rather HO_2 acts as a precursor to the production of H, O and OH as in autoignition scenarios [79]. This confirm that the flame is stabilised by autoignition.

The impact of the CSDR modelling on autoignition

To better understand the autoignition process, standalone zero-dimensional CMC (0DCMC) calculations are performed for each T_c. In these calculations, the convective and (physical space) diffusive terms in Eqs. (3.23) and (3.34) are turned off and the CSDR is modelled using the AMC [174]. This CSDR model is parametrised by its maximum value $\chi_\circ$ and it is given by $\langle\chi|\eta\rangle = \chi_\circ \exp\{-2[\text{erf}^{-1}(2\eta-1)]^2\}$ (Eq.(3.72)). The resulting homogeneous CMC equations are identical to those of the unsteady laminar flamelet model (with unity Lewis number) [178]. For a given $\chi_\circ$, the solution evolves from the inert mixing solution at $t = 0$ up to the moment when autoignition occurs, $t = \tau$. Autoignition is declared at the moment when the maximum OH mass fraction reaches 2×10^{-4} at any point in mixture fraction space, following Stanković and Merci [211]. Figure 6.10 displays the ignition delay (τ) as a function of $\chi_\circ$. These results are obtained using the mechanism of Mueller et al. [164] for T_c = 1030 K, 1045 K and 1060 K. It is evident from this figure that for a given coflow temperature, τ reaches an asymptotic limit as $\chi_\circ$ is gradually increased. This means that the occurrence of autoignition becomes impossible beyond a critical value of $\chi_\circ$, denoted here by $\chi_{\circ,c}$. The approximate values of $\chi_{\circ,c}$ are 227 s^{-1}, 482 s^{-1} and 991 s^{-1} for T_c = 1030 K, 1045 K and 1060 K, respectively. Therefore, $\chi_{\circ,c}$ increases with increasing T_c. In order to link these findings to the flow field of the flame under investigation, $\chi_\circ$ is first obtained by integrating Eq. (3.72) weighted by $\tilde{P}(\eta)$ over the mixture fraction space, as outlined in Eq. (3.74). This integration requires the usage of the readily available quantities $\tilde{\chi}$, $\tilde{\xi}$ and $\widetilde{\xi''^2}$. Figure 6.11 shows the Contours of $\chi_\circ$ computed from Eq. (3.74) for T_c = 1045 K. The contours for T_c = 1030 K and 1060 K are virtually the same and are not included here for brevity. The contour of Fig. 6.11 will be used in all of the subsequent analysis irrespective of the value of T_c. The thick contours represent the levels 227 s^{-1}, 482 s^{-1} and 991 s^{-1} which correspond to the $\chi_{\circ,c}$ values determined in Fig. 6.10. Also shown are the ignition kernel locations obtained from the different combinations of CSDR models and coflow temperatures. As expected, for all three coflow temperatures, ignition occurs

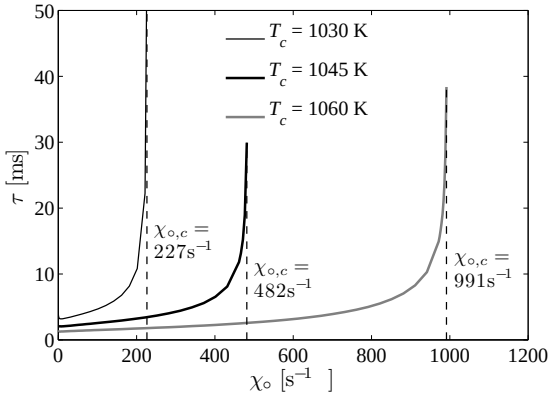

Figure 6.10: Ignition delays as a function of the peak scalar dissipation rate obtained using the mechanism of Mueller et al. [164] for $T_c = 1030$, 1045 and 1060 K. The vertical dashed lines represent the asymptotic limit beyond which ignition cannot occur ($\chi_\circ = \chi_{\circ,c}$).

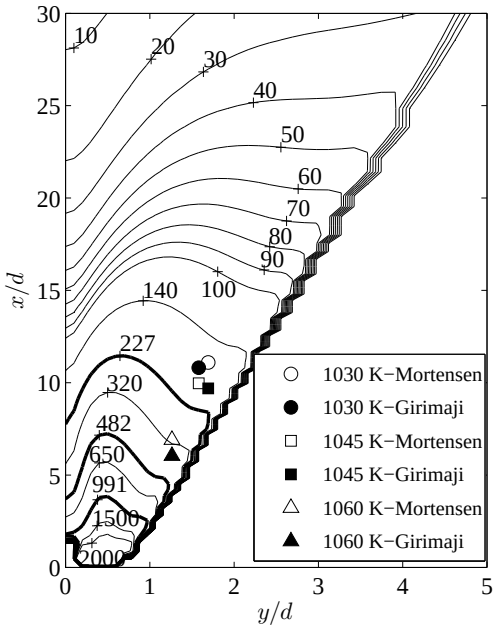

Figure 6.11: Contours of $\chi_\circ$ (Eq. 3.74). The thick contours correspond to $\chi_\circ = \chi_{\circ,c}$ for $T_c = 1030$ K (227 s^{-1}), 1045 K (482 s^{-1}) and 1060 K (991 s^{-1}). The symbols represent the ignition locations

Table 6.4: The most reactive mixture fraction, η_{mr}, and the CSDR values obtained from the AMC parametrised by $\chi_{\circ,c}$ at η_{mr}.

T_c [K]	η_{mr}	$\langle\chi\vert\eta_{mr}\rangle_c^{\mathrm{AMC}}$
1030	0.0620	21.27
1045	0.0543	36.65
1060	0.0465	59.02

at locations where $\chi_\circ$ is lower that $\chi_{\circ,c}$ (the circles, squares and triangles lie outside the 227 s^{-1}, 482 s^{-1} and 991 s^{-1} contour levels, respectively). Since $\tilde{\chi}$ decays away from the nozzle, autoignition does not take place until $\chi_\circ$ (which depends on $\tilde{\chi}$ via Eq. (3.74)) falls below $\chi_{\circ,c}$. This explains why increasing T_c results in earlier ignition and shorter liftoff from a mixing point of view.

In another set of 0DCMC calculations, the "most reactive" mixture fraction, η_{mr}, is computed for each T_c by setting $\chi_\circ$ in Eq. (3.72) to 10^{-20} s^{-1} (homogeneous reactor). The results are summarised in Table 6.4. Consistent with the findings of Stanković and Merci [211], η_{mr} decreases with increasing T_c. The objective behind determining η_{mr} is to compare the local CSDR values obtained using Mortensen's and Girimaji's models at $\eta = \eta_{mr}$, $\langle\chi\vert\eta_{mr}\rangle^{\mathrm{M}}$ and $\langle\chi\vert\eta_{mr}\rangle^{\mathrm{G}}$, respectively. As shown in Fig. 6.12, for all given coflow temperatures and radial locations, the axial profiles of $\langle\chi\vert\eta_{mr}\rangle^{\mathrm{M}}$ and $\langle\chi\vert\eta_{mr}\rangle^{\mathrm{G}}$ reveal that Mortensen's models generally results in higher scalar dissipation rate levels, and therefore yields longer ignition delays and higher liftoff heights. Also displayed in Fig. 6.12 are the critical CSDR values computed using the AMC model parametrised by $\chi_{\circ,c}$ at $\eta = \eta_{mr}$, that is $\langle\chi\vert\eta_{mr}\rangle_c^{\mathrm{AMC}} = \chi_{\circ,c}\exp\{-2[\mathrm{erf}^{-1}(2\eta_{mr}-1)]^2\}$ (horizontal grey lines). These values are also provided in Table 6.4 for all coflow temperatures. As expected, $\langle\chi\vert\eta_{mr}\rangle_c^{\mathrm{AMC}}$ increases with increasing T_c. Figure 6.12(a) (T_c = 1030 K) shows that ignition cannot occur as long as $\langle\chi\vert\eta_{mr}\rangle^{\mathrm{M}}$ or $\langle\chi\vert\eta_{mr}\rangle^{\mathrm{G}}$ is below $\langle\chi\vert\eta_{mr}\rangle_c^{\mathrm{AMC}}$. Indeed, when Mortensen's model is used, ignition happens at the first axial and radial locations where $\langle\chi\vert\eta_{mr}\rangle^{\mathrm{M}}$ falls below $\langle\chi\vert\eta_{mr}\rangle_c^{\mathrm{AMC}}$. This takes place at x/d = 11.09 and y/d = 1.69 (first pane from the top in Fig. 6.12(a)). A similar scenario is observed when Girimaji's model is used. Ignition occurs at the first axial and radial locations where $\langle\chi\vert\eta_{mr}\rangle^{\mathrm{G}}$ falls below $\langle\chi\vert\eta_{mr}\rangle_c^{\mathrm{AMC}}$, which happens at x/d = 10.81 and y/d = 1.58 (second pane from the top in Fig. 6.12(a)). Similar observation can be made in Figs. 6.12(b) (T_c = 1045 K) and (c) (T_c = 1060 K). However,

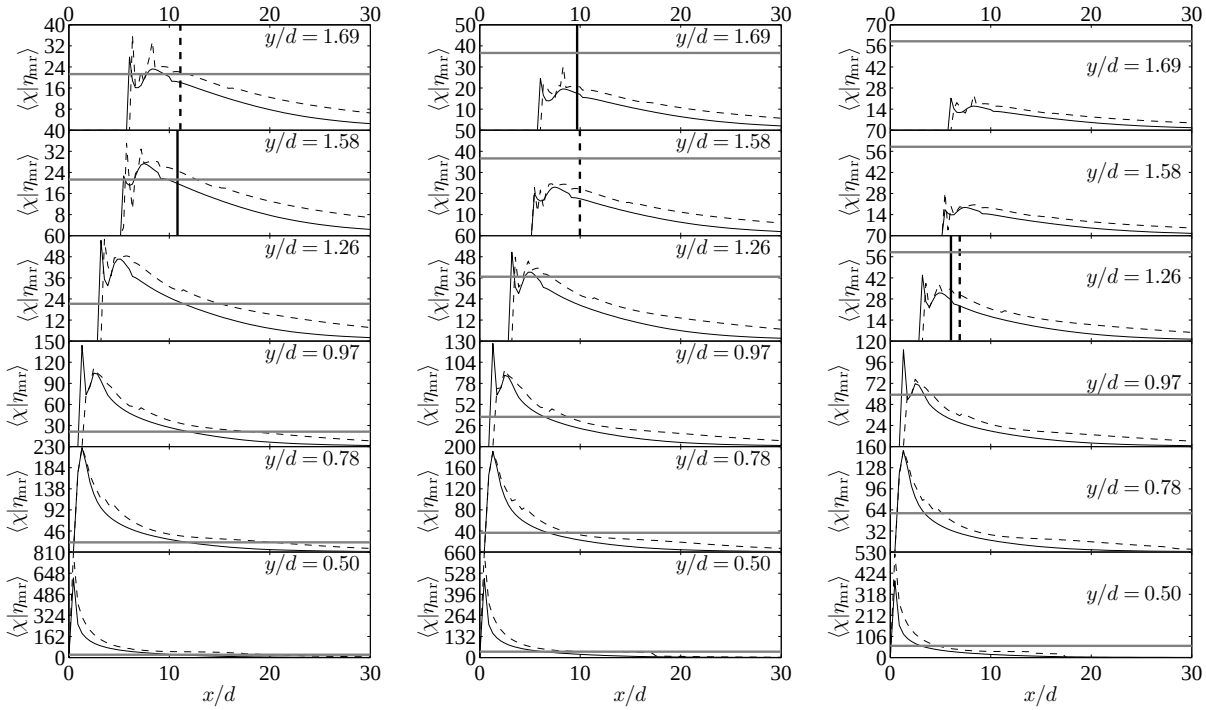

(a) $T_c = 1030$ K (b) $T_c = 1045$ K (c) $T_c = 1060$ K

Figure 6.12: Axial profiles of $\langle\chi|\eta_{mr}\rangle$ at several radial locations. (a) $T_c = 1030$ K, (b) $T_c = 1045$ K and (c) $T_c = 1060$ K. Solid black lines, Girimaji's model; dashed black lines, Mortensen's model. The vertical black lines indicate the radial locations where ignition occurs. The grey horizontal lines represent the value of the CSDR computed using the AMC model parametrised by $\chi_{\circ,c}$ at $\eta = \eta_{mr}$ ($\langle\chi|\eta_{mr}\rangle_c^{\mathrm{AMC}} = \chi_{\circ,c}\exp\{-2[\mathrm{erf}^{-1}(2\eta_{mr}-1)]^2\}$).

in these two cases, although $\langle\chi|\eta_{mr}\rangle^{\mathrm{M}}$ and $\langle\chi|\eta_{mr}\rangle^{\mathrm{G}}$ fall quickly below $\langle\chi|\eta_{mr}\rangle_c^{\mathrm{AMC}}$ at y/d locations smaller then the ones where ignition is indicated, ignition occurs at the first axial location with lowest $\langle\chi|\eta_{mr}\rangle$. As shown in Fig. 6.12(b) ($T_c = 1045$ K), ignition takes place at $x/d = 9.97$ and $y/d = 1.58$ using Mortensen's model, and at $x/d = 9.69$ and $y/d = 1.69$ using Girimaji's model. Similarly, in Fig. 6.12(c) ($T_c = 1060$ K), ignition happens at $x/d = 6.90$ and $y/d = 1.26$ using Mortensen's model, and at $x/d = 6.04$ and $y/d = 1.26$ using Girimaji's model.

The effect of the spurious sources

Ideally, the integration of the PDF-weighted CMC equations over η-space should lead to the unconditional set of equations without any additional source terms [120]. This outcome is guaranteed when the fully consistent inhomogeneous CSDR model of Mortensen is employed. On the other hand, when the inconsistent homogeneous CSDR model of Girimaji is used, the integration of the CMC equations results in additional spurious source terms. The spurious source associated with a species κ is calculated through [120, 226]:

$$\tilde{S}_\kappa = \frac{1}{2}\int_0^1 \left[\underbrace{\langle\chi|\eta\rangle^{\mathrm{G}}}_{\substack{\text{Inonsistent}\\ \text{CSDR model}}} - \underbrace{\langle\chi|\eta\rangle^{\mathrm{M}}}_{\substack{\text{Consistent}\\ \text{CSDR model}}} \right] \frac{\partial^2 Q_{\kappa,\mathrm{G}}}{\partial\eta^2}\tilde{P}(\eta)d\eta \tag{6.1}$$

where $Q_{\kappa,\mathrm{G}}$ is the conditional mass fraction of species κ obtained in the inconsistent realisation (using Girimaji's model). Figure 6.13 shows the radial profiles of the mean chemical sources (IT_{CS}) and spurious sources of O_2, H_2, H_2O and OH for $T_c = 1045$ K. In comparison to the mean chemical sources, the magnitudes of the spurious sources are small but non-negligible, in particular within the flame zone ($x/d = 14$ and 26). The effect of the spurious sources ahead of the predicted stabilisation heights ($x/d = 9$ and 10) is not sufficiently large to change the nature of the stabilisation mechanism, as the flame is stabilised by autoignition using both Mortensen's and Girimaji's models. However, the fact that Girimaji's model yields a relatively earlier ignition and a smaller liftoff height indicates that the spurious sources are influential. Although this is not the case in the calculations of the current flame, inconsistent CMC implementations may lead erroneous results and conclusions.

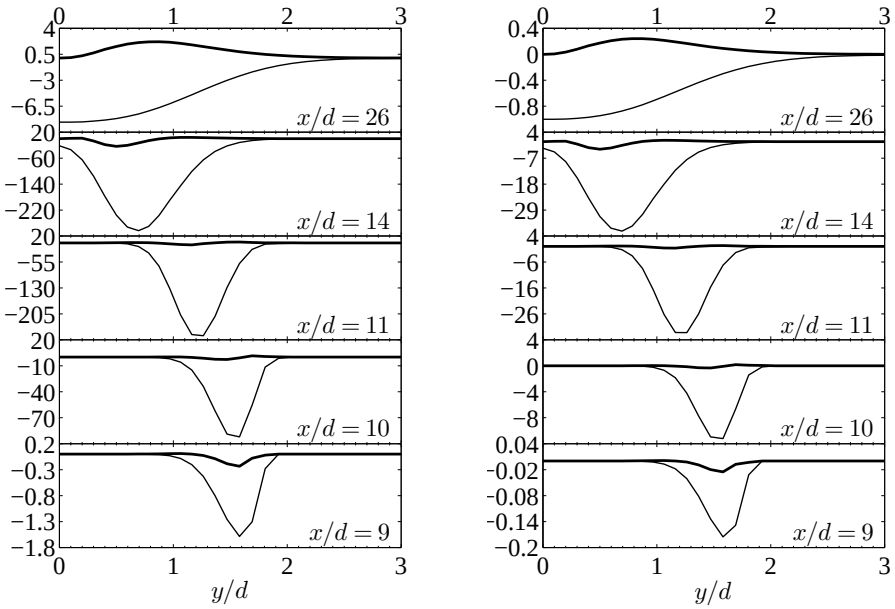

(a) O_2 (b) H_2

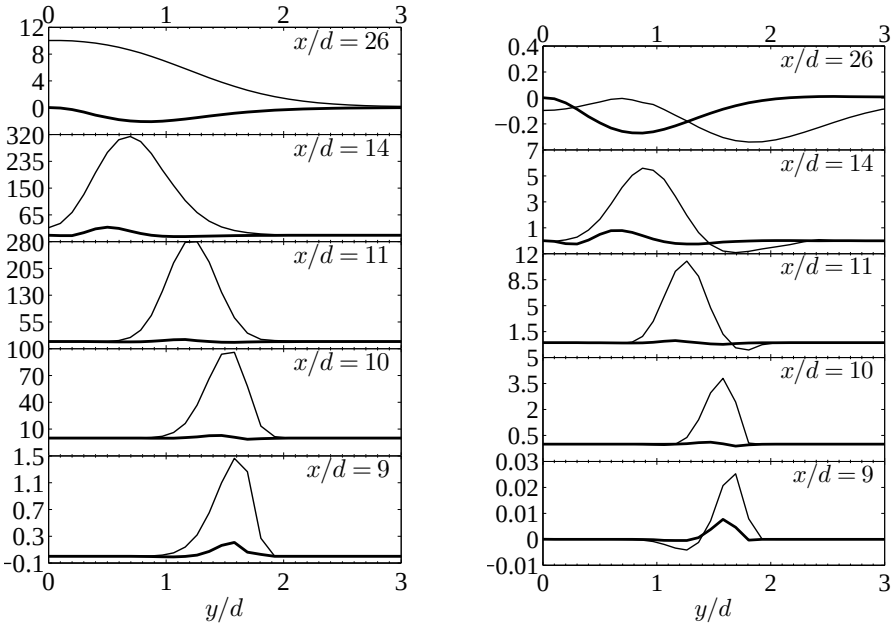

(c) H_2O (d) OH

Figure 6.13: Radial profiles of the chemical and spurious sources for $T_c = 1045$ K: (a) O_2, (b) H_2, (c) H_2O, and (d) OH. Thin lines, chemical sources; thick lines, spurious sources. The units are s^{-1}.

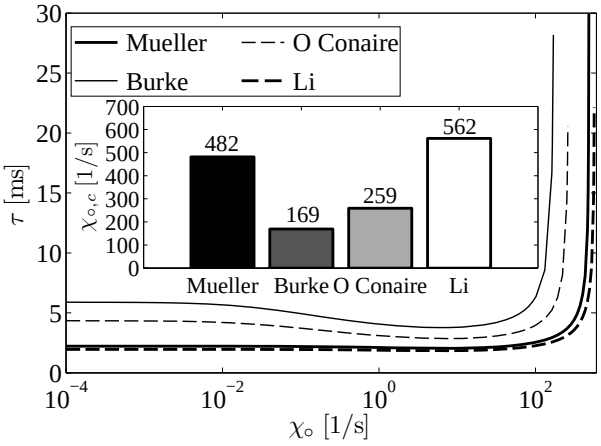

Figure 6.14: Ignition delay as a function of the peak scalar dissipation rate χ_o obtained using the Mueller et al. [165], Ó Conaire et al. [173], Li et al. [135] and Burke et al. [32] mechanisms for $T_c = 1045$ K. The inset shows the critical values $\chi_{\circ,c}$.

6.4.3 The effect of chemical kinetics

The mechanism of Mueller et al. [164] has been used in all of the results reported so far. The sensitivity of the flame to chemical kinetics is now assessed by testing the performance of the mechanisms of Li et al. [135], Burke et al. [32] and Ó Conaire et al. [173]. The coflow temperature is set the experimentally reported value of 1045 K.

Comparison of the chemical kinetics mechanisms

0DCMC *a priori analysis* 0DCMC calculations are first performed using the three mechanisms in order to determine the corresponding $\chi_{\circ,c}$ values. The results are shown in Fig. 6.14, along with those obtained with the Mueller mechanism in Sect. 6.4.2 for $T_c = 1045$ K. By inspecting the calculated $\chi_{\circ,c}$ values, and referring to Fig. 6.11, it can be postulated that the Li mechanism would yield the shortest ignition kernel and smallest liftoff height followed by the Mueller mechanism, then the Ó Conaire mechanism, and finally the Burke mechanism. This analysis provides a preliminary qualitative description of the sensitivity of liftoff height to the considered chemical kinetics.

Results in physical space To ascertain these findings, the flame is simulated using the three newly considered mechanisms. The CSDR is closed using Girimaji's model in all of the following calculations. The results are displayed in Fig. 6.15 at the axial locations $x/d = 9$, 10, 11, 14 and 26, along with those obtained using Mueller mechanism in Sect. 6.4.2. Unlike the Burke mechanism, the other three kinetic schemes are capable of reproducing the experimental trends. The results of the Mueller and Ó Conaire mechanisms show best agreement with the experimental data. The Mueller mechanism yields better predictions at $x/d = 9$ and 10, while Ó Conaire's results in better agreement with the measurements at $x/d = 11$. The differences between the two are small at $x/d = 14$ and 26. When the Li mechanism is employed, the temperature rises at early axial locations owing to the ability of the mixture to ignite at high scalar dissipation rate levels ($\chi_{o,c}^{\mathrm{Li}} = 562\ s^{-1}$). This effect propagates downstream and results in the deviation of the numerical predictions from the experiments. The performance of the Burke mechanisms is unsatisfactory, as the mixture fails to achieve early ignition ($\chi_{o,c}^{\mathrm{Burke}} = 169\ s^{-1}$) and remains inert up to approximately $x/d = 14$.

The contours of $\tilde{Y}_{\mathrm{OH}}$ ($\times 10^3$) are displayed in Fig 6.16. As predicted from the 0DCMC calculations, the Li and Burke mechanisms yield the smallest ($H/d = 9.73$) and largest ($H/d = 16.11$) liftoff heights, as shown in Figs. 6.16(a) and (b), respectively. Also consistent with the 0DCMC findings, the liftoff heights obtained using the Mueller and Ó Conaire mechanisms fall between those the Li and Burke mechanisms, as demonstrated in Figs. 6.16(c) and (d). However, the Mueller mechanism results in a slightly larger liftoff height ($H/d = 10.50$) in comparison to the Ó Conaire mechanism ($H/d = 10.26$), which contradicts with the 0DCMC predictions. Apart from the Burke mechanism, the liftoff heights computed from the remaining mechanisms are similar and are in close agreement with the experimental value $H_{\mathrm{exp}}/d = 10$. As for the radial location of liftoff, the Mueller, Li, and Ó Conaire mechanisms result is $W/d = 1.47$, whereas Burke's yields a wider flame base with $W/d = 1.92$.

As in the Mueller mechanism calculations, the flame is also stabilised by autoignition when the Ó conaire, Li and Burke mechanisms are employed. This can be clearly seen in Fig. 6.17 where H, O, OH and HO_2 exhibit the same trends observed in Fig. 6.9(a).

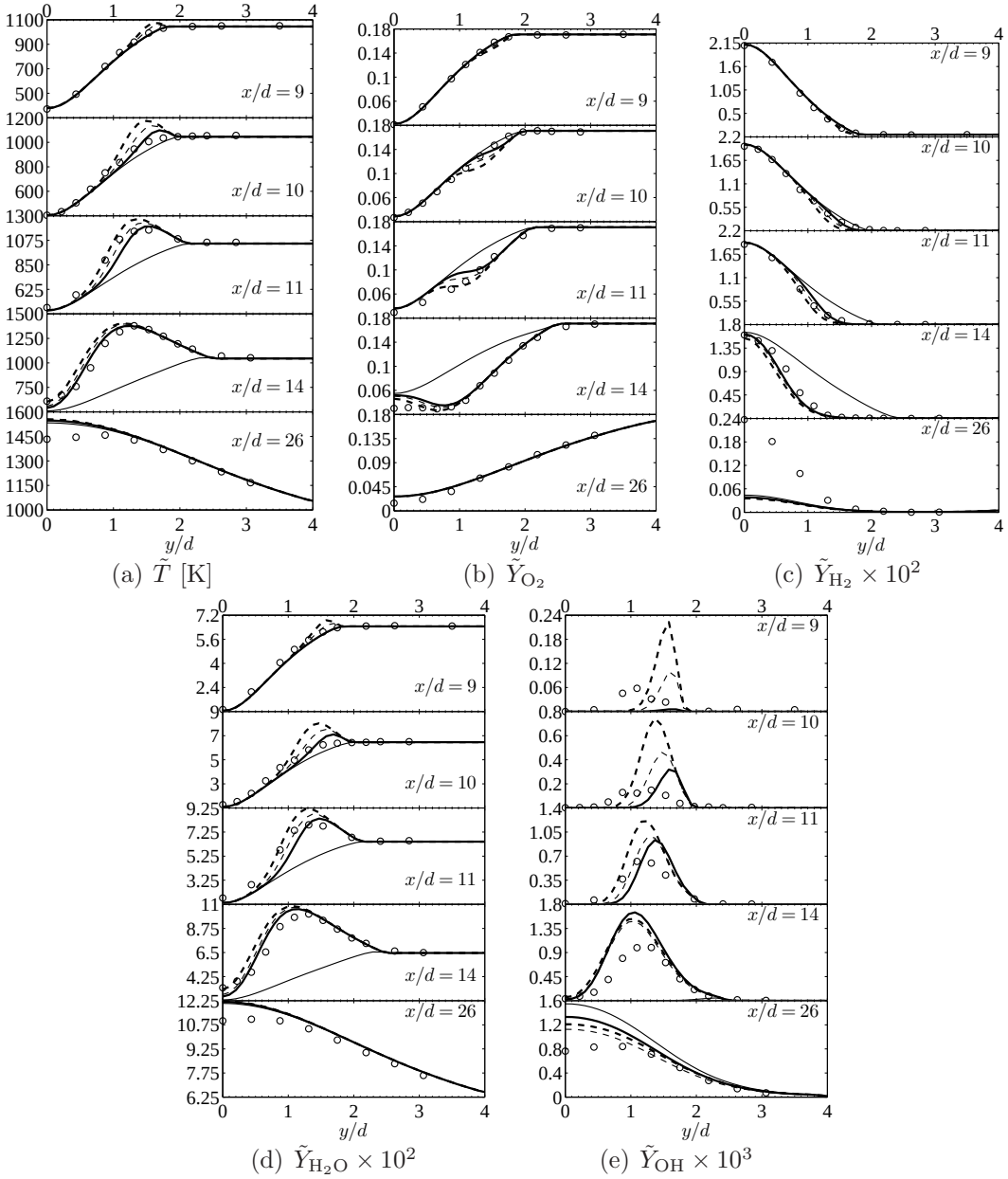

(a) $\tilde{T}$ [K] (b) $\tilde{Y}_{O_2}$ (c) $\tilde{Y}_{H_2} \times 10^2$

(d) $\tilde{Y}_{H_2O} \times 10^2$ (e) $\tilde{Y}_{OH} \times 10^3$

Figure 6.15: Radial profiles of (a) $\tilde{T}$, (b) $\tilde{Y}_{O_2}$, (c) $\tilde{Y}_{H_2}$ ($\times 10^2$), (d) $\tilde{Y}_{H_2O}$ ($\times 10^2$), and (e) $\tilde{Y}_{OH}$ ($\times 10^3$) using different chemical kinetic mechanisms. In (a)–(e): thick solid lines, Mueller et al. [164] mechanism; thick dashed lines, Li et al. [135] mechanism; thin solid lines, Burke et al. [32] mechanism; thin dashed lines, Ó Conaire et al. [173] mechanism; Symbols, experimental data [35]. Girimaji's model is used and $T_c = 1045$ K.

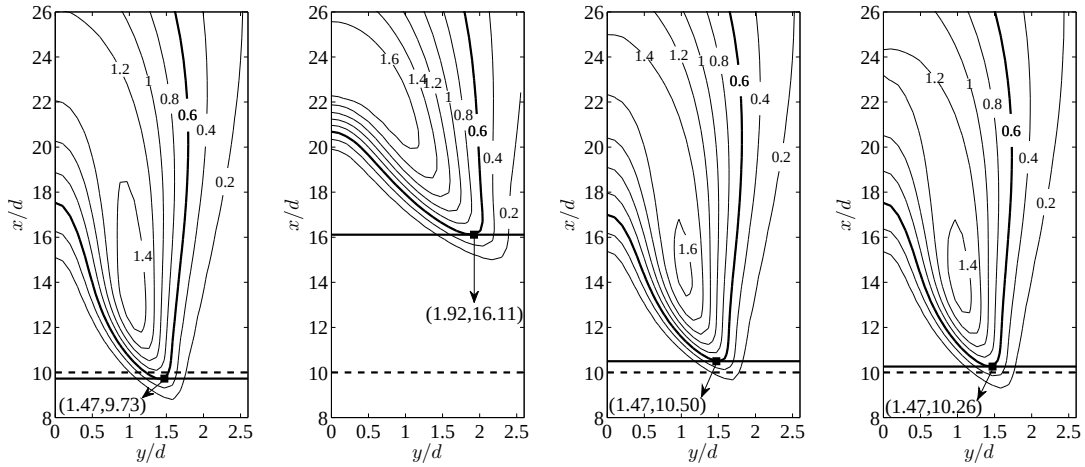

(a) Li (b) Burke (c) Mueller (d) Ó Conaire

Figure 6.16: Contours of $\tilde{Y}_{OH}$ ($\times 10^3$) obtained using the mechanisms of (a) Li et al. [135], (b) Burke et al. [32], (c) Mueller et al. [164], and (d) Ó Conaire et al. [173]. The thick contours correspond to 600 ppm. The solid and dashed horizontal lines correspond to the numerical and experimental liftoff heights, respectively. The CSDR is modelled using Girimaji's model and $T_c = 1045$ K.

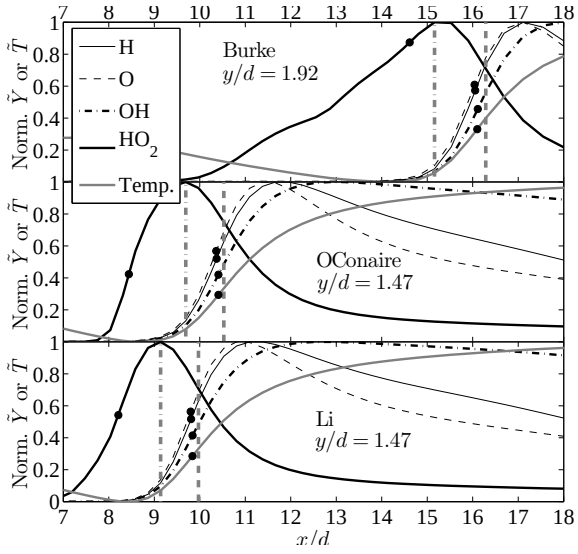

Figure 6.17: Axial profiles of the normalised Favre-averaged temperature and mass fractions of H, O, OH, and HO_2 obtained at the radial locations of liftoff using the mechanisms of Burke et al. [32], Ó conaire et al. [173], and Li et al. [135].

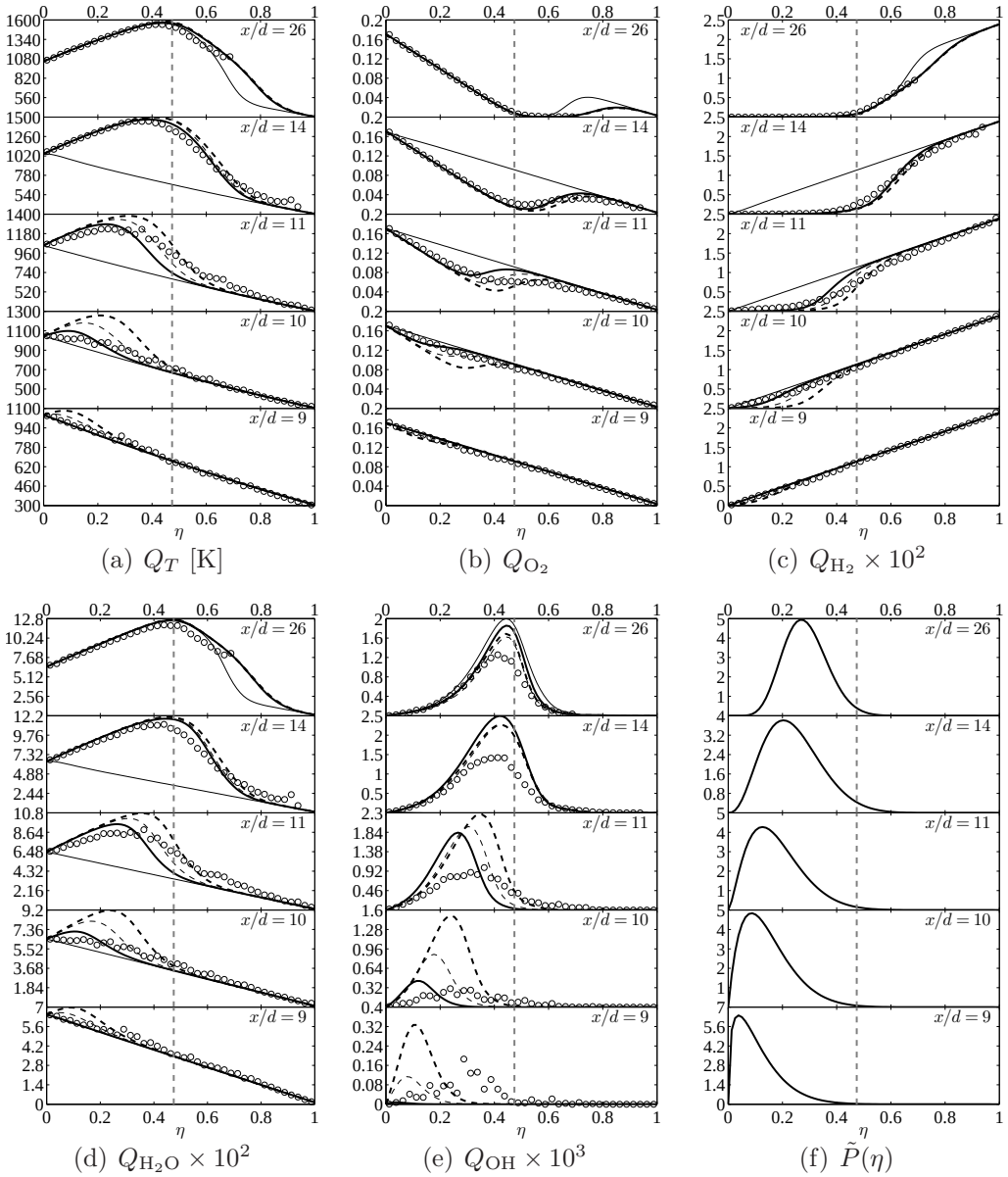

(a) Q_T [K] (b) Q_{O_2} (c) $Q_{H_2} \times 10^2$

(d) $Q_{H_2O} \times 10^2$ (e) $Q_{OH} \times 10^3$ (f) $\tilde{P}(\eta)$

Figure 6.18: Conditional profiles at x/d = 9, 10, 11, 14 and 26, and y/d = 1.47 using different chemical kinetic mechanisms: (a) Q_T, (b) Q_{O_2}, (c) Q_{H_2} ($\times 10^2$), (d) Q_{H_2O} ($\times 10^2$), (e) Q_{OH} ($\times 10^3$), and (f) $\tilde{P}(\eta)$. In (a)–(e): thick solid lines, Mueller et al. [164]; thick dashed lines, Li et al. [135]; thin solid lines, Burke et al. [32]; thin dashed lines, Ó Conaire et al. [173]; Symbols, experimental data (see Appendix A). The vertical dashed line indicates the location of η_{st}. The CSDR is modelled using Girimaji's model and T_c = 1045 K.

Results in mixture fraction space For completeness, the conditional profiles are shown in Fig. 6.18. The calculation of the conditional data from the experimental scatter is described in A. The numerical results are reported at $x/d = 9$, 10, 11, 14 and 26, and $y/d = 1.47$ (W/d obtained will all mechanisms except Burke's). Overall, the results of the Mueller and Ó Conaire mechanisms are in reasonable agreement with the experiments, especially within mixture fraction intervals where the PDF is large (see Fig. 6.18(f)). This explains the good agreement these two mechanisms yield with the measurements in physical space (Fig. 6.15). The Li mechanism predicts the highest OH levels up to $x/d = 11$ (Fig. 6.18(e)) which leads to the occurrence of the earliest ignition and consequently results in the smallest liftoff height among the considered kinetic schemes. In turn, this early ignition produces higher than expected temperature levels, an effect which propagates downstream resulting in the deviation of the conditional predictions from the experiments. In the three mechanisms discussed up to this point, the peak of Q_T in Fig. 6.18(a) shifts gradually from lean to stoichiometric mixtures as x/d increases, consistent with the axial evolution of the conditional heat release term T_{CS} in Fig. 6.7. The profiles of the Burke mechanism remain very close to the inert mixing solution up to $x/d = 14$. This behaviour results in the most delayed ignition and leads to the largest liftoff height. The conditional profiles at $y/d = 1.92$ where liftoff occurs undergo very similar trends (not shown here).

Diagnosis of the Burke mechanism

In order to diagnose the unsatisfactory performance of the Burke mechanism, the rate parameters of two of the key reactions are investigated. The recombination reaction

$$\mathrm{H + O_2(+M) \rightleftharpoons HO_2(+M)} \tag{R9}$$

and the chain-branching reaction

$$\mathrm{H + O_2 \rightleftharpoons O + OH} \tag{R1}$$

are two of the most important reactions in H_2 oxidation chemistry. R9 and R1 (labelled here as in [32, 135, 164, 173]) compete for H atoms, and therefore control the overall branching ratio and determine the second explosion limit in homogeneous H_2/O_2 systems [32]. The treatment of R9 and R1 in the Li and Burke mechanisms differs significantly from the Ó Conaire and Mueller mechanisms. The rate parameters of R9 are provided in Table 6.5.

The high-pressure limit rate parameters are identical in the Ó Conaire, Mueller and Li mechanisms [45]. Burke's mechanism uses a updated set of parameters [225]. In the low-pressure limit, the Ó Conaire and Mueller mechanisms use the same parameters [165]

Table 6.5: Rate parameters of Reaction R9: $H + O_2(+M) \rightleftharpoons HO_2(+M)$.

		Ó Conaire	Mueller	Li	Burke
High-pressure limit	A	1.475×10^{12}	1.475×10^{12}	1.475×10^{12}	4.65084×10^{12}
	n	0.6	0.6	0.6	0.44
	E_a	0	0	0	0
Low-pressure limit	A	3.482×10^{16}	3.482×10^{16}	6.366×10^{20}	6.366×10^{20}
	b	-0.411	-0.411	-1.72	-1.72
	E_a	-1.115×10^{3}	-1.115×10^{3}	5.248×10^{2}	5.248×10^{2}
	F_c	0.5	0.5	0.8	0.5
	ε_{H_2}	1.3	2.5	2	2
	ε_{H_2O}	14	12	11	14
	ε_{O_2}	1	1	0.78	0.78

Units are cm3-mole-sec-kcal-K; $k = AT^b \exp(-E_a/RT)$.
Nomenclature: A = pre-exponential coefficient; b = temperature exponent; E_a = activation energy; F_c = broadening factor; ε = third-body efficiency factor.

Table 6.6: Rate parameters of Reaction R1: $H + O_2 \rightleftharpoons O + OH$.

	Ó Conaire	Mueller	Li	Burke
A	1.915×10^{14}	1.915×10^{14}	3.547×10^{15}	1.040×10^{14}
b	0	0	-0.406	0
E_a	1.6439×10^{4}	1.6439×10^{4}	1.6599×10^{4}	1.5286×10^{4}

Units are cm3-mole-sec-kcal-K; $k = AT^b \exp(-E_a/RT)$.
Nomenclature: A = pre-exponential coefficient; b = temperature exponent; E_a = activation energy.

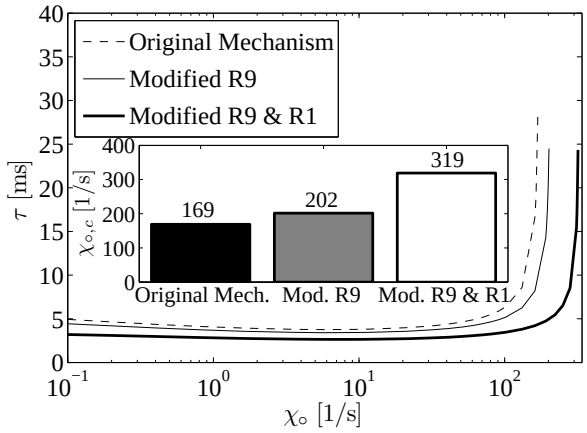

Figure 6.19: Ignition delay as a function of χ_o obtained using the original and modified mechanisms of Burke et al. [32]. The inset shows the critical values $\chi_{\circ,c}$.

except for the third-body efficiency factors of H_2 and H_2O. The Li mechanism employs a completely different set of parameters [152]. The Burke parameters differ from Li's by the broadening factor (decreased by a factor of 1.6 and equal to the ones employed in the Ó Conaire and Mueller mechanisms) and the third-body efficiency factor for H_2O (increased by a factor of 1.3) [32]. As for R1, the corresponding rate parameters are listed in Table 6.6. The parameters employed in the Ó Conaire and Mueller mechanisms are identical [182]. Two distinct sets of updated parameters are employed in the mechanisms of Li [84] and Burke [87]. In light of the above description, the variability of the predictions in Fig. 6.15, and the close agreement between the results of the Mueller and Ó Conaire mechanisms may be explained in part by the treatment of R9 and R1. This can be demonstrated for instance by adjusting the rate parameters of these two reactions in the Burke mechanism, in an attempt to improve its predictions. Since this mechanism is an updated version of Li's, two separate experiments are carried out as follows:

- The parameters of R9 are substituted by those of the Li mechanism, with the parameters of R1 left unchanged.
- The parameters of both R9 and R1 are substituted by those of the Li mechanism.

The preliminary 0DCMC calculations shown in Fig. 6.19 reveal that $\chi_{\circ,c}$ increases significantly when these modifications are applied. Therefore, the mixture is now anticipated to ignite earlier and the liftoff height is expected to decrease. Two additional CMC runs are performed using these modifications while keeping the same settings for the CSDR and

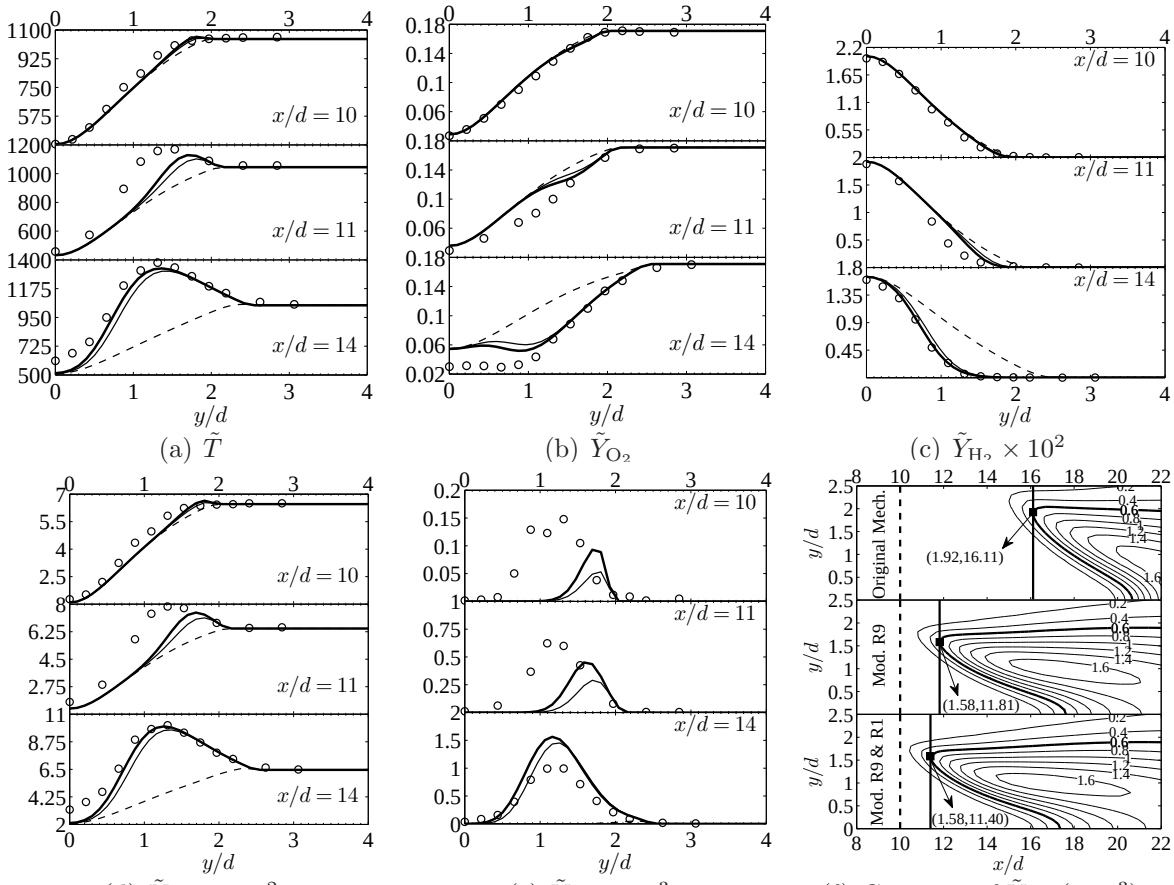

(a) $\tilde{T}$ (b) $\tilde{Y}_{O_2}$ (c) $\tilde{Y}_{H_2} \times 10^2$

(d) $\tilde{Y}_{H_2O} \times 10^2$ (e) $\tilde{Y}_{OH} \times 10^3$ (f) Contours of $\tilde{Y}_{OH}$ $(\times 10^3)$n

Figure 6.20: Radial profiles obtained using the original and modified versions of the Burke mechanism: (a) $\tilde{T}$, (b) $\tilde{Y}_{O_2}$, (c) $\tilde{Y}_{H_2}$ $(\times 10^2)$, (d) $\tilde{Y}_{H_2O}$ $(\times 10^2)$, and (e) $\tilde{Y}_{OH}$ $(\times 10^3)$. In (a)–(e): dashed lines, original mechanism; thin solid lines, modified R9; thick solid lines, modified R9 and R1; Symbols, experimental data [35]. Sub-figure (f) shows the contours of $\tilde{Y}_{OH}$ $(\times 10^3)$. The thick contour corresponds to 600 ppm. The solid and dashed horizontal lines correspond to the numerical and experimental liftoff heights, respectively. The CSDR is modelled using Girimaji's model and $T_c = 1045$ K.

the coflow temperature. The results are shown in Fig. 6.20 at $x/d = 10$, 11, and 14. It is evident that the modification of R9 alone brings a substantial improvement over the rate parameters of the original mechanism. The temperature (Fig. 6.20(a)) and the species mass fractions (Fig. 6.20(b)–(e)) are much better predicted, especially at $x/d = 11$ and

14. This further proves the importance of R9 as a precursor to autoignition reactions. Better agreement with the experimental data is obtained when both R9 and R1 are modified. As shown in Fig. 6.20(f), the liftoff height decreases by 26.69% when R9 is modified and by 29.24% when both R9 and R1 are modified. In both cases the computed liftoff heights are substantially closer to the experimentally measured value. Figure 6.20(f) also shows a remarkable decrease in W/d as liftoff occurs closer to the centreline. With the modified settings, both the axial and radial positions of liftoff become in line with those obtained using the Ó Conaire, Mueller and Li mechanisms. There should be further room for improvement by applying additional modifications to the rate parameters of other key reactions. However, extreme care must be taken while doing so because chemical kinetics mechanisms are usually optimised as a whole, rather than on an individual reaction basis. A sensitivity analysis is beyond the scope of this work and was not performed here. The modifications applied above are *ad hoc*.

6.5 Conclusions

A lifted H_2/N_2 jet flame issuing into a vitiated coflow was investigated using the first-order CMC. The flow and mixing fields were obtained using a modified version of the $k-\varepsilon$ model. The calculations included an additional transport equation for the Favre-averaged scalar dissipation rate. Two formulations were implemented for the CSDR, the homogeneous model of Girimaji and the inhomogeneous model of Mortensen. The CV was modelled using the PDF-gradient model. Calculations were performed for three coflow temperatures, 1030, 1045 and 1060 K, and four chemical kinetics mechanisms were assessed. In light of the previous results, the following conclusions are drawn:

1. The modification of the constant $C_{\varepsilon 1}$ in the $k-\varepsilon$ model from the standard value of 1.42 to 1.6 improves the predictions of the spreading rate of the jet.

2. The solution of a transport equation for the scalar dissipation rate in lieu of using the traditional algebraic modelling approach provides a more reliable mixing field.

3. The flame is very sensitive to small changes in the coflow temperature. A variation of roughly $\pm 1.44\%$ in the experimentally reported value of 1045 K results in substantial changes in the predictions. $T_c = 1045$ K yields best agreement with the experiments. The calculated liftoff height at the 1030 K level remains close to the experimentally measured value. A drastic decrease occurs when the coflow temperature is increased to 1060 K.

4. For all coflow temperatures, and using both CSDR models, the transport budgets in mixture fraction and physical spaces and the history of radical build-up ahead of the reaction zone indicate that the flame is stabilised by autoignition rather than premixed flame propagation. These findings agree in full with previous PDF calculations [37,79,146] and with the CMC results of Stanković and Merci [212], and in part with those of Navarro-Martinez and Kronenburg [169] and Patwardhan et al. [176].

5. Standalone zero-dimensional CMC calculation indicate that the mixture is capable of igniting at higher scalar dissipation levels as the coflow temperature is increased. This provides an explanation for the occurrence of ignition at locations closer to the nozzle exit and the decrease in liftoff height with increasing coflow temperature.

6. In comparison to Mortensen's model, Girimaji's model always results in lower CSDR at the "most reactive" mixture fraction, and therefore results in earlier ignition and smaller liftoff heights for all coflow temperatures.

7. The spurious sources resulting from the inconsistent modelling of the CSDR are in general small but non-negligible, mostly notably within the flame zone.

8. The flame shows high sensitivity to chemical kinetics. The results obtained with the Mueller, Li and Ó Conaire mechanisms reproduce the experimental trends with varying degrees of accuracy. The predictions are in general in good agreement with the experimental measurements, particularly those of the Mueller and Ó Conaire mechanisms. The three kinetic schemes predict very similar liftoff heights. Conversely, the performance of the Burke mechanism is unsatisfactory due to the inability of the mixture to achieve early ignition. The temperature and species mass fractions are not well predicted and the liftoff height is grossly overestimated. The modification of the rate parameters of some of the key reactions improves the predictions substantially.

Chapter 7

Modelling of a Lifted Hydrogen/Nitrogen Turbulent Jet Flame using the Presumed Mapping Function Approach

The lifted H_2/N_2 turbulent jet flame of Cabra et al. [35] (see Sect. 6.2) is revisited in order to assess the applicability of the PMF approach in the context of CMC. Using a prescribed reference field, the PMF approach provides a presumed PDF for the mixture fraction, which is used in closing the CSDR and the CV terms that are required for a fully consistent CMC implementation. The resulting PMF closures are applied here and the findings are compared to previous results obtained using β-PDF-based closures over a range of coflow temperatures (T_c). The PMF results are generally in line with those of the β-PDF closures and compare well to the experimental measurements. The transport budgets in mixture fraction and physical spaces and the radical history ahead of the stabilisation height indicate that the stabilisation mechanism is susceptible to T_c. Spontaneous ignition (autoignition) around the "most reactive" mixture fraction remains the controlling stabilisation mechanism for sufficiently high T_c. As T_c is decreased, stabilisation is achieved by means of premixed flame propagation as lean mixtures are heated by downstream burning mixtures in a pre-heat zone that develops ahead of the stabilisation height. The analysis of the spurious sources, which stem from inconsistent CSDR modelling, reveals that their effect is small but non-negligible, most notably within the flame zone. Overall, the PMF approach provides consistent, inexpensive, and reliable submodels for the closure of the CMC equations.

7.1 Introduction

In the previous chapter, the lifted H_2/N_2 turbulent jet flame of Cabra et al. [35] was thoroughly investigated using several CMC submodels and chemical kinetic mechanisms over a range of T_c values. For the most part, the study was aimed at the implementation of a fully consistent CMC realisation. Therefore, the consistency of the conditional CMC submodels with the mixture fraction PDF transport equation was emphasized. The commonly used β-distribution was adopted throughout to presume the PDF. The CV fluctuations were modelled using the PDF gradient diffusion model of Pope [188], which is consistent with the first and second moments of the PDF [43] and with the modelling of the unconditional passive and reactive scalar fluxes [160, 162]. As for the closure of the CSDR, the models of Girimaji [78] and Mortensen [157] were considered. Both models are derived by doubly-integrating the PDF transport equations and using the same set of boundary conditions. The former is based on the homogeneous form of the equation, while in the latter, the inhomogeneous terms are retained and PDF gradient diffusion modelling is applied to close the CV fluctuations. As such, Mortensen's model provides a fully consistent CSDR closure and degenerates exactly to Girimaji's when the inhomogeneous terms are discarded. In both CMC realisations, it was found that autoignition is the controlling stabilisation mechanism over the considered T_c range. This conclusion is in full agreement with the findings of Stanković and Merci [212] and in partial agreement with those of Patwardhan et al. [176] and Navarro-Martinez and Kronenburg [169] who report stabilisation via premixed flame propagation as T_c is decreased. Another conclusion drawn in the previous chapter is that Mortensen's fully consistent CSDR model results in delayed ignition, and consequently yields larger liftoff heights. Hence, the occurrence of earlier ignition in the realisation employing Girimaji's model is attributed to the spurious sources that arise from the inconsistency of this model with the CMC equations. Therefore, the consistent modelling of the CSDR is influential and ought to be investigated further.

In a recent study, Mortensen and Andersson [160] cast the solution of the mapping closure attained by Chen et al. [41] for homogeneous turbulence into a presumed mapping function for inhomogeneous turbulent flows. Using a Gaussian reference field, the PMF yields a presumed PDF for the mixture fraction. The resulting PMF-PDF is employed to derive analytical closures for the CV and the CSDR. The proposed CV closure is obtained by incorporating the PMF-PDF into the PDF gradient diffusion model of Pope [188]. The CSDR closure employs the PMF-PDF in the inhomogeneous formulation of Mortensen [157]. One invaluable feature of PMF is the ability to extend its applicability to scenarios involving multiple injections wherein the initial PDF is described by a combination of delta functions. Therefore, PMF is applicable to two-stream mixing scenarios (binary

mixing) such as the Cabra flame [35], to three-stream scenarios (trinary mixing) such as the Sandia piloted jet flames [12], and in general to scenarios involving any number of streams. The commonly used two-parameter β-PDF cannot describe the turbulent mixing of multiple injections. Nevertheless, some attempts have been made in the past to extend its applicability to the mixing of three streams. For instance, Kim et al. [114] propose a trimodal β-PDF to account for the presence of the pilot in the Sandia flames.

The early PMF assessment studies are confined within the context of passive scalar mixing and DNS. Mortensen and Andersson [160] validate the proposed closures against the DNS of a scalar mixing layer (binary mixing). They show that the closures based on the PMF-PDF outperform their β-PDF counterparts. The comparison of the homogeneous and inhomogeneous versions of Mortensen's CSDR model [157] reveals that the influence of the inhomogeneous modification is lower in the PMF approach, especially at low probabilities. The authors conclude that the PMF approach is well suited for mixture fraction-based combustion models that rely on presumed PDFs, such as CMC and the flamelet models [178]. Cha et al. [39] assess the applicability of the multiple injections extension by comparing the PMF closures to the DNS of a Double Scalar Mixing Layer (DSML) (trinary mixing). They show that the PMF approach is capable of accurately describing the fine-scale passive scalar mixing that takes place in the DSML as it captures complex features such as the trimodal PDF and the bimodal CSDR. Motivated by these findings, Mortensen et al. [163] incorporate the PMF approach in the CMC and stationary laminar flamelet of a Reacting DSML (RDSML). The considered scenario is a model problem for piloted diffusion flames wherein the fuel and oxidiser streams are initially separated by a pilot stream. The calculations employ single-step reversible chemistry and feature varying extinction levels. Given the negligible levels of the spurious source, the CSDR is closed using the homogeneous version of the multiple injections PMF closure. The findings are compared to the DNS results of the RDSML under investigation. The authors achieve a remarkable agreement between the considered combustion models and DNS at low-to-moderate extinction levels. At higher levels, they report deviations from DNS and they attribute the discrepancies to closures specific to the considered combustion models (e.g. the first-order closure for the conditional chemical source in CMC, which is not suitable for the modelling of extinction and reignition [120]).

To date, a limited number of attempts has been made to implement PMF in the CMC of laboratory-scale turbulent flames with detailed chemistry. Brizuela and Roudsari [29] use the PMF approach in the CMC calculations of Sandia flame D [12]. They make use of the trinary PMF-PDF in the pilot region and the binary PMF-PDF away from it. The CSDR is modelled using the homogeneous version of the PMF closure proposed in [160]. Two formulations of this simplified model are applied, depending on the type of mixing (binary

or trinary). In the binary mixing case the CSDR is equivalent to the PMF-PDF-based AMC [174] and counterflow model [177]. PDF gradient diffusion modelling is employed for the closure of the CV. The reported results show that the PMF closures outperform classical closures (in their case the β-distribution for the PDF, the β-PDF-based AMC for the CSDR, and the β-PDF gradient diffusion model for the CV). One nozzle diameter upstream of centre of the pilot (Fig. 3(a) in [29]), the CSDR profiles show two peaks with a local zero at around the mean mixture fraction of the pilot, $\tilde{\xi}_p$, and low dissipation levels around the stoichiometric mixture fraction $\tilde{\xi}_{st}$. These findings are consistent with the observations of Pitsch and Steiner [186] who note that the scalar dissipation rate within the pilot stream is zero because the scalar gradient over there is null. Hence, the CSDR at essentially zero at $\tilde{\xi}_p$, which causes the CSDR at $\tilde{\xi}_{st}$ to be small. It is also noted in [186] that this effect propagates to downstream locations and the shape of the CSDR remains influenced by the pilot. This behaviour is obvious two diameters upstream of the centre of the pilot (Fig. 3(b) in [29]) where the CSDR profile shows two peaks with a non-zero local minimum around $\tilde{\xi}_p$. Brizuela and Roudsari [29] also report better agreement with the experiments right downstream of the inlets (Fig. 5 in [29]). Therefore, even the homogeneous version of the PMF-based CSDR model is capable of capturing important mixing phenomena and yields reliable predictions in the near field. This shows that PMF has a promising potential in the context of CMC.

To the author's knowledge, the inhomogeneous PMF-based CSDR model has never been applied in CMC nor to lifted flames. The current study is an extension to the previous chapter. The lifted H_2/N_2 jet flame of Cabra et al. [35] is revisited and investigated using the two-dimensional first-order CMC and a modified version of the $k-\varepsilon$ model. The PDF, CV and CSDR are modelled here using the PMF approach. The objectives of this study are to assess the applicability of the PMF-based submodels and to compare the PMF results to previous β-PDF results. A range of coflow temperatures is considered and the stabilisation mechanism is determined by investigating the CMC budgets in mixture fraction and physical spaces, and through the analysis of the radical history ahead of the stabilisation height. In addition, the effect of the spurious sources is thoroughly investigated.

7.2 Mathematical model

The turbulence-chemistry interactions are modelled by means of the first-order CMC. The current implementation is exactly the same as in the previous chapter except that the submodels for $\tilde{P}(\eta)$, $\langle u_i|\eta\rangle$ and $\langle\chi|\eta\rangle$ required for the closure of Eqs. (3.23) and (3.34) are

Table 7.1: Summary of the CMC realisations.

Realisation	CMC-βG†	CMC-βM†	CMC-PMF‡
$\tilde{P}(\eta)$	β-PDF (Eq. (3.37))	β-PDF (Eq. (3.37))	PMF-PDF (Eq. (3.63))
$\langle u_i \vert \eta \rangle$	PDF gradient model based on the β-PDF (Eq. (3.70))	PDF gradient model based on the β-PDF (Eq. (3.70))	PDF gradient model based on the PMF-PDF (Eq. (3.71))
$\langle \chi \vert \eta \rangle$	Girimaji's model (Eq. (3.75))	Mortensen's model based on the β-PDF (Eqs. (3.81) and (3.85))	Mortensen's model based on the PMF-PDF (Eq. (3.87))
$\langle u_i'' y_\kappa'' \vert \eta \rangle$ and $\langle u_i'' T'' \vert \eta \rangle$	Gradient diffusion assumption (Eqs. (3.67) and (3.67)	Gradient diffusion assumption (Eqs. (3.67) and (3.67)	Gradient diffusion assumption (Eqs. (3.67) and (3.67)
$\langle \dot{\omega}_\kappa \vert \eta \rangle$	First-order closure (Eq. (3.90))	First-order closure (Eq. (3.90))	First-order closure (Eq. (3.90))
$\langle \dot{\omega}_r \vert \eta \rangle$	Optically thin assumption (Eq. (3.93))	Optically thin assumption (Eq. (3.93))	Optically thin assumption (Eq. (3.93))

† CMC realisations considered in Chapter 6.
‡ Current CMC realisation.

based on the PMF approach rather than the β-distribution. This realisation will be referred to as CMC-PMF. Some of the results of the realisations considered in the previous chapter are included here for the purpose of comparison with the those of CMC-PMF. Hereafter, they will be referred to as CMC-βG (the realisation employing Girimaji's model) and CMC-βM (the realisation employing Mortensen's model). For convenience, the submodels used in the three realisations are summarised in Table 7.1. The turbulent flow and mixing fields calculations follow the same procedure described in Sect. 6.3.2. The details of the numerical implementation of CMC are available in Sect. 6.3.3. The PMF closures for the PDF (Eq. (3.63)), the CV (Eq. (3.71)) and the CSDR (Eq. (3.87)) are computed using the open-source code *PMFpack* [159]. The H_2 oxidation chemical kinetics mechanism of Mueller et al. [164] is employed throughout this study (See Table 6.3).

7.3 Results and discussion

7.3.1 Comparison of PMF and β-PDF closures

In this section, the results of the realisations CMC-βG, CMC-βM and CMC-PMF are compared. The coflow temperature is set to the experimentally reported value of 1045 K [35].

Results in physical space

The contours of $\tilde{Y}_{\mathrm{OH}}$ ($\times 10^{-3}$) are shown in Fig. 7.1(a). As in the experiments of Cabra et al. [35], the criterion for the determination of the liftoff height is taken as the first location in the flow field where $\tilde{Y}_{\mathrm{OH}}$ reaches 600 ppm. Based on this criterion, the liftoff height (normalised by the nozzle diameter) predicted by CMC-PMF is 9.80 compared to 10.50 for CMC-βG and 10.61 for CMC-βM. In Comparison with the experimental value $H_{\mathrm{exp}}/d = 10$, CMC-PMF results in the smallest relative error. The usage of the PMF closures does not affect the radial location of stabilisation (the distance from the stabilisation point to the centreline normalised by d) as CMC-PMF yields 1.47, which is exactly the same value predicted by CMC-βG and CMC-βM. The radial profiles of the Favre-averaged temperature and species mass fractions are shown in Fig. 7.1(b)–(f) at the axial locations $x/d = 8$, 9, 10, 11, 14 and 26. The profiles obtained using the three CMC realisations overlap at $x/d = 8$ and 9 and agree well with the experimental data of Cabra et al. [35]. Compared to the results of CMC-PMF, those of CMC-βG and CMC-βM are in better agreement with the experiments at $x/d = 10$. The temperature and product mass fractions are overpredicted while the reactant mass fractions are underpredicted in the range $1.1 \leq y/d \leq 1.8$ when the PMF closures are used. As indicated earlier, CMC-PMF predicts a liftoff height of 9.8 compared to 10.50 for CMC-βG and 10.61 for CMC-βM. Therefore, at $x/d = 10$, the mixture is not inert and a flame is present, which explains the higher levels of temperature and products and the lower levels of reactants. This effect propagates downstream. As shown at $x/d = 11$, the CMC-PMF results are overall in better agreement with the measurements. The differences between the three CMC realisations diminish at $x/d = 14$, with CMC-βG and CMC-βM being slightly closer to the experiments. Further downstream at $x/d = 26$ the results are almost identical.

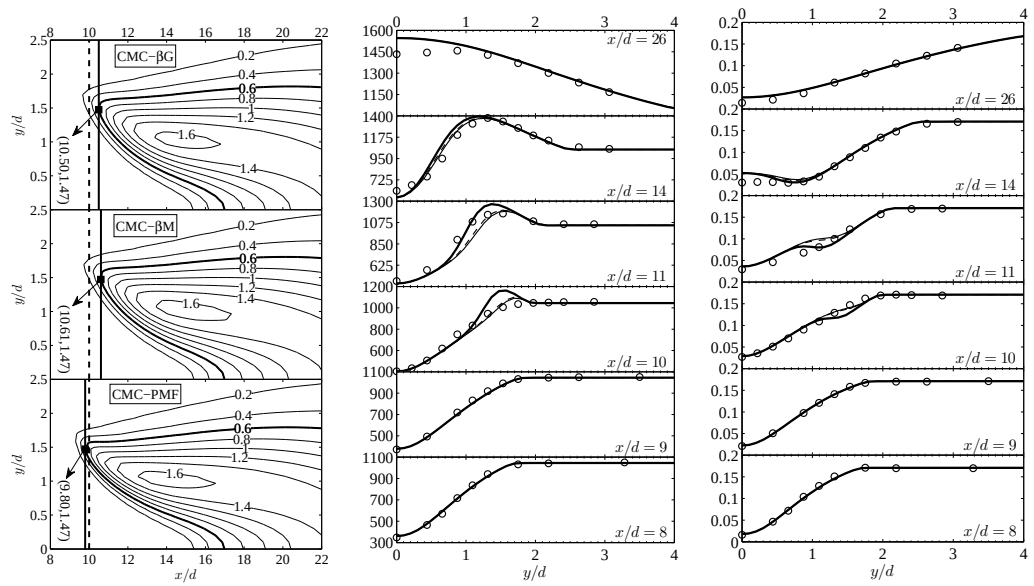

(a) Contours of $\tilde{Y}_{\mathrm{OH}}(\times 10^3)$ (b) $\tilde{T}$ [K] (c) $\tilde{Y}_{\mathrm{O_2}}$

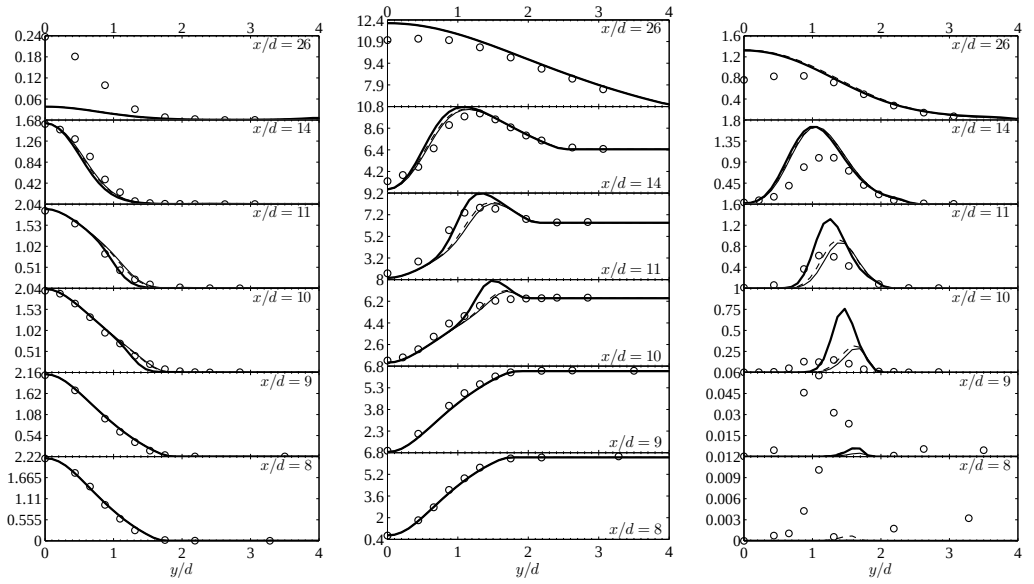

(d) $\tilde{Y}_{\mathrm{H_2}} \times 10^2$ (e) $\tilde{Y}_{\mathrm{H_2O}}(\times 10^2)$ (f) $\tilde{Y}_{\mathrm{OH}}(\times 10^3)$

Figure 7.1: Results of the three CMC realisations for $T_c = 1045$: (a) contours of $\tilde{Y}_{\mathrm{OH}}$ $(\times 10^3)$, and radial profiles of (b) $\tilde{T}$, (c) $\tilde{Y}_{\mathrm{O_2}}$, (d) $\tilde{Y}_{\mathrm{H_2}}$ $(\times 10^2)$, (e) $\tilde{Y}_{\mathrm{H_2O}}$ $(\times 10^2)$, and (f) $\tilde{Y}_{\mathrm{OH}}$ $(\times 10^3)$. In (a) the thick contours corresponds to 600 ppm. The solid and dashed vertical lines correspond to the normalised numerical and experimental liftoff heights, respectively. In (b)–(f): dashed lines, CMC-βG; thin solid lines, CMC-βM; thick solid lines, CMC-PMF; symbols, experimental data [35].

Results in mixture fraction space

Comparison of the reactive scalars Figures 7.2(a) and (b) show the axial evolution of the conditional temperature, Q_T, and the conditional OH mass fraction, Q_{OH}, around the stabilisation locations indicated in Fig. 7.1(a). In all three realisations, as x/d increases, the peaks of Q_T and Q_{OH} shift from lean mixtures towards stoichiometry and their amplitudes increase dramatically within roughly one and half nozzle diameters. Compared to CMC-βG and CMC-βM, CMC-PMF yields relatively higher Q_T and Q_{OH} levels and therefore leads to the smallest liftoff height (see Fig. 7.1(a)). The profiles of CMC-βG and CMC-βM are very similar, which explains why the liftoff heights resulting from these realisations are very close (see Fig. 7.1(a)). It is important to note that Q_T and Q_{OH} evolve differently in the CMC-PMF realisation. In CMC-βG and CMC-βM, Q_T and Q_{OH} start to increase around the "most reactive" mixture fraction ($\eta_{mr} = 0.0543$ (Sect. 6.4.2)), as shown at $x/d = 8.86$, and their peaks remain around η_{mr} up to $x/d = 9.42$ before shifting slowly to less lean mixtures at $x/d = 9.69$, and eventually closer towards stoichiometry at $x/d = 11.09$. This behaviour indicates the occurrence of spontaneous ignition (autoignition) ahead of the stabilisation height. In CMC-PMF, although Q_T and Q_{OH} reach their maxima at η_{mr} at $x/d = 8.86$, it is obvious that their peaks shift more aggressively towards stoichiometry as x/d increases. This shows that the flame is stabilised by a different mechanism other than autoignition. As it will be shown in Sect. 7.3.3, a pre-heat zone exists ahead of the stabilisation height where lean mixtures are preheated by downstream burning mixtures as in premixed flame propagation.

Comparison of the presumed PDFs The evolution of the PDF is displayed in Fig. 7.2(c). Both presumed PDFs peak at the same location in mixture fraction space. The PMF-PDF is slightly narrower than the β-PDF and presents a relatively higher peak. Although the differences between the two are small, the mildest changes in the shape of the PDF can have a non-negligible impact on the CV and CSDR distributions, and can affect the unconditional averages of the different reactive scalars (Eqs. (3.24) and (3.35)).

Comparison of the CSDR models Figure 7.2(d) shows the evolution of the CSDR. Girimaji's homogeneous model results in almost symmetric profiles whereas Mortensen's inhomogeneous models (based on the β-PDF and the PMF-PDF) yield skewed profiles. The effect of inhomogeneity manifests away from the mean of the mixture fraction ($\eta \gtrsim \tilde{\xi}$) as the PDF decays to zero (see Fig. 7.2(c)). Mortensen's models are in general less dissipative as they produce substantially lower CSDR levels for $\eta \gtrsim \tilde{\xi}$, most notably around stoichiometry and in rich mixtures. It is clear that the presumed form of the PDF in

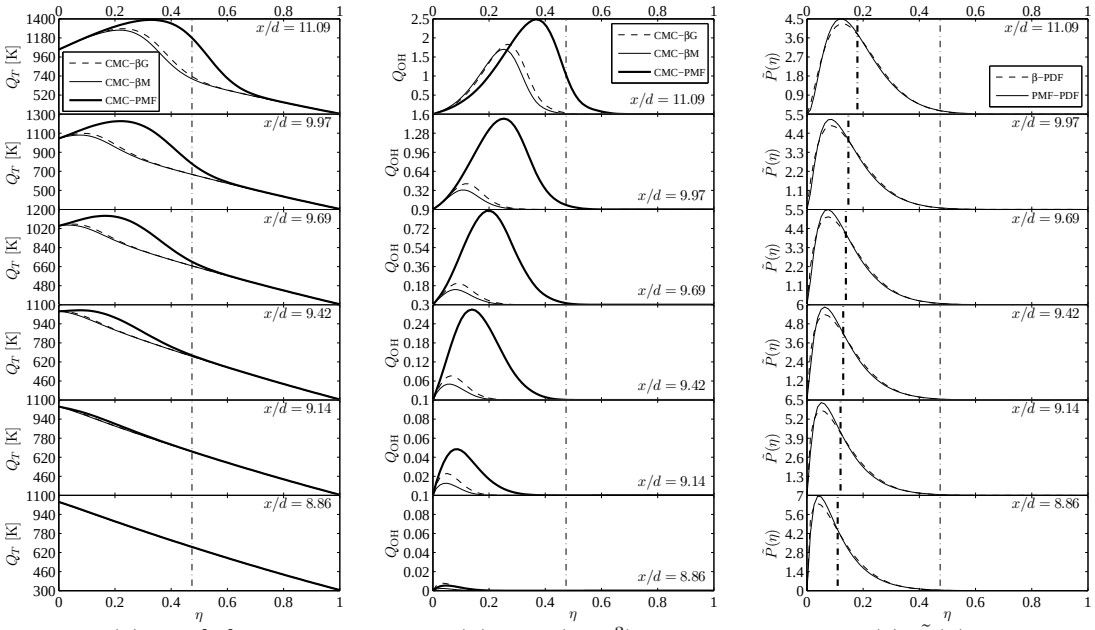

(a) Q_T [K] (b) $Q_{\mathrm{OH}}(\times 10^3)$ (c) $\tilde{P}(\eta)$

(d) $\langle\chi|\eta\rangle$ [1/s] (e) $\langle u|\eta\rangle$ [m/s] (f) $\langle v|\eta\rangle$ [m/s]

Figure 7.2: Axial evolution of (a) Q_T [K], (b) Q_{OH}, (c) $\tilde{P}(\eta)$, (d) $\langle\chi|\eta\rangle$ [1/s], (e) $\langle u|\eta\rangle$ [m/s], and (f) $\langle v|\eta\rangle$ [m/s] at $y/d = 1.47$ (the radial location of stabilisation). The thin vertical dash-dotted line indicates the location of the stoichiometric mixture fraction ($\eta = \tilde{\xi}_{st}$). The thick vertical dash-dotted line in (c)–(f) indicates the location of the mixture fraction mean ($\eta = \tilde{\xi}$). The coflow temperature is 1045 K.

Mortensen's model affects the shape of the CSDR. Although the trends of the β-PDF and the PMF-PDF versions of the model are similar, significant difference can be clearly seen around stoichiometry and in rich mixture, with the PMF-PDF version being less dissipative in these regions. This observation illustrates how influential the presumption of the PDF can be on the modelling of the CSDR.

Comparison of the CV models The axial and radial CV components, $\langle u|\eta\rangle$ and $\langle v|\eta\rangle$, are displayed in Figs. 7.2(e) and 7.2(f), respectively. The β-PDF and PMF-PDF gradient diffusion models yield very similar results within two-to-three standard deviations of the mixture fraction mean. As in the CSDR profiles, the differences between the two closures become substantial away from the mean. The β-PDF gradient model tends to $\pm\infty$ as the PDF approaches zero. The PMF-PDF closure is generally better-behaved over the whole mixture fraction space as it does not overshoot significantly at low probabilities. This behaviour demonstrates again the large influence of the presumed PDF. By inspecting Fig. 7.2(e), although the trends of $\langle u|\eta\rangle$ are quite different, the results of the β-PDF and PMF-PDF closures are of the same order of magnitude, and do not differ much from $\tilde{u}$. This is attributed to the fact that the axial velocity fluctuations are small, which is in turn due to the small magnitude of $\partial \ln[\tilde{P}(\eta)]/\partial x$ over the whole range of η. On the other hand, the magnitude of $\partial \ln[\tilde{P}(\eta)]/\partial y$ can vary substantially, depending on the radial variations of the PDF at the point of interest. As shown in Fig. 7.2(f), in the range where the PDF is finite ($0 < \eta \lesssim \tilde{\xi}_{st}$ in Fig. 7.2(c)), the magnitude of $\partial \ln[\tilde{P}(\eta)]/\partial y$ is small regardless whether the β-PDF or the PMF-PDF is used. However, at low probabilities ($\eta \gtrsim \tilde{\xi}_{st}$), the two PDFs yield substantially different velocities. When the β-PDF is employed, $\partial \ln[\tilde{P}(\eta)]/\partial y$ is one order of magnitude larger than the PMF-PDF fluctuations. In the absence of experimental measurements, it is difficult to judge which closure is more accurate. Nevertheless, the fact that the PMF closure does no overshoot at low probabilities is desirable for numerical stability.

The effect of the PMF and β-PDF closures Having identified the differences between the β-PDF and the PMF-PDF closures, it becomes obvious why the results of CMC-PMF differ from those of CMC-βG and CMC-βM (Figs. 7.2(a) and (b)). In chapter 6, the differences between the results of CMC-βG and CMC-βM were solely attributed to the distinct CSDR levels at the "most reactive" mixture fraction, simply because the same presumed PDF (β-PDF) and CV model (the β-PDF gradient diffusion model) were employed in both realisations. It is obvious from Fig. 7.2(d), that Mortensen's model based on the PMF-PDF results in comparable CSDR levels at η_{mr}, and produces profiles similar in shape and magnitude to those of the same model based on the β-PDF. Despite this, the

predictions of the CMC-PMF realisation shows departure from the CMC-βM results, as shown in Figs. 7.2(a) and (b). Thus, it becomes clear that the closure of the CV also plays an important role in the modelling of this flame. Therefore, arguments based exclusively on the grounds of intensity of micro-mixing at η_{mr} are not sufficient (though necessary) in order explain the variability in the results. To illustrate this, the axial profiles of the CSDR models employed in the three realisation are plotted in Figure 7.3 at η_{mr} ($\langle\chi|\eta_{mr}\rangle$). Although the flame is stabilised by autoignition in CMC-βM (Sect. 6.4.2) and by premixed flame propagation in CMC-PMF (Sect. 7.3.3), $\langle\chi|\eta_{mr}\rangle_{\text{CMC-PMF}}$ (thick solid lines) is lower than $\langle\chi|\eta_{mr}\rangle_{\text{CMC-}\beta\text{M}}$ (thin solid line). Hence, although the lower CSDR levels at η_{mr} favour the occurrence of autoignition, stabilisation is achieved by a different mechanism. For this reason, any analysis based exclusively on the CSDR is insufficient. Returning to Fig. 7.2, the lower CSDR levels around stoichiometry in the CMC-PMF realisation lead to a decrease in the leakage of fuel and oxidiser from stoichiometric mixtures towards lean and rich mixtures. Therefore, the oxidation of the fuel becomes more intense in the vicinity of the stoichiometric mixture fraction. This behaviour, accompanied by the heating of lean mixtures in the pre-heat zone, promotes the early formation of a flame. Further, the smaller magnitude of $\langle v|\eta\rangle$ around stoichiometry and in rich mixtures results in a long residence time, which leads to increased chemical activity and hence higher Q_T and Q_{OH} levels.

Comparison to conditional measurements The conditional profiles of the temperature and species mass fractions obtained from the three CMC realisations are shown in Fig. 7.4. The calculation of the conditional data from the experimental scatter is described in Appendix A. The numerical results are reported at the axial locations $x/d = 9$, 10, 11, 14 and 26 near the stoichiometric isocontour. As shown, the CMC-PMF results are generally in better agreement with the experimental data compared to CMC-βG and CMC-βM. The improved predictions are mostly notable in lean mixture at $x/d = 10$ and 11, and in rich mixtures at $x/d = 14$. This shows that the PMF approach is a reliable and accurate candidate for the closure of the CMC equations.

7.3.2 Sensitivity to the coflow temperature

Several CMC [169, 176, 212] and PDF [37, 79] calculations show that the flame under investigation is very sensitive to T_c. Cabra et al. [35] report an experimental uncertainty of 3% in the temperature measurements. As in Sect. 6.4.2, small perturbations ($\sim \pm 1.435\%$) are applied to T_c in order to assess flame response when the PMF closures are employed.

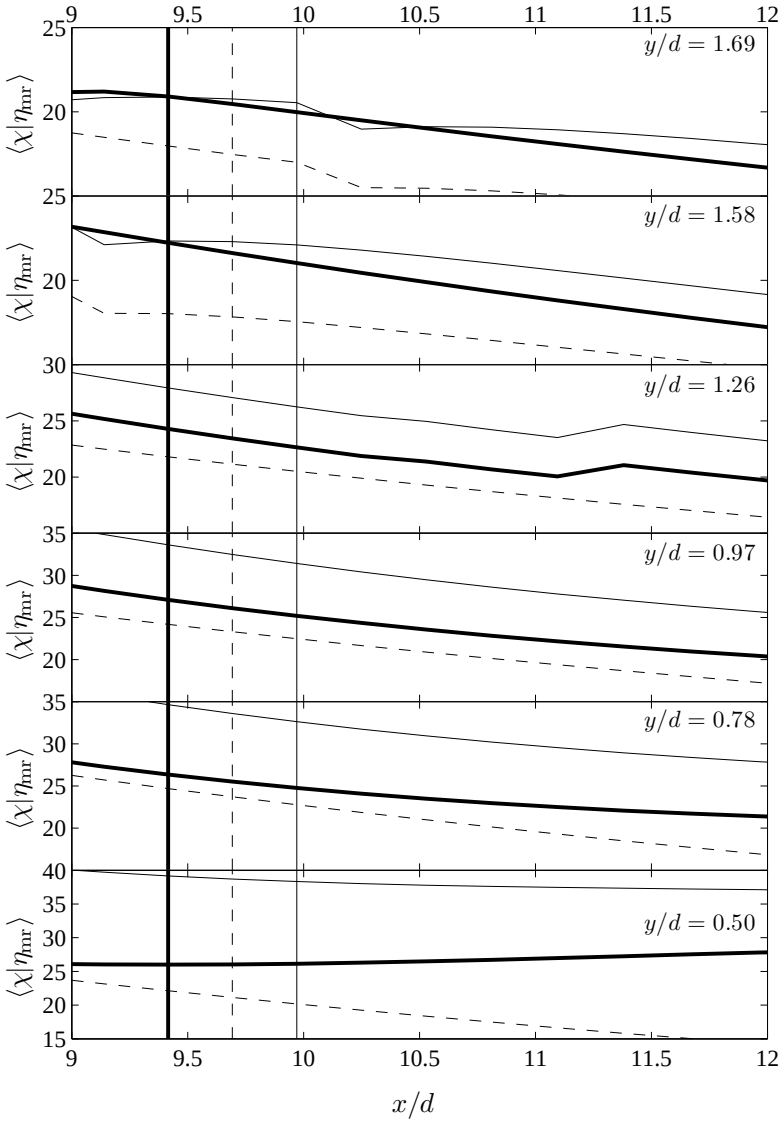

Figure 7.3: Axial profiles of $\langle\chi|\eta_{mr}\rangle$ at several radial locations for $T_c = 1045$ K: dashed lines, Girimaji's model ($\langle\chi|\eta_{mr}\rangle_{\text{CMC-}\beta\text{G}}$); thin solid lines, Mortensen's model based on the β-PDF ($\langle\chi|\eta_{mr}\rangle_{\text{CMC-}\beta\text{M}}$); thick solid lines, Mortensen's model based on the PMF-PDF ($\langle\chi|\eta_{mr}\rangle_{\text{CMC-PMF}}$). The vertical lines designate the ignition locations obtained with each CSDR model. The pattern of each vertical line follows that of the corresponding CSDR.

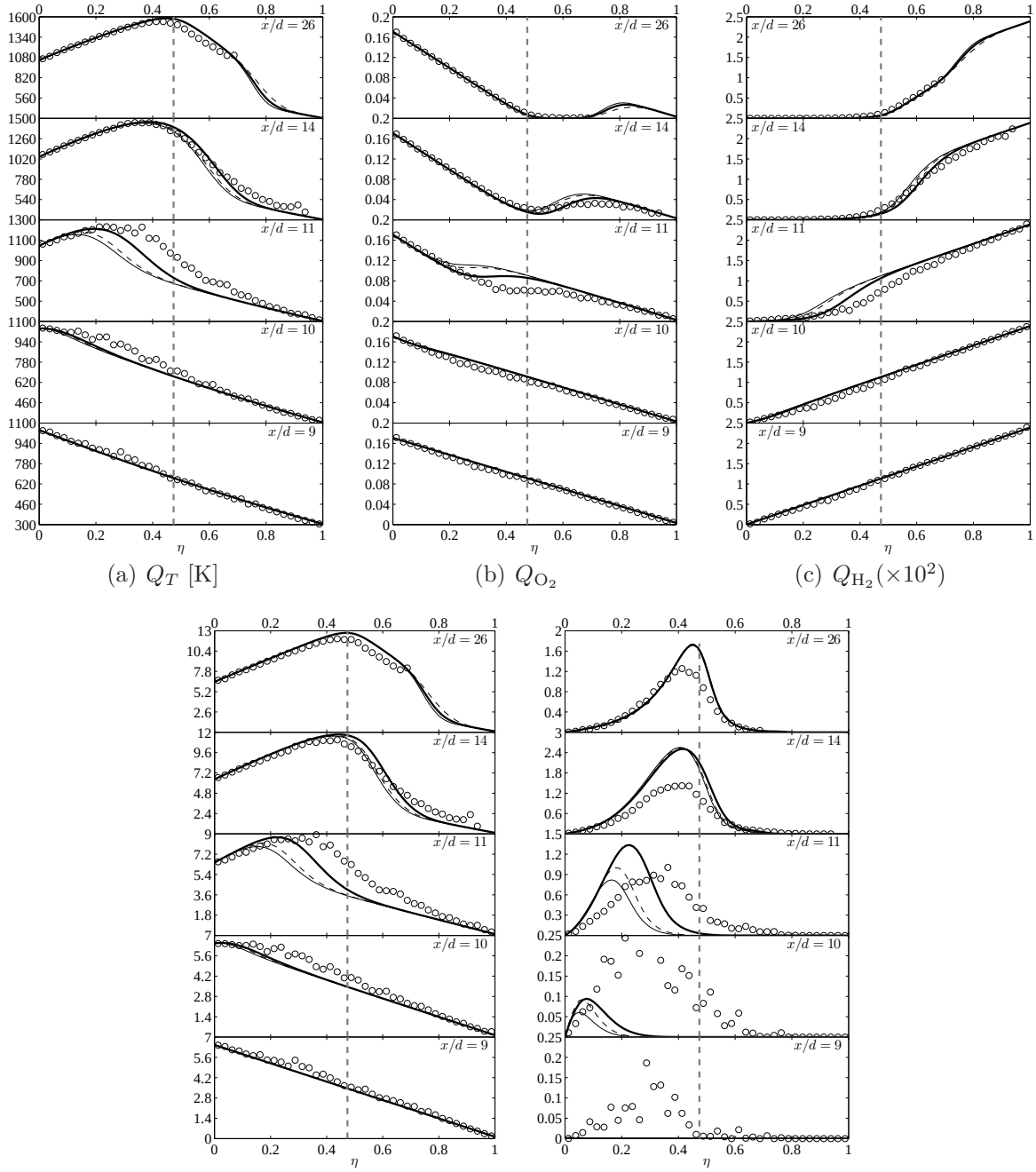

(a) Q_T [K] (b) Q_{O_2} (c) $Q_{H_2}(\times 10^2)$

(d) $Q_{H_2O}(\times 10^2)$ (e) $Q_{OH}(\times 10^3)$

Figure 7.4: Conditional profiles near the stoichiometric isocontour: (a) Q_T [K], (b) Q_{O_2}, (c) Q_{H_2} ($\times 10^2$), (d) Q_{H_2O} ($\times 10^2$), and (e) Q_{OH} ($\times 10^3$). Dashed lines, CMC-βG; thin solid lines, CMC-βM; thick solid lines, CMC-PMF; symbols, experimental data [35]. The vertical grey dashed line indicates the location of the stoichiometric mixture fraction.

Table 7.2: Locations of the stabilisation points obtained using the three CMC realisations with the coflow temperatures 1030 K and 1060 K.

	$T_c = 1030$ K		$T_c = 1060$ K	
Realisation	x/d	y/d	x/d	y/d
CMC-βG	11.48	1.58	6.61	1.16
CMC-βM	11.91	1.58	7.39	1.26
CMC-PMF	11.22	1.58	6.97	1.26

Figure 7.5 shows the radial profiles of the Favre-averaged temperature and species mass fractions at the axial locations $x/d = 8$, 9, 10, 11, 14 and 26 for $T_c = 1030$ and 1060 K. The results of all three realisations are displayed. When T_c is decreased to 1030 K (black lines), the profiles of CMC-PMF are in close agreement with those of CMC-βG. This trend differs from the $T_c = 1045$ K case (Fig. 7.1), where the profiles of CMC-βG and CMC-βM show closer agreement. In comparison to the experimental data, the predictions of CMC-PMF and CMC-βG are in general superior to those CMC-βM, particularly at $x/d = 11$ and 14. Overall, the results of all three realisations remain in reasonable agreement with the experiments. When T_c is increased to 1060 K (grey lines), the profiles of CMC-PMF are in close agreement with those of CMC-βM. Again, this trend differs from those observed in the $T_c = 1030$ and 1045 K cases. The experimental measurements are grossly mispredicted at all axial locations as a result of the occurrence of early ignition (discussed in Sect. 7.3.3), which is in turn due to the higher coflow temperature. From the results shown in Figs. 7.1 and 7.5, it can be seen that there is no clear qualitative trend in the relative outcome of the different CMC realisations as T_c is varied. The normalised stabilisation coordinates obtained using the three realisations are displayed Table 7.2. PMF-CMC yields the smallest liftoff height in the $T_c = 1030$ K case, followed by CMC-βG then CMC-βM. Quantitatively, the CMC-PMF prediction is the closest to H_{exp}/d. The predicted radial stabilisation location is the same in all realisations (1.58) and is slightly larger that the one calculated at $T_c = 1045$ K (1.47). Therefore, the flame base becomes wider as T_c is decreased. When $T_c = 1060$ K, the liftoff height predicted in CMC-PMF falls between the heights calculated in CMC-βG and CMC-βM. The radial stabilisation locations obtained in CMC-PMF and CMC-βM are the same (1.26), while the predicted CMC-βG value is slightly smaller (1.16). As such, it can be seen that the flame base becomes narrower when T_c is increased.

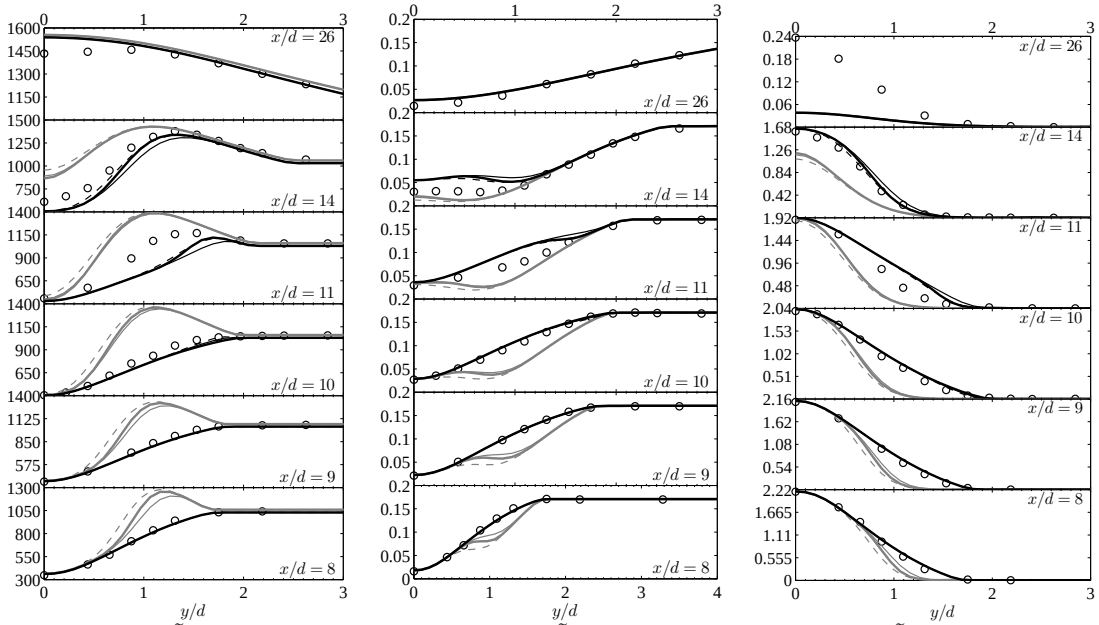

(a) $\tilde{T}$ [K] (b) $\tilde{Y}_{O_2}$ (c) $\tilde{Y}_{H_2} \times 10^2$

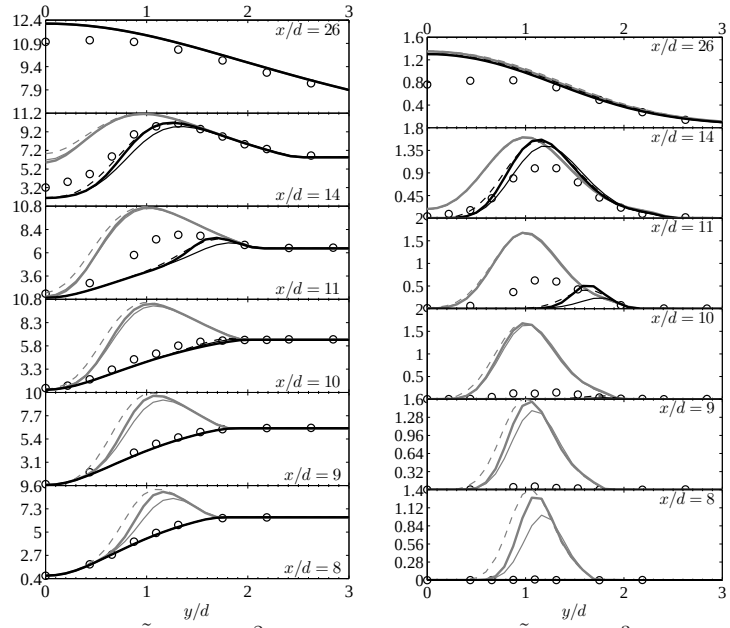

(d) $\tilde{Y}_{H_2O}(\times 10^2)$ (e) $\tilde{Y}_{OH}(\times 10^3)$

Figure 7.5: Radial profiles of (a) $\tilde{T}$, (b) $\tilde{Y}_{O_2}$, (c) $\tilde{Y}_{H_2}$ $(\times 10^2)$ (d) $\tilde{Y}_{H_2O}$ $(\times 10^2)$, and (e) $\tilde{Y}_{OH}$ $(\times 10^3)$ obtained from the three CMC realisations for $T_c = 1030$ K (black lines) and 1060 K (grey lines). Lines: dashed, CMC-βG; thin solid, CMC-βM; thick solid, CMC-PMF; symbols, experimental data [35].

7.3.3 The stabilisation mechanism

The flame under investigation was found in chapter 6 to be autoignition-stabilised over a range of coflow temperatures (1030-1060 K) when the β-PDF closures are used (CMC-βG and CMC-βM). The distinction between stabilisation by autoignition and premixed flame propagation was achieved by means of the numerical indicators developed by Gordon et al. [79], which involve the analyses of the transport budgets and the history of radical build-up ahead of the stabilisation height. In this section, these indicators are invoked in order to determine whether the usage of the PMF approach changes the previous conclusions.

Budgets in mixture fraction space

Figure 7.6 shows the transport budgets of the steady-state conditional temperature equation (the right-hand side terms of Eq. (3.34)) obtained using the CMC-PMF realisation for $T_c = 1030$, 1045 and 1060 K. For each T_c, the budgets are reported at three axial locations around the predicted stabilisation height covering the pre-flame, liftoff and post-flame regions. In the CMC-βG and CMC-βM realisations considered in chapter 6, a balance in lean mixtures between the chemical source, T_{CS}, the axial convection term, $T_{C,x}$, and micromixing, T_{MM}, was found in the pre-flame region for all T_c. The axial and radial diffusion terms, $T_{D,x}$ and $T_{D,y}$, and the radial convection term, $T_{C,y}$ were found to have little contribution to the overall budget. This balance lead to the conclusion that the mixtures ignites spontaneously, and therefore the flame was deemed to be stabilised by autoignition. As shown in Figs. 7.6(a) and (b), a different balance manifests in the pre-flame regions for $T_c = 1030$ and 1045 K (bottom panes) as $T_{C,x}$ is essentially counterbalanced by $T_{D,x}$. The contributions of the remaining terms are smaller in comparison, most notably that of T_{CS}. This balance suggests the presence of a pre-heat zone as in premixed flames. It is important to note that $T_{D,x}$ and $T_{C,x}$ do not peak at stoichiometry, but rather in lean mixtures. Therefore, as postulated by Patwardhan et al. [176], lean mixtures are preheated by downstream burning mixture. As such, a premixed flame front propagates upstream and anchors the base of the lifted flame in lean mixtures. It is worth noting that when $T_c = 1045$ K, T_{CS} yields a larger contribution compared to the $T_c = 1030$ K case. This observation indicates that there is a weak competition from autoignition. However, T_{CS} is not sufficiently large to change the nature of the stabilisation mechanism. When T_c is increased to 1060 K, T_{CS} peaks at η_{mr} and the T_{CS}-$T_{C,x}$-T_{MM} balance recurs in the pre-flame zone as displayed in Fig. 7.6(c) (bottom pane), which indicates the occurrence of autoignition as in the CMC-βG and CMC-βM realisations. At liftoff (middle panes in Figs. 7.6(a)-(c)), the peak of T_{CS} shifts to $\eta \approx 0.27$ and its amplitude increases dramatically. In

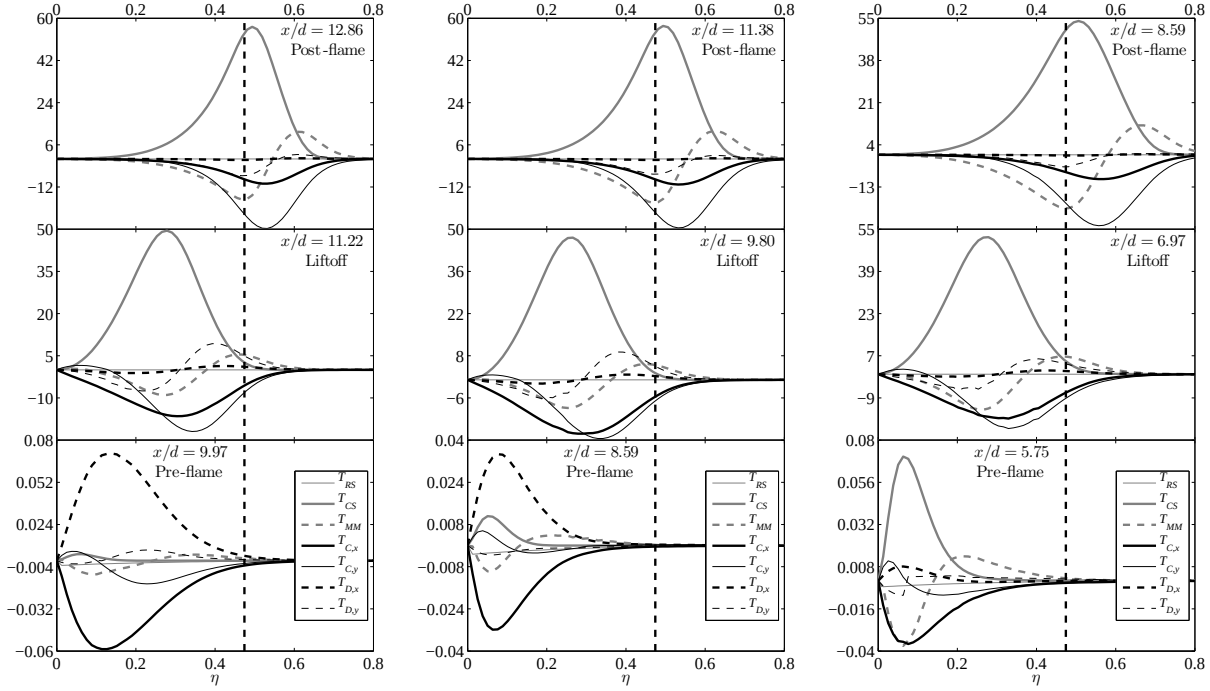

(a) $T_c = 1030$ K ($y/d = 1.58$) (b) $T_c = 1045$ K ($y/d = 1.47$) (c) $T_c = 1060$ K ($y/d = 1.26$)

Figure 7.6: Transport budget of the steady-state Q_T equation (r.h.s. terms of Eq.(3.34)) obtained using the CMC-PMF realisation for different coflow temperatures: (a) $T_c = 1030$ K ($y/d = 1.58$), (b) $T_c = 1045$ K ($y/d = 1.47$) and (c) $T_c = 1060$ K ($y/d = 1.26$). T_{RS}, radiative source; T_{CS}, chemical source; T_{MM}, micro-mixing; $T_{C,x}$, axial convection; $T_{C,y}$ radial convection; $T_{D,x}$, axial diffusion; $T_{D,y}$, radial diffusion. The vertical dashed line corresponds to the location of the stoichiometric mixture fraction. All terms are scaled down by a factor of 10^5 and the units are K/s.

the cases where $T_c = 1030$ and 1045 K, T_{CS} is balanced by $T_{C,x}$ and $T_{C,y}$. The terms, T_{MM} and $T_{D,y}$ are more important than in upstream locations and $T_{D,x}$ is negligible. A similar balance is observed when $T_c = 1060$ K, except that T_{MM} is more prevalent. Compared to the CMC-βG and CMC-βM realisations, when $T_c = 1060$ K the roles of T_{MM} and $T_{C,y}$ vary significantly due to the different shapes of the CSDR and CV predicted by the PMF closures. T_{MM} has a weaker effect because of the smaller CSDR levels for $\eta \gtrsim \tilde{\xi}$ (not shown). Conversely, $T_{C,y}$ is more influential due to the larger residence time caused by the smaller magnitude of $\langle v|\eta\rangle$ over the same range of η (not shown). Further downstream in the post-flame regions (top panes in Figs. 7.6(a)-(c)), T_{CS} peaks around the stoichiometric

mixture fraction and it is essentially balanced by T_{MM} and $T_{C,y}$. $T_{C,x}$ remains important but its role diminishes from upstream locations, and $T_{D,x}$ is virtually zero. In comparison to the CMC-βG and CMC-βM, for all T_c values, $T_{C,y}$ acts as the major heat sink around stoichiometry due to the larger residence time. Beyond the post-flame locations indicated in Fig. 7.6, $T_{C,x}$ and $T_{C,y}$ diminish gradually and the flame budgets approach the structure a non-premixed flame, which is largely characterised by a T_{CS}-T_{MM} balance.

Budgets in physical space

As in Sect. 6.4.2, the controlling stabilisation mechanism can be determined as well via the analysis the Integrated Transport (IT) budget of the conditional temperature in physical space. To compute the individual contributions, each term on the right-hand side of Eq. (3.34) is weighted by the appropriate presumed PDF and then integrated over the mixture fractions space. The axial profiles of the resulting contributions are shown in Fig. 7.7 for all combinations of CMC realisations and coflow temperatures. The indicated y/d values correspond to the radial locations of stabilisation obtained in each realisation. As shown in the top and middle panes of Figs. 7.7(a)-(c), for all coflow temperatures in the CMC-βG and CMC-βM realisations IT_{CS} is balanced by $IT_{C,x}$ and IT_{MM} in the pre-flame regions. The remaining terms have little contribution to the overall balance. However, they become more important right ahead of the stabilisation height. The IT_{CS}-$IT_{C,x}$-IT_{MM} balance indicates that the mixture ignites spontaneously, and therefore the flame is autoignition-stabilised for all T_c values. The nature of the controlling stabilisation mechanism in the CMC-PMF realisation depends on T_c. For $T_c = 1030$ (bottom pane in Fig. 7.7(a)), there is a clear balance between $IT_{D,x}$ and $IT_{C,x}$ up to $x/d \approx 10.25$ and IT_{CS} is small. This structure indicates the presence of a preheat zone, which is indicative of stabilisation by means of premixed flame propagation. Beyond this location and prior to liftoff, IT_{CS} increases rapidly. The terms IT_{MM}, $IT_{C,y}$ and $IT_{D,y}$ become more important and $IT_{D,x}$ has the smallest contribution to the overall budget. Similar trends are observed for $T_c = 1045$ K (bottom pane in Fig. 7.7(b)). However, in this case IT_{CS} is more significant in the pre-heat zone, which indicates that there is competition from the autoignition mechanism. Nevertheless, IT_{CS} is not sufficiently large in order for autoignition to happen. Increasing T_c further to 1060 K (bottom pane in Fig. 7.7(c)), the budgets in the pre-flame region are very similar to those of the CMC-βG and CMC-βM. IT_{CS} is primarily balanced by $IT_{C,x}$ and hence autoignition takes place. In the vicinity of the stabilisation height, the budgets of all realisations show similar structures as IT_{CS} is counterbalanced by $IT_{D,y}$, $IT_{C,x}$, $IT_{C,y}$ and IT_{MM}. However, the relative importance of $IT_{C,y}$ and IT_{MM} with respect to IT_{CS} and $IT_{C,x}$ varies significantly in the CMC-PMF realisations. Compared to CMC-βG and

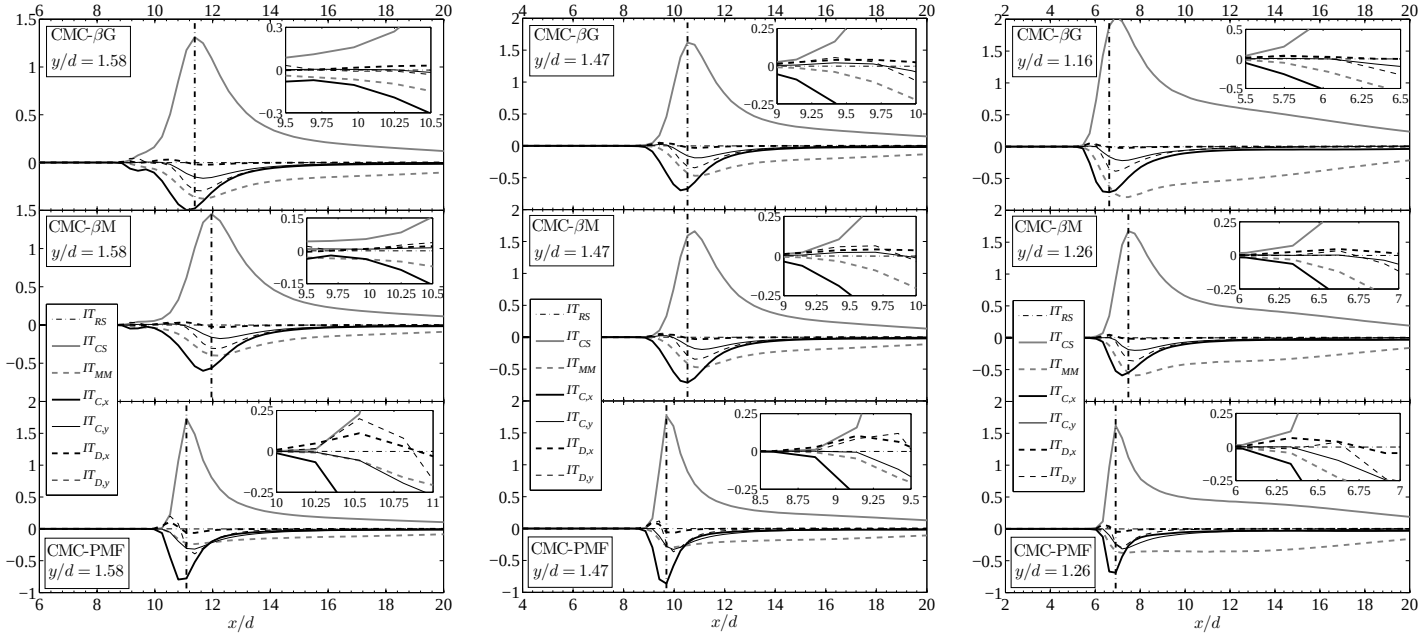

(a) $T_c = 1030$ K (b) $T_c = 1045$ K (c) $T_c = 1060$ K

Figure 7.7: Axial profiles of the Integrated Transport (IT) budget of the steady-state Q_T equation (integrated r.h.s. terms of Eq.(3.34)) obtained using the three CMC realisations: (a) $T_c = 1030$ K, (b) $T_c = 1045$ K and (c) $T_c = 1060$ K. The bottom, middle and top panes correspond to CMC-βG, CMC-βM and CMC-PMF, respectively. The indicated y/d values correspond the radial locations of stabilisation. IT_{RS}, radiative source; IT_{CS}, chemical source; IT_{MM}, micro-mixing; $IT_{C,x}$, axial convection; $IT_{C,y}$ radial convection; $IT_{D,x}$, axial diffusion; $IT_{D,y}$, radial diffusion. All terms are scaled down by a factor of 10^6 and the units are K/s.

CMC-βM, $IT_{C,y}$ is larger in magnitude due to the lower radial CV component (longer residence time) whereas IT_{MM} is smaller because of the lower CSDR levels. Beyond the stabilisation heights, the structure of a non-premixed flame is gradually approached as IT_{CS} is primarily balanced IT_{MM} with smaller contributions from the remaining terms.

Radical history ahead of the stabilisation height

The analyses of the transport budgets of the temperature in mixture fraction and physical spaces reveal that the nature of the stabilisation mechanism becomes sensitive to the coflow temperature when the PMF approach is employed. Further analysis of the history of radical build-up ahead of the stabilisation height can provide more insight into this matter. Figure 7.8 shows the axial profiles of the normalised Favre-averaged temperature $((\tilde{T}-\tilde{T}_{\min})/(\tilde{T}_{\max}-\tilde{T}_{\min}))$ and mass fractions $(\tilde{Y}/\tilde{Y}_{\max})$ of H, O, OH, and HO_2 for all combinations of CMC realisations and coflow temperatures. The subscripts "min" and "max" denote the minimum and maximum values of the reactive scalars at the axial locations of stabilisation. For all coflow temperatures, the CMC-βG and CMC-βM realisations (top and middle panes in Fig. 7.8) show that HO_2 builds-up rapidly prior to the runaway of H, O and OH. Therefore, HO_2 acts as a precursor to the production of H, O and OH as in autoignition scenarios [79]. The evolution of radicals in the CMC-PMF realisation (bottom panes in Fig. 7.8) shows similar trends, which is at first glance indicative of the occurrence of autoignition. As shown by Gordon et al. [79], in premixed flame propagation radicals build-up simultaneously in the pre-heat zone. It is obvious here that HO_2 builds-up prior to the remaining radicals. However, for $T_c = 1030$ and 1045 K, there is a notable decrease in the axial distance between the runaway location of HO_2 and those of the remaining radicals (see the filled circles), and between the peak of HO_2 and the stabilisation height (distance between dash-dotted and dashed vertical lines). Hence, although radicals do not start building-up at the same point, there is a clear tendency towards simultaneous radical production ahead of the stabilisation height. It is also important to note that when lifted flame are stabilised by means of premixed flame propagation, liftoff takes place at locations where the local mixture fraction mean, $\tilde{\xi}$, is equal to the stoichiometric mixture fraction, $\tilde{\xi}_{st}$ [228]. This is not the case here since the flame stabilises at $\tilde{\xi} = 0.183$ when $T_c = 1030$ K and $\tilde{\xi} = 0.139$ when $T_c = 1045$ K. These $\tilde{\xi}$ values are well below $\tilde{\xi}_{st} = 0.474$. Still, it is clear that $\tilde{\xi}$ approaches $\tilde{\xi}_{st}$ as T_c is decreased. A further decrease in T_c is therefore expected to lead to a more simultaneous radical build-up.

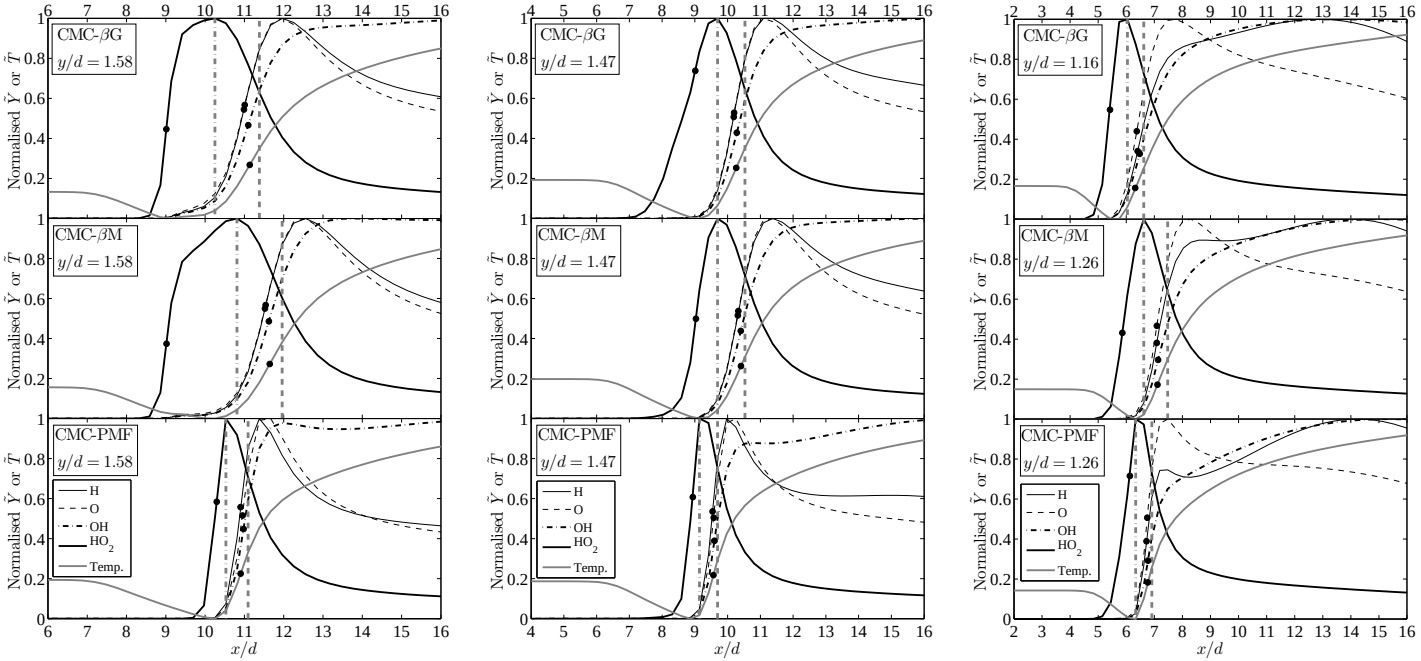

(a) $T_c = 1030$ K (b) $T_c = 1045$ K (c) $T_c = 1060$ K

Figure 7.8: Axial profiles of the normalised Favre-averaged temperature and mass fractions of H, O, OH, and HO_2 obtained using the three CMC realisations: (a) $T_c = 1030$ K, (b) $T_c = 1045$ K and (c) $T_c = 1060$ K. The bottom, middle and top panes correspond to CMC-βG, CMC-βM and CMC-PMF, respectively. The indicated y/d values correspond the radial locations of stabilisation. The vertical dash-dotted and dashed lines correspond the axial locations of maximum HO_2 and liftoff height, respectively. The circles indicate the locations of the maximum slopes.

7.3.4 The spurious sources

The effect of the spurious sources is assessed in the context of the PMF approach and compared to the findings obtained in the previous chapter using the β-PDF approach. The spurious source of a species κ is calculated as [120, 226]:

$$\tilde{S}_\kappa = \frac{1}{2}\int_0^1 \left[\langle\chi|\eta\rangle_i - \langle\chi|\eta\rangle_c\right] \frac{\partial^2 Q_{\kappa,i}}{\partial\eta^2}\tilde{P}(\eta)d\eta \tag{7.1}$$

where $\langle\chi|\eta\rangle_i$ and $\langle\chi|\eta\rangle_c$ are the inconsistent and consistent CSDR models, respectively (the same presumed PDF is used in both), and $Q_{\kappa,i}$ is the conditional mass fraction of species κ obtained in the inconsistent realisation. The consistent inhomogeneous CSDR model of Mortensen [157], Eq. (3.81), is benchmarked against its inconsistent homogeneous version with $\tilde{P}(\eta)$ presumed using both the β- and PMF-PDFs. As such, the difference $[\langle\chi|\eta\rangle_i - \langle\chi|\eta\rangle_c]$ in Eq. (7.1) is exactly the negative of the inhomogeneous contribution of the model. The details of the two cases are as follows:

- β-PDF case (previous chapter):
  - $\langle\chi|\eta\rangle_c$: Eq. (3.81) with $II(\eta)$ obtained from Eq. (3.85)
  - $\langle\chi|\eta\rangle_i$: Eq. (3.75) (the equivalent of the homogeneous version of Eq. (3.81))
- PMF-PDF case:
  - $\langle\chi|\eta\rangle_c$: Eq. (3.87)
  - $\langle\chi|\eta\rangle_i$: Eq. (3.89)

Figure 7.9 compares the axial evolution of the integrated conditional chemical sources (IT_{CS}) and spurious sources of HO_2, OH and H_2O for $T_c = 1045$ K. The profiles are plotted at the radial locations of stabilisation ($y/d = 1.47$ for the β-PDF case and $y/d = 1.37$ for the PMF-PDF case). As displayed in Fig. 7.9(a), $\tilde{S}_{HO_2}$ is negligible in both cases before the runaway of HO_2. Ahead of the stabilisation height, $\tilde{S}_{HO_2}$ acts as a source. It increases as the production of HO_2 proceeds and peaks in the vicinity of the maximum of IT_{CS,HO_2}, then decreases as soon as the consumption of HO_2 begins, reaching a local minimum right ahead of the base of the flame. As the consumption of HO_2 continues, $\tilde{S}_{HO_2}$ increases again and peaks downstream of the stabilisation height before it decays gradually inside the flame zone. Overall, the magnitude of $\tilde{S}_{HO_2}$ is more important ahead of the stabilisation height. Figure 7.9(b) displays the axial variation of $\tilde{S}_{OH}$. Similar to what is observed in Fig.

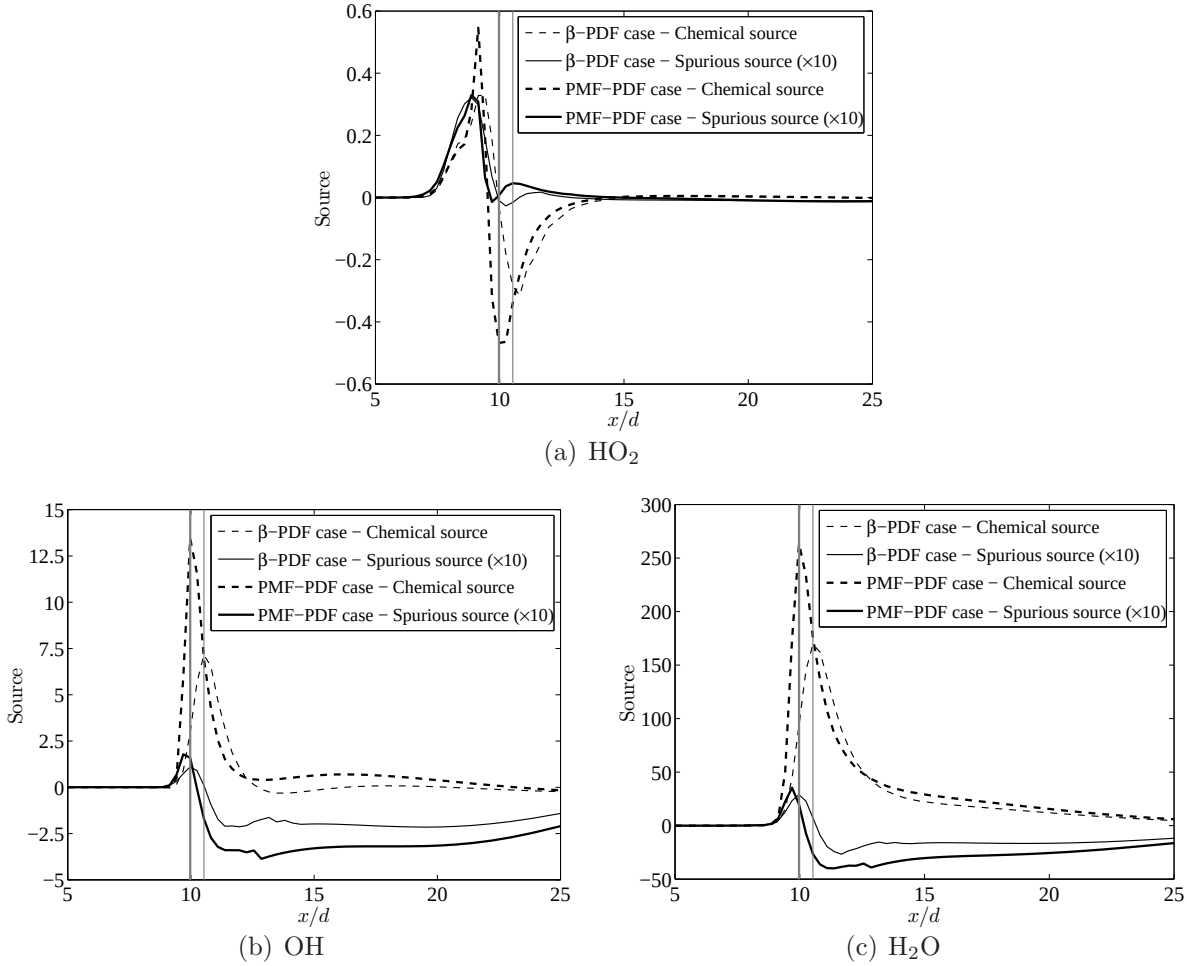

(a) HO_2

(b) OH

(c) H_2O

Figure 7.9: Axial profiles of the chemical and spurious sources at $y/d = 1.47$ (radial locations of stabilisation) for $T_c = 1045$ K: (a) HO_2, (a) OH and (c) H_2O. All spurious sources are multiplied by 10 and the units are s^{-1}. The vertical grey lines indicates the axial locations of the stabilisation heights: thin, β-PDF; thick, PMF-PDF.

7.9(a), $\tilde{S}_{OH}$ in Fig. 7.9(b) acts as a source ahead of the stabilisation height. Its magnitude is negligible before the runaway of OH then increases as OH is produced and peaks in the vicinity of the maximum of $IT_{CS,OH}$. $\tilde{S}_{OH}$ decreases sharply at the base of the flame before increasing at a much slower rate in the flame zone (its magnitude decreases gradually with increasing x/d) and continues to act as a sink. As opposed to $\tilde{S}_{HO_2}$, $\tilde{S}_{OH}$ is more important in the flame zone compared to the region located ahead of the stabilisation height. The trends observed in the axial variation of $\tilde{S}_{H_2O}$ (Fig. 7.9(c)) are similar to those of $\tilde{S}_{OH}$.

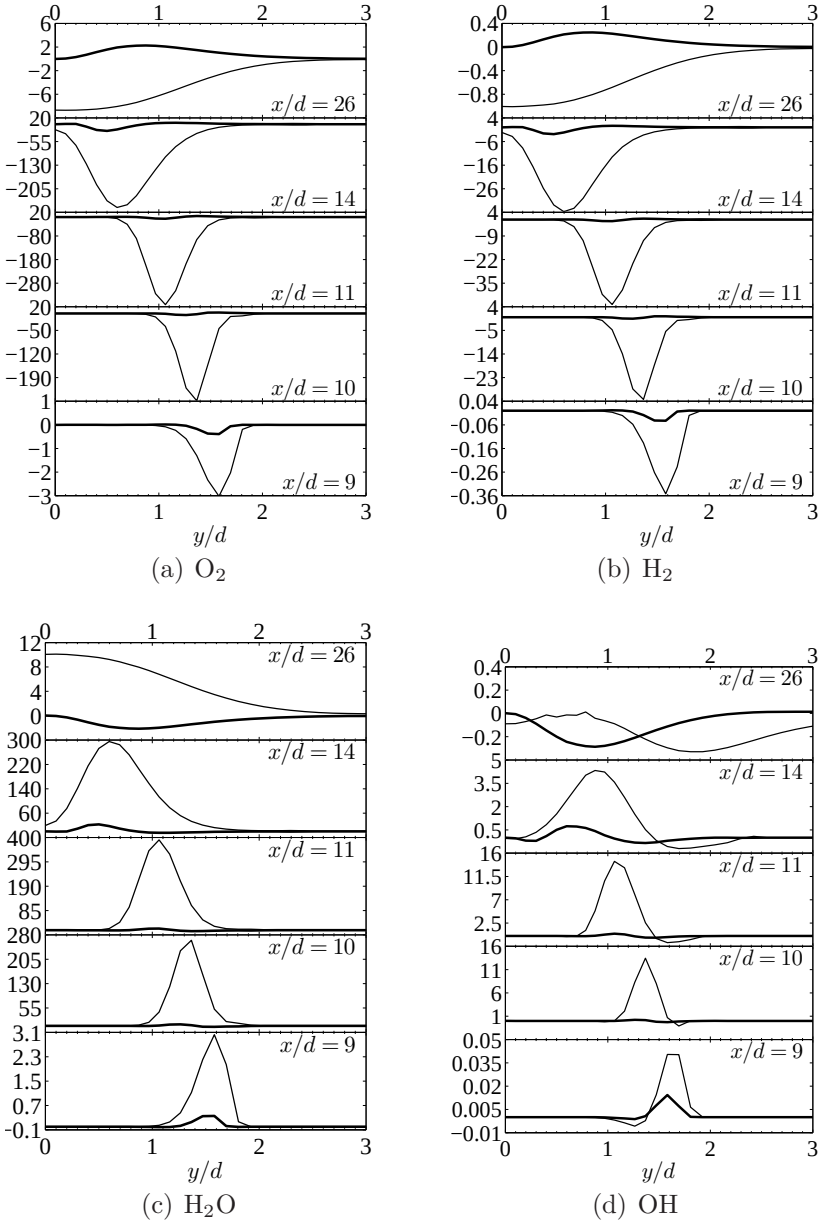

(a) O_2 (b) H_2

(c) H_2O (d) OH

Figure 7.10: Radial profiles of the chemical and spurious sources obtained in the PMF-PDF case for $T_c = 1045$ K: (a) O_2, (b) H_2, (c) H_2O, and (d) OH. Thin lines, chemical sources; thick lines, spurious sources. The units are s^{-1}.

The comparison of the results of the β-PDF and PMF-PDF cases ahead of the stabilisation heights in Figs. 7.9(a)-(c) reveals that the spurious sources in the PMF-PDF case yield higher maxima, however, prevail over narrower axial bands. In the flame zone, the magnitude of the spurious sources obtained in the β-PDF case is smaller at all axial locations.

Overall, it can be concluded that the errors arising from the inconsistent modelling of the CSDR are small but non-negligible. To ascertain this conclusion, the radial profiles of the chemical and spurious sources of O_2, H_2, H_2O and OH are plotted in Fig. 7.10. Only the PMF-PDF case is considered here. The results of the β-PDF case are very similar (see Sect. 6.4.2). It is evident that the effect of the spurious sources is non-negligible at all axial locations, particularly within the flame zone at $x/d = 14$ and 26. The ratios of spurious-to-chemical sources at the axial locations considered Fig. 7.10 (not shown) indicate that the spurious contribution increases with x/d, which is expected to take place as the scalar dissipation rate decays.

The findings presented in the current section show that inconsistent CMC implementations may influence the results as the additional spurious terms stemming from inconsistencies in the modelling of the CSDR can behave as significant sources or sinks.

7.4 Conclusions

A previously investigated lifted H_2/N_2 jet flame was revisited in order to assess the applicability of the PMF approach in the context of CMC. The findings were compared to previous results obtained using β-PDF-based closures over a range of coflow temperatures (T_c). In view of the current results, the following conclusions are drawn:

1. The PMF-PDF is in general narrower than the β-PDF and presents a higher peak. The shape of the PDF has a large influence on the modelling of the CSDR and the CV.

2. Girimaji's CSDR model results in nearly symmetric profiles whereas the Models of Mortensen (based on the PMF- and β-PDFs) yield skewed profiles. The latter models are less dissipative away from the mean of the mixture fraction.

3. The gradient diffusion CV model is well-behaved over the whole mixture fraction space when the PMF-PDF is employed as it does not overshoot significantly at low probabilities. The β-PDF-based model tends to infinity as the PDF approaches zero.

4. In comparison to the β-PDF-based closures at $T_c = 1045$ K, the PMF-based closures yield comparable results in physical space and superior predictions in mixture fraction space. Further, a smaller and more accurate liftoff height is obtained. The flame remains very sensitive to small perturbations in T_c. However, there is no clear qualitative trend in the relative outcome of the considered CMC realisations as T_c is varied.

5. As opposed to the β-PDF closures, the transport budgets in mixture fraction and physical spaces and the radical history ahead of the stabilisation height reveal that the nature of the stabilisation mechanism is sensitive to T_c when the PMF closures are used. For sufficiently high T_c (e.g. $T_c = 1060$ K), the mixture ignites spontaneously at the "most reactive" mixture fraction, and the flame is stabilised by autoignition. As T_c is decreased (e.g. to $T_c = 1045$ and 1030 K), lean mixtures are pre-heated by a premixed flame front propagating upstream, and therefore, the flame is stabilised by means of premixed flame propagation.

6. The effect of the spurious sources is overall small but non-negligible, in particular within the flame zone.

The PMF approach is a consistent and reliable candidate for the closure of the CMC equations. Further application to other combustion phenomena is necessary to fully assess its applicability.

Chapter 8

Doubly-Conditional Moment Closure: Model Formulation and Parametric Assessment

A DCMC method is proposed for the accurate treatment of highly fluctuating phenomena encountered in non-premixed and partially premixed flames. A normalised PV is introduced beside the mixture fraction as a second conditioning variable. The unburnt and burnt states employed in the normalisation of the PV are specified such that they are mixture fraction-dependent. A transport equation for the normalised PV is first obtained. The doubly-conditional species, enthalpy and temperature transport equations are then derived using the decomposition approach and the primary closure hypothesis is applied. Submodels for the doubly-conditioned unclosed terms which arise from the derivation are suggested and boundary conditions are discussed. The homogeneous version of the proposed method is implemented and a standalone parametric assessment is performed by varying the levels of strain rate in mixture fraction and PV spaces.

8.1 Introduction

The modelling of the conditional chemical reaction rate is critical for the successful application of CMC. In situations where fluctuations about the conditional means of the reactive scalars are small, the first-order closure (Sect. 3.3.5) is sufficient. A higher-order level of modelling becomes necessary when fluctuations are significant as in extinction

and re-ignition scenarios. The second-order closure (Sect. 3.6.2) has the advantage of incorporating the conditional variances and covariances of the reactive scalars in the modelling of the conditional reaction rates, and thereby provides an explicit treatment for the conditional fluctuations.

Another approach for the treatment of fluctuations is to introduce a second conditioning variable beside ξ, while maintaining a first-order closure for the conditional reaction rates. First proposed by Bilger [18, 19], this approach is known as the first-order DCMC. Contrary to the second-order CMC, the treatment of fluctuations in the first-order DCMC is implicit. The inclusion of a second conditioning variable renders the conditioning process more constrictive so that doubly-conditional means contain more information about the scalar field than singly-conditional means. Therefore, doubly-conditional fluctuations are of smaller order than their singly-conditional counterparts, which justifies the usage of the first-order closure. Despite this advantage, DCMC gives rise to a number of unclosed terms and increases the dimensionality of the governing equations.

The selection of the second conditioning variable is a challenging task. Three factors must be taken into account:

1. The strength of the correlation between the reactive scalars and the selected variable.
   A temperature-related reactive variable satisfies this factor due to the dependence of the reactive scalars on the temperature through the chemical reaction rates. On the other hand, a conserved (non-reactive) variable cannot correlate well with the reactive scalars unless it is somehow strongly coupled with the chemical time scales. Such variable is difficult to define.

2. The level of modelling complexity introduced by the variable.
   A conserved variable is more appealing due to the absence of chemical sources. It yields relatively simpler doubly-conditional transport equations and allows for a less complicated modelling for the resulting unclosed terms.

3. The description of joint statistics.
   Information regarding the nature of the correlation between ξ and the selected variable must be available in order to presume the joint PDF. Reactive variables are in general strongly dependent of ξ, making the assumption of statistical independence crude.

Several definitions for the second conditioning variable have been proposed. Based on experimental observations, Bilger suggests using a non-normalised reaction PV [18] or the temperature [19]. Following flamelet modelling strategies, Cha et al. [40] propose

the usage of the scalar dissipation rate, χ, since extinction events are associated with high levels of this quantity. Their *a priori* analysis shows that the model is capable of describing some features of extinction, but predicts the onset of re-ignition too early. They attribute this discrepancy to the neglect of the significant fluctuations about the doubly-conditional means, which occur at low values of the scalar dissipation rate with respect to the extinction value. Kronenburg [122,128] notes that although χ is a suitable indicator for extinction, this variable does not correlate well with the reactive scalars after the occurrence of extinction and neglects the role of the relevant chemical time scales. He argues that a temperature-related quantity is a more suitable choice because chemical reaction rates have a strong dependence on temperature. An obvious choice is the temperature itself, as proposed by Bilger [19]. However, Kronenburg [122] notes that the modelling of the conditional chemical source in the temperature equation is complicated due to the temperature-species cross gradient in the interdiffusion term. Instead, he suggests employing the sensible enthalpy, h_s. This choice is motivated by the fact that the modelling of the conditional source of h_s is more tractable under the assumption of unity Lewis numbers. The *a priori* assessment of the proposed formulation shows a remarkable agreement with DNS as local extinction and the onset of re-ignition are captured accurately. The homogeneous implementations of Cha et al. [40] and Kronenburg [122] rely on DNS databases in order to obtain the joint PDF and to close the doubly conditional dissipation terms. No modelling attempts are made in their studies. The chemistry included in both works is simple due to the computational restrictions of DNS. Cha et al. [40] use a single-step reversible reaction, whereas Kronenburg [122] employs a relatively more detailed kinetic scheme comprising two irreversible steps.

In this chapter, a DCMC method is proposed by introducing a normalised temperature-related PV as second conditioning variable beside ξ. The normalisation of the PV is performed such that unburnt and burnt states are dependent on ξ. Transport equations for the normalised PV and the doubly-conditional reactive scalars are derived. The primary closure hypothesis is applied and submodels for the unclosed doubly-conditioned unclosed terms are proposed. The model equations are then simplified for homogeneous turbulence and a parametric assessment is performed to investigate the effect of strain in mixture fraction and PV spaces. The conditions of the piloted CH_4/air Sandia flames are considered using reduced chemical kinetics.

8.2 The second conditioning variable

The second conditioning variable chosen for the current DCMC formulation is a temperature-related quantity following Bilger [18,19] and Kronenburg [122]. Possible definitions are the mass fraction of a species (or a combination of species) or the sensible enthalpy. At this stage, it is simply denoted by the generic variable ϕ. Here, ϕ is normalised such that it varies between 0 and 1. The unburnt and burnt states involved in the normalisation of ϕ are specified such that they are mixture fraction-dependent. The resulting second conditioning variable, c, is therefore written as:

$$c = \frac{\phi(\mathbf{x},t) - \phi_{min}(\xi(\mathbf{x},t))}{\phi_{max}(\xi(\mathbf{x},t)) - \phi_{min}(\xi(\mathbf{x},t))} \tag{8.1}$$

where $\phi_{max}(\xi(\mathbf{x},t))$ and $\phi_{min}(\xi(\mathbf{x},t))$ are, respectively, the maximum (burnt, $c=1$) and minimum (unburnt, $c=0$) values of ϕ at a given mixture fraction value. Assuming $\mathrm{Le}_\phi = 1$, ϕ is governed by the generic transport equation:

$$\underbrace{\rho\frac{\partial\phi}{\partial t}}_{\substack{\text{Local rate}\\ \text{of change}}} + \underbrace{\rho u_i\frac{\partial\phi}{\partial x_i}}_{\text{Convection}} = \underbrace{\frac{\partial}{\partial x_i}\left(\rho D\frac{\partial\phi}{\partial x_i}\right)}_{\text{Diffusion}} + \underbrace{\dot{\omega}_\phi}_{\substack{\text{Chemical}\\ \text{source}}} \tag{8.2}$$

To derive a transport equation for c, Eq. (8.1) is first rearranged as:

$$\phi = c\left[\phi_{max}(\xi) - \phi_{min}(\xi)\right] + \phi_{min}(\xi) \tag{8.3}$$

where the dependence of ϕ and ξ on $\mathbf{x}$ and t has been omitted for simplicity of notation. Using Eq. (8.3), the time derivative and gradient of ϕ and the diffusive term in Eq. (8.2) are transformed as:

$$\frac{\partial\phi}{\partial t} = \left[\phi_{max}(\xi) - \phi_{min}(\xi)\right]\frac{\partial c}{\partial t} + c\frac{d[\phi_{max}(\xi) - \phi_{min}(\xi)]}{d\xi}\frac{\partial\xi}{\partial t} + \frac{d\phi_{min}(\xi)}{d\xi}\frac{\partial\xi}{\partial t} \tag{8.4}$$

$$\frac{\partial\phi}{\partial x_i} = \left[\phi_{max}(\xi) - \phi_{min}(\xi)\right]\frac{\partial c}{\partial x_i} + c\frac{d[\phi_{max}(\xi) - \phi_{min}(\xi)]}{d\xi}\frac{\partial\xi}{\partial x_i} + \frac{d\phi_{min}(\xi)}{d\xi}\frac{\partial\xi}{\partial x_i} \tag{8.5}$$

$$\begin{aligned}\frac{\partial}{\partial x_i}\left(\rho D\frac{\partial\phi}{\partial x_i}\right) =& \left[\phi_{max}(\xi) - \phi_{min}(\xi)\right]\frac{\partial}{\partial x_i}\left(\rho D\frac{\partial c}{\partial x_i}\right)\\ &+ c\frac{d[\phi_{max}(\xi) - \phi_{min}(\xi)]}{d\xi}\frac{\partial}{\partial x_i}\left(\rho D\frac{\partial\xi}{\partial x_i}\right)\\ &+ \frac{d\phi_{min}(\xi)}{d\xi}\frac{\partial}{\partial x_i}\left(\rho D\frac{\partial\xi}{\partial x_i}\right) + \rho\frac{d[\phi_{max}(\xi) - \phi_{min}(\xi)]}{d\xi}\chi_{\xi,c}\\ &+ \rho c\frac{d^2[\phi_{max}(\xi) - \phi_{min}(\xi)]}{d\xi^2}\frac{\chi_\xi}{2} + \rho\frac{d^2\phi_{min}(\xi)}{d\xi^2}\frac{\chi_\xi}{2}\end{aligned} \tag{8.6}$$

where

$$\chi_\xi = 2D\frac{\partial \xi}{\partial x_i}\frac{\partial \xi}{\partial x_i} \tag{8.7}$$

and

$$\chi_{\xi,c} = 2D\frac{\partial \xi}{\partial x_i}\frac{\partial c}{\partial x_i} \tag{8.8}$$

are the dissipation of ξ and the cross-dissipation of ξ and c, respectively. Substituting Eqs. (8.4)-(8.6) in Eq. (8.2) yields:

$$\begin{aligned}
&[\phi_{max}(\xi) - \phi_{min}(\xi)]\left[\rho\frac{\partial c}{\partial t} + \rho u_i\frac{\partial c}{\partial x_i} - \frac{\partial}{\partial x_i}\left(\rho D\frac{\partial c}{\partial x_i}\right)\right] \\
&+c\frac{d}{d\xi}[\phi_{max}(\xi) - \phi_{min}(\xi)]\left[\rho\frac{\partial \xi}{\partial t} + \rho u_i\frac{\partial \xi}{\partial x_i} - \frac{\partial}{\partial x_i}\left(\rho D\frac{\partial \xi}{\partial x_i}\right)\right] \\
&+\frac{d\phi_{min}(\xi)}{d\xi}\left[\rho\frac{\partial \xi}{\partial t} + \rho u_i\frac{\partial \xi}{\partial x_i} - \frac{\partial}{\partial x_i}\left(\rho D\frac{\partial \xi}{\partial x_i}\right)\right] = \\
&\rho\frac{d[\phi_{max}(\xi) - \phi_{min}(\xi)]}{d\xi}\chi_{\xi,c} + \rho c\frac{d^2[\phi_{max}(\xi) - \phi_{min}(\xi)]}{d\xi^2}\frac{\chi_\xi}{2} + \rho\frac{d^2\phi_{min}(\xi)}{d\xi^2}\frac{\chi_\xi}{2} + \dot{\omega}_\phi
\end{aligned} \tag{8.9}$$

The second and third bracketed quantities on the left-hand side (l.h.s.) of Eq. (8.9) are zero via the mixture fraction transport equation (Eq. (2.77)). Dividing Eq. (8.9) by $[\phi_{max}(\xi) - \phi_{min}(\xi)]$ and rearranging lead to the transport equation of c:

$$\begin{aligned}
\rho\frac{\partial c}{\partial t} + \rho u_i\frac{\partial c}{\partial x_i} - \frac{\partial}{\partial x_i}\left(\rho D\frac{\partial c}{\partial x_i}\right) &= \frac{\rho}{\phi_{max}(\xi) - \phi_{min}(\xi)}\frac{d[\phi_{max}(\xi) - \phi_{min}(\xi)]}{d\xi}\chi_{\xi,c} \\
&+\frac{\rho}{\phi_{max}(\xi) - \phi_{min}(\xi)}\left(c\frac{d^2[\phi_{max}(\xi) - \phi_{min}(\xi)]}{d\xi^2} + \frac{d^2\phi_{min}(\xi)}{d\xi^2}\right)\frac{\chi_\xi}{2} + \dot{\omega}_c
\end{aligned} \tag{8.10}$$

where

$$\dot{\omega}_c = \frac{\dot{\omega}_\phi}{\phi_{max}(\xi) - \phi_{min}(\xi)} \tag{8.11}$$

Similar transport equations for c are derived in [28, 55, 56, 138].

8.3 Doubly-Conditional Moment Closure

The derivation of the doubly-conditional transport equations follows the same procedure outlined in Sect. 3.2. However, it is slightly more complicated due to the presence of two conditioning variables rather than one. In the following sections, the assumptions of unity Lewis numbers and equal diffusivities are invoked for simplicity.

8.3.1 Doubly-conditional species equation

The doubly conditional average of Y_κ is defined as:

$$Q_\kappa(\eta,\theta,\mathbf{x},t) = \langle Y_\kappa(\mathbf{x},t)|\xi=\eta, c=\theta\rangle \tag{8.12}$$

where η and θ are sample space variables of ξ and c, respectively. The decomposition approach proposed by Bilger [18,19] is adopted. Y_κ is decomposed into doubly-conditional average, Q_κ, and a fluctuation, y''_κ:

$$Y_\kappa(\mathbf{x},t) = Q_\kappa(\xi(\mathbf{x},t), c(\mathbf{x},t), \mathbf{x}, t) + y''_\kappa(\mathbf{x},t) \tag{8.13}$$

such that $\langle y''_\kappa(\mathbf{x},t)|\xi=\eta, c=\theta\rangle = 0$. Using Eq. (8.13), the time derivative and gradient of Y_κ and the diffusive term in the species transport equation, Eq. (3.1), are transformed as:

$$\frac{\partial Y_\kappa}{\partial t} = \frac{\partial Q_\kappa}{\partial \eta}\frac{\partial \xi}{\partial t} + \frac{\partial Q_\kappa}{\partial \theta}\frac{\partial c}{\partial t} + \frac{\partial Q_\kappa}{\partial t} + \frac{\partial y''_\kappa}{\partial t} \tag{8.14}$$

$$\frac{\partial Y_\kappa}{\partial x_i} = \frac{\partial Q_\kappa}{\partial \eta}\frac{\partial \xi}{\partial x_i} + \frac{\partial Q_\kappa}{\partial \theta}\frac{\partial c}{\partial x_i} + \frac{\partial Q_\kappa}{\partial x_i} + \frac{\partial y''_\kappa}{\partial x_i} \tag{8.15}$$

$$\begin{aligned}\frac{\partial}{\partial x_i}\left(\rho D\frac{\partial Y_\kappa}{\partial x_i}\right) =& \frac{\partial Q_\kappa}{\partial \eta}\frac{\partial}{\partial x_i}\left(\rho D\frac{\partial \xi}{\partial x_i}\right) + \rho\frac{\chi_\xi}{2}\frac{\partial^2 Q_\kappa}{\partial \eta^2} + \rho D\frac{\partial \xi}{\partial x_i}\frac{\partial}{\partial x_i}\left(\frac{\partial Q_\kappa}{\partial \eta}\right)\\ &+ \frac{\partial Q_\kappa}{\partial \theta}\frac{\partial}{\partial x_i}\left(\rho D\frac{\partial c}{\partial x_i}\right) + \rho\frac{\chi_c}{2}\frac{\partial^2 Q_\kappa}{\partial \theta^2} + \rho\chi_{\xi,c}\frac{\partial^2 Q_\kappa}{\partial \eta\partial\theta}\\ &+ \rho D\frac{\partial c}{\partial x_i}\frac{\partial}{\partial x_i}\left(\frac{\partial Q_\kappa}{\partial \theta}\right) + \frac{\partial}{\partial x_i}\left(\rho D\frac{\partial Q_\kappa}{\partial x_i}\right) + \frac{\partial}{\partial x_i}\left(\rho D\frac{\partial y''_\kappa}{\partial x_i}\right)\end{aligned} \tag{8.16}$$

where χ_ξ and $\chi_{\xi,c}$ are given by Eqs. (8.7) and (8.8), respectively, and

$$\chi_c = 2\rho D\frac{\partial c}{\partial x_i}\frac{\partial c}{\partial x_i} \tag{8.17}$$

is the dissipation of c. Substituting Eqs. (8.14)-(8.16) in Eq. (3.1) and grouping the terms having $\partial Q_\kappa/\partial\eta$ and $\partial Q_\kappa/\partial\theta$ lead to:

$$\begin{aligned}&\rho\frac{\partial Q_\kappa}{\partial t} + \rho u_i\frac{\partial Q_\kappa}{\partial x_i} + \frac{\partial Q_\kappa}{\partial \eta}\left[\rho\frac{\partial \xi}{\partial t} + \rho u_i\frac{\partial \xi}{\partial x_i} - \frac{\partial}{\partial x_i}\left(\rho D\frac{\partial \xi}{\partial x_i}\right)\right]\\ &+\frac{\partial Q_\kappa}{\partial \theta}\left[\rho\frac{\partial c}{\partial t} + \rho u_i\frac{\partial c}{\partial x_i} - \frac{\partial}{\partial x_i}\left(\rho D\frac{\partial c}{\partial x_i}\right)\right] = \rho\frac{\chi_\xi}{2}\frac{\partial^2 Q_\kappa}{\partial \eta^2} + \rho\frac{\chi_c}{2}\frac{\partial^2 Q_\kappa}{\partial \theta^2} + \rho\chi_{\xi,c}\frac{\partial^2 Q_\kappa}{\partial\eta\partial\theta}\\ &+\left[\rho D\frac{\partial \xi}{\partial x_i}\frac{\partial}{\partial x_i}\left(\frac{\partial Q_\kappa}{\partial \eta}\right) + \rho D\frac{\partial c}{\partial x_i}\frac{\partial}{\partial x_i}\left(\frac{\partial Q_\kappa}{\partial \theta}\right) + \frac{\partial}{\partial x_i}\left(\rho D\frac{\partial Q_\kappa}{\partial x_i}\right)\right]\\ &-\left[\rho\frac{\partial y''_\kappa}{\partial t} + \rho u_i\frac{\partial y''_\kappa}{\partial x_i} - \frac{\partial}{\partial x_i}\left(\rho D\frac{\partial y''_\kappa}{\partial x_i}\right)\right] + \dot{\omega}_\kappa\end{aligned} \tag{8.18}$$

The first bracketed quantity on the l.h.s of Eq. (8.18) is zero via the transport equation of ξ, Eq. (2.77). Substituting the second bracketed quantity by the r.h.s. of the transport equation of c, Eq. (8.10), and rearranging result in:

$$\begin{aligned}
&\rho\frac{\partial Q_\kappa}{\partial t}+\rho u_i\frac{\partial Q_\kappa}{\partial x_i}= \\
&\rho\frac{\chi_\xi}{2}\left[\frac{\partial^2 Q_\kappa}{\partial\eta^2}-\frac{1}{\phi_{max}(\xi)-\phi_{min}(\xi)}\left(c\frac{d^2[\phi_{max}(\xi)-\phi_{min}(\xi)]}{d\xi^2}+\frac{d^2\phi_{min}(\xi)}{d\xi^2}\right)\frac{\partial Q_\kappa}{\partial\theta}\right] \\
&+\rho\frac{\chi_c}{2}\frac{\partial^2 Q_\kappa}{\partial\theta^2}+\rho\chi_{\xi,c}\left(\frac{\partial^2 Q_\kappa}{\partial\eta\partial\theta}-\frac{1}{\phi_{max}(\xi)-\phi_{min}(\xi)}\frac{d[\phi_{max}(\xi)-\phi_{min}(\xi)]}{d\xi}\frac{\partial Q_\kappa}{\partial\theta}\right) \\
&+\left[\rho D\frac{\partial\xi}{\partial x_i}\frac{\partial}{\partial x_i}\left(\frac{\partial Q_\kappa}{\partial\eta}\right)+\rho D\frac{\partial c}{\partial x_i}\frac{\partial}{\partial x_i}\left(\frac{\partial Q_\kappa}{\partial\theta}\right)+\frac{\partial}{\partial x_i}\left(\rho D\frac{\partial Q_\kappa}{\partial x_i}\right)\right] \\
&-\left[\rho\frac{\partial y''_\kappa}{\partial t}+\rho u_i\frac{\partial y''_\kappa}{\partial x_i}-\frac{\partial}{\partial x_i}\left(\rho D\frac{\partial y''_\kappa}{\partial x_i}\right)\right]+\dot\omega_\kappa-\dot\omega_c\frac{\partial Q_\kappa}{\partial\theta}
\end{aligned}\tag{8.19}$$

Finally, taking the doubly-conditional average of Eq. (8.19) with respect to $\xi(\mathbf{x},t)=\eta$ and $c(\mathbf{x},t)=\theta$ while neglecting density fluctuations results in the doubly-conditional species transport equation[1]:

$$\begin{aligned}
&\frac{\partial Q_\kappa}{\partial t}+\langle u_i|\eta,\theta\rangle\frac{\partial Q_\kappa}{\partial x_i}= \\
&\frac{\langle\chi_\xi|\eta,\theta\rangle}{2}\left[\frac{\partial^2 Q_\kappa}{\partial\eta^2}-\frac{1}{\phi_{max}(\eta)-\phi_{min}(\eta)}\left(\theta\frac{d^2[\phi_{max}(\eta)-\phi_{min}(\eta)]}{d\eta^2}+\frac{d^2\phi_{min}(\eta)}{d\eta^2}\right)\frac{\partial Q_\kappa}{\partial\theta}\right] \\
&+\langle\chi_{\xi,c}|\eta,\theta\rangle\left(\frac{\partial^2 Q_\kappa}{\partial\eta\partial\theta}-\frac{1}{\phi_{max}(\eta)-\phi_{min}(\eta)}\frac{d[\phi_{max}(\eta)-\phi_{min}(\eta)]}{d\eta}\frac{\partial Q_\kappa}{\partial\theta}\right) \\
&+\frac{\langle\chi_c|\eta,\theta\rangle}{2}\frac{\partial^2 Q_\kappa}{\partial\theta^2}+\frac{\langle\dot\omega_\kappa|\eta,\theta\rangle}{\langle\rho|\eta,\theta\rangle}-\frac{\langle\dot\omega_c|\eta,\theta\rangle}{\langle\rho|\eta,\theta\rangle}\frac{\partial Q_\kappa}{\partial\theta}+\frac{e_{Q_\kappa}}{\langle\rho|\eta,\theta\rangle}+\frac{e_{y''_\kappa}}{\langle\rho|\eta,\theta\rangle}
\end{aligned}\tag{8.20}$$

where

$$e_{Q_\kappa}=\frac{\partial}{\partial x_i}\left(\rho D\frac{\partial Q_\kappa}{\partial x_i}\right)+\left\langle\rho D\frac{\partial\xi}{\partial x_i}\frac{\partial}{\partial x_i}\left(\frac{\partial Q_\kappa}{\partial\eta}\right)+\rho D\frac{\partial c}{\partial x_i}\frac{\partial}{\partial x_i}\left(\frac{\partial Q_\kappa}{\partial\theta}\right)\middle|\eta,\theta\right\rangle \tag{8.21}$$

and

$$e_{y''_\kappa}=-\left\langle\rho\frac{\partial y''_\kappa}{\partial t}+\rho u_i\frac{\partial y''_\kappa}{\partial x_i}-\frac{\partial}{\partial x_i}\left(\rho D\frac{\partial y''_\kappa}{\partial x_i}\right)\middle|\eta,\theta\right\rangle \tag{8.22}$$

[1]The notation $\langle\cdot|\eta,\theta\rangle$ is used in Eqs. (8.20)–(8.22) instead of $\langle\cdot|\xi(\mathbf{x},t)=\eta,c(\mathbf{x},t)=\theta\rangle$ for brevity.

As it stands, Eq. (8.20) is similar to the equation derived by Kronenburg [122]. In comparison to Eq. (6) in [122] (with equal diffusivities), Eq. (8.20) contains additional terms involving the ordinary derivatives of $\phi_{max}(\eta)$ and $\phi_{min}(\eta)$. These terms arise from the normalisation of ϕ and from the dependence of ϕ_{max} and ϕ_{min} on ξ (see Eq. (8.1)).

8.3.2 Doubly-conditional energy equation

This section outlines the derivation of the doubly-conditional enthalpy, sensible enthalpy and temperature transport equations.

Enthalpy

Assuming unity Lewis numbers and equal diffusivities, and neglecting viscous heating and pressure effects, the enthalpy transport equation (Eq. (2.19)) reduces to:

$$\rho\frac{\partial h}{\partial t}+\rho u_i\frac{\partial h}{\partial x_i}=\frac{\partial}{\partial x_i}\left(\rho D\frac{\partial h}{\partial x_i}\right)+\frac{\partial p}{\partial t}+\dot{\omega}_r \tag{8.23}$$

The enthalpy is decomposed as $h(x_i,t)=Q_h(\xi(\mathbf{x},t),c(\mathbf{x},t),\mathbf{x},t)+h''(\mathbf{x},t)$ such that $\langle h''(\mathbf{x},t)|\xi=\eta,c=\theta\rangle=0$. Using the transformations given by Eqs. (8.4), (8.5) and (8.6), and following the procedure outlined in Sect. 8.3.1, it can be easily shown that:

$$\begin{aligned}\frac{\partial Q_h}{\partial t}+\langle u_i|\eta,\theta\rangle\frac{\partial Q_h}{\partial x_i}&=\frac{\langle\chi_\xi|\eta,\theta\rangle}{2}\left[\frac{\partial^2 Q_h}{\partial\eta^2}\right.\\&\left.-\frac{1}{\phi_{max}(\eta)-\phi_{min}(\eta)}\left(\theta\frac{d^2[\phi_{max}(\eta)-\phi_{min}(\eta)]}{d\eta^2}+\frac{d^2\phi_{min}(\eta)}{d\eta^2}\right)\frac{\partial Q_h}{\partial\theta}\right]\\&+\langle\chi_{\xi,c}|\eta,\theta\rangle\left(\frac{\partial^2 Q_h}{\partial\eta\partial\theta}-\frac{1}{\phi_{max}(\eta)-\phi_{min}(\eta)}\frac{d[\phi_{max}(\eta)-\phi_{min}(\eta)]}{d\eta}\frac{\partial Q_h}{\partial\theta}\right)\\&+\frac{\langle\chi_c|\eta,\theta\rangle}{2}\frac{\partial^2 Q_h}{\partial\theta^2}-\frac{\langle\dot{\omega}_c|\eta,\theta\rangle}{\langle\rho|\eta,\theta\rangle}\frac{\partial Q_h}{\partial\theta}+\frac{\langle\dot{\omega}_r|\eta,\theta\rangle}{\langle\rho|\eta,\theta\rangle}+\frac{\langle\partial p/\partial t|\eta,\theta\rangle}{\langle\rho|\eta,\theta\rangle}+\frac{e_{Q_h}}{\langle\rho|\eta,\theta\rangle}+\frac{e_{h''}}{\langle\rho|\eta,\theta\rangle}\end{aligned} \tag{8.24}$$

where e_{Q_h} and $e_{h''}$ are given by Eqs. (8.21) and (8.22) with Q_{Y_κ} and y''_κ replaced by Q_h and h'', respectively.

Sensible enthalpy

The sensible enthalpy equation has the same form as Eq. (8.23) with h replaced by h_s in addition to the chemical source term $\dot{\omega}_{h_s}=-\sum_{\kappa=1}^{N_s}h^\circ_{f,\kappa}\dot{\omega}_\kappa$ on the r.h.s. of the equa-

tion. Therefore, the doubly-conditional sensible enthalpy equation follows directly from Eq. (8.24) with an additional conditional chemical source on the r.h.s.:

$$\begin{aligned}
&\frac{\partial Q_{h_s}}{\partial t} + \langle u_i|\eta,\theta\rangle \frac{\partial Q_{h_s}}{\partial x_i} = \frac{\langle \chi_\xi|\eta,\theta\rangle}{2}\left[\frac{\partial^2 Q_{h_s}}{\partial \eta^2}\right. \\
&\left. -\frac{1}{\phi_{max}(\eta)-\phi_{min}(\eta)}\left(\theta\frac{d^2[\phi_{max}(\eta)-\phi_{min}(\eta)]}{d\eta^2} + \frac{d^2\phi_{min}(\eta)}{d\eta^2}\right)\frac{\partial Q_{h_s}}{\partial \theta}\right] \\
&+\langle \chi_{\xi,c}|\eta,\theta\rangle\left(\frac{\partial^2 Q_{h_s}}{\partial\eta\partial\theta} - \frac{1}{\phi_{max}(\eta)-\phi_{min}(\eta)}\frac{d[\phi_{max}(\eta)-\phi_{min}(\eta)]}{d\eta}\frac{\partial Q_{h_s}}{\partial\theta}\right) \\
&+\frac{\langle\chi_c|\eta,\theta\rangle}{2}\frac{\partial^2 Q_{h_s}}{\partial\theta^2} - \frac{\sum_{\kappa=1}^{N_s} h^\circ_{f,\kappa}\langle\dot\omega_\kappa|\eta,\theta\rangle}{\langle\rho|\eta,\theta\rangle} - \frac{\langle\dot\omega_c|\eta,\theta\rangle}{\langle\rho|\eta,\theta\rangle}\frac{\partial Q_{h_s}}{\partial\theta} + \frac{\langle\dot\omega_r|\eta,\theta\rangle}{\langle\rho|\eta,\theta\rangle} \\
&+\frac{\langle\partial p/\partial t|\eta,\theta\rangle}{\langle\rho|\eta,\theta\rangle} + \frac{e_{Q_{h_s}}}{\langle\rho|\eta,\theta\rangle} + \frac{e_{h_s''}}{\langle\rho|\eta,\theta\rangle}
\end{aligned} \tag{8.25}$$

Similarly, $e_{Q_{h_s}}$ and $e_{h_s''}$ are given by Eqs. (8.21) and (8.22) with Q_{Y_κ} and y_κ'' replaced by Q_{h_s} and h_s'', respectively.

Temperature

A detailed derivation of the doubly-conditional temperature equation is provided in Appendix B. Assuming that the specific heats are independent of position and setting all Lewis numbers to unity, the end result is given by:

$$
\begin{aligned}
&\frac{\partial Q_T}{\partial t} + \langle u_i|\eta,\theta\rangle\frac{\partial Q_T}{\partial x_i} = \\
&\frac{\langle\chi_\xi|\eta,\theta\rangle}{2}\left\{\frac{\partial^2 Q_T}{\partial\eta^2} + \frac{1}{\langle c_p|\eta,\theta\rangle}\left[\frac{\partial\langle c_p|\eta,\theta\rangle}{\partial\eta} + \sum_{\kappa=1}^{N_s}\left(\langle c_{p,\kappa}|\eta,\theta\rangle\frac{\partial Q_\kappa}{\partial\eta}\right)\right]\frac{\partial Q_T}{\partial\eta}\right. \\
&\left. -\frac{1}{\phi_{max}(\eta)-\phi_{min}(\eta)}\left(c\frac{d^2[\phi_{max}(\eta)-\phi_{min}(\eta)]}{d\eta^2} + \frac{d^2\phi_{min}(\eta)}{d\eta^2}\right)\frac{\partial Q_T}{\partial\theta}\right\} \\
&+\frac{\langle\chi_c|\eta,\theta\rangle}{2}\left\{\frac{\partial^2 Q_T}{\partial\theta^2} + \frac{1}{\langle c_p|\eta,\theta\rangle}\left[\frac{\partial\langle c_p|\eta,\theta\rangle}{\partial\theta} + \sum_{\kappa=1}^{N_s}\left(\langle c_{p,\kappa}|\eta,\theta\rangle\frac{\partial Q_\kappa}{\partial\theta}\right)\right]\frac{\partial Q_T}{\partial\theta}\right\} \\
&+\langle\chi_{\xi,c}|\eta,\theta\rangle\left\{\frac{\partial^2 Q_T}{\partial\eta\partial\theta} + \frac{1}{2\langle c_p|\eta,\theta\rangle}\left[\frac{\partial\langle c_p|\eta,\theta\rangle}{\partial\eta} + \sum_{\kappa=1}^{N_s}\left(\langle c_{p,\kappa}|\eta,\theta\rangle\frac{\partial Q_\kappa}{\partial\eta}\right)\right]\frac{\partial Q_T}{\partial\theta}\right. \\
&+\frac{1}{2\langle c_p|\eta,\theta\rangle}\left[\frac{\partial\langle c_p|\eta,\theta\rangle}{\partial\theta} + \sum_{\kappa=1}^{N_s}\left(\langle c_{p,\kappa}|\eta,\theta\rangle\frac{\partial Q_\kappa}{\partial\theta}\right)\right]\frac{\partial Q_T}{\partial\eta} \\
&\left. -\frac{1}{\phi_{max}(\eta)-\phi_{min}(\eta)}\frac{d[\phi_{max}(\eta)-\phi_{min}(\eta)]}{d\eta}\frac{\partial Q_T}{\partial\theta}\right\} + \frac{\langle\partial p/\partial t|\eta,\theta\rangle}{\langle\rho|\eta,\theta\rangle\langle c_p|\eta,\theta\rangle} \\
&-\frac{\sum_{\kappa=1}^{N_s}\langle h_\kappa|\eta,\theta\rangle\langle\dot\omega_\kappa|\eta,\theta\rangle}{\langle\rho|\eta,\theta\rangle\langle c_p|\eta,\theta\rangle} - \frac{\langle\dot\omega_c|\eta,\theta\rangle}{\langle\rho|\eta,\theta\rangle}\frac{\partial Q_T}{\partial\theta} + \frac{\langle\dot\omega_r|\eta,\theta\rangle}{\langle\rho|\eta,\theta\rangle\langle c_p|\eta,\theta\rangle} + \frac{e_{Q_T}+e_{T''}+e_{c_p}}{\langle\rho|\eta,\theta\rangle\langle c_p|\eta,\theta\rangle}
\end{aligned}
\tag{8.26}
$$

where

$$
e_{Q_T} = \frac{\partial}{\partial x_i}\left(\rho c_p D\frac{\partial Q_T}{\partial x_i}\right) + \left\langle c_p\left[\rho D\frac{\partial\xi}{\partial x_i}\frac{\partial}{\partial x_i}\left(\frac{\partial Q_T}{\partial\eta}\right) + \rho D\frac{\partial c}{\partial x_i}\frac{\partial}{\partial x_i}\left(\frac{\partial Q_T}{\partial\theta}\right)\right]\middle|\eta,\theta\right\rangle \tag{8.27}
$$

$$
e_{T''} = \left\langle c_p\left[\rho\frac{\partial T''}{\partial t} + \rho u_i\frac{\partial T''}{\partial x_i} - \frac{\partial}{\partial x_i}\left(\rho D\frac{\partial T''}{\partial x_i}\right)\right]\middle|\eta,\theta\right\rangle \tag{8.28}
$$

$$
\begin{aligned}
e_{c_p} = &\left\langle\rho D\left\{\sum_{\kappa=1}^{N_s}\left[c_{p,\kappa}\left(\frac{\partial Q_T}{\partial x_i}+\frac{\partial T''}{\partial x_i}\right)\left(\frac{\partial Q_\kappa}{\partial\eta}\frac{\partial\xi}{\partial x_i}+\frac{\partial Q_\kappa}{\partial\theta}\frac{\partial c}{\partial x_i}\right)\right.\right.\right. \\
&\left.+\left(\frac{\partial Q_\kappa}{\partial x_i}+\frac{\partial y''_\kappa}{\partial x_i}\right)\left(\frac{\partial Q_T}{\partial\eta}\frac{\partial\xi}{\partial x_i}+\frac{\partial Q_T}{\partial\theta}\frac{\partial c}{\partial x_i}+\frac{\partial Q_T}{\partial x_i}+\frac{\partial T''}{\partial x_i}\right)\right] \\
&\left.\left.+\left(\frac{\partial Q_T}{\partial x_i}+\frac{\partial T''}{\partial x_i}\right)\left(\frac{\partial\langle c_p|\eta,\theta\rangle}{\partial\eta}\frac{\partial\xi}{\partial x_i}+\frac{\partial\langle c_p|\eta,\theta\rangle}{\partial\theta}\frac{\partial c}{\partial x_i}\right)\right\}\right|\eta,\theta\right\rangle
\end{aligned}
\tag{8.29}
$$

It is obvious that Eq. (8.26) involves more assumptions compared to the conditional enthalpy equations, Eqs. (8.24) and (8.25). In the former, c_p is assumed to be independent from $\mathbf{x}$, hence the spatial derivatives of $\langle c_p|\eta,\theta\rangle$ and c_p'' are neglected. Further, Eq. (8.26) yields the additional unclosed term e_{c_p}. The relevance of this term is not easy to quantify. Therefore, Eqs. (8.24) and (8.25) are in general more accurate.

8.3.3 Primary closure hypothesis

The primary closure hypothesis [18,20,120] employed in CMC is invoked in order to model the terms e_{Q_κ} (Eq. (8.21)) and $e_{y_\kappa''}$ (Eq. (8.22)). The procedure described in Sect. 3.2.1 is followed here. Given finite Sc, ρD scales as Re^{-1}. Therefore, all the terms in Eq. (8.21) may be neglected in high Re flows, leading to:

$$e_{Q_\kappa} \approx 0 \tag{8.30}$$

As in Eq. (3.14), the unconditional mean of $e_{y_\kappa''}$ is obtained via:

$$\int_0^1\int_0^1 e_{y_\kappa''}P_{\xi,c}(\eta,\theta)d\eta d\theta = -\frac{\partial\left\langle\rho y_\kappa''\right\rangle}{\partial t} - \frac{\partial\left\langle\rho u_i y_\kappa''\right\rangle}{\partial x_i} + \frac{\partial}{\partial x_i}\left\langle\rho D\frac{\partial y_\kappa''}{\partial x_i}\right\rangle \tag{8.31}$$

where $P_{\xi,c}(\eta,\theta)$ is the joint PDF of ξ and c. The first and last terms on the r.h.s. of Eq. (8.31) may be discarded if the density and diffusivity fluctuations are neglected ($\langle y_\kappa''|\eta,\theta\rangle = 0 \Rightarrow \langle y_\kappa''\rangle = \int_0^1\int_0^1\langle y_\kappa''|\eta,\theta\rangle P_{\xi,c}(\eta,\theta)d\eta d\theta = 0$). By further decomposing the velocity into the sum of a doubly-conditional mean and a fluctuation, its is easy to show that Eq. (8.31) reduces to (see Eq. (3.20)):

$$\int_0^1\int_0^1 e_{y_\kappa''}P_{\xi,c}(\eta,\theta)d\eta d\theta \approx \int_0^1\int_0^1 \frac{\partial}{\partial x_i}\left(\langle\rho|\eta,\theta\rangle\langle u_i''y_\kappa''|\eta,\theta\rangle P_{\xi,c}(\eta,\theta)\right)d\eta d\theta \tag{8.32}$$

which leads to:

$$e_{y_\kappa''} \approx -\frac{\langle\rho|\eta,\theta\rangle}{\langle\rho\rangle\tilde{P}_{\xi,c}(\eta,\theta)}\frac{\partial}{\partial x_i}\left(\langle u_i''y_\kappa''|\eta,\theta\rangle\langle\rho\rangle\tilde{P}_{\xi,c}(\eta,\theta)\right) \tag{8.33}$$

where $\tilde{P}_{\xi,c}$ is the Favre joint PDF of ξ and c.

The treatment of the terms e_{Q_h}, $e_{Q_{h_s}}$, e_{Q_T}, $e_{h''}$, $e_{h_s''}$ and $e_{T''}$ is accomplished in a similar fashion. If the temperature equation is adopted, the term e_{c_p} may be neglected in high Re flows (since $\rho D \sim \mathrm{Re}^{-1}$).

8.3.4 Unconditional averages

Upon solving the system of doubly-conditional transport equations, the Favre-averaged species mass fractions and temperature are obtained from:

$$\tilde{Y}_\kappa = \int_0^1 \int_0^1 \langle Y_\kappa|\eta,\theta\rangle \tilde{P}_{\xi,c}(\eta,\theta)d\eta d\theta = \int_0^1 \int_0^1 Q_\kappa \tilde{P}_{\xi,c}(\eta,\theta)d\eta d\theta; \quad \kappa = 1,2,\ldots,N_s \tag{8.34}$$

and

$$\tilde{T} = \int_0^1 \int_0^1 \langle T|\eta,\theta\rangle \tilde{P}_{\xi,c}(\eta,\theta)d\eta d\theta = \int_0^1 \int_0^1 Q_T \tilde{P}_{\xi,c}(\eta,\theta)d\eta d\theta \tag{8.35}$$

The mean density is computed using:

$$\langle\rho\rangle = \left(\int_0^1 \int_0^1 \langle\rho|\eta,\theta\rangle^{-1} \tilde{P}_{\xi,c}(\eta,\theta)d\eta d\theta\right)^{-1} \tag{8.36}$$

8.4 Doubly-conditional submodels

The closure of the DCMC equations requires the modelling of $\tilde{P}_{\xi,c}(\eta,\theta)$, $\langle u_i''\psi''|\eta,\theta\rangle$ ($\psi = \{y_\kappa''|\kappa = 1,2,\ldots,N_s\}$, and h'', h_s'' or T''), $\langle u_i|\eta,\theta\rangle$, $\langle\chi_\xi|\eta,\theta\rangle$, $\langle\chi_c|\eta,\theta\rangle$, $\langle\chi_{\xi,c}|\eta,\theta\rangle$, $\langle\dot{\omega}_\kappa|\eta,\theta\rangle$ ($\kappa = 1,2,\ldots,N_s$) and $\langle\dot{\omega}_r|\eta,\theta\rangle$. This section presents possible closures for these quantities.

8.4.1 Joint probability density function

Using Bayes' theorem, the joint PDF of ξ and c is written as:

$$\tilde{P}_{\xi,c}(\eta,\theta) = \tilde{P}_\xi(\eta)\tilde{P}_{c|\xi}(\theta|\eta) \tag{8.37}$$

where $\tilde{P}_\xi(\eta)$ is the marginal PDF of ξ and $\tilde{P}_{c|\xi}(\theta|\eta)$ is the conditional PDF of c with respect to ξ. If ξ and c are statistically independent,

$$\tilde{P}_{c|\xi}(\theta|\eta) = \tilde{P}_c(\theta) \tag{8.38}$$

where $\tilde{P}_c$ is the marginal PDF of c. In this case, Eq. (8.37) becomes:

$$\tilde{P}_{\xi,c} = \tilde{P}_\xi(\eta)\tilde{P}_c(\theta) \tag{8.39}$$

Although the assumption of statistical independence between c and ξ is questionable (notice the explicit dependence of c on ξ in Eq. (8.1)), Eq. (8.39) is often employed [55, 69–71, 75, 153, 229] for simplicity. Unlike the marginal PDF of ξ, there is no clear consensus in the literature in regards to the presumed form of the conditional and marginal PDFs of c.

Marginal PDF of ξ

The most commonly presumed distribution for $\tilde{P}_\xi(\eta)$ is the β-PDF (Eq. (3.37)). Other options include include the PMF-PDF (Eq. (3.63)), the CG-PDF (Eq. (3.42)) or the three-part composite PDF [57]. All four distributions require the solution of the $\tilde{\xi}$ and $\widetilde{\xi''^2}$ transport equations given by Eqs. (2.80) and (2.86), respectively.

Conditional PDF of c with respect to ξ

Kronenburg et al. [127,129] set $\phi = h_s$ in Eq. (8.1) and presume $\tilde{P}_{\xi|c}(\eta,\theta)$ using the β-PDF, which is given by Eq. (3.37) with $\tilde{\xi}$ and $\widetilde{\xi''^2}$ in Eqs. (3.38)-(3.40) replaced by $\langle c|\xi=\eta\rangle$ and $\langle c''^2|\xi=\eta\rangle$, respectively. A such, this distribution requires the knowledge of the first and second conditional moments of c with respect to ξ. Taking the conditional average of c as defined in Eq. (8.1) with respect to $\xi=\eta$ yields:

$$\langle c|\eta\rangle = \frac{\langle\phi|\eta\rangle - \phi_{min}(\eta)}{\phi_{max}(\eta) - \phi_{min}(\eta)} \tag{8.40}$$

where $\langle\phi|\eta\rangle$ is obtained from $\langle\phi|\eta,\theta\rangle$:

$$\langle\phi|\eta\rangle = \int_0^1 \langle\phi|\eta,\theta\rangle^D \tilde{P}_{c|\xi}(\theta|\eta)d\theta \tag{8.41}$$

The superscript "D" in Eq. (8.41) indicates that the quantity involved is obtained from the DCMC solution. Using the decomposition $c = \langle c|\eta\rangle + c''$, the conditional variance of c is written as:

$$\langle c''^2|\eta\rangle = \langle c^2|\eta\rangle - \langle c|\eta\rangle^2 \tag{8.42}$$

Substituting the conditional average of c^2 with respect to $\xi=\eta$ and Eq. (8.40) in Eq. (8.42) results in:

$$\langle c''^2|\eta\rangle = \frac{\langle\phi''^2|\eta\rangle}{[\phi_{max}(\eta) - \phi_{min}(\eta)]^2} \tag{8.43}$$

where $\langle\phi''^2|\eta\rangle$ is the conditional variance of ϕ. Hence, to evaluate $\langle c''^2|\eta\rangle$, the transport equation of $\langle\phi''^2|\eta\rangle$ needs to be solved. When c is defined in terms of some species mass fractions, this equation can be easily obtained from Eq. (3.100) by applying the following manipulations: (1) y_ι'' and y_κ'' are replaced with ϕ'', (2) Q_ι and Q_κ are replaced by $\langle\phi|\eta\rangle$,

(3) $\dot{\omega}_\iota''$ and $\dot{\omega}_\kappa''$ are replaced by $\dot{\omega}_\phi''$ (4) $J_{g,\iota\kappa}$ is replaced by $J_{g,\phi\phi}$ and (5) the subscript ξ is added to $P(\eta)$, χ and χ''. The resulting expression takes the form:

$$\begin{aligned}\frac{\partial\langle\phi''^2|\eta\rangle}{\partial t} =& -\langle u_i|\eta\rangle\frac{\partial\langle\phi''^2|\eta\rangle}{\partial x_i} + \frac{\langle\chi_\xi|\eta\rangle}{2}\frac{\partial^2\langle\phi''^2|\eta\rangle}{\partial\eta^2} - \frac{1}{\langle\rho|\eta\rangle P_\xi(\eta)}\frac{\partial}{\partial x_i}\left[\langle\rho|\eta\rangle\langle u_i''\phi''^2|\eta\rangle P_\xi(\eta)\right] \\ & - 2\langle u_i''\phi''|\eta\rangle\frac{\partial\langle\phi|\eta\rangle}{\partial x_i} + \frac{1}{\langle\rho|\eta\rangle P_\xi(\eta)}\frac{\partial J_{g,\phi\phi}}{\partial x_i} - 2\left\langle D\frac{\partial\phi''}{\partial x_i}\frac{\partial\phi''}{\partial x_i}\middle|\eta\right\rangle \\ & + 2\langle\dot{\omega}_\phi''\phi''|\eta\rangle + \langle\chi_\xi''\phi''|\eta\rangle\frac{\partial^2\langle\phi|\eta\rangle}{\partial\eta^2}\end{aligned} \tag{8.44}$$

All the r.h.s. terms are unclosed. Closures were presented in Sect. 3.6.2. The manipulations used in the process of obtaining Eq. (8.44) apply to these closures.

Marginal PDF of c

When ξ and c are assumed to be statistically independent, their joint PDF is expressed as the product of their corresponding marginal PDFs (see Eq. (8.39)). In this case a model for $\tilde{P}_c(\theta)$ is required. In several numerical studies [55,69–71,75,153,229], $\tilde{P}_c(\theta)$ is presumed using the β distribution, which is given by Eq. (3.37) with $\tilde{\xi}$ and $\widetilde{\xi''^2}$ in Eqs. (3.38)-(3.40) replaced by $\tilde{c}$ and $\widetilde{c''^2}$, respectively. One discrepancy of this PDF is its inability to describe distributions involving a peak at $c = 0$ (unburnt gases) or $c = 1$ (burnt gases) with an intermediate maximum in the range $0 < c < 1$ [187]. The CG-PDF described in Sect. 3.3.1 could be employed instead in order to resolve this issue. Such PDFs require the first and second moments of c. Formally, these moments should obtained from their respective transport equations. However, since these equations involve several unclosed requiring additional modelling, a different approach is adopted. As in [55, 69–71, 75, 153, 229], it is possible to approximate $\tilde{c}$ and $\widetilde{c''^2}$ from $\tilde{\phi}$ and $\widetilde{\phi^2}$, which are described by relatively less complicated transport equations. The mean is obtained from (see Appendix C):

$$\tilde{c} = \frac{\tilde{\phi} - \tilde{\phi}_{min}}{\tilde{\phi}_{max} - \tilde{\phi}_{min}} \tag{8.45}$$

where

$$\begin{aligned}\tilde{\phi} &= \int_0^1\int_0^1 \langle\phi|\eta,\theta\rangle^D \tilde{P}_\xi(\eta)\tilde{P}_c(\theta)d\eta d\theta; \\ \tilde{\phi}_{min} &= \int_0^1 \phi_{min}(\eta)\tilde{P}_\xi(\eta)d\eta; \quad \tilde{\phi}_{max} = \int_0^1 \phi_{max}(\eta)\tilde{P}_\xi(\eta)d\eta\end{aligned} \tag{8.46}$$

The variance is calculated as (see Appendix C):

$$\widetilde{c''^2} = \frac{1}{\widetilde{(\Delta\phi)^2}}\left[\widetilde{\phi^2} - \left(\frac{\tilde{\phi}-\tilde{\phi}_{min}}{\tilde{\phi}_{max}-\tilde{\phi}_{min}}\right)^2 \widetilde{(\Delta\phi)^2} - 2\left(\frac{\tilde{\phi}-\tilde{\phi}_{min}}{\tilde{\phi}_{max}-\tilde{\phi}_{min}}\right)(\widetilde{\phi_{max}\phi_{min}} - \widetilde{\phi^2_{min}}) - \widetilde{\phi^2_{min}}\right] \tag{8.47}$$

where

$$\widetilde{\phi_{max}\phi_{min}} = \int_0^1 \phi_{max}(\eta)\phi_{min}(\eta)\tilde{P}_\xi(\eta)d\eta;$$
$$\widetilde{\phi^2_{min}} = \int_0^1 \phi^2_{min}(\eta)\tilde{P}_\xi(\eta)d\eta; \quad \widetilde{(\Delta\phi)^2} = \int_0^1 [\phi_{max}(\eta)-\phi_{min}(\eta)]^2\tilde{P}_\xi(\eta)d\eta \tag{8.48}$$

The same expression is employed in [70, 71], whereas a simpler form is used in [55, 75, 153, 229] (in these studies, $\phi_{min}(\eta) = 0$ and therefore, $\tilde{\phi}_{min} = \widetilde{\phi_{max}\phi_{min}} = \widetilde{\phi^2_{min}} = 0$ and $\widetilde{(\Delta\phi)^2} = \widetilde{\phi^2_{max}}$). The condition $0 \leq \widetilde{c''^2} \leq \max(\widetilde{c''^2})$ where $\max(\widetilde{c''^2}) = \tilde{c}(1-\tilde{c})$ must be checked. $\widetilde{\phi^2}$ may be obtained in two different ways. Ideally,

$$\widetilde{\phi^2} = \int_0^1\int_0^1 \langle\phi^2|\eta,\theta\rangle^D \tilde{P}_\xi(\eta)\tilde{P}_c(\theta)d\eta d\theta \tag{8.49}$$

If the doubly-conditional variance of ϕ is neglected to a first-order approximation, $\widetilde{\phi^2}$ may be estimated from:

$$\widetilde{\phi^2} \approx \int_0^1\int_0^1 [\langle\phi|\eta,\theta\rangle^D]^2\tilde{P}_\xi(\eta)\tilde{P}_c(\theta)d\eta d\theta \tag{8.50}$$

Alternatively, the transport equation of $\widetilde{\phi^2}$ (see Appendix C) may be solved:

$$\bar{\rho}\frac{\partial\widetilde{\phi^2}}{\partial t} + \bar{\rho}\tilde{u}_i\frac{\partial\widetilde{\phi^2}}{\partial x_i} = \underbrace{\frac{\partial}{\partial x_i}\left(\overline{\rho D\frac{\partial\phi^2}{\partial x_i}}\right)}_{\substack{\text{Transport by}\\ \text{molecular diffusion}}} - \underbrace{\frac{\partial(\bar{\rho}\widetilde{u_i''\phi^2})}{\partial x_i}}_{\substack{\text{Turbulent}\\ \text{transport}}} - \underbrace{\bar{\rho}\tilde{\chi}_\phi}_{\text{dissipation}} + \underbrace{2\bar{\rho}\widetilde{\phi\dot{\omega}_\phi}}_{\substack{\text{Chemical}\\ \text{source}}} \tag{8.51}$$

Transport by molecular diffusion may be neglected in high Re flows. The turbulent flux $\widetilde{u_i''\phi^2}$ can be closed using the gradient diffusion assumption. The dissipation of ϕ may modelled as:

$$\tilde{\chi}_\phi = C_\phi\frac{\tilde{\varepsilon}}{\tilde{k}}\widetilde{\phi''^2} = C_\phi\frac{\tilde{\varepsilon}}{\tilde{k}}(\widetilde{\phi^2}-\tilde{\phi}^2) \tag{8.52}$$

where C_ϕ is a modelling constant. Formally, the source term should be obtained from:

$$\widetilde{\phi\dot{\omega}_\phi} = \int_0^1 \int_0^1 \langle \phi\dot{\omega}_\phi|\eta,\theta\rangle^D \tilde{P}_\xi(\eta)\tilde{P}_c(\theta)d\eta d\theta \tag{8.53}$$

If the doubly-conditional covariance of ϕ and $\dot{\omega}_\phi$ is neglected, the source term may calculated to a first-order approximation as:

$$\widetilde{\phi\dot{\omega}_\phi} \approx \int_0^1 \int_0^1 \langle \phi|\eta,\theta\rangle^D \langle \dot{\omega}_\phi|\eta,\theta\rangle^D \tilde{P}_\xi(\eta)\tilde{P}_c(\theta)d\eta d\theta \tag{8.54}$$

8.4.2 Conditional turbulent fluxes

The doubly-conditional turbulent fluxes may be modelled using the gradient diffusion assumption:

$$\langle u_i''\phi''|\eta,\theta\rangle = -D_t\frac{\partial Q_\phi}{\partial x_i} \quad \phi'' = \{y_\kappa''|\kappa = 1,\ldots,N_s\}, h'', h_s'' \text{ or } T'' \tag{8.55}$$

where D_t is given by Eq. (2.56). This expression may not be suitable for the modelling of partially-premixed flames as it does not account for counter-gradient effects. The addition of a counter-gradient correction may be necessary.

8.4.3 Conditional velocity

The PDF-gradient model [190] may be easily extended to account for the second conditioning variable by replacing the marginal PDF of ξ by the joint PDF of ξ and c. The resulting model for the doubly-conditional velocity reads:

$$\langle u_i|\eta,\theta\rangle = \tilde{u}_i - \frac{D_t}{\tilde{P}_{\xi,c}(\eta,\theta)}\frac{\partial \tilde{P}_{\xi,c}(\eta,\theta)}{\partial x_i} = \tilde{u}_i - D_t\frac{\partial[\ln(\tilde{P}_{\xi,c}(\eta,\theta))]}{\partial x_i} \tag{8.56}$$

8.4.4 Conditional dissipation rates

The modelling of the doubly-conditional dissipation and cross-dissipation terms is one of the most challenging aspects of DCMC. No rigorous attempts are made here to model these terms. Simple closures are suggested.

Dissipation of ξ

Zero-dimensional estimate from $\tilde{\chi}_{\xi}$ The doubly-conditional dissipation of ξ, $\langle\chi_{\xi}|\eta,\theta\rangle$, is assumed to be equal to $\tilde{\chi}_{\xi}$. This leads to (see Eq. (2.87)):

$$\langle\chi_{\xi}|\eta,\theta\rangle \approx \tilde{\chi}_{\xi} = C_{\chi_{\xi}}\frac{\tilde{\varepsilon}}{\tilde{k}}\widetilde{\xi''^2} \tag{8.57}$$

where $C_{\chi_{\xi}}$ is a modelling constant usually set to 2. Accordingly, $\langle\chi_{\xi}|\eta,\theta\rangle$ is assumed to be uniform in η- and θ-spaces.

One-dimensional estimate from $\langle\chi_{\xi}|\eta\rangle$ Rather than assuming a uniform distribution, $\langle\chi_{\xi}|\eta,\theta\rangle$ may be set equal to its mixture fraction-conditioned counterpart, i.e.:

$$\langle\chi_{\xi}|\eta,\theta\rangle \approx \langle\chi_{\xi}|\eta\rangle \tag{8.58}$$

Several closures for $\langle\chi_{\xi}|\eta\rangle$ are available in the literature [78, 157, 160, 174]. When Eq. (8.58) is employed, $\langle\chi_{\xi}|\eta,\theta\rangle$ is assumed to be independent of c and therefore, constant at every θ plane. This approximations is less aggressive than Eq. (8.57) since it retains the dependence of $\langle\chi_{\xi}|\eta,\theta\rangle$ on η.

Two-dimensional estimate from $\langle\chi_{\xi}|\eta\rangle$ using inverse theory $\langle\chi_{\xi}|\eta,\theta\rangle$ is related to $\langle\chi_{\xi}|\eta\rangle$ by:

$$\langle\chi_{\xi}|\eta\rangle(x_i,t) \approx \int_0^1 \langle\chi_{\xi}|\eta,\theta\rangle(x_i,t)\tilde{P}_{c|\xi}(x_i,t,\theta|\eta)d\theta \tag{8.59}$$

where the dependence on x_i and t are included for clarity. At a given $t = t^*$ and for a given $\eta = \eta^*$, Eq. (8.59) is a Fredholm equation of the first kind where the function $\langle\chi_{\xi}|\eta^*\rangle(x_i,t^*)$ is modelled, the kernel $\tilde{P}_{c|\xi}(x_i,t^*,\theta|\eta^*)$ is presumed, and $\langle\chi_{\xi}|\eta^*,\theta\rangle(x_i,t^*)$ is the unknown function. In order to solve for $\langle\chi_{\xi}|\eta^*,\theta\rangle(x_i,t^*)$, Eq. (8.59) needs to be inverted. However, inversion is not straightforward since this problem is ill-posed (the inverse in not unique). Equation (8.59) may be solved using the Tikhonov linear regularisation or the truncated singular value decomposition methods described in [193, 200].

Dissipation of c

Zero-dimensional estimate from $\tilde{\chi}_{c}$ The doubly-conditional dissipation of c, $\langle\chi_{c}|\eta,\theta\rangle$, is assumed to be uniform in η- and θ-spaces and set equal to $\tilde{\chi}_{c}$:

$$\langle\chi_{c}|\eta,\theta\rangle \approx \tilde{\chi}_{c} \approx C_{\chi_{c}}\frac{\tilde{\varepsilon}}{\tilde{k}}\widetilde{c''^2} \tag{8.60}$$

where C_{χ_c} is a modelling constant. The level of modelling of $\tilde{\chi}_c$ in Eq. (8.60) is the same as that of $\tilde{\chi}_\xi$ in Eq. (8.57). However, the approximation in this case is crude since the chemical contribution of c is not accounted for in the modelling to $\tilde{\chi}_c$.

One-dimensional estimate from $\langle \chi_c|\eta\rangle$ $\langle \chi_c|\eta,\theta\rangle$ is assumed to be independent of ξ and therefore constant at every η plane. Accordingly,

$$\langle \chi_c|\eta,\theta\rangle \approx \langle \chi_c|\eta\rangle \approx C_{\chi_c}\frac{\tilde{\varepsilon}}{\tilde{k}}\langle c''^2|\eta\rangle \tag{8.61}$$

where $\langle c''^2|\eta\rangle$ is obtained from Eq. (8.43) upon solving Eq. (8.44). If c is assumed to be statistically independent from ξ, $\langle c''^2|\eta\rangle = \widetilde{c''^2}$ and Eq. (8.61) reduces to Eq. (8.60).

Two-dimensional estimate from $\langle \chi_c|\eta\rangle$ using inverse theory As in Eq. (8.59), $\langle \chi_c|\eta,\theta\rangle$ is related to $\langle \chi_c|\eta\rangle$ via the Fredholm equation of the first kind:

$$\langle \chi_c|\eta\rangle(x_i,t) \approx \int_0^1 \langle \chi_c|\eta,\theta\rangle(x_i,t)\tilde{P}_{x|\xi}(x_i,t,\theta|\eta)d\theta \tag{8.62}$$

At $t=t^*$ and for $\eta=\eta^*$, the function $\langle \chi_c|\eta^*\rangle(x_i,t^*)$ is modelled following Eq. (8.61), the kernel $\tilde{P}_{x|\xi}(x_i,t^*,\theta|\eta^*)$ is presumed, and $\langle \chi_c|\eta^*,\theta\rangle(x_i,t^*)$ is the unknown function.

Cross-dissipation of ξ and c

The doubly-conditional cross-dissipation of ξ and c may be approximated from $\langle \chi_\xi|\eta,\theta\rangle$ and $\langle \chi_c|\eta,\theta\rangle$ via:

$$\langle \chi_{\xi,c}|\eta,\theta\rangle \approx \langle \chi_\xi|\eta,\theta\rangle^{1/2}\langle \chi_c|\eta,\theta\rangle^{1/2}\mathbf{n}_\xi\cdot\mathbf{n}_c \tag{8.63}$$

where $\mathbf{n}_\xi = -\nabla\xi/|\nabla\xi|$ and $\mathbf{n}_c = -\nabla c/|\nabla c|$ are, respectively, the unit vectors normal to the ξ and c isosurfaces. The outcome of the scalar product of $\mathbf{n}_\xi$ and $\mathbf{n}_c$ depends on the combustion mode. Three modes can be distinguished [172]:

1. Non-premixed flames: when these flames are mildly curved, $\nabla\xi$ and ∇c are almost aligned, leading to $\mathbf{n}_\xi\cdot\mathbf{n}_c \approx \pm 1$. When this is the case, the magnitude of $\langle \chi_{\xi,c}|\eta,\theta\rangle$ is highest.

2. Premixed and weakly stratified flames: the flame front is perpendicular to the mixture fraction isosurfaces. Therefore, $\nabla\xi$ and ∇c are almost orthogonal, leading to $\mathbf{n}_\xi\cdot\mathbf{n}_c \approx 0$. In this case, $\langle \chi_{\xi,c}|\eta,\theta\rangle \approx 0$ and the role of cross-dissipation is insignificant.

3. Partially premixed flames: the relative orientations of $\nabla\xi$ and ∇c are intermediate between those in non-premixed and premixed flames. Therefore, $-1 < \mathbf{n}_\xi \cdot \mathbf{n}_c < 1$ and $\langle \chi_{\xi,c} | \eta, \theta \rangle$ is non-negligible.

8.4.5 Conditional reactions rates

The doubly conditional reaction rates, $\langle \dot{\omega}_\kappa (\rho, T, \mathbf{Y}) | \eta, \theta \rangle$, may be modelled using the first order closure [18,120,122]. This simple closure is reasonable when DCMC is applied to the modelling of highly fluctuating phenomena. Its validity is attributed to the small order of doubly-conditional fluctuations. Therefore, $\langle \dot{\omega}_\kappa (\rho, T, \mathbf{Y}) | \eta, \theta \rangle$ is simply modelled as a function of $\langle \rho | \eta, \theta \rangle$, $\langle T | \eta, \theta \rangle$ and $\langle \mathbf{Y} | \eta, \theta \rangle$:

$$\langle \dot{\omega}_\kappa (\rho, T, \mathbf{Y}) | \eta, \theta \rangle \approx \langle \dot{\omega}_\kappa (\langle \rho | \eta, \theta \rangle, \langle T | \eta, \theta \rangle, \langle \mathbf{Y} | \eta, \theta \rangle) | \eta, \theta \rangle = \dot{\omega}_\kappa (\langle \rho | \eta, \theta \rangle, Q_T, \mathbf{Q}) \quad (8.64)$$

where $\mathbf{Q} = \{ Q_\kappa | \kappa = 1, 2, \ldots, N_s \}$.

8.4.6 Conditional radiative source

In open flames where soot concentration is negligible, the optically thin assumption may be used to model the conditional radiative source. To a first-order approximation, the double-conditioning of Eq. (2.61) yields:

$$\langle \dot{\omega}_r | \eta, \theta \rangle = 4\sigma \sum_{\kappa=1}^{N_r} p_\kappa a_{p,\kappa} (\langle T | \eta, \theta \rangle^4 - T_b^4) = 4\sigma \sum_{\kappa=1}^{N_r} p_\kappa a_{p,\kappa} (Q_T^4 - T_b^4) \quad (8.65)$$

8.5 Implementation for homogeneous turbulence

This section describes the implementation of the homogeneous DCMC. A standalone parametric assessment of the method is performed by specifying different combinations of strain levels in η- and θ-spaces. The conditions of the piloted CH_4/air Sandia flames [12] are considered (see Sect. 5.2).

8.5.1 Simplification for homogeneous turbulence

The DCMC equations are solved for the simple case of homogeneous turbulence. All terms involving gradients of conditional mean quantities are dropped from Eqs. (8.20)

and (8.24). Accordingly, convective transport and the terms e_{Q_κ}, e_{Q_h}, $e_{y''_\kappa}$ and $e_{h''}$ are discarded from the governing equations. It is noted here that no modelling assumptions are required for the closure of e_{Q_κ} and e_{Q_h} in the computations of homogeneous turbulence. These terms are identically zero as they consist of terms involving means of conditional quantities [122]. As for $e_{y''_\kappa}$ and $e_{h''}$, these quantities are closed in terms of the gradients of the doubly-conditional turbulent fluxes via the primary closure hypothesis (Sect. 8.3.3). When these fluxes are modelled using the gradient diffusion assumption (Sect. 8.4.2), the final expressions of $e_{y''_\kappa}$ and $e_{h''}$ involve the gradients of the Q_κ and Q_h, and thereby vanish from the DCMC equations. With the above simplifications, the species equation reduces to:

$$\begin{aligned}\frac{\partial Q_\kappa}{\partial t} =& \underbrace{\frac{\langle\chi_\xi|\eta,\theta\rangle}{2}\left[\frac{\partial^2 Q_\kappa}{\partial\eta^2} - \frac{1}{\Delta\phi^{max}_{min}(\eta)}\left(\theta\frac{d^2[\Delta\phi^{max}_{min}(\eta)]}{d\eta^2} + \frac{d^2\phi_{min}(\eta)}{d\eta^2}\right)\frac{\partial Q_\kappa}{\partial\theta}\right]}_{T_1} \\ &+ \underbrace{\langle\chi_{\xi,c}|\eta,\theta\rangle\left(\frac{\partial^2 Q_\kappa}{\partial\eta\partial\theta} - \frac{1}{\Delta\phi^{max}_{min}(\eta)}\frac{d[\Delta\phi^{max}_{min}(\eta)]}{d\eta}\frac{\partial Q_\kappa}{\partial\theta}\right)}_{T_2} + \underbrace{\frac{\langle\chi_c|\eta,\theta\rangle}{2}\frac{\partial^2 Q_\kappa}{\partial\theta^2}}_{T_3} \\ &+ \underbrace{\frac{\langle\dot\omega_\kappa|\eta,\theta\rangle}{\langle\rho|\eta,\theta\rangle}}_{T_4} \underbrace{-\frac{\langle\dot\omega_c|\eta,\theta\rangle}{\langle\rho|\eta,\theta\rangle}\frac{\partial Q_\kappa}{\partial\theta}}_{T_5}\end{aligned} \tag{8.66}$$

where the notation $\Delta\phi^{max}_{min}(\eta) = \phi_{max}(\eta) - \phi_{min}(\eta)$ has been introduced for simplicity. Similarly, the enthalpy equation reduces to:

$$\begin{aligned}\frac{\partial Q_h}{\partial t} =& \frac{\langle\chi_\xi|\eta,\theta\rangle}{2}\left[\frac{\partial^2 Q_h}{\partial\eta^2} - \frac{1}{\Delta\phi^{max}_{min}(\eta)}\left(\theta\frac{d^2[\Delta\phi^{max}_{min}(\eta)]}{d\eta^2} + \frac{d^2\phi_{min}(\eta)}{d\eta^2}\right)\frac{\partial Q_h}{\partial\theta}\right] \\ &+ \langle\chi_{\xi,c}|\eta,\theta\rangle\left(\frac{\partial^2 Q_h}{\partial\eta\partial\theta} - \frac{1}{\Delta\phi^{max}_{min}(\eta)}\frac{d[\Delta\phi^{max}_{min}(\eta)]}{d\eta}\frac{\partial Q_h}{\partial\theta}\right) + \frac{\langle\chi_c|\eta,\theta\rangle}{2}\frac{\partial^2 Q_h}{\partial\theta^2} \\ &- \frac{\langle\dot\omega_c|\eta,\theta\rangle}{\langle\rho|\eta,\theta\rangle}\frac{\partial Q_h}{\partial\theta} + \frac{\langle\dot\omega_r|\eta,\theta\rangle}{\langle\rho|\eta,\theta\rangle} + \frac{\langle\partial p/\partial t|\eta,\theta\rangle}{\langle\rho|\eta,\theta\rangle}\end{aligned} \tag{8.67}$$

When viscous heating, radiation, and pressure effects are neglected and all Lewis numbers are set to unity, the enthalpy transport equations (Eq. (2.19)) has no source terms and h is conserved. Under such circumstances, the transport equations of h and ξ have exactly the same form. Therefore, h can be related to ξ via by the linear coupling relation [178]:

$$h = h_O + \xi(h_F - h_O) \tag{8.68}$$

where h_O and h_F are, respectively, the enthalpies in the oxidiser and fuel streams. Equation (8.68) can be conditionally averaged with respect to $\xi = \eta$ and $c = \theta$ leading to:

$$Q_h = h_O + \eta(h_F - h_O) \tag{8.69}$$

This expression implies that Q_h is linear in η-space and remains constant in θ-space. As such,

$$\frac{\partial^2 Q_h}{\partial \eta^2} = \frac{\partial Q_h}{\partial \theta} = \frac{\partial^2 Q_h}{\partial \eta \partial \theta} = \frac{\partial^2 Q_h}{\partial \theta^2} = 0 \tag{8.70}$$

Using this result in Eq. (8.67) upon eliminating the radiation and pressure terms, all the r.h.s. vanish. Therefore, Q_h can be simply obtained from Eq. (8.69) and the solution of its transport equation is avoided. Q_T is computed iteratively from Q_h upon solving Eq. (8.66).

8.5.2 Modelling of the conditional dissipation terms

The first-order modelling of the conditional chemical reaction rate leaves the conditional dissipations $\langle \chi_\xi | \eta, \theta \rangle$ and $\langle \chi_c | \eta, \theta \rangle$ and the cross-dissipation $\langle \chi_{\xi,c} | \eta, \theta \rangle$ in Eq. (8.66) unclosed. In previous *a priori* DCMC analyses [40, 122], these quantities are obtained from DNS. The zero-, one- and two-dimensional estimates proposed in Sect. 8.4.4 are applicable in DCMC implementations that are fully coupled with a flow solver providing a set of local variables. Since the current implementation is concerned with the parametric assessment of DCMC, a different approach is adopted in order to close these terms. Nguyen et al. [172] employ the following expressions in MFM tabulation[2]:

$$\langle \chi_\xi | \eta, \theta \rangle = \frac{a}{\pi} G(\eta); \quad G(\eta) = \exp\left\{-2\left[\mathrm{erf}^{-1}(2\eta - 1)\right]^2\right\} \tag{8.71}$$

$$\begin{gathered} \langle \chi_c | \eta, \theta \rangle = 2bH(\eta)L(\theta); \\ H(\eta) = \exp\left\{-2\left[\mathrm{erf}^{-1}\left(\frac{\eta}{\eta_{st}} - 1\right)\right]^2\right\}; \quad L(\theta) = \exp\left\{-2\left[\mathrm{erf}^{-1}(2\theta - 1)\right]^2\right\} \end{gathered} \tag{8.72}$$

$$\langle \chi_{\xi,c} | \eta, \theta \rangle = \langle \chi_\xi | \eta, \theta \rangle^{1/2} \langle \chi_c | \eta, \theta \rangle^{1/2} \mathbf{n}_\xi \cdot \mathbf{n}_c \tag{8.73}$$

The parameter a in Eq. (8.71) is the strain rate in η-space and the parameter b in Eq. (8.72) plays a similar role in θ-space. In Eq. (8.73), Nguyen et al. [172] consider the

[2]Equations (8.71) and (8.72) correspond to Eqs. (23) and (24) in [172] multiplied by 2 since the definition of the dissipation terms in this work involves an additional factor of 2, which is absent in [172].

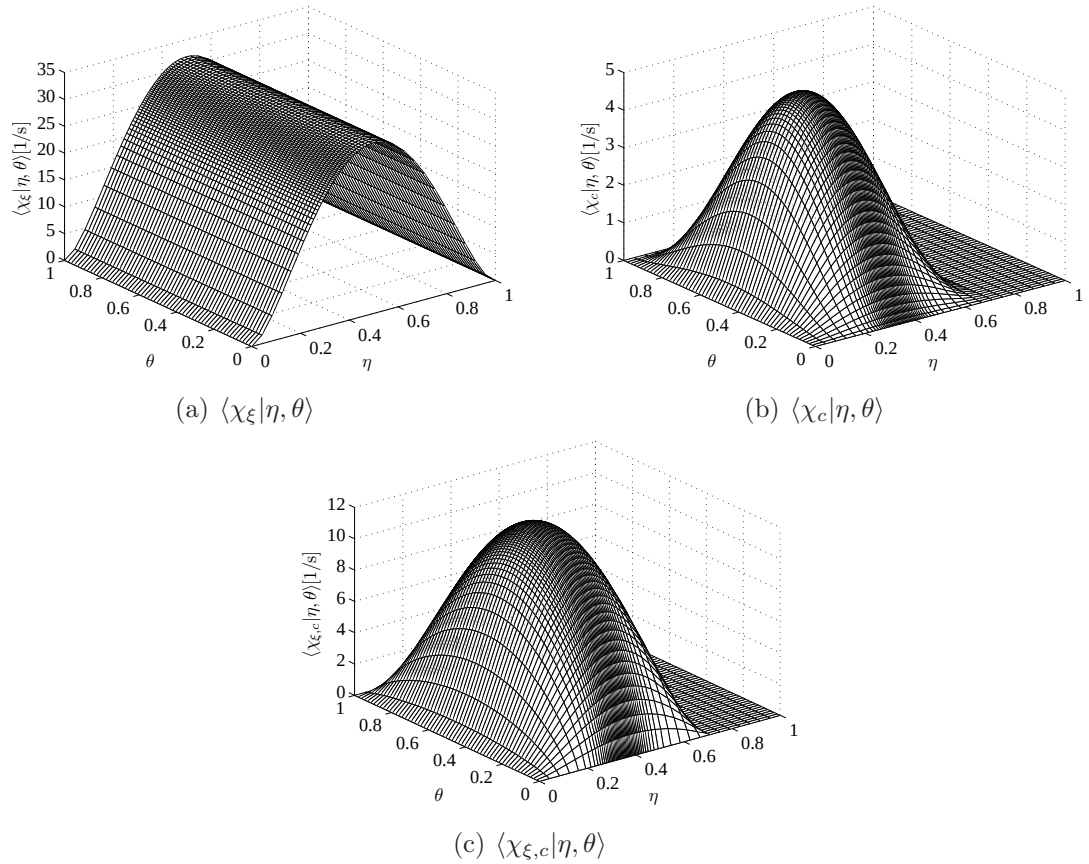

(a) $\langle\chi_\xi|\eta,\theta\rangle$ (b) $\langle\chi_c|\eta,\theta\rangle$

(c) $\langle\chi_{\xi,c}|\eta,\theta\rangle$

Figure 8.1: Doubly-conditional scalar dissipation rates: (a) $\langle\chi_\xi|\eta,\theta\rangle$, (b) $\langle\chi_c|\eta,\theta\rangle$, and (c) $\langle\chi_{\xi,c}|\eta,\theta\rangle$. $a = 100$ s^{-1}; $b = 2.5$ s^{-1}; $\mathbf{n}_\xi \cdot \mathbf{n}_c = +1$.

limiting cases $\mathbf{n}_\xi \cdot \mathbf{n}_c = 0$, +1 and -1. Equations (8.71)–(8.73) are plotted in Fig. 8.1 for $a = 100$ s^{-1}, $b = 2.5$ s^{-1} and $\mathbf{n}_\xi \cdot \mathbf{n}_c = +1$. As shown in Fig. 8.1(a), $\langle\chi_\xi|\eta,\theta\rangle$ is uniform in θ-space and reaches its maximum, a/π, at $\eta = 0.5$ ($G(\eta)$ is symmetric). In Fig. 8.1(b), the peak of $\langle\chi_c|\eta,\theta\rangle$, $2b$, is reached at $\eta = \eta_{st}$ and $\theta = 0.5$ ($H(\eta)$ peaks at $\eta = \eta_{st}$ and $L(\theta)$ is symmetric). Figure 8.1(b) also shows that $\langle\chi_c|\eta,\theta\rangle$ vanishes at $\eta = 2\eta_{st}$ since $\lim_{\eta\to 2\eta_{st}} \mathrm{erf}^{-1}(\eta/\eta_{st} - 1) = +\infty$. $H(\eta)$ is undefined in $2\eta_{st} < \eta \leq 1$. Therefore, $\langle\chi_c|\eta,\theta\rangle$ set to zero in this range. As result, $\langle\chi_{\xi,c}|\eta,\theta\rangle$ in Fig. 8.1(c) vanishes in $2\eta_{st} \leq \eta \leq 1$ because $\langle\chi_c|\eta,\theta\rangle^{1/2}$ appears as factor in its expression (see Eq. (8.73)).

In MFM, several combinations of a and b are chosen and multidimensional look-up tables are precomputed prior to the performance of the combustion calculations. If Eqs. (8.71)–(8.73) are adopted in fully coupled DCMC implementations, a and b must be cal-

culated from known flow field variables at each grid point in physical space. The double integration of Eqs. (8.71) and (8.72) weighted by the joint PDF over η- and θ-spaces yields:

$$a = \pi \frac{\tilde{\chi}_\xi}{\int_0^1 \int_0^1 G(\eta)\tilde{P}_\xi(\eta)\tilde{P}_{c|\xi}(\theta|\eta)d\eta\, d\theta} \tag{8.74}$$

and

$$b = \frac{\tilde{\chi}_c}{2\int_0^1 \int_0^1 H(\eta)L(\theta)\tilde{P}_\xi(\eta)\tilde{P}_{c|\xi}(\theta|\eta)d\eta\, d\theta} \tag{8.75}$$

It is obvious from these two expressions that a and b depend on the moments of ξ and the conditional moments of c through $\tilde{P}_\xi$ and $\tilde{P}_{c|\xi}$, respectively. If ξ and c are assumed to be statistically independent, Eqs. (8.74) and (8.75) simplify to:

$$a = \pi \frac{\tilde{\chi}_\xi}{\int_0^1 G(\eta)\tilde{P}_\xi(\eta)d\eta} \tag{8.76}$$

and

$$b = \frac{\tilde{\chi}_c}{2\left(\int_0^1 H(\eta)\tilde{P}_\xi(\eta)d\eta\right)\left(\int_0^1 L(\theta)\tilde{P}_c(\theta)d\theta\right)} \tag{8.77}$$

Since the current calculations are not coupled with a flow solver, the only way to close Eq. (8.66) is to set a and b parametrically. As such, the current homogeneous DCMC implementation and MFM are the same apart from the definition of the PV and the treatment of the fully burnt boundary in PV-space. Nguyen et al. [172] do not normalize their PV, and therefore their solution domain is not square. Instead, the fully burnt boundary is allowed to freely propagate and adaptive meshing is employed. Here, the location of the fully burnt boundary is predefined and the solution domain is square. Boundary conditions are discussed next.

8.5.3 Boundary conditions

Assuming that the flame does not lose mass or heat in unburnt and fully burnt mixture, zero-flux boundary conditions are imposed in θ-space at $c = 0$ and $c = 1$, i.e.:

$$\left.\frac{\partial Q_\kappa}{\partial \theta}\right|_{c=0} = 0 \tag{8.78a}$$

$$\left.\frac{\partial Q_\kappa}{\partial \theta}\right|_{c=1} = 0 \tag{8.78b}$$

Further, according to Eqs. (8.72) and (8.73):

$$\langle\chi_\xi|\eta, c=0\rangle = (a/\pi)G(\eta); \quad \langle\chi_c|\eta, c=0\rangle = 0; \quad \langle\chi_{\xi,c}|\eta, c=0\rangle = 0 \tag{8.79a}$$

$$\langle\chi_\xi|\eta, c=1\rangle = (a/\pi)G(\eta); \quad \langle\chi_c|\eta, c=1\rangle = 0; \quad \langle\chi_{\xi,c}|\eta, c=1\rangle = 0 \tag{8.79b}$$

Substituting Eqs. (8.78a) and (8.79a) in Eq. (8.66) and setting $\langle\omega_\kappa|\eta, c=0\rangle$ to zero (mixture in non-reacting at $c=0$) yield:

$$\frac{\partial Q_\kappa}{\partial t}\Big|_{c=0} = \frac{aG(\eta)}{2\pi}\frac{\partial^2 Q_\kappa}{\partial \eta^2}\Big|_{c=0} \tag{8.80}$$

At steady state, Eq. (8.80) becomes:

$$\frac{\partial^2 Q_\kappa}{\partial \eta^2}\Big|_{c=0} = 0 \tag{8.81}$$

which has the linear solution:

$$Q_\kappa(\eta, c=0) = Y_{\kappa,O} + \eta(Y_{\kappa,F} - Y_{\kappa,O}) \tag{8.82}$$

where $Y_{\kappa,O}$ and $Y_{\kappa,F}$ are the species mass fractions in the oxidiser and fuel streams, respectively. When species κ is absent from the two streams, $Q_\kappa(\eta, c=0) = 0$ since $Y_{\kappa,O} = Y_{\kappa,F} = 0$. The inert mixing solution of the temperature, the enthalpy and the mass fractions O_2, N_2 and CH_4 are shown in Fig. 8.2. Here, $Q_T(\eta, c=0)$ is constant over η-space because $T_O = T_F = 300$K and $Q_T(\eta, c=0)$ in $0 < \eta < 1$ cannot physically fall below 300 K. In general, $Q_T(\eta, c=0)$ is not linear when $T_O \neq T_F$ due to the dependence of Q_T on the specific heats. On the other hand, $Q_h(\eta, c=0)$ is linear (see Eq. (8.69)). The unburnt state described by $\phi_{min}(\eta)$ is obtained from this boundary.

A similar procedure is followed to specify the boundary conditions at $c=1$. The substitution of Eqs. (8.78b) and (8.79b) in Eq. (8.66) while retaining the chemical reaction rate (mixture is reacting) results in:

$$\frac{\partial Q_\kappa}{\partial t}\Big|_{c=1} = \frac{aG(\eta)}{2\pi}\frac{\partial^2 Q_\kappa}{\partial \eta^2}\Big|_{c=1} + \frac{\langle\dot{\omega}_\kappa|\eta, c=1\rangle}{\langle\rho|\eta, c=1\rangle} \tag{8.83}$$

Equation (8.83) is equivalent to the well known specie equation of the laminar flamelet model (with unity Lewis numbers) [178]. The solution of this equation provides $\phi_{max}(\eta)$. In homogeneous calculations, Eq. (8.83) is solved before the solution of Eq. (8.66) is undertaken. The solution for $a = 100$ s^{-1} is shown in Fig. 8.3.

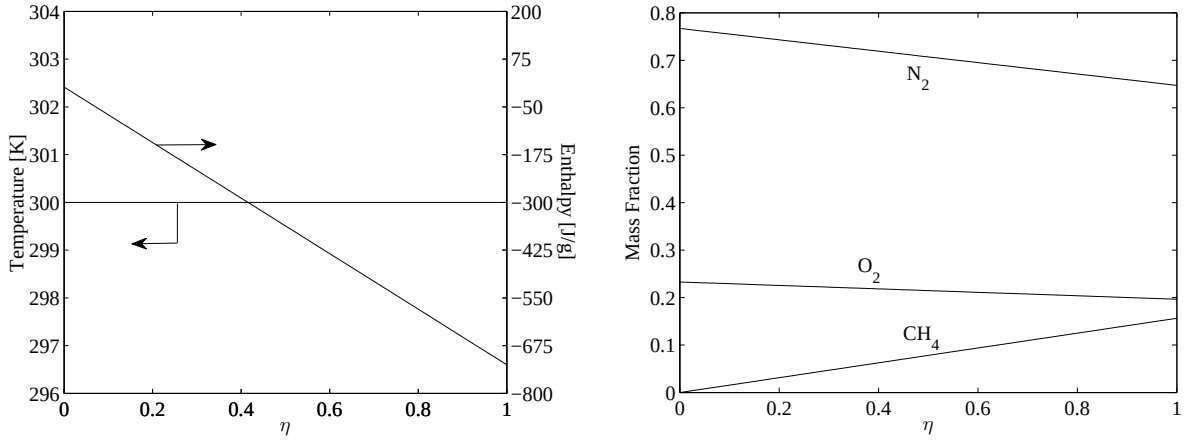

Figure 8.2: Inert mixing (frozen chemistry) solution: (a) temperature and enthalpy; (b) species mass fractions.

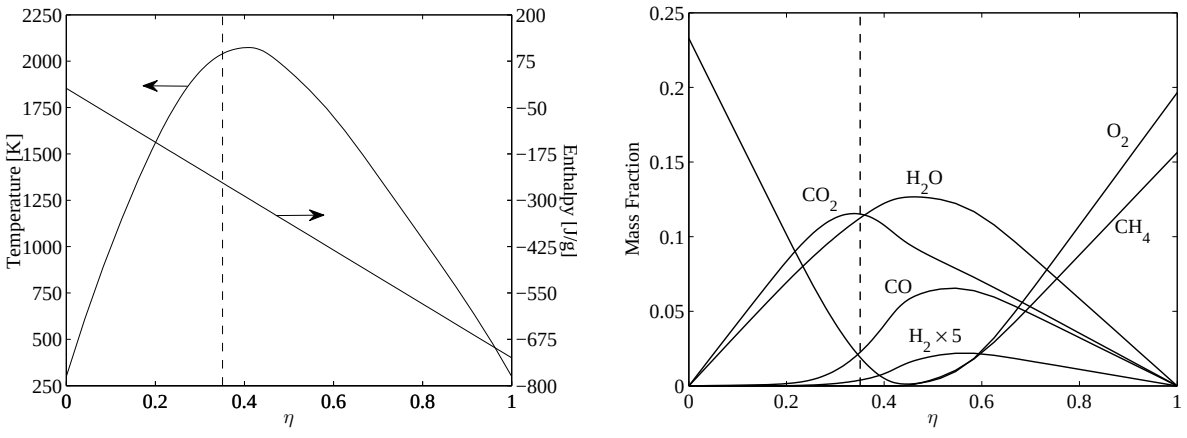

Figure 8.3: Flamelet solution for $a = 100\ s^{-1}$: (a) temperature and enthalpy; (b) selected species mass fractions. The vertical dashed lines correspond to $\xi = \eta_{st}$.

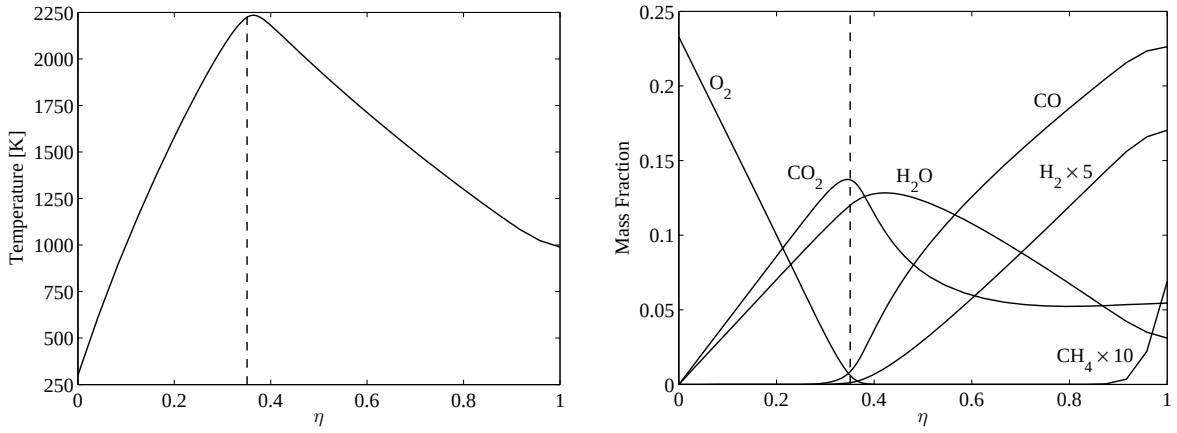

(a) (b)

Figure 8.4: Chemical equilibrium solution: (a) temperature (adiabatic flame temperature); (b) selected species mass fractions. The vertical dashed lines correspond to $\xi = \eta_{st}$.

Ideally, when $a = 0$, $\phi_{max}(\eta)$ corresponds to the chemical equilibrium solution of ϕ. For a given set of species, this solution is obtained from the knowledge of $Y_{\kappa,O}$, T_O, $Y_{\kappa,F}$ and T_F. However, this solution is problematic in flames where the fuel stream contains O_2, such as the piloted Sandia flames considered here. Difficulties arise at the $\xi = 1$ boundary where the equilibrium solution yields temperatures and mass fractions different from $Y_{\kappa,F}$ and T_F. CH_4 in the fuel stream consumes the available O_2 which results in a temperature higher than T_F and non-zero product mass fractions, as shown in Fig. 8.4. Alternatively, Eq. (8.83) may be solved subject to a very low strain rate. Figure 8.5 shows the temperature solution for increasing strain rate values. The resulting profiles are virtually the same as those of the equilibrium solution in lean mixtures. Non-equilibrium effects arising from straining manifest around stoichiometry and in rich mixtures.

As for the remaining boundaries, Dirichlet boundary conditions are set at $(\xi = 0, \theta)$ and $(\xi = 1, \theta)$. The temperature (or enthalpy) and the species mass fractions are set to their respective values in the oxidiser ($\xi = 0$) and fuel ($\xi = 1$) streams:

$$Q_\kappa(\xi = 0, \theta) = Y_{\kappa,O} \quad Q_T(\xi = 0, \theta) = T_O \quad Q_h(\xi = 0, \theta) = h_O \tag{8.84a}$$

$$Q_\kappa(\xi = 1, \theta) = Y_{\kappa,F} \quad Q_T(\xi = 1, \theta) = T_F \quad Q_h(\xi = 1, \theta) = h_F \tag{8.84b}$$

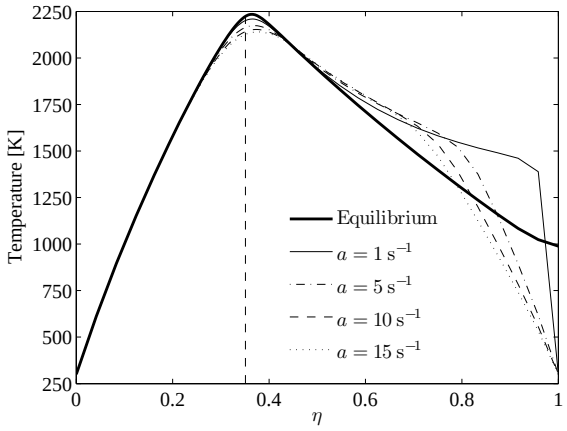

Figure 8.5: Chemical equilibrium and flamelet solutions of the temperature for different strain rates. The vertical dashed lines correspond to $\xi = \eta_{st}$.

8.5.4 Definition of ϕ

Two possible definitions for ϕ are the mass fraction of some combination of products or reactants [55, 69–71, 75, 153, 229] or the sensible enthalpy [122]. Details related to both definitions are provided in this section. The former is considered in the current implementation.

Combination of species

To monitor reaction progress, ϕ may be defined as the mass fraction of combination of monotonically and slowly varying products or reactants [69]. The choice of species depends on the nature of the fuel. For H_2 combustion, Galpin et al. [75] set $\phi = Y_{H_2O} - Y_H$, whereas for CH_4 combustion, Fiorina et al. [69] employ $\phi = Y_{CO} + Y_{CO_2}$. Since the Sandia piloted flames burn a CH_4/air mixture, the latter definition is adopted here. Accordingly, c is expressed as:

$$c = \frac{[Y_{CO}(\mathbf{x},t) + Y_{CO_2}(\mathbf{x},t)] - [Y_{CO,min}(\xi(\mathbf{x},t)) + Y_{CO_2,min}(\xi(\mathbf{x},t))]}{[Y_{CO,max}(\xi(\mathbf{x},t)) + Y_{CO_2,max}(\xi(\mathbf{x},t))] - [Y_{CO,min}(\xi(\mathbf{x},t)) + Y_{CO_2,min}(\xi(\mathbf{x},t))]} \tag{8.85}$$

The unity Lewis number transport equation of ϕ is obtained by simply adding those of Y_{CO} and Y_{CO_2} (Eq. (2.4) with $\kappa = CO$ and CO_2, and $D_\kappa = D$). Accordingly, the source term of the ϕ equation becomes $\dot{\omega}_\phi = \dot{\omega}_{CO} + \dot{\omega}_{CO_2}$ and that of the c equation, Eq. (8.10),

takes the form:

$$\dot{\omega}_c = \frac{\dot{\omega}_{\mathrm{CO}} + \dot{\omega}_{\mathrm{CO_2}}}{[Y_{\mathrm{CO},max}(\xi(\mathbf{x},t)) + Y_{\mathrm{CO_2},max}(\xi(\mathbf{x},t))] - [Y_{\mathrm{CO},min}(\xi(\mathbf{x},t)) + Y_{\mathrm{CO_2},min}(\xi(\mathbf{x},t))]} \tag{8.86}$$

The double-conditioning of Eq. (8.86) with respect to $\xi = \eta$ and $c = \theta$ leads to:

$$\langle \dot{\omega}_c | \eta, \theta \rangle = \frac{\langle \dot{\omega}_{\mathrm{CO}} | \eta, \theta \rangle + \langle \dot{\omega}_{\mathrm{CO_2}} | \eta, \theta \rangle}{[Y_{\mathrm{CO},max}(\eta) + Y_{\mathrm{CO_2},max}(\eta)] - [Y_{\mathrm{CO},min}(\eta) + Y_{\mathrm{CO_2},min}(\eta)]} \tag{8.87}$$

Since the oxidiser and fuel streams in Sandia flames do not contain CO and CO_2, $Y_{\mathrm{CO},min}(\eta) = Y_{\mathrm{CO_2},min}(\eta) = 0$, which leads to $\phi_{min}(\eta) = 0$. Therefore, the following simplifications apply in Eq. (8.66):

$$\begin{gathered}
\Delta\phi^{max}_{min}(\eta) = \phi^{max}(\eta) = Y_{\mathrm{CO},max}(\eta) + Y_{\mathrm{CO_2},max}(\eta); \qquad \frac{d^2\phi_{min}(\eta)}{d\eta^2} = 0; \\
\frac{d\Delta\phi^{max}_{min}(\eta)}{d\eta} = \frac{d\phi_{max}(\eta)}{d\eta}; \qquad \frac{d^2\Delta\phi^{max}_{min}(\eta)}{d\eta^2} = \frac{d^2\phi_{max}(\eta)}{d\eta^2}; \\
\langle \dot{\omega}_c | \eta, \theta \rangle = \frac{\langle \dot{\omega}_{\mathrm{CO}} | \eta, \theta \rangle + \langle \dot{\omega}_{\mathrm{CO_2}} | \eta, \theta \rangle}{Y_{\mathrm{CO},max}(\eta) + Y_{\mathrm{CO_2},max}(\eta)}
\end{gathered} \tag{8.88}$$

The construction of $\phi_{max}(\eta)$ from $Y_{\mathrm{CO},max}(\eta)$ and $Y_{\mathrm{CO_2},max}(\eta)$ is shown in Fig. 8.6(a) for $a = 100\ \mathrm{s}^{-1}$. Figure 8.6(b) displays the first and second derivatives of $\phi_{max}(\eta)$ with respect to η for the same level of strain. As shown, these derivatives are non-negligible. Therefore, the terms involving them in Eq. (8.66) ought not to be neglected.

Sensible Enthalpy

Alternatively, ϕ may be defined in terms of the sensible enthalpy. With this setting, c acts as a marker for heat loss. Setting $\phi = h_s$, Eq. (8.1) becomes:

$$c = \frac{h_s(\mathbf{x},t) - h_{s,min}(\xi(\mathbf{x},t))}{h_{s,max}(\xi(\mathbf{x},t)) - h_{s,min}(\xi(\mathbf{x},t))} \tag{8.89}$$

where

$$h_{s,min}(\xi(\mathbf{x},t)) = h_{min}(\xi(\mathbf{x},t)) - \sum_{\kappa=1}^{N_s} \Delta h^\circ_{f,\kappa} Y_{\kappa,min}(\xi(\mathbf{x},t)) \tag{8.90a}$$

$$h_{s,max}(\xi(\mathbf{x},t)) = h_{max}(\xi(\mathbf{x},t)) - \sum_{\kappa=1}^{N_s} \Delta h^\circ_{f,\kappa} Y_{\kappa,max}(\xi(\mathbf{x},t)) \tag{8.90b}$$

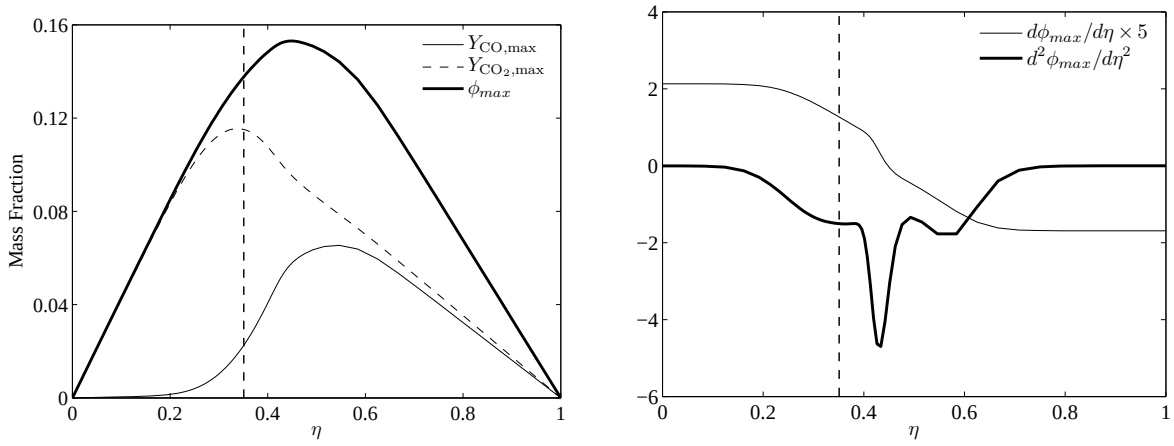

(a) (b)

Figure 8.6: Definition of ϕ based on the sum of the CO and CO_2 mass fractions: (a) construction of ϕ_{max} from $Y_{CO,max}$ and $Y_{CO_2,max}$;(b) first and second derivatives of ϕ_{max} with respect to η. The vertical dashed lines indicate the location of $\xi = \eta_{st}$. $a = 100$ s^{-1}.

When pressure variations, viscous heating, and radiation are neglected, and all Lewis numbers are set to unity, the sensible enthalpy transport equation has the same form as that of ϕ (Eq. (8.10)) with $\dot{\omega}_\phi = \dot{\omega}_{h_s} = -\sum_{\kappa=1}^{N_s} \Delta h^\circ_{f,\kappa} \dot{\omega}_\kappa$. Hence, the source term of c becomes:

$$\dot{\omega}_c = -\frac{\sum_{\kappa=1}^{N_s} \Delta h^\circ_{f,\kappa} \dot{\omega}_\kappa}{h_{s,max}(\xi(\mathbf{x},t)) - h_{s,min}(\xi(\mathbf{x},t))} \tag{8.91}$$

The double-conditioning of Eq. (8.91) with respect to $\xi = \eta$ and $c = \theta$ results in:

$$\langle \dot{\omega}_c | \eta, \theta \rangle = -\frac{\sum_{\kappa=1}^{N_s} \Delta h^\circ_{f,\kappa} \langle \dot{\omega}_\kappa | \eta, \theta \rangle}{h_{s,max}(\eta) - h_{s,min}(\eta)} \tag{8.92}$$

At the boundary $c = 0$, $h_{min}(\eta)$ and $Y_{\kappa,min}(\eta)$ are linear in η-space ($h_{min}(\eta) = h_O + \eta(h_F - h_O)$ and $Y_{\kappa,min}(\eta) = Y_{\kappa,O} + \eta(Y_{\kappa,F} - Y_{\kappa,O})$). Therefore, $\phi_{min}(\eta) = h_{s,min}(\eta)$ is also a linear function of η. As such, the following simplifications apply in Eq. (8.66):

$$\frac{d^2\phi_{min}(\eta)}{d\eta^2} = \frac{d^2 h_{s,min}(\eta)}{d\eta^2} = 0; \qquad \frac{d^2 \Delta\phi^{max}_{min}(\eta)}{d\eta^2} = \frac{d^2 h_{s,max}(\eta)}{d\eta^2} \tag{8.93}$$

The profiles of $h_{s,min}(\eta)$ and $h_{s,max}(\eta)$ are shown in Fig. 8.7(a) and those of the first and second derivatives of $h_{s,max}$ with respect to η are displayed in Fig. 8.7(b). As in the case where $\phi = Y_{CO} + Y_{CO_2}$, the derivatives of ϕ_{max} play an important role in Eq. (8.66).

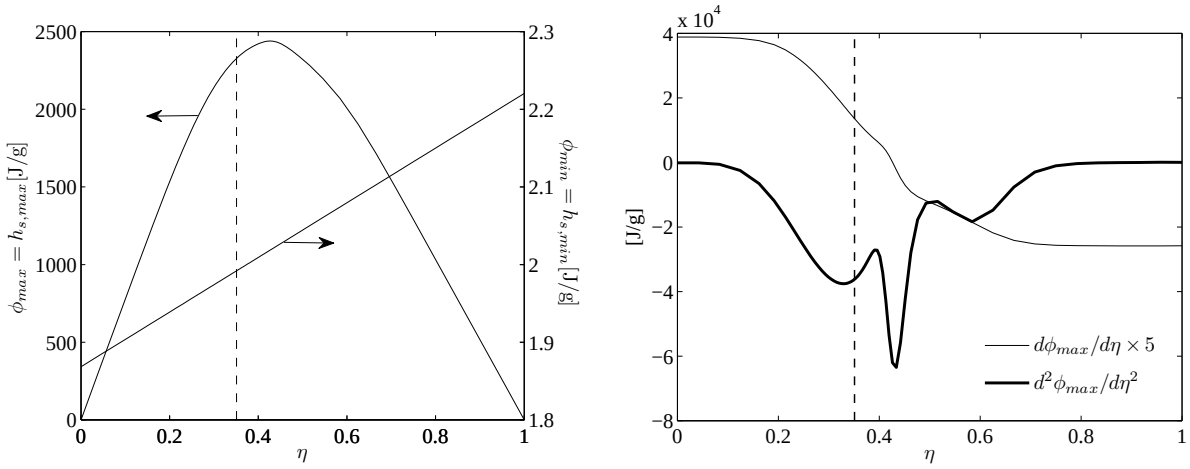

(a) (b)

Figure 8.7: Profiles of (a) $\phi_{max} = h_{s,max}$ and $\phi_{min} = h_{s,min}$ and (b) first and second derivatives of $\phi_{max} = h_{s,max}$ with respect to η. The vertical dashed lines indicate the location of $\xi = \eta_{st}$. $a = 100$ s^{-1}.

8.5.5 Numerical method

The augmented reduced chemical kinetic mechanism ARM2 [1] (see Table 5.2) is employed throughout the calculations. A grid resolution of 60×60 is employed in both η and θ spaces. The η-grid is clustered around the stoichiometric mixture fraction ($\eta = 0.351$), whereas the θ-grid is uniformly distributed. The resulting grid is shown in Fig. 8.8. The finite difference method is employed to discretise the partial derivatives of Q_κ. The first and second-order derivatives are discretized using the first-order upwind and second-order central difference schemes, respectively. Steady state is obtained via the relaxation of the solution by time-marching. The calculations are initialized by applying linear interpolation between the unburnt ($c = 0$) and burnt ($c = 1$) states. The stiff ODE solver VODPK [30, 31, 33] is employed to advance the solution in time. A time-step of 10^{-6} is employed. The absolute tolerances for major and minor species are set to 10^{-7} and 10^{-10}, respectively, and the relative solver tolerance is set to 10^{-5}. A three-step fractional method is used in order to speed up the calculations by treating the stiff chemical sources separately. To advance the solution from time $t = t_\circ$ to $t = t_\circ + \Delta t$, Eq. (8.66) is split as follows:

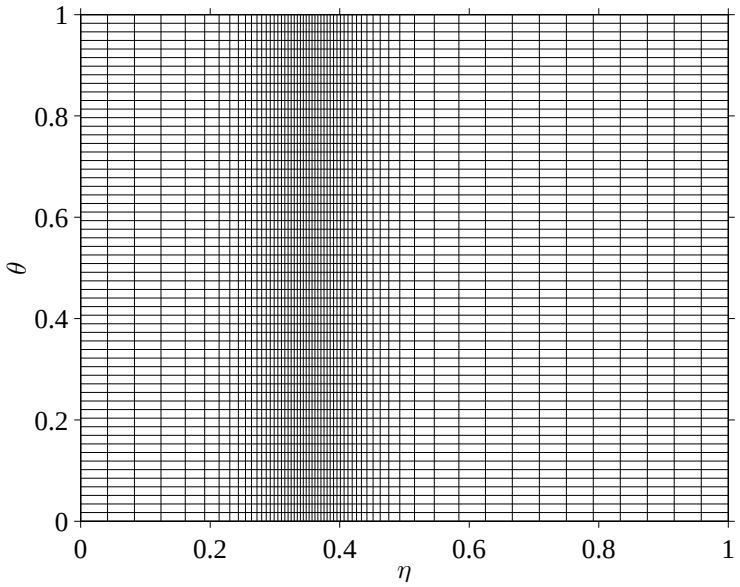

Figure 8.8: Computational domain.

- **Step 1**: the diffusion terms T_1, T_2 and T_3 are solved over the first half of the time step:

$$\frac{\partial Q_\kappa}{\partial t} = T_1 + T_2 + T_3 \qquad t_\circ \leq t \leq t_\circ + \frac{\Delta t}{2} \tag{8.94}$$

- **Step 2**: the sources T_4 and T_5 are solved over the whole time step:

$$\frac{\partial Q_\kappa}{\partial t} = T_4 + T_5 \qquad t_\circ \leq t \leq t_\circ + \Delta t \tag{8.95}$$

- **Step 3**: the diffusion terms T_1, T_2 and T_3 are solved over the second half of the time step:

$$\frac{\partial Q_\kappa}{\partial t} = T_1 + T_2 + T_3 \qquad t_\circ + \frac{\Delta t}{2} \leq t \leq t_\circ + \Delta t \tag{8.96}$$

Each fractional step is initialised using the solution of the previous one. Steps 1 and 3 are non-stiff (solved using Adam's method), whereas step 2 is stiff (solved using the BDF). Steady state is considered to be reached when the criterion given by Eq. (8.97) is met.

$$\max\left(\frac{|Q_T^{t+\Delta t}(\eta,\theta) - Q_T^t(\eta,\theta)|}{Q_T^t(\eta,\theta)}\right) < 10^{-10} \tag{8.97}$$

8.5.6 Effect of strain in η-space

To assess the effect of strain in η-space, the parameter a in Eq. (8.71) is varied while holding the parameter b in Eq. (8.72) constant. The product $\mathbf{n}_\xi \cdot \mathbf{n}_c$ in Eq. (8.73) is taken to be $+1$. Three values of a are considered, namely 350, 900 and 1450 s^{-1}, and b is set to 50 s^{-1}. Beside modifying the distributions of $\langle \chi_\xi | \eta, \theta \rangle$ and $\langle \chi_{\xi,c} | \eta, \theta \rangle$ via Eqs. (8.71) and (8.73), the variation of a affects the boundary conditions at $\theta = 1$ since Eq. (8.83) yields different solutions when a is changed. Figure 8.9 shows the doubly-conditional profiles of the temperature and the mass fraction of CH_4, H_2O, CO_2, CO, and OH. The left panes display the results in η-space at different θ-planes, whereas the right ones depict the results in θ-space at different η-planes. The chosen values for θ (0.3, 0.5, 0.65, 0.80 and 0.95) cover the intermediate states between unburnt and fully burnt conditions. The values of η are selected such that lean ($\eta = 0.12$ and 0.24), stoichiometric ($\eta = 0.35$) and rich ($\eta = 0.52$ and 0.67) conditions are represented.

As a is increased, the solution in η-space at every θ-plane tends to the inert mixing solution, and the extinction state is gradually approached. To demonstrate this, the steady state form of Eq. (8.66) is first multiplied by $2\Delta\phi^{max}_{min}(\eta)/\langle \chi_\xi | \eta, \theta \rangle$ then rearranged as:

$$\begin{aligned}
\Delta\phi^{max}_{min}(\eta)\frac{\partial^2 Q_\kappa}{\partial \eta^2} = &\left(\theta\frac{d^2[\Delta\phi^{max}_{min}(\eta)]}{d\eta^2} + \frac{d^2\phi_{min}(\eta)}{d\eta^2}\right)\frac{\partial Q_\kappa}{\partial \theta} \\
&- 2\frac{\langle \chi_{\xi,c} | \eta, \theta \rangle}{\langle \chi_\xi | \eta, \theta \rangle}\left(\Delta\phi^{max}_{min}(\eta)\frac{\partial^2 Q_\kappa}{\partial \eta \partial \theta} - \frac{d[\Delta\phi^{max}_{min}(\eta)]}{d\eta}\frac{\partial Q_\kappa}{\partial \theta}\right) \\
&- \Delta\phi^{max}_{min}(\eta)\frac{\langle \chi_c | \eta, \theta \rangle}{\langle \chi_\xi | \eta, \theta \rangle}\frac{\partial^2 Q_\kappa}{\partial \theta^2} - 2\frac{\Delta\phi^{max}_{min}(\eta)}{\langle \chi_\xi | \eta, \theta \rangle}\frac{\langle \dot{\omega}_\kappa | \eta, \theta \rangle}{\langle \rho | \eta, \theta \rangle} \\
&+ 2\frac{\Delta\phi^{max}_{min}(\eta)}{\langle \chi_\xi | \eta, \theta \rangle}\frac{\langle \dot{\omega}_c | \eta, \theta \rangle}{\langle \rho | \eta, \theta \rangle}\frac{\partial Q_\kappa}{\partial \theta}
\end{aligned} \tag{8.98}$$

In the limit of very large a, the solution of Eq. (8.83) yields the inert mixing solution, $Y_{\kappa,min}(\eta)$. Therefore, as a is increased $\phi_{max}(\eta)$ tends gradually towards $\phi_{min}(\eta)$ ($=Y_{\mathrm{CO,min}}(\eta) + Y_{\mathrm{CO_2,min}}(\eta) = 0$ for the flame under investigation). As a result, $\Delta\phi^{max}_{min}(\eta)$ and its first and second derivatives with respect to η tend to zero. As such, all the terms on the r.h.s. of Eq. (8.98) approach zero, leading to:

$$\lim_{a \to +\infty} \Delta\phi^{max}_{min}(\eta)\frac{\partial^2 Q_\kappa}{\partial \eta^2} = 0 \tag{8.99}$$

Although $\lim_{a \to +\infty} \Delta\phi^{max}_{min}(\eta) = 0$, $\partial^2 Q_\kappa / \partial \eta^2$ in Eq. (8.99) is not arbitrary. Since $Q_\kappa(\eta, \theta)$ is bounded by $Y_{\kappa,min}(\eta)$ at $\theta = 0$ and $Y_{\kappa,max}(\eta)$ at $\theta = 1$, and since $Y_{\kappa,max}(\eta)$ tends to

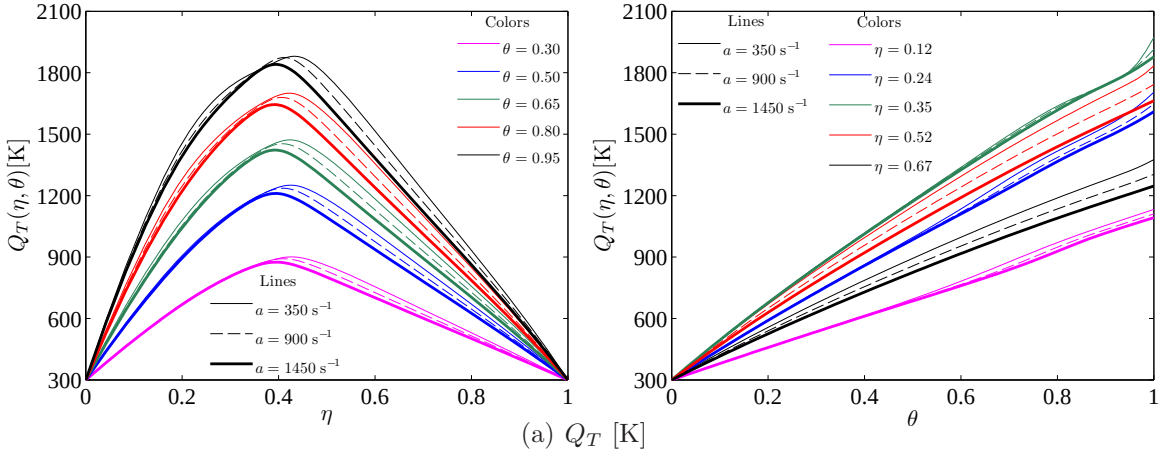

(a) Q_T [K]

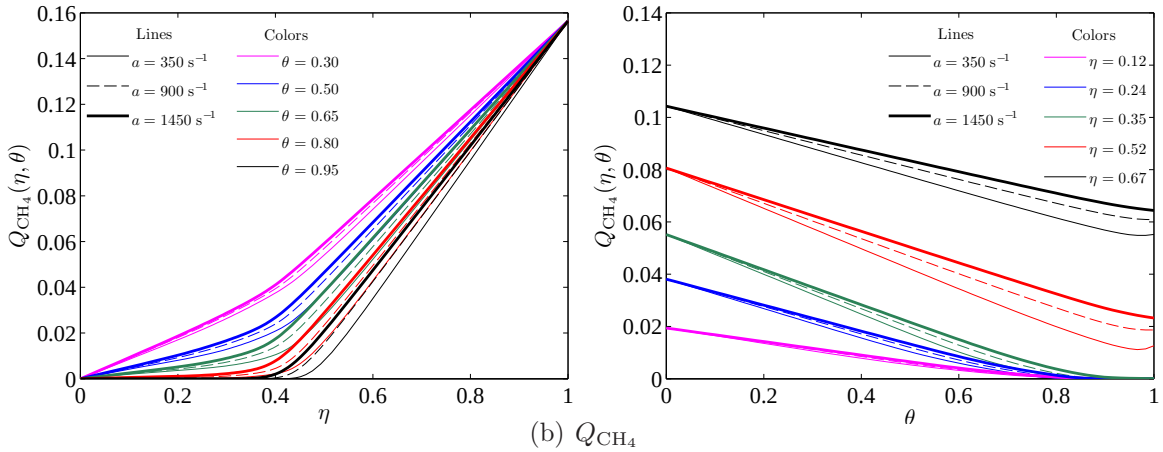

(b) Q_{CH_4}

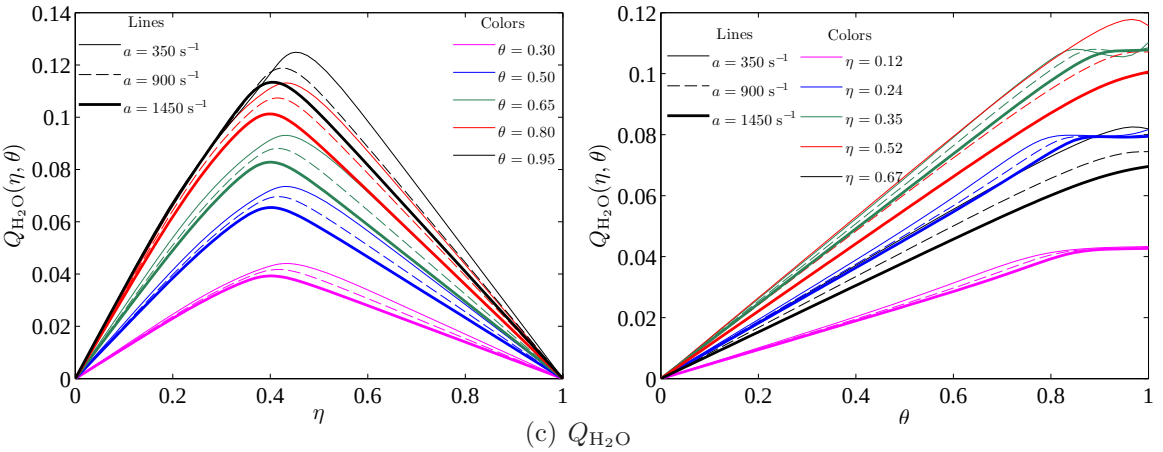

(c) Q_{H_2O}

Figure 8.9: Profiles of (a) Q_T [K], (b) Q_{CH_4}, (c) Q_{H_2O}, (d) Q_{CO_2}, (e) Q_{CO}, and (f) Q_{OH} for $a = 350$, 900 and 1450 s^{-1}, $b = 50$ s^{-1}, and $\mathbf{n}_\xi \cdot \mathbf{n}_c = +1$ (continued on next page).

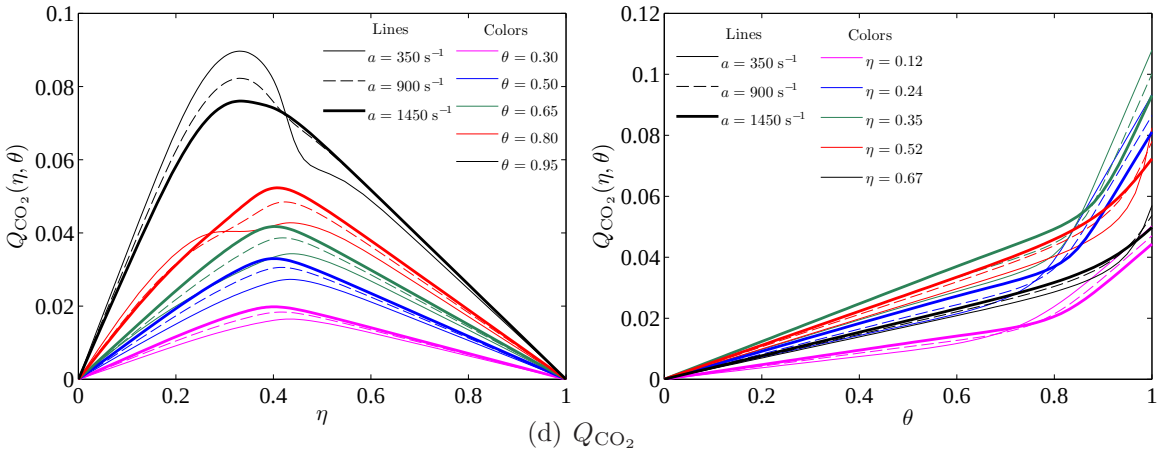

(d) $Q_{\mathrm{CO_2}}$

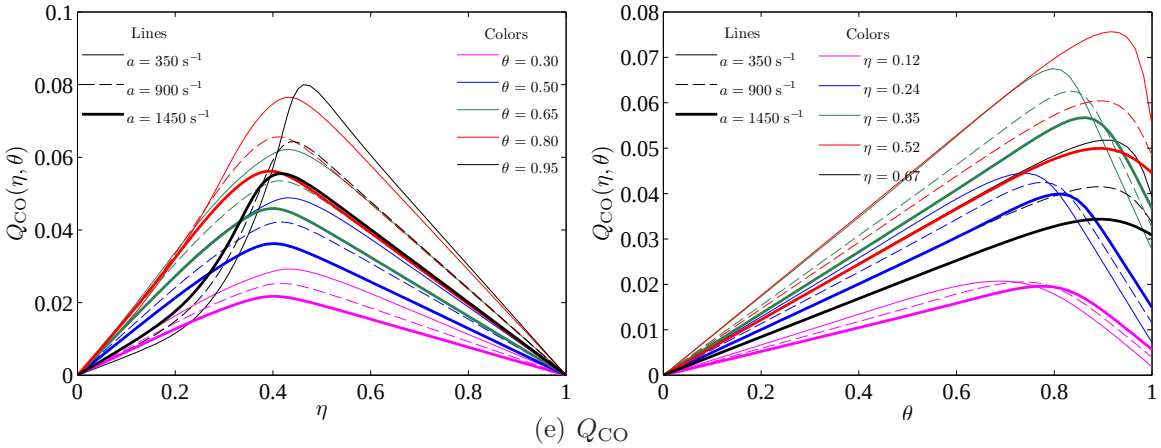

(e) Q_{CO}

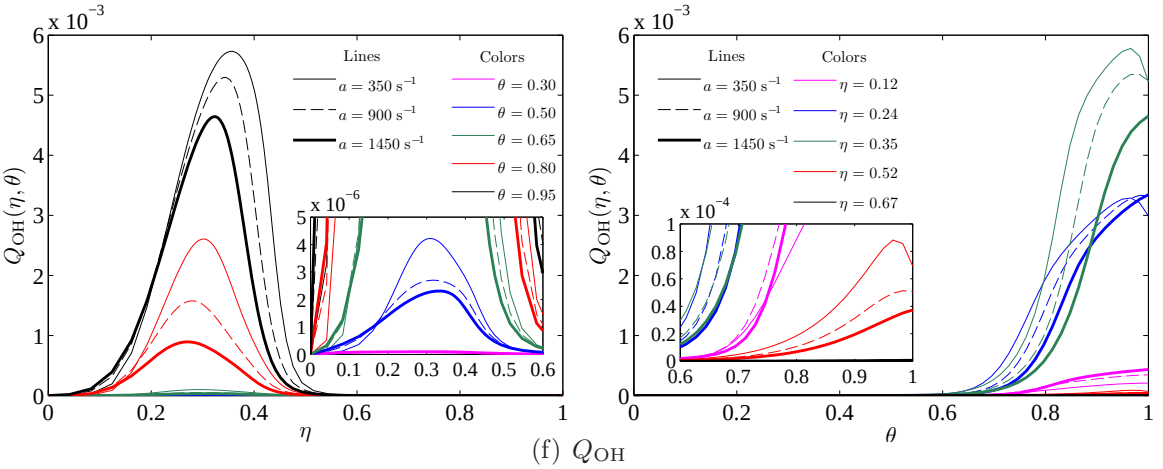

(f) Q_{OH}

Figure 8.9: Profiles of (a) Q_T [K], (b) $Q_{\mathrm{CH_4}}$, (c) $Q_{\mathrm{H_2O}}$, (d) $Q_{\mathrm{CO_2}}$, (e) Q_{CO}, and (f) Q_{OH} for $a = 350$, 900 and 1450 s^{-1}, $b = 50\ \mathrm{s}^{-1}$, and $\mathbf{n}_\xi \cdot \mathbf{n}_c = +1$.

$Y_{\kappa,min}(\eta)$ in the limit of large a, it follows that $Q_\kappa(\eta, 0 < \theta < 1)$ tends to $Y_{\kappa,min}(\eta)$. Hence,

$$\lim_{a\to+\infty} Q_\kappa(\eta,\theta) = Y_{\kappa,min}(\eta) \tag{8.100}$$

This limit satisfies $\lim_{a\to+\infty} \partial^2 Q_\kappa/\partial\eta^2 = 0$ because $Y_{\kappa,min}(\eta)$ is linear.

8.5.7 Effect of strain in θ-space

Similar to the procedure followed in the previous section, the assessment of the effect of strain in θ-space is performed by varying the parameter b in Eq. (8.72), while holding the parameter a in Eq. (8.71) constant. The product $\mathbf{n}_\xi \cdot \mathbf{n}_c$ in Eq. (8.73) is taken to be $+1$. The considered values of b are 2.5, 250, 2500 s^{-1}. a is set to 350 s^{-1}. Since a is constant, the boundary conditions at $\theta = 1$ and $\langle\chi_\xi|\eta,\theta\rangle$ remain unchanged. The variation of b affects the distributions of $\langle\chi_c|\eta,\theta\rangle$ and $\langle\chi_{\xi,c}|\eta,\theta\rangle$ via Eqs. (8.71) and (8.72). The results are displayed in Figure 8.10.

As b is increased, $Q_\kappa(\eta,\theta)$ at a given η tends towards a linear solution in θ-space bounded by the unburnt state at $\theta = 0$ and the burnt state at $\theta = 1$. To demonstrate this, the steady-state form of Eq. (8.66) is first multiplied by $2/\langle\chi_c|\eta,\theta\rangle$ and then rearranged as:

$$\begin{aligned}\frac{\partial^2 Q_\kappa}{\partial\theta^2} = &-\frac{\langle\chi_\xi|\eta,\theta\rangle}{\langle\chi_c|\eta,\theta\rangle}\left[\frac{\partial^2 Q_\kappa}{\partial\eta^2} - \frac{1}{\Delta\phi^{max}_{min}(\eta)}\left(\theta\frac{d^2[\Delta\phi^{max}_{min}(\eta)]}{d\eta^2} + \frac{d^2\phi_{min}(\eta)}{d\eta^2}\right)\frac{\partial Q_\kappa}{\partial\theta}\right] \\ &- 2\frac{\langle\chi_{\xi,c}|\eta,\theta\rangle}{\langle\chi_c|\eta,\theta\rangle}\left(\frac{\partial^2 Q_\kappa}{\partial\eta\partial\theta} - \frac{1}{\Delta\phi^{max}_{min}(\eta)}\frac{d[\Delta\phi^{max}_{min}(\eta)]}{d\eta}\frac{\partial Q_\kappa}{\partial\theta}\right) \\ &- \frac{2}{\langle\chi_c|\eta,\theta\rangle}\frac{\langle\dot\omega_\kappa|\eta,\theta\rangle}{\langle\rho|\eta,\theta\rangle} + \frac{2}{\langle\chi_c|\eta,\theta\rangle}\frac{\langle\dot\omega_c|\eta,\theta\rangle}{\langle\rho|\eta,\theta\rangle}\frac{\partial Q_\kappa}{\partial\theta}\end{aligned} \tag{8.101}$$

As b is increased, $\langle\chi_c|\eta,\theta\rangle$ becomes larger in magnitude compared to $\langle\chi_\xi|\eta,\theta\rangle$, $\langle\chi_{\xi,c}|\eta,\theta\rangle$, $\langle\dot\omega_\kappa|\eta,\theta\rangle$ and $\langle\dot\omega_c|\eta,\theta\rangle$. Therefore, in the limit of very large b all the terms on the r.h.s. of Eq. (8.101) tend to zero, leading to:

$$\lim_{b\to+\infty} \frac{\partial^2 Q_\kappa}{\partial\theta^2} = 0 \tag{8.102}$$

Since Q_κ is bounded by $Y_{\kappa,min}(\eta)$ at $\theta = 0$ and $Y_{\kappa,max}(\eta)$ at $\theta = 1$, Eq. (8.102) has the simple linear solution:

$$\lim_{b\to+\infty} Q_\kappa(\eta,\theta) = Y_{\kappa,min}(\eta) + (Y_{\kappa,max}(\eta) - Y_{\kappa,min}(\eta))\theta \tag{8.103}$$

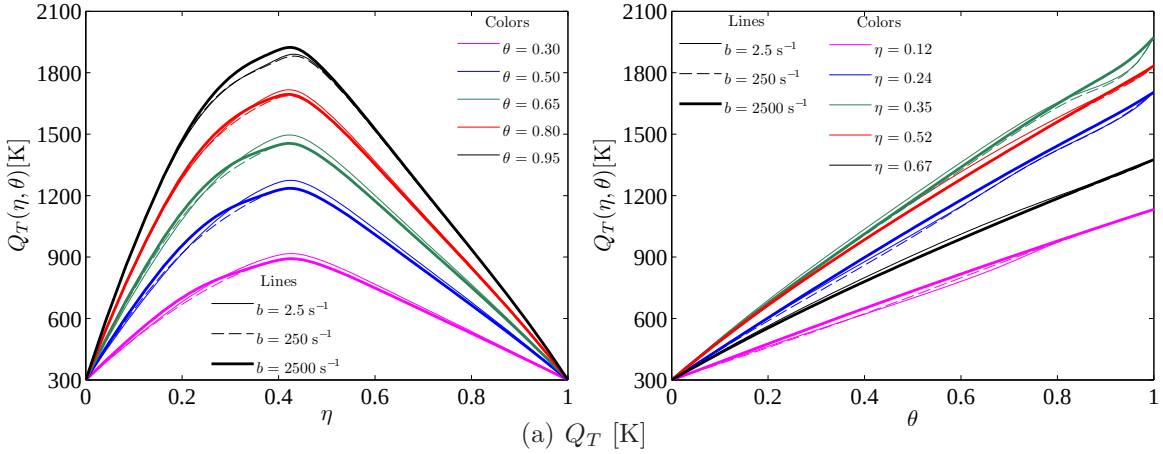

(a) Q_T [K]

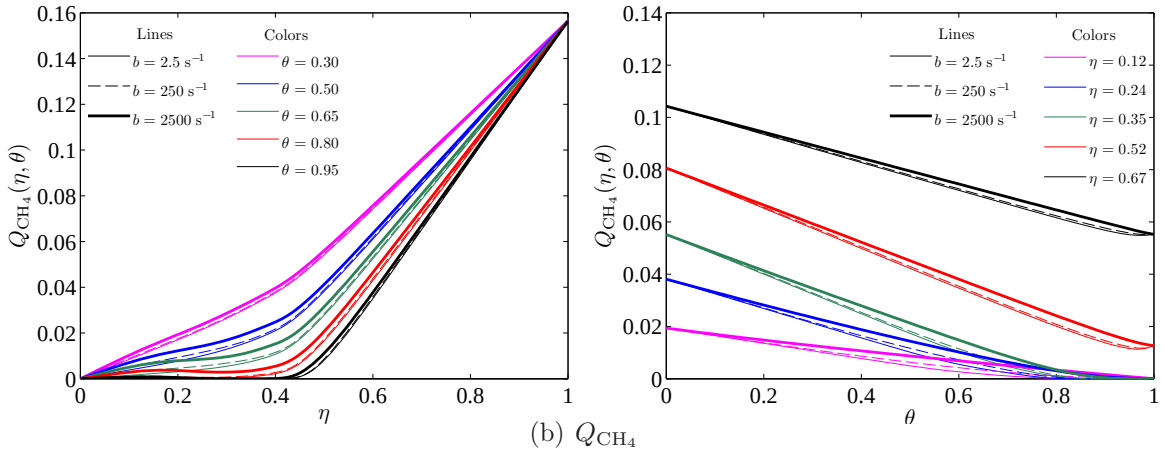

(b) Q_{CH_4}

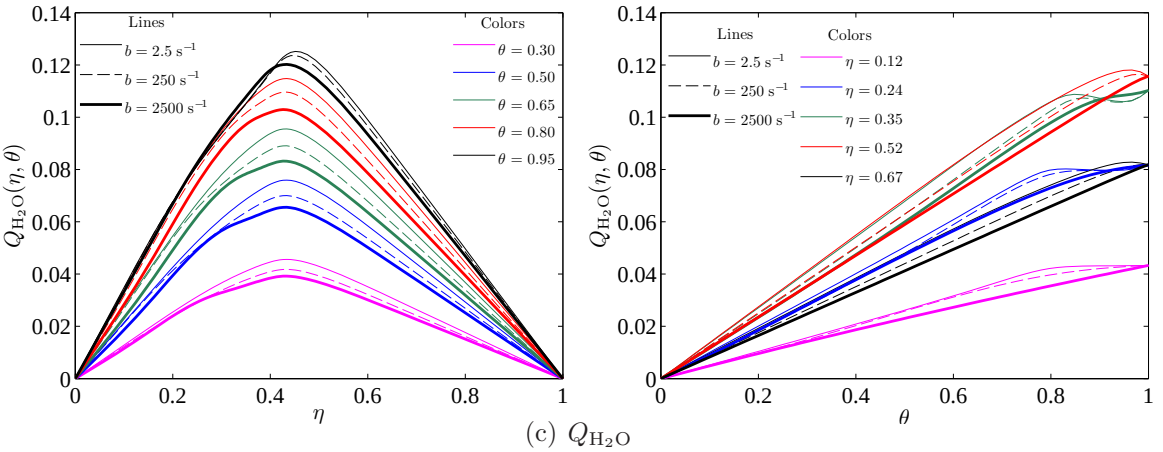

(c) Q_{H_2O}

Figure 8.10: Profiles of (a) Q_T [K], (b) Q_{CH_4}, (c) Q_{H_2O}, (d) Q_{CO2}, (e) Q_{CO}, and (f) Q_{OH} for $a = 350$ s^{-1}, $b = 2.5$, 250 and 2500 s^{-1}, and $\mathbf{n}_\xi \cdot \mathbf{n}_c = +1$ (continued on next page).

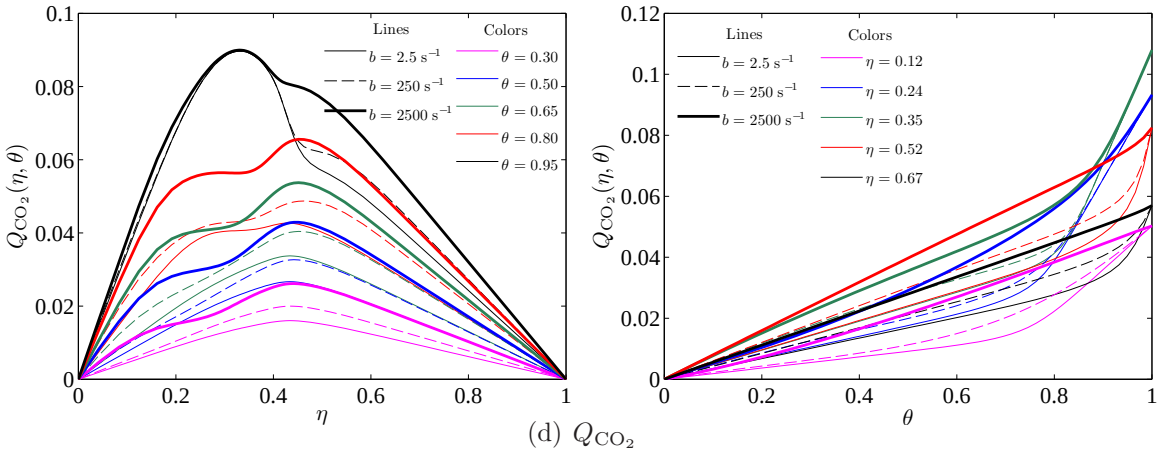

(d) Q_{CO_2}

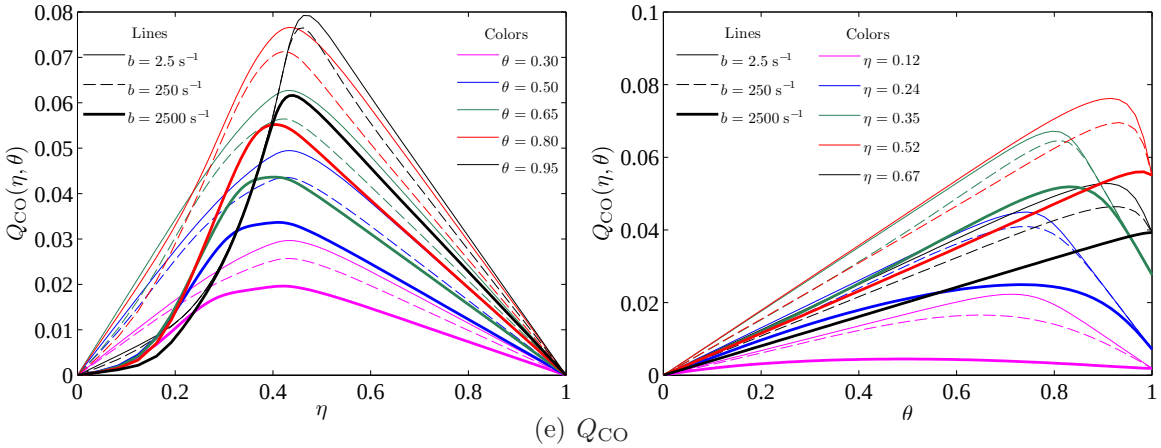

(e) Q_{CO}

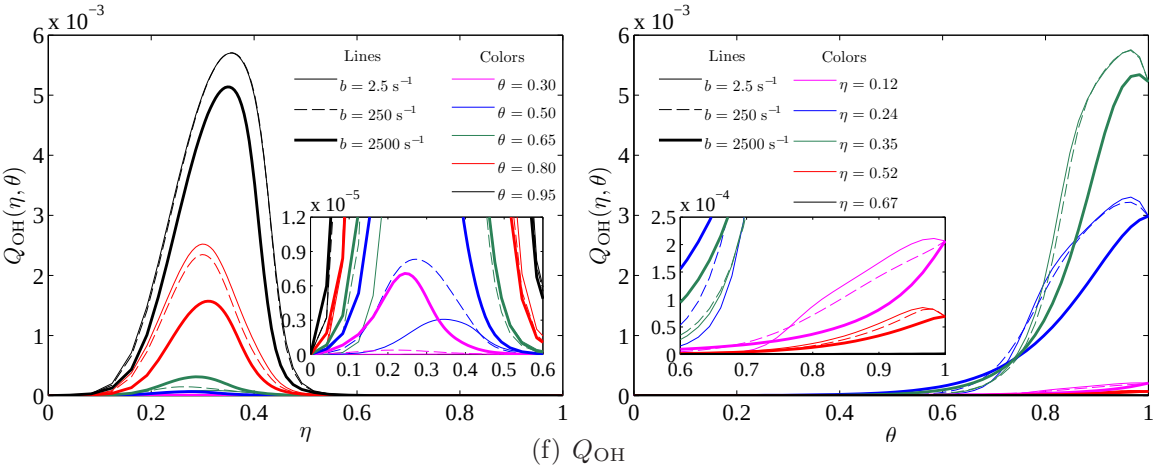

(f) Q_{OH}

Figure 8.10: Profiles of (a) Q_T [K], (b) Q_{CH_4}, (c) Q_{H_2O}, (d) Q_{CO2}, (e) Q_{CO}, and (f) Q_{OH} for $a = 350\ s^{-1}$, $b = 2.5$, 250 and 2500 s^{-1}, and $\mathbf{n}_\xi \cdot \mathbf{n}_c = +1$.

As such, at a given η, Q_κ tends to vary linearly in θ-space between the unburnt and burnt states as b is increased. This can be observed in the right panes of Fig. 8.10. By increasing b, the slopes of the profiles of the reactive scalars in θ-space tend towards $Y_{\kappa,max}(\eta) - Y_{\kappa,min}(\eta)$. This behaviour can be clearly seen in the case where $b = 2500\ s^{-1}$.

8.5.8 Effect of cross-dissipation

In order to analyse the role of the doubly-conditional cross-dissipation, $\langle \chi_{\xi,c} | \eta, \theta \rangle$, the parameters a and b are held constant and $\mathbf{n}_\xi \cdot \mathbf{n}_c$ is varied. a and b are set to 200 and 50 s^{-1}, respectively, and $\mathbf{n}_\xi \cdot \mathbf{n}_c$ is assigned the values -1, 0 and +1 in three separate realisations. The case where $\mathbf{n}_\xi \cdot \mathbf{n}_c = 0$ corresponds to the absence of cross-dissipation (the term T_2 in Eq. (8.66) is turned off), whereas the cases where $\mathbf{n}_\xi \cdot \mathbf{n}_c$ = -1 and +1 correspond to the two extremes where $\langle \chi_{\xi,c} | \eta, \theta \rangle$ is smallest (negative) and largest (positive), respectively. Since a and b are constant, the distributions of $\langle \chi_\xi | \eta, \theta \rangle$ and $\langle \chi_c | \eta, \theta \rangle$ and the boundary conditions at $\theta = 1$ remain unchanged in all three realisations. The doubly-conditional profiles of the reactive scalars are shown in Fig. 8.11. It is obvious that the role of $\langle \chi_{\xi,c} | \eta, \theta \rangle$ is non-negligible. The temperature and species mass fractions profiles obtained in the $\mathbf{n}_\xi \cdot \mathbf{n}_c = 0$ case are intermediate between those of the $\mathbf{n}_\xi \cdot \mathbf{n}_c$ -1 and +1 cases, as shown in Figs. 8.11(a)-(f). The difference in η-space are small near the burnt boundary ($\theta = 0.95$) and confined within a narrow range of η. The response to the variation of $\mathbf{n}_\xi \cdot \mathbf{n}_c$ becomes more notable with decreasing θ. Larger differences are observed between the three realisations over a wider range of η ($\theta = 0.85$, 0,75 and 0.5). As the unburnt boundary is approached, the differences diminish gradually but remain substantial ($\theta = 0.3$).

8.5.9 Effect of strain on heat release

The contours of the volumetric heat release rate, $-\sum_{\kappa=1}^{N_s} \langle h_\kappa | \eta, \theta \rangle \langle \dot{\omega}_\kappa | \eta, \theta \rangle$ [J/m^{3}s], are shown in Figs. 8.12 for different combinations of a and b. In all cases $\mathbf{n}_\xi \cdot \mathbf{n}_c$ is set to +1. In each subplot, b is held constant at the indicated value and a is assigned the values 50, 100 and 35 s^{-1}. As a is increased (compare the panes in each of Figs. 8.12(a), (b) and (c) from top to bottom), the reaction zone stretches and propagates towards the fully burnt boundary most notably in rich mixtures. The maximum rate of heat release decreases in magnitude and its location (filled circles) shifts from slightly rich mixtures towards stoichiometric mixtures and closer towards the burnt boundary. As b is increased (compare the top, middle and bottom panes in Figs. 8.12(a)–(c)), burning is enhanced. The reaction zone becomes notably larger and the maximum rate of heat release increases. The

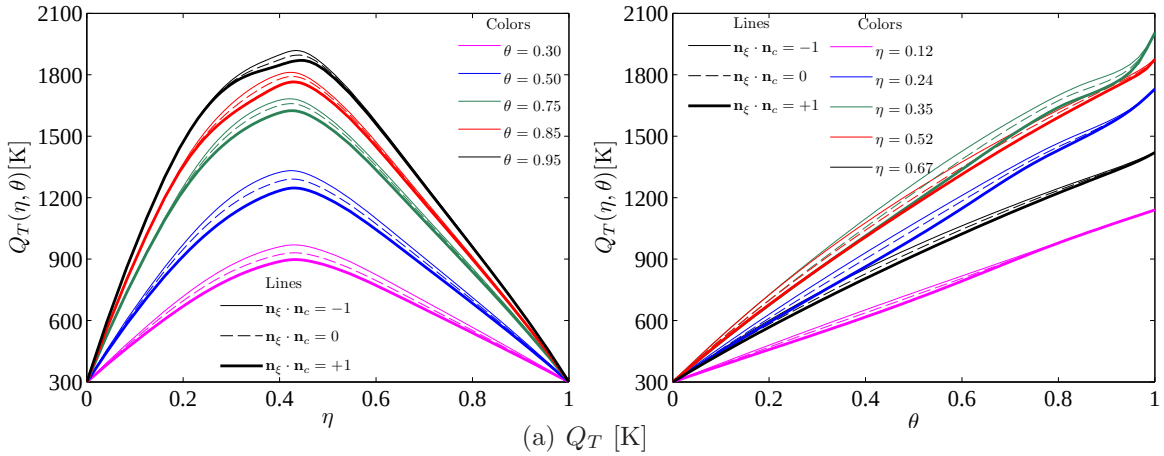

(a) Q_T [K]

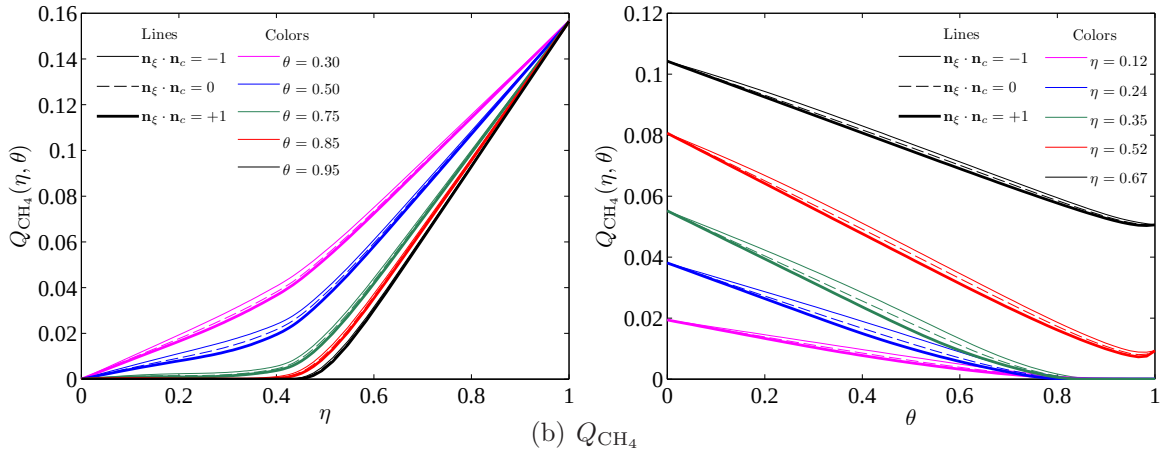

(b) Q_{CH_4}

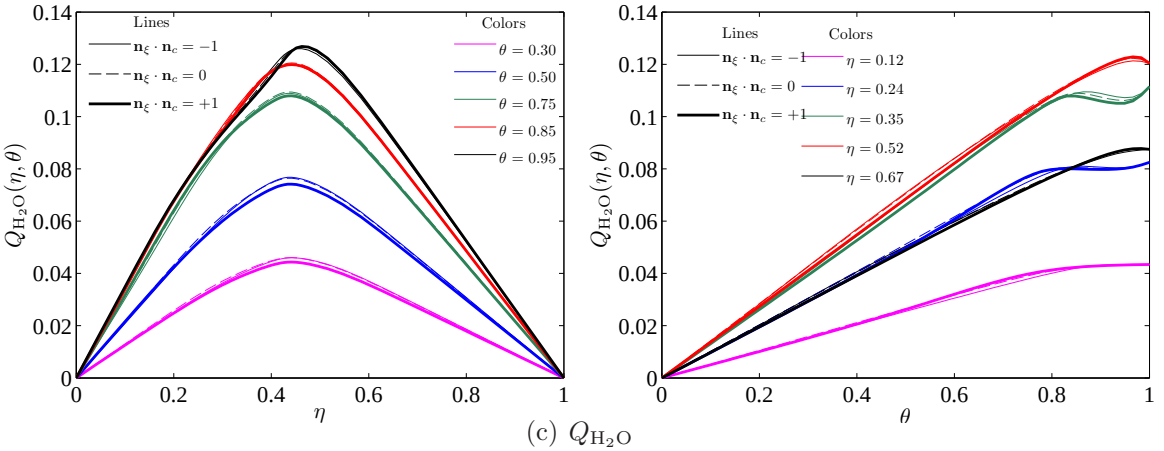

(c) Q_{H_2O}

Figure 8.11: Profiles of (a) Q_T [K], (b) Q_{CH_4}, (c) Q_{H_2O}, (d) Q_{CO_2} (e) Q_{CO}, and (f) Q_{OH} for $a = 200$ s^{-1}, $b = 50$ s^{-1} and $\mathbf{n}_\xi \cdot \mathbf{n}_c$ = -1, 0, +1 (continued on next page).

8.11

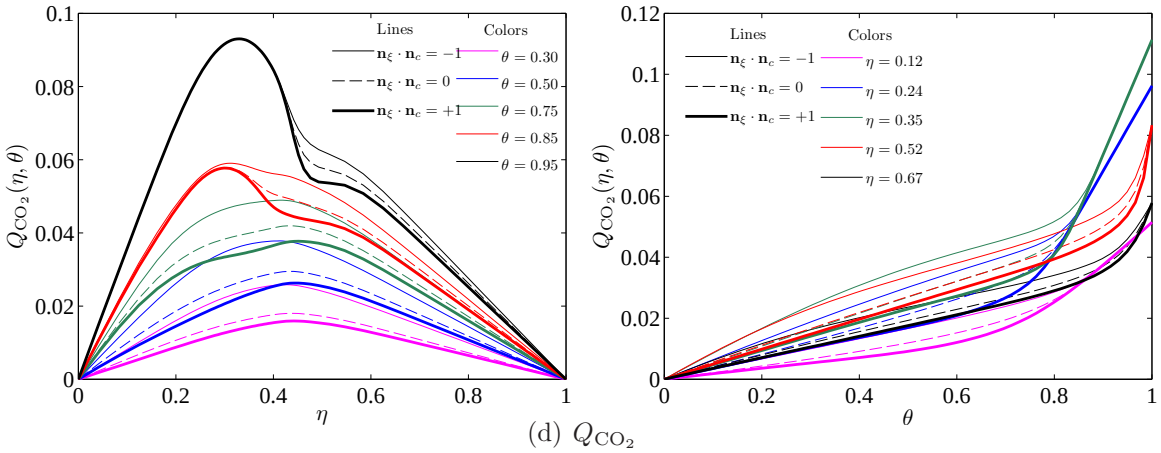

(d) $Q_{\mathrm{CO_2}}$

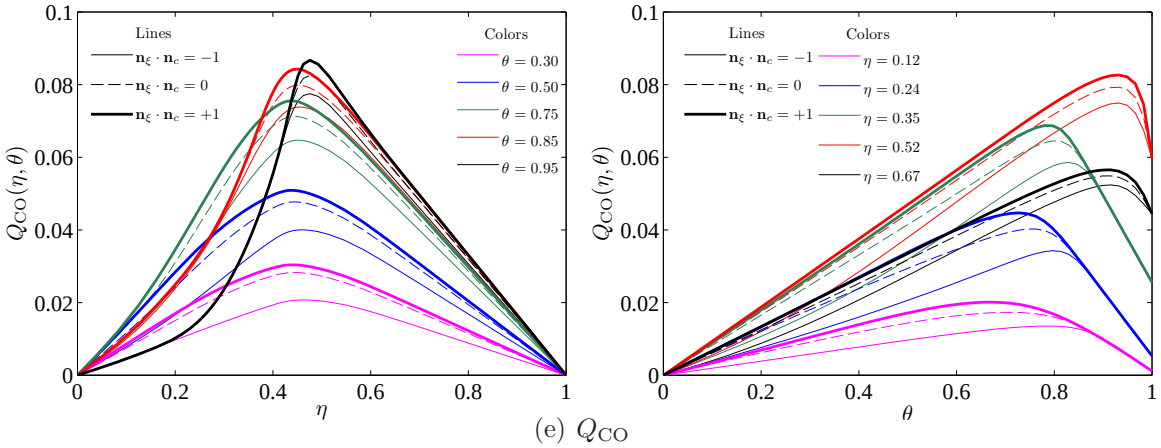

(e) Q_{CO}

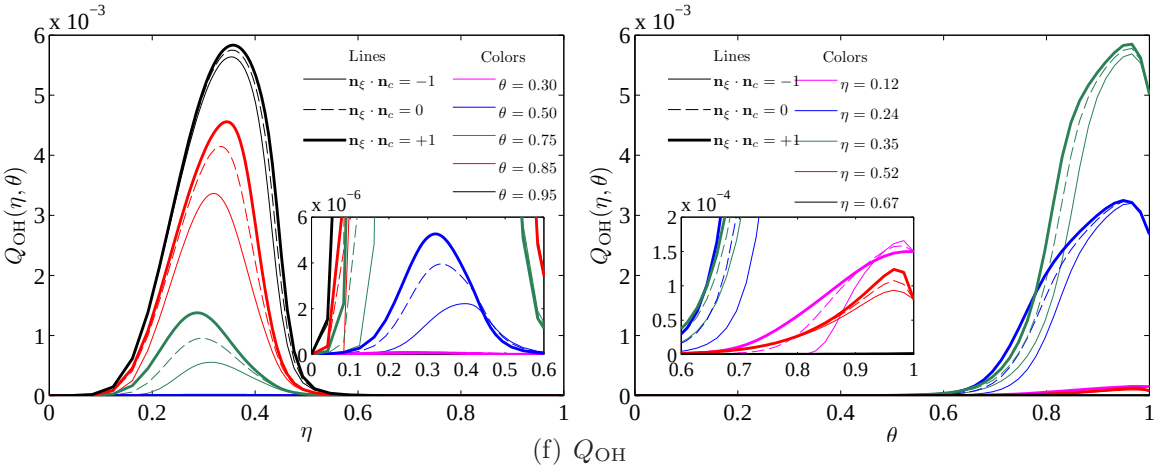

(f) Q_{OH}

Figure 8.11: Profiles of (a) Q_T [K], (b) $Q_{\mathrm{CH_4}}$, (c) $Q_{\mathrm{H_2O}}$, (d) $Q_{\mathrm{CO_2}}$ (e) Q_{CO}, and (f) Q_{OH} for $a = 200$ s^{-1}, $b = 50$ s^{-1} and $\mathbf{n}_\xi \cdot \mathbf{n}_c$ = -1, 0, +1

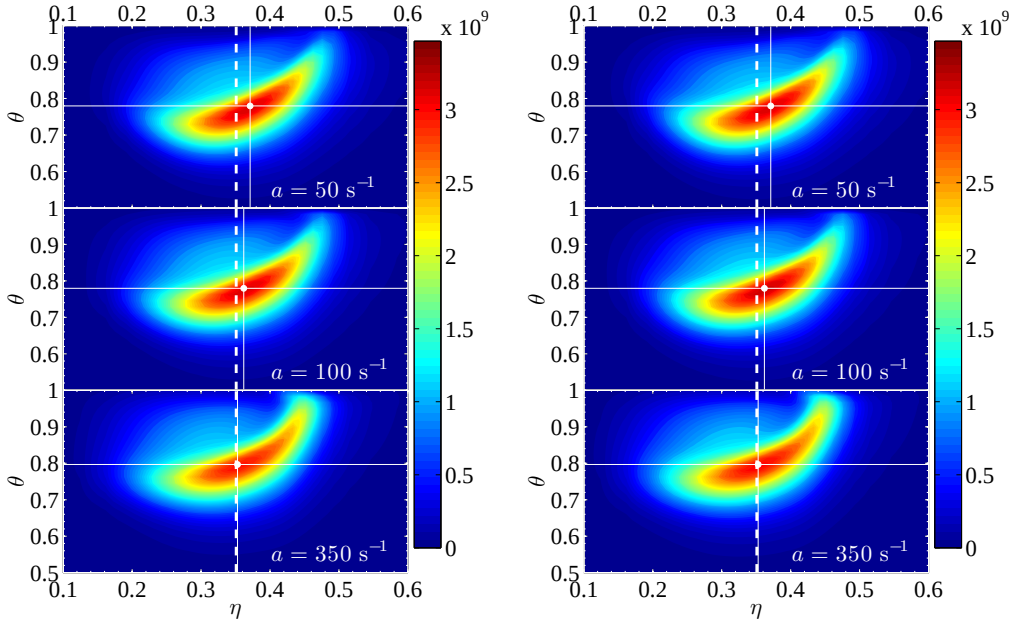

(a) $b = 25$ s^{-1} (b) $b = 50$ s^{-1}

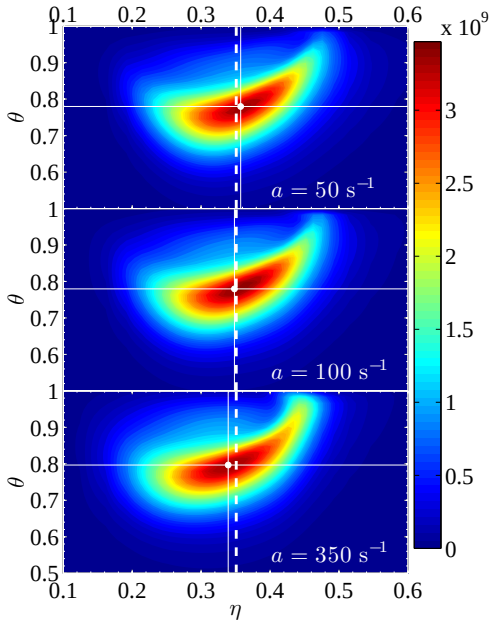

(c) $b = 250$ s^{-1}

Figure 8.12: Contours of the volumetric heat release [J/m^{3}s] for $a = 50$, 100 and 350 s^{-1} and $\mathbf{n}_\xi \cdot \mathbf{n}_c = +1$: (a) $b = 25$ s^{-1}, (b) $b = 50$ s^{-1}, and (c) $b = 250$ s^{-1}. The dashed lines correspond to $\eta = \xi_{st}$ and the intersections of the solid lines indicate locations of maximum heat release (filled circles).

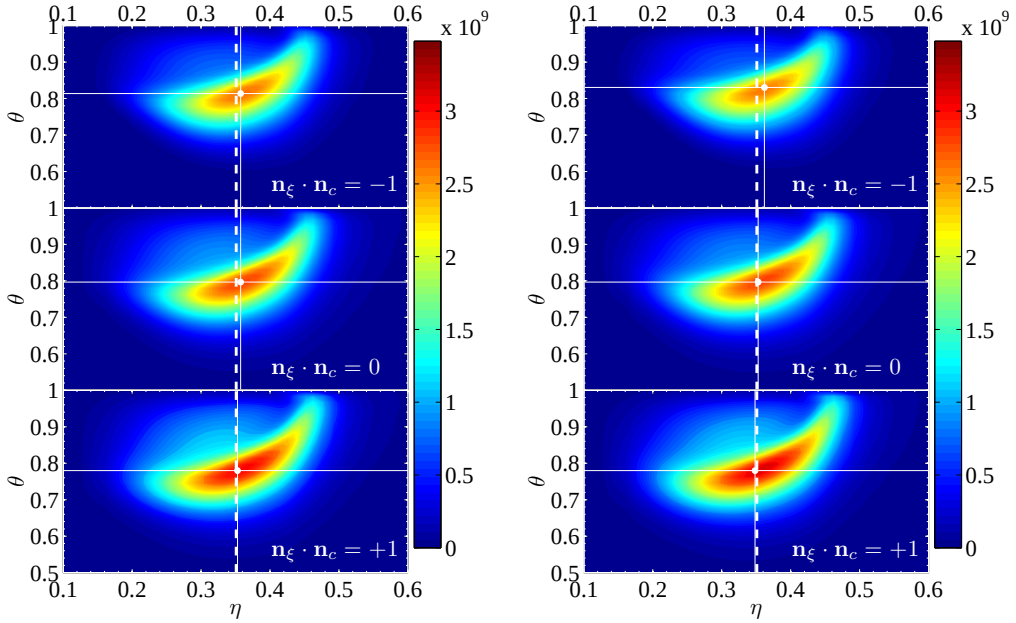

(a) $b = 25$ s^{-1} (b) $b = 50$ s^{-1}

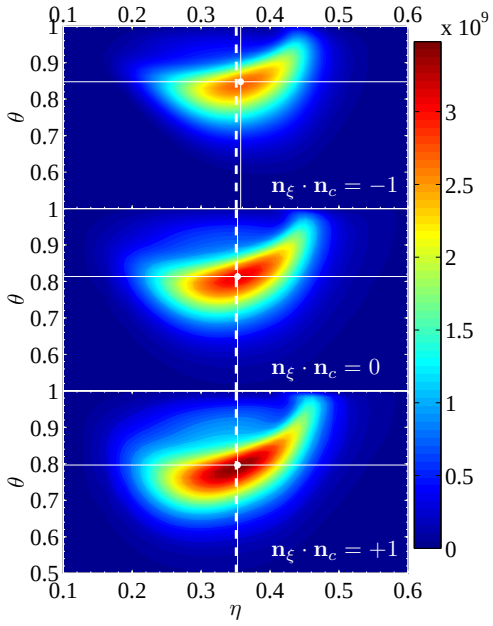

(c) $b = 250$ s^{-1}

Figure 8.13: Contours of the volumetric heat release [J/m^{3}s] for $a = 200$ s^{-1} and $\mathbf{n}_\xi \cdot \mathbf{n}_c =$ -1, 0, +1: (a) $b = 25$ s^{-1}, (b) $b = 50$ s^{-1}, and (c) $b = 250$ s^{-1}. The dashed lines correspond to $\eta = \xi_{st}$ and the intersections of the solid lines indicate locations of maximum heat release (filled circles).

location of maximum heat release shifts move from rich mixtures towards stoichiometric or lean mixtures, depending on the value of a. No appreciable change in the locations of the maxima is observed in θ-space.

Figure 8.13 displays the contours of the volumetric heat release rate for several combinations of b and $\mathbf{n}_\xi \cdot \mathbf{n}_c$. In each sub-figure, a is held constant at 200 s^{-1} and b is set the indicated value. Three sets of calculations are performed using the prescribed values of a and b with $\mathbf{n}_\xi \cdot \mathbf{n}_c$ assigned the values -1, 0 and +1. Common observations can be made as $\mathbf{n}_\xi \cdot \mathbf{n}_c$ is increased (compare the panes in each of Figs. 8.13(a), (b) and (c) from top to bottom). Burning is enhanced and the reaction zone propagates in all directions. The maximum rate of heat release moves from slightly rich towards stoichiometric mixtures and away from the burnt boundary. For a given $\mathbf{n}_\xi \cdot \mathbf{n}_c$ value, the rate of burning increases with increasing b (compare the top, middle and bottom panes in Figs. 8.13(a)–(c)). The findings described in Fig. 8.13 illustrate the importance of the doubly-conditional cross-dissipation in DCMC modelling. The response of heat release to variations in $\mathbf{n}_\xi \cdot \mathbf{n}_c$ demonstrates the sensitivity of the results to the orientation of the ξ and c isosurfaces.

8.6 Conclusions

This chapter presented a new DCMC method for the modelling of conditional fluctuations in non-premixed and partially premixed flames. The proposed method differs from previous formulations [40, 122] by the approach followed to define the second conditioning variable. A normalised, mixture-fraction-dependent progress variable was introduced. The dependence of the selected variable on mixture fraction was accomplished through normalisation using the unburnt and burnt states. The doubly-conditional species and energy equations were derived based on a generic definition for the progress variable. Simple submodels for the doubly-conditional unclosed terms resulting from the derivation were proposed. A preliminary parametric assessment of the homogeneous version of the method was performed. The conditions of Sandia flame D were considered with the progress variable defined as the sum of the CO and CO_2 mass fractions. The unburnt and burnt states were set to the inert mixing and homogeneous CMC solutions, respectively. For simplicity, the doubly-conditional dissipation terms were closed using the parametric expression proposed in [172]. The first- and second-order derivatives in the DCMC transport equations were discretised using the finite difference method and a fractional step method was implemented in order to treat the stiff chemical terms separately. The steady state solution was obtained by relaxation of the time step.

The parametric assessment was focused on the sensitivity of the structure of the reactive

scalars to variations in the strain rate levels in both mixture fraction and progress variable spaces. The performed numerical experiments reveal that:

1. The profiles of the reactive scalars in mixture fraction space tend to the inert mixing as the mixture fraction strain rate parameter is increased.

2. The profiles in progress variable space tend to vary linearly between the unburnt and burnt states as the progress variable strain rate parameter is increased.

3. The doubly-conditional cross-dissipation plays an important role in DCMC modelling, and therefore should not be neglected

4. The relative orientation of the unit vectors normal to the mixture fraction and progress variables isosurfaces has a non-negligible effect on the structure of the reactive scalars.

The assessment performed in this work is preliminary in nature. Further analysis using DNS is necessary in order to explore the potential of the proposed method and the validity of the suggested submodels.

Chapter 9

Conclusions and recommendations

The objectives of this thesis were to assess the applicability of the first-order Conditional Moment Closure (CMC) to a number of combustion problems using classical and advanced CMC submodels and to propose a Doubly-Conditional Moment Closure (DCMC) formulation for the treatment of conditional fluctuations in non-premixed and partially premixed combustion.

CMC was first implemented to model the autoignition of CH_4-based fuel blends in a shock tube facility [240]. The experimental conditions of the shock tube simulate the autoignition environment in a direct-injection compression-ignition engine. The considered sets of measurements and the employed chemical kinetic mechanisms have not been previously investigated using CMC. Although the accurate CMC modelling of autoignition necessitates a second-order closure for the conditional reaction rates, the application of the first-order closure was found to be useful when placed into the perspective of the level of accuracy required for practical engine calculations.

The piloted CH_4/air jet flame [12] and lifted H_2/N_2 jet flame [35] that were investigated in this work have been previously analysed using the first-order CMC. However, previous investigations overlook the importance of the consistency of the Conditional Velocity (CV) and the Conditional Scalar Dissipation Rate (CSDR) submodels with the modelling of the mixture fraction Probability Density Function (PDF). The CV submodel needs to be fully consistent with the closures employed in the modelling of the turbulent fluxes of the first and second moments of the mixture fraction. Additionally, the CSDR submodel must guarantee the absence of spurious sources in the unconditional transport equations of the reactive scalars. This condition is fulfilled if the CSDR modelling is consistent with the presumed PDF (through the PDF transport equation). The commonly used CV and

CSDR submodels in the CMC literature violate these two requirements, and therefore lead to inconsistent CMC implementations. To quantify the impact of this discrepancy in CMC modelling, the piloted CH_4/air and lifted H_2/N_2 jet flames were revisited in order to compare the performance of classical (inconsistent) and advanced (consistent) submodels.

Double-conditioning of reactive scalars in non-premixed combustion has been previously shown to simplify the modelling of the chemical reaction rates in situations where the conditional fluctuations about the singly-conditional means of the scalars are significant [40, 122]. The incorporation of a second conditioning variable beside the mixture fraction has the advantage of making conditioning more constrictive so that doubly-conditional means comprise more refined information about the flow field compared to singly-conditional means. Consequently, doubly-conditional fluctuations are smaller in magnitude than their singly-conditional counterparts, and the first-order closure holds for the treatment of highly fluctuating combustion phenomena. In this work, a new DCMC method was proposed in order to explore the potential of double-conditioning in the modelling of both non-premixed and partially premixed combustion modes.

This chapter summarises the major results and main conclusion reached in this work. Further improvements are proposed.

9.1 Conclusions

9.1.1 Autoignition CH_4-based fuel blends

The shock tube autoignition of low temperature, high pressure, transient CH_4-based fuel jets injected into lower pressure heated air was investigated using the first-order CMC and the standard k-ε model. Fuel mixtures consisting of 100% CH_4, 90% CH_4/10% C_2H_6, 80% CH_4/20% H_2, and 80% CH_4/20% N_2 were considered over a wide range of pre-combustion air temperatures. The PDF was presumed using using the β-distribution and the CV was closed using the linear model [131]. Two submodels were implemented for the modelling of the CSDR: Girimaji's model [78] and the AMC [174]. Optimised chemical kinetic mechanisms specific to each fuel blend were employed.

The first-order closure was found to be suitable for the modelling of the conditional chemical sources since the CSDR decays rapidly below its critical value downstream of the injector. The calculated ignition delays and kernel locations are in fair agreement with the experimental measurements of Wu [240]. The AMC predicts slightly shorter ignition delays compared to Girimaji's model. Both CSDR submodels lead to slight underpredictions at

high air temperatures and larger overpredictions at lower temperatures. The effect of C_2H_6, H_2 and N_2 additives on the autoignition of CH_4 was well reproduced. C_2H_6 and H_2 additives do not change the main CH_4 reaction pathways, however, their oxidation provides additional ignition-promoting radical, which in turn enhance the oxidation of CH_4, and therefore leads to shorter ignition delays. The presence of N_2 additives in the fuel stream reduces the fraction of CH_4 available for reaction, and hence causes delayed ignition. The autoignition in all blends was found to take place in lean mixtures and at low scalar dissipation rates, consistent with previous DNS studies [147, 149].

One shortcoming of the presented calculations is the inconsistent modelling of the CV and CSDR. Firstly, the linear CV model is exact only if the joint PDF of the velocity and the mixture fraction is Gaussian [22, 120], which is not the case in the considered autoignition problem. Further, the linear model is not consistent with the modelling of the mean flux of the mixture fraction variance (the second moment of the PDF) [43]. Secondly, the AMC and Girimaji's CSDR submodels are valid for homogeneous turbulence and therefore, contribute spurious sources. Additionally, the AMC is a particular solution of the homogeneous PDF transport equation, wherein the employed mapping function is Gaussian. Hence, the modelling of the CSDR with the AMC while presuming the PDF with a β-distribution is mathematically flawed. Nevertheless, the good agreement between the CMC results and the experimental measurements suggests that the employed CV and CSDR submodels, although inconsistent, are capable of producing reliable predictions.

9.1.2 Piloted CH_4/air jet flame

The piloted CH_4/air turbulent jet flame Sandia D [12] was investigated using the two-dimensional CMC and a modified version of the Reynolds stress model. Following previous CMC studies [62, 66, 199], a first-order closure was employed for the modelling of the conditional chemical reaction rates. This closure is sufficient because the probability of local extinction in the considered flame is small [12]. The PDF was presumed using the β-distribution. The CV was closed using the PDF-gradient model [190], which is consistent with the modelling of the mean fluxes of the first and second moments of the mixture fraction. Two CSDR closures based on the double integration of the PDF transport equation were investigated: Girimaji's model [78] and Mortensen's model [157]. The former relies on the homogeneous form of the equation, whereas the latter retains the inhomogeneous terms and employs consistent PDF-gradient modelling for the modelling for the CV fluctuations. Girimaji's model is the exact equivalent of the homogeneous portion of Mortensen's.

The comparison of the predictions with experimental measurements show that the levels of all reactive scalars, including minor intermediates and radicals, are in general

better predicted when the CSDR is modelled using Mortensen's model. Improvements are mostly observed in lean and rich mixture near the inflow-pilot shear layer with some discrepancies around the stoichiometric mixture fraction. Differences between the results of the inconsistent and consistent realisations were found to diminish at downstream locations where both CSDR models tend to yield similar distributions. Overall, the obtained results indicate that that spurious sources have a non-negligible effect on the modelling of the flame, particularly downstream of the fuel and pilot streams where the modelling of mixing is critical.

One drawback in the adopted PDF modelling approach is the inability of the two-parameter β-distribution, and thereby Mortensen's β-PDF-based CSDR closure, to capture the fine mixing characteristics that manifest in the double-scalar in the double scalar mixing layer formed by the fuel, pilot and oxidiser streams. The PMF approach employed by Brizuela and Roudsari [29] seems to resolve this discrepancy by using the trinary PDF and CSDR closures proposed in [160] in the pilot region and the binary closures elsewhere. The calculations reported in [29] employ the homogeneous version of the binary and trinary CSDR closures. The application of the fully consistent inhomogeneous closures can offer additional improvements by providing a better description of the double scalar mixing layer.

9.1.3 Lifted H_2/N_2 jet flame

A lifted H_2/N_2 jet flame issuing into a vitiated coflow [35] was analysed using the two-dimensional CMC and a modified version of the $k-\varepsilon$ model. The first-order closure was employed to model the conditional chemical reactions rates following previous CMC investigations of the same flame [169,176,212]. Two PDF modelling approaches were investigated: the β-PDF and the PMF-PDF. The flow and mixing solver was supplemented by an additional transport equation for the Favre averaged scalar dissipation rate. The flame response was analysed by perturbating the experimentally reported coflow temperatures (T_c). The numerical indicators developed by Gordon et al. [79] were employed to determine the stabilisation mechanism and the effects of chemical kinetics and spurious sources were analysed.

β-PDF approach

The CV and CSDR were modelled based on the β-PDF using the PDF gradient model and Mortensen's model, respectively. Girimaji's CSDR model, the exact equivalent of

the homogeneous version of Mortensen's model, was also considered in order to assess the role of the spurious sources. The results indicate that the flame is very sensitive to small perturbations in T_c. The transport budgets in mixture fraction and physical spaces, and the history of radical build-up ahead of the stabilisation height reveal that the flame is stabilised by autoignition irrespective of the value of T_c. The neglect of inhomogeneity in Girimaji's CSDR model yields lower dissipation level at the most reactive mixture fraction, resulting in earlier ignition and smaller liftoff heights. The analysis of the spurious sources arising from inconsistent CSDR modelling show that the effect of this phenomenon is small but non-negligible within the flame zone. The assessment of different H_2 oxidation mechanisms show that the flame is very sensitive to chemical kinetics.

PMF-PDF approach

The consistent CV and CSDR submodels developed by Mortensen and Andersson [160] based on the PMF-PDF were applied. The PMF-PDF distributions around the stabilisation height are slightly narrower than those of the β-PDF and present higher peaks. Although small, the differences between the two distributions have an important impact on the CV and CSDR distributions. Compared to the β-PDF approach, the CSDR and radial CV components are lower in stoichiometric and rich mixtures, whereas the axial CV components are higher. These differences have an important influence on mixing and the residence time of the reactive scalars. The predicted temperature and mass fraction profiles and stabilisation heights were found to be qualitatively similar to those obtained using the β-PDF approach. The transport budgets and radical history indicate that autoignition remains the controlling stabilisation mechanism for sufficiently high T_c. However, as T_c is decreased, stabilisation is achieved by means of premixed flame propagation. The effect of the spurious sources remains non-negligible within the flame zone.

Despite the variability in the nature of the stabilisation mechanism, the close agreement between the predictions obtained using the PMF- and β-PDF modelling approaches suggests that former is reliable for the modelling of the unclosed CMC terms. Further application to other combustion problems, such as autoignition, extinction and re-ignition, and other flame configurations is necessary in order to fully assess the applicability of this approach.

9.1.4 Doubly-Conditional Moment Closure

A new DCMC method was devised for the implicit treatment of conditional fluctuations in non-premixed and partially premixed flames by introducing a normalised PV as a second

conditioning variable beside the mixture fraction. The normalisation was performed such that the unburnt and burnt states of the PV are dependent on the mixture fraction. A transport equation for the normalised PV was obtained and the doubly-conditional transport equations were derived using the decomposition approach assuming unity Lewis numbers and negligible density fluctuations. Simple closures for the marginal and joint PDFs, and the doubly-conditional turbulent fluxes, velocity and dissipation terms were suggested. The treatment of boundary conditions in mixture fraction and PV spaces was discussed.

A standalone parametric assessment was performed using the homogeneous form of the proposed method. The doubly conditional dissipation terms were parametrised by variable strain rate factors. By increasing the strain rate in mixture fraction space, the extinction state is approached gradually as the profiles in mixture fraction space tend to the inert mixing solution. The increase of strain rate in the PV space leads to a linear variation between the unburnt and burnt states of the reactive scalars. The doubly conditional cross-dissipation and the orientation of the isosurfaces of the conditioning variables were found to have a non-negligible effect on the structure of the reactive scalars.

The proposed DCMC method and submodels provide a framework for the modelling of non-premixed and partially premixed turbulent combustion. The preliminary parametric analysis performed in this thesis provides insight into the effect of strain levels in homogeneous turbulence. Further analysis is necessary in order to validate the proposed method. As a first step, an *a priori* analysis relying on DNS needs to be performed as in [40,122]. In such analysis, the PDFs and the doubly-conditional dissipation terms are obtained directly from DNS at every time step in order to advance the system of DCMC equations in time. The DCMC solution can be then compared to the DNS results. DNS also allows the validation of the proposed submodel. If the *a priori* assessment of the method and its submodels proves to be successful, proceeding to coupling with a RANS solver becomes possible. The computational cost is anticipated to be high. The usage of reduced chemical kinetics and code parallelisation can offer a tremendous increase in computational efficiency. Cross-stream averaging may be applied in shear flows in order to reduce the dimensionality of the governing equations. Further, the inert mixing assumption may invoked if the conditions of the considered flow allow. DCMC can be filtered for LES. However, compared to RANS, the computations are expected to be substantially more expensive.

9.2 Further recommendations

9.2.1 Solver coupling

The inert (frozen) mixing assumption adopted in the modelling of the shock tube autoignition and the lifted flame offers significant reductions in computational cost. In combustion problems, heat release due to reaction has a non-negligible effect on the density of the flow and mixing fields. Therefore, coupling between the combustion and CFD solvers is necessary. The inert mixing assumption is suitable in situations where density variations are too small to influence the flow and mixing fields. In the autoignition problem, the amount of heat released due to reaction during the pre-ignition phase is small and the density does not change significantly. Therefore, this assumption holds. The occurrence of autoignition is characterised by a sudden and significant heat release, which leads to substantial density variations. Accurate analysis of flame propagation in the post-ignition phase requires full coupling between the CMC and CFD solvers. In the modelling of the lifted flame, the inert mixing assumption is invoked because the flow reacts slowly in regions located below the stabilisation height. However, the flame may anchor at locations in the flow field where the axial velocity and scalar dissipation rate decrease due to thermal expansion at the base of the flame. Decoupling of CMC from the flow and mixing solver does not allow the detection of this phenomenon, and therefore may be classified as a source of discrepancy.

9.2.2 Counter-gradient diffusion

The gradient diffusion assumption employed in the modelling of the conditional turbulent fluxes does not account for counter-gradient effects. Encountered in premixed and partially premixed flames, counter-gradient diffusion arise from differential buoyancy effects between unburnt (cold) and burnt (hot) gases [187]. Richardson and Mastorakos [196] have recently proposed a new closure for the modelling of the conditional turbulent fluxes wherein a treatment of counter-gradient diffusion is provided. The model consists of the classical gradient diffusion assumption supplemented by an additional correction term that accounts counter-gradient transport. This correction is inspired from well established closures developed for the modelling of turbulent fluxes in premixed flames. In essence, it involves a bimodally distributed normalised reaction PV and the difference between the conditional velocities of the burnt products and unburnt reactants for which further modelling is proposed. The application of this model to the lifted flame considered in this work can influence the structure of the physical space diffusion term in the CMC trans-

port budget, and thereby may lead to different conclusions in regards to the stabilisation mechanism.

9.2.3 Differential diffusion

The neglect of differential diffusion (assumption of unity Lewis numbers) in the first-order CMC modelling of the piloted and lifted flames was based on experimental observations. The measurements of the piloted Sandia flame series [13] show that the role of differential diffusion diminishes with increasing fuel jet Reynolds number. In particular, those of flame D, which was considered in this work, reveal that differential diffusion has a minor effect near the base of the flame. The measurements of the H_2/air lifted flame [34, 35] indicate that the effects of differential diffusion are negligible despite the fact that the molecular diffusivity of H_2 is significantly different from those of heavier species, particularly N_2. Based on the above observations, the inclusion of differential diffusion in the calculations was deemed to be unnecessary. In practice, care should be taken when this phenomenon is present. Although the complexity of CMC modelling increases when non-unity Lewis numbers are employed (see Sect. 3.6.4), the inclusion of differential diffusion effects can improve the predictions of radicals and capture super-equilibrium effects, as demonstrated in [124].

9.2.4 Second-order modelling

Although most second-order studies in the CMC literature employ inconsistent CV and CSDR submodels [50, 63, 65, 115], such calculations were proven to yield superior results compared to first-order implementations employing the same set of submodels. In some second-order investigations [110, 113], the CSDR is obtained from the numerical double-integration of the PDF transport equation over the mixture fraction space while neglecting the CV fluctuations (the CV is set to equal to the Favre-averaged velocity). This approach is in general more consistent than the closures employed in [50, 63, 65, 115], however, modelling inconsistencies remain present due to the neglect of the CV fluctuations. The findings obtained in [110, 113] are not compared to the predictions of other second-order realisations employing different closures for the CV and CSDR. Therefore, it is difficult to judge whether the used submodels have any appreciable impact on the outcome of the second-order CMC. Nonetheless, as demonstrated in the calculations of the piloted and lifted flames, the consistent implementation of the first-order CMC eliminates spurious sources and leads to reliable predictions. Therefore, it is anticipated that additional improvements

can be achieved by employing a second-order closure for the conditional reaction rates. The CV and CSDR closures proposed in [157, 160] should incorporate a marginal increase in the overhead cost of the calculations.

Appendices

Appendix A

Conditional averaging of the experimental data of the lifted hydrogen/ nitrogen flame

For each of the axial locations $x/d = 1$, 8, 9, 10, 11, 14 and 26, single-shot measurements are reported by Cabra et al. [35] at several radial locations. For a given axial location, the data is conditionally averaged at each radius following the procedure described in [120]:

1. The range of the mixture fraction is subdivided into 40 bins.
2. The experimental scatter is sorted into the bins.
3. The average of the data in each bin is taken to be the conditional average with respect to the mixture fraction value at the centre of the bin.

As an example, the radial profiles of the experimental conditional temperature at $x/d = 14$ are shown in Fig. A.1(a). The weak radial dependence of the conditional data is obvious. A similar behaviour was obtained at the remaining axial locations (not shown). Therefore, steps 1-3 were repeated for all axial locations using all of the experimental scatter irrespective of the radial location. The conditional temperature profile at $x/d = 14$ is displayed in Fig. A.1(b).

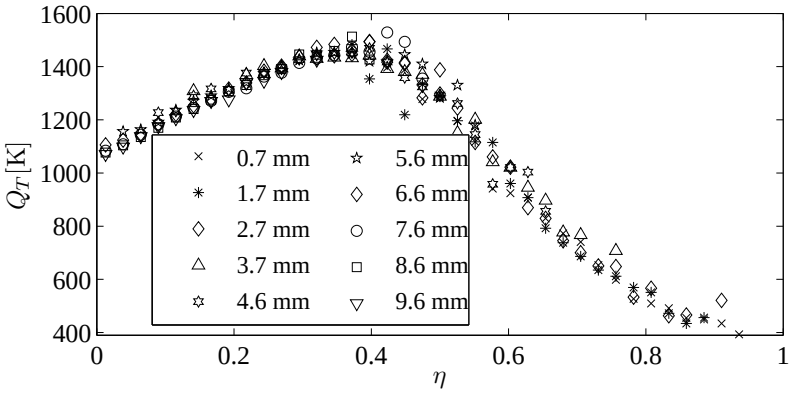

(a) Radial Q_T profiles

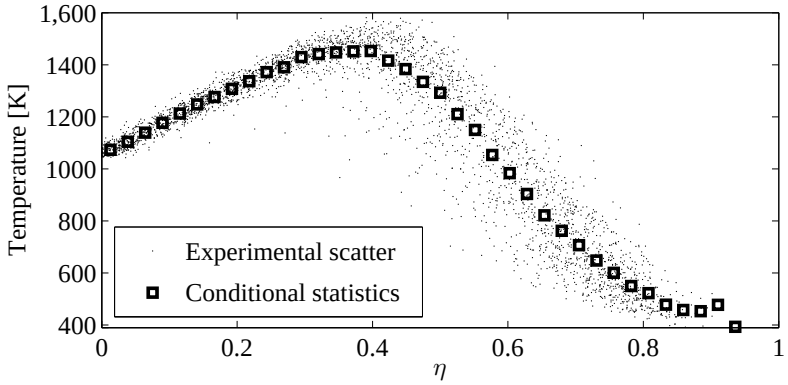

(b) Q_T from all samples

Figure A.1: Computation of the conditional temperature from the experimental scatter of the lifted H_2/N_2 jet flame of Cabra et al. [35] at $x/d = 14$: (a) profiles obtained from measurements at fixed radii (b) profile obtained from all samples superimposed over the experimental scatter.

Appendix B

Derivation of the doubly-conditional temperature equation

The temperature is decomposed as $T(\mathbf{x},t) = Q_T(\xi(\mathbf{x},t), c(\mathbf{x},t), \mathbf{x}, t) + T''(\mathbf{x},t)$ such that $\langle T''(\mathbf{x},t)|\xi=\eta, c=\theta\rangle = 0$. The partial derivatives of T in Eq. (3.25) are transformed as:

$$\frac{\partial T}{\partial t} = \frac{\partial Q_T}{\partial \eta}\frac{\partial \xi}{\partial t} + \frac{\partial Q_T}{\partial \theta}\frac{\partial c}{\partial t} + \frac{\partial Q_T}{\partial t} + \frac{\partial T''}{\partial t} \tag{B.1}$$

and

$$\frac{\partial T}{\partial x_i} = \frac{\partial Q_T}{\partial \eta}\frac{\partial \xi}{\partial x_i} + \frac{\partial Q_T}{\partial \theta}\frac{\partial c}{\partial x_i} + \frac{\partial Q_T}{\partial x_i} + \frac{\partial T''}{\partial x_i} \tag{B.2}$$

The diffusion term is expanded as:

$$\frac{\partial}{\partial x_i}\left(\rho c_p D \frac{\partial T}{\partial x_i}\right) = c_p \frac{\partial}{\partial x_i}\left(\rho D \frac{\partial T}{\partial x_i}\right) + \rho D \frac{\partial T}{\partial x_i}\frac{\partial c_p}{\partial x_i} \tag{B.3}$$

Using Eq. (B.2), the first term on the r.h.s. of Eq. (B.3) is transformed as:

$$\begin{aligned}
c_p \frac{\partial}{\partial x_i}\left(\rho D \frac{\partial T}{\partial x_i}\right) =& c_p \frac{\partial}{\partial x_i}\left[\rho D\left(\frac{\partial Q_T}{\partial \eta}\frac{\partial \xi}{\partial x_i} + \frac{\partial Q_T}{\partial \theta}\frac{\partial c}{\partial x_i} + \frac{\partial Q_T}{\partial x_i} + \frac{\partial T''}{\partial x_i}\right)\right] \\
=& c_p \frac{\partial Q_T}{\partial \eta}\frac{\partial}{\partial x_i}\left(\rho D \frac{\partial \xi}{\partial x_i}\right) + \rho c_p \frac{\chi_\xi}{2}\frac{\partial^2 Q_T}{\partial \eta^2} + \rho c_p D \frac{\partial \xi}{\partial x_i}\frac{\partial}{\partial x_i}\left(\frac{\partial Q_T}{\partial \eta}\right) \\
&+ c_p \frac{\partial Q_T}{\partial \theta}\frac{\partial}{\partial x_i}\left(\rho D \frac{\partial c}{\partial x_i}\right) + \rho c_p \frac{\chi_c}{2}\frac{\partial^2 Q_T}{\partial \theta^2} + \rho c_p \chi_{\xi,c}\frac{\partial^2 Q_T}{\partial \eta \partial \theta} \\
&+ \rho c_p D \frac{\partial c}{\partial x_i}\frac{\partial}{\partial x_i}\left(\frac{\partial Q_T}{\partial \theta}\right) + c_p \frac{\partial}{\partial x_i}\left(\rho D \frac{\partial Q_T}{\partial x_i}\right) + c_p \frac{\partial}{\partial x_i}\left(\rho D \frac{\partial T''}{\partial x_i}\right)
\end{aligned} \tag{B.4}$$

The transformation of the second term on the r.h.s. of Eq. (B.3) may be simplified by assuming that the specific heat of the mixture is independent of $\mathbf{x}$ but remains a function of η and θ. Using the decomposition $c_p = \langle c_p|\eta,\theta\rangle + c_p''$, $\partial c_p/\partial x_i$ can be transformed as in Eq. (B.2) with T, Q_T and T'' replaced by c_p, $\langle c_p|\eta,\theta\rangle$ and c_p'', respectively. When c_p is assumed to be independent of $\mathbf{x}$, $\partial\langle c_p|\eta,\theta\rangle/\partial x_i = \partial c_p''/\partial x_i = 0$. In this case, the second term on the r.h.s. of Eq. (B.3) is transformed as:

$$\begin{aligned}
\rho D\frac{\partial T}{\partial x_i}\frac{\partial c_p}{\partial x_i} =& \rho D\left(\frac{\partial Q_T}{\partial \eta}\frac{\partial \xi}{\partial x_i} + \frac{\partial Q_T}{\partial \theta}\frac{\partial c}{\partial x_i} + \frac{\partial Q_T}{\partial x_i} + \frac{\partial T''}{\partial x_i}\right)\times \\
& \left(\frac{\partial\langle c_p|\eta,\theta\rangle}{\partial \eta}\frac{\partial \xi}{\partial x_i} + \frac{\partial\langle c_p|\eta,\theta\rangle}{\partial \theta}\frac{\partial c}{\partial x_i}\right) \\
=& \rho\frac{\chi_\xi}{2}\frac{\partial Q_T}{\partial \eta}\frac{\partial\langle c_p|\eta,\theta\rangle}{\partial \eta} + \rho\frac{\chi_{\xi,c}}{2}\frac{\partial Q_T}{\partial \theta}\frac{\partial\langle c_p|\eta,\theta\rangle}{\partial \eta} \\
& + \rho\frac{\chi_{\xi,c}}{2}\frac{\partial Q_T}{\partial \eta}\frac{\partial\langle c_p|\eta,\theta\rangle}{\partial \theta} + \rho\frac{\chi_c}{2}\frac{\partial Q_T}{\partial \theta}\frac{\partial\langle c_p|\eta,\theta\rangle}{\partial \theta} \\
& + \rho D\left(\frac{\partial Q_T}{\partial x_i} + \frac{\partial T''}{\partial x_i}\right)\left(\frac{\partial\langle c_p|\eta,\theta\rangle}{\partial \eta}\frac{\partial \xi}{\partial x_i} + \frac{\partial\langle c_p|\eta,\theta\rangle}{\partial \theta}\frac{\partial c}{\partial x_i}\right)
\end{aligned} \tag{B.5}$$

Finally, the cross-gradient in the interdiffusion term of Eq. (3.25) is transformed as:

$$\begin{aligned}
\rho c_{p,\kappa} D\frac{\partial Y_\kappa}{\partial x_i}\frac{\partial T}{\partial x_i} =& \rho c_{p,\kappa} D\left(\frac{\partial Q_\kappa}{\partial \eta}\frac{\partial \xi}{\partial x_i} + \frac{\partial Q_\kappa}{\partial \theta}\frac{\partial c}{\partial x_i} + \frac{\partial Q_\kappa}{\partial x_i} + \frac{\partial y_\kappa''}{\partial x_i}\right)\times \\
& \left(\frac{\partial Q_T}{\partial \eta}\frac{\partial \xi}{\partial x_i} + \frac{\partial Q_T}{\partial \theta}\frac{\partial c}{\partial x_i} + \frac{\partial Q_T}{\partial x_i} + \frac{\partial T''}{\partial x_i}\right) \\
=& \rho c_{p,\kappa}\frac{\chi_\xi}{2}\frac{\partial Q_\kappa}{\partial \eta}\frac{\partial Q_T}{\partial \eta} + \rho c_{p,\kappa}\frac{\chi_{\xi,c}}{2}\frac{\partial Q_\kappa}{\partial \theta}\frac{\partial Q_T}{\partial \eta} \\
& + \rho c_{p,\kappa}\frac{\chi_c}{2}\frac{\partial Q_\kappa}{\partial \theta}\frac{\partial Q_T}{\partial \theta} + \rho c_{p,\kappa}\frac{\chi_{\xi,c}}{2}\frac{\partial Q_\kappa}{\partial \eta}\frac{\partial Q_T}{\partial \theta} \\
& + \rho D\left[c_{p,\kappa}\left(\frac{\partial Q_T}{\partial x_i} + \frac{\partial T''}{\partial x_i}\right)\left(\frac{\partial Q_\kappa}{\partial \eta}\frac{\partial \xi}{\partial x_i} + \frac{\partial Q_\kappa}{\partial \theta}\frac{\partial c}{\partial x_i}\right)\right. \\
& \left. + \left(\frac{\partial Q_\kappa}{\partial x_i} + \frac{\partial y_\kappa''}{\partial x_i}\right)\left(\frac{\partial Q_T}{\partial \eta}\frac{\partial \xi}{\partial x_i} + \frac{\partial Q_T}{\partial \theta}\frac{\partial c}{\partial x_i} + \frac{\partial Q_T}{\partial x_i} + \frac{\partial T''}{\partial x_i}\right)\right]
\end{aligned} \tag{B.6}$$

Substituting Eqs. (B.1), (B.2) and (B.4)-(B.6) in Eq. (3.25) and rearranging lead to:

$$
\begin{aligned}
&\rho c_p \frac{\partial Q_T}{\partial t} + \rho c_p u_i \frac{\partial Q_T}{\partial x_i} + c_p \frac{\partial Q_T}{\partial \eta}\left[\rho \frac{\partial \xi}{\partial t} + \rho u_i \frac{\partial \xi}{\partial x_i} - \frac{\partial}{\partial x_i}\left(\rho D \frac{\partial \xi}{\partial x_i}\right)\right] \\
&\quad + c_p \frac{\partial Q_T}{\partial \theta}\left[\rho \frac{\partial c}{\partial t} + \rho u_i \frac{\partial c}{\partial x_i} - \frac{\partial}{\partial x_i}\left(\rho D \frac{\partial c}{\partial x_i}\right)\right] = \\
&\quad \rho \frac{\chi_\xi}{2}\left\{c_p \frac{\partial^2 Q_T}{\partial \eta^2} + \left[\frac{\partial \langle c_p|\eta,\theta\rangle}{\partial \eta} + \sum_{\kappa=1}^{N_s}\left(c_{p,\kappa}\frac{\partial Q_\kappa}{\partial \eta}\right)\right]\frac{\partial Q_T}{\partial \eta}\right\} \\
&\quad + \rho \frac{\chi_c}{2}\left\{c_p \frac{\partial^2 Q_T}{\partial \theta^2} + \left[\frac{\partial \langle c_p|\eta,\theta\rangle}{\partial \theta} + \sum_{\kappa=1}^{N_s}\left(c_{p,\kappa}\frac{\partial Q_\kappa}{\partial \theta}\right)\right]\frac{\partial Q_T}{\partial \theta}\right\} \\
&\quad + \rho \chi_{\xi,c}\left\{c_p \frac{\partial^2 Q_T}{\partial \eta \partial \theta} + \frac{1}{2}\left[\frac{\partial \langle c_p|\eta,\theta\rangle}{\partial \eta} + \sum_{\kappa=1}^{N_s}\left(c_{p,\kappa}\frac{\partial Q_\kappa}{\partial \eta}\right)\right]\frac{\partial Q_T}{\partial \theta}\right. \\
&\quad \left. + \frac{1}{2}\left[\frac{\partial \langle c_p|\eta,\theta\rangle}{\partial \theta} + \sum_{\kappa=1}^{N_s}\left(c_{p,\kappa}\frac{\partial Q_\kappa}{\partial \theta}\right)\right]\frac{\partial Q_T}{\partial \eta}\right\} \\
&\quad + c_p\left[\rho D \frac{\partial \xi}{\partial x_i}\frac{\partial}{\partial x_i}\left(\frac{\partial Q_T}{\partial \eta}\right) + \rho D \frac{\partial c}{\partial x_i}\frac{\partial}{\partial x_i}\left(\frac{\partial Q_T}{\partial \theta}\right) + \frac{\partial}{\partial x_i}\left(\rho D \frac{\partial Q_T}{\partial x_i}\right)\right] \\
&\quad - c_p\left[\rho \frac{\partial T''}{\partial t} + \rho u_i \frac{\partial T''}{\partial x_i} - \frac{\partial}{\partial x_i}\left(\rho D \frac{\partial T''}{\partial x_i}\right)\right] \\
&\quad + \rho D\left\{\sum_{\kappa=1}^{N_s}\left[c_{p,\kappa}\left(\frac{\partial Q_T}{\partial x_i} + \frac{\partial T''}{\partial x_i}\right)\left(\frac{\partial Q_\kappa}{\partial \eta}\frac{\partial \xi}{\partial x_i} + \frac{\partial Q_\kappa}{\partial \theta}\frac{\partial c}{\partial x_i}\right)\right.\right. \\
&\quad + \left(\frac{\partial Q_\kappa}{\partial x_i} + \frac{\partial y''_\kappa}{\partial x_i}\right)\left(\frac{\partial Q_T}{\partial \eta}\frac{\partial \xi}{\partial x_i} + \frac{\partial Q_T}{\partial \theta}\frac{\partial c}{\partial x_i} + \frac{\partial Q_T}{\partial x_i} + \frac{\partial T''}{\partial x_i}\right)\Big] \\
&\quad \left. + \left(\frac{\partial Q_T}{\partial x_i} + \frac{\partial T''}{\partial x_i}\right)\left(\frac{\partial \langle c_p|\eta,\theta\rangle}{\partial \eta}\frac{\partial \xi}{\partial x_i} + \frac{\partial \langle c_p|\eta,\theta\rangle}{\partial \theta}\frac{\partial c}{\partial x_i}\right)\right\} \\
&\quad + \frac{\partial p}{\partial t} - \sum_{\kappa=1}^{N_s} h_\kappa \dot{\omega}_\kappa + \dot{\omega}_r
\end{aligned}
\tag{B.7}
$$

The first bracketed quantity on the l.h.s of Eq. (B.7) is zero by means of the transport equation of ξ, Eq. (2.77). The second bracketed quantity on the l.h.s. can be simplified by introducing the r.h.s. of Eq. (8.10). Taking the doubly-conditional average of Eq. (B.7) with respect to $\xi(\mathbf{x},t) = \eta$ and $c(\mathbf{x},t) = \theta$ and dividing the resulting expression by $\langle \rho|\eta,\theta\rangle\langle c_p|\eta,\theta\rangle$ yield the desired doubly-conditional temperature equation:

$$\frac{\partial Q_T}{\partial t} + \langle u_i|\eta,\theta\rangle\frac{\partial Q_T}{\partial x_i} =$$
$$\frac{\langle\chi_\xi|\eta,\theta\rangle}{2}\left\{\frac{\partial^2 Q_T}{\partial\eta^2} + \frac{1}{\langle c_p|\eta,\theta\rangle}\left[\frac{\partial\langle c_p|\eta,\theta\rangle}{\partial\eta} + \sum_{\kappa=1}^{N_s}\left(\langle c_{p,\kappa}|\eta,\theta\rangle\frac{\partial Q_\kappa}{\partial\eta}\right)\right]\frac{\partial Q_T}{\partial\eta}\right.$$
$$\left. -\frac{1}{\phi_{max}(\eta)-\phi_{min}(\eta)}\left(c\frac{d^2[\phi_{max}(\eta)-\phi_{min}(\eta)]}{d\eta^2} + \frac{d^2\phi_{min}(\eta)}{d\eta^2}\right)\frac{\partial Q_T}{\partial\theta}\right\}$$
$$+\frac{\langle\chi_c|\eta,\theta\rangle}{2}\left\{\frac{\partial^2 Q_T}{\partial\theta^2} + \frac{1}{\langle c_p|\eta,\theta\rangle}\left[\frac{\partial\langle c_p|\eta,\theta\rangle}{\partial\theta} + \sum_{\kappa=1}^{N_s}\left(\langle c_{p,\kappa}|\eta,\theta\rangle\frac{\partial Q_\kappa}{\partial\theta}\right)\right]\frac{\partial Q_T}{\partial\theta}\right\}$$
$$+\langle\chi_{\xi,c}|\eta,\theta\rangle\left\{\frac{\partial^2 Q_T}{\partial\eta\partial\theta} + \frac{1}{2\langle c_p|\eta,\theta\rangle}\left[\frac{\partial\langle c_p|\eta,\theta\rangle}{\partial\eta} + \sum_{\kappa=1}^{N_s}\left(\langle c_{p,\kappa}|\eta,\theta\rangle\frac{\partial Q_\kappa}{\partial\eta}\right)\right]\frac{\partial Q_T}{\partial\theta}\right. \tag{B.8}$$
$$+\frac{1}{2\langle c_p|\eta,\theta\rangle}\left[\frac{\partial\langle c_p|\eta,\theta\rangle}{\partial\theta} + \sum_{\kappa=1}^{N_s}\left(\langle c_{p,\kappa}|\eta,\theta\rangle\frac{\partial Q_\kappa}{\partial\theta}\right)\right]\frac{\partial Q_T}{\partial\eta}$$
$$\left. -\frac{1}{\phi_{max}(\eta)-\phi_{min}(\eta)}\frac{d[\phi_{max}(\eta)-\phi_{min}(\eta)]}{d\eta}\frac{\partial Q_T}{\partial\theta}\right\} + \frac{\langle\partial p/\partial t|\eta,\theta\rangle}{\langle\rho|\eta,\theta\rangle\langle c_p|\eta,\theta\rangle}$$
$$-\frac{\sum_{\kappa=1}^{N_s}\langle h_\kappa|\eta,\theta\rangle\langle\dot\omega_\kappa|\eta,\theta\rangle}{\langle\rho|\eta,\theta\rangle\langle c_p|\eta,\theta\rangle} - \frac{\langle\dot\omega_c|\eta,\theta\rangle}{\langle\rho|\eta,\theta\rangle}\frac{\partial Q_T}{\partial\theta} + \frac{\langle\dot\omega_r|\eta,\theta\rangle}{\langle\rho|\eta,\theta\rangle\langle c_p|\eta,\theta\rangle} + \frac{e_{Q_T}+e_{T''}+e_{c_p}}{\langle\rho|\eta,\theta\rangle\langle c_p|\eta,\theta\rangle}$$

where

$$e_{Q_T} = \frac{\partial}{\partial x_i}\left(\rho c_p D\frac{\partial Q_T}{\partial x_i}\right) + \left\langle c_p\left[\rho D\frac{\partial\xi}{\partial x_i}\frac{\partial}{\partial x_i}\left(\frac{\partial Q_T}{\partial\eta}\right) + \rho D\frac{\partial c}{\partial x_i}\frac{\partial}{\partial x_i}\left(\frac{\partial Q_T}{\partial\theta}\right)\right]\middle|\eta,\theta\right\rangle \tag{B.9}$$

$$e_{T''} = \left\langle c_p\left[\rho\frac{\partial T''}{\partial t} + \rho u_i\frac{\partial T''}{\partial x_i} - \frac{\partial}{\partial x_i}\left(\rho D\frac{\partial T''}{\partial x_i}\right)\right]\middle|\eta,\theta\right\rangle \tag{B.10}$$

$$e_{c_p} = \left\langle \rho D\left\{\sum_{\kappa=1}^{N_s}\left[c_{p,\kappa}\left(\frac{\partial Q_T}{\partial x_i} + \frac{\partial T''}{\partial x_i}\right)\left(\frac{\partial Q_\kappa}{\partial\eta}\frac{\partial\xi}{\partial x_i} + \frac{\partial Q_\kappa}{\partial\theta}\frac{\partial c}{\partial x_i}\right)\right.\right.\right.$$
$$\left. + \left(\frac{\partial Q_\kappa}{\partial x_i} + \frac{\partial y''_\kappa}{\partial x_i}\right)\left(\frac{\partial Q_T}{\partial\eta}\frac{\partial\xi}{\partial x_i} + \frac{\partial Q_T}{\partial\theta}\frac{\partial c}{\partial x_i} + \frac{\partial Q_T}{\partial x_i} + \frac{\partial T''}{\partial x_i}\right)\right] \tag{B.11}$$
$$\left.\left. + \left(\frac{\partial Q_T}{\partial x_i} + \frac{\partial T''}{\partial x_i}\right)\left(\frac{\partial\langle c_p|\eta,\theta\rangle}{\partial\eta}\frac{\partial\xi}{\partial x_i} + \frac{\partial\langle c_p|\eta,\theta\rangle}{\partial\theta}\frac{\partial c}{\partial x_i}\right)\right\}\middle|\eta,\theta\right\rangle$$

Appendix C

Approximation of the mean and variance of c

C.1 Approximation of $\tilde{c}$ and $\widetilde{c''^2}$

When c is assumed to be statistically independent from ξ, $\langle c|\eta\rangle = \tilde{c}$. Inserting this approximation in

$$\langle c|\eta\rangle = \frac{\langle \phi|\eta\rangle - \phi_{min}(\eta)}{\phi_{max}(\eta) - \phi_{min}(\eta)} \tag{C.1}$$

and rearranging lead to:

$$\langle \phi|\eta\rangle = \tilde{c}[\phi_{max}(\eta) - \phi_{min}(\eta)] + \phi_{min}(\eta) \tag{C.2}$$

Integrating Eq. (C.2) weighted by $\tilde{P}_\xi(\eta)$ over η-space results in:

$$\tilde{c} = \frac{\tilde{\phi} - \tilde{\phi}_{min}}{\tilde{\phi}_{max} - \tilde{\phi}_{min}} \tag{C.3}$$

where

$$\begin{aligned} \tilde{\phi} &= \int_0^1 \int_0^1 \langle \phi|\eta,\theta\rangle^D \tilde{P}_\xi(\eta)\tilde{P}_c(\theta)d\eta d\theta \\ \tilde{\phi}_{min} &= \int_0^1 \phi_{min}(\eta)\tilde{P}_\xi(\eta)d\eta \\ \tilde{\phi}_{max} &= \int_0^1 \phi_{max}(\eta)\tilde{P}_\xi(\eta)d\eta \end{aligned} \tag{C.4}$$

Taking the conditional average of the square of c with respect to ξ and noting that $\langle c^2|\eta\rangle = \widetilde{c^2}$ (due to the assumption of statistical independence) give:

$$\langle\phi^2|\eta\rangle = \widetilde{c^2}[\phi_{max}(\eta) - \phi_{min}(\eta)]^2 + 2\langle\phi|\eta\rangle\phi_{min}(\eta) - \phi_{min}^2(\eta) \tag{C.5}$$

Taking the square of Eq. (C.2) results in:

$$\langle\phi|\eta\rangle^2 = \tilde{c}^2[\phi_{max}(\eta) - \phi_{min}(\eta)]^2 + 2\tilde{c}[\phi_{max}(\eta) - \phi_{min}(\eta)]\phi_{min}(\eta) + \phi_{min}^2(\eta) \tag{C.6}$$

Subtracting Eq. (C.6) from Eq. (C.5) and using Eq. (C.2) result in the following expression for the conditional variance of ϕ:

$$\underbrace{\langle\phi^2|\eta\rangle - \langle\phi|\eta\rangle^2}_{\langle\phi''^2|\eta\rangle} = \widetilde{c''^2}[\phi_{max}(\eta) - \phi_{min}(\eta)]^2 \tag{C.7}$$

where $\widetilde{c''^2} = \widetilde{c^2} - \tilde{c}^2$. The terms of Eq. (C.7) are now integrated over η-space as follows:

$$\int_0^1 \langle\phi^2|\eta\rangle\tilde{P}_\xi(\eta)d\eta = \widetilde{\phi^2} \tag{C.8}$$

$$\begin{aligned}\int_0^1 \langle\phi|\eta\rangle^2\tilde{P}_\xi(\eta)d\eta = \int_0^1 \{&\tilde{c}^2[\phi_{max}(\eta) - \phi_{min}(\eta)]^2 + 2\tilde{c}[\phi_{max}(\eta) - \phi_{min}(\eta)]\phi_{min}(\eta) \\ &+ \phi_{min}^2(\eta)\}\tilde{P}_\xi(\eta)d\eta = \tilde{c}^2\widetilde{(\Delta\phi)^2} + 2\tilde{c}(\widetilde{\phi_{max}\phi_{min}} - \widetilde{\phi_{min}^2}) + \widetilde{\phi_{min}^2}\end{aligned} \tag{C.9}$$

$$\int_0^1 \widetilde{c''^2}[\phi_{max}(\eta) - \phi_{min}(\eta)]^2\tilde{P}_\xi(\eta)d\eta = \widetilde{c''^2}\widetilde{(\Delta\phi)^2} \tag{C.10}$$

where

$$\begin{aligned}\widetilde{\phi_{max}\phi_{min}} &= \int_0^1 \phi_{max}(\eta)\phi_{min}(\eta)\tilde{P}_\xi(\eta)d\eta \\ \widetilde{\phi_{min}^2} &= \int_0^1 \phi_{min}^2(\eta)\tilde{P}_\xi(\eta)d\eta \\ \widetilde{(\Delta\phi)^2} &= \int_0^1 [\phi_{max}(\eta) - \phi_{min}(\eta)]^2\tilde{P}_\xi(\eta)d\eta\end{aligned} \tag{C.11}$$

As such, the integration of Eq. (C.7) yields:

$$\widetilde{\phi^2} - \tilde{c}^2\widetilde{(\Delta\phi)^2} - 2\tilde{c}(\widetilde{\phi_{max}\phi_{min}} - \widetilde{\phi_{min}^2}) - \widetilde{\phi_{min}^2} = \widetilde{c''^2}\widetilde{(\Delta\phi)^2} \tag{C.12}$$

Introducing Eq. (C.3) in Eq. (C.12) and rearranging, the variance is finally expressed as:

$$\widetilde{c''^2} = \frac{1}{\widetilde{(\Delta\phi)^2}}\left[\widetilde{\phi^2} - \left(\frac{\tilde{\phi}-\tilde{\phi}_{min}}{\tilde{\phi}_{max}-\tilde{\phi}_{min}}\right)^2 \widetilde{(\Delta\phi)^2} - 2\left(\frac{\tilde{\phi}-\tilde{\phi}_{min}}{\tilde{\phi}_{max}-\tilde{\phi}_{min}}\right)(\widetilde{\phi_{max}\phi_{min}} - \widetilde{\phi^2_{min}}) - \widetilde{\phi^2_{min}}\right] \tag{C.13}$$

C.2 Transport equation of $\widetilde{\phi^2}$

To obtain the transport equation of $\widetilde{\phi^2}$, the conservative and non-conservative forms of the ϕ transport equation are first multiplied by ϕ:

$$\phi\frac{\partial(\rho\phi)}{\partial t} + \phi\frac{\partial(\rho u_i\phi)}{\partial x_i} = \phi\frac{\partial}{\partial x_i}\left(\rho D\frac{\partial\phi}{\partial x_i}\right) + \rho\phi\dot{\omega}_\phi \tag{C.14}$$

$$\rho\phi\frac{\partial\phi}{\partial t} + \rho u_i\phi\frac{\partial\phi}{\partial x_i} = \phi\frac{\partial}{\partial x_i}\left(\rho D\frac{\partial\phi}{\partial x_i}\right) + \rho\phi\dot{\omega}_\phi \tag{C.15}$$

Adding Eqs. (C.14) and (C.15) yields the ϕ^2 equation:

$$\frac{\partial(\rho\phi^2)}{\partial t} + \frac{\partial(\rho u_i\phi^2)}{\partial x_i} = \frac{\partial}{\partial x_i}\left(\rho D\frac{\partial\phi^2}{\partial x_i}\right) - \underbrace{2\rho D\frac{\partial\phi}{\partial x_i}\frac{\partial\phi}{\partial x_i}}_{\rho\chi_\phi} + 2\rho\phi\dot{\omega}_\phi \tag{C.16}$$

Finally, the averaging of Eq. (C.16) results in:

$$\bar{\rho}\frac{\partial\widetilde{\phi^2}}{\partial t} + \bar{\rho}\tilde{u}_i\frac{\partial\widetilde{\phi^2}}{\partial x_i} = \frac{\partial}{\partial x_i}\left(\overline{\rho D\frac{\partial\phi^2}{\partial x_i}}\right) - \frac{\partial(\widetilde{\bar{\rho}u_i''\phi^2})}{\partial x_i} - \bar{\rho}\tilde{\chi}_\phi + 2\widetilde{\bar{\rho}\phi\dot{\omega}_\phi} \tag{C.17}$$

where conservation of mass has been employed to expand the material derivative.

Appendix D

Publications

Journal articles:

- **A. El Sayed**, A. Milford and C. B. Devaud. Modelling of autoignition for methane-based fuel blends using Conditional Moment Closure. *Proc. Combust. Inst.*, 32(1):1621-1628, 2009 (Chap. 4).

Articles awaiting submission:

- **A. El Sayed** and R. A. Fraser. Consistent Conditional Moment Closure modelling of Sandia flame D (Chap. 5).
- **A. El Sayed** and R. A. Fraser. Conditional Moment Closure modelling of a lifted hydrogen/nitrogen jet flame issuing into a vitiated coflow (Chap. 6).
- **A. El Sayed** and R. A. Fraser. Conditional Moment Closure modelling of a lifted jet flame using the Presumed Mapping Function approach (Chap. 7).

Articles in preparation:

- **A. El Sayed** and R. A. Fraser. A Doubly-Conditional Moment Closure based on the mixture fraction and a normalised reaction progress variable (Chap. 8).

Conference Proceedings:

- **A. El Sayed** and R. A. Fraser. Modelling of a lifted hydrogen jet flame in a vitiated coflow using the Conditional Moment Closure. In: Proceedings of the 35$^{\text{th}}$ Combustion Institute/Canadian Section Spring Technical Meeting, Toronto, ON, Canada, Pages 291-296, 2012.

- **A. El Sayed** and R. A. Fraser. Conditional moment closure modelling of Sandia flame D. Part 1: assessment of submodels. In: Proceedings of the 34$^{\text{th}}$ Combustion Institute/Canadian Section Spring Technical Meeting, Winnipeg, MB, Canada, Pages 53–58, 2011.

- **A. El Sayed** and R. A. Fraser. Conditional moment closure modelling of Sandia flame D. Part 2: simulation results using consistent submodels. In: Proceedings of the 34$^{\text{th}}$ Combustion Institute/Canadian Section Spring Technical Meeting, Winnipeg, MB, Canada, Pages 59-64, 2011.

- **A. El Sayed** and C. B. Devaud. A Doubly Conditional Moment Closure method for the modelling of ignition and extinction in turbulent non-premixed combustion. In: Proceedings of the 32$^{\text{nd}}$ Combustion Institute/Canadian Section Spring Technical Meeting, Montreal, QC, Canada, Pages 90–95, 2009.

- **A. El Sayed** and C. B. Devaud. Autoignition of CH_4, CH_4/C_2H_6, CH_4/H_2, and CH_4/N_2 mixtures using Conditional Moment Closure. In: Proceedings of the 31$^{\text{st}}$ Combustion Institute/Canadian Section Spring Technical Meeting, Toronto, ON, Canada, Pages 159–164, 2008.

Posters:

- **A. El Sayed**, A. Milford and C.B. Devaud. Modelling of autoignition for methane-based fuel blends using Conditional Moment Closure. In: the 32$^{\text{nd}}$ International Symposium on Combustion, Montréal, QC, Canada, August 3–8, 2008.

References

[1] http://www.sandia.gov/TNF/chemistry.html, accessed May 2010.

[2] http://www.sandia.gov/TNF/DataArch/FlameD.html, accessed September 2011.

[3] M. M. M. Abou-Ellail, K. R. Beshay, and M. S. Mansour. A flamelet model for premixed methane-air flames. *Combust. Sci. Tech.*, 153(1):223–245, 2000.

[4] ANSYS, Inc. ANSYS CFX 10.0, 2006.

[5] ANSYS Inc. ANSYS FlUENT 12.1, 2009.

[6] ANSYS Inc. ANSYS FLUENT 12.1 Theory Guide, April 2009.

[7] ANSYS Inc. ANSYS FLUENT 12.1 User's Guide, April 2009.

[8] ANSYS Inc. ANSYS ICEM CFD, 2009.

[9] S. Ayache and E. Mastorakos. Conditional moment closure/large eddy simulation of the Delft-III natural gas non-premixed jet flame. *Flow Turb. Combust.*, 88(1–2):207–231, 2011.

[10] B. J. McBride and S. Gordon and M. A. Reno. Coefficients for calculating thermodynamic and transport properties of individual species. Technical Report TM-4513, NASA, 1993.

[11] R. Barlow and J. Frank. Piloted CH_4/Air Flames C, D, E, and F – Release 2.1. TNF Workshop, June 2007.

[12] R. S. Barlow and J. H. Frank. Effects of turbulence on species mass fractions in methane/air jet flames. *Symp. (Int.) Combust.*, 27(1):1087–1098, 1998.

[13] R. S. Barlow, J. H. Frank, A. N. Karpetis, and J. Y. Chen. Piloted methane/air jet flames: Transport effects and aspects of scalar structure. *Combust. Flame*, 143(4):433–449, 2005.

[14] R. S. Barlow, A. N. Karpetis, J. H. Frank, and J. -Y. Chen. Scalar profiles and NO formation in laminar opposed-flow partially premixed methane/air flames. *Combust. Flame*, 127(3):2102–2118, 2001.

[15] R. S. Barlow, N. S. A. Smith, J. -Y. Chen, and R. W. Bilger. Nitric oxide formation in dilute hydrogen jet flames: isolation of the effects of radiation and turbulence-chemistry submodels. *Combust. Flame*, 117(1–2):4–31, 1999.

[16] T. J. Barth and D. C. Jesperson. The design and application of upwind schemes on unstructured meshes. In *Twenty-Seventh Aerospace Sciences Exhibit and Meeting*, Reno, Nevada, U.S.A., 1989. AIAA Paper 89–0366.

[17] H. Barths, N. Peters, N. Brehm, A. Mack, M. Pfitzner, and V. Smiljanovski. Simulation of pollutant formation in a gas-turbine combustor using unsteady flamelets. *Symp. (Int.) Combust.*, 27(2):1841–1847, 1998.

[18] R. W. Bilger. Conditional moment methods for turbulent reacting flow using Crocco variable conditions. Technical Report TNF-99, Charles Kolling Laboratory Report, Department of Mechanical Engineering, The University of Sydney, 1991.

[19] R. W. Bilger. Advanced laser diagnostics: implication of recent results and advanced combustor models. In R. S. Lee, J. H. Whitelaw, and T. S. Wung, editors, *Aerothermodynamics in Combustors*, pages 3–16. Springer-Verlag, Berlin, Germany, 1992.

[20] R. W. Bilger. Conditional moment closure for turbulent reacting flow. *Phys. Fluids A*, 5(2):436–444, 1993.

[21] R. W. Bilger. Future progress in turbulent combustion research. *Prog. Energy Combust. Sci.*, 26(4–6):367–380, 2000.

[22] R. W. Bilger. Some aspects of scalar dissipation. *Flow Turb. Combust.*, 72(2–4):93–114, 2004.

[23] R. W. Bilger, L. R. Saetran, and L. Y. Krishnamoorthy. Reaction in a scalar mixing layer. *J. Fluid Mech.*, 233:211–242, 1991.

[24] G. Blanquart and H. Pitsch. Modeling autoignition in non-premixed turbulent combustion using a stochastic flamelet approach. *Proc. Combust. Inst.*, 30(2):2745–2753, 2005.

[25] G. Borghesi, E. Mastorakos, C. B. Devaud, and R. W. Bilger. Modeling evaporation effects in conditional moment closure for spray autoignition. *Combust. Theory Model.*, 15(5):725–752, 2011.

[26] R. Borghi. Turbulent combustion modelling. *Prog. Energy Combust. Sci.*, 14(4):245–292, 1988.

[27] C. T. Bowman, R. K. Hanson, D. F. Davidson, W. C. Gardiner Jr., V. Lissianski, G. P. Smith, D. M. Golden, M. Frenklach, and M. Goldenberg. http://diesel.me.berkeley.edu/~gri_mech/new21/version21/text21.html, 1995.

[28] K. Bray, P. Domingo, and L. Vervisch. Role of the progress variable in models for partially premixed turbulent combustion. *Combust. Flame*, 141(4):431–437, 2005.

[29] E. A. Brizuela and M. Z. Roudsari. Comparison of RANS/CMC modeling of Flame D with conventional and with Presumed Mapping Function statistics. *Combust. Theory Model.*, 15(5):671–690, 2011.

[30] P. N. Brown, G. D. Byrne, and A. C. Hindmarsh. VODE, a Variable-Coefficient ODE solver. *SIAM J. Sci. Stat. Comput.*, 10(5):1038–1051, 1988.

[31] P. N. Brown and A. C. Hindmarsh. Reduced storage matrix methods in stiff ODE systems. *J.Appl. Math. & Comp.*, 31:40–91, 1989.

[32] M. P. Burke, M. Chaos, Y. Ju, F. L. Dryer, and S. J. Klippenstein. Comprehensive H_2/O_2 kinetic model for high-pressure combustion. *Int. J. Chem. Kinet.*, 44(7):444–474, 2012.

[33] G. D. Byrne. Pragmatic experiments with Krylov methods in the stiff ODE setting. In J. Cash and I. Gladwell, editors, *Computational Ordinary Differential Equations*, pages 323–356. Oxford University Press, Oxford, 1992.

[34] R. Cabra. *Turbulent Jet Flames Into a Vitiated Coflow*. PhD thesis, University of California, Berkeley, Berkeley, California, 2004.

[35] R. Cabra, T. Myhrvold, J. Y. Chen, R. W. Dibble, A. N. Karpetis, and R. S. Barlow. Simultaneous laser Raman-Rayleigh-LIF measurements and numerical modeling results of a lifted turbulent H_2/N_2 jet flame in a vitiated coflow. *Proc. Combust. Inst.*, 29(2):1881–1888, 2002.

[36] R. S. Cant and E. Mastorakos. *An Introduction to Turbulent Reacting Flows*. Imperial College Press, London, U.K., 2008.

[37] R. R. Cao, S. B. Pope, and A. R. Masri. Turbulent lifted flames in a vitiated coflow investigated using joint PDF calculations. *Combust. Flame*, 142(4):438–453, 2005.

[38] M. G. Carvalho and T. L. Farias. Modelling of heat transfer in radiating and combusting systems. *Chem. Eng. Res. Des.*, 76(2):175–184, 1998.

[39] C. M. Cha, S. M. de Bruyn Kops, , and M. Mortensen. Direct numerical simulations of the double scalar mixing layer. Part I: Passive scalar mixing and dissipation. *Phys. Fluids*, 18(6):067106, 2006.

[40] C. M. Cha, G. Kosály, and H. Pitsch. Modeling extinction and reignition in turbulent nonpremixed combustion using a doubly-conditional moment closure approach. *Phys. Fluids*, 13(12):3824–3834, 2001.

[41] H. Chen, S. Chen, and R. H. Kraichnann. Probability distribution of a stochastically advected scalar field. *Phys. Rev. Lett.*, 63(24):2657–2660, 1989.

[42] T. J. Chung. *Computational fluid dynamics*. Cambridge University Press, Cambridge, U.K., 2002.

[43] M. J. Cleary. *CMC Modelling of Enclosure Fires*. PhD thesis, University of Sydney, Sydney, Australia, 2004.

[44] M. J. Cleary and J. H. Kent. Modelling of species in hood fires by conditional moment closure. *Combust. Flames*, 143(4):357–368, 2005.

[45] C. J. Cobos, H. Hippler, and J. Troe. High-pressure falloff curves and specific rate constants for the reactions $H + O_2 \rightleftharpoons HO_2 \rightleftharpoons HO + O$. *J. Phys. Chem.*, 89(2):342–349, 1985.

[46] P. J. Coelho and N. Peters. Unsteady modelling of a piloted methane/air jet flame based on the Eulerian particle flamelet model. *Combust. Flame*, 124(3):444–465, 2001.

[47] B. J. Daly and F. H. Harlow. Transport equations in turbulence. *Phys. Fluids*, 13(11):2634–2649, 1970.

[48] S. M. de Bruyn Kops and M. Mortensen. Conditional mixing statistics in a self-similar scalar mixing layer. *Phys. Fluids*, 17:095107, 2005.

[49] G. De Paola. *Conditional Moment closure for autoignition in turbulent flows*. PhD thesis, University of Cambridge, Cambridge, U.K., 2007.

[50] G. De Paola, I. S. Kim, and E. Mastorakos. Second-order conditional moment closure simulations of autoignition of an n-heptane plume in a turbulent coflow of heated air. *Flow Turb. Combust.*, 82(4):455–475, 2009.

[51] G. De Paola, Y. M. Wright, K. Boulouchos, and E. Mastorakos. Diesel engine simulations with multi-dimensional conditional moment closure. *Combust. Sci. Tech.*, 180(5):883–899, 2008.

[52] J. de Vries and E. L. Petersen. Autoignition of methane-based fuel blends under gas turbine conditions. *Proc. Combust. Inst.*, 31(2):3163–3171, 2007.

[53] C. B. Devaud, R. W. Bilger, and T. Liu. A new method of modeling the conditional scalar dissipation rate. *Phys. Fluids*, 16(6):2004–2011, 2004.

[54] C. B. Devaud and K. N. C. Bray. Assessment of the applicability of conditional moment closure to a lifted turbulent flame: first order model. *Combust. Flame*, 132(1):102–114, 2003.

[55] P. Domingo, L. Vervisch, and K. Bray. Partially premixed flamelets in LES of non-premixed turbulent combustion. *Combust. Theory Model.*, 6(4):529–551, 2002.

[56] C. Duwig and C. Fureby. Large eddy simulation of unsteady lean stratified premixed combustion. *Combust. Flame*, 151(1–2):85–103, 2007.

[57] E. Effelsberg and N. Peters. A composite model for the conserved scalar PDF. *Combust. Flame*, 52(complete):351–360, 1983.

[58] E. Effelsberg and N. Peters. Scalar dissipation rates in turbulent jets and jet diffusion flames. *Symp. (Int.) Combust.*, 22(1):693–700, 1988.

[59] A. El Sayed and C. B. Devaud. Conditional moment closure (CMC) applied to autoignition of high pressure methane jets in a shock tube. *Combust. Theory Model.*, 12(5):943–972, 2008.

[60] V. Eswaran and S. B. Pope. Direct numerical simulation of the turbulent mixing of a passive scalar. *Phys. Fluids*, 31(3):506–520, 1988.

[61] M. Fairweather and R. M. Woolley. First-order conditional moment closure modeling of turbulent, nonpremixed hydrogen flames. *Combust. Flame*, 133(4):393–405, 2003.

[62] M. Fairweather and R. M. Woolley. First-order conditional moment closure modeling of turbulent, nonpremixed methane flames. *Combust. Flame*, 138(1–2):3–19, 2004.

[63] M. Fairweather and R. M. Woolley. Conditional moment closure modelling of turbulent jet diffusion flames of helium-diluted hydrogen. *Combust. Theory Model.*, 9(3):433–447, 2005.

[64] M. Fairweather and R. M. Woolley. Conditional moment closure calculations of a swirl-stabilized, turbulent nonpremixed methane flame. *Combust. Flame*, 151(3):397–411, 2007.

[65] M. Fairweather and R. M. Woolley. First- and second-order elliptic conditional moment closure calculations of piloted methane diffusion ames. *Combust. Flame*, 150(1–2):92–107, 2007.

[66] M. Fairweather, R. M. Woolley, and Y. Yunardi. Analysis of kinetic mechanism performance in conditional moment closure modelling of turbulent, non-premixed methane flames. *Combust. Theory Model.*, 10(3):413–438, 2006.

[67] A. Favre. Statistical equations of turbulent cases. In *Problems of hydrodynamics and continuum mechanics*, pages 231–266. SIAM, Philadelphia, PA, U.S.A., 1969.

[68] J. H. Ferziger and M. Perić. *Computational methods for fluid dynamics*. Springer, Berlin, Germany, third edition, 2002.

[69] B. Fiorina, R. Baron, O. Gicquel, D. Thevenin, S. Carpentier, and N. Darabiha. Modelling non-adiabatic partially premixed flames using flame-prolongation of ILDM. *Combust. Theory Model.*, 7(3):449–470, 2003.

[70] B. Fiorina, O. Gicquel, L. Vervisch, S. Carpentier, and N. Darabiha. Premixed turbulent combustion modeling using tabulated detailed chemistry and PDF. *Proc. Combust. Inst.*, 30(1):867–874, 2005.

[71] B. Fiorina, O. Gicquel, and D. Veynante. Turbulent flame simulation taking advantage of tabulated chemistry self-similar properties. *Proc. Combust. Inst.*, 32(2):1687–1694, 2009.

[72] R. A. Fraser, D. L. Siebers, and C. F. Edwards. Autoignition of methane and natural gas in a simulated diesel environment. *SAE*, Technical Paper No. 910227, 1991.

[73] M. Frenklach, H. Wang, C. -L. Yu, M. Goldenberg, C. T. Bowman, R. K. Hanson, D. F. Davidson, E. J. Chang, G. P. Smith, D. M. Golden, W. C. Gardiner, and V. Lissianski. http://diesel.me.berkeley.edu/~gri_mech/new21/version12/text12.html, 1995.

[74] S. Fu, B. E. Launder, and D. P. Tselepidakis. Accommodating the effects of high strain rates in modeling the pressure-strain correlation. Technical Report TFD/87/5, UMIST, 1987.

[75] J. Galpin, C. Angelberger, A. Naudin, and L. Vervisch. Large-eddy simulation of $h_2$air auto-ignition using tabulated detailed chemistry. *J. Turb.*, 9(13):1–21, 2008.

[76] F. Gao. An analytical solution for the scalar probability density function in homogeneous turbulence. *Phys. Fluids A*, 3(4):511–513, 1991.

[77] S. S. Girimaji. Assumed β-pdf model for turbulent mixing: Validation and extension to multiple scalar mixing. *Combust. Sci. Tech.*, 78(4–6):177–196, 1991.

[78] S. S. Girimaji. On the modeling of scalar diffusion in isotropic flows. *Phys. Fluids A*, 4(11):2529–2537, 1992.

[79] R. L. Gordon, A. R. Masri, S. B. Pope, and G. M. Goldin. A numerical study of autoignition in turbulent lifted flames issuing into a vitiated co-flow. *Combust. Theory Model.*, 11(3):351–376, 2007.

[80] I. R. Gran and B. F. Magnussen. A numerical study of a bluff-body stabilized diffusion flame. Part 2. Influence of combustion modeling and finite-rate chemistry. *Combust. Sci. Tech*, 119(1–6):191–217, 1996.

[81] W. L. Grosshandler. RADCAL: a narrow-band model for radiation calculations in a combustion environment. Technical Report 1402, National Institute of Standards and Technology, April 1993.

[82] R. Grout, W. K. Bushe, and C. Blair. Predicting the ignition delay of turbulent methane jet using conditional source-term estimation. *Combust. Theory Model.*, 11(6):1009–1028, 2007.

[83] C. Hasse and N. Peters. A two mixture fraction flamelet model applied to split injections in a di diesel engine. *Proc. Combust. Inst.*, 30(2):2755–2762, 2005.

[84] J. P. Hessler. Calculation of reactive cross sections and microcanonical rates from kinetic and thermochemical data. *J. Phys. Chem. A*, 102(24):4517–4526, 1998.

[85] P. G. Hill and P. Ouellette. Transient turbulent gaseous fuel jets for diesel engine. *J. Fluids Eng.*, 121(1):93–101, 1999.

[86] C. Hirsch. *Numerical computation of internal and external flows: the fundamentals of computational fluid dynamics*. Butterworth Heinemann. Elsevier, Great Britain, second edition, 2007.

[87] Z. Hong, D. F. Davidson, E. A. Barbour, and R. K. Hanson. A new shock tube study of the $H + O_2 \rightarrow OH + O$ reaction rate using tunable diode laser absorption of H_2O near 2.5 μm. *Proc. Comb. Inst.*, 33(1):309–316, 2011.

[88] J. Huang and W. K. Bushe. Experimental and kinetic study of autoignition in methane/ethane/air and methane/propane/air mixtures under engine-relevant conditions. *Combust. Flame*, 144(1):74–88, 2006.

[89] J. Huang and W. K. Bushe. Simulation of an igniting methane jet using conditional source-term estimation with a trajectory generated low-dimensional manifold. *Combust. Theory Model.*, 11(6):977–1008, 2007.

[90] J. Huang, P. G. Hill, W. K. Bushe, and S. R. Munshi. Shock-tube study of methane ignition under engine-relevant conditions: experiments and modeling. *Combust. Flame*, 136(1–2):25–42, 2004.

[91] J. Huang, P.G. Hill, W. K. Bushe, and S. R. Munshi. Shock initiated ignition in homogeneous methane-hydrogen-air mixtures at high pressure. *Int. J. Chem. Kinet.*, 38(4):221–233, 2006.

[92] M. Ihme and H. Pitsch. Prediction of extinction and reignition in nonpremixed turbulent flames using a flamelet/progress variable model 2. Application in LES of Sandia ames D and E. *Combust. Flame*, 155(1-2):90–107, 2008.

[93] J. Janicka, W. Kolbe, and W. Kollman. Closure of the transport equation for the probability density function of turbulent scalar fields. *J. Non-Equilibrium Thermodyn.*, 4(1):47–66, 1977.

[94] W. P. Jones and B. E. Launder. The prediction of laminarization with a two-equation model of turbulence. *Int. J. Heat Mass Transfer.*, 15(2):301–314, 1972.

[95] W. P. Jones and P. Musonge. Closure of the Reynolds stress and scalar flux equations. *Phys. Fluids*, 31(12):3589–3604, 1988.

[96] W. P. Jones and S. Navarro-Martinez. Large eddy simulation of autoignition with a subgrid probability density function method. *Combust. Flame*, 150(3):170–187, 2007.

[97] W. P. Jones and S. Navarro-Martinez. Numerical study of n-heptane auto-ignition using LES-PDF methods. *Flow Turb. Combust.*, 83(3):407–423, 2007.

[98] W. P. Jones and J. H. Whitelaw. Calculation methods for reacting turbulent flows: A review. *Combust. Flame*, 48:1–26, 1982.

[99] A. N. Karpetis and R. S. Barlow. Measurements of flame orientation and scalar dissipation in turbulent partially premixed methane flames. *Proc. Combust. Inst.*, 30(1):665–672, 2005.

[100] J. E. Kent. BE thesis, University of Sydney, Sydney, Australia, 2003.

[101] A. R. Kerstein. A linear eddy model of turbulent scalar transport and mixing. *Combust. Sci. Tech*, 60(4-6):391–421, 1988.

[102] A. R. Kerstein. Linear eddy modelling turbulent transport. part 3. mixing and differential molecular diffusion in round jets. *J. Fluid Mech.*, 216:411–435, 1990.

[103] A. R. Kerstein. Linear eddy modelling turbulent transport. part 4. structure of diffusion flames. *Combust. Sci. Tech*, 81(1-3):75–96, 1992.

[104] A. R. Kerstein. Linear eddy modelling turbulent transport. part 7. finite rate chemistry and multi-stream chemistry. *J. Fluid Mech.*, 240:289–313, 1992.

[105] I. S. Kim and E. Mastorakos. Simulations of turbulent lifted jet flames with two-dimensional conditional moment closure. *Combust. Flame*, 30(1):911–918, 2005.

[106] I. S. Kim and E. Mastorakos. Simulations of turbulent non-premixed counterflow flames with first-order conditional moment closure. *Flow Turb. Combust.*, 76(2):133–162, 2006.

[107] J. S. Kim and F. A. Williams. Structures of flow and mixture-fraction fields for counterflow diffusion flames with small stoichiometric mixture fractions. *SIAM J. Appl. Math.*, 53(6):1551–1566, 1993.

[108] S. -K. Kim, Y. Yu, J. Ahn, and Y. -M. Kim. Numerical investigation of the autoignition of turbulent gaseous jets in a high-pressure environment using the multiple-RIF model. *Fuel*, 83(3):375–386, 2004.

[109] S. H. Kim. On the conditional variance and covariance equations for second-order conditional moment closure. *Phys. Fluids*, 14(6):2011–2014, 2002.

[110] S. H. Kim, C. H. Choi, and K. Y. Huh. Second-order conditional moment closure modeling of a turbulent $CH_4/H_2/N_2$ jet diffusion flame. *Proc. Combust. Inst.*, 30(1):735–742, 2005.

[111] S. H. Kim and K. Y. Huh. Application of the elliptic conditional moment closure model to a two-dimensional nonpremixed methanol bluff-body flame. *Combust. Flame*, 120(1–2):75–90, 2000.

[112] S. H. Kim and K. Y. Huh. Use of the conditional moment closure model to predict NO formation in a turbulent CH_4/H_2 flame over a bluff-body. *Combust. Flame*, 130(1–2):94111, 2002.

[113] S. H. Kim and K. Y. Huh. Second-order conditional moment closure modeling of turbulent piloted jet diffusion flames. *Combust. Flame*, 138(4):336–352, 2004.

[114] S. H. Kim and K. Y. Huh. Second-order conditional moment closure modeling of turbulent piloted jet diffusion flames. *Combust. Flame*, 138(4):336–352, 2004.

[115] S. H. Kim, K. Y. Huh, and R. W. Bilger. Second-order conditional moment closure modeling of local extinction and reignition in turbulent non-premixed hydrocarbon flames. *Proc. Combust. Inst.*, 29(2):2131–2137, 2002.

[116] S. H. Kim, K. Y. Huh, and R. A. Fraser. Modeling autoignition of a turbulent methane jet by the Conditional Moment Closure model. *Proc. Combust. Inst.*, 28(1):185–191, 2000.

[117] W. T. Kim and K. Y. Huh. Numerical simulation of spray autoignition by the first order Conditional Moment Closure model. *Proc. Combust. Inst.*, 29(1):569–576, 2002.

[118] A. Yu. Klimenko. Multicomponent diffusion of various admixtures in turbulent flow. *Fluid Dyn.*, 25(3):327–334, 1990.

[119] A. Yu. Klimenko. Note on the conditional moment closure in turbulent shear flows. *Phys. Fluids*, 7(2):446–448, 1995.

[120] A. Yu. Klimenko and R. W. Bilger. Conditional moment closure for turbulent combustion. *Prog. Energy Combust. Sci.*, 25(6):595–687, 1999.

[121] B. Koren. A robust upwind discretization method for advection, diffusion and source terms. In C. B. Vreugdenhil and B. Koren, editors, *Numerical methods for advection-diffusion problems, notes on numerical fluid mechanics*, volume 45, pages 117–138. Vieweg, Braunschweig, Germany, 1993.

[122] A. Kronenburg. Double conditioning of reactive scalar transport equations in turbulent nonpremixed flames. *Phys. Fluids*, 16(7):2640–2648, 2004.

[123] A. Kronenburg and R. W. Bilger. Modeling of differential diffusion effects in nonpremixed nonreacting turbulent flow. *Phys. Fluids*, 9(5):1435–1447, 1997.

[124] A. Kronenburg and R. W. Bilger. Modelling differential diffusion in nonpremixed reacting turbulent flow: application to turbulent jet flames. *Combust. Sci. Tech.*, 166(1):175–194, 2001.

[125] A. Kronenburg and R. W. Bilger. Modelling differential diffusion in nonpremixed reacting turbulent flow: model development. *Combust. Sci. Tech.*, 166(1):195–227, 2001.

[126] A. Kronenburg, R. W. Bilger, and J. H. Kent. Second-order conditional moment closure for turbulent jet diffusion flames. *Proc. Combust. Inst.*, 27(1):1097–1104, 1998.

[127] A. Kronenburg and M. Kostka. Modeling extinction and reignition in turbulent flames. *Combust. Flame*, 143(4):342–356, 2005.

[128] A. Kronenburg and E. Mastorakos. The conditional moment closure model. In T. Echekki and E. Mastorakos, editors, *Turbulent Combustion Modeling*, volume 95 of *Fluid Mechanics and Its Applications*, pages 91–117. Springer, The Netherlands, 2011.

[129] A. Kronenburg and A. E. Papoutsakis. Conditional moment closure modeling of extinction and re-ignition in turbulent non-premixed flames. *Proc. Combust. Inst.*, 30(1):759–766, 2005.

[130] K. K. Kuo. *Principles of Combustion*. John Wiley & Sons, Inc., Hoboken, New Jersey, U.S.A., second edition, 2005.

[131] V. R. Kuznetsov and V. A. Sabel'nikov. *Turbulence and combustion.* English Edition Editor: P. A. Libby. Hemisphere Publishing Corporation, New York, U.S.A., 1990.

[132] K. N. Lakshmisha, B. Rogg, and K. N. C. Bray. PDF modelling of autoignition in nonpremixed turbulent flows. *Combust. Sci. Tech.*, 105(4–6):229–243, 1995.

[133] B. E. Launder, G. J. Reece, and W. Rodi. Progress in the developments of a reynolds-stress turbulence closure. *J. Fluid Mech.*, 68(3):537–566, 1975.

[134] C. K. Law. *Combustion physics.* Cambridge University Press, Cambridge, U.K., 2006.

[135] J. Li, Z. Zhao, A. Kazakov, and F. L. Dryer. An updated comprehensive kinetic model of hydrogen combustion. *Int. J. Chem. Kinet.*, 32(10):566–575, 2004.

[136] J. D. Li and R. W. Bilger. Measurement and prediction of the conditional variance in a turbulent reactive-scalar mixing layer. *Phys. Fluids A*, 15(12):3255–3264, 1993.

[137] F. S. Lien and M. A. Leschziner. Assessment of turbulence-transport models including non-linear RNG eddy-viscosity formulation and second-moment closure for flow over a backward-facing step. *Comput. Fluids*, 23(8):983–1004, 1994.

[138] D. O. Lignell, J. H. Chen, and H. A. Schmutz. Effects of Damköhler number on flame extinction and reignition in turbulent non-premixed flames using DNS. *Combust. Flame*, 158(5):949–963, 2011.

[139] F. C. Lockwood and A. S. Naguib. The prediction of the fluctuations in the properties of free, round-jet, turbulent, diffusion flames. *Combust. Flame*, 24:109–124, 1975.

[140] B. F. Magnussen. On the structure of turbulence and a generalized eddy dissipation concept for chemical reaction in turbulent flow. In *Nineteenth AIAA Meeting*, St. Louis, U.S.A., 1981.

[141] B. F. Magnussen and B. H. Hjertager. On mathematical modeling of turbulent combustion with special emphasis on soot formation and combustion. *Symp. (Int.) Combust.*, 16(1):719–729, 1977.

[142] C. N. Markides. *Autoignition in turbulent flows.* PhD thesis, University of Cambridge, Cambridge, U.K., 2005.

[143] C. N. Markides, G. De Paola, and E. Mastorakos. Measurements and simulations of mixing and autoignition of an n-heptane plume in a turbulent flow of heated air. *Exp. Therm. Fluid Sci.*, 31(5):393–401, 2007.

[144] B. Marracino and D. Lentini. Radiation modelling in non-luminous nonpremixed turbulent flames. *Combust. Sci. Tech.*, 128(1–6):23–48, 1997.

[145] S. M. Martin, J. C. Kramlich, G. Kosály, and J. J. Riley. The premixed conditional moment closure method applied to idealized lean premixed gas turbine combustors. *J. Eng. Gas Turbine Power*, 125(4):895–900, 2003.

[146] A. R. Masri, R. Cao, S. B. Pope, and G. M. Goldin. PDF calculations of turbulent lifted flames of H_2/N_2 fuel issuing into a vitiated co-flow. *Combust. Theory Model.*, 8(1):1–22, 2003.

[147] E. Mastorakos, T. A. Baritaud, and T. J. Poinsot. Numerical simulations of autoignition in turbulent mixing flows. *Combust. Flame*, 109(1–2):198–223, 1997.

[148] E. Mastorakos and R. W. Bilger. Second-order conditional moment closure for the autoignition of turbulent flows. *Phys. Fluids*, 10(6):1246–1248, 1998.

[149] E. Mastorakos, A. Pires da Cruz, T. A. Baritaud, and T. J. Poinsot. A model for the effects of mixing on the autoignition of turbulent flows. *Combust. Sci. Tech*, 125(1–6):243–282, 1997.

[150] P. A. McMurty, S. Menon, and A.R. Kerstein. Linear eddy modeling of turbulent combustion. *Energy Fuels*, 7(6):817–826, 1993.

[151] B. Merci, E. Dick, J. Vierendeels, and C. De Langhe. Determination of ε at inlet boundaries. *Int. J. Numer. Meth. Heat Fluid Flow*, 12(1):65–80, 2002.

[152] J. V. Michael, M. C. Su, J. W. Sutherland, J. J. Carroll, and A. F. Wagner. Rate constants for $H + O_2 + M \rightarrow HO_2 + M$ in seven bath gases. *J. Phys. Chem.*, 106(21):5297–5313, 2002.

[153] J. -B. Michel, O. Colin, and D. Veynante. Comparison of differing formulations of the pcm model by their application to the simulation of an auto-igniting H_2/air jet. *Flow Turb. Combust.*, 83(1):33–60, 2009.

[154] A. Milford and C. B. Devaud. Investigation of an inhomogeneous turbulent mixing model for conditional moment closure applied to autoignition. *Combust. Flame*, 157(8):1467–1483, 2010.

[155] A. P. Morse. *Axisymmetric free shear flows with and without swirl*. PhD thesis, University of London, U.K., 1977.

[156] M. Mortensen. Implementation of a conditional moment closure for mixing sensitive reactions. *Chem. Eng. Sci.*, 59(24):5709–5723, 2004.

[157] M. Mortensen. Consistent modeling of scalar mixing for presumed, multiple parameter probability density functions. *Phys. Fluids*, 17(1):018106, 2005.

[158] M. Mortensen, 2012. Private communication.

[159] M. Mortensen. PMFpack (Revision 11). https://launchpad.net/pmfpack, accessed May 2012.

[160] M. Mortensen and B. Andersson. Presumed mapping functions for eulerian modelling of turbulent mixing. *Flow Turb. Combust.*, 76(2):199–219, 2006.

[161] M. Mortensen and R. W. Bilger. Derivation of the conditional moment closure equations for spray combustion. *Combust. Flame*, 156(1):62–72, 2009.

[162] M. Mortensen and S. M. de Bruyn Kops. Conditional velocity statistics in the double scalar mixing layer - A mapping closure approach. *Combust. Theory Model.*, 12(5):929–941, 2008.

[163] M. Mortensen, S. M. de Bruyn Kops, and C. M. Cha. Direct numerical simulations of the double scalar mixing layer: Part II: Reactive scalars. *Combust. Flame*, 149(4):392–408, 2007.

[164] M. A. Mueller, T. J. Kim, R. A. Yetter, and F. L. Dryer. Flow reactor studies and kinetic modeling of the H_2/O_2 reaction. *Int. J. Chem. Kinet.*, 31(2):113–125, 1999.

[165] M. A. Mueller, R. A. Yetter, and F. L. Dryer. Measurement of the rate constant for $H + O_2 + M \rightarrow HO_2 + M$ ($M = N_2$, Ar) using kinetic modeling of the high-pressure $H_2/O_2/NO_x$ reaction. *Symp. (Int.) Combust.*, 27(1):177–184, 1998.

[166] J. D. Naber, D. L. Siebers, J. A. Caton, C. K. Westbrook, and S. S. Di Julio. Natural gas autoignition under diesel conditions: experiments and chemical kinetic modeling. *SAE*, Technical Paper No. 942034, 1994.

[167] S. Navarro-Martinez and A. Kronenburg. LES-CMC simulations of a turbulent bluff-body flame. *Proc. Combust. Inst.*, 31(2):1721–1728, 2007.

[168] S. Navarro-Martinez and A. Kronenburg. LES-CMC simulations of a lifted methane flame. *Proc. Combust. Inst.*, 32(1):1509–1516, 2009.

[169] S. Navarro-Martinez and A. Kronenburg. Flame stabilization mechanisms in lifted flames. *Flow Turb. Combust.*, 87(2–3):377–406, 2011.

[170] S. Navarro-Martinez, A. Kronenburg, and F. Di Mare. Conditional moment closure for large eddy simulations. *Flow Turb. Combust.*, 75(1–4):245–274, 2005.

[171] S. Navarro-Martinez and S. Rigopoulos. Large eddy simulation of a turbulent lifted flame using conditional moment closure and rate-controlled constrained equilibrium. *Flow Turb. Combust.*, 87(2–3):407–423, 2011.

[172] P. -D. Nguyen, L. Vervisch, V. Subramanian, and P. Domingo. Multidimensional flamelet-generated manifolds for partially premixed combustion. *Combust. Flame*, 157(1):43–61, 2010.

[173] M. Ó Conaire, H. J. Curran, J. M. Simmie, , W. J. Pitz, and C. K. Westbrook. A comprehensive modeling study of hydrogen oxidation. *Int. J. Chem. Kinet.*, 36(11):603–622, 2004.

[174] E. E. O'Brian and T. L. Jiang. The conditional dissipation rate of an initially binary scalar in homogeneous turbulence. *Phys. Fluids A*, 3(12):3121–3123, 1991.

[175] E. S. Oran and J. P. Boris. *Numerical simulation of reactive flow*. Elsevier Science Publishing, New York, U.S.A., second edition, 2001.

[176] S. S. Patwardhan, S. De, K. N. Lakshmisha, and B. N. Raghunandan. CMC simulations of lifted turbulent jet flame in a vitiated coflow. *Proc. Combust. Inst.*, 32(2):1705–1712, 2009.

[177] N. Peters. Laminar diffusion flamelet models in non-premixed turbulent combustion. *Prog. Energy Combust Sci.*, 10(3):319–339, 1984.

[178] N. Peters. *Turbulent Combustion*. Cambridge University Press, Cambridge, U.K., 2000.

[179] N. Peters and F. A. Williams. Lift-off characteristics of turbulent jet diffusion flames. *AIAA*, 21(3):423–429, 1983.

[180] C. D. Pierce and P. Moin. Progress-variable approach for large-eddy simulation of non-premixed turbulent combustion. *J. Fluid Mech.*, 504:73–97, 2004.

[181] R. Piessens, E. de Doncker-Kapenga, and C. W. Ueberhuber. *Quadpack: A Subroutine Package for Automatic Integration*. Springer (Springer Series in Computational Mathematics), Berlin, 1983.

[182] A. N. Pirraglia, J. V. Michael, J. W. Sutherland, and R. B. Klemm. A flash photolysis-shock tube kinetic study of the hydrogen atom reaction with oxygen: $H + O_2 \rightleftharpoons OH + O$ (962 k $\leq t \leq$ 1705 k) and $H + O_2 + Ar \rightarrow HO_2 + Ar$ (746 k $\leq t \leq$ 987 k). *J. Phys. Chem.*, 93(1):282–291, 1989.

[183] H. Pitsch, M. Chen, and N. Peters. Unsteady flamelet modeling of turbulent hydrogen-air diffusion flames. *Symp. (Int.) Combust.*, 27(1):1057–1064, 1998.

[184] H. Pitsch and N. Peters. A consistent flamelet formulation for non-premixed combustion considering differential diffusion effects. *Combust. Flame.*, 114(1–2):26–40, 1998.

[185] H. Pitsch and H. Steiner. Large-eddy simulation of a turbulent piloted methane/air diffusion flame sandia ame d. *Phys. Fluids*, 12(10):2541–2554, 2000.

[186] H. Pitsch and H. Steiner. Scalar mixing and dissipation rate in large-eddy simulations of non-premixed turbulent combustion. *Proc. Combust. Inst.*, 28(1):41–49, 2000.

[187] T. Poinsot and D. Veynante. *Theoretical and Numerical Combustion*. Edwards, Philadelphia, PA, U.S.A., second edition, 2005.

[188] S. B. Pope. The probability approach to the modelling of turbulent reacting flows. *Combust. Flame*, 27(3):299–312, 1976.

[189] S. B. Pope. An explanation of the turbulent round-jet/plane-jet anomaly. *AIAA J.*, 16(3):279–281, 1978.

[190] S. B. Pope. PDF methods for turbulent reactive flows. *Prog. Energy Combust. Sci.*, 11(2):119–192, 1985.

[191] S. B. Pope. Combustion modeling using probability density function methods. In E. S. Oran and J. P. Boris, editors, *Numerical approaches to combustion modeling*, pages 349–364. AIAA, New York, U.S.A., 1991.

[192] S. B. Pope. *Turbulent Flows*. Cambridge University Press, Cambridge, U.K., first edition, 2000.

[193] W. H. Press, S. A. Teukolsky, W. T. Vetterling, and B. P. Flannery. *Numerical recipes in Fortran 77, the art of scientific computing*. Cambridge University Press, Cambridge, Second edition, 1992.

[194] R. J. Kee and F. M. Rupley and J. A. Miller. Chemkin-II: a Fortran chemical kinetics package for the analysis of gas-phase chemical kinetics. Technical Report SAND89-8009, Sandia National Laboratories, 1989.

[195] J. Réveillon and L. Vervisch. *Accounting for spray vaporization in turbulent combustion modeling*. Proceedings of the Summer Program. Center for Turbulence Research, Stanford University, Stanford, CA, U.S.A., 1998.

[196] E. S. Richardson and E. Mastorakos. Simulations of non-premixed edge-flame propagation in turbulent non-premixed jets. In *Third European Combustion Meeting*, Chania, Crete, Greece, April 2007.

[197] C. J. F. Ridders. Accurate computation of $F'(x)$ and $F'(x)F''(x)$. *Adv. Eng. Software*, 4(2):75–76, 1982.

[198] M. R. Roomina and R. W. Bilger. Conditional moment closure modelling of turbulent methanol jet flames. *Combust. Theory Model.*, 3(4):689–708, 1999.

[199] M. R. Roomina and R. W. Bilger. Conditional moment closure (CMC) predictions of a turbulent methane-air jet flame. *Combust. Flame*, 125(3):1176–1195, 2001.

[200] M. M. Salehi, W. K. Bushe, and K. J. Daun. Application of the conditional source-term estimation model for turbulence-chemistry interactions in a premixed flame. *Combust. Theory Model.*, 16(2):301–320, 2012.

[201] J. P. H. Sanders and I. Göklap. Scalar dissipation rate modelling in variable density turbulent axisymmetric jets and diffusion flames. *Phys. Fluids*, 10(4):938–948, 1998.

[202] S. Sarkar and L. Balakrishnan. Application of a reynolds stress turbulence model to the compressible shear layer. Technical Report 91-18, ICASE, 1990.

[203] Ch. Schneider, A. Dreizler, J. Janicka, and E. P. Hassel. Flow field measurements of stable and locally extinguishing hydrocarbon-fuelled jet flames. *Combust. Flame*, 135(1-2):185–190, 2003.

[204] R. Siegel and J. Howell. *Thermal radiation heat transfer*. Taylor and Francis, New York, U.S.A., fourth edition, 2002.

[205] N. S. A. smith, R. W. Bilger, and J. -Y. Chen. Modelling of nonpremixed hydrogen jet flames using a conditional moment closure method. *Symp. (Int.) Combust.*, 24(1):263–269, 1992.

[206] N. S. A. Smith, C. M. Cha, H. Pitsch, and J. C. Oefelein. *Simulation and modeling of the behavior of conditional scalar moments in turbulent spray combustion.* Proceedings of the Summer Program. Center for Turbulence Research, Stanford University, Stanford, CA, U.S.A., 2000.

[207] C. G. Speziale and S. Sarkar. Second-order closure models for supersonic turbulent flows. Technical Report 91-1, ICASE, 1991.

[208] C. G. Speziale, S. Sarkar, and T. B. Gatski. Modelling the pressure-strain correlation of turbulence: an invariant dynamical systems approach. *J. Fluid Mech.*, 227:245–272, 1991.

[209] S. Sreedhara and K. N. Lakshmisha. Assessment of conditional moment closure models of turbulent autoignition using DNS data. *Proc. Combust. Inst.*, 29(2):2069–2077, 2002.

[210] S. Sreedhara, Y. Lee, K. Y. Huh, and D. H. Ahn. Comparison of submodels for conditional velocity and scalar dissipation in CMC simulation of piloted jet and bluff-body flames. *Combust. Flame*, 152(1-2):282–286, 2008.

[211] I. Stanković and B. Merci. Analysis of auto-ignition of heated hydrogen–air mixtures with different detailed reaction mechanisms. *Combust. Theory Model.*, 15(3):409–436, 2011.

[212] I. Stanković and B. Merci. LES-CMC simulations of turbulent hydrogen flame in a vitiated air co-flow. In *Seventh Mediterranean Combustion Symposium*, Sardinia, Italy, September 2011.

[213] G. Strang. On the construction and comparison of difference schemes. *SIAM J. Numer. Anal.*, 5(3):506–517, 1968.

[214] S. Subramaniam and S. B. Pope. A mixing model for turbulent reactive flows based on Euclidean minimum spanning trees. *Combust. Flame*, 115(4):487–514, 1998.

[215] G. D. Sullivan, J. Huang, T. X. Wang, W. K. Bushe, and S. N. Rogak. Emissions variability in gas fuel direct injection compression ignition combustion. *SAE*, Technical Paper No. 2005-01-0917, 2005.

[216] N. Swaminathan and R. W. Bilger. Assessment of combustion submodels for turbulent nonpremixed hydrocarbon flames. *Combust. Flame*, 116(4):519–545, 1999.

[217] N. Swaminathan and R. W. Bilger. Study of the conditional covariance and variance equations for second order conditional moment closure. *Phys. Fluids*, 11(9):2679–2695, 1999.

[218] N. Swaminathan and R. W. Bilger. Analyses of conditional moment closure for turbulent premixed flames. *Combust. Theory Model.*, 5(2):241–260, 2001.

[219] N. Swaminathan and R. W. Bilger. Scalar dissipation, diffusion and dilatation in turbulent H_2-air premixed flames with complex chemistry. *Combust. Theory Model.*, 5(3):429–446, 2001.

[220] N. Swaminathan and B. B. Dally. Cross stream dependence of conditional averages in elliptic region of flows behind a bluff-body. *Phys. Fluids*, 9(10):2424–2426, 1998.

[221] N. Swaminathan and S. Mahalingam. Assessment of conditional moment closure for single and multistep chemistry. *Combust. Sci. and Tech.*, 112(1):301–326, 1996.

[222] B. Thornber, R. W. Bilger, A. R. Masri, and E. R. Hawkes. An algorithm for les of premixed compressible flows using the conditional moment closure model. *J. Comp. Phys.*, 230(20):7687–7705, 2011.

[223] A. Triantafyllidis and E. Mastorakos. Large eddy simulations of forced ignition of a non-premixed bluff-body methane flame with conditional moment closure. *Combust. Flame*, 156(12):2328–2345, 2009.

[224] A. Triantafyllidis and E. Mastorakos. Implementation issues of the conditional moment closure model in large eddy simulations. *Flow Turb. Combust.*, 84(3):481–512, 2010.

[225] J. Troe. Detailed modeling of the temperature and pressure dependence of the reaction $H + O2(+M) \leftarrow HO2(+M)$. *Proc. Combust. Inst.*, 28(2):1463–1469, 2000.

[226] K. Tsai and R. O. Fox. Modeling multiple reactive scalar mixing with the generalized IEM model. *Phys. Fluids*, 7(11):2820–2830, 1995.

[227] S. Ukai, A. Kronenburg, and O. T. Stein. LES-CMC of a dilute acetone spray flame. *Proc. Combust. Inst.*, 34(1):1643–1650, 2013.

[228] L. Vanquickenborne and A. van Tiggelen. The stabilisation mechanism of lifted diffusion flames. *Combust. Flame*, 10(1):59–69, 1966.

[229] L. Vervisch, R. Hauguel, P. Domingo, and M. Rullaud. Three facets of turbulent combustion modelling: DNS of premixed V-flame, LES of lifted nonpremixed flame and RANS of jet-flame. *J. Turb.*, 5:N4, 2004.

[230] D. Veynante and L. Vervisch. Turbulent combustion modeling. *Prog. Energy Combust. Sci.*, 28(3):193–266, 2002.

[231] J. Villermaux and J. C. Devillon. Représentation de la coalescence et de la redispersion des domaines de ségrégation dans un fluide par un modèle d'interaction phénoménologique. In *Second Int. Symp. on Chemical Reaction Engineering*, New York, 1972. Elsevier.

[232] R. Viskanta and M. P. Mengüç. Radiation heat transfer in combustion systems. *Prog. Energy Combust. Sci.*, 13(2):97–160, 1987.

[233] K. Vogiatzaki, M. J. Cleary, A. Kronenburg, and J. H. Kent. Modeling of scalar mixing in turbulent jet flames by multiple mapping conditioning. *Phys. Fluids*, 21:025105, 2009.

[234] Y. P. Wan, H. Pitsch, and N. Peters. Simulation of autoignition delay and location of fuel sprays under diesel-engine relevant conditions. *SAE*, Technical Paper No 971590, 1997.

[235] H. Wang and Y. Chen. Steady flamelet modelling of a turbulent non-premixed flame considering scalar dissipation rate uctuations. *Fluid Dyn. Res.*, 37(3):133–153, 2005.

[236] M. Wang and W. K. Bushe. Conditional source-term estimation with laminar flamelet decomposition in large eddy simulation of a turbulent nonpremixed flame. *Phys. Fluids*, 19:115103, 2007.

[237] D. C. Wilcox. Reassessment of the scale determining equation for advanced turbulence models. *AIAA J.*, 26(11):1299–1310, 1988.

[238] Y. M. Wright, K. Boulouchos, G. De Paola, and E. Mastorakos. Multi-dimensional conditional moment closure modelling applied to a heavy-duty common-rail diesel engine. *SAE*, Technical Paper No. 2009-01-0717, 2009.

[239] Y. M. Wright, G. De Paola, K. Boulouchos, and E. Mastorakos. Simulations of spray autoignition and flame establishment with two-dimensional CMC. *Combust. Flame*, 143(4):402–419, 2005.

[240] N. Wu. *Autoignition and emission characteristics of gaseous fuel direct-injection compression-ignition combustion*. PhD thesis, University of British Columbia, BC, Canada, 2007.

[241] J. Xu and S. B. Pope. PDF calculations of turbulent nonpremixed flames with local extinction. *Combust. Flame*, 123(3):281–307, 2000.

[242] C. S. Yoo, R. Sankaran, and J. H. Chen. Three-dimensional direct numerical simulation of a turbulent lifted hydrogen jet flame in heated coflow: flame stabilization and structure. *J. Fluid Mech.*, 640:453–481, 2009.

[243] M. Zakyani and C. Lacor. LES-CMC simulations for piloted non-premixed flames. *AIP Conference Proceedings*, 1190(1):90–97, 2009.

[244] V. Zimont, W. Polifke, M. Bettelini, and W. Weisenstein. An efficient computational model for premixed turbulent combustion at high reynolds numbers based on a turbulent flame speed closure. *J. Eng. Gas Turb. Power*, 120(3):526–532, 1998.